The Response of the Atmospheric Convective Boundary Layer to Surface Inhomogeneities

by Mark Gregory Hadfield

Colorado State University

DEPARTMENT OF ATMOSPHERIC SCIENCE

PAPER NO.
433

THE RESPONSE OF THE ATMOSPHERIC CONVECTIVE BOUNDARY LAYER TO SURFACE INHOMOGENEITIES

by
Mark Gregory Hadfield
Department of Atmospheric Science
Colorado State University
Fort Collins, CO 80523

Research Supported by

The Electric Power Research Institute
under Project #1630-53

and by

The U.S. Army Research Office
under Project #DAAL03-86-K-0175

and by

The National Science Foundation
under Grant #ATM-8616662

Atmospheric Science Paper No. 433

ABSTRACT

THE RESPONSE OF THE ATMOSPHERIC CONVECTIVE BOUNDARY LAYER TO SURFACE INHOMOGENEITIES

Large-eddy simulations (LES) of the atmospheric convective boundary layer have been conducted with a surface sensible heat flux that either is constant or varies on a spatial scale comparable to the boundary layer depth.

The horizontally homogeneous simulations have been compared with previous LES, laboratory and atmospheric studies. The dynamics of the simulated turbulence and the model's sensitivity to the subgrid diffusivity have been investigated. In general the present model gives results similar to previous large-eddy simulations. All the LES models simulate a field of convective eddies having approximately the correct velocity and spatial scales, and with the crucial property that kinetic energy is transported vigorously upwards through the middle levels. Several failings of the models have been identified, including a tendency to underpredict temperature variance and to overpredict vertical velocity skewness in the upper boundary layer.

The surface heat-flux variations are one-dimensional and sinusoidal with a wavelength between one and four times the boundary layer depth. Simulations have been carried out with zero wind or with a light mean wind perpendicular to the perturbations. Several effects have been identified, though some are evident only after a great deal of averaging. They include mean circulations in phase with the surface perturbations, modulation of the turbulence throughout the boundary layer and modifications (usually slight) to the profiles of horizontally averaged statistics. The mean boundary layer depth remains horizontally uniform. Most of the effects increase as the wavelength of the surface perturbation is increased and decrease with an imposed mean wind.

The processes maintaining the mean temperature field and the mean circulation have been analysed. A time scale for kinetic energy transfer from the circulation to the turbulence has been defined and found to be surprisingly short in some cases. The turbulent stress budgets have also been examined: the effects of turbulent buoyancy fluctuations and of interactions between the circulation and the turbulence have been distinguished.

Elevated-plume dispersion has been studied using a Lagrangian particle model. Circulations driven by the surface heat-flux perturbations affect the ground level concentration.

ACKNOWLEDGEMENTS

I would like to thank my advisors, Prof. Roger Pielke and Prof. William Cotton, for their guidance throughout my program of study and for their support of this research. Thanks also to the other members, past and present, of my committee: Prof. Thomas McKee, Prof. Richard Johnson and Dr. Douglas Fox.

The students and staff at the Department of Atmospheric Science have been a valuable source of ideas and advice. Dr. Gregory Tripoli was largely responsible for developing the numerical model that I have used and Dr. Chaing Chen adapted it to large-eddy simulation. Ms. Judy Sorbie has drafted many of the figures in this dissertation.

I have benefitted from discussions with Dr. Chin-Hoh Moeng, Dr. John Wyngaard and others at the National Center for Atmospheric Research.

I cannot overstate my gratitude to my wife, Sally, for her companionship and encouragement. Each of my children, Kate, Jennifer and Rachel, has assisted in her own way.

The New Zealand Meteorological Service (Director, Mr. John Hickman) has shown remarkable trust and generosity by supporting my family and me throughout the last four years at Colorado State University.

Substantial support for the research was provided by the Electric Power Research Institute (1630-53), the U.S. Army Research Office (DAAL03-86-K-0175) and the National Science Foundation (ATM-8616662). Computations were performed at the National Center for Atmospheric Research, which is sponsored by the National Science Foundation.

Table of Contents

List of Tables

List of Figures

Chapter 1

Introduction

In the limit of high surface sensible-heat flux, light winds and little cloud cover, the atmospheric boundary layer tends to assume a relatively simple form, called the convective boundary layer, with an inversion capping a strongly turbulent, well-mixed layer. To a large extent the behaviour of such a boundary layer can be predicted in terms of a few scaling parameters, based on the boundary layer depth and the surface heat flux. Numerical and laboratory models of the convective boundary layer, both pioneered by Deardorff and his co-workers (Deardorff, 1974a,b; Deardorff and Willis, 1985), have simulated its behaviour in considerable detail and have been largely confirmed by atmospheric observations (Caughey, 1982).

The numerical model used by Deardorff would now be called a large-eddy simulation (LES) model, i.e., a three-dimensional, non-hydrostatic model with grid spacing sufficiently small to resolve the larger boundary layer eddies and a subgrid closure scheme that parameterises the smaller ones. It is noteworthy that this model has been able to predict phenomena that had not been anticipated. For example, Lamb's (1978) simulations of an elevated plume in the LES fields showed that the plume centreline descends immediately after release. This surprising result was confirmed in the laboratory (Willis and Deardorff, 1978) and several years later in the atmosphere (Moninger *et al.*, 1983).

The LES and laboratory models have used a homogeneous surface, and in most observational studies an effort has been made to select a site where this condition is satisfied, at least approximately. However on land the surface sensible heat flux can vary a great deal owing to variations in land use. Segal *et al.* (1988a), reviewing a number of other studies, report mesoscale differences in near-surface air temperature between areas of irrigated vegetation and bare soil of a few degrees Celsius, with the vegetated surface being cooler than the bare soil, and differences in surface radiometric temperature in excess of 10°C. They estimate that over vegetated areas more than 70% of the typical net radiation is converted to latent heat flux and less than 30% to sensible heat flux, whereas over dry, bare soil the latent heat flux is much lower and the sensible heat flux much higher. On a smaller scale, air-borne radiometric observations in the vicinity of the Boulder Atmospheric Observatory (BAO) during July have shown the surface temperature varying from less than 28°C to more than 52°C on scales of a few kilometres (Schneider, 1987, personal communication); similar observations at the site of Boundary Layer Experiment–1983 (BLX83) in Oklahoma give a standard deviation in surface temperature of 2.5°C and peak-to-peak fluctuations of more than 10°C (Hechtel and Stull, 1985; Hechtel, 1988a). Businger and Frisch (1972) report surface radiometric temperatures as low as 30°C in irrigated fields or ponds in Kansas, versus 50°C in the surrounding land; they find the sensible heat flux reversed over the cooler surfaces at a height of 30 m, but not at 100 m.

This dissertation addresses the question of how the convective boundary layer is affected by modest variations in surface sensible heat flux on a scale comparable to the boundary layer depth. Two different aspects of the question are considered:

1. Is there a consistent tendency for variations in the boundary layer to be associated with the pattern of surface variation? One expects, for example, that over a region of enhanced surface heat flux the air temperature near the surface will be higher than elsewhere, but one wonders whether this temperature perturbation extends to higher levels and to what extent the associated buoyancy perturbation drives vertical motion. Such an effect might be significant in the dispersion of pollutants from point sources. One also expects that, near the surface, turbulence will be strongest immediately over a heat-flux maximum and one would like to know if this effect can be seen throughout the depth of the boundary layer.

2. Do the surface variations change profiles of turbulence statistics? For example, it seems reasonable that near-surface variations in air temperature will contribute directly to a higher temperature variance, relative to the horizontal average. One can also speculate that surface forcing on the preferred scale of the convective eddies might in some sense increase the efficiency with which the eddies transport heat and kinetic energy vertically.

The questions will be expressed more exactly in later chapters once appropriate averaging operators have been defined.

With regard to the first question above, it is well known that thermal contrasts between *extended* areas can drive circulations, sometimes quite vigorous, such as the land-sea breeze (Defant, 1951). Less well-known are circulations driven by vegetation contrasts (Segal *et al.*, 1988a,b) and by urban-rural contrasts (Ackerman, 1974a,b). These circulations are typically accompanied by modulation of the boundary-layer turbulence (Raynor *et al.*, 1979; Hildebrand and Ackerman, 1984). However it is not clear what effect *smaller-scale* thermal contrasts have on the convective boundary layer. Abe and Yoshida (1982) have simulated sea-breeze circulations induced by peninsulas between 8 km and 150 km wide with zero geostrophic wind. They find that the maximum vertical velocity is $0.25\,\mathrm{m\,s^{-1}}$ and it occurs when the peninsula width is about 30 km; with a width of 8 km the maximum vertical velocity is only $0.02\,\mathrm{m\,s^{-1}}$. This result suggests that surface thermal contrasts on scales of a few kilometres cannot drive circulations with significant mean vertical velocities. On the other hand, the experience of glider pilots (Wallington, 1961; Scorer, 1978) indicates that surface features (fields, forests, hills, small towns) with horizontal dimensions of a kilometre or less can be preferred sources for convective boundary layer updraughts; it remains to be seen whether such an effect will be manifested as a mean circulation.

With regard to the second question, several studies of the convective boundary layer over moderately inhomogeneous surfaces have failed to find any significant effects of the inhomogeneity. Young (1986, 1988a) has compared turbulence statistics gathered in the vicinity of the BAO with comparable statistics from studies in a variety of other locations. The BAO is surrounded by rolling terrain, with height variations of the order of 100 m, and has a major mountain range a few tens of kilometres to the west; as mentioned above, large spatial variations in surface temperature have been observed there during the summer. Nevertheless the normalised turbulence statistics are not consistently different from those of the other studies. Kaimal *et al.* (1982) have measured turbulence spectra at the same site and found no significant difference from flat, uniform sites. Jochum (1988) has measured turbulence statistics over hilly terrain (maximum height variation 100 m) in South Germany and found only minor differences from measurements over flat, uniform terrain. Hechtel (1988a,b) has simulated a convective boundary layer over a heterogeneous surface with an irregular, two-dimensional pattern of variations in heat and moisture fluxes characteristic of the BLX83 site. She finds no consistent differences from a similar simulation over a homogeneous surface.

For the present investigation the primary tool is an LES version of the RAMS time-split, compressible model (Tripoli and Cotton, 1982). The surface perturbations are of plausible magnitude but idealised geometry. The emphasis is on building basic understanding, which can then aid in planning and interpreting atmospheric observations. One can justify using an LES model in such a way because such a model does seem to describe much of the basic structure of a convective boundary layer with little *a priori* input of assumptions about the turbulence. It is certainly not suggested that the model is infallible—verification is discussed in Chapter 7

Simplicity in the simulations is desirable for two reasons. First, it makes it easier to formulate averaging operators to separate the phenomena of interest from the chaos of the boundary layer eddies. This advantage is particularly relevant in answering the first of the questions posed above. Second, it reduces the number of conceivable explanations for any phenomenon that is observed. Therefore, only a simple surface configuration is considered, namely a one-dimensional sinusoidal perturbation in heat flux with wavelength between one and four times the boundary layer depth. Furthermore the variation of the surface fluxes with time is kept as simple as possible. (No attempt is made to simulate a diurnal cycle, for example). In a typical numerical experiment a quasi-steady convective boundary layer is produced over a homogeneous surface, then the perturbation is imposed suddenly. The transient behaviour is sometimes interesting, but the main focus is on the steady state that is assumed to exist when the transients have died down. (The extent to which this assumption is confirmed will be examined critically.)

Chapter 2 introduces a number of averaging operators used in formulating and analysing the model. The model equations are then described and several aspects of the analysis are discussed, including the definition of scaling parameters relevant to the convective boundary layer. Further details of the analysis are considered in Appendix A.

Chapter 3 deals for the most part with a single simulation of a convective boundary layer over a homogeneous, heated surface. It is found that the present model gives similar results to previous large-eddy models, and that the large-eddy models generally are successful insofar as they simulate a field of convective updraughts and downdraughts of approximately the right scale, with the crucial property that kinetic energy is transported vigorously upwards.

Chapter 4 describes a series of simulations over surfaces with spatial variations in the sensible heat flux, with and without a light mean wind. The results are described with reference to the questions posed above, and a number of effects of the surface variations are identified. These effects are found to be sensitive both to the scale of the surface perturbations and to the wind speed. In Chapter 5 the same simulations are analysed in dynamical terms. (The distinction between the material covered in Chapters 4 and 5 is somewhat arbitrary.) Simplifying concepts are identified where possible.

In Chapter 6 the concentration field resulting from elevated releases of a non-buoyant pollutant is simulated using a Lagrangian particle model driven by the LES fields. The major finding is that dispersion is affected by the surface heat-flux perturbations: mean circulations driven by the surface variations can increase or decrease ground-level concentrations according to the position of the source.

Chapter 7 summarises the principal conclusions of the dissertation and includes recommendations for further work.

CHAPTER 2

AVERAGING AND MODEL FORMULATION

2.1 Averaging

The following sections describe the averages that will be used in describing and analysing the model. Because of the number of these averages it is necessary to develop a flexible notation; the one used here is adapted from Reiter (1969).

Consider a general variable a and a general averaging operator $\langle\,\rangle_r$. The result when $\langle\,\rangle_r$ operates on a is written $\langle a\rangle_r$ and the deviation is $(a)_r$, i.e.,

$$a = \langle a\rangle_r + (a)_r\,. \tag{2.1}$$

Repeated averaging is indicated by repeated subscripts:

$$\langle a\rangle_{r,s} \stackrel{\text{def}}{=} \langle\langle a\rangle_r\rangle_s. \tag{2.2}$$

There are several desirable properties for the averages. One would like them to satisfy the Reynolds postulates,

$$\begin{aligned} \langle (a)_r\rangle_r &= 0 & \qquad \langle a+b\rangle_r &= \langle a\rangle_r + \langle b\rangle_r \\ \langle \langle a\rangle_r (b)_r\rangle_r &= 0 & \qquad \langle a\rangle_{r,r} &= \langle a\rangle_r\,, \end{aligned} \tag{2.3}$$

from which it follows that

$$\langle ab\rangle_r = \langle a\rangle_r\langle b\rangle_r + \langle (a)_r(b)_r\rangle_r. \tag{2.4}$$

Furthermore one would like the averages to be commutative with differentiation, and with each other:

$$\begin{gathered} \frac{\partial}{\partial t}\langle a\rangle_r = \left\langle\frac{\partial a}{\partial t}\right\rangle_r \qquad \frac{\partial}{\partial x_i}\langle a\rangle_r = \left\langle\frac{\partial a}{\partial x_i}\right\rangle_r \\ \langle a\rangle_{r,s} = \langle a\rangle_{s,r}\,. \end{gathered} \tag{2.5}$$

2.1.1 *The grid average*

There is a lower limit to the scale of turbulent fluctuations that can be resolved on a grid, so each turbulent field $\tilde{a}$ is divided into a resolved component $\langle\tilde{a}\rangle_g$ and an unresolved, or subgrid, component $(\tilde{a})_g$. For brevity the resolved component is also indicated by *omitting* the tilde, i.e., $\langle\tilde{a}\rangle_g \equiv a$. (This notation is a little unconventional, but convenient when one is usually describing the resolved variables.) The resolved variables are assumed to be *defined* continuously, but *evaluated* in the model only at discrete intervals in time and space.

The grid-averaged value of a stress $\tilde{u}_i\tilde{u}_j$ can be decomposed as

$$\begin{aligned}\langle\tilde{u}_i\tilde{u}_j\rangle_g &= \langle\tilde{u}_i\rangle_g\langle\tilde{u}_j\rangle_g + \langle(\tilde{u}_i)_g(\tilde{u}_j)_g\rangle_g \\ &\quad + \left[\langle\langle\tilde{u}_i\rangle_g\langle\tilde{u}_j\rangle_g\rangle_g - \langle\tilde{u}_i\rangle_g\langle\tilde{u}_j\rangle_g\right] + \langle\langle\tilde{u}_i\rangle_g(\tilde{u}_j)_g\rangle_g + \langle(\tilde{u}_i)_g\langle\tilde{u}_j\rangle_g\rangle_g .\end{aligned} \tag{2.6}$$

(A similar decomposition applies to the temperature flux $\tilde{u}_j\tilde{\theta}$ or to any other second moment.) The first term on the right-hand side is the one that the model's centered-difference advection scheme calculates, although in doing so it introduces errors that arise in large part because of contradictory assumptions about whether the grid-point values represent samples or spatial averages of the resolved fields. The second term on the right-hand side is the usual "Reynolds stress." The remaining terms would be zero if the grid average were to obey the Reynolds postulates, but in general it does not. The term enclosed in square brackets has been called the "Leonard stress" after Leonard (1974): it can be evaluated explicitly *if* the form of the grid average is known. In pseudospectral models a Gaussian filter has commonly been assumed (e.g., Moeng, 1984), but the present study follows Mason and Callen (1986) in considering $\langle\,\rangle_g$ as a low-pass spatial filter—the exact form of which is not known—effectively determined by the subgrid closure. The sum of *all terms but the first* on the right-hand side of Equation 2.6 is parameterised according to Deardorff's (1980) scheme as described in Section 2.2.2.

To simplify notation the following second-order quantities are defined:

$$\phi_i \stackrel{\text{def}}{=} \langle\tilde{u}_i\tilde{\theta}\rangle_g - u_i\theta \tag{2.7}$$

$$\tau_{ij} \stackrel{\text{def}}{=} \langle \tilde{u}_i \tilde{u}_j \rangle_g - u_i u_j \tag{2.8}$$

$$e \stackrel{\text{def}}{=} \tau_{ii}/2 \tag{2.9}$$

where ϕ_i is the subgrid flux in potential temperature, τ_{ij} is the subgrid stress, and e is the subgrid kinetic energy. (In accordance with the usual convention, summation over i is implied by the repeated subscripts in the expression for e.)

2.1.2 *The horizontal and phase averages*

In a horizontally homogeneous simulation all points at the same height are equivalent, so it is logical to analyse the model fields in term of the horizontal average, which is written $\langle\,\rangle_h$ and defined

$$\langle a \rangle_h (z,t) \stackrel{\text{def}}{=} \frac{\int_{Y_1}^{Y_2} \int_{X_1}^{X_2} a(x,y,z,t)\, dx\, dy}{(X_2 - X_1)(Y_2 - Y_1)}, \tag{2.10}$$

where X_1, X_2, Y_1 and Y_2 are the positions of the lateral boundaries of the model domain. It is simply an average over all points at the same height z.

Chapter 4 and subsequent chapters examine how a convective boundary layer responds to forcing by one-dimensional surface heat-flux perturbations with wavelength λ_p in the x direction. A new horizontal coordinate $\hat{x}$ can be defined,

$$\hat{x} \stackrel{\text{def}}{=} \left[x - x_p + \frac{\lambda_p}{2} \right]_{\operatorname{mod} \lambda_p} - \frac{\lambda_p}{2}, \tag{2.11}$$

where x_p is a reference point in the surface perturbation, namely, the position of a heat flux maximum. In other words, $\hat{x}$ is the phase relative to the surface perturbation and takes values in the interval $[-\lambda_p/2, +\lambda_p/2]$. For a simulation in which there are n wavelengths λ_p within the domain, there are n values of the x coordinate with the same $\hat{x}$: let these be called $x_1, x_2, \ldots x_n$. The phase average[1] $\langle\,\rangle_p$ is defined as

$$\langle a \rangle_p (\hat{x},z,t) \stackrel{\text{def}}{=} \frac{1}{n} \sum_{k=1}^{n} \frac{\int_{Y_1}^{Y_2} a(x_k,y,z,t)\, dy}{(Y_2 - Y_1)}. \tag{2.12}$$

[1]The phase average is named after a similar average in the time domain introduced by Hussain and Reynolds (1970).

It is an average over all points with the same $\hat{x}$ and z.

Listed below are several properties of the horizontal average $\langle\,\rangle_h$ and the phase average $\langle\,\rangle_p$:

$$\begin{aligned} \frac{\partial}{\partial x}\langle a\rangle_h &= 0 & \qquad \frac{\partial}{\partial y}\langle a\rangle_h &= 0 \\ \frac{\partial}{\partial y}\langle a\rangle_p &= 0 & \qquad \langle a\rangle_{p,h} &= \langle a\rangle_h \ . \end{aligned} \tag{2.13}$$

2.1.3 *Averaging over several model realisations*

An ensemble of model realisations can be defined as an infinite set of simulations with identical initial and boundary conditions, except that the field of initial temperature perturbations (see Section 2.2.3) in each realisation is generated from a different set of random numbers. In the present case the dimensionality of the ensemble average is determined by the surface heat flux: for a variable $a(x, y, z, t)$ the ensemble average is a function of z and t when the surface is homogeneous, then becomes a function of $\hat{x}$ also when the perturbation is introduced. It should be emphasised that this ensemble average does evolve with time, although one expects it to evolve more smoothly than an average over a single realisation.

One cannot simulate an infinite number of realisations, but the estimates of the ensemble average state of the system can be improved by combining the results from several simulations. This technique will be used extensively.

2.1.4 *The time average*

The time average is labelled $\langle\,\rangle_t$. Different definitions are discussed in Appendix A, and the one adopted is shown to satisfy the Reynolds postulates and the commutativity properties (Equations 2.3 and 2.5). There are at least two reasons for looking at time-averaged statistics. The first is that when the ensemble average is stationary, or nearly so, averaging a small number of realisations over time may improve the estimate of that ensemble average. The second reason arises during the discussion in Appendix A: the time average allows one to relate a simulation with well-defined and possibly unrealistic initial conditions (e.g., a heat flux perturbation applied suddenly) to the sort of heterogeneous ensemble that can be constructed in the atmosphere.

2.2 The model

The model is the time-split, compressible model which has been described in the literature by Tripoli and Cotton (1982). The model equations used in the present LES application are described below.

2.2.1 *Equations of motion*

The grid-averaged prognostic equation for velocity is

$$\begin{aligned}\frac{\partial u_i}{\partial t} + \theta_0 \frac{\partial}{\partial x_i}(\pi - \pi_0) &= + \delta_{i3}\frac{g}{\theta_0}(\theta - \theta_0) - u_j \frac{\partial u_i}{\partial x_j} \\ &\quad - \frac{1}{\rho_0}\frac{\partial}{\partial x_j}(\rho_0 \tau_{ij}) - \alpha_R (u_i - u_{i0}),\end{aligned} \tag{2.14}$$

where the terms on the right-hand side represent tendencies[2] due to buoyancy, advection, and subgrid stresses, as well as a fictitious damping process (Rayleigh friction) introduced near the upper boundary. The Coriolis force is neglected. The symbols are described in the Glossary. A zero subscript indicates the "base state" value of a variable. The base state is horizontally homogeneous; in general it is constant with time and equal to the initial state of the model, but the base state *velocity* sometimes changes during the simulation as described in Section 4.3.

The pressure-gradient force has been written on the left-hand side of Equation 2.14 to illustrate the way the equation is solved using the time-split scheme. The "slow" forces on the right-hand side are evaluated on a long time step Δt_l, subject to linear stability criteria for internal gravity waves, advection and diffusion. The equation is then integrated on a small time step Δt_s, subject to linear stability criteria for sound waves, along with a prognostic equation for pressure,

$$\frac{\partial \pi}{\partial t} + \frac{c_s^2}{\rho_0 \theta_0^2}\frac{\partial}{\partial x_j}(\rho_0 \theta_0 u_j) = 0. \tag{2.15}$$

---

[2]Tendencies in the velocity equation will be described, somewhat loosely, as forces. They have the dimensions of acceleration.

Following Drogemeier (1985) the speed of sound c_s is reduced below its atmospheric value of $\sim 330\,\mathrm{m\,s^{-1}}$ in order to allow a larger Δt_s. The simulations reported in Chapters 3 and 4 use $c_s \approx 60\,\mathrm{m\,s^{-1}}$, with $\Delta t_s = 1\,\mathrm{s}$ and $\Delta t_l = 10\,\mathrm{s}$, and require 60% of real time on a Cray X-MP CPU. This is a fivefold increase in computational speed relative to a simulation with $c_s = 330\,\mathrm{m\,s^{-1}}$. It makes it practicable to run the model several times to accumulate statistics and this capability has turned out to be crucial for the current work. The computational saving is gained at very little expense in model accuracy. As c_s is reduced there is a slight increase—at most a few percent—in the magnitude of pressure fluctuations (but see further discussion in Section A.4). Otherwise, model fields are unaffected.

In the thermodynamic equation, radiation and moist processes are ignored and the equation for θ is

$$\frac{\partial \theta}{\partial t} \quad = \quad -u_j\frac{\partial \theta}{\partial x_j} - \frac{1}{\rho_0}\frac{\partial}{\partial x_j}(\rho_0\phi_j) - \alpha_R(\theta - \theta_0), \tag{2.16}$$

with tendencies due to advection, the subgrid flux and Rayleigh friction.

As long as the maximum phase velocities of the model fields remain small relative to c_s, the acoustic pressure computation forces the velocity field to satisfy approximately the following condition:

$$\frac{\partial}{\partial x_j}(\rho_0\theta_0 u_j) = 0. \tag{2.17}$$

The left-hand side of this equation can be rewritten as

$$\frac{1}{\rho_0\theta_0}\frac{\partial}{\partial x_j}(\rho_0\theta_0 u_j) = \frac{\partial u_j}{\partial x_j} + u_j\left(H_\rho^{-1} + H_\theta^{-1}\right) \tag{2.18}$$

where

$$H_\rho \stackrel{\text{def}}{=} \frac{\rho_0}{\partial\rho_0/\partial z} \quad \text{and} \quad H_\theta \stackrel{\text{def}}{=} \frac{\theta_0}{\partial\theta_0/\partial z}$$

are scale heights for ρ_0 and θ_0. For a typical large-eddy simulation, H_ρ is about 10 km and H_θ is at least 40 km, whereas a typical boundary layer depth is 1 km. The variation in θ_0 can therefore be ignored, in which case Equation 2.17 reduces to the anelastic continuity equation,

$$\frac{\partial}{\partial x_j}(\rho_0 u_j) = 0. \tag{2.19}$$

The advective tendency in a variable a can then be written in flux-divergence form:

$$- u_j \frac{\partial a}{\partial x_j} = -\frac{1}{\rho_0} \frac{\partial}{\partial x_j} (\rho_0 u_j a). \tag{2.20}$$

If one assumes the anelastic continuity equation (Equation 2.19) and takes the divergence of ρ_0 times the prognostic equation for velocity (Equation 2.14), one derives a diagnostic equation for pressure,

$$\rho_0 \theta_0 \nabla_a^2 (\pi - \pi_0) = + \frac{\partial}{\partial z} \left(\rho_0 g \frac{\theta - \theta_0}{\theta_0} \right) - \frac{\partial^2}{\partial x_i \partial x_j} (\rho_0 u_i u_j) - \frac{\partial^2}{\partial x_i \partial x_j} (\rho_0 \tau_{ij}), \tag{2.21}$$

where the Rayleigh friction term has been neglected and summation is implied over i and j. The symbol ∇_a^2 stands for a differential operator,

$$\nabla_a^2 \stackrel{\text{def}}{=} \frac{\partial^2}{\partial x_i^2} + \left(H_\rho^{-1} + H_\theta^{-1} \right) \frac{\partial}{\partial z}, \tag{2.22}$$

that reduces to a Laplacian when $H_\rho, H_\theta \to \infty$. Equation 2.21 is not used to evaluate the pressure during model integration, but it has been used during analysis and gives good agreement with the model pressure field (see Section A.4). It also allows decomposition of the pressure field into components induced by each of the forces on the right-hand side of Equation 2.14.[3] The components will be labelled the buoyancy pressure π_b, the advection pressure π_a and the subgrid pressure π_s. (The last is not to be confused with the subgrid pressure fluctuation $(\tilde{\pi})_g$.) This decomposition will be shown to be a valuable aid to understanding. In later chapters various further decompositions of the advection pressure will be introduced.

The velocity equation (Equation 2.14) can be rewritten, ignoring Rayleigh friction, as

$$\begin{aligned} \frac{\partial u_i}{\partial t} = & + \left(\delta_{i3} \frac{g}{\theta_0} (\theta - \theta_0) - \theta_0 \frac{\partial \pi_b}{\partial x_i} \right) + \left(-u_j \frac{\partial u_i}{\partial x_j} - \theta_0 \frac{\partial \pi_a}{\partial x_i} \right) \\ & + \left(-\frac{1}{\rho_0} \frac{\partial}{\partial x_j} (\rho_0 \tau_{ij}) - \theta_0 \frac{\partial \pi_s}{\partial x_i} \right), \end{aligned} \tag{2.23}$$

[3] A similar decomposition has long been used in the turbulence literature (Wyngaard, 1980) and has recently been applied to analysing large-eddy simulations of the convective boundary layer (Moeng and Wyngaard, 1986b).

where each force on the right-hand side of Equation 2.14 has been paired with the pressure-gradient that balances its divergence. The sum of each pair is therefore the non-divergent part of the force, or the "non-divergent force."

In the simulations reported here, subsidence has been imposed to maintain the boundary layer depth approximately constant. The mass that enters through the top boundary is *not* removed through the lateral boundaries (because that would complicate the formulation of the cyclic boundary conditions) so the velocity field is forced to be convergent. It is found that the model then maintains $\partial(\rho_0 u_j)/\partial x_j$ constant (but non-zero) over the domain so the velocity can be split into two parts:

$$u_i = \delta_{i3} \langle w \rangle_h + (u_i - \delta_{i3} \langle w \rangle_h). \tag{2.24}$$

The first part varies more or less linearly with height and the second satisfies the anelastic balance. The effects of advection by $\langle w \rangle_h$ have been examined thoroughly; its only significant effect is its intended one, namely warming the stable region above the boundary layer.

2.2.2 *The subgrid parameterisation*

Subgrid quantities have been estimated using the scheme of Deardorff (1980), in which the grid-averaged subgrid fluxes are diagnosed via down-gradient diffusion relationships:

$$\begin{aligned} \phi_i &= K_h \frac{\partial \theta}{\partial x_i} && (2.25) \\ \tau_{ij} - \frac{2}{3}\delta_{ij} e &= K_m \left(\frac{\partial u_i}{\partial x_j} + \frac{\partial u_j}{\partial x_i} \right). && (2.26) \end{aligned}$$

The eddy diffusivities, K_h and K_m, are estimated as functions of the subgrid kinetic energy e for which the following prognostic equation is solved,

$$\frac{\partial e}{\partial t} = \frac{g}{\theta_0}\phi_3 - \tau_{ij}\frac{\partial u_i}{\partial x_j} - u_j \frac{\partial e}{\partial x_j} + \frac{1}{\rho_0}\frac{\partial}{\partial x_j}\left(\rho_0 2 K_m \frac{\partial e}{\partial x_j}\right) - C_e e^{3/2}/l. \tag{2.27}$$

In writing this equation the approximation has been made, among others, that $\langle \rangle_g$ satisfies the Reynolds postulates. The tendencies on the right-hand side are due to buoyancy production, shear-stress production, advection, subgrid transport and molecular dissipation. The subgrid length scale l appearing in the dissipation term is set equal to a grid-length scale l_g when $\partial\theta/\partial z \leq 0$, and to the minimum of l_g and a stability-dependent length scale l_s when $\partial\theta/\partial z > 0$. The expressions for l_g and l_s are

$$l_g = C_g(\Delta x \Delta y \Delta z)^{\frac{1}{3}} \qquad l_s = 0.76\, e^{\frac{1}{2}} \left(\frac{g}{\theta_0}\frac{\partial\theta}{\partial z}\right)^{-\frac{1}{2}}. \tag{2.28}$$

Deardorff assumed $C_g \equiv 1$, but in the present study the sensitivity of the model to C_g has been investigated (Section 3.4) and a value of $C_g = 1.5$ has been adopted for most simulations. The dissipation constant C_e is

$$C_e = 0.19 + 0.51\, l/l_g, \tag{2.29}$$

except at the lowest level, where it is increased by a wall factor of 3.9. The subgrid diffusion coefficients are given by

$$K_m = C_K\, l\, e^{\frac{1}{2}} \qquad K_h = K_m(1 + 2l/l_g) \tag{2.30}$$

where $C_K = 0.1$.

At most points within the boundary layer $l = l_g$, so the dissipation constant C_e and the ratio K_h/K_m assume their neutral values of $C_e = 0.7$ and $K_h/K_m = 3$. The neutral value of C_e was established by Deardorff (1973) in a series of numerical turbulence experiments, in which C_e was adjusted to give the expected value for the critical Richardson number. It is close to the value of 0.93 that Lilly (1967) estimated by relating the unresolved energy in a truncated, inertial-subrange spectrum to the dissipation rate. The ratio K_h/K_m was determined empirically by Deardorff (1972) who found that "... K_h had to be nearly three times larger than K_m before the simulated transfer of scalar variance to subgrid scales could keep up with its directly calculated rate of cascade..." (quotation from Deardorff, 1973).

2.2.3 *Grid resolution, boundary conditions, initial conditions*

The large-eddy simulations described in later chapters all share several common features as follows: The grid has $36 \times 36 \times 39$ points covering a $4500\,\mathrm{m} \times 4500\,\mathrm{m} \times 2340\,\mathrm{m}$

domain at a resolution of $125\,\mathrm{m} \times 125\,\mathrm{m} \times 60\,\mathrm{m}$. Cyclic boundary conditions are used in the x and y directions, which means that each point in the model is indistinguishable from any other point at the same level, at least until horizontal variations are introduced into the initial conditions or the surface forcing. The momentum flux at the lower boundary is diagnosed with the Businger *et al.* (1971) surface layer profile formulas, whereas the potential temperature flux Φ is prescribed. The upper boundary is a rigid wall, with an absorbing layer occupying the twelve grid levels immediately below. Within this layer the Rayleigh friction relaxation coefficient α_R increases linearly with height from zero at the base to $(200\,\mathrm{s})^{-1}$at the top.

The initial stratification is weakly stable ($\partial\theta_0/\partial z = 0.8\,\mathrm{K\,km^{-1}}$) up to $z = 1200\,\mathrm{m}$ and strongly stable ($\partial\theta_0/\partial z = 7.4\,\mathrm{K\,km^{-1}}$) above. At $t = 0\,\mathrm{min}$ the heat flux is turned on, and convective eddies near the surface are initiated by small random perturbations in θ at the lowest grid level. The convective eddies grow rapidly through the weakly stable layer, then more slowly when the strongly stable layer is reached. Subsidence is imposed at the top boundary to keep the boundary layer depth approximately constant. (The justification for imposing the subsidence is twofold: it eliminates any explanations of model phenomena that are based on evolution in the boundary layer depth, and it makes it possible to deal with long-period time averages without the complication of "smearing" in the vertical fine structure near the capping inversion.) The subsidence velocity is initially $-0.090\,\mathrm{m\,s^{-1}}$, and it is reduced to $-0.065\,\mathrm{m\,s^{-1}}$ after 100 minutes.

The aim of the simulations is to produce a quasi-stationary daytime boundary layer with minimum computational expense; no attempt is made to simulate the gradual increase of surface heat flux around sunrise, or the break-up of the nocturnal inversion.

2.3 Scaling parameters

Turbulence acts to warm the convective boundary layer, but to cool the capping inversion above, so it is reasonable to define the boundary layer depth h_* as the level where the turbulent tendency in θ crosses zero, i.e., where

$$\frac{\partial}{\partial t}\langle\theta\rangle_{h,t} + \langle w\rangle_{h,t}\,\frac{\partial}{\partial z}\langle\theta\rangle_{h,t} = 0, \tag{2.31}$$

or equivalently where the vertical heat flux $\langle w'\theta' + \phi_3 \rangle_{h,t}$ has a minimum. (The definition has been written in terms of time-averaged statistics, but it can also be expressed in terms of instantaneous statistics.) The mixed layer scales (Deardorff, 1970) for velocity, potential temperature, pressure and Exner pressure are then respectively

$$\begin{aligned} w_* &= \left(g \langle \Phi \rangle_h h_* / \theta_{0S}\right)^{\frac{1}{3}} & \qquad \theta_* &= \langle \Phi \rangle_h / w_* \\ p_* &= \rho_{0S} w_*^2 & \qquad \pi_* &= w_*^2 / \theta_{0S} \ , \end{aligned} \tag{2.32}$$

where θ_{0S} and ρ_{0S} are the surface values of the base state potential temperature and density. In a weakly sheared, horizontally homogeneous convective boundary layer many turbulent statistics scale with the mixed layer parameters (Caughey, 1982).

When perturbations in heat flux or terrain height are imposed at the lower boundary layer, additional scales are introduced. For the one-dimensional, sinusoidal, heat-flux perturbations considered here, one of these is the wavelength λ_p of the perturbation and another is the mean velocity in the boundary layer perpendicular to the axes of the perturbations. (A wind *parallel* to the perturbations should have very little effect unless it is strong enough for shear to organize the flow.) This mean velocity is approximately equal to the base state x-component velocity u_0. An appropriate way of making the new scales dimensionless is to form the ratios λ_p/h_* and $(u_0 h_*)/(\lambda_p w_*)$. The former is self-explanatory; the latter is the ratio between the "eddy turnover time" h_*/w_* and the time λ_p/u_0 required for advection at velocity u_0 through distance λ_p.

With an inhomogeneous lower surface the boundary layer depth may vary with $\hat{x}$. In view of the way h_* has been defined in Equation 2.31, a logical definition of the local boundary layer depth (let us call this h) is the height where

$$\frac{\partial}{\partial t}\langle \theta \rangle_{p,t} + \langle w \rangle_{h,t} \frac{\partial}{\partial z}\langle \theta \rangle_{p,t} = 0. \tag{2.33}$$

In principle one could calculate mixed layer scales based on the local boundary layer depth and fluxes, but it is simpler to have them constant in space and based on horizontally averaged quantities. In making this choice one is certainly not assuming that the turbulent statistics still obey the scaling relations for a horizontally homogeneous boundary layer.

Finally, a minor complication must be introduced into the mixed-layer scaling because of the variation of base state density ρ_0 with height. For consistency with the model's governing equations, vertical integrals are weighted by $\rho_0(z)$. The density-weighted integral over the depth of the domain is written $\int_Z$ and is defined as

$$\int_Z a \stackrel{\text{def}}{=} \frac{1}{\rho_{0s}} \int_0^Z \rho_0 a \, dz. \tag{2.34}$$

Consider a variable that scales as $a \sim f(h_*, w_*, \theta_*, \pi_*)$ within the boundary layer and is small above it. The density-weighted vertical integral of this variable then scales as

$$\int_Z a \sim h_{\rho *} \times f(h_*, w_*, \theta_*, \pi_*)$$

where $h_{\rho *}$ is the *density-weighted* depth of the boundary layer, defined as

$$h_{\rho *} \stackrel{\text{def}}{=} \frac{1}{\rho_{0s}} \int_0^{h_*} \rho_0 \, dz. \tag{2.35}$$

(It is assumed here that $h_{\rho *}/h_* \approx 1$, i.e., that the boundary layer is not very deep. In a deep boundary layer $h_{\rho *}/h_*$ would enter the scaling as an extra parameter in a more complicated way.)

Chapter 3

The Horizontally Homogeneous Boundary Layer

The following chapter deals for the most part with a single simulation of a convective boundary layer over a homogeneous surface. The simulation is described in Section 3.1 and its evolution is briefly discussed. In Section 3.2 various profiles of time-averaged statistics are presented and compared with the results of other large-eddy models, and with laboratory and observational data. The results also serve as a basis for comparison in later chapters. The dynamics of the model are investigated in Section 3.3, with reference to the budgets of turbulence kinetic energy, heat flux and temperature variance, and with brief reference to the third moment budgets. Particular attention is paid to the role of pressure-gradient forces. Some comparisons with other studies will be made here, too. In Section 3.4 the sensitivity of the model to a change in its subgrid length scale is examined. Finally in Section 3.5 aspects of the model's description of a real convective boundary layer are discussed briefly.

3.1 The simulation

The simulation is labelled "Run A" and was set up as described in Section 2.2.3. The surface potential temperature flux Φ was constant at $0.2\,\mathrm{K\,m\,s^{-1}}$ (equivalent to a sensible heat flux of $250\,\mathrm{W\,m^{-2}}$ at sea level), which is typical of a dry land surface under strong insolation. The initial horizontal velocities, u_0 and v_0, were zero.

For the first 30 minutes after initialisation the boundary layer grows rapidly through the weakly stable layer below 1200 m, then it grows very slowly in approximate balance with the imposed subsidence. For the first 200 minutes there is a steady increase in the temperature contrast across the capping inversion, which leads to a reduction in the rate of entrainment of mass into the boundary layer, such that the entrainment heat flux remains approximately constant at -0.2 times the surface heat flux. The boundary layer height reaches a maximum of 1220 m at 200 minutes then decreases steadily to 1090 m by 500 minutes, when the simulation is terminated.

The evolution of the velocity variances is shown in Figure 3.1. The variances are expressed as vertical integrals, made dimensionless with $w_*^2 h_{\rho *}$. The vertical velocity variance reaches a dimensionless integral value of 0.30 by $t = 40$ min and thereafter fluctuates within $\pm 20\%$ of that value. The horizontal velocity variances take much longer to develop, and never do become particularly steady. Their evolution during Run A can be described as a steady increase until 100 minutes, followed by a slower increase to a maximum around 350 minutes and a slight decrease thereafter, but other similar simulations do not follow exactly the same pattern. Willis and Deardorff's (1974) early laboratory model results show that the horizontal velocity variance tends to increase with an reduction in the entrainment rate, so one can probably relate the increase observed in the first 200 minutes of the present simulation to the increase in the temperature contrast across the capping inversion. Much of the later variation seems to be random.

An interesting aspect of this and other simulations is that the horizontal average velocities, $\langle u \rangle_h$ and $\langle v \rangle_h$, fluctuate through $\sim \pm 0.1 w_*$ in such a way that the vertically-integrated momentum remains approximately zero. The velocity fluctuations are associated with fluctuations in the corresponding momentum fluxes of up to $\pm 0.05 w_*^2$, which typically extend throughout the depth of the boundary layer and last for one or two convective time scales h_*/w_*. Since the physical situation being modelled is symmetrical in the x and y directions, the *ensemble average* horizontal velocities and momentum fluxes must be exactly zero, and on this basis it might seem that the fluctuations are unphysical. However in each individual simulation the symmetry is broken by the random temperature perturbations that initiate convection. This asymmetry causes the simulation to develop asymmetrical circulations, and therefore non-zero *horizontal average* horizontal velocities and fluxes.

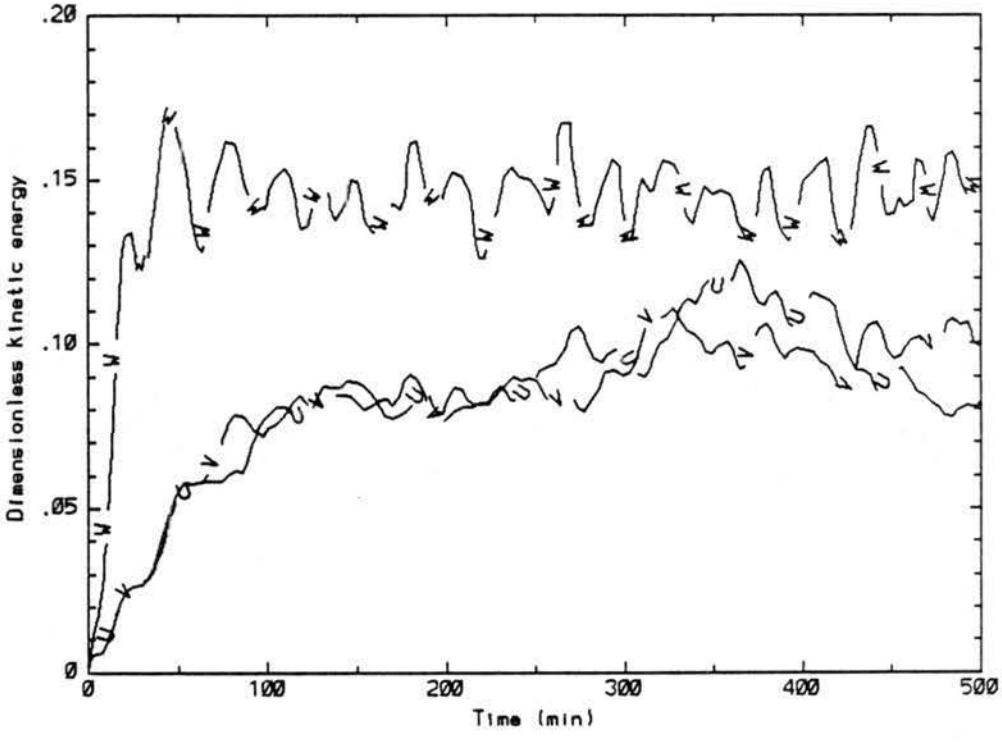

Figure 3.1. Evolution of the velocity variances in Run A. The curves show one-half the vertical integrals of the resolved velocity variances, made dimensionless with $w_*^2 h_{\rho *}$, for the u (—U—), v (—V—) and w (—W—) velocity components.

If the model were horizontally infinite, one would expect the horizontal averages to approach the ensemble averages. The problem of estimating ensemble average momentum fluxes with a LES model of finite area is similar to the problem of estimating them from observations over a finite area in the atmosphere, discussed by Wyngaard (1983). The present simulation implies that for a domain with sides $\sim 4h_*$ long the maximum deviation between the instantaneous, horizontal average momentum fluxes and the ensemble average values will be of the order of $0.05w_*^2$, and that time averaging over several periods of h_*/w_* will reduce this deviation somewhat.

For some perspective on the form of the eddies that contribute to the statistics discussed below, Figure 3.2 shows horizontal cross-sections of the vertical velocity and potential temperature perturbations at two levels in Run A. At the lower level ($z = 290\,\mathrm{m} = 0.25\mathrm{h}_*$) the updraughts are organised in intersecting ribbon-like structures—presumably vertical sheets in three dimensions—occupying somewhat less than half of the horizontal area. The regions with positive temperature perturbations correspond closely to the regions with positive vertical velocity perturbations, and the most-positive θ' is substantially larger in magnitude than the most-negative θ'. Several aspects of the statistics to be discussed below are already evident, namely the high positive correlation coefficient between w and θ, and the skewed probability density functions, indicated by positive third moments in w and θ. At the upper level ($z = 880\,\mathrm{m} = 0.75\mathrm{h}_*$) the updraughts are rounder and relatively isolated, but generally they are located above the updraughts at the lower level. There is no obvious correspondence at this level between the w and θ perturbations.

3.2 Comparison of time-averaged statistics with data from other studies

Deardorff's (1974a,b) pioneering large-eddy simulations of a convective boundary layer produced a wealth of data and helped provide a framework for a number of atmospheric and laboratory studies. Various points of agreement and disagreement between the large-eddy simulations and observations have been mentioned in the literature since

(a)

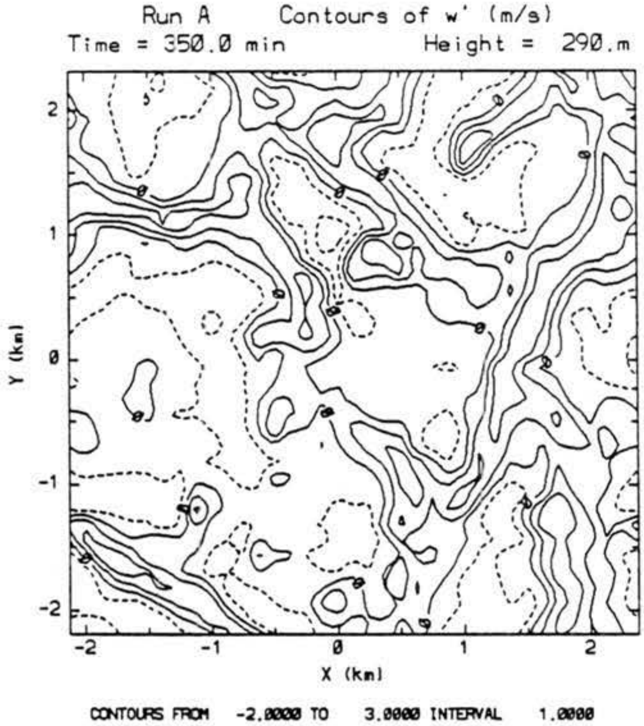

(b)

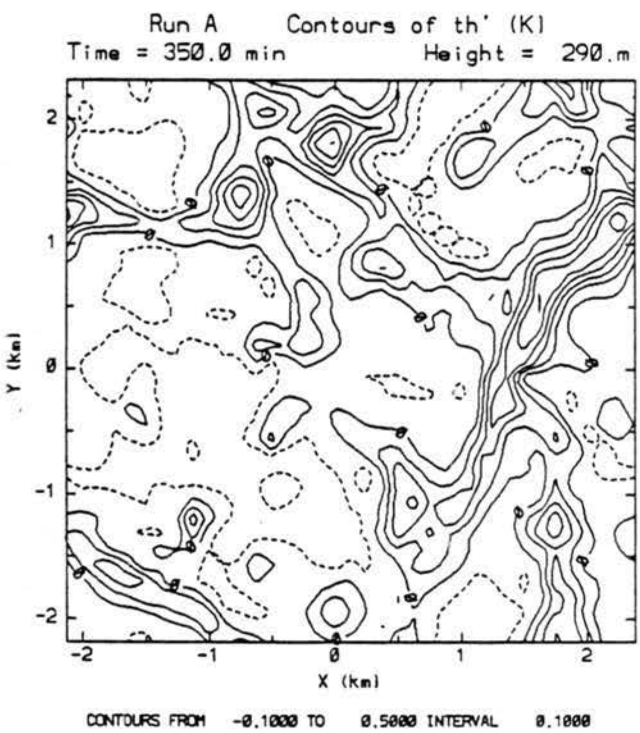

Figure 3.2. Cross-sections of w' and θ' at $t = 350$ min from Run A. (a) w' at $z = 0.25h_*$. (b) θ' at $z = 0.25h_*$. (c) w' at $z = 0.75h_*$. (d) θ' at $z = 0.75h_*$. The contour interval is $1.0\,\mathrm{m\,s^{-1}}$ for w' and 0.1 K for θ'.

Continued on following page.

(c)

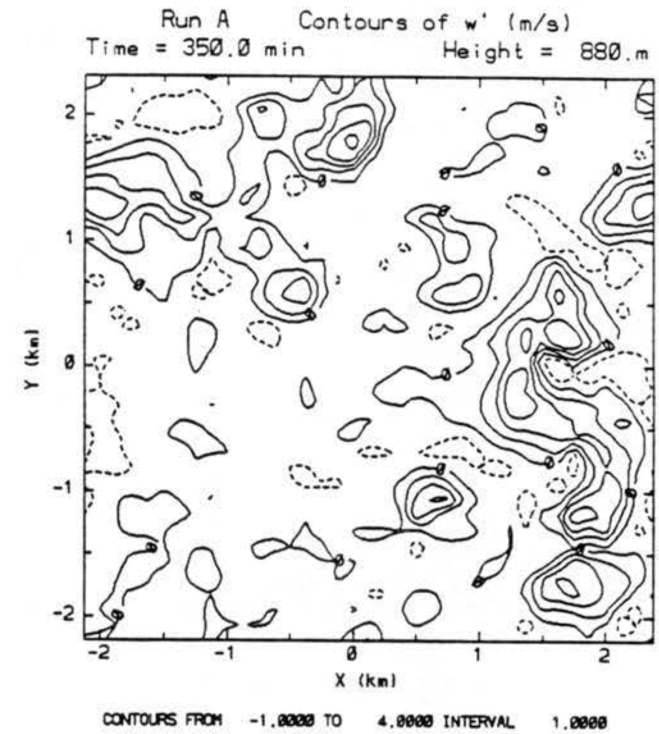

(d)

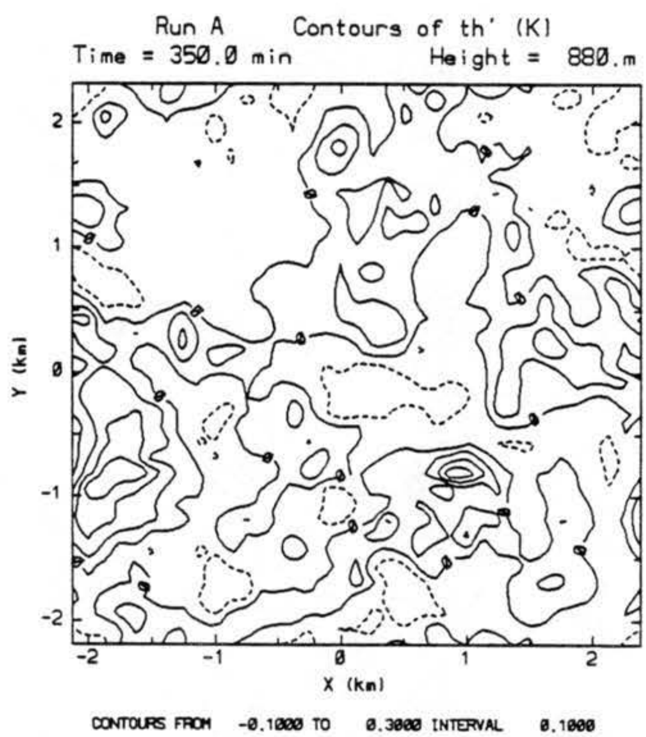

Figure 3.2 (continued).

then—and some points of disagreement have not received the attention they deserve—but there has been no comprehensive comparison based on up-to-date observations. A number of statistics from the present simulation will be presented below and compared with results from obtained from large-eddy simulation, laboratory and atmospheric studies.

Among the other large-eddy simulations are Deardorff's work and a series of more recent papers by Moeng and her co-workers, including Moeng (1984), Moeng and Wyngaard (1984), Moeng and Wyngaard (1986a), Moeng and Wyngaard (1986b) and Carruthers and Moeng (1987). Deardorff's model uses finite-differencing in all directions and a subgrid scheme which differs from the later Deardorff (1980) scheme in two important respects: first, prognostic equations are carried for *all* the relevant second-order subgrid moments and second, the subgrid length scale is held constant with height rather than being reduced in stable regions. Moeng's model is pseudospectral in the horizontal and finite-difference in the vertical and uses the Deardorff (1980) subgrid scheme. In addition, however, it employs an explicit calculation of the Leonard stress (the term enclosed in square brackets in Equation 2.6), which also extracts energy from the resolved scales.

As mentioned in Section 2.2, the present model uses finite-differencing in all directions with no explicit calculation of the Leonard stress—like Deardorff's—and the simpler Deardorff (1980) subgrid scheme—like Moeng's. One feature which distinguishes the present model from both Deardorff's and Moeng's is that it solves the acoustic equation prognostically, whereas they diagnose the pressure from the anelastic continuity equation. The success of the anelastic pressure diagnosis in the model analysis suggests that this is not a significant difference, however. In summary, then, there are a number of differences in detail between the three models. All have a similar domain size and grid spacing.

The laboratory study that will serve as the primary basis for comparison is Deardorff and Willis (1985). Compared to the earlier study of Willis and Deardorff (1974), convection in this study was less constrained by the lateral boundaries and the results agree better with atmospheric data.

There have been a large number of observational studies of the atmospheric convective boundary layer. Some of them have been carried out under conditions where mixed layer scaling should clearly be applicable, while others have been subject to various disturbing influences (baroclinicity, cloud cover, terrain variations). Caughey (1982) has written a good summary of the observed structure of the atmospheric convective boundary layer and Young (1986, 1988a) has presented comparisons of statistics from different studies. Among the data that will be used for comparison with the models are the analyses of the Minnesota and Ashchurch experiments by Caughey and Palmer (1979) and Caughey (1982), the analysis of the AMTEX experiments by Lenschow *et al.* (1980), the Phoenix 78 analyses of Young (1986, 1988a,b) and some measurements reported by Druilhet *et al.* (1983).

A number of time-averaged statistics will be examined below, with the averaging period being from 300 to 400 minutes.[4] There is little need for such a long averaging period in calculating the statistics that will be examined in the present chapter, but it is convenient to use the same period as is used for examining surface-forced circulations in Chapters 4 and 5, and there it is desirable to average over long times. The boundary layer scaling parameters based on the time-averaged statistics are summarised in table 3.1. Note that, between $t = 300\,\mathrm{min}$ and $t = 400\,\mathrm{min}$, h_* decreases by 50 m, or 4%, so time averaging will introduce slight smoothing of vertical fine structure near the inversion.

A Reynolds number based on the subgrid diffusivity can be defined as follows (Moeng and Wyngaard, 1988)

$$Re = \frac{w_* h_*}{C_K \mathcal{L} \mathcal{E}^{1/2}} \tag{3.1}$$

where $\mathcal{E}$ is a typical subgrid kinetic energy within the boundary layer (taken here to be $1/h_*$ times the vertical integral of e), $\mathcal{L}$ is a typical subgrid length scale (taken to be the grid length scale l_g), and C_K is the constant in the equation for K_m (Equation 2.30). For the present simulation $\mathcal{E} = 0.11 w_*^2$ and $\mathcal{L} = 147\,\mathrm{m} = 0.125\mathrm{h}_*$, so a typical subgrid diffusivity for momentum is $C_K \mathcal{L} \mathcal{E}^{1/2} = 10\,\mathrm{m^2\,s^{-1}}$, giving $Re = 240$.

---

[4]For the remainder of this chapter the t subscript, indicating time averaging, will be omitted from the notation for compactness.

Table 3.1. Boundary layer scaling parameters based on statistics of Run A averaged from 300 to 400 minutes. The symbols are all listed in the Glossary, and most have been described in Section 2.3.

Parameter	Value
h_*	$1171\,\mathrm{m}$
w_*	$2.00\,\mathrm{m\,s^{-1}}$
θ_*	$0.100\,\mathrm{K}$
p_*	$5.1\,\mathrm{Pa}$
h_*/w_*	$585\,\mathrm{s}$
$-L/h_*$	$\sim 10^{-5}$
z_0/h_*	$\sim 10^{-5}$
w_s	$-0.014w_*$
$\partial h_*/\partial t$	$-0.004w_*$
$w_e = (\partial h_*/\partial t) - w_s$	$0.010w_*$

3.2.1 *The potential temperature profile*

The potential temperature gradient is dynamically significant because it enters the budgets for quantities like heat flux and temperature variance: Figure 3.3 shows its profile. A log-linear transformation, $y=(x/|x|)\ln(1+|x|/x_0)$, is used on the horizontal axis, with x_0 chosen to suit the data. This transformation will be employed as appropriate in later figures. The model domain extends up to $2.0h_*$, but profiles are plotted only up to $1.4h_*$, which is just below the base of the absorbing layer. The short, dashed vertical line in the figure indicates the temperature gradient in the absorbing layer, and this is approximately the gradient that would be produced by subsidence alone. The maximum in stability near $1.4h_*$ and the minimum near $1.25h_*$ result from circulations which are evident in the profiles of vertical velocity variance and heat flux. It will be concluded in Section 3.3.3 that these circulations are numerical artefacts, resulting from a combination of truncation errors plus inadequate diffusion.

Also plotted in Figure 3.3 is an estimate of the potential temperature gradient based on the "bottom-up" and "top-down" scalar diffusion expressions of Wyngaard and Brost (1984) and Moeng and Wyngard (1984), namely

$$\frac{h_*}{\theta_*}\frac{\partial\langle\theta\rangle_h}{\partial z} = -0.4(z/h_*)^{-\frac{3}{2}} + R\times 0.7(1-z/h_*)^{-2}. \tag{3.2}$$

These expressions were based on large-eddy simulations with two different models, and the bottom-up gradient (the first term on the right-hand side) has circumstantial support from surface layer measurements in the Kansas experiments (Businger *et al.*, 1971). The ratio R between the surface flux and the entrainment flux has been given a value of -0.2. Near the surface agreement is very good (although it will be shown in Section 3.4 that the gradient in this region is sensitive to the subgrid parameterisation). The profile calculated from Equation 3.2 crosses zero at a higher level than the present results, however, and has gradients weaker by a factor of two or more in the upper boundary layer.

The average potential temperature gradient in the interior of the atmospheric boundary layer is very small: in the present simulation, for example, the mixed-layer scale for

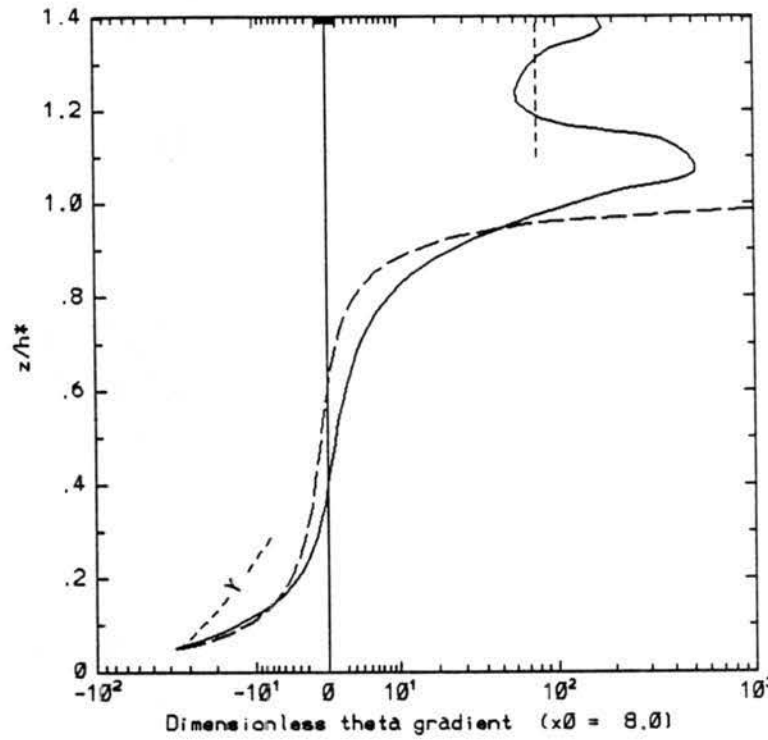

Figure 3.3. Profile of the dimensionless potential temperature gradient in Run A (solid line) compared with Equation 3.2 (long dashes) and the profile of Young (1986) (--Y--). The short vertical dashed line indicates the gradient that would be produced by subsidence.

this gradient, θ_*/h_*, is only $0.08\,\mathrm{K\,km^{-1}}$. Measuring it therefore presents instrumental and statistical problems. Lenschow *et al.* (1985) have presented results from aircraft and tower soundings in the upper boundary layer that "tentatively indicate that the measured top-down scalar gradient may be two to four times greater than that predicted by large-eddy simulation [of Wyngaard and his co-workers]." This supports the present model, although the uncertainties in the measurements are large. For the lower boundary layer, Young (1986) has published a potential temperature gradient profile based on measurements made on the 300 m tower at the Boulder Atmospheric Observatory (BAO) during the Phoenix 78 experiment (Hooke, 1979). This profile is also shown in Figure 3.3. It agrees with the LES data at $z=0.05h_*$, (which is approximately the lowest level where $\partial \langle\theta\rangle_h /\partial z$ is computed in the model) but gives gradients two to three times as large between $z = 0.1h_*$ and $z = 0.3h_*$. There is reason to suspect, however, that the BAO profiles may not be representative of the surrounding area, because substantial variations in surface temperature have been observed in the vicinity (Schneider, 1987, personal communication) and because there may be interaction between local topography and the prevailing mesoscale flow (Young, 1987, personal communication). So, given the uncertainties in the observational data, the present model's potential temperature profile seems plausible.

3.2.2 *Velocity variances*

The profile of the simulated vertical velocity variance is shown in Figure 3.4, both with and without a subgrid contribution. The subgrid variance is estimated by dividing the subgrid kinetic energy equally amongst the three velocity components. (Note that Deardorff (1973, 1974b), who estimated the subgrid variances individually, found them nearly equal.) Figure 3.5 summarises comparable profiles from a number of LES, fluid tank and atmospheric studies. The data from all the different sources are in reasonably good agreement: in all cases the variance has a maximum of about $0.4w_*^2$ near the middle of the boundary layer and drops to about $0.1w_*^2$ at $z=h_*$.

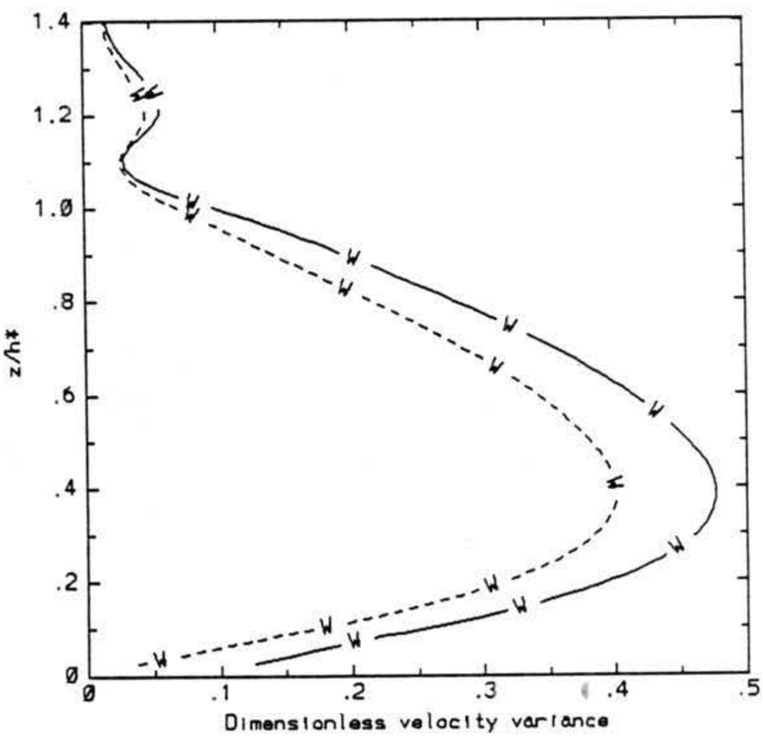

Figure 3.4. Profile of the dimensionless vertical velocity variance for Run A. The dashed curve shows the resolved part only and the solid curve includes a subgrid contribution.

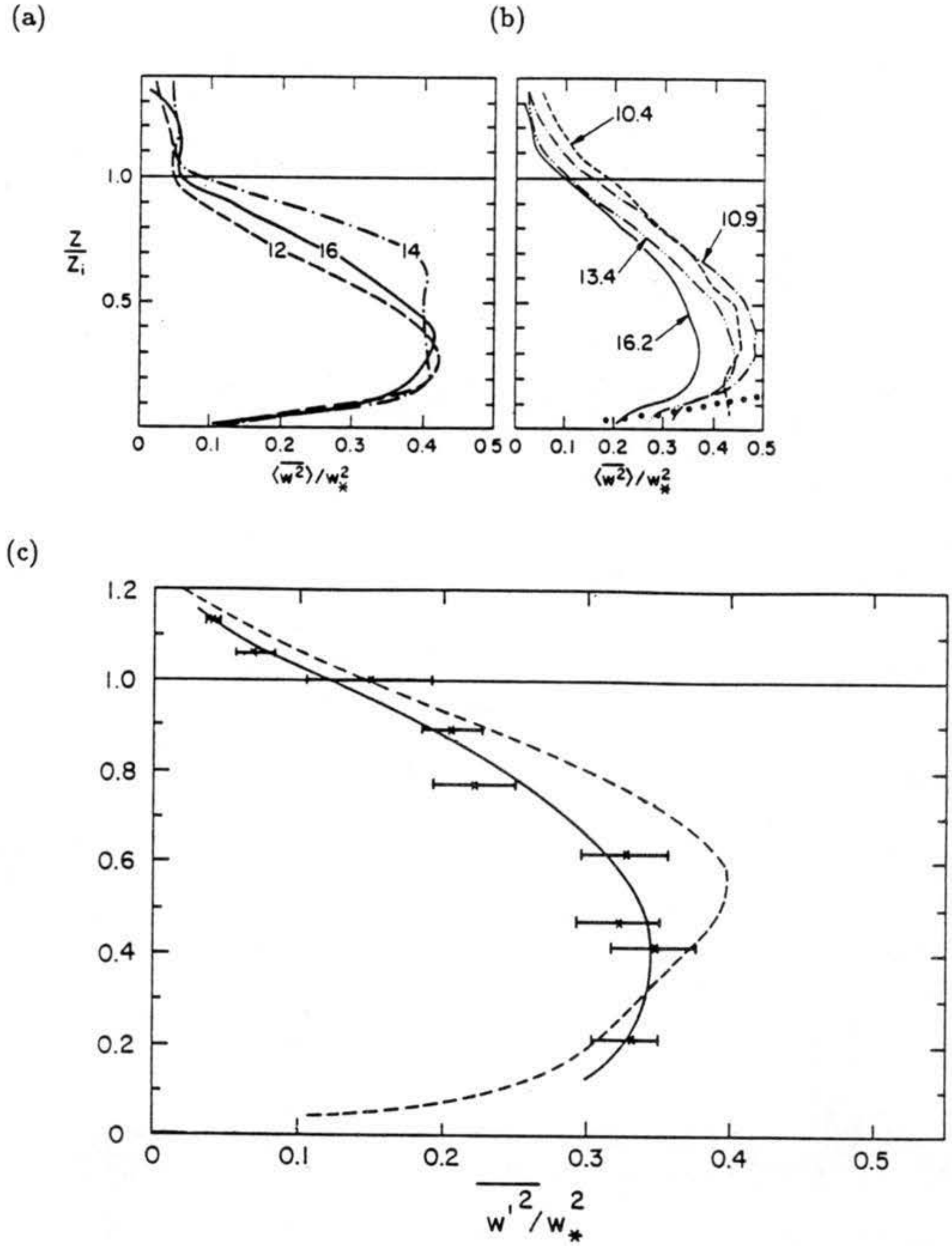

Figure 3.5. Vertical velocity variance profiles from other studies. (a) LES results from Moeng (1984), with a subgrid contribution. (b) LES results from Deardorff (1974b), without a subgrid contribution. (c) Fluid-tank model results from Deardorff and Willis (1985) (solid line and error bars) with atmospheric measurements from the Minnesota and Ashchurch experiments (Caughey, 1982) (dashed line). (d) Atmospheric measurements from several sources summarised by Young (1986).

Continued on following page.

(d)

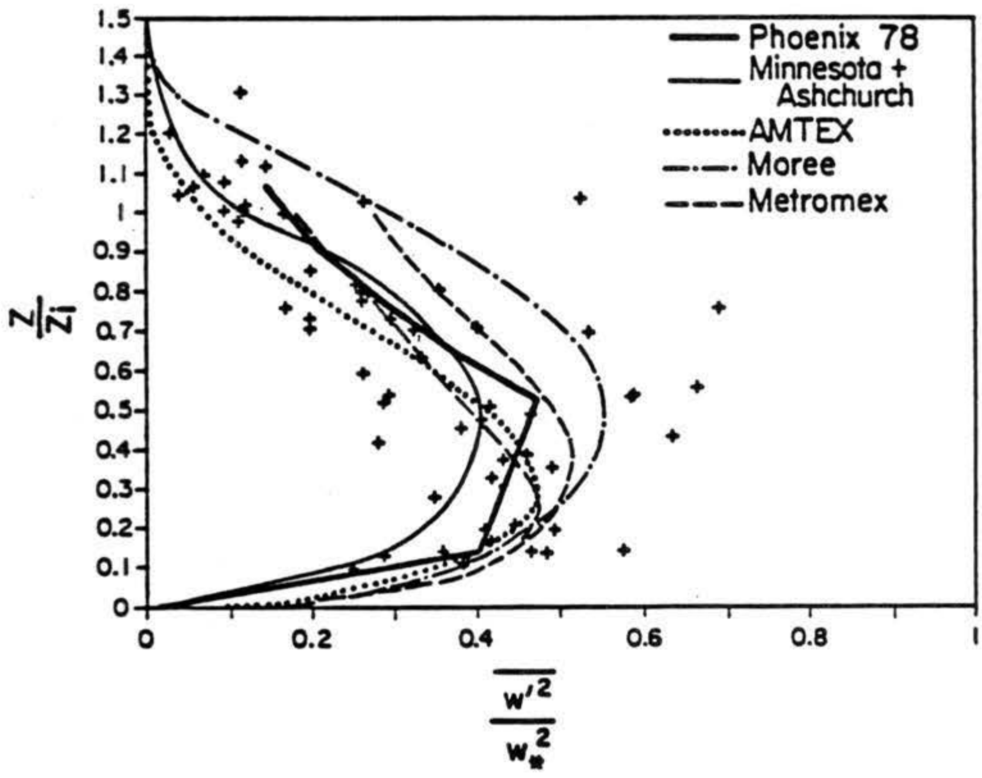

Figure 3.5 (continued).

The simulated horizontal velocity variances are shown in Figure 3.6 and can be compared with profiles from previous studies in Figure 3.7. The fluid tank and atmospheric data are rather scattered, but all are consistent with the magnitude of the variances being around $0.3w_*^2$ in the middle of the boundary layer, and all have weak maxima near the surface and in the vicinity of $z=h_*$. The LES models underestimate the variance at mid-levels and have a pronounced low-level maximum, which is not so prominent in the fluid tank or atmospheric data. Among the LES results, Moeng's (1984) model shows more variance at all levels than Deardorff's (1974b) and the present model is somewhere in between. (In making this comparison note that Deardorff includes a subgrid contribution, whereas Moeng does not.)

With regard to the low-level maximum in horizontal velocity variance that is apparent in the LES models, Moeng (1988, personal communication) has remarked that this maximum is "*very* sensitive" (her emphasis) to the surface roughness length z_0, and that the maximum can vanish if the roughness length is made sufficiently large. A brief sensitivity experiment was performed with the present model, where z_0 was increased from 0.01 m to 1.0 m. The former is typical of level grassland, and it is the value used in the present study and by Deardorff (1974a,b), whereas the latter is typical of forests and large towns (Panofsky and Dutton, 1984). With the larger roughness length, there was a modest (16%) reduction in the horizontal velocity variance near the surface and the low-level maximum remained evident. It appears that the low-level maximum in horizontal velocity variance is an unrealistic and reasonably robust feature of the LES models.

Finally, note that in Run A the variance in the u component is greater than in the v component in the upper boundary layer. Presumably this difference reflects the geometry of outflow from the large eddies. In other simulations, and at other times in the present simulation, the difference is absent or reversed in sign.

3.2.3 *Temperature variance*

Figure 3.8 shows the profile of the resolved potential temperature variance $\langle\theta'^2\rangle_h$ along with data from LES, fluid tank and atmospheric studies. A maximum between

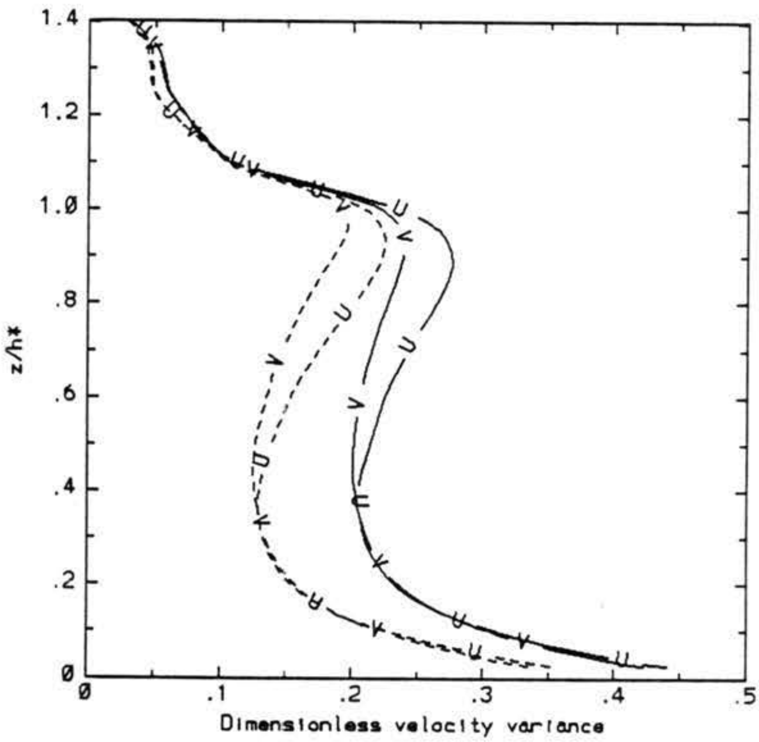

Figure 3.6. Profiles of the dimensionless horizontal velocity variances for Run A. The curves are labelled U for the u component and V for the v component; the dashed curves show the resolved part only and the solid curves include a subgrid contribution.

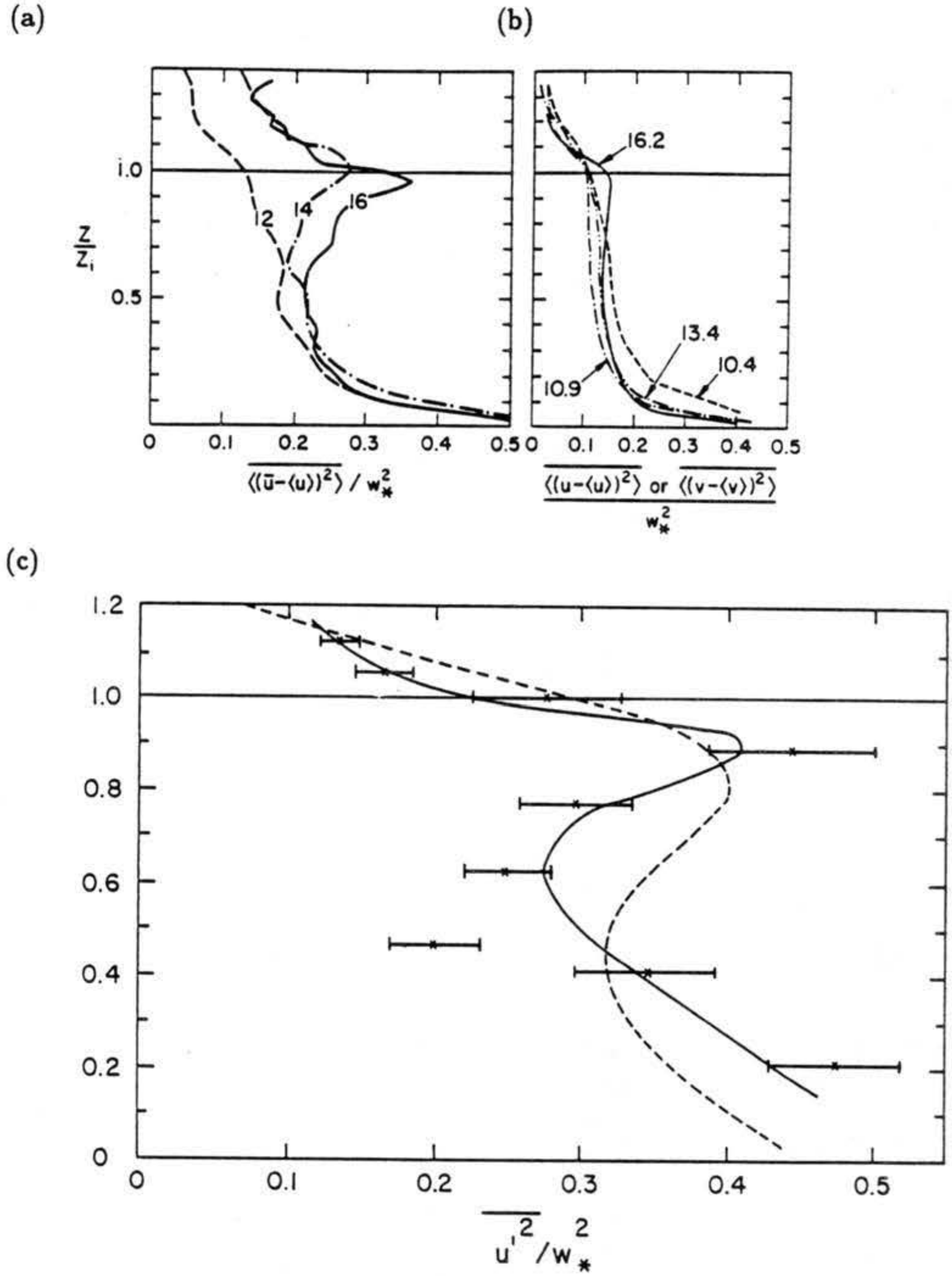

Figure 3.7. As Figure 3.5, but for the horizontal velocity variances.

Continued on following page.

(d)

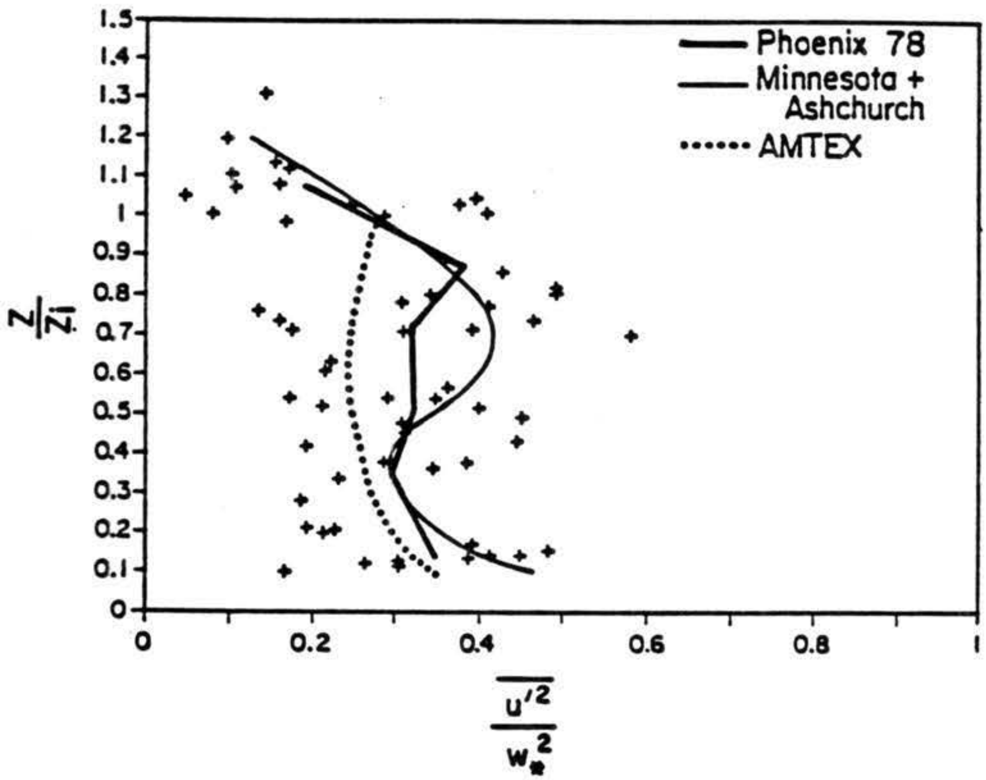

Figure 3.7 (continued).

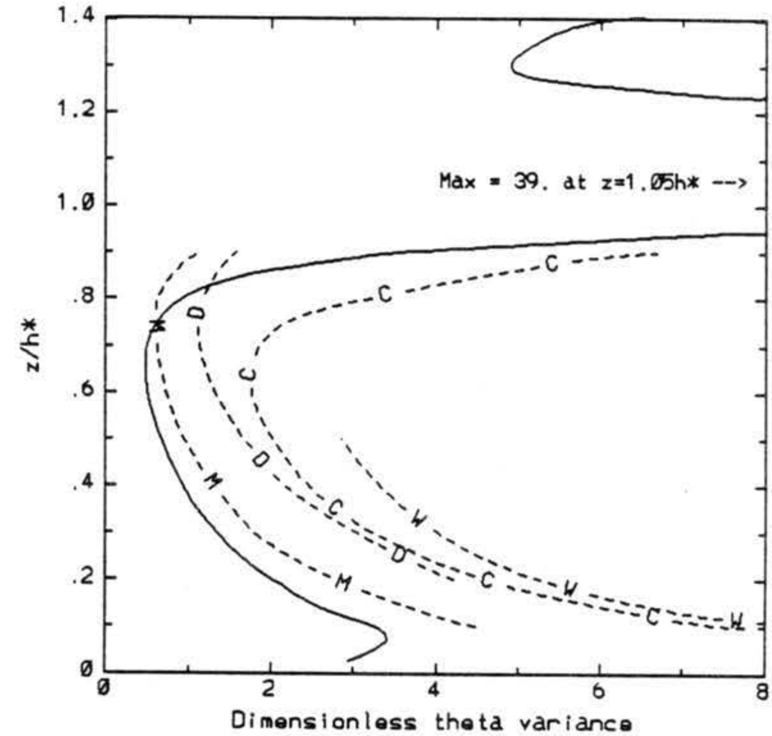

Figure 3.8. Profiles of the dimensionless resolved variance in potential temperature. The profile from Run A is shown by a solid line with a label indicating the position and magnitude of the maximum. Several other comparable profiles are shown as follows: Fluid tank results of Deardorff and Willis (1985) (--D--). Atmospheric observations from Caughey (1982) (--C--). Surface-layer free-convection expression of Wyngaard *et al.* (1971) (--W--). Resolved potential temperature variance from Moeng and Wyngaard (1984) and Moeng (1988, personal communication) (--M--).

$z = 1.0h_*$ and $z = 1.1h_*$ has been observed in all these studies, but its magnitude is highly variable and so appears not to follow mixed-layer scaling. In the lower and middle boundary layer the observational data are reasonably consistent, and they show two to four times as much variance as the present model resolves. Moeng and Wyngaard's (1984) large-eddy simulation[56] has the variance somewhat larger than the present model, but still substantially less than the observations.

Neither of the LES models shown in Figure 3.8 estimates the subgrid temperature variance. On the other hand, Deardorff (1974b) does estimate the subgrid contribution and finds the total (resolved plus subgrid) potential temperature variance comparable to the observations. However, he has the subgrid contribution accounting for approximately 75% of the total, even in the middle of the boundary layer. Observed temperature spectra (Caughey, 1982, Deardorff and Willis, 1985) are not consistent with such large temperature fluctuations on small scales. Furthermore, Young (1986) has investigated the effect of filtering aircraft data on scales comparable to the large-eddy grid scales and has found that the temperature variance is not significantly reduced.

Recently Moeng and Wyngaard (1988) have conducted simulations on a $96 \times 96 \times 96$ grid with grid spacing less than one half of their earlier runs. The resolved temperature variance profile from one of these simulations (Moeng, 1988, personal communication) shows a modest increase ($\sim 20\%$) relative to the the earlier simulation plotted in Figure 3.8. Futhermore, Moeng and Wyngaard (1988) have argued that Deardorff used an erroneous constant in his parameterisation of subgrid temperature variance. Their estimates of the subgrid variance for their own simulations—based on the temperature spectra—are of the order of 0.10 times the resolved variance. Allowing for this subgrid contribution, the total temperature variance from their $96 \times 96 \times 96$ model is of the order of 0.75 times the Deardorff and Willis (1985) and Caughey (1982) data.

---

[6]The temperature variance profile is not shown in Moeng and Wyngaard (1984), but was kindly supplied by Moeng (1988, personal communication).

3.2.4 *Pressure variance*

The profile of resolved Exner pressure variance is shown in Figure 3.9, expressed as a standard deviation to facilitate comparison with other workers' results in Figure 3.10. Moeng and Wyngaard (1986b) simulate pressure fluctuations approximately twice as large as Deardorff (1974b) whereas the present model is intermediate. Gal-Chen and Kropfli (1984) have estimated pressure fields from dual-Doppler radar velocity observations of a convective boundary layer during the Phoenix 78 experiment and find the standard deviation of pressure larger than any of the models. They suggest that the difference might be due to mean shear or rapid growth in the case they observed, but the possibility must also be considered that the LES models are underestimating pressure fluctuations significantly.

As well as the total pressure variance, Figure 3.9 shows the variances of the components,

$$\pi - \pi_0 = \pi_b + \pi_m + \pi_t + \pi_s, \tag{3.3}$$

which are induced by buoyancy (π_b), turbulence/mean-flow interaction (π_m), turbulence/ turbulence interaction (π_t) and subgrid forces (π_s), respectively. They are calculated from elliptic equations,

$$\begin{aligned}
\rho_0\theta_0\nabla_a^2\pi_b &= \frac{\partial}{\partial z}\left(\rho_0 g\frac{\theta-\theta_0}{\theta_0}\right) && (3.4)\\
\rho_0\theta_0\nabla_a^2\pi_m &= -2\frac{\partial^2}{\partial x_i \partial x_j}\left(\rho_0\left\langle u_i\right\rangle_h u_j'\right) && (3.5)\\
\rho_0\theta_0\nabla_a^2\pi_t &= -\frac{\partial^2}{\partial x_i \partial x_j}\left(\rho_0 u_i' u_j'\right) && (3.6)\\
\rho_0\theta_0\nabla_a^2\pi_s &= -\frac{\partial^2}{\partial x_i \partial x_j}\left(\rho_0 \tau_{ij}\right), && (3.7)
\end{aligned}$$

plus boundary conditions. Here ∇_a^2 is a differential operator (Section 2.2.1, Equation 2.22) which would reduce to a Laplacian if ρ_0 and θ_0 were constant.

The pressure components in Figure 3.9 can be compared to those calculated by Moeng and Wyngaard (1986b) and plotted in Figure 3.10b. The turbulence/mean-flow contribution to the pressure variance is small in Run A—which is to be expected since

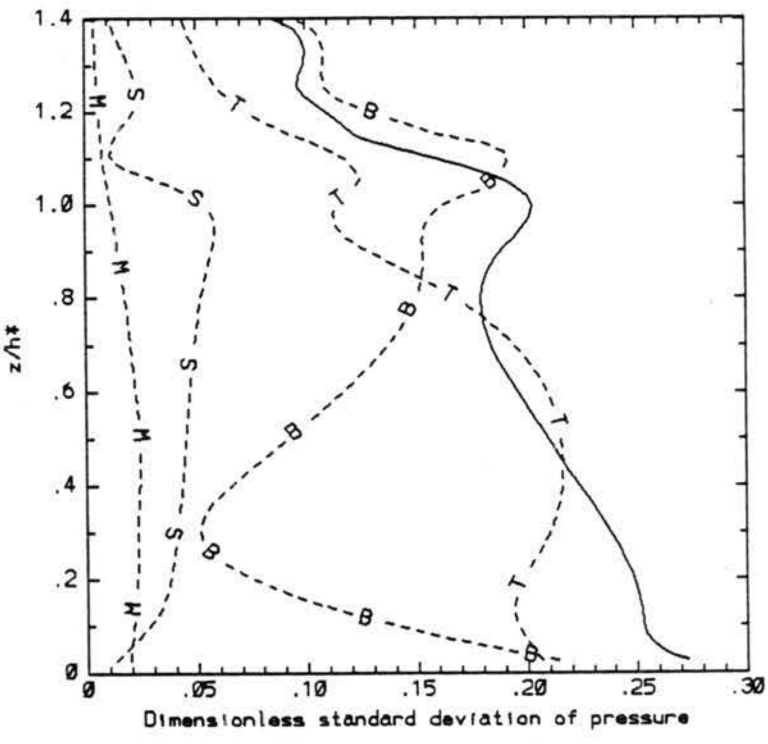

Figure 3.9. Profiles of the dimensionless standard deviation of Exner pressure from Run A. The solid line shows the total pressure and the dashed lines show contributions from the buoyancy pressure π_b (--B--), the turbulence/mean-shear pressure π_m (--M--), the turbulence/turbulence pressure π_t (--T--) and the subgrid pressure π_s (--S--).

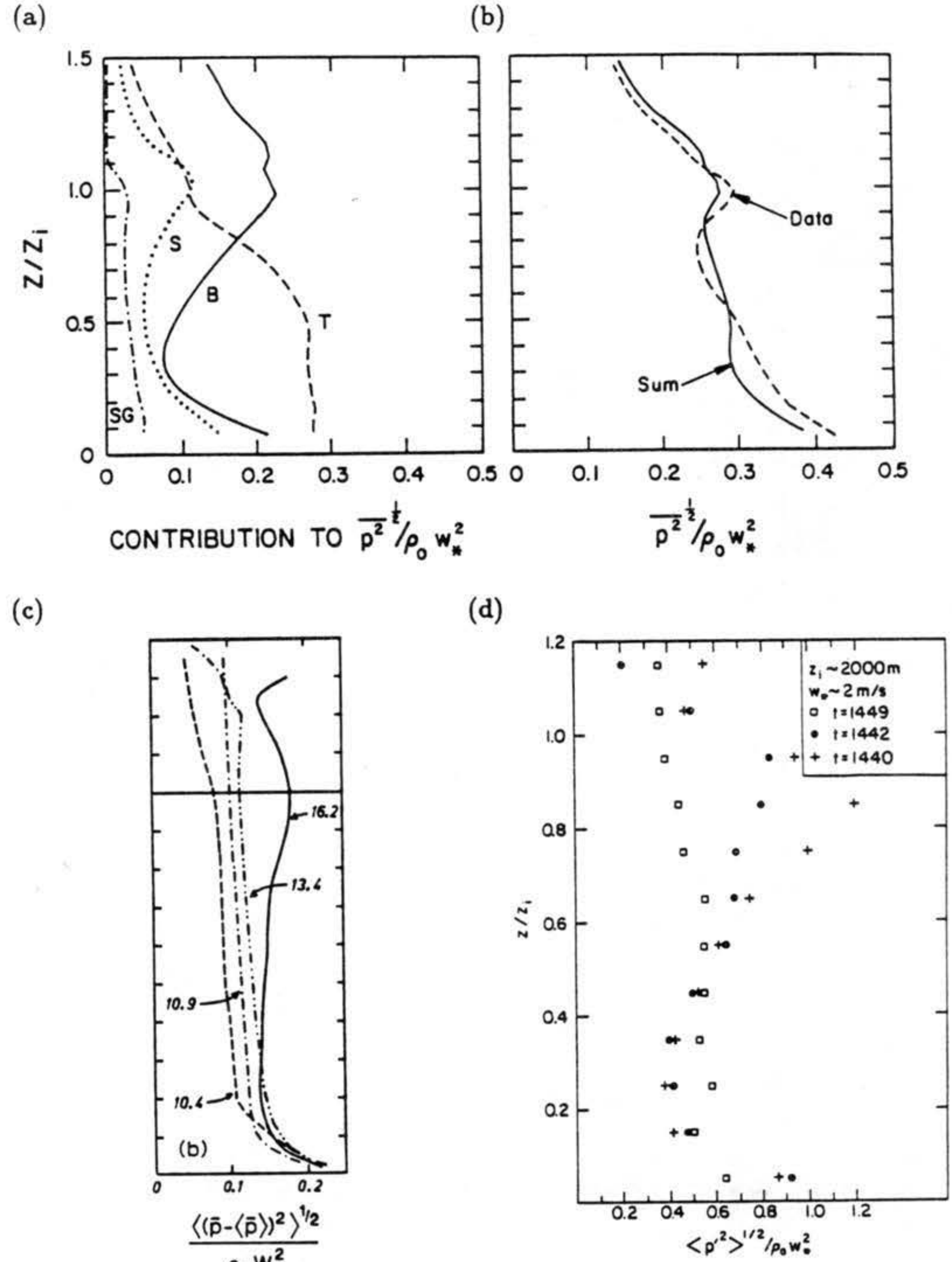

Figure 3.10. Profiles of the dimensionless standard deviation of pressure from other studies. (a) Contributions induced by buoyancy (B), turbulence/turbulence interaction (T), mean-shear (S) and subgrid (SG) forces from Moeng and Wyngaard (1986b). (b) Total pressure standard deviation from Moeng and Wyngaard (1986b). (c) LES results from Deardorff (1974b). (d) Results derived from dual-Doppler radar observations by Gal-Chen and Kropfli (1984).

the simulation was initialised with zero mean wind—and a little larger in Moeng and Wyngaard's more strongly sheared case. The other pressure components have similar profiles in the two simulations, although Moeng and Wyngaard's turbulence/turbulence contribution is somewhat larger, and this is probably the cause of their larger overall pressure variance. It would be very interesting to see a similar decomposition of radar-derived pressure fields (and there appears to be no reason why such a decomposition could not be done).

3.2.5 *Heat flux and budget of potential temperature*

The equation for the evolution of the horizontally averaged potential temperature is

$$\frac{\partial}{\partial t}\langle\theta\rangle_h = -\langle w\rangle_h \frac{\partial\langle\theta\rangle_h}{\partial z} - \frac{1}{\rho_0}\frac{\partial}{\partial z}\langle\rho_0 w'\theta'\rangle_h - \frac{1}{\rho_0}\frac{\partial}{\partial z}\langle\rho_0\phi_3\rangle_h . \tag{3.8}$$

The time-averaged terms in this equation are plotted in Figure 3.11a and the resolved heat flux $\langle w'\theta'\rangle_h$ and total heat flux $\langle w'\theta' + \phi_3\rangle_h$ are plotted in Figure 3.11b. In the layer near the surface, subgrid diffusion acts to warm and destabilise the air and turbulent advection responds by cooling and stabilising it, carrying heat upwards. A good measure of the depth of this layer is the height of the maximum in resolved heat flux, which for this simulation is $0.15h_*$. Because potential temperature gradients remain small in the boundary layer, the net tendency in $\langle\theta\rangle_h$ is nearly constant with height (at $1.25w_*\theta_*/h_{\rho *}$) and the total heat flux is very nearly linear. There is a powerful constraint maintaining this linearity: if the heat flux in the middle of the boundary layer increases, say, then the lower boundary layer will be cooled relative to the upper boundary layer, resulting in a reduction in the instability driving the convection and a negative feedback on the heat flux.

In Figure 3.12 the correlation coefficient between the resolved w and θ,

$$C_{w\theta} = \frac{\langle w'\theta'\rangle_h}{\sqrt{\langle w'^2\rangle_h\langle\theta'^2\rangle_h}},$$

is plotted and compared with atmospheric data. The modelled correlation coefficient is between 0.8 and 0.9 below $z = 0.4h_*$ whereas the atmospheric value is smaller, ~ 0.6 or

(a)

(b)

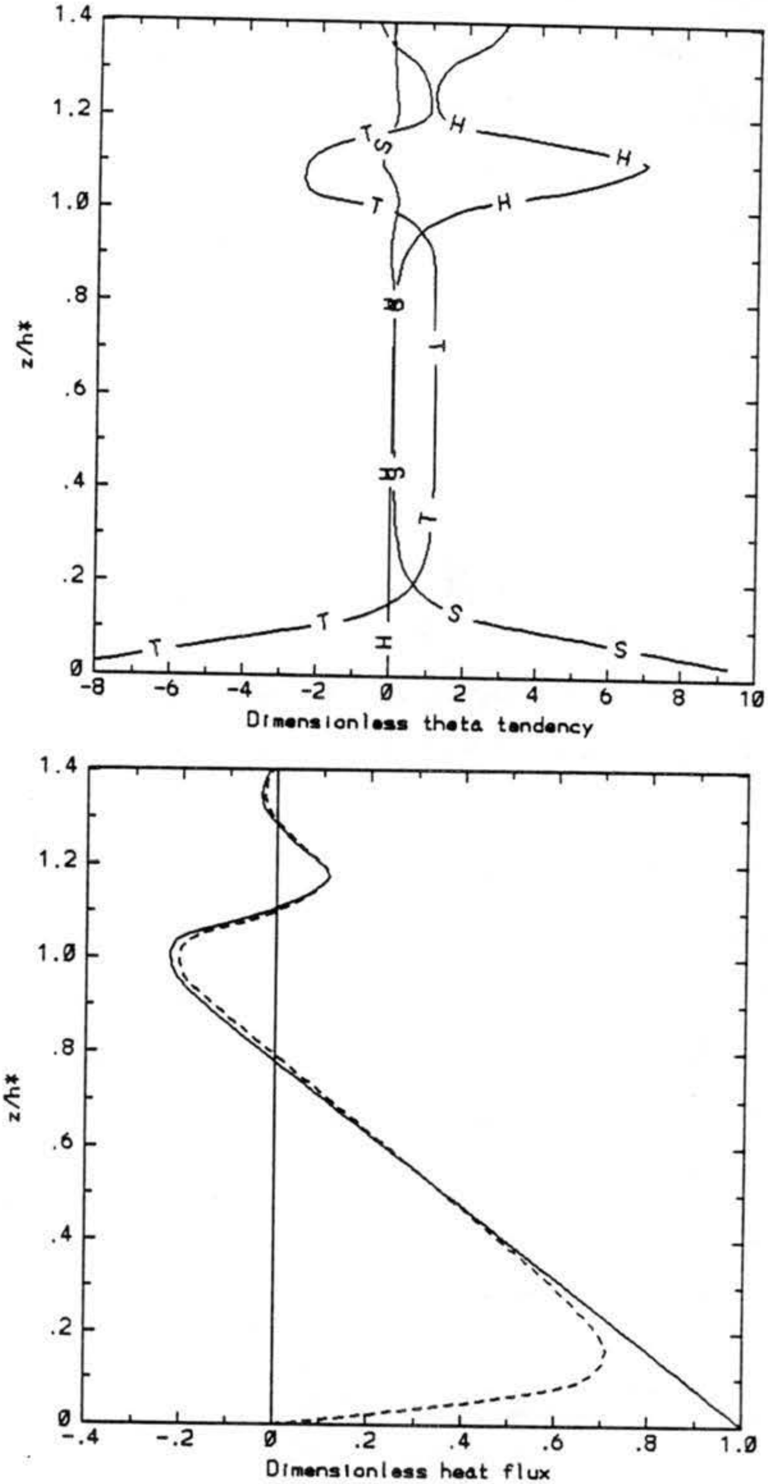

Figure 3.11. Potential-temperature budget and heat flux profiles from Run A. (a) Terms in $\partial\langle\theta\rangle_{h,t}/\partial t$, made dimensionless with $w_*\theta_*/h_{\rho*}$: advection by subsidence (—H—), resolved flux divergence (—T—) and subgrid flux divergence (—S—). (b) Resolved (dashed line) and resolved plus subgrid (solid line) vertical heat flux, made dimensionless with $w_*\theta_*$.

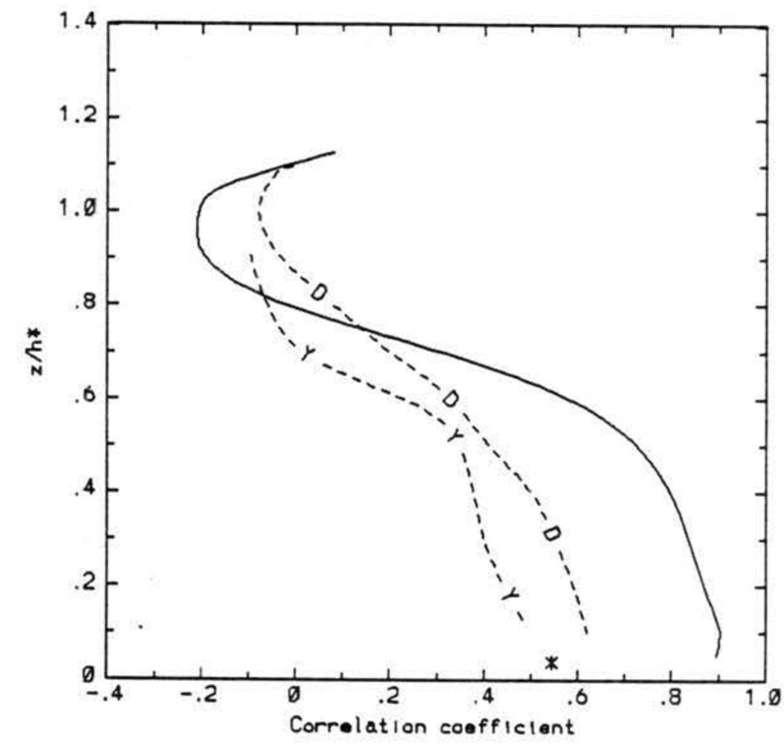

Figure 3.12. Correlation coefficient $C_{w\theta}$ of resolved w and θ from Run A. Also the free-convection surface-layer value of Wyngaard *et al.* (1971) (*) and the atmospheric observations of Young (1986) (--Y--) and Druilhet *et al.* (1983) (--D--).

less. The discrepancy is mostly due to the model's under-estimate of the temperature variance, but the point to be made is that in the lower boundary layer the model is achieving almost the maximum heat flux it can with the fluctuations it resolves in w and θ. Really, it is more appropriate to say that the model resolves fluctuations in w and θ just large enough to transport the heat it needs to. The atmosphere is more extravagant.

3.2.6 *Conditionally sampled statistics*

Figure 3.13 shows the fraction of the model grid points at each level where the resolved vertical velocity perturbation w' is greater than zero, along with similar data calculated by Lamb (1978) from Deardorff's (1974a,b) model. Both show updraughts occupying less than half of the area throughout most of the boundary layer, with a minimum coverage of 0.36 near $0.8h_*$, although they do differ near the surface where Deardorff's model has coverage greater than 0.5 below $0.1h_*$. Similar calculations have been made by Young (1986) from Phoenix aircraft data, with the distinction between updraughts and downdraughts being based on whether the low-pass filtered vertical velocity is positive or negative. Young's filtering scale is $0.1h_*$, which is not too different from the models' grid scale, so his results can reasonably be compared with the LES results. His results have support from measurements reported by Caughey *et al.* (1983) for the middle and upper boundary layer. Young finds that the fractional coverage has a minimum of 0.42 near the middle of the boundary layer. His profile is much closer to 0.5 in the upper boundary layer than the LES models.

The updraught-mean vertical velocity perturbation is plotted in Figure 3.14a, along with comparable results from Lamb (1978) and Young (1986). Agreement amongst the models and the observations is very good. Another quantity that Young calculates is the updraught-mean temperature perturbation (Figure 3.14b), which does not appear to have been computed for large-eddy models before now. The model shows temperature perturbations slightly larger than the observed values, which is interesting given that it underpredicts the temperature variance substantially.

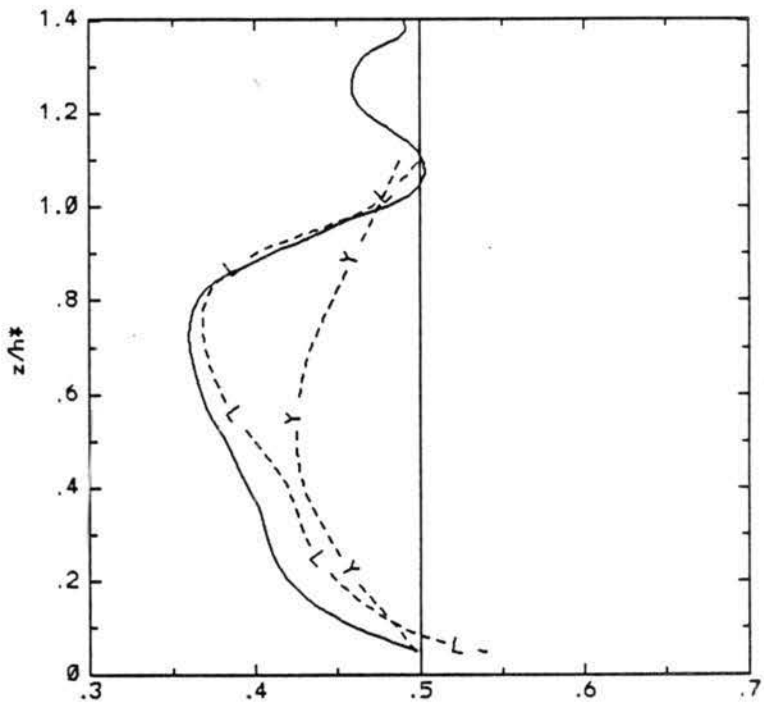

Figure 3.13. Profile of the fraction of points at each level in Run A with $w' > 0$ (solid line). Also similar data extracted by Lamb (1978) from Deardorff's (1974a, 1974b) model (--L--) and atmospheric results of Young (1986) (--Y--).

(a)

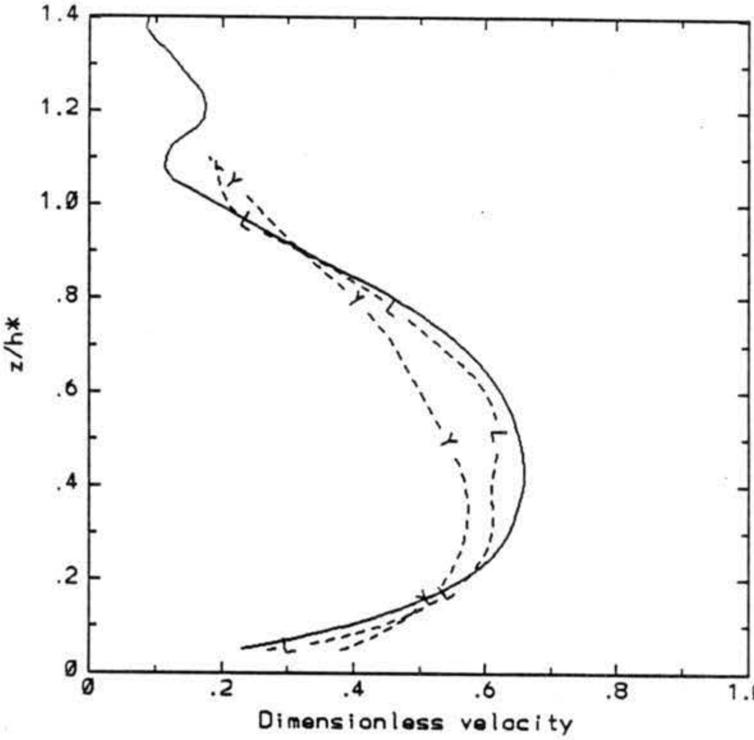

(b)

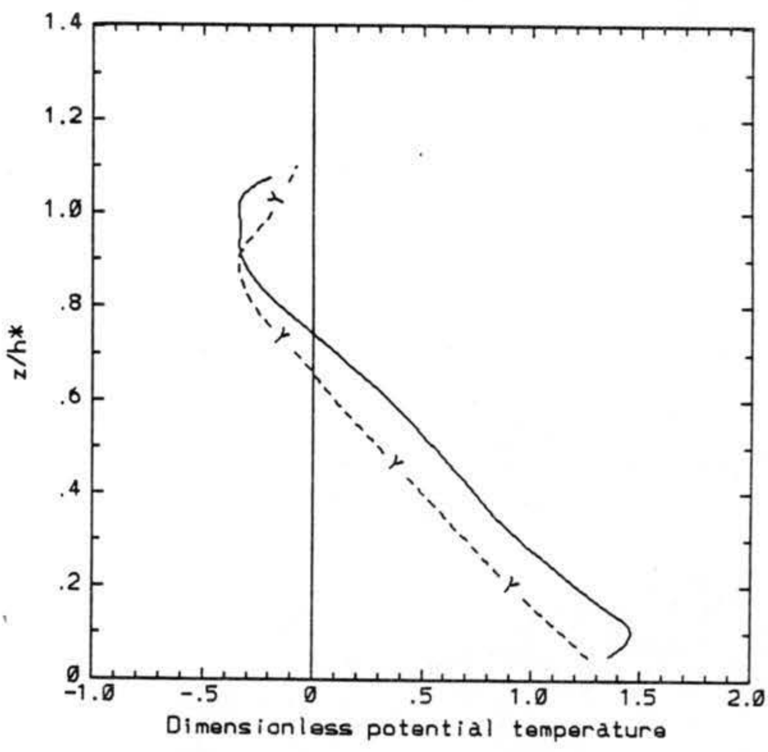

Figure 3.14. Profiles of conditionally sampled statistics from Run A. (a) Dimensionless updraught-mean w' along with data of Lamb (1978) (--L--) and Young (1986) (--Y--). (b) Dimensionless updraught-mean θ' along with data of Young (1986) (--Y--).

Young has estimated the "top-hat" contribution of the updraughts and downdraughts to different statistics (i.e., the value calculated for that statistic assuming that the flow consists entirely of uniform updraughts and downdraughts) and finds that this contribution accounts for 50% to 60% of $\langle w'^2 \rangle_h$ and $\langle w'\theta' \rangle_h$, but for only 20% of $\langle \theta'^2 \rangle_h$ near the surface and no more than a few percent above $0.6h_*$. In the model (Figure 3.15) the top-hat contribution accounts for a little more of the resolved vertical velocity variance and heat flux—up to 75% near the surface—but for *much more*—up to 60%—of the temperature variance. In other words, whereas the atmospheric convective boundary layer generates excess temperature fluctuations that are not directly involved in carrying heat upwards, the model does not.

3.2.7 *Skewness coefficient*

The fact that the fractional coverage of updraughts is less than 0.5 is an indicator of positive vertical velocity skewness, which has important implications for dispersion, as discussed by Lamb (1982). The ability of Deardorff's model to predict the sign of this skewness was one of its greatest successes. Another measure of the skewness is the skewness coefficient,

$$S_w = \left\langle w'^3 \right\rangle_h / \left\langle w'^2 \right\rangle_h^{3/2},$$

which is plotted in Figure 3.16[7] along with data from Deardorff (1974b), Moeng (1984) and Young (1986). The LES profiles are all similar, the major difference being that Deardorff's model has a more pronounced region of negative skewness near the surface. This feature will be discussed in Section 3.4. As one might expect from the profiles of updraught coverage, Young's atmospheric observations have S_w substantially closer to zero than the models in the upper boundary layer.

---

[7]Actually the numerator in S_w has not been calculated as a single-point third moment, but in a vertically interpolated form which arises from the finite-difference expression for turbulent transport of vertical velocity variance—see Section 3.3.1. If the single-point form of $\langle w'^3 \rangle_h$ is used the skewness coefficient becomes slightly negative at the lowest level (value about -0.1), but otherwise the profile is essentially unchanged.

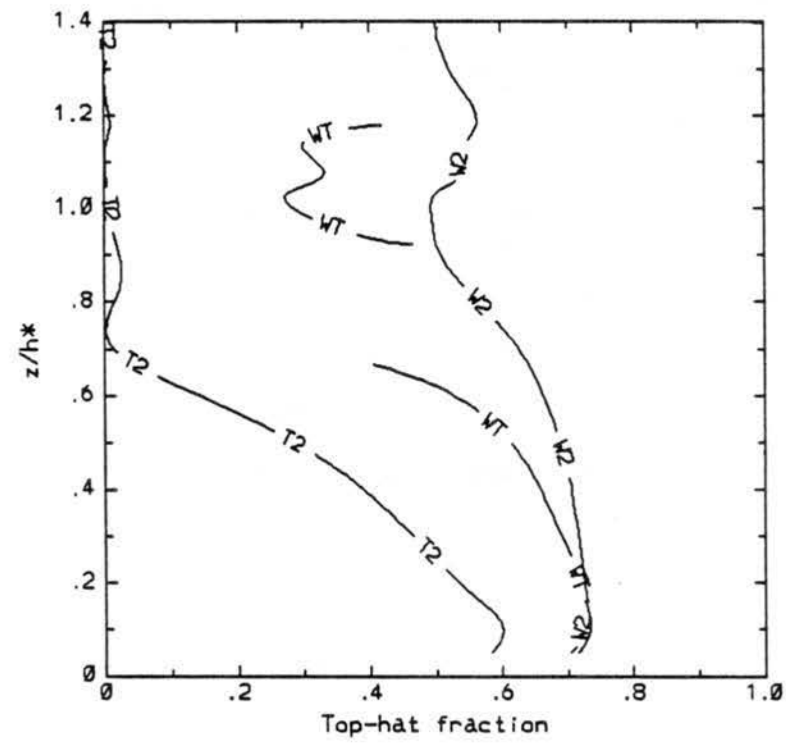

Figure 3.15. Profiles of the fraction of the resolved covariances accounted for by the top-hat contribution in Run A (see text). Curves are for vertical velocity variance (—W2—), vertical heat flux (—WT—) and potential temperature variance (—T2—). The heat flux curve is suppressed where the magnitude of the dimensionless flux is less than 0.1.

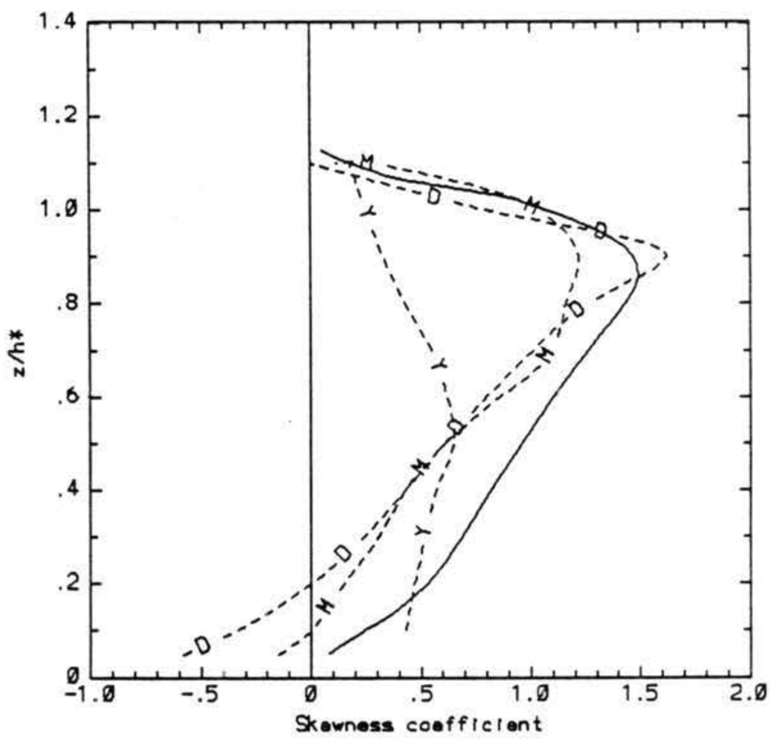

Figure 3.16. Skewness coefficient S_w of resolved w from Run A. Also LES data from Deardorff (1974b) (--D--) and Moeng (1984) (--M--), and atmospheric data from Young (1986) (--Y--).

3.2.8 *Spectra*

Figure 3.17 shows power spectra for potential temperature and vertical velocity at five heights: $0.05h_*$, $0.25h_*$, $0.50h_*$, $0.75h_*$ and $1.00h_*$. The spectra are calculated along lines in the x and y directions, then averaged over the perpendicular horizontal direction and over time. They are functions of horizontal wavenumber, $k = 2\pi/\lambda$, and have units of variance per unit interval in k. As plotted they are multiplied by k (to give variance per unit interval in ln$k$) and made dimensionless with θ_*^2 and w_*^2 respectively.

At the three middle levels ($0.25h_*$, $0.50h_*$ and $0.75h_*$) both temperature and vertical velocity spectra have broad peaks in the vicinity of $kh_* = 4$ ($\lambda = 1.5h_*$), in agreement with a number of observational studies (Caughey, 1982). Furthermore one can, with a little imagination, identify in these spectra a region around $kh_* = 10$ ($\lambda = 0.6h_*$) where the spectra have slopes approximating the inertial subrange value. (It will be shown in Section 3.4 that, with the grid length-scale constant C_g equal to 1, this region extends out to the maximum wavenumber resolved by the model.) However, a crucial property of the inertial subrange, namely isotropy, is not satisfied. The spectral density of vertical velocity at the middle and high wavenumbers is approximately twice the transverse[8] spectral density of horizontal velocity (not shown), whereas in the inertial subrange they should be equal. A similar ratio is apparent in Deardorff's (1974b) simulation.

Near the surface ($z = 0.05h_*$) the spectral peaks shift towards higher wavenumber, as expected. A similar, but more pronounced, shift also occurs near the top of the boundary layer to the extent that at $z = 1.00h_*$ the spectra of w and θ remain flat or increase slightly as the wavenumber approaches its maximum value of $kh_* = 30$ ($\lambda = 0.2h_* = 2\Delta x$). Although some atmospheric and laboratory studies (Caughey and Palmer, 1979; Deardorff and Willis, 1985) find evidence for a such a shift in the w spectra and (less clearly) in the θ spectra near $z = h_*$, the fact remains that numerical models do not

---

[8]Transverse velocity spectra are those taken along lines perpendicular to the velocity component, and longitudinal spectra are taken along lines parallel to the velocity component.

(a) θ:

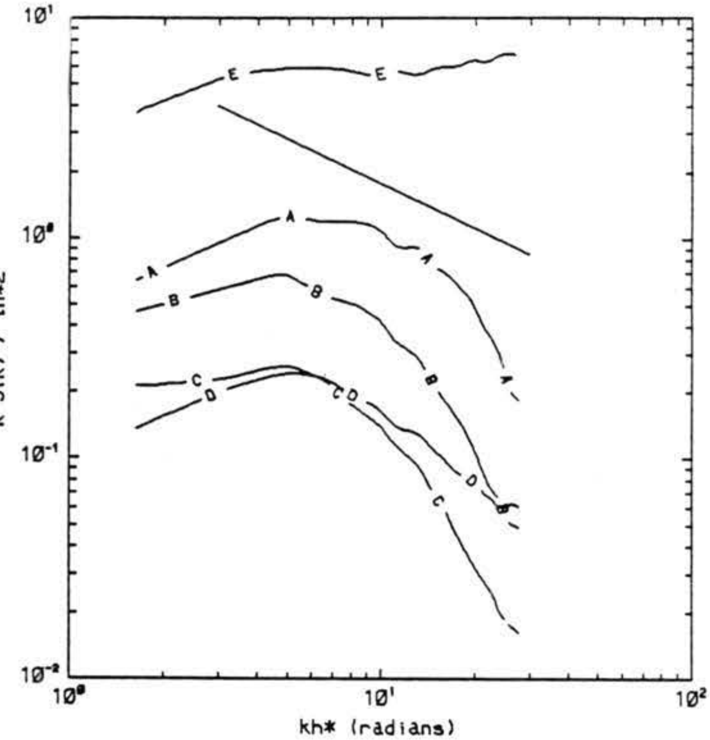

(b) w:

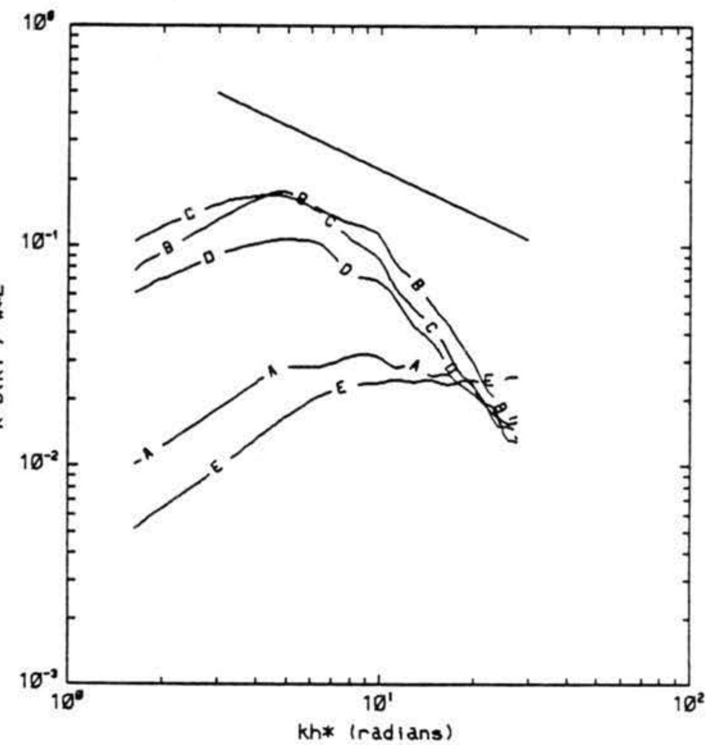

Figure 3.17. One-dimensional horizontal power spectra from Run A plotted against dimensionless wavenumber kh_*. (a) Potential temperature spectra, made dimensionless by θ_*^2. (b) Vertical velocity spectra, made dimensionless by w_*^2. Heights are $0.05h_*$ (—A—), $0.25h_*$ (—B—), $0.50h_*$ (—C—), $0.75h_*$ (—D—) and $1.00h_*$ (—E—). The straight solid lines have inertial subrange slope $-2/3$.

simulate wavelengths near $2\Delta x$ at all well, so processes occurring near the inversion in the model must be suspect.

3.2.9 *Discussion*

This concludes the section devoted in large part to comparing the present model with other LES models and with observations, although other comparisons will be made when appropriate in the following section on the dynamics of boundary layer turbulence.

Taken as a group the large-eddy models share several common features. They all predict realistic magnitudes for the vertical velocities in the boundary layer eddies and predict that the vertical velocities are postively skewed, though they overestimate that skewness in the upper boundary layer. The vertical variation of $\langle\theta\rangle_h$ is plausible, and seems to agree with observations where these are available. Common failings include horizontal velocity variances that are too small in the middle of the boundary layer and too large (relatively) near the surface, and temperature and pressure variances that are too small. In some sense the models seem to be less "turbulent" than a real fluid. This is not too surprising given the limited range of scales of motion available to the models, at least with the number of grid points used in the simulations described here.

Amongst the models, Moeng's develops substantially larger horizontal velocity variances and pressure variances (but not larger temperature variances) than Deardorff's, with the present model in between. On this basis it *appears* that Moeng's model is a little more realistic than the finite-difference models at the same resolution.

3.3 Dynamics of the large eddies

3.3.1 *Turbulence kinetic energy budget*

The tendency equation in the model for the components of resolved turbulence kinetic energy is most simply written as

$$\begin{aligned}\frac{1}{2}\frac{\partial}{\partial t}\left\langle u_i'^2\right\rangle_h &= +\delta_{i3}\frac{g}{\theta_0}\left\langle w'\theta'\right\rangle_h - \theta_0\left\langle u_i'\frac{\partial\pi'}{\partial x_i}\right\rangle_h - \left\langle u_i' u_j\frac{\partial u_i}{\partial x_j}\right\rangle_h \\ &\quad -\frac{1}{\rho_0}\left\langle u_i'\frac{\partial}{\partial x_j}(\rho_0\tau_{ij}')\right\rangle_h - \alpha_R\left\langle u_i'^2\right\rangle_h\end{aligned} \tag{3.9}$$

where the terms on the right-hand side are due to buoyancy, the pressure-gradient force, advection, the subgrid force and Rayleigh friction, the last of these being active only in the absorbing layer.

The advection term is discussed further in Appendix A. If the small contribution from subsidence is ignored it can be written as the sum of two parts,

$$-\left\langle u_i' u_j \frac{\partial u_i}{\partial x_j} \right\rangle_h = -\langle w' u_i' \rangle_h \frac{\partial}{\partial z} \langle u_i \rangle_h - \frac{1}{\rho_0} \frac{\partial}{\partial z} \left\langle \rho_0 w' u_i'^2 / 2 \right\rangle_h \qquad (3.10)$$

called, respectively, velocity-gradient production and turbulent transport. The velocity-gradient term exchanges kinetic energy between turbulence and the mean flow. It is small at any instant—since the instantaneous mean shear and momentum fluxes are never large (Section 3.1)—and smaller still when time-averaged because there is no consistent tendency for transfer of energy either to or from the mean flow. The advective tendency in turbulence kinetic energy, then, is dominated by turbulent transport.

It should be mentioned that the quantities calculated in the model analysis are not direct finite-difference implementations of the expressions in Equation 3.10. Rather the finite-diference advection tendency is broken into parts as described in Appendix A (Equation A.6), using the same advection algorithms as the model, and these parts are then evaluated. For example, the turbulent transport term is estimated by calculating the tendency in u_i due to advection of turbulent velocity fluctuations by the turbulent velocity field (i.e., the finite-difference counterpart of $u_j' \partial u_i' / \partial x_j$), then taking the covariance of that tendency with u_i. It is *not* calculated by differentiating a triple velocity covariance. It so happens that for single-point variances (like velocity variances and temperature variance) the second-order, centred-difference equations share with the continuum equations the property that the turbulent transport term reduces to the gradient of a flux and so integrates to zero over the domain.

It is common to split the pressure term in Equation 3.9 into two parts,

$$-\theta_0 \left\langle u_i' \frac{\partial \pi'}{\partial x_i} \right\rangle_h = -\delta_{i3} \frac{1}{\rho_0} \frac{\partial}{\partial z} \left\langle \rho_0 \theta_0 w' \pi' \right\rangle_h + \frac{1}{\rho_0} \left\langle \pi' \frac{\partial}{\partial x_i} (\rho_0 \theta_0 u_i') \right\rangle_h . \qquad (3.11)$$

The former is called pressure transport and the δ_{i3} symbol indicates that it acts only on the vertical velocity variance. The latter is called intercomponent transfer and it vanishes when the sum is taken over the three velocity components.

Figure 3.18a shows the time-averaged terms of Equation 3.9 in the budget for turbulence kinetic energy and Figure 3.18b shows the contribution to the pressure term from the pressure fields generated by buoyancy, advection and subgrid forces. (The advection pressure π_a is dominated by the turbulence/turbulence part π_t and generally the distinction between them can be ignored.) Figures 3.19 and 3.20 show similar budgets for one-half the vertical velocity variance and one-half the sum of the horizontal velocity variances, respectively. Vertical velocity variance is generated in the lower and middle boundary layer by buoyancy. It is transported vertically, mainly by turbulent advection, to maintain entrainment in the upper boundary layer and is converted into horizontal velocity variance by pressure forces. A number of aspects of the turbulence kinetic energy and velocity variance budgets are examined below, beginning with the pressure forces.

Let us first consider the pressure induced by the buoyancy force. For a single Fourier component of the fluctuating temperature field,

$$\theta' = \Theta \exp(ik_x x + ik_y y + ik_z z), \tag{3.12}$$

one finds on solving the elliptic equation for π_b (ignoring variations in θ_0 and ρ_0) that the pressure gradient force opposes the buoyancy force according to

$$-\theta_0 \frac{\partial \pi_b'}{\partial z} = -A \frac{g}{\theta_0} \theta' \quad \text{where} \quad A = k_z^2/(k_x^2 + k_y^2 + k_z^2). \tag{3.13}$$

When $k_z^2 \gg k_x^2 + k_y^2$ the factor A approaches its hydrostatic limiting value of 1, whereas if $k_x = k_y = k_z$ then $A = 1/3$.

It is convenient here to consider a general second- or third-order moment of the form $\langle w'^m \theta'^n \rangle_h$, where $m + n$ equals two or three. (The budget with $m + n = 3$ is written later in Equation 3.35.) A simple parameterisation suggested by Equation 3.13 for the relationship between the buoyancy and buoyancy-pressure terms in such a budget is

$$-\theta_0 \left\langle w'^{m-1} \theta'^n \frac{\partial \pi_b'}{\partial z} \right\rangle_h = -A \frac{g}{\theta_0} \left\langle w'^{m-1} \theta'^n \theta' \right\rangle_h \tag{3.14}$$

(a)

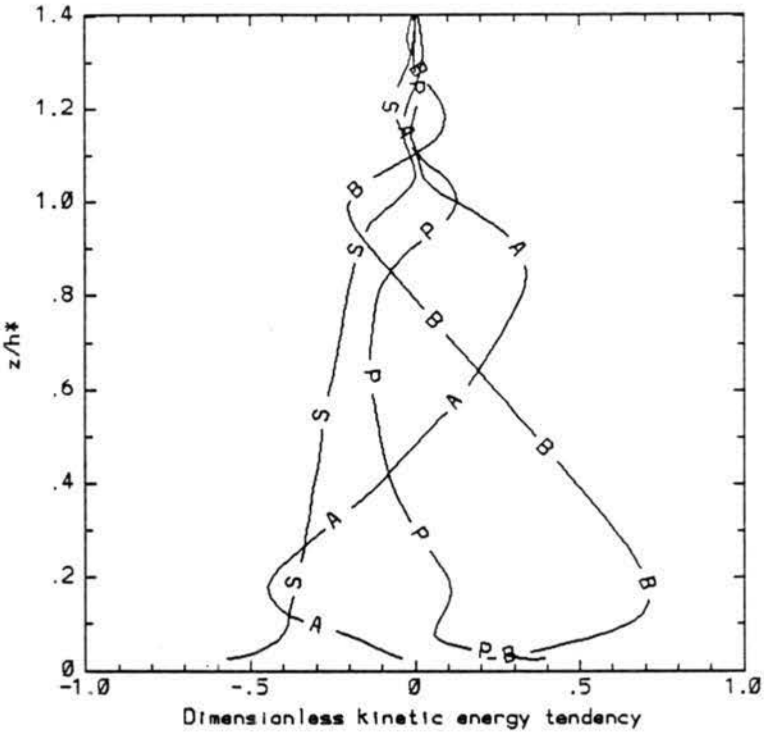

(b)

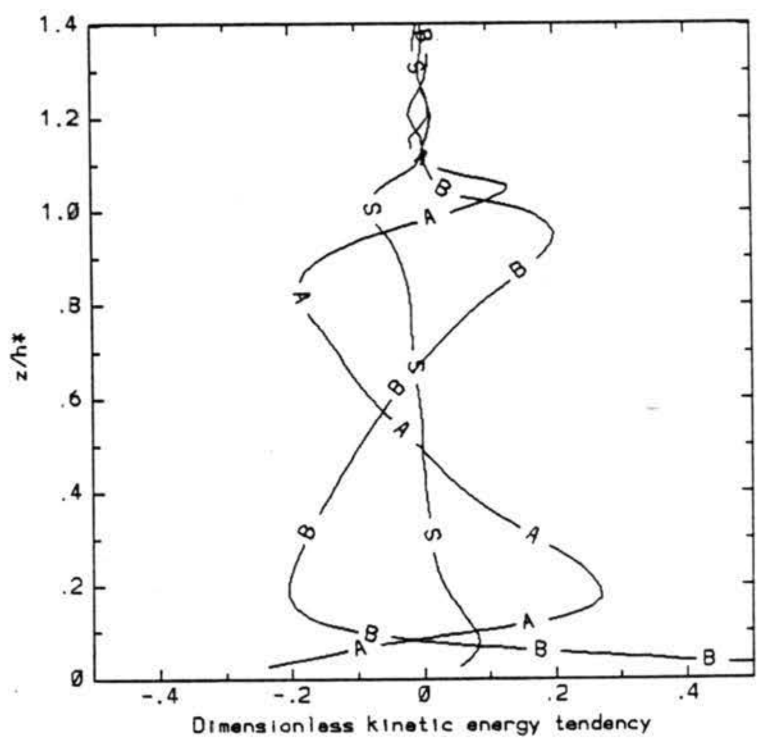

Figure 3.18. Terms in the resolved turbulence kinetic energy budget $(\partial/\partial t)\langle u_i'^2\rangle_{h,t}/2$ from Run A. (a) Buoyancy (—B—), pressure (—P—), advection (—A—) and subgrid (—S—). (b) Velocity/π-gradient contributions from buoyancy pressure π_b (—B—), advection pressure π_a (—A—) and subgrid pressure π_s (—S—). All made dimensionless with w_*^3/h_*.

(a)

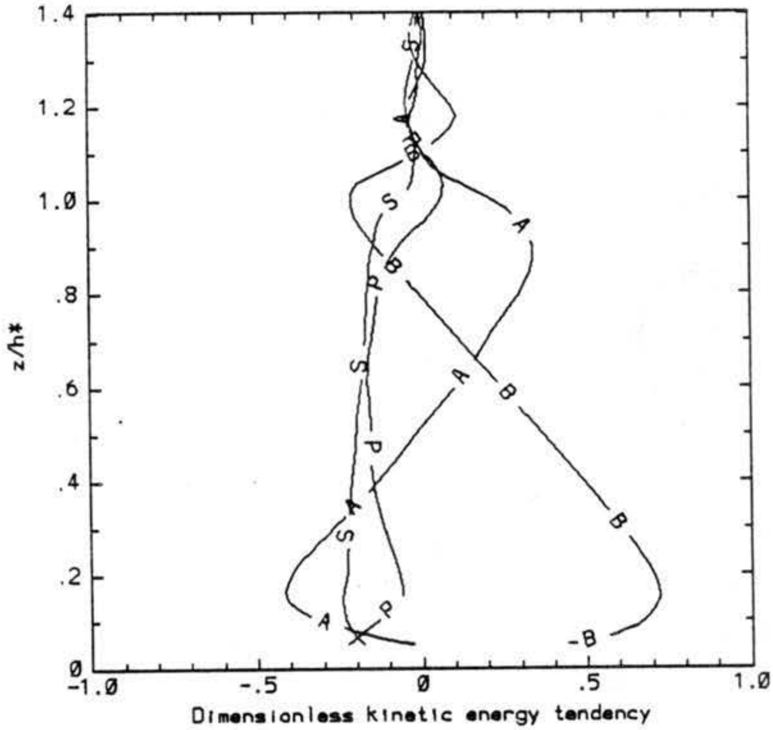

(b)

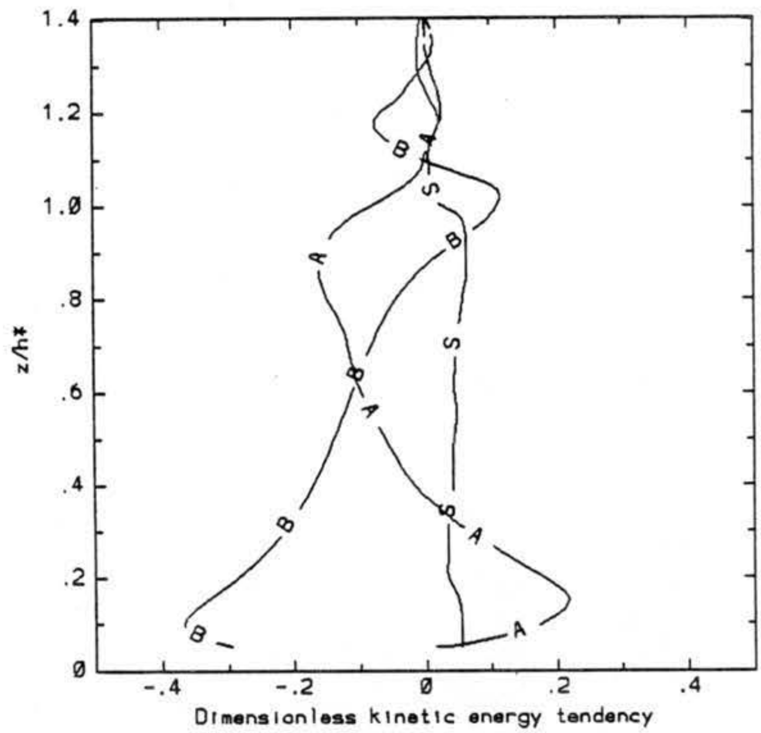

Figure 3.19. As figure 3.18, but for the budget of one-half the vertical velocity variance $(\partial/\partial t)\langle w'^2\rangle_{h,t}/2$.

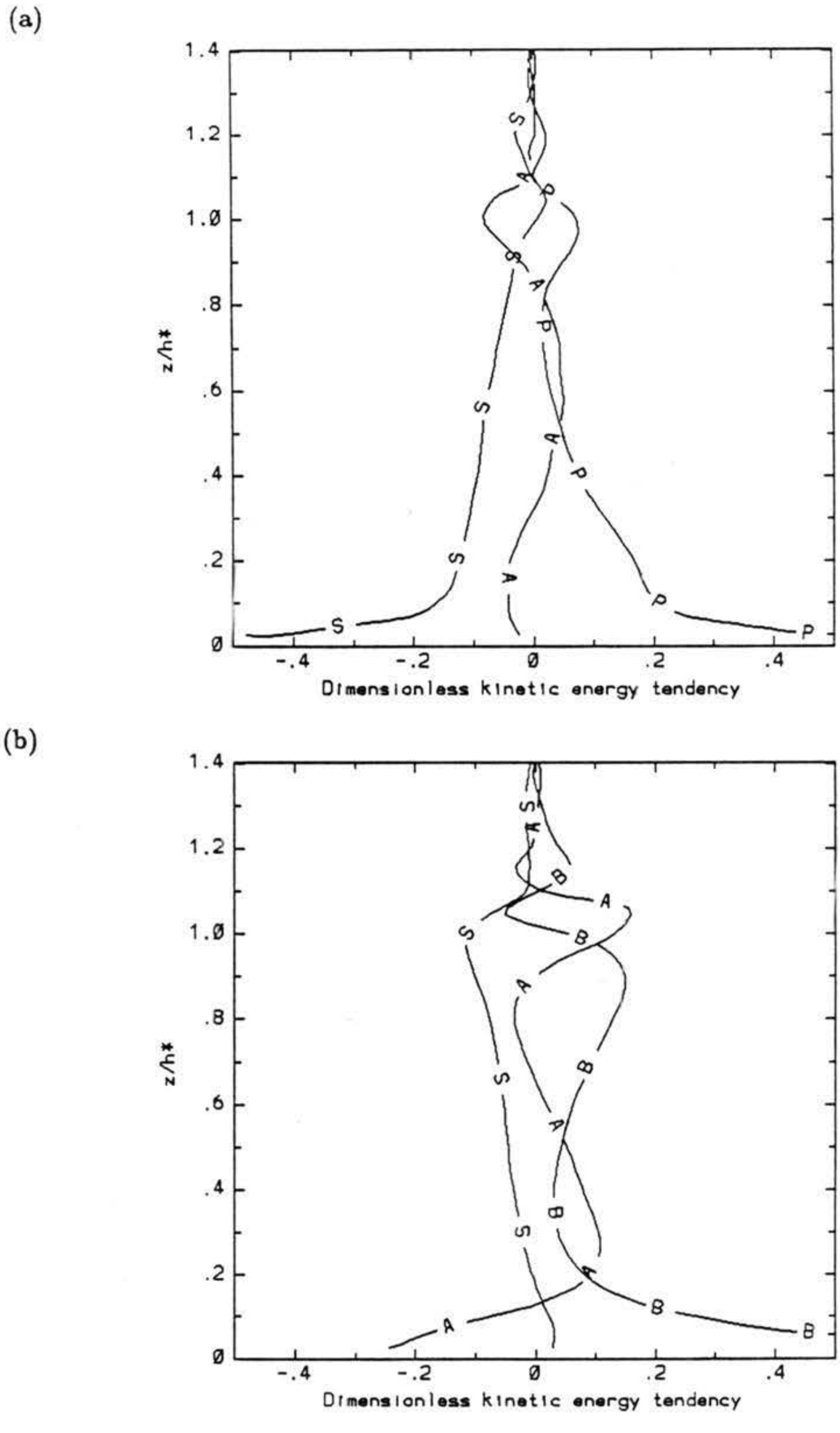

Figure 3.20. As figure 3.18, but for the budget of one-half the sum of the horizontal velocity variances $(\partial/\partial t)\langle u'^2 + v'^2\rangle_{h,t}/2$.

where A depends on the geometry of the dominant buoyancy fluctuations and on the boundary conditions imposed on π_b. For the particular case of the vertical velocity variance budget ($m=2$, $n=0$) this reduces to

$$-\theta_0 \left\langle w' \frac{\partial \pi_b'}{\partial z} \right\rangle_h = -A \frac{g}{\theta_0} \left\langle w'\theta' \right\rangle_h. \tag{3.15}$$

Moeng and Wyngaard (1986b) have evaluated an expression analogous to Equation 3.14 in their scalar flux budgets and found the best agreement with $A = 0.5$. In the present work budgets have been examined for all the second and third moments of w and θ. The profiles of A calculated from each one are compared in Figure 3.21. The pattern of vertical variation is very consistent. (The third moment budgets have A a little smaller than the second moment budgets: this suggests a difference in the geometry of the buoyancy fluctuations contributing most strongly at the different orders.) A simple cubic expression,

$$A(z) = \begin{cases} 0.80 - 2.75\left(\dfrac{z}{h_*}\right) + 4.90\left(\dfrac{z}{h_*}\right)^2 - 2.35\left(\dfrac{z}{h_*}\right)^3 & z < h_* \\ 0.60 & z \geq h_*, \end{cases} \tag{3.16}$$

summarises the data in Figure 3.21 well. This has $A = 0.8$ at the surface, dropping off rapidly to a minimum of 0.33 at $z=0.4h_*$ and increasing to 0.6 at $z=h_*$ and above. The left- and right-hand sides of Equation 3.15 are compared in Figure 3.22. Agreement is very good, with the greatest discrepancy near the zero-crossing in heat flux at $z=0.8h_*$.

Launder (1975) has proposed a parameterisation similar to Equation 3.15, but for the intercomponent-transfer part only of the pressure covariance terms. In the present nomenclature his parameterisation is

$$\frac{\theta_0}{\rho_0} \left\langle \pi_b' \frac{\partial}{\partial z}(\rho_0 w') \right\rangle_h \equiv \theta_0 \left\langle u' \frac{\partial \pi_b'}{\partial x} + v' \frac{\partial \pi_b'}{\partial y} \right\rangle_h = -A_1 \frac{g}{\theta_0} \left\langle w'\theta' \right\rangle_h, \tag{3.17}$$

with $A_1 = 0.4$. It is readily apparent from the vertical and horizontal velocity variance budgets already presented in Figures 3.19 and 3.20 that this expression does not describe the model profiles well. In particular it fails to predict the strong transfer of kinetic energy to the horizontal velocity fields near the surface.

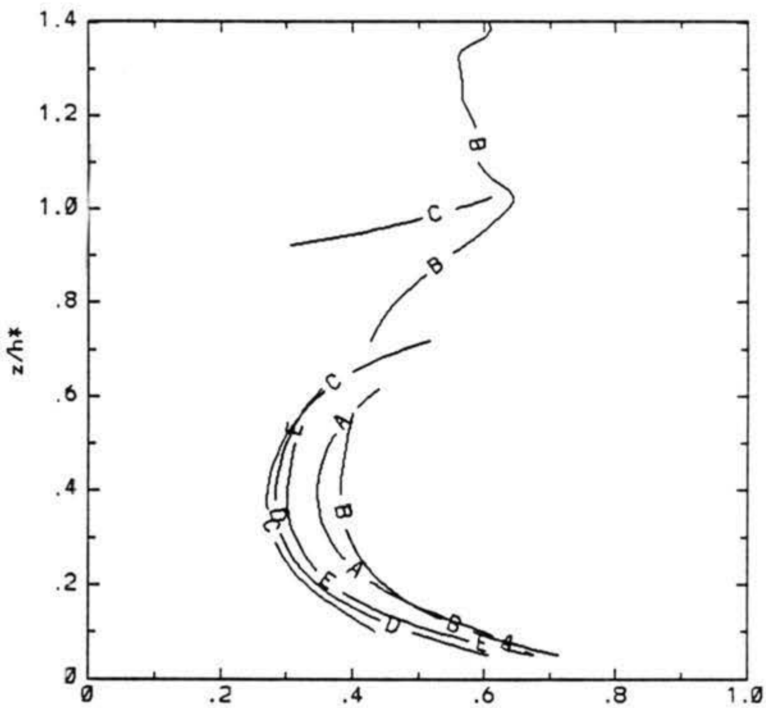

Figure 3.21. Profiles of the ratio between the π_b-gradient term and the buoyancy term in second- and third-moment budgets for Run A. The moments are $\langle w'^2 \rangle_{h,t}$ (—A—), $\langle w'\theta' \rangle_{h,t}$ (—B—), $\langle w'^3 \rangle_{h,t}$ (—C—), $\langle w'^2\theta' \rangle_{h,t}$ (—D—) and $\langle w'\theta'^2 \rangle_{h,t}$ (—E—). Profiles are suppressed where the buoyancy term approaches zero. The profiles for the $\langle w'^2\theta' \rangle_{h,t}$ and $\langle w'\theta'^2 \rangle_{h,t}$ budgets are suppressed above $z = 0.9h_*$, where the budgets become erratic.

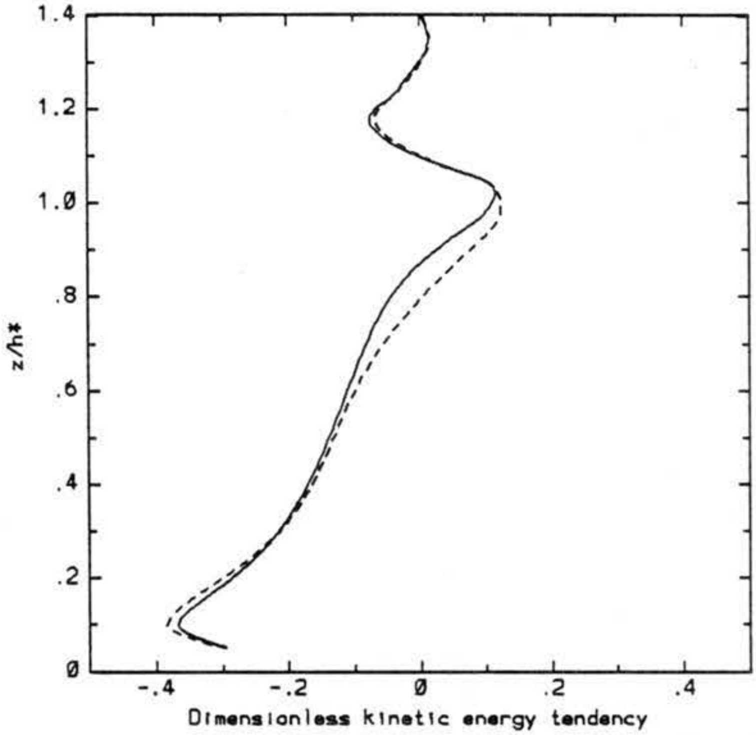

Figure 3.22. Comparison of the velocity/π_b-gradient term in the $\langle w'^2 \rangle_{h,t}/2$ budget of Run A (solid line) with the right-hand side of Equation 3.15 (dashed line). The constant of proportionality A is given by Equation 3.16.

The notion that the vertical π_b-gradient force opposes a certain fraction of the buoyancy force is appealingly simple and one might speculate (ignoring the fact that the advective force is three-dimensional) that a similar relationship holds between the vertical component of the turbulence/turbulence advection force and the turbulence/turbulence pressure gradient, i.e., that

$$-\theta_0 \frac{\partial \pi_t'}{\partial z} \sim B \left(u_j' \frac{\partial w'}{\partial x_j} \right)_h . \tag{3.18}$$

Here the $\sim$ symbol implies a statistical tendency rather than equality. For the vertical velocity variance budget this implies

$$-\theta_0 \left\langle w' \frac{\partial \pi_t'}{\partial z} \right\rangle_h = B \frac{1}{\rho_0} \left\langle \rho_0 \frac{w'^3}{2} \right\rangle_h , \tag{3.19}$$

which has the π_t-gradient forces opposing the vertical transport of vertical velocity variance. The expression actually works quite well in the lower and upper boundary layer with $B = 0.5$ (Figure 3.23); it is not satisfactory in the middle of the boundary layer, predicting $-\theta_0 \langle w' \partial \pi_t' / \partial z \rangle_h$ too positive, and it also errs in predicting a vertical integral of zero.

A more conventional view of the turbulence/turbulence component of pressure has it tending to restore isotropy and, in fact, π_t is sometimes called the "return-to-isotropy" pressure, although that name will not be used here. A typical assumption for the convective boundary layer is

$$\frac{\theta_0}{\rho_0} \left\langle \pi_t' \frac{\partial}{\partial z} (\rho_0 w') \right\rangle_h \equiv \theta_0 \left\langle u' \frac{\partial \pi_t'}{\partial x} + v' \frac{\partial \pi_t'}{\partial y} \right\rangle_h = -\frac{1}{\tau} \left\langle w'^2 - \frac{1}{3} u_i'^2 \right\rangle_h , \tag{3.20}$$

where τ is a positive time scale. The comparison of the left- and right-hand sides of Equation 3.20 is made in Figure 3.24, with τ chosen as $1.0 h_* / w_*$ to give reasonable agreement near the surface. The return-to-isotropy assumption is tenable in the lower boundary layer, but generally of the wrong sign above $0.5 h_*$, and fails to predict the strong transfer from the vertical velocity variance to the horizontal velocity variances by π_t-gradient forces in the vicinity of the inversion.

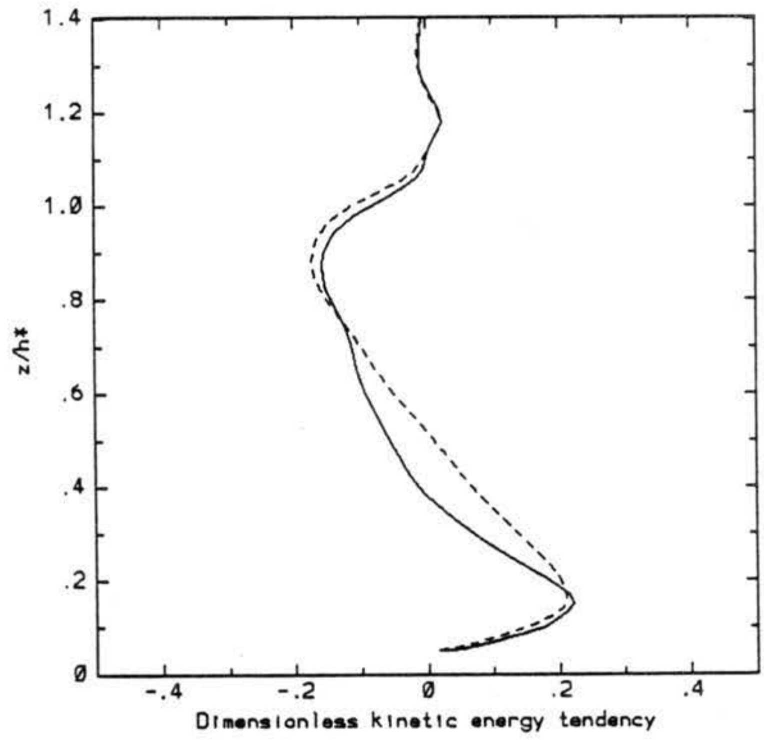

Figure 3.23. Comparison of the velocity/π_t-gradient term in the $\langle w'^2 \rangle_{h,t}/2$ budget of Run A (solid line) with the right-hand side of Equation 3.19 (dashed line). The constant of proportionality B is 0.5.

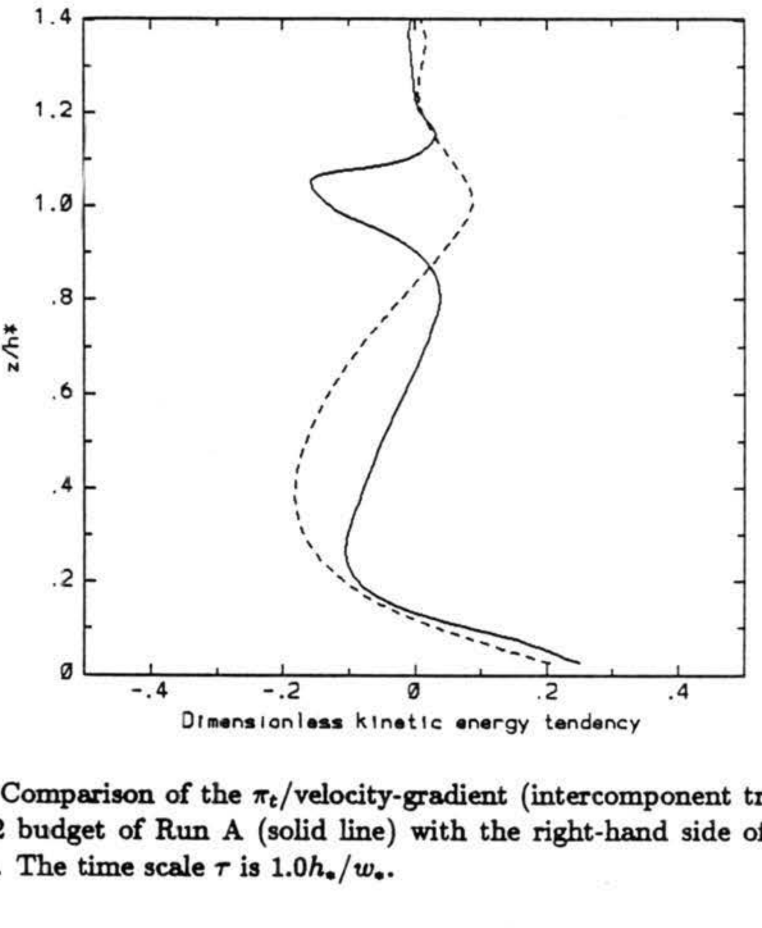

Figure 3.24. Comparison of the π_t/velocity-gradient (intercomponent transfer) term in the $\langle w'^2 \rangle_{h,t}/2$ budget of Run A (solid line) with the right-hand side of Equation 3.20 (dashed line). The time scale τ is $1.0h_*/w_*$.

Let us now turn our attention briefly to the subgrid stresses and the pressure field they maintain. The subgrid force can be divided into two parts,

$$-\frac{1}{\rho_0}\frac{\partial \rho_0 \tau_{ij}}{\partial x_j} = -\frac{1}{\rho_0}\frac{\partial \rho_0 2e/3}{\partial x_i} - \frac{1}{\rho_0}\frac{\partial \rho_0(\tau_{ij} - \delta_{ij}2e/3)}{\partial x_j}. \tag{3.21}$$

The first of these is dynamically somewhat like a pressure, exactly so if ρ_0 is constant. The second is parameterised in the model by a down-gradient diffusion relationship so its divergence is small, zero if the eddy viscosity K_m is constant. Neither ρ_0 nor K_m is constant, nevertheless to a very good approximation it is found that $\theta_0 \pi'_s \approx -2e'/3$, so the π_s-gradient force essentially just cancels the force due to gradients in e. The remaining, non-divergent, part of the subgrid force should dissipate the resolved velocity variances. If the model were to resolve an inertial subrange, then that dissipation would act mainly on the smallest scales and would be the same for all three velocity components. This assumption is tested in Figure 3.25 and found lacking. In the middle of the boundary layer, where a well-developed inertial subrange is most likely to be found, subgrid dissipation is two to three times as strong for the vertical velocity as it is for the horizontal velocities. This is consistent with the anisotropy noted earlier in the velocity spectra.

The transfer of turbulence kinetic energy between vertical and horizontal velocity components is summarised, in a vertically integrated sense, in Figure 3.26. Of the dimensionless buoyancy production of 0.306, 46% is dissipated by the non-divergent subgrid force acting on the w' field, 53% is transferred to the u' and v' fields and dissipated there, and a little more than 1% is exported to the absorbing layer. (This latter effect is described further below.) The time scale based on the vertically integrated kinetic energy divided by the vertically integrated subgrid destruction is $1.17h_*/w_*$. The net rate of change of vertically integrated kinetic energy is very small; it would be larger—around 5% of the buoyancy production—in the absence of subsidence. Of the energy transfer from the vertical to the horizontal velocity fields, about 85% is achieved by the buoyancy pressure and the remainder by the turbulence/turbulence pressure.

It has been argued above that if the model were more isotropic at small scales (and therefore more realistic) a greater fraction of the kinetic energy transfer to the

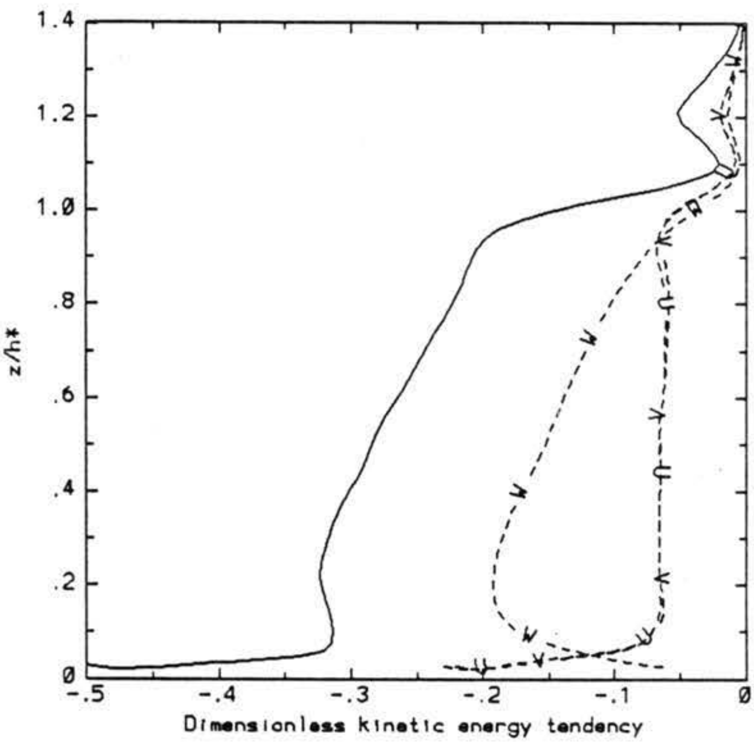

Figure 3.25. Profiles of the non-divergent subgrid terms in the turbulence kinetic energy and velocity variance budgets from Run A. The solid line shows the tendency in turbulence kinetic energy and the dashed lines (labelled u, v and w) show the tendencies in one-half the velocity variances.

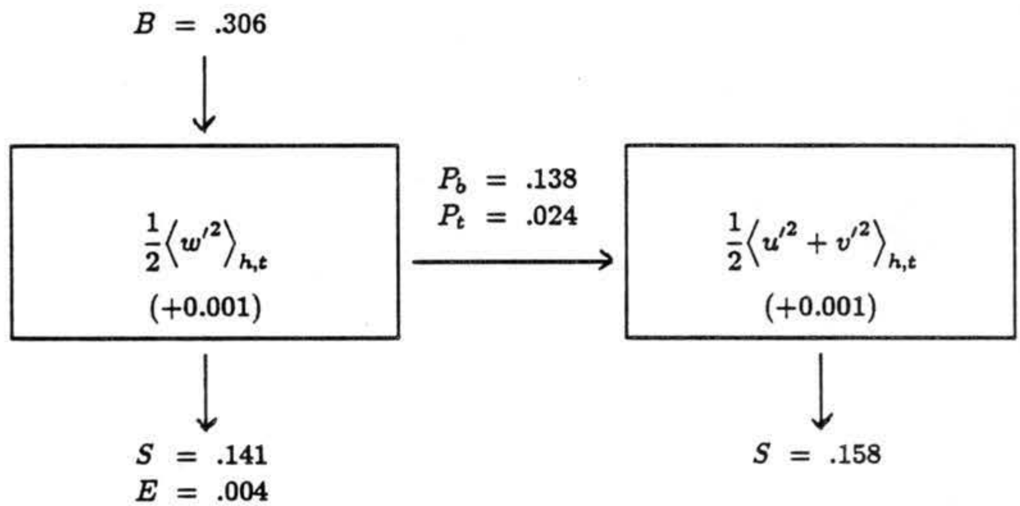

Figure 3.26. Vertical integrals of terms in the $\langle u_i'^2 \rangle_{h,t}/2$ budget of Run A. The terms are buoyancy (B), buoyancy pressure (P_b), turbulence pressure (P_t), non-divergent subgrid force (S) and export via $\langle w'\pi_b' \rangle_{h,t}$ to the absorbing layer (E). Energy transfer is in the direction indicated by the arrows. The numbers in parentheses inside the boxes indicate the observed rate of change of the turbulence kinetic energy components. All terms are made dimensionless with $w_*^3 h_{\rho *}/h_*$.

subgrid would be from the horizontal velocity fields; assuming small-scale isotropy at all levels, this fraction should be two thirds. How could the extra transfer from the vertical velocity field to the horizontal be achieved? It is hard to believe that the fraction A of buoyancy production transferred directly by the π_b-gradients should be much higher, since this would require that the buoyancy fluctuations dominating the heat flux have larger horizontal dimensions than vertical dimensions. One suspects, therefore, that the intercomponent transfer by the π_t-gradients should be more vigorous.

Several quantities that can be identified as kinetic energy fluxes appear in the budget equations. The velocity triple covariances $\langle w'u_i'^2/2\rangle_h$ appear in the turbulent transport term for their respective variances, and the velocity/pressure covariance $\langle w'\pi'\rangle_h$ appears in the pressure transport term in the vertical velocity variance budget. They are plotted in Figure 3.27. Not shown is another flux, $\langle 2w'e'/3\rangle_h$, that can be extracted from the isotropic part of the subgrid term. In the middle of the boundary layer $\langle w'^3/2\rangle_h$ is large and positive: it carries $\langle w'^2\rangle_h$ from the lower boundary layer, where buoyancy production is largest, to the upper boundary layer, where buoyancy production is small or negative. The horizontal velocity variance fluxes are much smaller, but it is apparent nevertheless from the budget in Figure 3.20 that they are significant in maintaining $\langle u'^2\rangle_h$ and $\langle v'^2\rangle_h$ in the middle of the boundary layer. The velocity triple covariances can be compared with atmospheric and fluid tank data, shown in Figure 3.28. The $\langle w'^3/2\rangle_h$ profile seems to be predicted well by the model (surprisingly well given that the skewness is definitely overestimated in the upper boundary layer). Deardorff and Willis' (1985) profile of horizontal velocity variance flux has a low-level maximum that is missing in the LES results, but this is based on a single data point and they comment that it may not be real.

The individual contributions to the velocity/pressure covariance are shown in Figure 3.29. The subgrid-pressure part just cancels out the $\langle 2w'e'/3\rangle_h$ flux mentioned above. Note also that the buoyancy-pressure supports a kinetic energy flux of a little less than $0.005w_*^3$ from just above $z = h_*$ up to the base of the absorbing layer. Presumably this

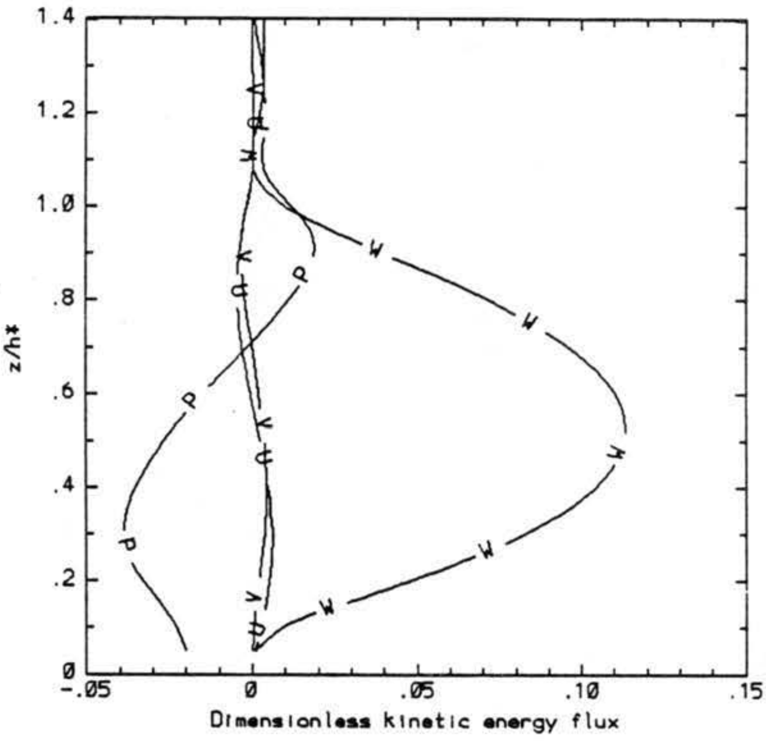

Figure 3.27. Profiles of vertical fluxes in resolved turbulence kinetic energy for Run A. The curves are $\langle w'u'^2\rangle_{h,t}/2$ (—U—), $\langle w'v'^2\rangle_{h,t}/2$ (—V—), $\langle w'^3\rangle_{h,t}/2$ (—W—) and $\langle w'\pi'\rangle_{h,t}$ (—P—). The first three are made dimensionless by w_*^3 and the last by $w_*\pi_*$.

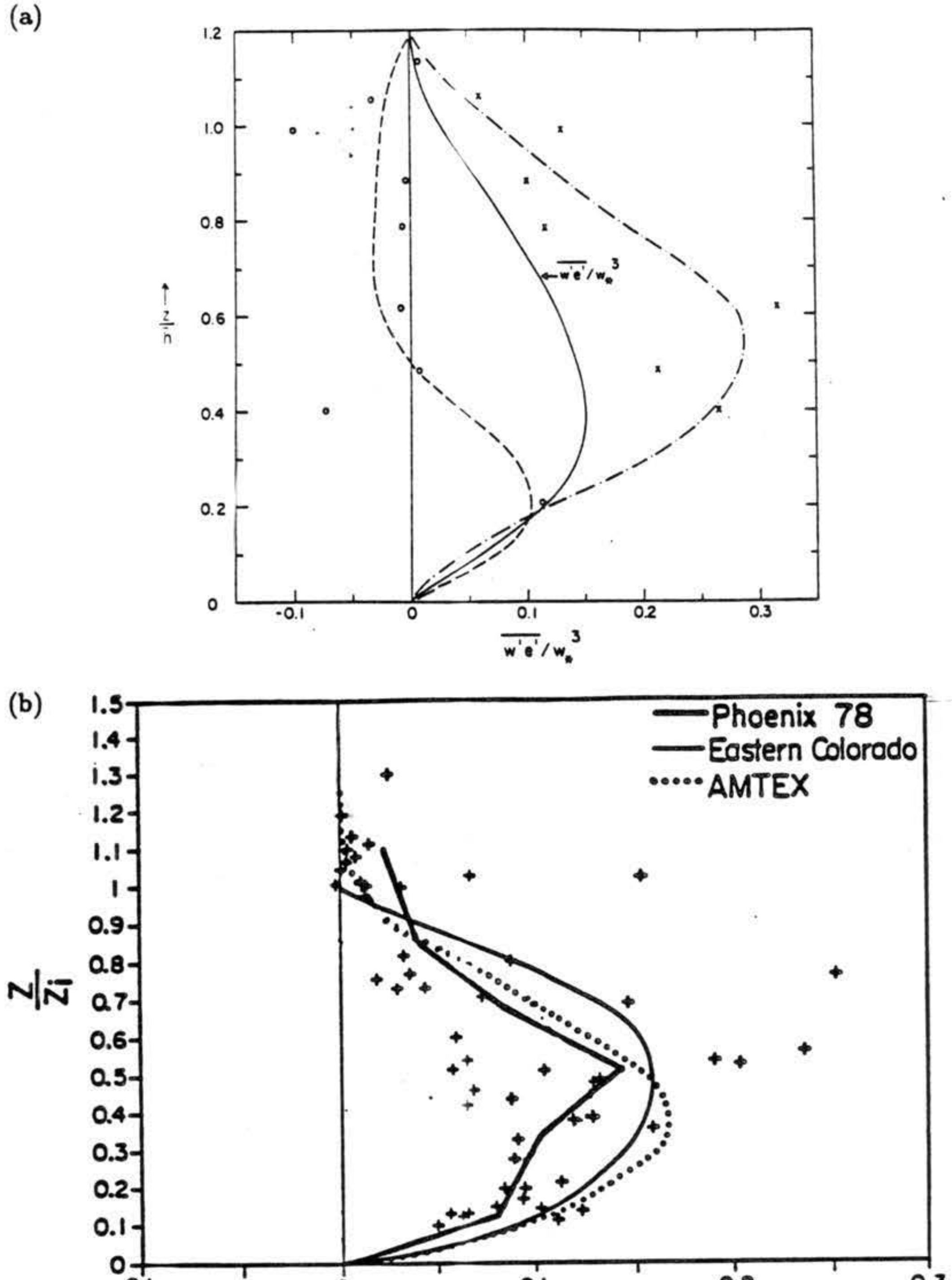

Figure 3.28. Profiles of turbulence kinetic energy flux from other studies. (a) Fluid tank results of Deardorff and Willis (1985): flux of horizontal velocity variance (dashed curve and o's), flux of vertical velocity variance (dash-dot curves and x's), and flux of turbulence kinetic energy (solid curve). (b) Atmospheric observations summarised by Young (1986).

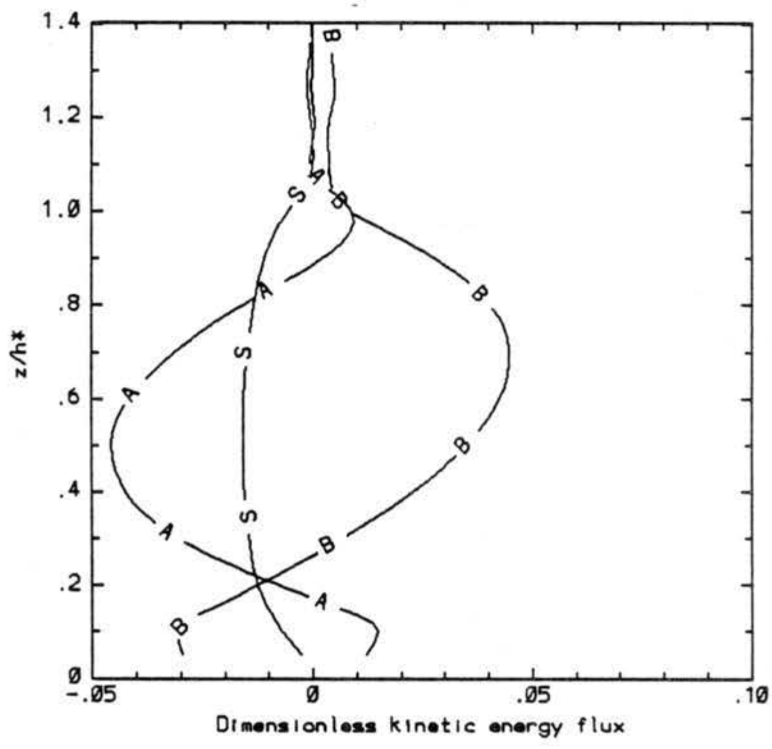

Figure 3.29. Profiles of contributions to dimensionless $\langle w'\pi' \rangle_{h,t}$ for Run A. Contributions are from the buoyancy pressure π_b (—B—), the turbulence pressure π_t (—T—) and the subgrid pressure π_s (—S—).

involves the propagation of gravity waves, which are evident in the instantaneous velocity and temperature fields above the inversion. The kinetic energy exported from the boundary layer in this way is dissipated by Rayleigh friction forces in the absorbing layer.

The buoyancy-pressure and advection-pressure fluxes can be compared with the predictions of isotropic tensor modelling (Zeman and Lumley, 1976), namely

$$\theta_0 \left\langle w'\pi_b' \right\rangle_h = 0 \tag{3.22}$$

$$\theta_0 \left\langle w'\pi_t' \right\rangle_h = -\frac{2}{5}\left\langle w'\frac{u_i'^2}{2}\right\rangle_h , \tag{3.23}$$

where summation over i is implied in the latter. Equation 3.22 is clearly not even approximately correct, since $\theta_0 \langle w'\pi_b' \rangle_h$ is comparable to the other fluxes in the upper boundary layer. The left-hand and right-hand sides of Equation 3.23 are compared in Figure 3.30. The curves agree to within a few percent at $z = 0.5h_*$, but elsewhere $\langle w'\pi_t' \rangle_h$ is less negative than predicted by the Zeman-Lumley expression. Note especially the regions of positive flux near $z = 0$ and $z = h_*$.

On the basis of the flux profiles just presented, along with profiles of moments and conditionally sampled statistics presented earlier, a qualitative model of the temperature, velocity and pressure structure in the boundary layer updraughts and downdraughts has been developed, and it is presented in Figure 3.31. (Conditionally sampled statistics of the pressure components have also been examined, but they are not presented because they do not show anything that is not apparent from the w/π covariances.) The temperature field (Figure 3.31a) is essentially a visualisation of the conditionally sampled θ fluctuations. The π_b field (Figure 3.31b) is constructed assuming that its pressure-gradient force in the vertical opposes the buoyancy; the zero contour at $z = 0.25h_*$ is implied by the pronounced minimum in $\langle \pi_b'^2 \rangle_h$ plus the zero-crossing in $\langle w'\pi_b' \rangle_h$. Given inflow at the base of the updraughts and outflow at the top, this π_b field transfers energy to $\langle u'^2 \rangle_h$ and $\langle v'^2 \rangle_h$ in the upper boundary layer and near the surface, which is indeed seen in the budgets in Figure 3.20.

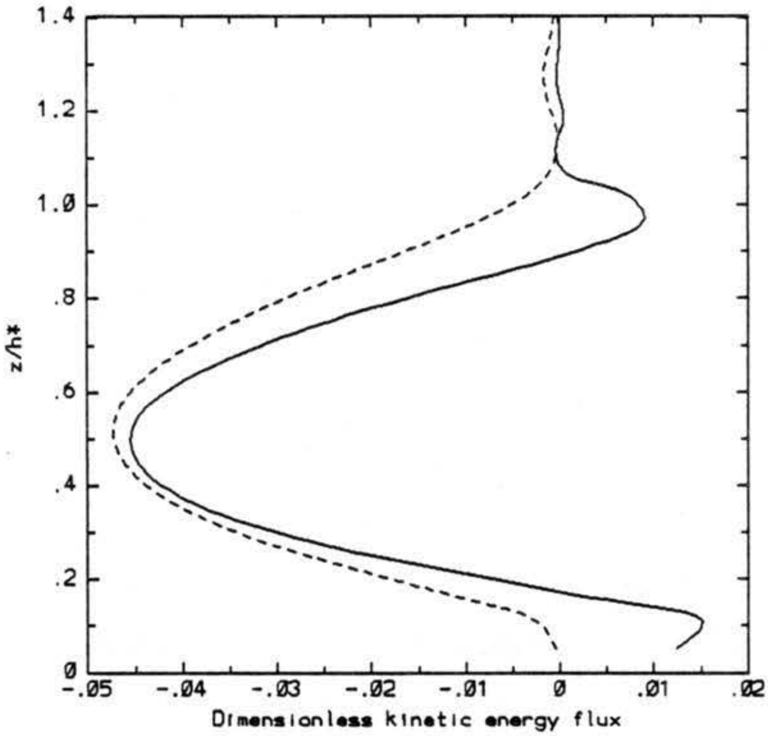

Figure 3.30. Comparison of dimensionless $\langle w'\pi_t' \rangle_{h,t}$ (solid line) with the right-hand-side of Equation 3.23 (dashed line) for Run A.

(a) θ':

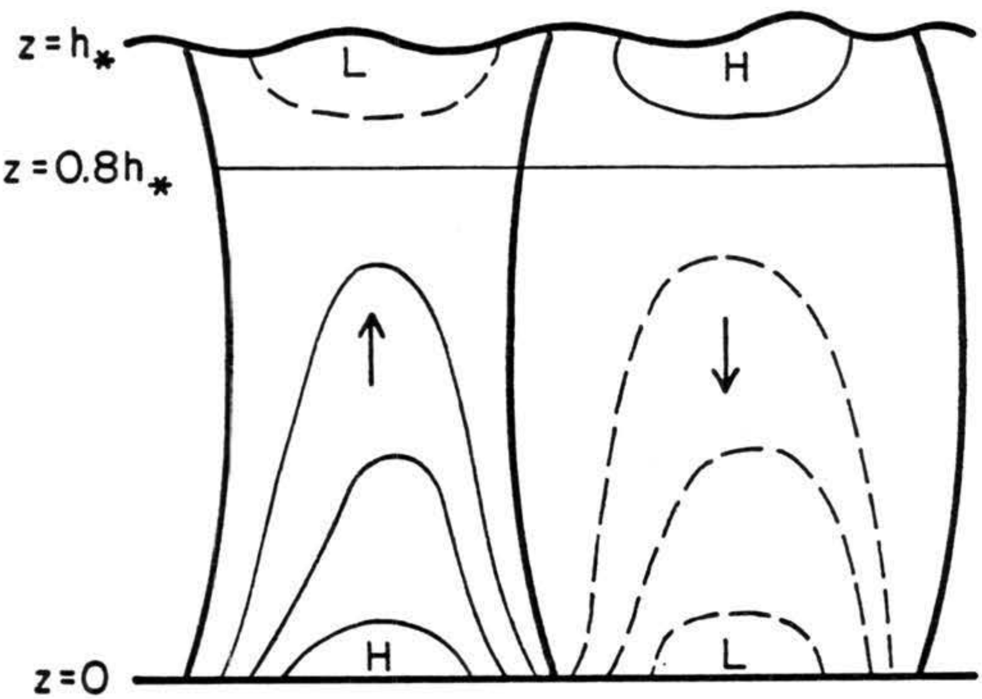

(b) π'_b:

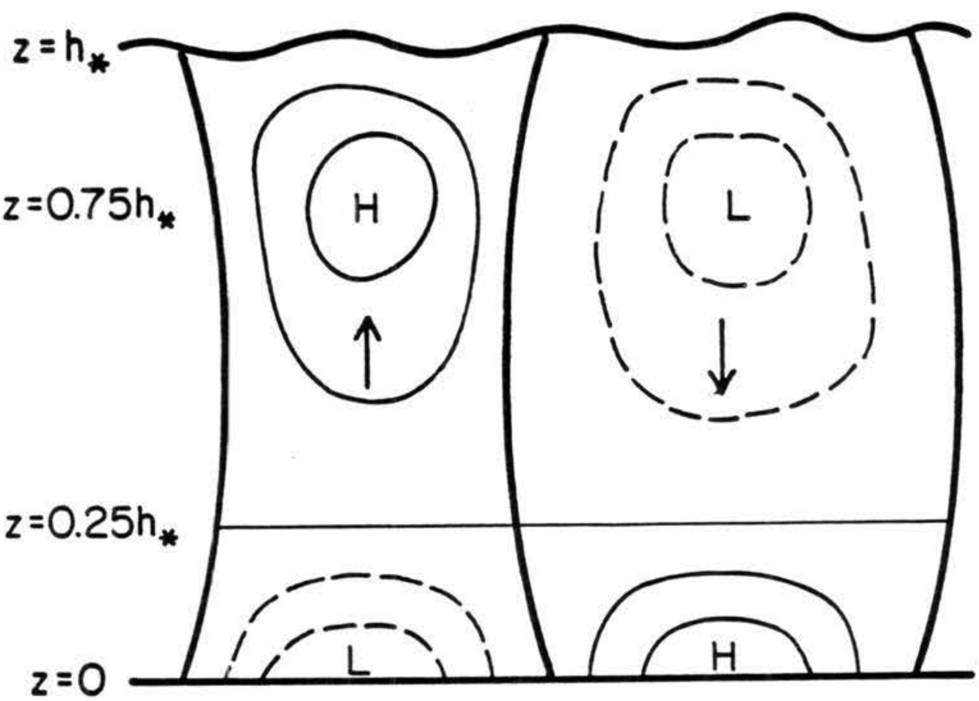

Figure 3.31. Qualitative model of the structure of updraughts and downdraughts. (a) Contours of θ'. (b) Contours of π'_b. (c) Contours of $\nabla^2\pi_t$. (d) Contours of π_t. Negative contours are dashed; zero and positive contours are solid.

Continued on following page.

(c) $\nabla^2 \pi_t$:

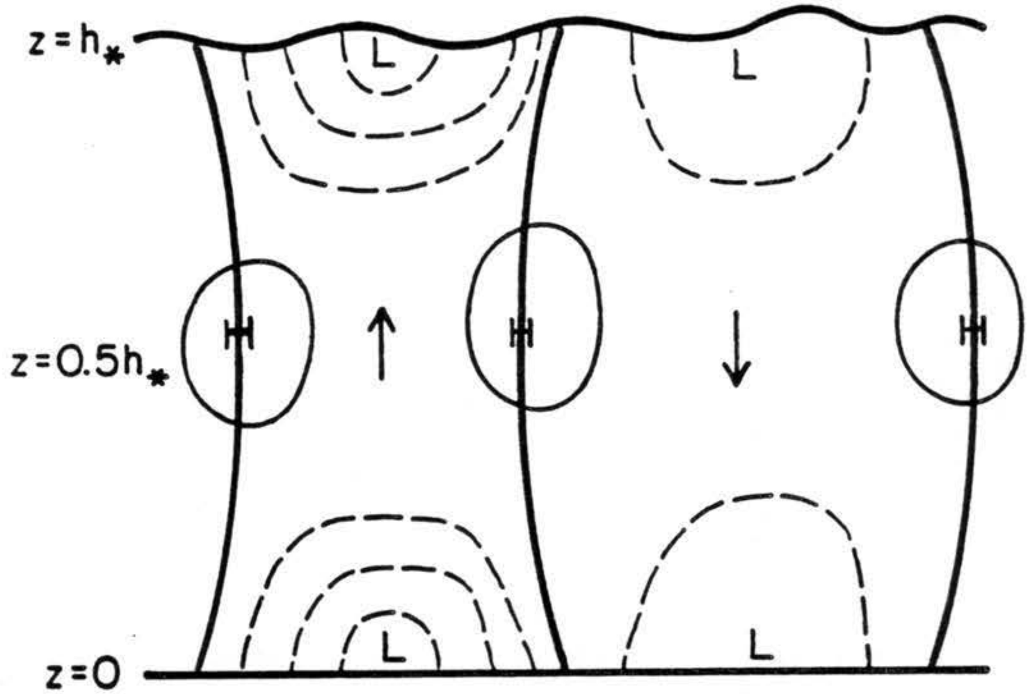

(d) π_t:

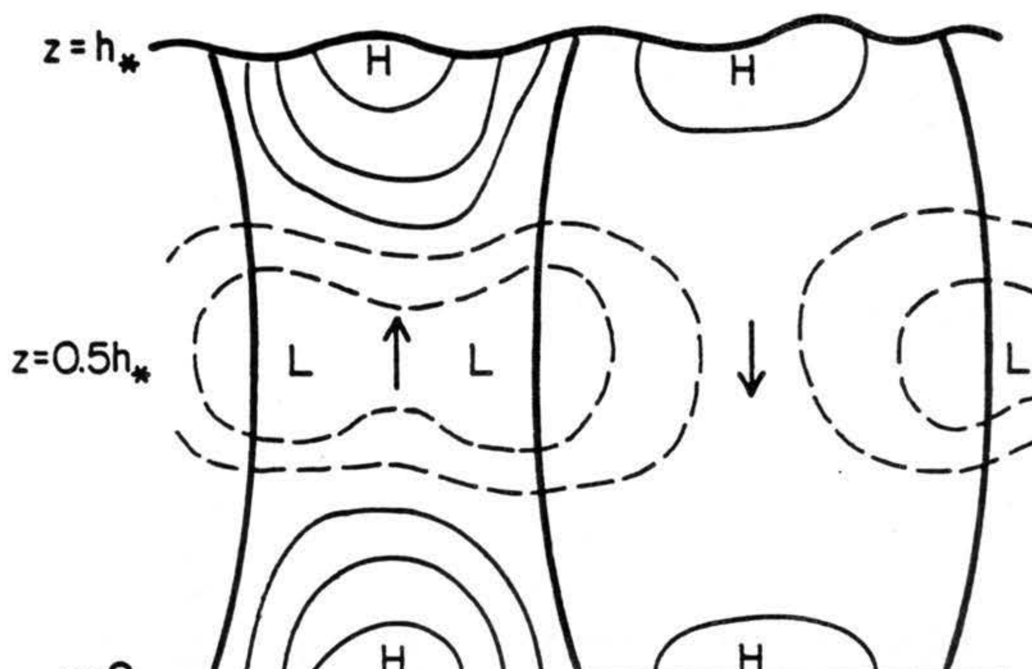

Figure 3.31 (continued).

To visualise the turbulence/turbulence component of pressure consider first a very simple two-dimensional vertical velocity field,

$$w' = W\cos(\pi x/l)\,\sin(\pi z/h), \tag{3.24}$$

bounded by solid surfaces at $z=0$ and $z=h$. (The symbol π here stands for the ratio of the circumference of a circle to its diameter, rather than pressure, but this should not cause any confusion.) The updraughts have width l and are centred at $x=2nl$ where n is an integer. Assuming ρ_0 and θ_0 are constant, the horizontal velocity field required for mass continuity is

$$u' = -(l/h)W\sin(\pi x/l)\,\cos(\pi z/h) \tag{3.25}$$

and the elliptic equation for pressure is

$$\theta_0\nabla^2\pi_t = (\pi/h)^2\,W^2\left(\sin^2\frac{\pi x}{l}\,\sin^2\frac{\pi z}{h} - \cos^2\frac{\pi x}{l}\,\cos^2\frac{\pi z}{h}\right). \tag{3.26}$$

It is straightforward to show that

$$\theta_0\pi_t = \frac{W}{4}\left(\cos\frac{2\pi z}{h} + \frac{l^2}{h^2}\cos\frac{2\pi x}{h}\right). \tag{3.27}$$

This has local maxima in pressure ($\nabla^2\pi_t < 0$) on the axes of the updraughts and downdraughts at $z=0$ and $z=h$; it has local minima in pressure ($\nabla^2\pi_t > 0$) on the boundaries between the updraughts and downdraughts at $z=0.5h$. The pressure variance $\langle\pi_t'^2\rangle_h$ is constant with height and by symmetry $\langle w'^3\rangle_h$ and $\langle w'\pi_t'\rangle_h$ are both zero everywhere.

The qualitative model of π_t in boundary layer updraughts and downdraughts (Figures 3.31c and 3.31d) takes account of the simple model presented above, but recognises that the updraughts are narrower and more vigorous than the downdraughts. Because the updraughts are narrower, the neighbouring regions of maximum $\nabla^2\pi_t$ on either side of the updraught are hypothesised to produce lower pressure within the updraught than within the downdraught. In other words $\langle w'\pi_t'\rangle_h$ opposes $\langle w'^3\rangle_h$, which is roughly the phenomenon described by Equations 3.19 and 3.23. It is also hypothesised that the maxima in π_t at the base of the updraughts are stronger than the maxima at the base of the downdraughts (the updraughts being more vigorous) so that $\langle w'\pi_t'\rangle_h$ is positive near the surface and, by a similar argument, near the inversion.

The qualitative model is thus consistent with the profile of $\langle w'\pi_t'\rangle_h$ in the large-eddy model. Furthermore it predicts the destruction of horizontal velocity variance by the velocity/π_t-gradient term near the surface and its production near the inversion. (The former is also predicted by a return-to-isotropy mechanism, but the latter is not.) It is unclear whether the qualitative model is consistent with the observed intercomponent transfer in the middle of the boundary layer and one expects that in this term unsteady flow structures are crucial.

3.3.2 *Heat flux budget*

The heat flux budget equation is

$$\begin{aligned}\frac{\partial}{\partial t}\langle w'\theta'\rangle_h &= +\frac{g}{\theta_0}\left\langle\theta'^2\right\rangle_h - \theta_0\left\langle\theta'\frac{\partial\pi'}{\partial z}\right\rangle_h - \left\langle w'^2\right\rangle_h\frac{\partial\langle\theta\rangle_h}{\partial z}\\ &\quad -\frac{1}{\rho_0}\frac{\partial}{\partial z}\left\langle\rho_0 w'^2\theta'\right\rangle_h - \frac{1}{\rho_0}\left\langle\theta'\frac{\partial}{\partial x_j}\rho_0\tau_{3j}' + w'\frac{\partial}{\partial x_j}\rho_0\phi_j'\right\rangle_h.\end{aligned} \tag{3.28}$$

The first term on the right-hand side is buoyancy production, proportional to the θ variance; the second is a temperature/pressure-gradient term; the third is (potential temperature) gradient production, which drives the heat flux down-gradient; the fourth is turbulent transport and the last is the subgrid term. These terms are plotted in Figure 3.32a. In the lower boundary layer, heat flux is generated by buoyancy production and gradient production. These are balanced by the pressure-gradient term, turbulent transport and subgrid diffusion. Between $z = 0.4h_*$ and $z = 0.8h_*$, where the lapse rate is stable, the positive heat flux is maintained by turbulent transport and buoyancy production (which itself is largely maintained by turbulent transport of variance—see Section 3.3.3). Near the top of the boundary layer the major terms are the gradient term, which is driving the negative heat flux, the buoyancy term, which opposes it, and the pressure term. In Figure 3.32b the pressure term is divided into contributions from the pressure fields generated by buoyancy, advection (dominated as before

(a)

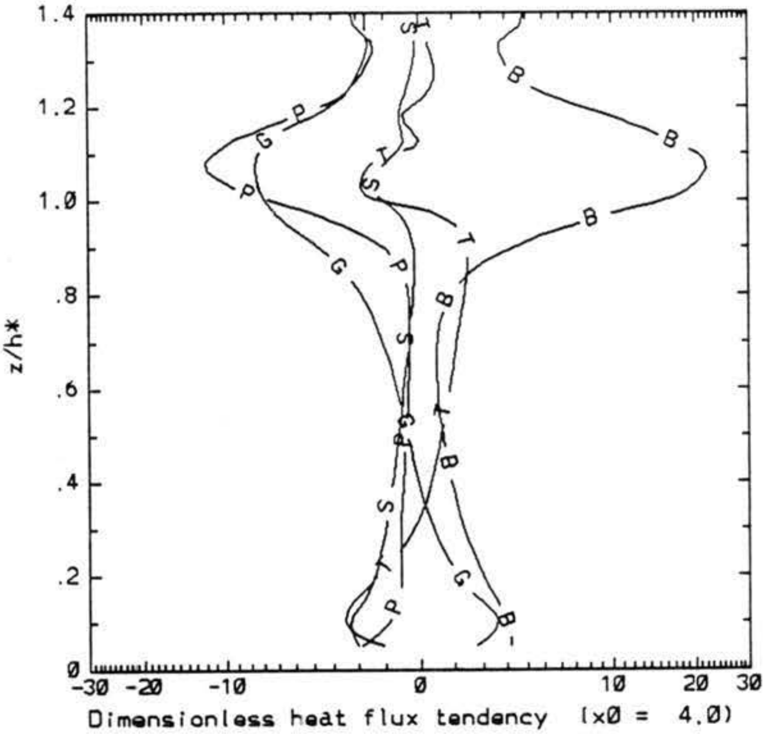

(b)

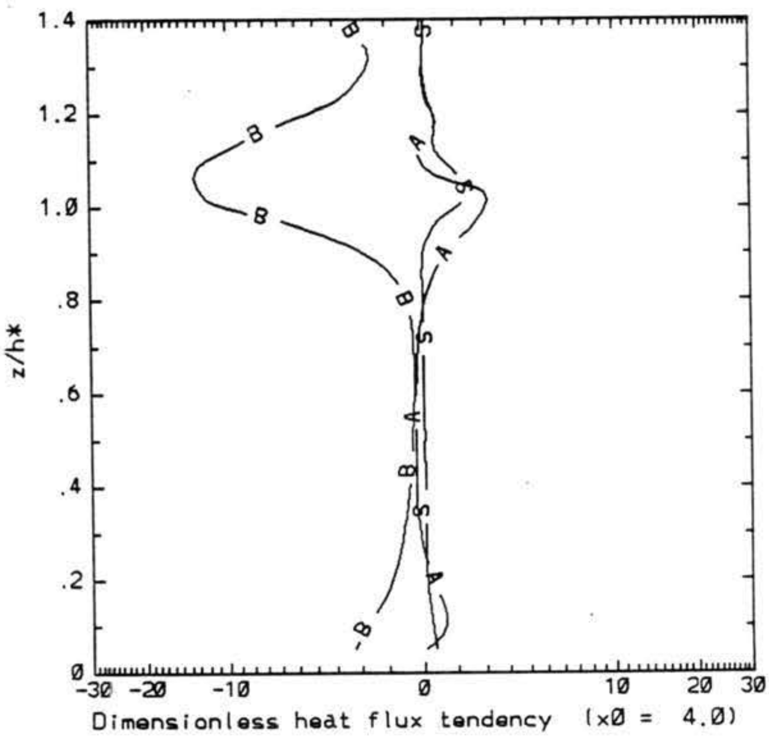

Figure 3.32. Profiles of terms in the resolved heat flux budget $(\partial/\partial t)\langle w'\theta'\rangle_{h,t}$ for Run A. (a) Buoyancy (—B—), pressure (—P—), gradient production (—G—), turbulent transport (—T—) and subgrid (—S—). (b) Temperature/π-gradient contributions from buoyancy pressure π_b (—B—), advection pressure π_a (—A—) and subgrid pressure π_s (—S—). All terms made dimensionless with $w_*^2\theta_*/h_*$.

by turbulence/turbulence interaction) and subgrid stresses. These will be discussed below.

It is interesting to divide the heat flux tendency into two parts

$$\frac{\partial}{\partial t}\langle w'\theta'\rangle_h = \left\langle \theta' \frac{\partial w'}{\partial t} \right\rangle_h + \left\langle w' \frac{\partial \theta'}{\partial t} \right\rangle_h \tag{3.29}$$

associated respectively with tendencies in w' and θ'. These are plotted in Figure 3.33 and it is apparent that at all levels the balance in heat flux is maintained by net positive acceleration in warm regions and net cooling in regions where the vertical velocity is positive.[9] In the lower boundary layer, $\langle \theta' \partial w'/\partial t \rangle_h$ and $\langle w' \partial \theta'/\partial t \rangle_h$ are each much smaller than the individual tendencies that produce them, so here it should be satisfactory to assume that updraughts and downdraughts are each close to a steady state. (An analogous assumption is implicit in Young's (1986) conditional-sampling analysis of boundary layer dynamics, for example.) At and above the top of the boundary layer, such an assumption is clearly not satisfactory. Here regions with rising motion are continually becoming cooler, but this does not continue indefinitely at any place because buoyancy forces eventually become large enough to reverse the vertical motion.

Let us now examine the dynamics of the inversion and its vicinity a little more closely. Long (1978) and Carruthers and Hunt (1987) have argued that entrainment is effected by the overturning of gravity waves trapped in the vicinity of the inversion. Carruthers and Moeng (1987) have shown that the heat flux budget in this region of Moeng's model is consistent with the existence of a resonant gravity wave mode, with properties depending on the thickness and stratification of the inversion layer. The major terms in the heat flux budget are then the buoyancy term, the buoyancy-pressure term and the gradient production term. Carruthers and Moeng find that the turbulent transport term is much smaller than the three just listed and this is also true (to a slightly lesser extent) for the

[9]This sentence could just have well been written with every occurrence of "positive" replaced by "negative", every occurrence of "warm" replaced by "cool", and so on. The fact that a second moment like $\langle a'b' \rangle_h$ is positive, say, does not imply whether it is dominated by positive-a'/positive-b' or negative-a'/negative-b' events. In general only one such set of possibilities will be made explicit.

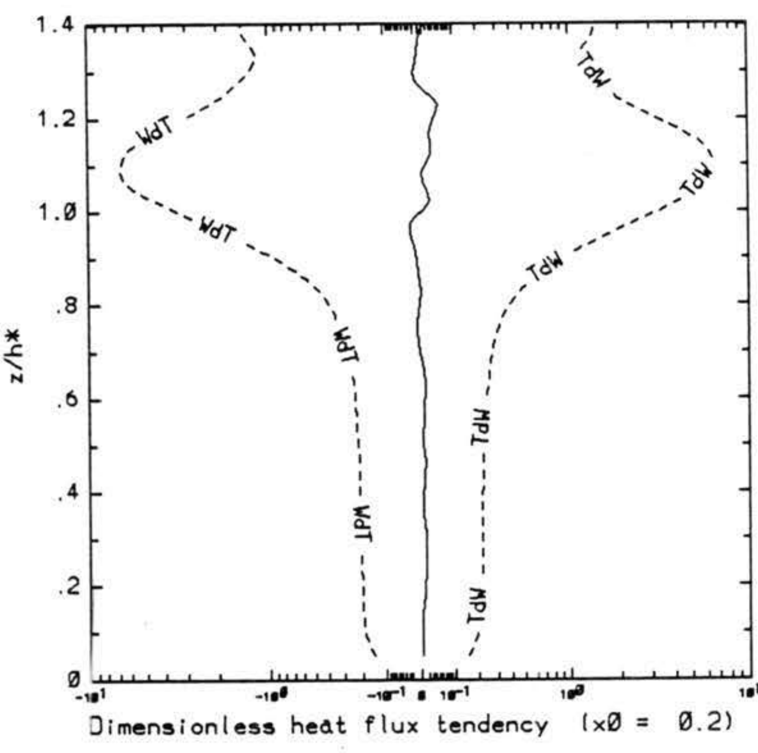

Figure 3.33. Decomposition of the heat-flux tendency $(\partial/\partial t)\langle w'\theta'\rangle_{h,t}$ (solid line) in Run A into $\langle w'\partial\theta'/\partial t\rangle_{h,t}$ (--WdT--) and $\langle \theta'\partial w'/\partial t\rangle_{h,t}$ (--TdW--).

present model. It is interesting, however, to decompose the turbulent transport into the parts associated with turbulent advection of w' and θ', i.e.,

$$-\frac{1}{\rho_0}\frac{\partial}{\partial z}\left\langle \rho_0 w'^2\theta'\right\rangle_h = -\left\langle \theta' u'_j \frac{\partial w'}{\partial x_j}\right\rangle_h - \left\langle w' u'_j \frac{\partial \theta'}{\partial x_j}\right\rangle_h . \tag{3.30}$$

These are shown in Figure 3.34. In the lower boundary layer w'-advection and θ'-advection both act to reduce the positive heat flux, but near the inversion they oppose each other. The former is negative there and describes a tendency for turbulent advection to impart negative momentum to warm regions. The latter term is positive near the inversion and describes a tendency for turbulent cooling of regions where the flow is downward. These processes act together to incorporate air from above the inversion into the boundary layer and generate a negative heat flux. Note that, whereas the "gravity wave" terms in the heat flux budget remain large well above the top of the boundary layer, the turbulent advection terms drop off sharply at $z = 1.10h_*$. This is the height of the second zero-crossing in the heat flux, which Nieuwstadt and de Valk (1987) have found is the maximum height reached by material released within the boundary layer of their large-eddy simulation. It is also close to the maximum height reached by particles released in the boundary layer in the present model (Chapter 6).

Turning now to the effect of pressure-gradient forces, first it should be noted that the subgrid pressure π_s again essentially cancels the isotropic part of the subgrid force. The sum of the subgrid and π_s-gradient tendencies in heat flux (the non-divergent subgrid term) is very small near the inversion, but increases towards the surface. In the lower boundary layer it is comparable to the turbulent transport term.

The temperature/π_b-gradient term (Figure 3.35) is described very well by the expression

$$-\theta_0\left\langle \theta' \frac{\partial \pi'_b}{\partial z}\right\rangle_h = -A(z)\,\frac{g}{\theta_0}\left\langle \theta'^2\right\rangle_h , \tag{3.31}$$

where $A(z)$ has the same profile defined earlier (Equation 3.16). Moeng and Wyngaard (1986b) have proposed a similar expression for their scalar flux budgets, with $A = 0.5$. The justification for letting A be a function of height was presented in the previous section.

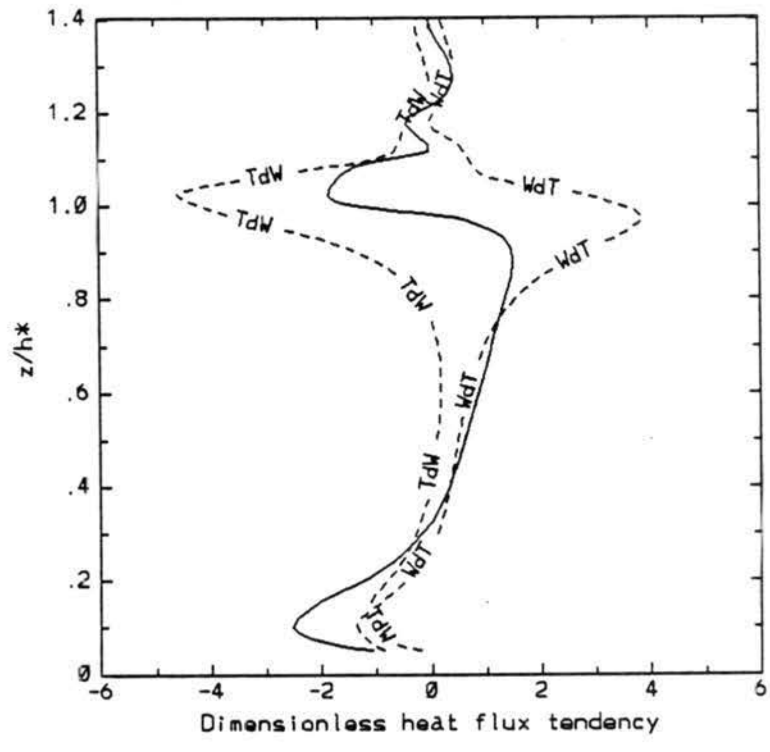

Figure 3.34. Decomposition of the turbulent transport term (solid line) in the $\langle w'\theta'\rangle_{h,t}$ budget of Run A into terms associated with turbulent advection of θ' (--WdT--) and turbulent advection of w' (--TdW--).

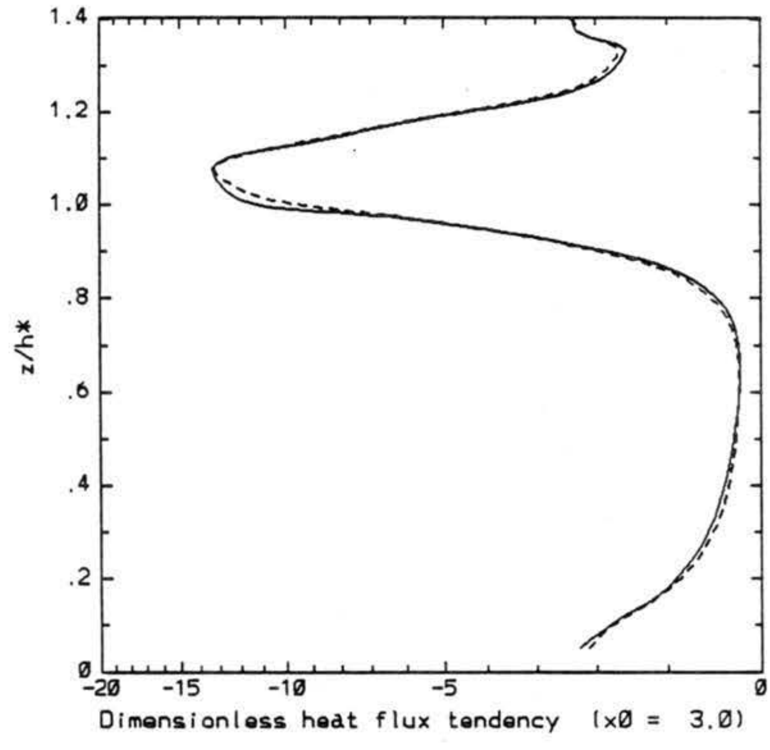

Figure 3.35. Comparison of the temperature/π_b-gradient term (solid line) in the $\langle w'\theta' \rangle_{h,t}$ budget of Run A with the right-hand side of Equation 3.31 (dashed line). The constant of proportionality A is given by Equation 3.16.

The temperature/π_t-gradient term is described tolerably well by an expression analogous to Equation 3.19, namely

$$-\theta_0 \left\langle \theta' \frac{\partial \pi_t'}{\partial z} \right\rangle_h = B \left\langle \theta' u_j' \frac{\partial w'}{\partial x_j} \right\rangle_h . \tag{3.32}$$

(Unlike Equation 3.19 this is not really a *closure* expression, because the right-hand side does not by itself reduce to an easily measured quantity.) The comparison is made in Figure 3.36 with $B = 0.5$. Again agreement is good near the surface and near the inversion, but poor in the middle of the boundary layer. Moeng and Wyngaard, on the other hand, have

$$-\theta_0 \left\langle \theta' \frac{\partial \pi_t'}{\partial z} \right\rangle_h < 0$$

throughout the lower boundary layer.[10] They propose a return-to-isotropy expression (also plotted in Figure 3.36),

$$-\theta_0 \left\langle \theta' \frac{\partial \pi_t'}{\partial z} \right\rangle_h = -\frac{1}{\tau} \langle w'\theta' \rangle_h , \tag{3.33}$$

with τ a positive time scale. For Run A this expression has the wrong sign below $z = 0.25h_*$. It will be argued below that in both the models the role of the π_t-gradient in the heat flux budget is significantly different from its role in a real fluid.

Two quantities that can be identified as fluxes of heat flux can be extracted from the budget equations. The first, $\langle w'^2\theta' \rangle_h$, appears in the turbulent transport term and the second, $\langle \pi'\theta' \rangle_h$, can be extracted from the pressure term (see, for example, Moeng and Wyngaard, 1986b). The former is plotted in Figure 3.37, along with a profile from Moeng and Wyngaard (1986b) and a profile derived by Lenschow *et al.* (1980) from data collected during the Air Mass Transformation Experiment (AMTEX). The profile from Run A is rather different from Moeng and Wyngaard's, being more positive throughout the lower and middle boundary layer. Note that their profile is negative below $z = 0.1h_*$, which may be related to the negative skewness in vertical velocity noted earlier (Section 3.2.7).

---

[10]Note that Figures 2 and 3 in Moeng and Wyngaard (1986b) are wrongly labelled, and that it is Figure 3 which shows the pressure terms in the heat flux budget.

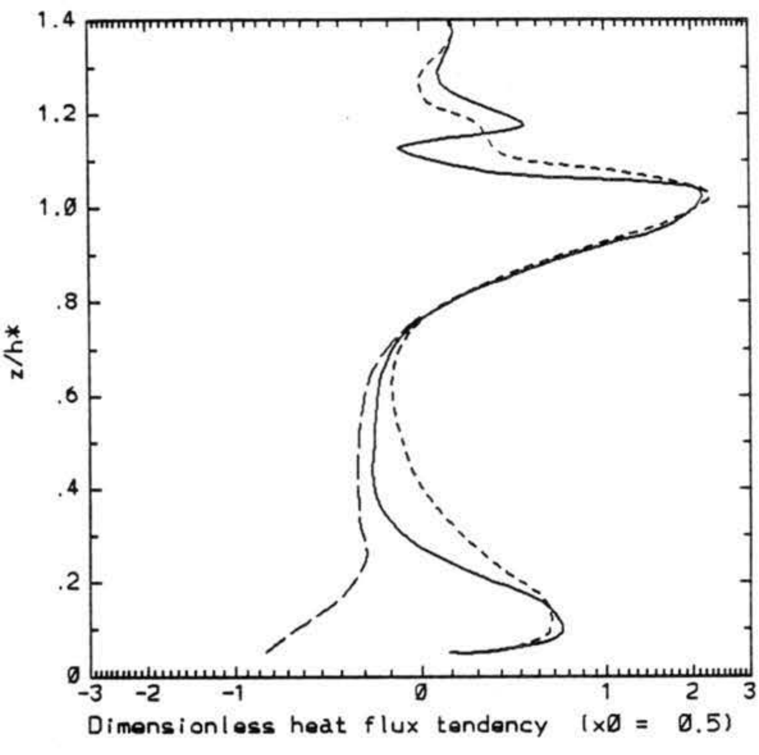

Figure 3.36. Comparison of the temperature/π_t-gradient term (solid line) in the $\langle w'\theta'\rangle_{h,t}$ budget of Run A with the right-hand sides of Equations 3.32 (short dashes) and 3.33 (long dashes). The constant of proportionality B in Equation 3.32 is 0.5 and the time scale τ in Equation 3.33 is calculated from the Moeng and Wyngaard's (1986b) Equation 45.

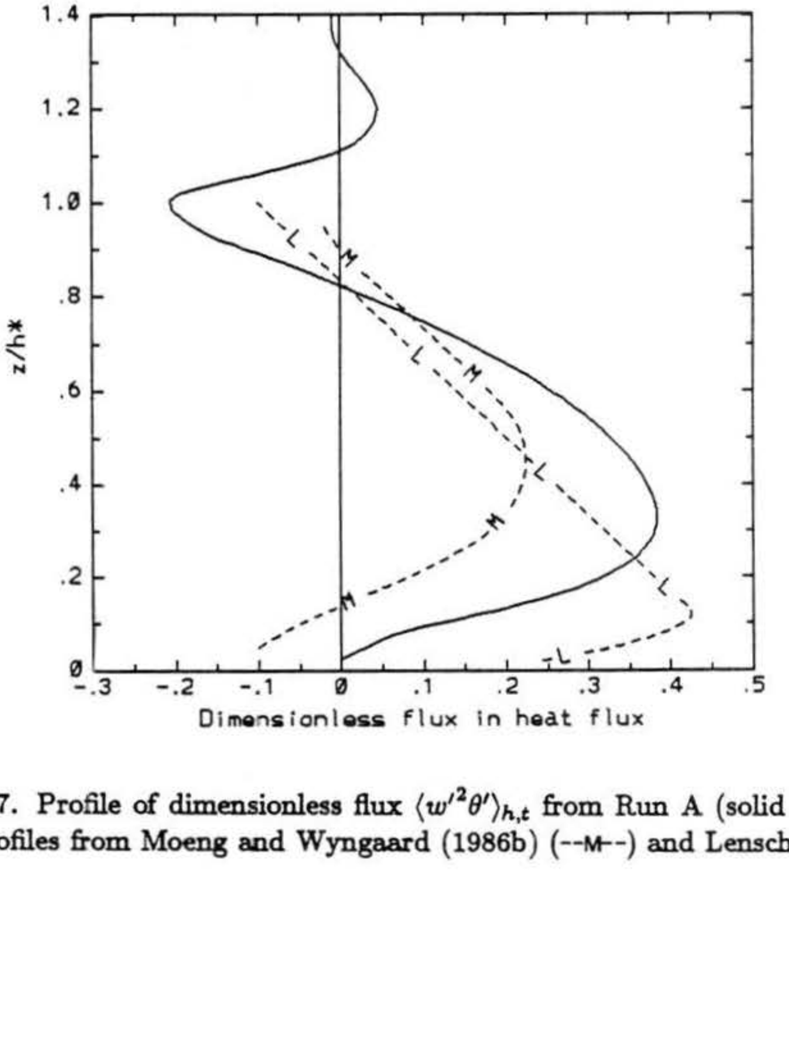

Figure 3.37. Profile of dimensionless flux $\langle w'^2\theta' \rangle_{h,t}$ from Run A (solid line) with comparable profiles from Moeng and Wyngaard (1986b) (--M--) and Lenschow *et al.* (1980) (--L--).

The atmospheric profile differs from the LES profile mainly in that its maximum is at a much lower level. This has important implications for the turbulent transport term in the budget, as will be discussed below. Moeng and Wyngaard (1988) have recently presented $\langle w'^2\theta'\rangle_h$ profiles from their 96 × 96 × 96 simulation. Those results are much more similar to the present ones, having a maximum of $0.4w_*\theta_*^2$ at $z=0.3h_*$ and lacking a negative region near the surface.

The profile of pressure/temperature covariance is plotted in Figure 3.38a along with the profile from Moeng and Wyngaard (1986b). Again the two models differ, Moeng and Wyngaard having this quantity approximately twice as negative throughout the lower boundary layer. The net transport of heat flux towards the surface by $\langle w'^2\theta'\rangle_h + \langle\pi'\theta'\rangle_h$ is therefore considerably stronger in their model. In Figure 3.38b the contributions to $\langle\pi'\theta'\rangle_h$ from the buoyancy and advection forces are shown. The profiles are consistent with the qualitative model of updraught temperature and pressure structure in Figure 3.31. Note in particular that the turbulence/turbulence part $\langle\pi_t'\theta'\rangle_h$ is positive near the surface, which, given the high correlation between w and θ at these levels, is consistent with the idea that π_t is higher at the base of updraughts than at the base of downdraughts.

It is interesting to consider what relationship the budget for resolved heat flux in the model has with the budget for turbulent heat flux covering all scales—i.e., $\langle\tilde{w}'\tilde{\theta}'\rangle_h$—in the atmosphere or the laboratory. Consider the layer between $z=0.1h_*$ and $z=0.4h_*$. The former height can be loosely identified as the top of the surface free convection layer and the latter is the height where the temperature gradient (in the model at least) changes sign. Throughout this layer the model underestimates the buoyancy production (temperature variance) by a factor between two and four. From fluid tank and observational data presented earlier in Figure 3.8, $\langle\theta'^2\rangle_h$ is $\sim 8\theta_*^2$ at $z=0.1h_*$ and $\sim 2\theta_*^2$ at $z=0.4h_*$, so the average dimensionless buoyancy production within the layer is $\sim 4w_*^2\theta_*/h_*$. On the other hand the gradient production calculated by the model, which averages $\sim 1w_*^2\theta_*/h_*$ in the layer, is probably approximately correct because the model has a realistic vertical velocity variance and a plausible potential temperature gradient. Certainly it is hard to

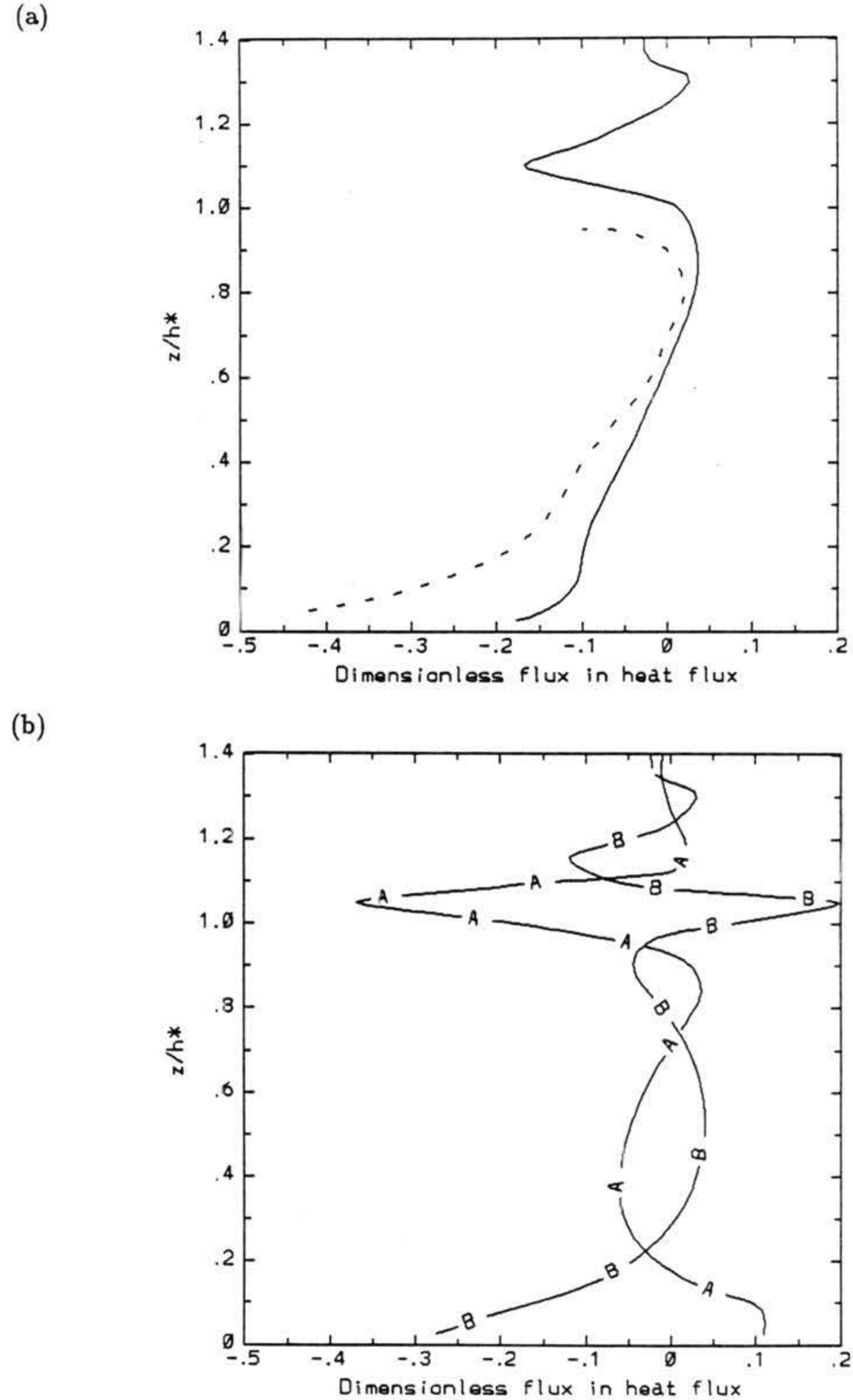

Figure 3.38. Profiles of dimensionless pressure/temperature covariance $\langle\theta'\pi'\rangle_{h,t}$ from Run A. (a) Pressure/temperature covariance (solid line) with a comparable profile from Moeng and Wyngaard (1986b) (dashed line). (b) Contributions to $\langle\theta'\pi'\rangle_{h,t}$ from buoyancy pressure π_b (—B—) and advection pressure π_a (—A—).

imagine that $\partial\langle\theta\rangle_h/\partial z$ could be sufficiently *stable* for gradient production to cancel much of the buoyancy production. How then are these production terms balanced?

In the model the major sink terms are due to resolved turbulent advection (turbulent transport) and subgrid processes. The latter are absent from the $\langle\tilde{w}'\tilde{\theta}'\rangle_h$ budget, of course, and the molecular diffusion terms which replace them are expected to be zero because of local isotropy (Wyngaard, 1980). Furthermore from the Lenschow *et al.* profile in Figure 3.37, turbulent transport in the atmosphere is not a sink but a weak source, $\sim 0.4w_*^2\theta_*/h_*$, in the layer. This leaves a surplus production of $\sim 6w_*^2\theta_*/h_*$ to be balanced by the temperature/pressure-gradient covariances. If the buoyancy-pressure term acts in the same way in a real fluid as it does in the model, i.e., to oppose about one-half of the buoyancy force, then the turbulence/turbulence contribution to $\theta_0\langle\theta'\partial\pi'/\partial z\rangle_h$ must be negative in the layer, with average value $\sim -4w_*^2\theta_*/h_*$. This is consistent with a return-to-isotropy expression like Equation 3.33, but the time scale required is quite short, of order $0.2h_*/w_*$. In the present model the time scale is negative in the lower boundary layer, and in Moeng and Wyngaard's it is positive but still much too large, ~ 1 to $2h_*/w_*$.

3.3.3 *Temperature variance budget*

The temperature variance budget equation is

$$\frac{\partial}{\partial t}\left\langle\theta'^2\right\rangle_h = -2\langle w'\theta'\rangle_h\frac{\partial}{\partial z}\langle\theta\rangle_h - \frac{1}{\rho_0}\frac{\partial}{\partial z}\left\langle\rho_0 w'\theta'^2\right\rangle_h - \frac{2}{\rho_0}\left\langle\theta'\frac{\partial}{\partial x_j}\left(\rho_0\phi_j'\right)_h\right\rangle_h \tag{3.34}$$

where the terms on the right-hand side are gradient production, turbulent transport and subgrid dissipation, respectively. They are plotted in Figure 3.39. Variance is generated by down-gradient heat flux near the surface; most is dissipated locally but some is transported up into the middle boundary layer to maintain the variance against the counter-gradient heat flux there. There is a second maximum in gradient production associated with the entrainment flux near $z = h_*$. The vertical flux $\langle w'\theta'^2\rangle_h$ is plotted in Figure 3.40, along with a profile from Lenschow *et al.* (1980) based on AMTEX observations. The model is unable to resolve the very large fluxes near the surface, but

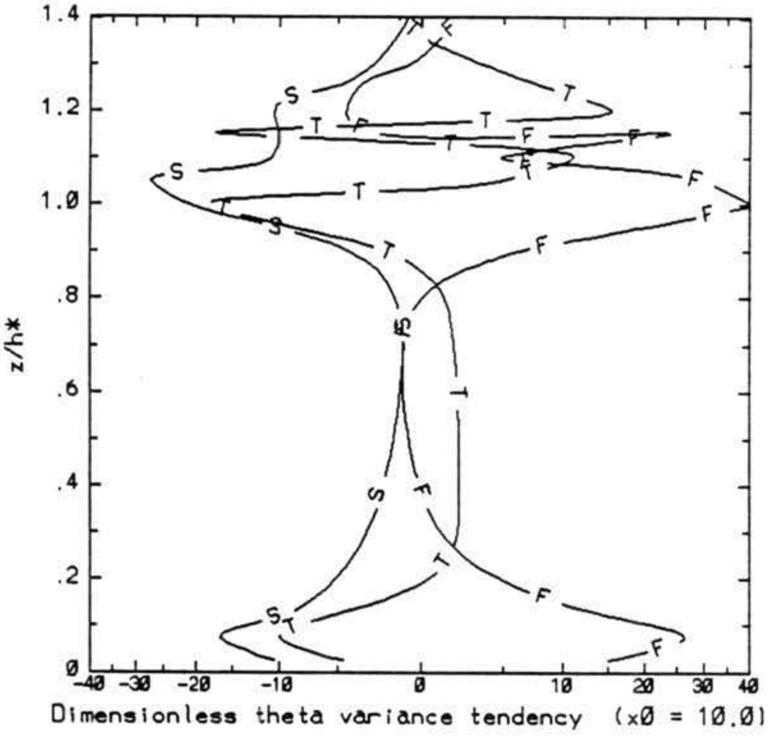

Figure 3.39. Profiles of terms in the resolved θ variance budget $(\partial/\partial t)\langle\theta'^2\rangle_{h,t}$ for Run A. The terms are gradient production (—G—), transport (—T—), and subgrid diffusion (—S—). All are made dimensionless with $w_*\theta_*^2/h_*$.

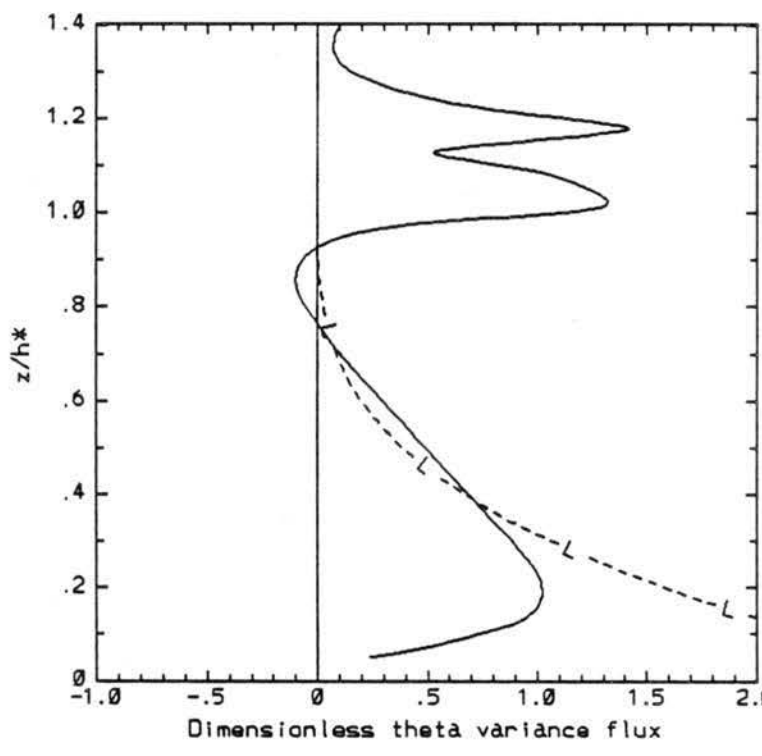

Figure 3.40. Profile of the dimensionless flux in temperature variance $\langle w'\theta'^2\rangle_{h,t}$ from Run A (solid line) compared with the profile of Lenschow *et al.* (1980) (--L--).

it is in agreement with the observed profile above $z=0.3h_*$. The small region of negative flux around $z=0.9h_*$ has some observational support too, according to Lenschow *et al.*, although that is not reflected in their profile. On the other hand the large positive flux above $z=h_*$ is not apparent in observations, which admittedly are very widely scattered in this region.

It is now appropriate to look at the circulations centred around $z=1.2h_*$ that were mentioned in connection with the $\partial\langle\theta\rangle_h/\partial z$ profile. There is a secondary maximum in $\langle w'^2\rangle_h$ at this level (Figure 3.4) which is also apparent in some of Moeng's (1984) profiles (Figure 3.5a). Carruthers and Hunt (1987) have postulated that it is due to the presence of trapped waves. Looking at the vertical velocity variance budget (Figure 3.19a), one sees that the only positive term in this region is buoyancy production, associated with a secondary maximum in the heat flux. A secondary heat flux maximum has been noted by Deardorff (1980) and is also apparent in Moeng's (1984) profile, although it is smaller in magnitude in both those simulations. The major source term for heat flux near $z=1.2h_*$ is buoyancy production driven by the temperature variance (Figure 3.32), and the major source term for temperature variance is turbulent transport (Figure 3.39). Overall the layer between $z = 1.1h_*$ and $z = 1.4h_*$ resembles a secondary mixed layer, driven by "leakage" of buoyancy fluctuations from below.

It has been noted already that temperature fluctuations near the inversion are found on horizontal scales that are not well resolved by the model. Furthermore the inversion has a small vertical scale, and one can expect spurious temperature fluctuations to be generated when it is advected up and down. The laboratory measurements of Deardorff *et al.* (1980) could be expected to observe a secondary mixed layer if it existed, but they do not. There is therefore good reason to believe that the secondary mixed layer is unrealistic. The Deardorff (1980) subgrid scheme, as implemented in the present model, has both the subgrid kinetic energy and the subgrid length scale going to very small values in the stable layer, so the subgrid diffusivity is several orders of magnitude less than within the boundary layer. An exploratory simulation with increased diffusivity in the stable layer has been found to have much less prominent maxima in vertical velocity variance and heat flux, and a less pronounced minimum in temperature gradient. The fundamental problem, however, seems to be inadequate resolution.

3.3.4 *Third moments*

From the analysis of the second moment budgets in previous sections it is clear that the turbulent transport terms are important. These are associated with divergences in third moments like $\langle w'^3\rangle_h$, $\langle w'^2\theta'\rangle_h$ and $\langle w'\theta'^2\rangle_h$, which are all positive throughout most of the boundary layer. It is tempting to try to explain how the third moments are maintained in terms of their budget equations, which can be written for a general moment, $\langle w'^m\theta'^n\rangle_h$ where $m+n=3$, as follows:

$$\begin{aligned}\frac{\partial}{\partial t}\langle w'^m\theta'^n\rangle_h \;=\;& +m\frac{g}{\theta_0}\left\langle w'^{m-1}\theta'^{n+1}\right\rangle_h - m\theta_0\left\langle w'^{m-1}\theta'^n\frac{\partial\pi'}{\partial z}\right\rangle_h \\ & - n\left\langle w'^{m+1}\theta'^{n-1}\right\rangle_h\frac{\partial\langle\theta\rangle_h}{\partial z} \\ & - m\left\langle w'^{m-1}\theta'^n\left(u'_j\frac{\partial w'}{\partial x_j}\right)_h\right\rangle_h - n\left\langle w'^m\theta'^{n-1}\left(u'_j\frac{\partial\theta'}{\partial x_j}\right)_h\right\rangle_h \\ & - S_w \;-\; S_\theta\;.\end{aligned} \tag{3.35}$$

The first term on the right-hand side is buoyancy production, and the second is the pressure-gradient term. The relationship between the former and the buoyancy-induced part of the latter has already been discussed in Section 3.3.1. The third term is potential temperature gradient production. The fourth and fifth terms are associated with turbulence/turbulence advection. They can be rearranged to form a transport term involving a fourth moment, plus other terms involving second moments. Furthermore the fourth moments in the transport term can be approximated by products of second moments (the quasi-normal approximation) leading to further simplifications. The final two terms stand for subgrid diffusion of w and θ and seem to be generally dissipative.

Note that each $\langle w'^m\theta'^n\rangle_h$ budget has a buoyancy term proportional to the third moment one order lower in w (i.e., $\langle w'^{m-1}\theta'^{n+1}\rangle_h$) and a gradient production term proportional to the third moment one order higher in w (i.e., $\langle w'^{m+1}\theta'^{n-1}\rangle_h$). If the lapse rate is unstable there is therefore positive feedback between all the third moments via these terms. A similar feedback is seen between the $\langle w'^2 \rangle_h$, $\langle w'\theta' \rangle_h$ and $\langle \theta'^2 \rangle_h$ budgets: it is kept in check by the linearity constraint on the heat flux profile acting through the temperature gradient profile, and also by the third moments which export second moments from the unstable region.

There is one third moment, namely $\langle \theta'^3 \rangle_h$, which does not enter the second moment budgets directly, but which is coupled to the other third moments by buoyancy. This quantity is shown in Figure 3.41, along with data published by Druilhet *et al.* (1983). The model's profile is of the right sign, but the magnitude is *much* too low (the disagreement being masked somewhat in the figure by the log-linear horizontal axis).

There is therefore little justification for analysing the $\langle \theta'^3 \rangle_h$ budget, and the $\langle w'\theta'^2 \rangle_h$ budget must be unrealistic because its buoyancy term is greatly underestimated. The other third moment budgets may be somewhat realistic, but one must be sceptical, in particular, about the role of the turbulence/turbulence pressure, which has been shown to be somewhat unrealistic in the second moment budgets.

3.4 Sensitivity to the subgrid closure

To investigate the sensitivity of the model to its subgrid closure a pair of simulations was conducted with different values for the constant C_g that appears in the equation (Equation 2.28) specifying the grid length scale l_g. The stability-dependent length scale l_s was not changed. The sensitivity experiment was motivated in part by the attractive idea, proposed by Mason and Callen (1986), that the scale of the grid average $\langle \rangle_g$ is determined by the subgrid parameterisation (rather than vice versa) and so can be controlled independently of the model's grid spacing. The primary effect of an increase in l_g should be a reduction in resolved variance at high wavenumbers and a compensating increase in subgrid variance, where this is parameterised. The subgrid diffusivity should also increase, since it is proportional to the product of l and $e^{1/2}$.

The first of the test simulations is called "Run E1." It was identical to the control, Run A, except that $C_g = 1$ instead of 1.5. The second is called "Run E2" and was

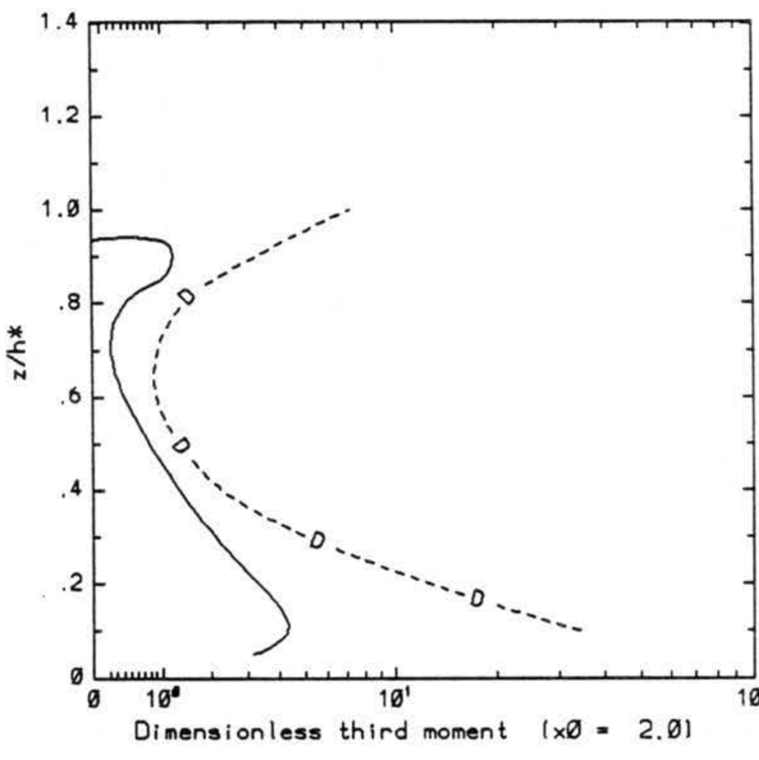

Figure 3.41. Profile of the third moment of potential temperature $\langle\theta'^3\rangle_{h,t}$ (solid line) compared with observational data of Druilhet *et al.* (1983) (--D--).

initialised with the fields of Run E1 at $t = 200\,\mathrm{min}$, but with C_g thereafter set equal to 2. There is a transient response to the change in C_g which lasts around 50 minutes and has been described by Cotton *et al.* (1988); it will not be discussed further here. Runs E1 and E2 were both integrated until $t = 400\,\mathrm{min}$. Statistics averaged from 300 to 400 minutes are described below and compared with statistics from the same period in Run A.

To establish the statistical significance of any differences between Runs A, E1, and E2, several time-averaged statistics have been calculated for a wider set of control simulations. In all there are four such simulations, labelled "Run A" to "Run D" and described in Section 4.3. In all of them, C_g has the value 1.5 and the surface heat flux is homogeneous; some have a light mean wind and some do not. In total, nine 100-minute periods between $t = 200\,\mathrm{min}$ and $t = 500\,\mathrm{min}$ are available.

It is found that an increase in C_g does indeed produce an increase in subgrid kinetic energy: relative to Run A the typical value of e within the boundary layer is reduced by 21% in Run E1 and increased by 24% in Run E2. The Reynolds numbers (Equation 3.1) for the latter two simulations are 400 and 160 respectively.

Figure 3.42 shows the vertical velocity spectra at several levels for Runs E1 and E2 (c.f. Figure 3.17b for Run A). The expected reduction in spectral density at high wavenumbers with increasing C_g is seen, but there is also a modest increase in spectral density at low wavenumbers at all levels but the lowest. With $C_g = 1$ the spectra at mid-levels have an inertial subrange slope up to the maximum wavenumber at $kh_* = 30$ ($\lambda = 0.2h_*$), although this certainly doesn't imply that a true inertial subrange exists. With $C_g = 1.5$ they steepen substantially above about $kh_* = 10$ ($\lambda = 0.6h_*$), and with $C_g = 2$ they steepen above $kh_* = 7$ ($\lambda = 0.9h_*$) and the region with inertial subrange slope is vanishingly small. The spectra at $z = 0.05h_*$ also fall away at high wavenumbers with an increase in C_g, but the spectra at $z = h_*$ are much less affected. Near $z = h_*$ the subgrid length scale assumes its stability-dependent value l_s much of the time, so the subgrid diffusivity is not affected greatly by changes in C_g.

(a) Run E1:

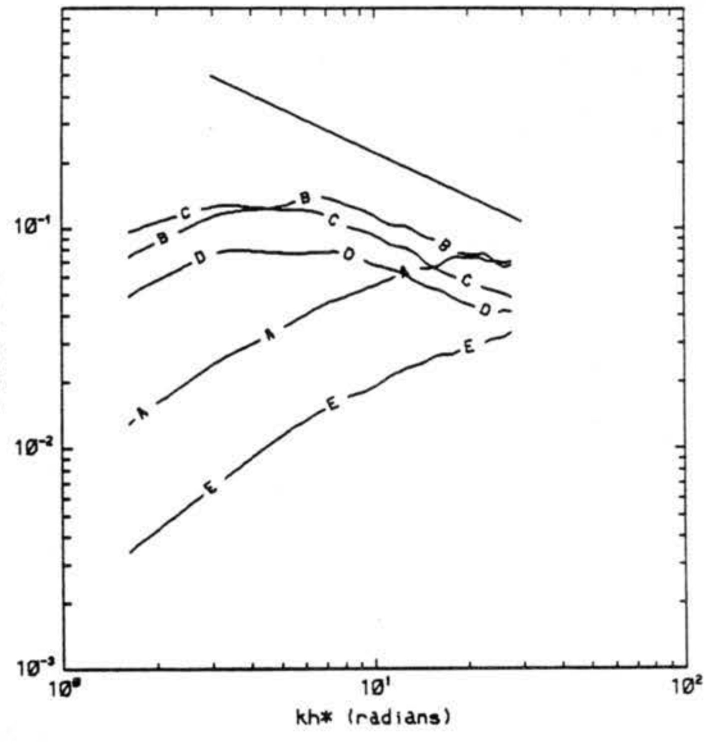

(b) Run E2:

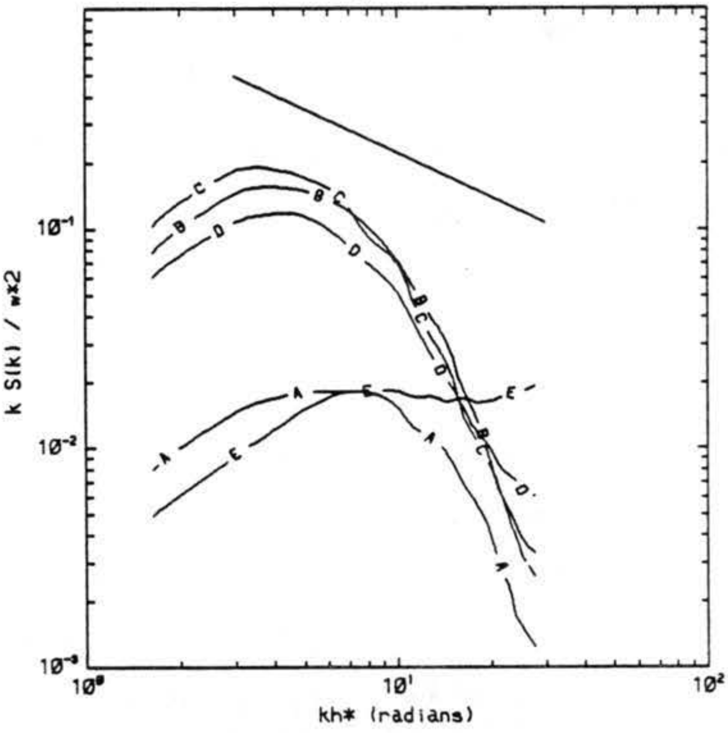

Figure 3.42. Dimensionless power spectra of vertical velocity for (a) Run E1 and (b) Run E2. Heights are $0.05h_*$ (—A—), $0.25h_*$ (—B—), $0.50h_*$ (—C—), $0.75h_*$ (—D—) and $1.00h_*$ (—E—). The straight solid lines have inertial subrange slope $-2/3$.

For the most part, changes in the profiles of variances, covariances, etc. with changes in C_g are slight, as one might hope. Most of the conclusions of previous sections would not be changed if either of the test simulations had been analysed in place of Run A. Nevertheless some changes are observed and can be confidently attributed to the change in subgrid parameterisation. One is a change in the depth of the layer where subgrid heating is significant, or equivalently a change in the height of maximum resolved heat flux (Figure 3.43). With $C_g = 1$ the heat flux maximum is found at $z = 0.10h_*$ (which is only $2\Delta z$), with $C_g = 1.5$ it is at $z = 0.15h_*$ and with $C_g = 2$ it is at $z = 0.21h_*$.

A change in the resolved heat flux implies changes in the resolved θ variance or the resolved w variance or the correlation coefficient, or all three. In practice it is found that as C_g increases the correlation coefficient near the surface increases a little (remaining around 0.9) and the vertical velocity variance decreases (see below), but the largest change is in the temperature variance (Figure 3.44), which decreases by a factor of more than two near the surface. Above $z = 0.2h_*$, however, it does not change at all. Another consequence of the increase in C_g is an increase in the temperature gradient near the surface (Figure 3.45). The maximum effect is found near $z = 0.1h_*$ and consists of an approximate doubling in $\partial \langle\theta\rangle_h / \partial z$ with the doubling in C_g. With $C_g = 1.5$ the profile conforms quite closely to a $z^{-3/2}$ dependence (as in Equation 3.2), but when C_g is either increased or reduced it does not. Note that the change in $\partial \langle\theta\rangle_h / \partial z$ means that an *increase* in the subgrid diffusivity has produced a *decrease* in the diffusivity,

$$-\frac{\langle w'\theta' + \phi_3\rangle_h}{\partial \langle\theta\rangle_h / \partial z},$$

based on the total heat flux.

The changes in the velocity variance profiles are shown in Figure 3.46. The increase in C_g leads to a reduction in resolved velocity variance at low levels and an increase in the level of the maximum, from $z = 0.37h_*$ for $C_g = 1$ to $z = 0.43h_*$ for $C_g = 2$. Both are statistically significant at 95% confidence. In the horizontal velocity variance there is a decrease at low levels and an increase at high levels; variability in the horizontal velocity variances is quite high, however, and these changes are only marginally significant.

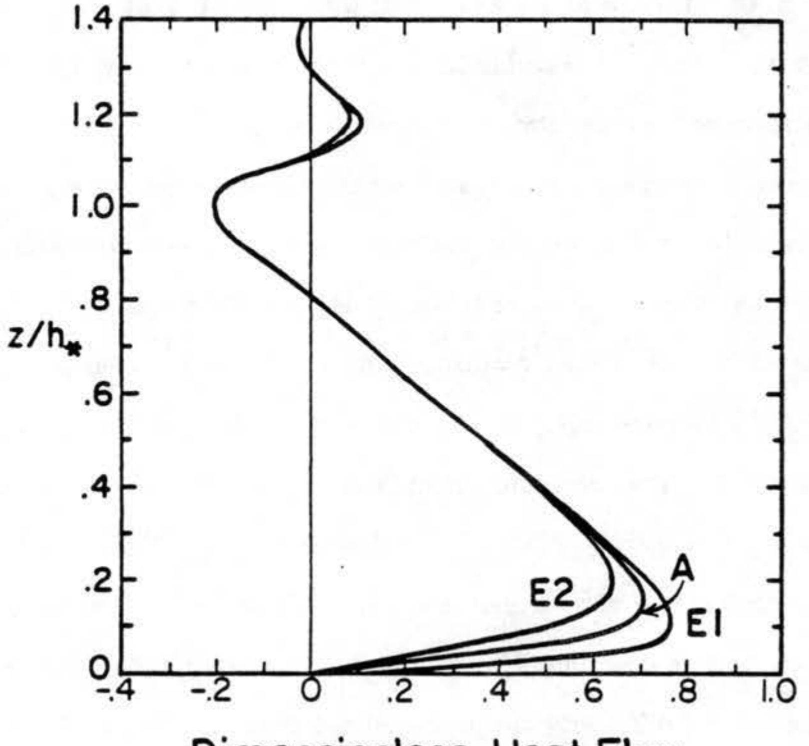

Figure 3.43. Profiles of dimensionless, resolved heat flux for Runs A, E1 and E2.

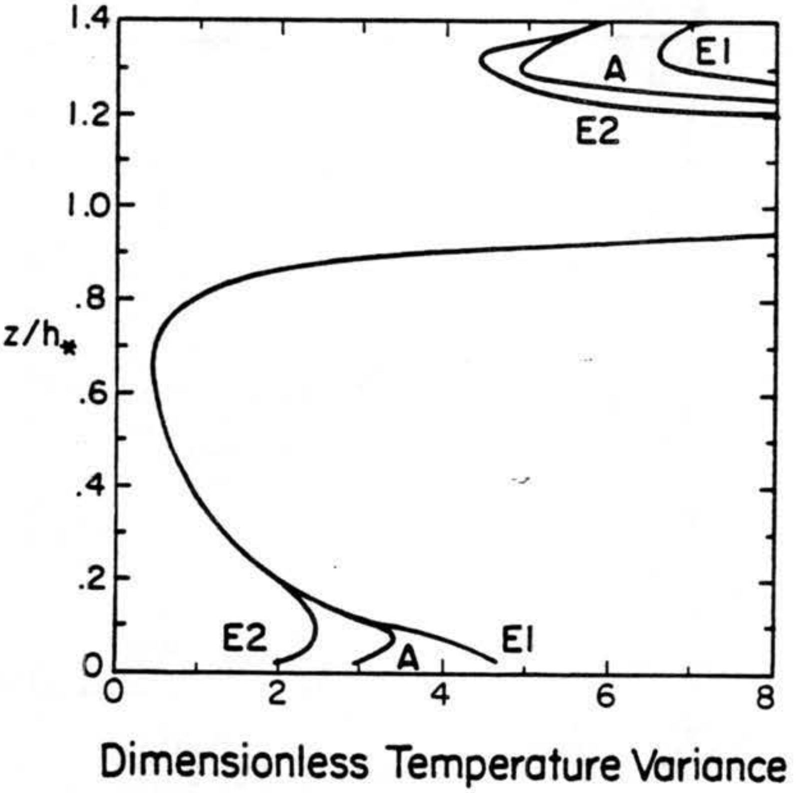

Figure 3.44. Profiles of dimensionless, resolved potential temperature variance for Runs A, E1 and E2.

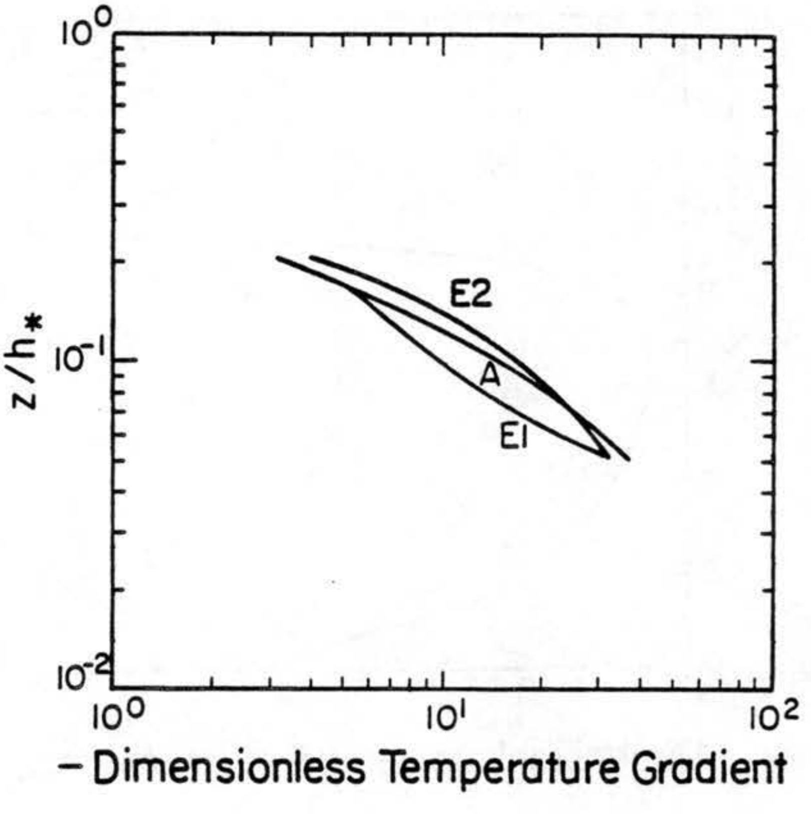

Figure 3.45. Profiles of dimensionless potential temperature gradient for Runs A, E1 and E2.

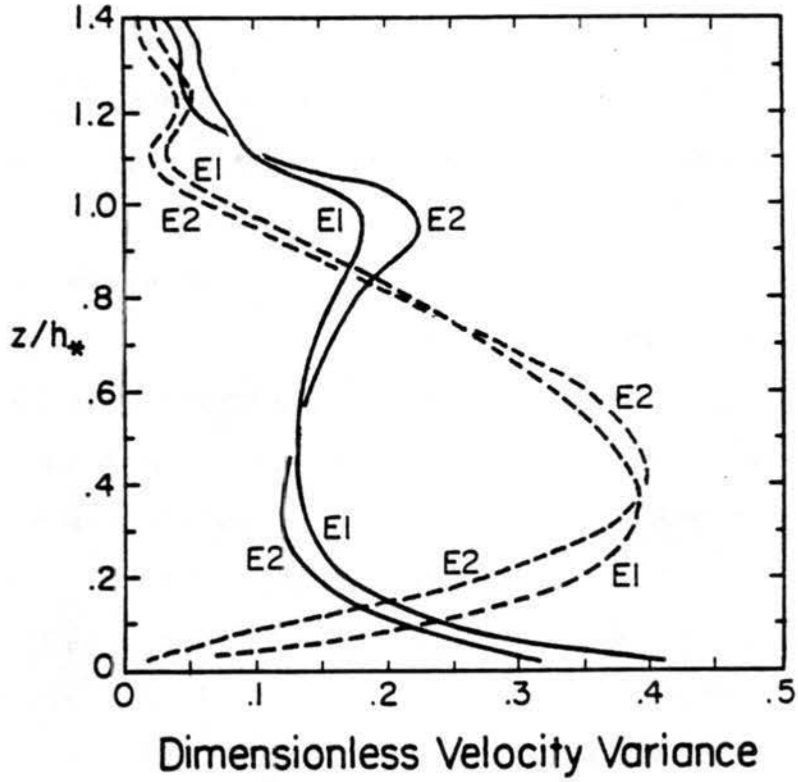

Figure 3.46. Profiles of dimensionless horizontal velocity variance $\langle u'^2 + v'^2 \rangle_{h,t}/2$ (solid lines) and vertical velocity variance $\langle w'^2 \rangle_{h,t}$ (dashed lines) for Runs E1 and E2.

There is evidence, then, of subtle changes in the structure of the convective eddies and the obvious place to look next is the skewness profile (Figure 3.47). With an increase in C_g there is an increase in skewness at low levels and a decrease at high levels. Recall from Section 3.2.7 that the numerator in the skewness coefficient is actually the turbulent flux in vertical velocity variance and not the single-point third moment in w. It was stated that the difference between these two quantities is very small. This is true with $C_g = 1.5$ and with $C_g = 2$, but it is not so true with $C_g = 1$, especially near the surface where the vertical velocity field has more fine structure. If the skewness coefficient is calculated from the single-point third moment, then with $C_g = 1$ the value at the lowest level ($z = 0.05h_* = \Delta z$) is -0.4, which is similar to the value reported by Deardorff (1974b). Deardorff suggested that the negative skewness near the surface might be a consequence of the spatial averaging—which he assumed to be grid-volume averaging—involved in defining the resolved variables. Given that it is sensitive to both the magnitude of the subgrid diffusivity and to the way in which the skewness coefficient is calculated, it appears to be attributable to inadequate resolution near the surface, perhaps to having too few grid levels within the layer below the resolved heat flux maximum.

The noticeable changes in the skewness profile would appear to imply noticeable changes in the profile of the flux of vertical velocity variance. Actually little change in this profile is apparent as C_g is increased (Figure 3.48). The increase in skewness at low levels is largely a result of the reduction in $\langle w'^2 \rangle_h$. At high levels there is a reduction in $\langle w'^3 \rangle_h$, but it occurs where this quantity is dropping off steeply with height so it is not conspicuous on the figure. The magnitude and position of the maximum in $\langle w'^3 \rangle_h$ are essentially unchanged. On the other hand the profile of $\langle w'\pi' \rangle_h$ (also in Figure 3.48) does change visibly as C_g is increased, there being, in particular, a more prominent maximum near $z = 0.9h_*$.

The change with C_g in the standard deviation of pressure is shown in Figure 3.49a. The doubling of C_g produces an increase in $\langle \pi'^2 \rangle_h^{1/2}$ of between 10% and 30%. The difference is insignificant (at 5% confidence) at $z = 0.1h_*$, marginally significant at $z = 0.5h_*$ and highly significant at $z = 0.9h_*$. In Figure 3.49b the buoyancy and turbulence/

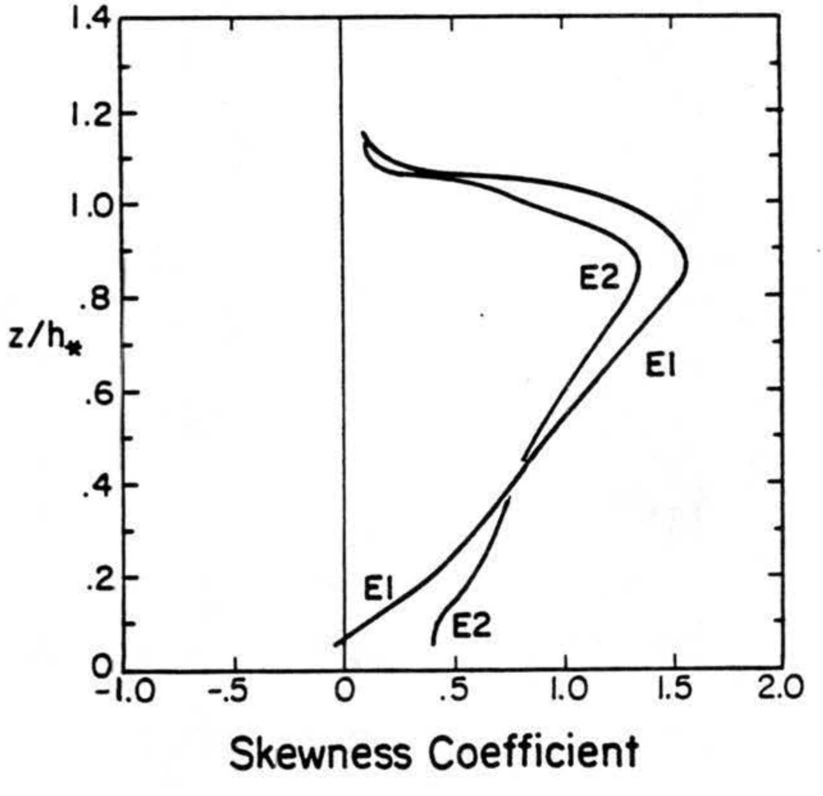

Figure 3.47. Profiles of skewness coefficient S_w for Runs E1 and E2.

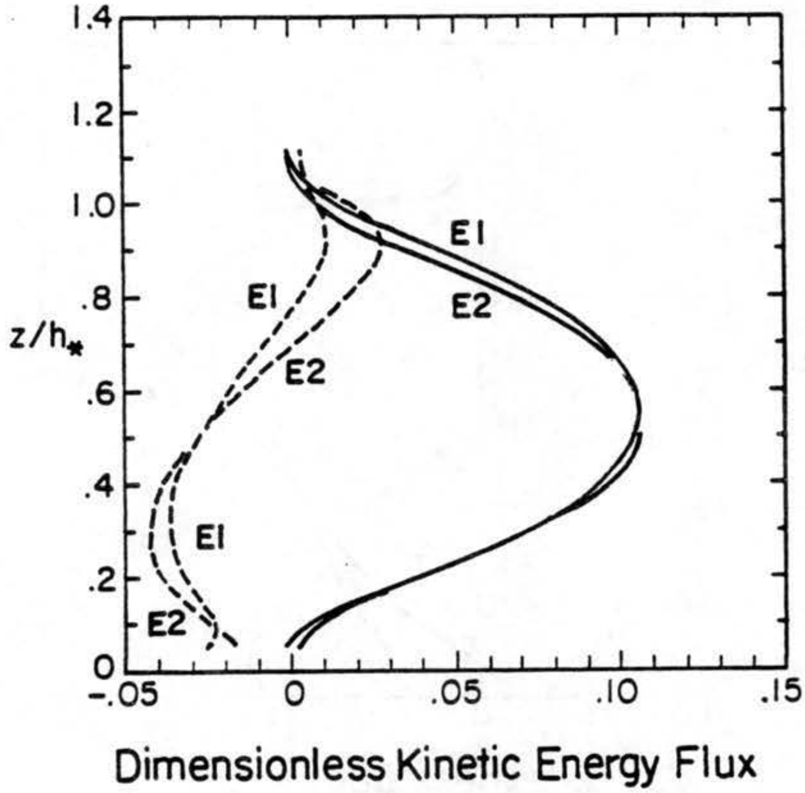

Figure 3.48. Profiles of dimensionless kinetic energy fluxes $\langle w'^3 \rangle_{h,t}/2$ (solid lines) and $\langle w'\pi' \rangle_{h,t}$ (dashed lines) for Runs E1 and E2.

(a)

(b)

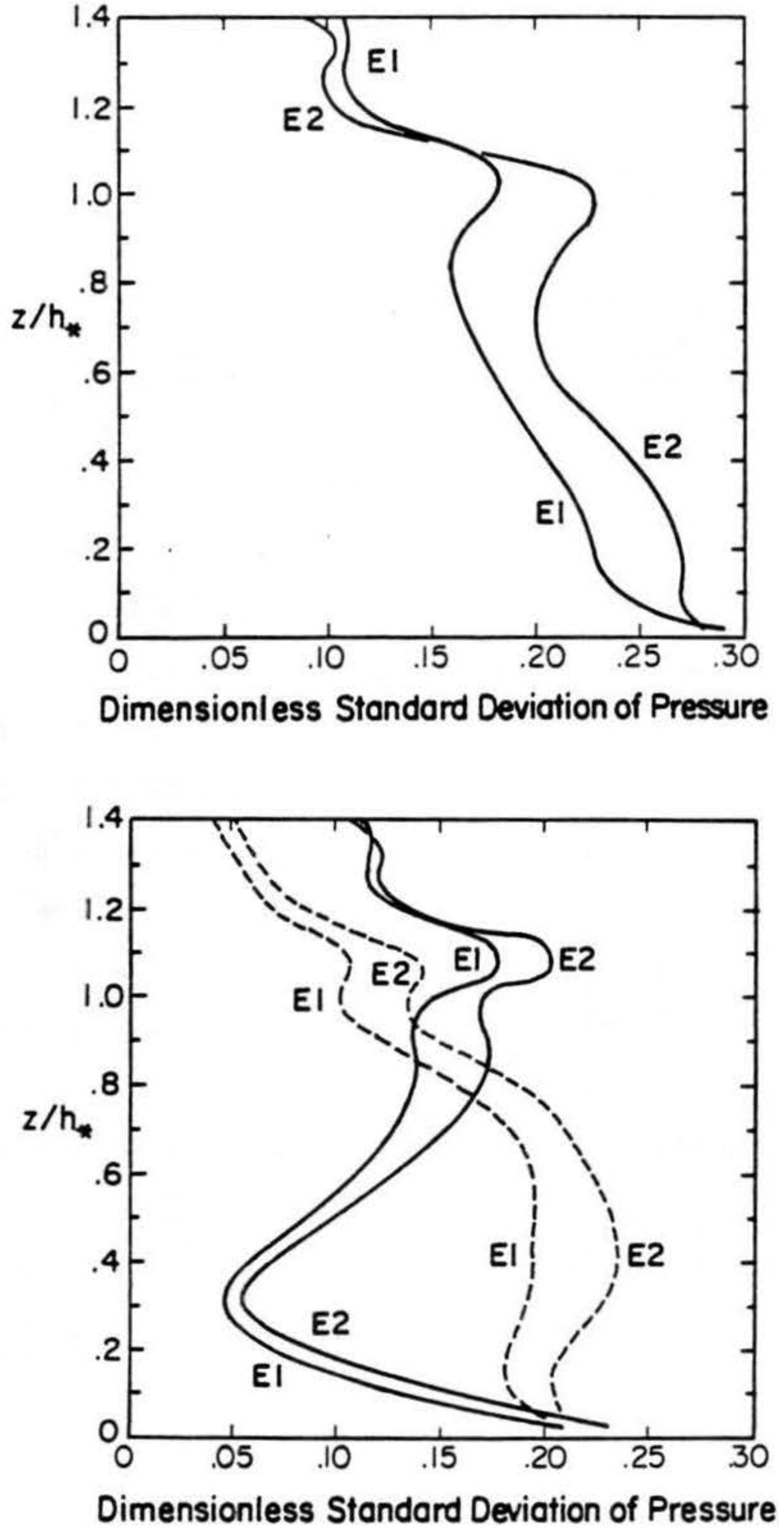

Figure 3.49. Profiles of the dimensionless standard deviation of pressure for Runs E1 and E2. (a) Total pressure π. (b) Turbulence pressure π_t (solid lines) and buoyancy pressure π_b (dashed lines) .

turbulence components of the pressure are shown. The standard deviations of both increase with C_g, the former dominating in the upper boundary layer and the latter in the middle of the boundary layer.

It is not clear how to interpret the increase in the standard deviation of pressure with C_g, but a few observations can be made. First, regarding the buoyancy pressure π_b, the stronger fluctuations in the upper boundary layer are associated with stronger forcing of the horizontal velocity variances via the velocity/π_b-gradient covariance (not shown). Second, regarding the turbulence/turbulence pressure π_t, one might expect this to be quite sensitive to the geometry of the large eddies: for example with the two-dimensional, sinusoidal eddy structure defined by Equations 3.24 to 3.27 the standard deviation of the pressure is proportional to the square of the horizontal scale, for a given velocity scale and vertical scale. The increase in the standard deviation of π_t with C_g is thus consistent with the shift in energy from small to large scales seen in the vertical velocity spectra. The increase in the magnitude of the π_t fluctuations does *not* imply that they are more effective in transferring energy from the vertical velocity variance to the horizontal variances. On the contrary the vertically integrated energy budgets (Figure 3.50) show that as C_g increases, the rate of intercomponent transfer by π_t gradient forces decreases markedly, from 15% of the resolved buoyancy production for $C_g = 1$ to only 5% for $C_g = 2$.

Recently Moeng and Wyngaard (1988) have examined the sensitivity of their model to changes in the subgrid scheme. Among other changes they varied the subgrid diffusivity by changing the dissipation rate constant C_ϵ in the range 0.7 to 1.2. (An increase in C_ϵ causes a decrease in diffusivity.) They report that the large-eddy structure is essentially unaffected, and support this with a profile of $\langle w'^3 \rangle_h$. At first glance this contradicts the result of the present study, that there are modest effects in the large-eddy structure. Several comments are in order. First, between the extremes in C_ϵ in Moeng and Wyngaard's study, the diffusivity changes by a factor of only 1.2, versus 2.5 in the present study. Second, their simulation is at a higher resolution ($52\,\mathrm{m} \times 52\,\mathrm{m} \times 21\,\mathrm{m}$) and Reynolds number ($\sim 10^3$), where the large eddies should be less sensitive to the

(a) Run E1:

$$
\begin{tikzcd}
B = .334 \arrow[d] & & \\
\boxed{\frac{1}{2}\left\langle w'^2 \right\rangle_{h,t}} \arrow[rr, "\begin{matrix} P_b = .136 \\ P_t = .050 \end{matrix}"] \arrow[d] & & \boxed{\frac{1}{2}\left\langle u'^2 + v'^2 \right\rangle_{h,t}} \arrow[d] \\
\begin{matrix} S = .145 \\ E = .004 \end{matrix} & & S = .183
\end{tikzcd}
$$

(b) Run E2:

$$
\begin{tikzcd}
B = .283 \arrow[d] & & \\
\boxed{\frac{1}{2}\left\langle w'^2 \right\rangle_{h,t}} \arrow[rr, "\begin{matrix} P_b = .140 \\ P_t = .015 \end{matrix}"] \arrow[d] & & \boxed{\frac{1}{2}\left\langle u'^2 + v'^2 \right\rangle_{h,t}} \arrow[d] \\
\begin{matrix} S = .126 \\ E = .003 \end{matrix} & & S = .148
\end{tikzcd}
$$

Figure 3.50. Vertically integrated budgets of resolved turbulence kinetic energy for (a) Run E1 and (b) Run E2. For definitions of terms see Figure 3.26.

subgrid scales. Third, in addition to explicit subgrid diffusion, Moeng and Wyngaard use spatial filtering with a sharp spectral cutoff. Finally, the profile they have presented is of a quantity which is not conspicuously affected in the present study. Nevertheless their profiles do suggest a decrease (albeit very small) in $\langle w'^3 \rangle_h$ with increasing diffusivity, as has been noted above.

To summarise the results of this section, an increase in the subgrid length scale has caused substantantial changes in the mean and fluctuating temperature field near the surface and more subtle, but detectable, changes in the large-eddy structure throughout the boundary layer. Many of the changes with increasing length scale are in the direction of better agreement with observations: namely, a less pronounced peak in horizontal velocity variances near the surface, larger horizontal velocity variances in the upper boundary layer, smaller vertical velocity skewness coefficient in the upper boundary layer and larger pressure variance. However there is also a substantial decrease in the intercomponent transfer of energy by the turbulence/turbulence pressure field. In that sense the model has become less "turbulent" and the assumption on which large-eddy simulation has been justified—that it can realistically deal with processes well into the inertial range—is less tenable.

The value of C_g used for all the simulations but Runs E1 and E2, namely 1.5, was chosen to be as small as possible without signs of inadequate resolution (specifically negative vertical velocity skewness near the surface and large spectral density at $\lambda = 2\Delta x$).

3.5 The relationship between large-eddy simulations and real fluids

It is clear that the success of large-eddy models of the horizontally homogeneous convective boundary layer, at least at the moderate resolution described here, does *not* lie in their correctly predicting the dynamics of a large range of spatial scales of boundary layer turbulence. What they do is simulate a field of updraughts and downdraughts with the characteristic velocity and dimensions approximately correct and with the crucial property that turbulence kinetic energy—specifically vertical velocity variance—is transported upwards. The buoyancy fluctuations driving the turbulence are too small in magnitude, however, in the sense that the temperature variance is substantially underpredicted, although it is encouraging that the conditionally sampled updraught-mean and downdraught-mean temperature perturbations are approximately correct. In addition there is evidence that the pressure gradient forces due to turbulence/turbulence interaction are not coupling the vertical and horizontal velocity components sufficiently tightly.

It is possible with current supercomputers (specifically a Cray X–MP/48) to increase the resolution of the model by a factor of two or more, as Moeng and Wyngaard (1988) have done recently. It is also possible to increase the resolution near the surface and at the inversion—both regions where there is evidence of inadequate resolution—using either variable grid spacing in the vertical or nested fine grids. All these developments seem well worth pursuing. It is currently the author's opinion that the most promising route is to combine a modest increase in overall resolution with nested grids near the surface and the inversion, and to give some more attention to filtering out unresolvable features. It will be very interesting to see whether such improvements result in a substantially better description of turbulence dynamics. The present work has suggested several statistics that should be examined critically.

At higher resolutions the models are expensive to run, but certainly not unreasonably so if one contemplates only one or two simulations of a few hours duration each. The following chapters address a problem for which series of several simulations and/or long averaging times are found to be necessary. For these experiments it is not feasible to use a domain with much more than the $36 \times 36 \times 39$ grid points used here and the question must be asked: is the model's description of reality sufficiently correct to justify taking its predictions seriously? The answer suggested by the present chapter is a very cautious yes.

CHAPTER 4

BOUNDARY LAYER RESPONSE TO SURFACE HEAT-FLUX PERTURBATIONS: DESCRIPTION

4.1 Introduction

Chapter 1 presented two questions about the effect of surface heat-flux perturbations on the boundary layer. They are paraphrased here as follows:

1. Is there a consistent tendency for variations in the boundary layer to be associated with the pattern of surface variation?

2. Do the surface variations change profiles of turbulence statistics?

The present chapter addresses these questions. Section 4.2 describes the various decompositions of the variables that are appropriate to answering the questions. Section 4.3 describes the simulations, which can be organised into five groups according to the wavelength of the heat-flux perturbation and the mean wind speed. Sections 4.4 to 4.8 describe the results from each of these groups in turn and Section 4.9 discusses and summarises the results.

4.2 Averages

One decomposition of a variable—the one that was used in looking at the horizontally homogeneous boundary layer in chapter 3—divides it into its horizontal average and deviations from that average,

$$a = \langle a \rangle_h + a'. \tag{4.1}$$

In this context a' is called turbulence. This division is relevant to the second of the questions posed above. Statistics calculated using it will be labelled "horizontal-average" statistics.

In answering the first question, the regularity of the surface variation allows one to use the phase average in dividing a' into a mean part and a deviation,

$$a = \langle a \rangle_h + \langle a' \rangle_p + (a')_p \,. \tag{4.2}$$

With this division $\langle a' \rangle_p$ is called the circulation (the name will be used even if the variable is not a velocity) and $(a')_p$ is now turbulence. It will be found, however, that the circulation fields can fluctuate in time in a way that one would like to ignore, so it is appropriate to look at the time-averaged circulation $\langle a' \rangle_{p,t}$, and the decomposition becomes

$$a = \langle a \rangle_h + \langle a' \rangle_{p,t} + (a')_{p,t} \,. \tag{4.3}$$

The deviation $(a')_{p,t}$ will also be called turbulence; obviously there is room for confusion in using the word, but the meaning will be made clear by the context.

Various and diverse aspects of the decompositions described above are considered in more detail in Appendix A, but there is one subtlety that should be mentioned here. Equation 4.2 could just as well have been written

$$a = \langle a \rangle_h + \langle a' \rangle_p + (a)_p \,, \tag{4.4}$$

since $(a)_p \equiv (a')_p$. Replacing the phase averages in Equation 4.4 with phase-time averages then yields the decomposition

$$a = \langle a \rangle_{h,t} + \langle a' \rangle_{p,t} + (a)_{p,t} \,, \tag{4.5}$$

but this is *not* the same as Equation 4.3. The difference is that in Equation 4.5 the time-varying part of the horizontal average, namely $(\langle a \rangle_h)_t$, is included in the turbulence, whereas in Equation 4.3 it was included in the horizontal average term. The distinction is not important for the velocity fields, but it is crucial for the temperature and pressure fields which evolve steadily. A decomposition like Equation 4.5 inteprets the evolution as turbulence, resulting—among other problems—in temperature and pressure variances that become larger as the length of the averaging period is increased.

4.3 The simulations

In all the simulations described in this chapter the surface heat flux Φ was either horizontally homogeneous or perturbed according to

$$\Phi = \langle\Phi\rangle_h + \Phi_p \cos 2\pi \frac{x - x_p}{\lambda_p} \tag{4.6}$$

The horizontal average $\langle\Phi\rangle_h$ was constant throughout all runs at $0.2\,\mathrm{K\,m\,s^{-1}}$, which is the value used for the simulations described in chapter 3. The amplitude Φ_p (when non-zero) was always $0.1\,\mathrm{K\,m\,s^{-1}}$, i.e., one-half of the horizontal average. Two values of the wavelength were used: $\lambda_p = 1500\,\mathrm{m}$ and $\lambda_p = 4500\,\mathrm{m}$. With the former there are three identical cycles of the heat-flux perturbation within the domain and with the latter there is just one. With $\lambda_p = 4500\,\mathrm{m}$ each phase average is calculated over 36 points and with $\lambda_p = 1500\,\mathrm{m}$ it is calculated over $3 \times 36 = 108$ points.

The simulations are listed in Table 4.1. Run A is the horizontally homogeneous simulation analysed in chapter 3. Run B is a repetition of Run A, but with a different set of random temperature fluctuations to initiate convection. Runs C and D were initialised from the fields of Run A at $t = 200\,\mathrm{min}$, at which time a constant, u_0, was added to the x-component of velocity everywhere. No attempt was made to simulate the realistic evolution of the horizontal velocity profile—in the absence of Coriolis force the boundary layer simply loses momentum (but very slowly) through surface drag. Run C had $u_0 = 1\,\mathrm{m\,s^{-1}}$ and Run D had $u_0 = 2\,\mathrm{m\,s^{-1}}$. Together Runs A to D comprise a horizontally homogeneous control group, from which various statistics have been extracted for comparison with the perturbed simulations.

The perturbed simulations cover five combinations of λ_p and u_0. Simulations with a name starting with "F" had $\lambda_p = 1500\,\mathrm{m}$ and $u_0 = 0\,\mathrm{m\,s^{-1}}$. The other combinations are: $\lambda_p = 1500\,\mathrm{m}$ and $u_0 = 1\,\mathrm{m\,s^{-1}}$ (G), $\lambda_p = 4500\,\mathrm{m}$ and $u_0 = 0\,\mathrm{m\,s^{-1}}$ (H), $\lambda_p = 4500\,\mathrm{m}$ and $u_0 = 1\,\mathrm{m\,s^{-1}}$ (I), and $\lambda_p = 4500\,\mathrm{m}$ and $u_0 = 2\,\mathrm{m\,s^{-1}}$ (J). With one exception, the perturbed simulations were initialised from Run A or Run B at $t = 200\,\mathrm{min}$, with the heat-flux perturbation imposed suddenly at that time and maintained thereafter. They were run

Table 4.1. List of the simulations.

Run	u_0 ($\mathrm{m\,s^{-1}}$)	λ_p (m)	x_p	Remarks
A	0	–	–	Horizontally homogeneous control run.
B	0	–	–	Repetition of Run A, but with different random temperature fluctuations.
C	1	–	–	Initialised from Run A at $t=200$ min.
D	2	–	–	Initialised from Run A at $t=200$ min.
F1	0	1500	0	Initialised from Run A at $t=200$ min.
F2			$\lambda_p/2$	
F3			0	Initialised from Run B at $t=200$ min.
F4			$\lambda_p/2$	
F5			0	Initialised from Run A at $t=0$ min.
G1	1	1500	0	Initialised from Run A at $t=200$ min.
G2			$\lambda_p/2$	
H1	0	4500	0	Initialised from Run A at $t=200$ min.
H2			$\lambda_p/2$	
I1	1	4500	0	Initialised from Run A at $t=200$ min.
I2			$\lambda_p/2$	
J1	2	4500	0	Initialised from Run A at $t=200$ min.
J2			$\lambda_p/2$	

in pairs, with the members of each pair differing from each other only in that the phase x_p of the heat-flux perturbation was zero in the first and $\lambda_p/2$ in the second. (Since the lateral boundary conditions are cyclic, the origin for x_p is arbitrary.) The odd-one-out is Run F5, in which the heat-flux perturbation was imposed at $t=0\,\mathrm{min}$, before random convection had developed.

Later sections will examine averages over the groups of simulations with the same u_0 and λ_p. These groups are labelled "Set F," "Set G," etc. Table 4.2 summarises the five groups and the simulations that comprise them. Note that Run F5 is not included in Set F.

All the simulations were run until $t = 400\,\mathrm{min}$, except Run A which was run to $t=500\,\mathrm{min}$. All told, the total simulated time was 3900 minutes, or 63 hours, which took approximately 38 hours of Cray X-MP CPU time. Clearly it would have been expensive to use a less-efficient model or a higher resolution.

4.4 Simulations with $\lambda_p=1500\,\mathrm{m}$ and $u_0=0\,\mathrm{m\,s^{-1}}$

4.4.1 *Evolution of surface-driven circulations*

A convenient measure of the strength of the instantaneous, phase-average circulations is the circulation kinetic energy,

$$E_c=\sum_i E_{ci} \quad \text{where} \quad E_{ci} \stackrel{\text{def}}{=} \frac{1}{2}\int_Z \left\langle \langle u_i' \rangle_p^2 \right\rangle_h . \tag{4.7}$$

The $\int_Z$ symbol indicates density-weighted vertical integration, and was defined in Equation 2.34. The naive expectation is that E_c will be "small" in the absence of a surface heat-flux perturbation, and that when such a perturbation is imposed it will increase (perhaps over a period of a few h_*/w_*) to a more or less steady, "large" value. Figures 4.1a and 4.1b show the evolution of the circulation kinetic energy and its components for Run F1 and for the horizontally homogeneous Run A. (For some perspective on the magnitudes note that the vertical integral of resolved turbulence kinetic energy $\langle u_i'^2 \rangle_h/2$ has a dimensionless value of 0.35.) The naive expectation is not borne out in Figure 4.1a. There E_c is small at $t=100\,\mathrm{min}$, but starts to increase *before* the heat-flux perturbation

Table 4.2. List of the groups of simulations.

	$u_0 = 0\,\mathrm{m\,s^{-1}}$	$u_0 = 1\,\mathrm{m\,s^{-1}}$	$u_0 = 2\,\mathrm{m\,s^{-1}}$
$\lambda_p = 1500\,\mathrm{m}$	Set F (F1 to F4)	Set G (G1 & G2)	–
$\lambda_p = 4500\,\mathrm{m}$	Set H (H1 & H2)	Set I (I1 & I2)	Set J (J1 & J2)

(a)

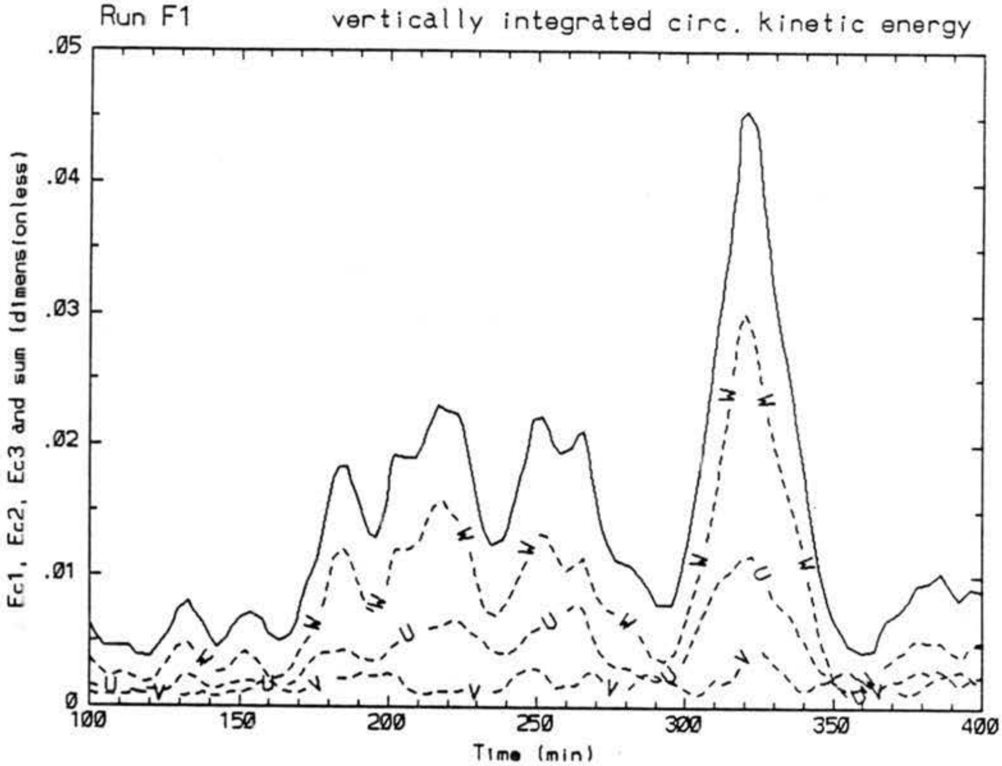

(b)

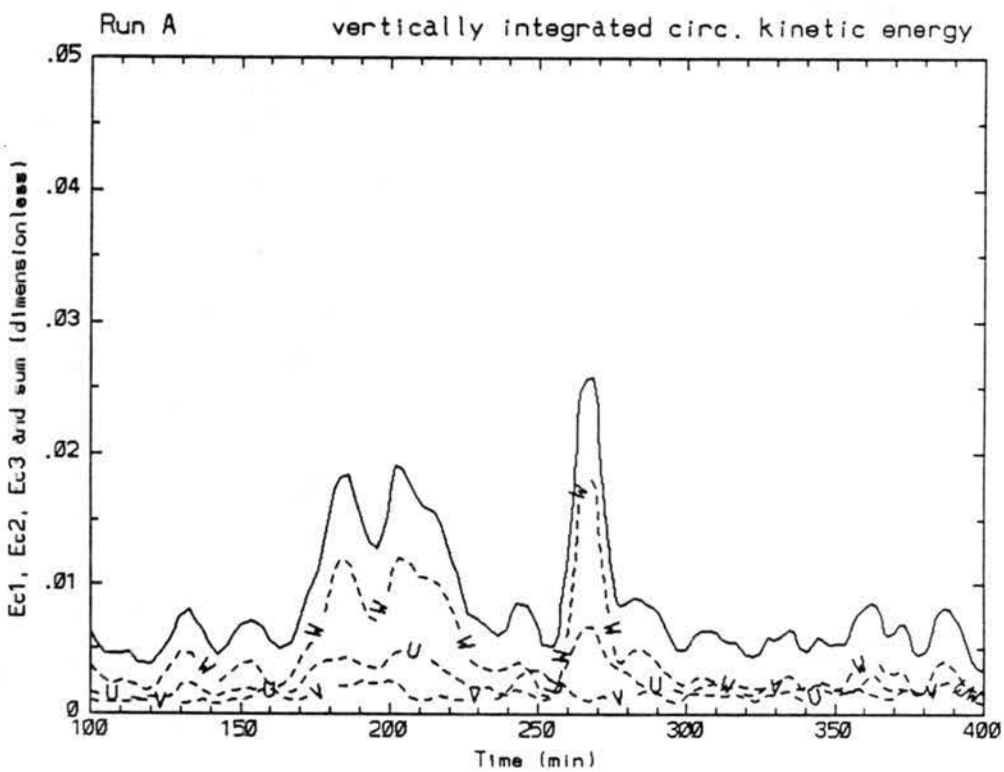

Figure 4.1. Evolution of the circulation kinetic energy for (a) Run F1 and (b) Run A. The dashed lines (labelled U, V and W) show the components of the dimensionless, vertically integrated, circulation kinetic energy E_{ci} and the solid line shows their sum E_c.

is applied at $t = 200\,\text{min}$ and certainly never approaches a steady value. Comparison between Figures 4.1a and 4.1b shows that the two simulations do evolve differently after $t = 200\,\text{min}$, so the heat-flux perturbation *does* have an effect. (But so, perhaps, might any change in the model.) On the whole the effect of the heat-flux perturbation seems to be to increase the strength of the circulation, but the result is not clear-cut.

In order to estimate the ensemble average response of the boundary layer to surface heat-flux perturbations it has been necessary to average over several simulations and also over time. The simulations have been arranged in pairs, differing in the phase of the perturbation by $\lambda_p/2$, as has already been described. The motivation for arranging them in this way is as follows. Consider the period before the surface perturbation is imposed. The phase averages should be horizontally homogeneous, but spurious circulations exist due to random organisation of the eddies. The phase average fields of one member of a pair differ from the phase average fields of the other member only by a horizontal displacement of $\lambda_p/2$, so a phase average formed over both members tends to exclude the spurious circulations. (To be specific it excludes all components with wavelength λ_p/m, where m is odd.) Furthermore, assume that, when the perturbation is imposed, the eddies are arranged so that in the first member of the pair there is, on average, ascent over the heat-flux maxima. In the second member there will be descent over the heat-flux maxima. One expects the perturbation to reinforce the first pattern and oppose the second. Therefore, *before the heat-flux perturbation is imposed and for some time after*, a phase average over the pair should in general be closer to the ensemble average than an average over either individually, and also closer than an average over two independent simulations. The problem with this argument is that it is not clear how long "some time after" is. It seems likely that over the periods considered here, typically 100 to 200 minutes, the two simulations in a pair will lose their special relationship to each other and can be considered independent.

In the present case there are two pairs of simulations: Runs F1 and F2, and Runs F3 and F4. An average over all four is labelled "Set F." The circulation kinetic energy based on phase average fields from Set F is shown in Figure 4.2. (Note the change in vertical

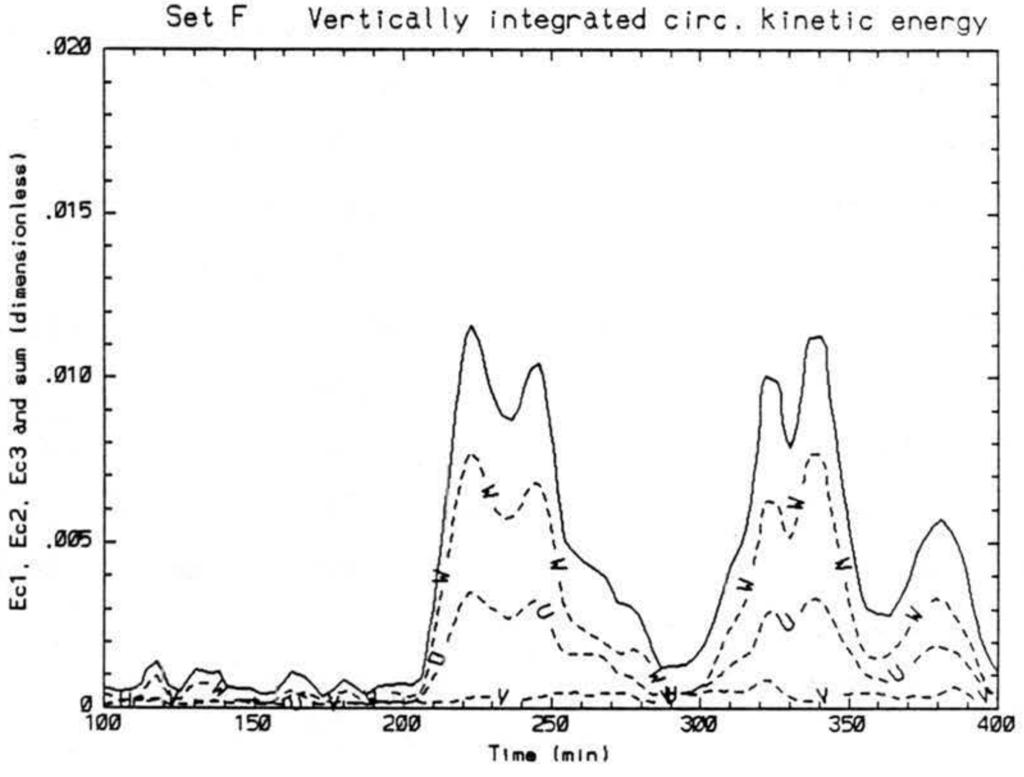

Figure 4.2. Evolution of circulation kinetic energy for Set F.

scale from Figure 4.1.) The troublesome circulations before $t = 200\,\mathrm{min}$ have largely cancelled out, as expected, and the evolution of E_c conforms a little more closely to the expectation. There is still no sign of approach to a steady value, however. It is not clear whether the quasi-periodic variation after $t = 200\,\mathrm{min}$ is real, in the sense that it would appear in the ensemble average. At its maximum the instantaneous circulation accounts for only 3% of the total resolved turbulence kinetic energy.

When the heat-flux perturbation is imposed before random convection has developed, as it was in Run F5, the evolution of E_c is rather different (Figure 4.3). In that case a strong circulation grows during the first 20 minutes, accounting for up to one-half of the total turbulence kinetic energy. After $t = 50\,\mathrm{min}$ it decays and after $t = 200\,\mathrm{min}$ the E_c curve does not look very different from the one for Run F1.

At this point it is appropriate to mention briefly an earlier pair of simulations, described by Cotton *et al.* (1988). These were labelled "NSH" and "NSI" and were similar to Run F1 and Run F2 respectively, except that there was no subsidence, the heat-flux perturbation was imposed at $t = 50\,\mathrm{min}$ and the simulations were terminated at $t = 200\,\mathrm{min}$. Figure 4.4 (adapted from Cotton *et al.*'s Figure 5.1) shows the evolution of E_c for NSH plus NSI. Note that the maximum in E_c in Figure 4.4 has a dimensionless value of ~ 0.04, versus ~ 0.01 in Figure 4.2. Cotton *et al.* tentatively advanced the hypothesis that the decrease in E_c after $t = 110\,\mathrm{min}$ was a result of strong sensitivity to the ratio λ_p/h_*, which decreased by about 15% between $t = 100\,\mathrm{min}$ and $t = 200\,\mathrm{min}$. Subsidence was imposed in the present series of simulations to hold the boundary layer depth constant and allow a test of this hypothesis. The observed fluctuations in E_c in Set F, in the absence of changes of more than a few percent in λ_p/h_*, suggest that the hypothesis is not justified, although evidence will be presented later that surface-driven circulations *are* sensitive to *large* changes in λ_p/h_*. The following interpretation of the earlier results is proposed. At $t = 50\,\mathrm{min}$, when the heat-flux perturbation was first imposed, the horizontal velocity variances were still relatively low (see Figure 3.1) and the weak horizontal mixing allowed a vigorous circulation to develop. After $t = 110\,\mathrm{min}$ the circulation died away in much the same way as it does in Run F5, either as a result of the

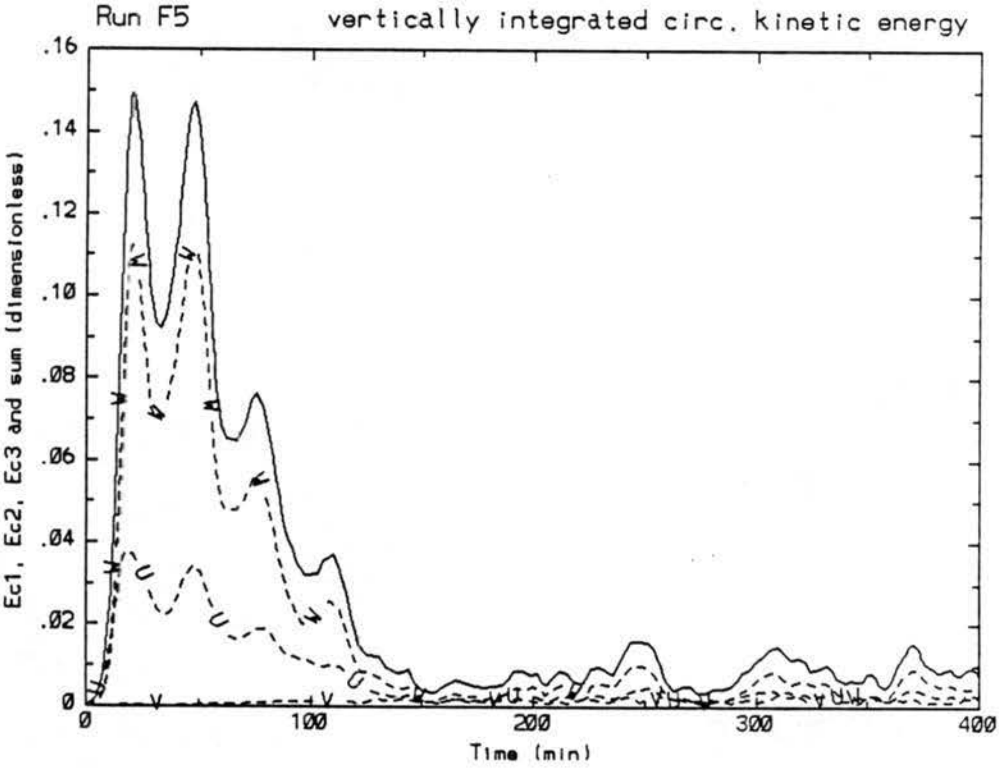

Figure 4.3. Evolution of circulation kinetic energy for Run F5.

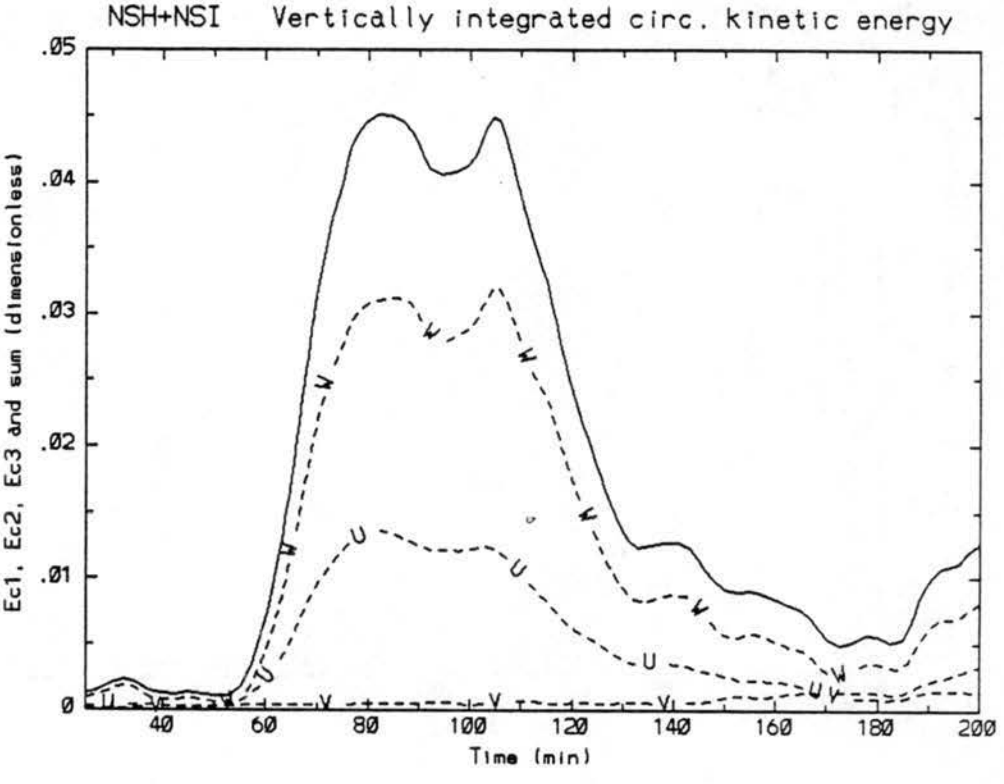

Figure 4.4. Evolution of circulation kinetic energy for simulations NSH plus NSI of Cotton *et al.* (1988).

steady build-up of horizontal velocity variance or because of a transient effect associated with the sudden imposition of the perturbation earlier. At $t=200$ min the circulation had settled down to a quasi-steady state characterised by E_c fluctuating with dimensionless magnitude of order 0.01, not too different from the present study. This explanation suggests that horizontal mixing is very important in dissipating the circulations.

4.4.2 *Averages over individual simulations*

The phase average fields from Set F have been further averaged over time and some aspects will be described in detail in following sections. Two reasons for being interested in such a time average have been advanced in Section 2.1.4: First, one suspects that the ensemble average circulation is reasonably steady over the period and that averaging over time will remove fluctuations about that average. Second, even if the ensemble average is not steady, the time average should be relevant to a more heterogeneous—and realistic—situation where the heat flux perturbation is not applied suddenly and where different regions of the flow have different histories.

Before examining time averages taken over Set F, let us look briefly at time averages from the individual simulations. The four fields of the circulation potential temperature $\langle\theta'\rangle_{p,t}$, averaged between $t = 300$ min and $t = 400$ min, are shown in Figure 4.5. All distances are made dimensionless by h_* and the temperature is made dimensionless by θ_*. In all four simulations the air near the surface is warmer over the heat-flux maximum ($\hat{x} = 0$) than it is over the heat-flux minimum ($\hat{x} = \pm\lambda_p/2$). The limiting amplitude of the variation as $z \to 0$ is about $2\,\theta_*$, or 0.2 K. (Actually, the lowest level at which the air temperature is evaluated in the model is at $z=\Delta z/2=0.03h_*$ and below there the θ field is extrapolated linearly. The simulated temperature perturbation *at the surface* has a much larger amplitude, approximately 4 K.) Away from the surface the $\langle\theta'\rangle_{p,t}$ pattern varies more between the different simulations. In all cases $\langle\theta'\rangle_{p,t} > 0$ at $\hat{x}=0$ up to at least $z=0.5h_*$; in all but Run F2 $\langle\theta'\rangle_{p,t} < 0$ at $\hat{x}=0$ near $z=h_*$.

One expects the buoyancy perturbations forced by the surface to drive a symmetrical circulation with ascent over the heat flux maxima and descent over the heat-flux minima.

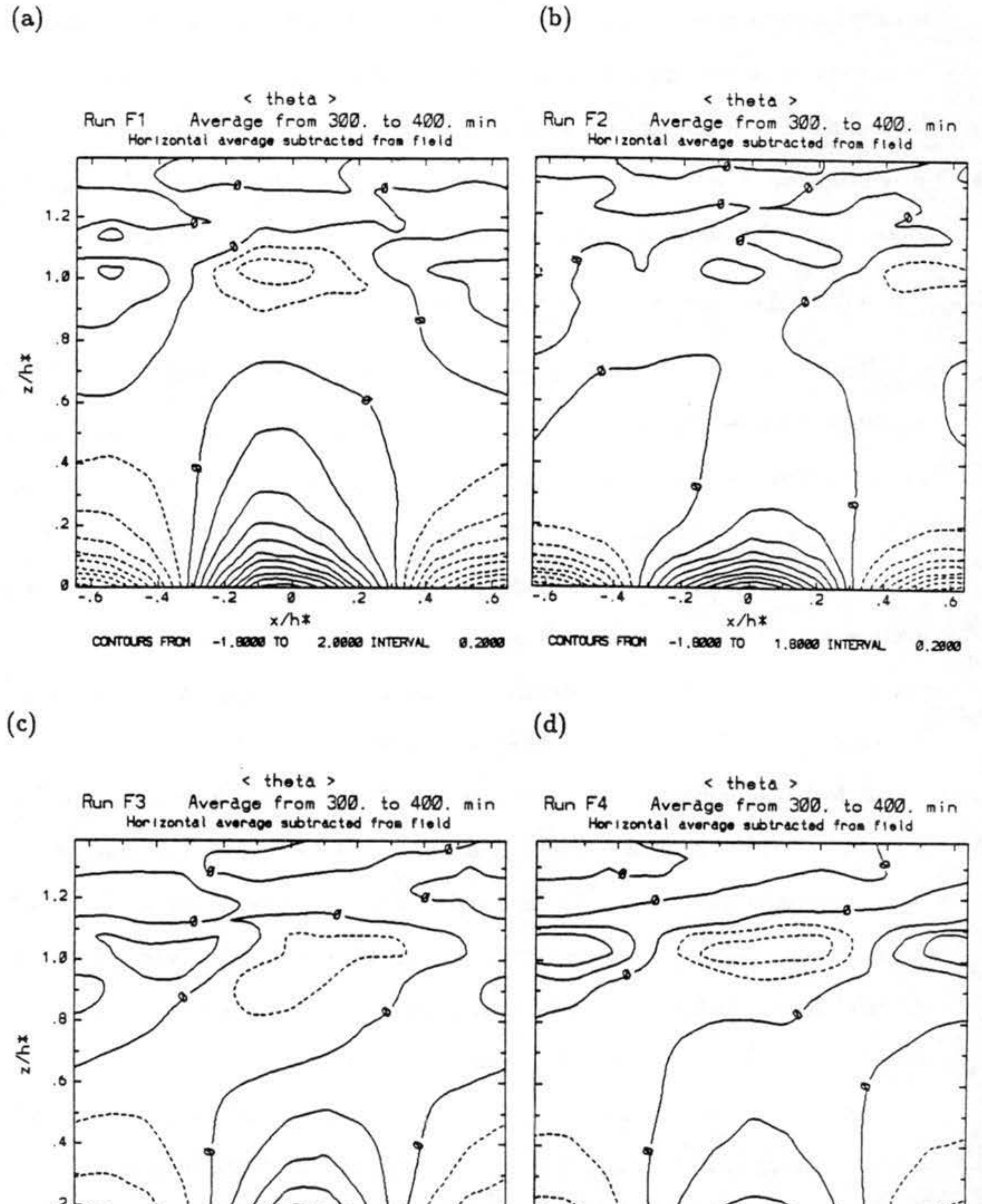

Figure 4.5. Circulation potential temperature perturbation $\langle\theta'\rangle_{p,t}$ for (a) Run F1, (b) Run F2, (c) Run F3 and (d) Run F4. Contour interval $0.2\,\theta_*$ for all figures. Positive and zero contour lines are solid; negative contour lines are dashed.

Figure 4.6 shows the $\langle w' \rangle_{p,t}$ fields. In three of the simulations the expected pattern is seen, with maximum velocities of order $0.1w_*$ to $0.2w_*$; in the other (puzzlingly) it is not. An examination of similar time averages from the horizontally homogeneous simulations with $u_0 = 0\,\mathrm{m\,s^{-1}}$ (Runs A and B) suggests that circulations with random phase and vertical velocities up to $\sim 0.1w_*$ can arise by chance, so the question arises whether the surface heat-flux perturbation really does drive an ensemble-average circulation.

The following procedure has been used to test for the statistical significance of the circulations observed in Runs F1 to F4. A parameter,

$$W \stackrel{\text{def}}{=} \left.\frac{\langle w' \rangle_{p,t}}{2}\right|_{\hat{x}=0,z=0.4h_*} - \left.\frac{\langle w' \rangle_{p,t}}{2}\right|_{\hat{x}=0.5\lambda_p,z=0.4h_*},$$

is defined to capture a circulation that is symmetrical about $\hat{x} = 0$ and has maximum vertical velocity near the middle of the boundary layer. From the fields of Figure 4.6 one finds

$$W = \quad 0.10w_*, -0.01w_*, \quad 0.23w_*, \quad 0.12w_*,$$

for Runs F1 to F4 respectively. The mean of this sample is $0.11w_*$ and the standard deviation is $0.10w_*$. The null hypothesis is that the sample is drawn from a population with mean zero, and the alternative hypothesis is that the population mean is non-zero (positive *or* negative, since a deviation of either sign cannot be excluded *a priori*). Based on a t test with 3 degrees of freedom (Devore, 1982) the null hypothesis can be rejected with approximately 90% confidence. This is a lower level of confidence than the traditional thresholds (95%, 99%), but it is suggestive nonetheless. Corroborating evidence comes from a second series of averages calculated between $t = 200\,\mathrm{min}$ and $t = 300\,\mathrm{min}$, for which

$$W = \quad 0.19w_*, \quad 0.08w_*, \quad 0.16w_*, \quad 0.08w_*,$$

for Runs F1 to F4. Although this earlier period would be affected by any transient effects associated with the sudden imposition of the perturbation, the E_c/t curve in Figure 4.2 suggests that the two periods are comparable. The mean of the second sample is $0.13w_*$ and the standard deviation is $0.06w_*$, and the null hypothesis can be rejected at better

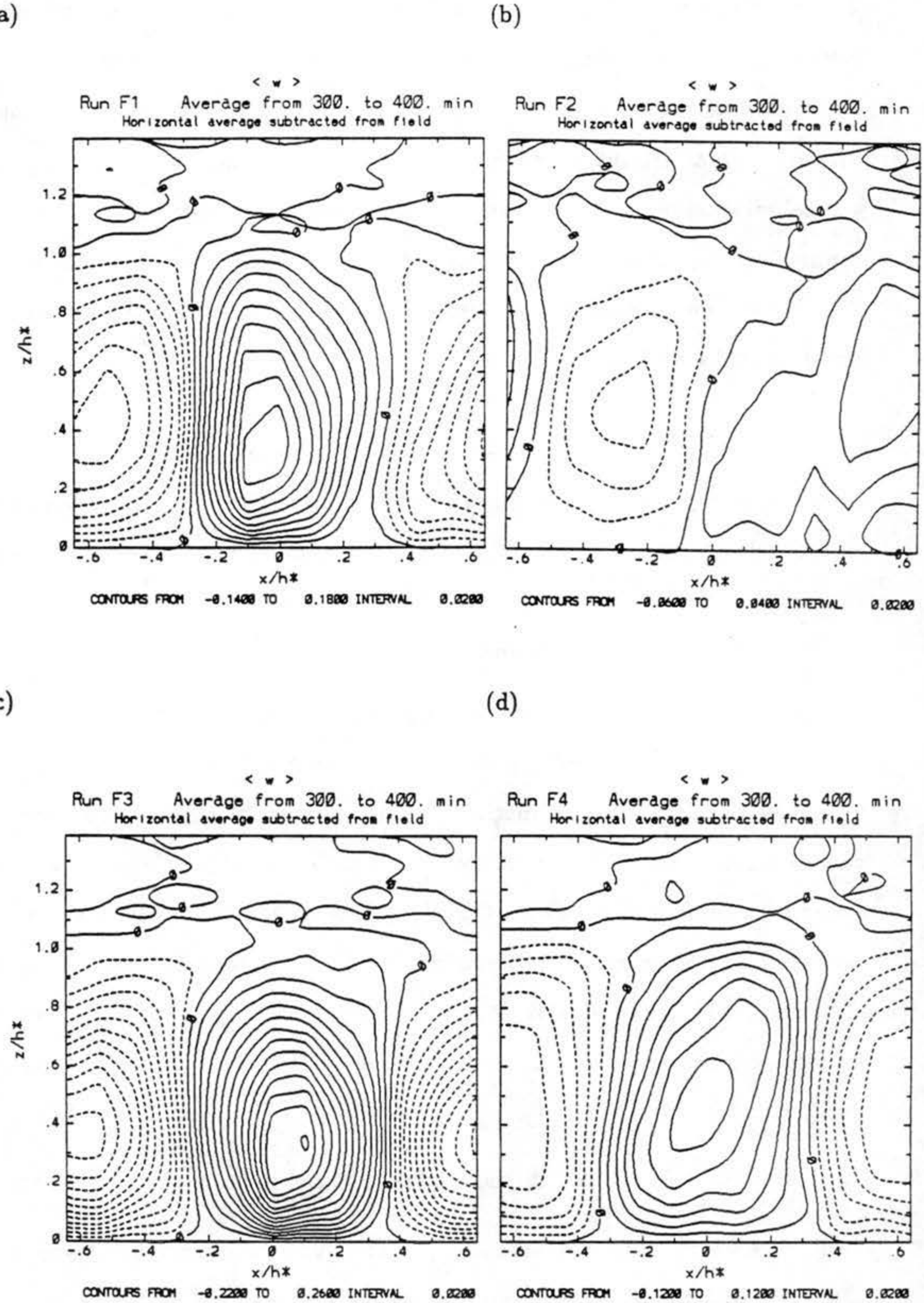

Figure 4.6. As Figure 4.5, but the vertical velocity perturbation $\langle w' \rangle_{p,t}$. Contour interval $0.02 w_*$.

than 95% confidence. The t test requires that the underlying distribution be Gaussian and that the members of the sample be independent. The former assumption is plausible, but the latter one is not strictly true, since each pair of simulations is initialised from a single field. Still, there is little evidence from two sets of values quoted above that W for the first member of each pair is either positively or negatively correlated with W from the second member.

Based on the values of W presented above and on the symmetry of *most* of the $\langle w' \rangle_{p,t}$ fields calculated from the individual simulations, it is concluded that the surface heat-flux perturbations *probably* drive mean ascent over the heat-flux maxima and descent over the heat-flux minima. From all eight values of W one can estimate that the typical maximum vertical velocity is $\sim 0.12 w_*$ and the uncertainty (standard error) is $\sim 0.03 w_*$. It is worth noting that the result has come only after a great deal of averaging in a situation with a high degree of regularity.

4.4.3 *Scaling parameters*

The boundary layer depth h_* based on the time-averaged heat flux profile of Set F is 1170 m. For comparison, over a sample of four horizontally homogeneous simulations (Runs A to D), h_* had mean 1160 m and standard deviation 8 m—the difference is not statistically significant. The dimensionless wavelength of the surface perturbation is therefore

$$\frac{\lambda_p}{h_*} = 1.28.$$

In principle the boundary layer depth can vary with $\hat{x}$: this depth is called h to distinguish it from h_*, which is based on horizontally averaged statistics. In Section 2.3 (Equation 2.33), h was defined as the height where the net tendency in $\langle \theta \rangle_{p,t}$, excluding the effect of subsidence, crosses zero. With this definition it is found that h in Set F varies by less than $\pm 1\%$ with $\hat{x}$. Other indicators of the top of the boundary layer are the maxima in potential temperature gradient $\partial \langle \theta \rangle_{p,t} / \partial z$ and temperature variance $\langle (\theta')^2_{p,t} \rangle_{p,t}$ (Section 4.4.5 below). They are both at $z = 1.08 h_*$ and also vary by less than 1% horizontally.

4.4.4 *The time-averaged circulation*

Figure 4.7 shows $\langle u\rangle_{p,t}$, $\langle w\rangle_{p,t}$ and $\langle\theta\rangle_{p,t}$ fields averaged over time between $t=300$ min and $t=400$ min for Set F. (The $\langle v\rangle_{p,t}$ field has not been shown, incidentally, because its magnitude is negligibly small, as expected from symmetry considerations.) The graphs on the right-hand edge of the figures show profiles of the horizontal averages $\langle a\rangle_{h,t}$ and the contour plots show the deviations from the horizontal average $\langle a'\rangle_{p,t}$ on an $\hat{x}$-z plane.[11]

The $\langle w'\rangle_{p,t}$ field is approximately symmetrical about $\hat{x}=0$—whereas the ensemble average must be exactly symmetrical—and has maximum amplitude near $z=0.35h_*$. The maximum velocity in the updraught is slightly larger in magnitude than the maximum in the downdraught ($0.14w_*$ versus $-0.12w_*$ to the nearest contour interval). The $\langle u'\rangle_{p,t}$ field is related to the $\langle w'\rangle_{p,t}$ field by mass continuity. Below $z=0.35h_*$ it has inflow into the base of the ascending branch, with maximum velocity ($\sim 0.18w_*$) near the surface, and above $z=0.35h_*$ it has substantially weaker outflow with maximum velocity ($\sim 0.04w_*$) near $z=0.9h_*$. The $\langle\theta'\rangle_{p,t}$ field has the air over $\hat{x}=0$ warmer in the lower and middle boundary layer and cooler in the upper boundary layer, with the reversal in sign near $z=0.7h_*$. At the surface the amplitude of the perturbation is $2.0\,\theta_*$, as was noted above, but in the middle and upper boundary layer the perturbations are an order of magnitude less, i.e., $\sim 10^{-1}\theta_*$ or $\sim 10^{-2}K$.

The $\langle\pi\rangle_{p,t}$ field can be decomposed as follows

$$\langle\pi\rangle_{p,t} = \langle\pi_b\rangle_{p,t} + \langle\pi_t\rangle_{p,t} + \langle\pi_c\rangle_{p,t} + \langle\pi_s\rangle_{p,t}, \tag{4.8}$$

where π_b (buoyancy pressure) is induced by the buoyancy force, π_t (turbulence pressure) is induced by turbulence/turbulence interaction, π_c (circulation pressure) is induced by circulation/circulation interaction, and π_s (subgrid pressure) is induced by the subgrid stresses. The buoyancy and subgrid pressures have already been defined in Equations 3.4

[11] A similar format will be used extensively in later figures, but in some cases the horizontal average will *not* be subtracted from the contoured field and this fact will be indicated in the title.

(a)

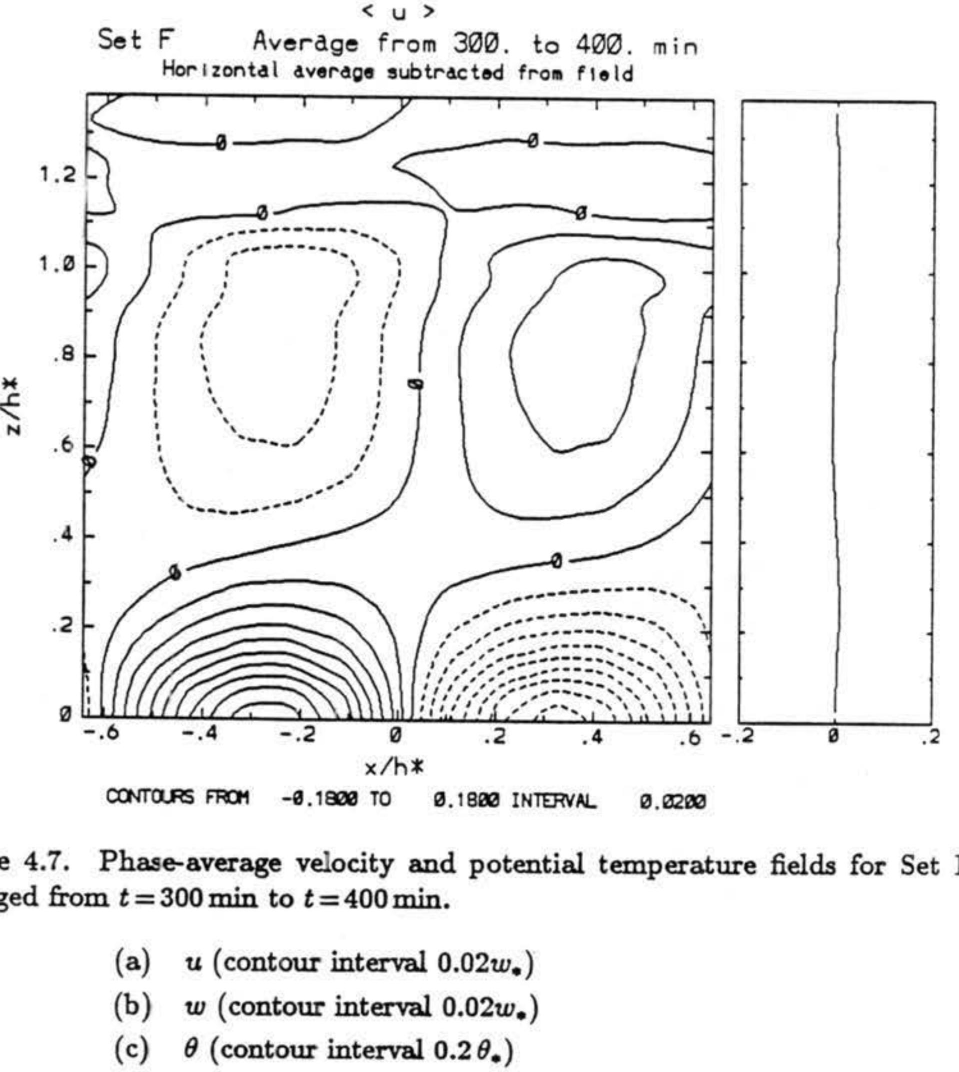

Figure 4.7. **Phase-average velocity and potential temperature fields for Set F, time-averaged from $t = 300$ min to $t = 400$ min.**

(a) **u (contour interval $0.02w_*$)**

(b) **w (contour interval $0.02w_*$)**

(c) **θ (contour interval $0.2\,\theta_*$)**

The contour plots show fields of the form $\langle a' \rangle_{p,t}$ and the profiles on the right-hand side show $\langle a \rangle_{h,t}$.

Continued on following page.

(b)

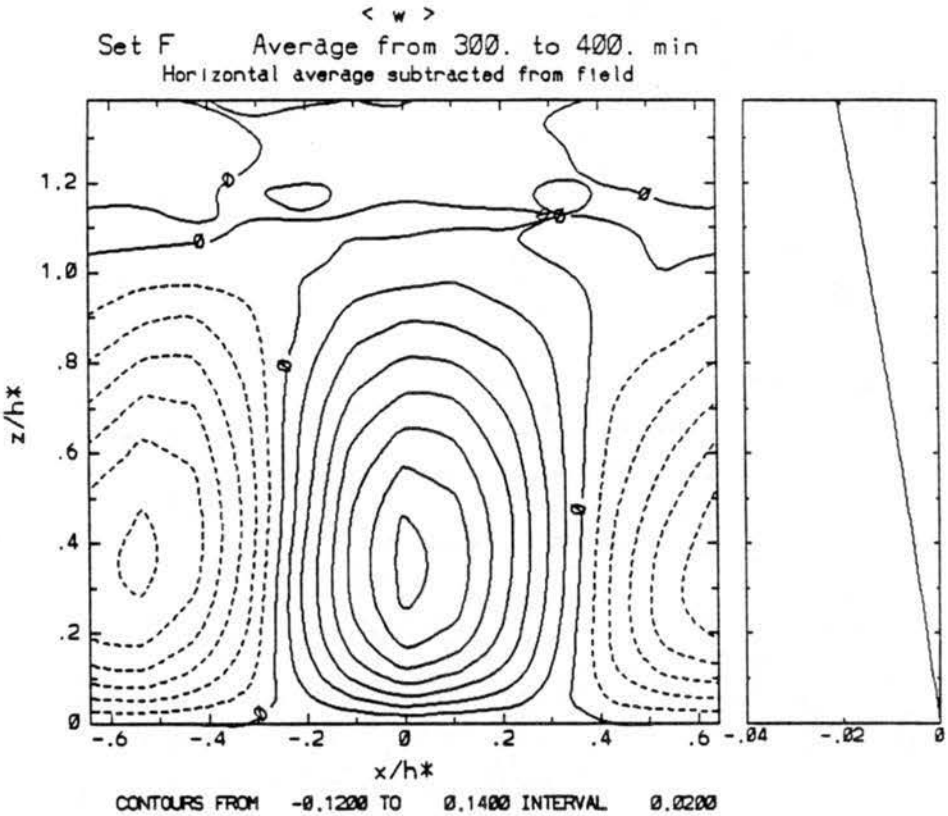

(c)

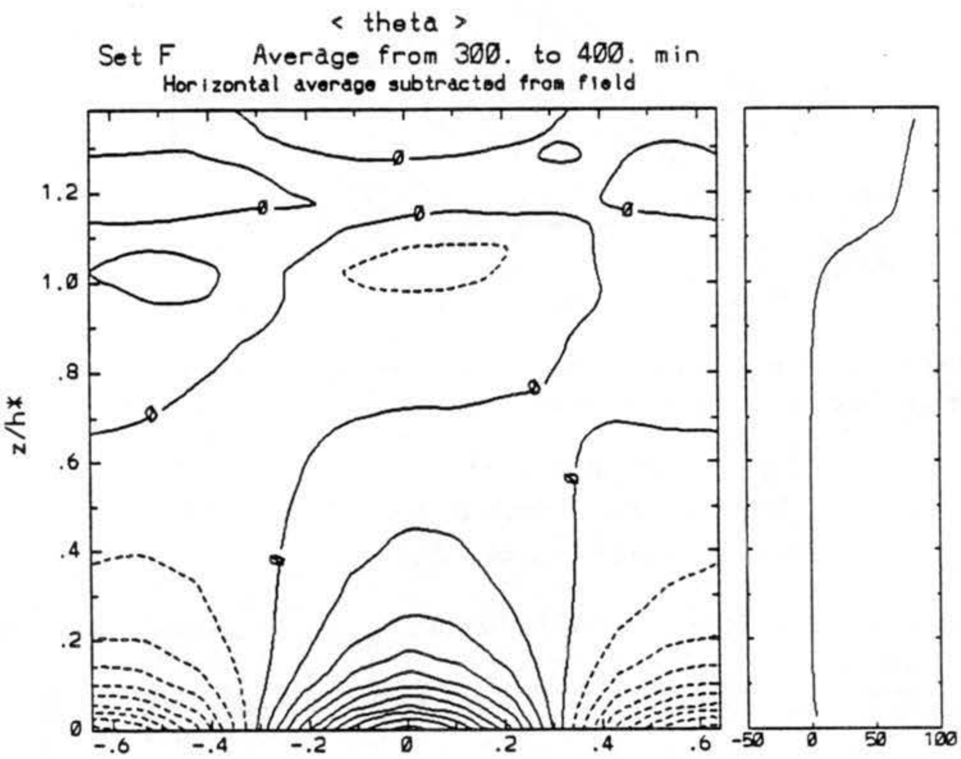

Figure 4.7 (continued).

and 3.7 (Section 2.2.1). The other two components are calculated respectively as

$$\rho_0\theta_0\nabla_a^2\pi_t = -\frac{\partial^2}{\partial x_i \partial x_j}\left(\rho_0 (u_i')_{p,t}(u_j')_{p,t}\right) \tag{4.9}$$

$$\rho_0\theta_0\nabla_a^2\pi_c = -\frac{\partial^2}{\partial x_i \partial x_j}\left(\rho_0 \langle u_i'\rangle_{p,t}\langle u_j'\rangle_{p,t}\right). \tag{4.10}$$

The definition of the turbulence pressure has changed from the one used in chapter 3—although the symbol π_t has been retained—in that the "turbulence" is now $(u_i')_{p,t}$. There is also a residual pressure, associated with interaction between circulation and the horizontal average flow, which is extremely small.

The pressure field and its components are shown in Figure 4.8. The maximum amplitude of the net pressure perturbation is about $0.14\pi_*$, which corresponds to an amplitude in p of only 0.7 Pa. Pressure is generally low above the heat-flux maximum, this effect being largely due to a minimum in the buoyancy pressure near the surface plus minima in the turbulence pressure and subgrid pressure in the middle of the boundary layer. The circulation pressure is much smaller than the others and has a pattern with wavelength $\lambda_p/2$ reminiscent of the two-dimensional updraught/downdraught model described in Section 3.3.1.

Moeng and Wyngaard (1986b) have proposed that surface temperature perturbations of a few kelvin beneath a convective boundary layer should produce buoyancy-pressure perturbations of the order of 10^2 Pa, much larger than are found here. However Hadfield *et al.* (1988) have argued that large temperature perturbations will be confined to a shallow layer near the surface, and shown that Moeng and Wyngaard's analysis fails to account properly for the strong temperature gradients within that layer.

The magnitude of the time-averaged circulation can be described in terms of the profiles of quantities like $\langle\langle a'\rangle_{p,t}\langle b'\rangle_{p,t}\rangle_h$, which will be called the circulation variances and covariances. A few simple ratios based on these quantities have been devised to characterise the circulation—their values are listed in Table 4.3. Most of the ratios are self-explanatory: they compare a circulation variance or covariance with the corresponding moment of the form $\langle a'b'\rangle_{h,t}$, at selected heights (numbers 1 to 5) or in terms of their

(a)

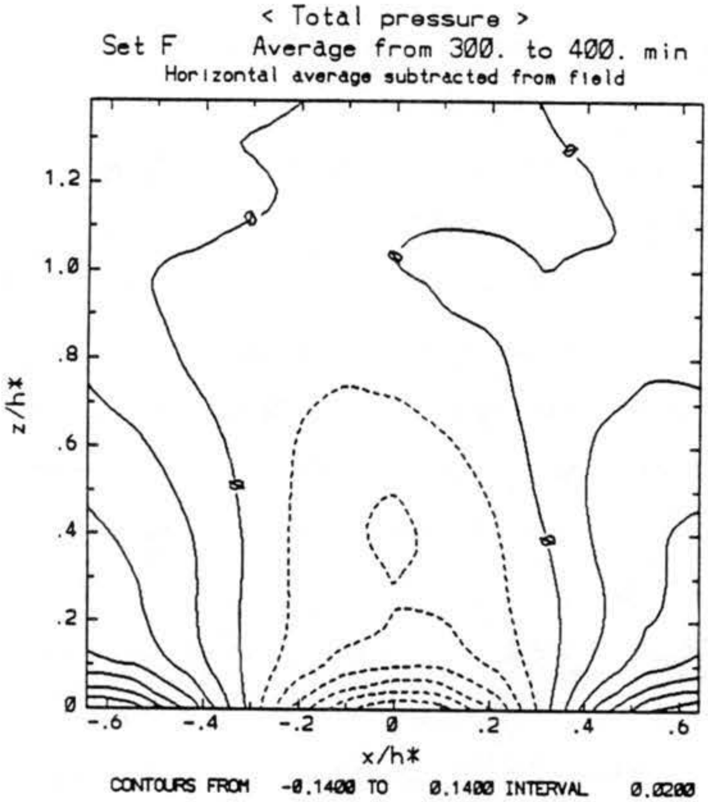

Figure 4.8. Phase-time averaged pressure fields for Set F.

- (a) total pressure π (contour interval $0.02\pi_*$)
- (b) buoyancy pressure π_b (contour interval $0.02\pi_*$)
- (c) turbulence pressure π_t (contour interval $0.02\pi_*$)
- (d) circulation pressure π_c (contour interval $0.002\pi_*$)
- (e) subgrid pressure π_s (contour interval $0.01\pi_*$)

The horizontal-average profiles for π and π_b are not included because they are calculated with respect to an arbitrary base state.

Continued on following pages.

(b)

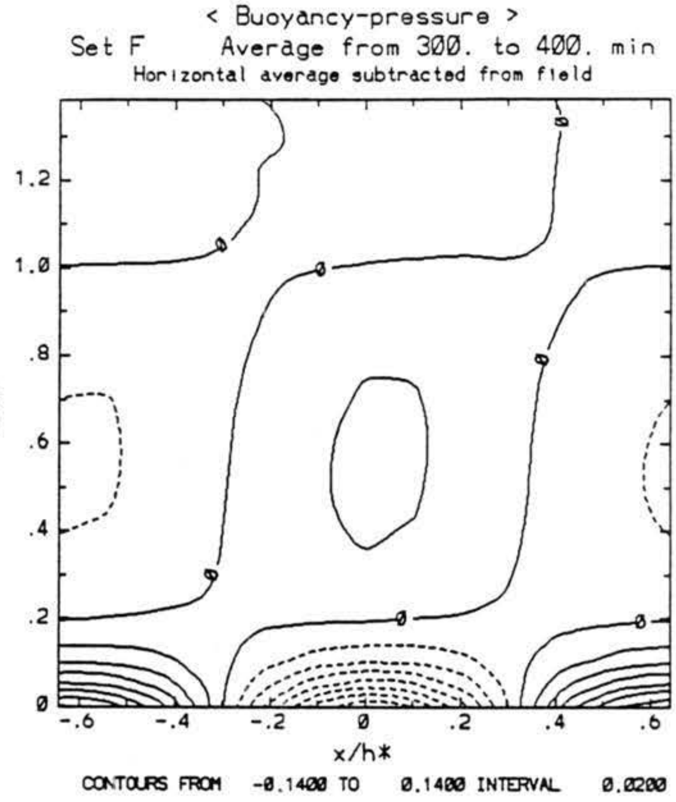

(c)

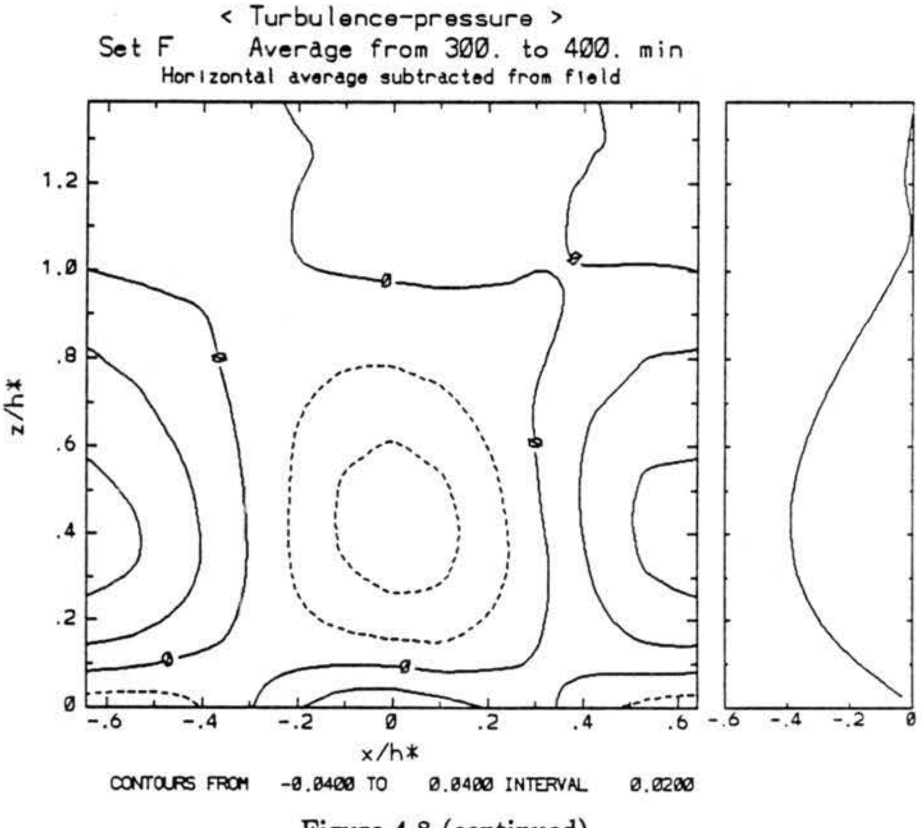

Figure 4.8 (continued).

Continued.

(d)

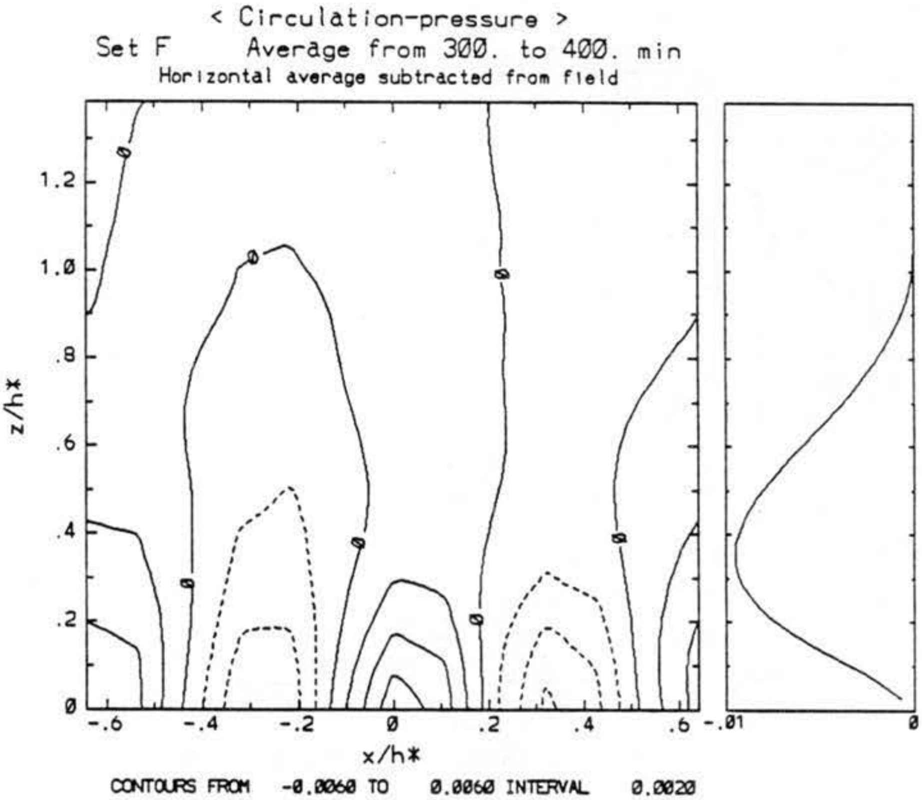

(e)

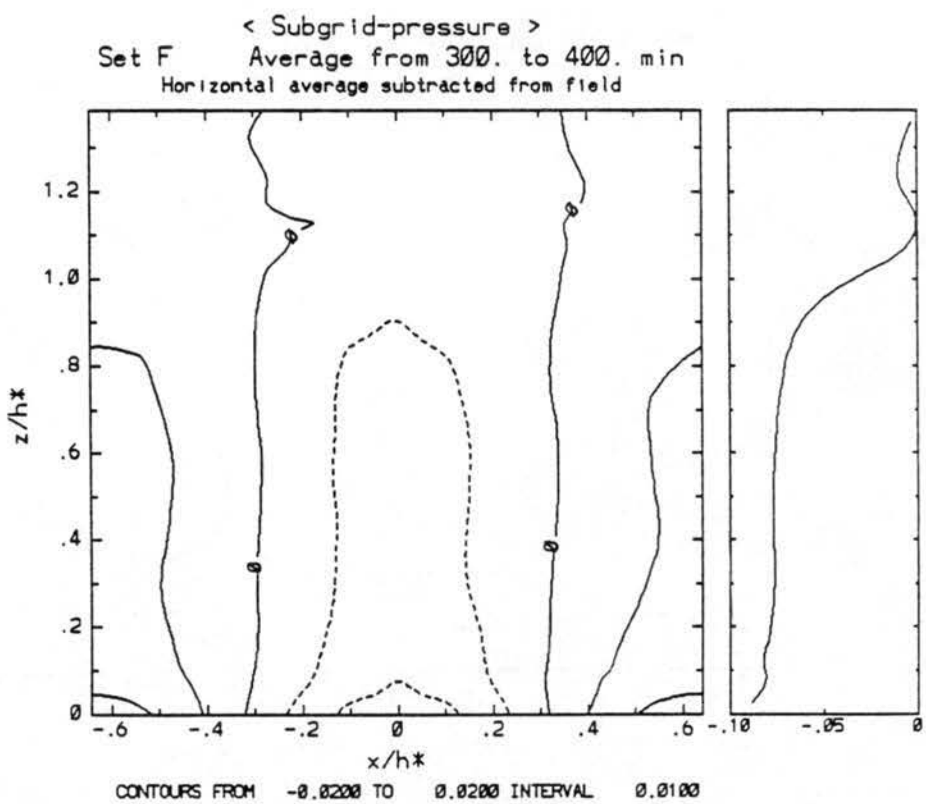

Figure 4.8 (continued).

Table 4.3. Ratios characterising the time-averaged circulation in Set F.

No.	Ratio	Height	Value
1	$\left\langle \langle u' \rangle_{p,t}^2 \right\rangle_h / \left\langle u'^2 \right\rangle_{h,t}$	$0.1h_*$	0.03
		$0.9h_*$	0.006
2	$\left\langle \langle w' \rangle_{p,t}^2 \right\rangle_h / \left\langle w'^2 \right\rangle_{h,t}$	$0.4h_*$	0.02
3	$\left\langle \langle \theta' \rangle_{p,t}^2 \right\rangle_h / \left\langle \theta'^2 \right\rangle_{h,t}$	$0.1h_*$	0.10
		$0.9h_*$	0.003
4	$\left\langle \langle \pi' \rangle_{p,t}^2 \right\rangle_h / \left\langle \pi'^2 \right\rangle_{h,t}$	$0.1h_*$	0.03
		$0.9h_*$	0.002
5	$\left\langle \langle w' \rangle_{p,t} \langle \theta' \rangle_{p,t} \right\rangle_h / \left\langle w'\theta' \right\rangle_{h,t}$	$0.2h_*$	0.04
		$1.0h_*$	0.007
6	$\sum_i \int_Z \left\langle \langle u_i' \rangle_{p,t}^2 \right\rangle_h / \sum_i \int_Z \left\langle u_i'^2 \right\rangle_{h,t}$	–	0.011
7	$\int_Z \left\langle \langle w' \rangle_{p,t} \langle \theta' \rangle_{p,t} \right\rangle_h / \int_Z \left\langle w'\theta' \right\rangle_{h,t}$	–	0.04
8	$\int_Z \left\langle \langle u' \rangle_{p,t}^2 \right\rangle_h / \sum_i \int_Z \left\langle \langle u_i' \rangle_{p,t}^2 \right\rangle_h$	–	0.34
9	$-(\theta_0^2/g) \int_Z \left\langle \langle w' \rangle_{p,t} \frac{\partial}{\partial z} \langle \pi_b' \rangle_{p,t} \right\rangle_h / \int_Z \left\langle \langle w' \rangle_{p,t} \langle \theta' \rangle_{p,t} \right\rangle_h$	–	0.45

vertical integrals (numbers 6 and 7). It is apparent that in general the time-averaged circulation accounts for only a small fraction (a few percent) of the variability in the boundary layer; the only exception is in the temperature variance near the surface, where the fraction is 0.10 at $z = 0.1h_*$. The last two ratios (numbers 8 and 9) in Table 4.3 are each based on two different integrals of the circulation. Number 8 compares the energy in the horizontal velocity field to the total kinetic energy. Number 9 will be discussed in Section 5.2, but is included in the table for completeness. It is the fraction of the buoyancy production in the vertically integrated, circulation vertical velocity variance $\langle\langle w'\rangle_{p,t}^2\rangle_h$ that is opposed by the π_b-gradient; in other words it is a crude measure of "how hydrostatic" the buoyancy pressure field is. For circulation fields of a given shape, both the ratios will increase with an increase in the aspect ratio (defined as the vertical length scale divided by the horizontal length scale).

Another interesting indicator of the strength of the circulation is shown in Figure 4.9. It is the fraction of the points at any position on the $\hat{x}$-z plane that have $w' > 0$. The profile on the right-hand side of the figure shows the horizontal average; throughout most of the boundary layer $w' > 0$ between 35% and 45% of the time, as in the horizontally homogeneous case. The contour plot shows the phase-average field, but note that the horizontal average has *not* been subtracted. Upward motion is found more frequently where $\langle w'\rangle_{p,t} > 0$ than where $\langle w'\rangle_{p,t} < 0$, as one might expect, but even at $\hat{x} = 0$ it is found less than 50% of the time everywhere above $z = 0.2h_*$.

4.4.5 *Turbulence: deviations from the time-averaged circulation*

Figure 4.10 shows a number of turbulent moments calculated for Set F. These are quantities of the form $\langle(a')_{p,t}^2\rangle_{p,t}$ and $\langle(a')_{p,t}(b')_{p,t}\rangle_{p,t}$ where a and b are velocity components or temperature; the former will be labelled the a variance and the latter the a/b covariance. The fields of u/v covariance, v/w covariance and v/θ covariance are not shown, since they are expected to be zero in the ensemble average and are found to be very small.

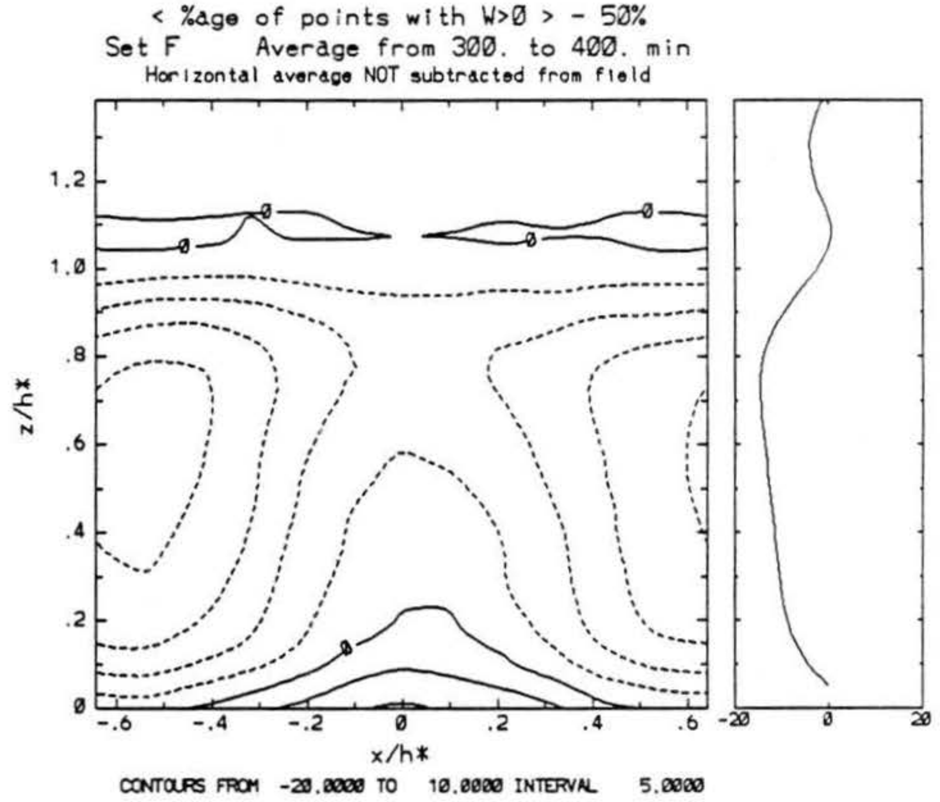

Figure 4.9. The percentage of points at each position $(\hat{x},z)$ with $w' > 0$, minus 50%, for Set F. Contour interval 5%.

(a)

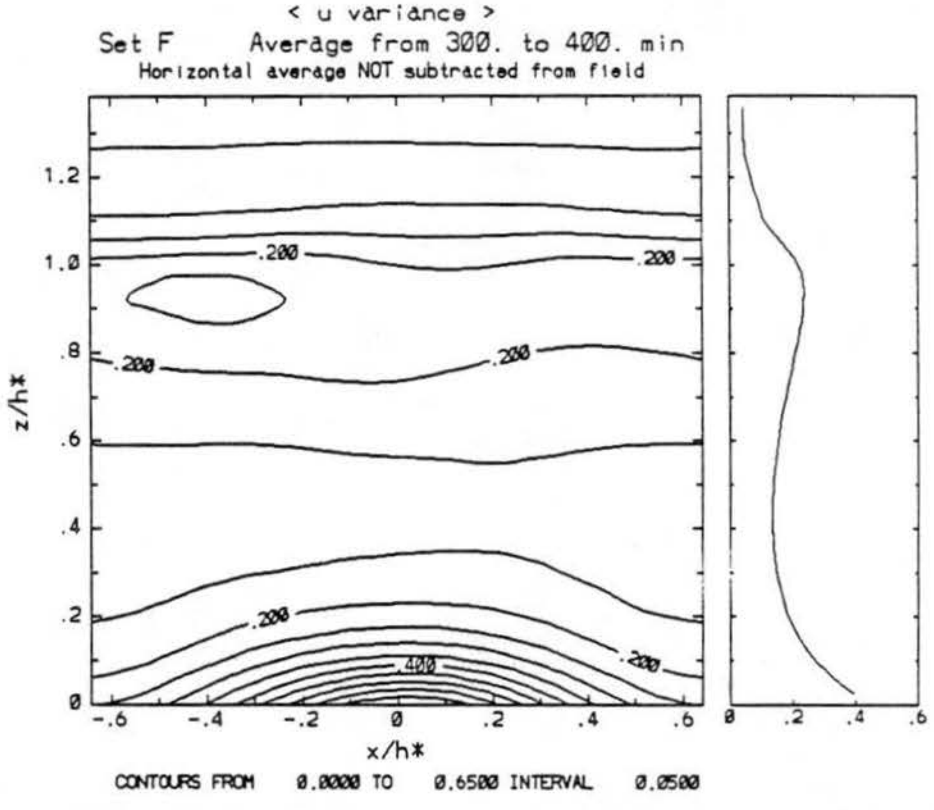

Figure 4.10. Fields of turbulent variances and covariances of the form $\langle (a')_{p,t}(b')_{p,t}\rangle_{p,t}$ for Set F.

(a) u variance (contour interval $0.05w_*^2$)

(b) v variance (contour interval $0.05w_*^2$)

(c) w variance (contour interval $0.05w_*^2$)

(d) u/w covariance (contour interval $0.01w_*^2$)

(e) square root of θ variance (contour interval $0.5\,\theta_*$)

(f) u/θ covariance (contour interval $0.1w_*\theta_*$)

(g) w/θ covariance (contour interval $0.1w_*\theta_*$)

Continued on following pages.

(b)

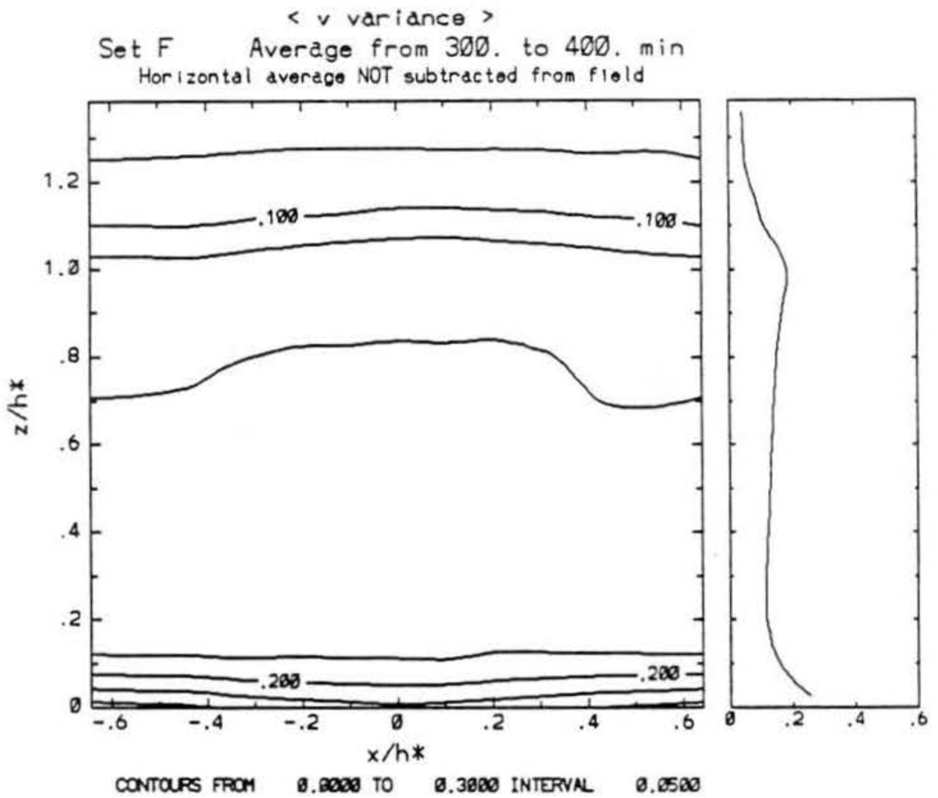

(c)

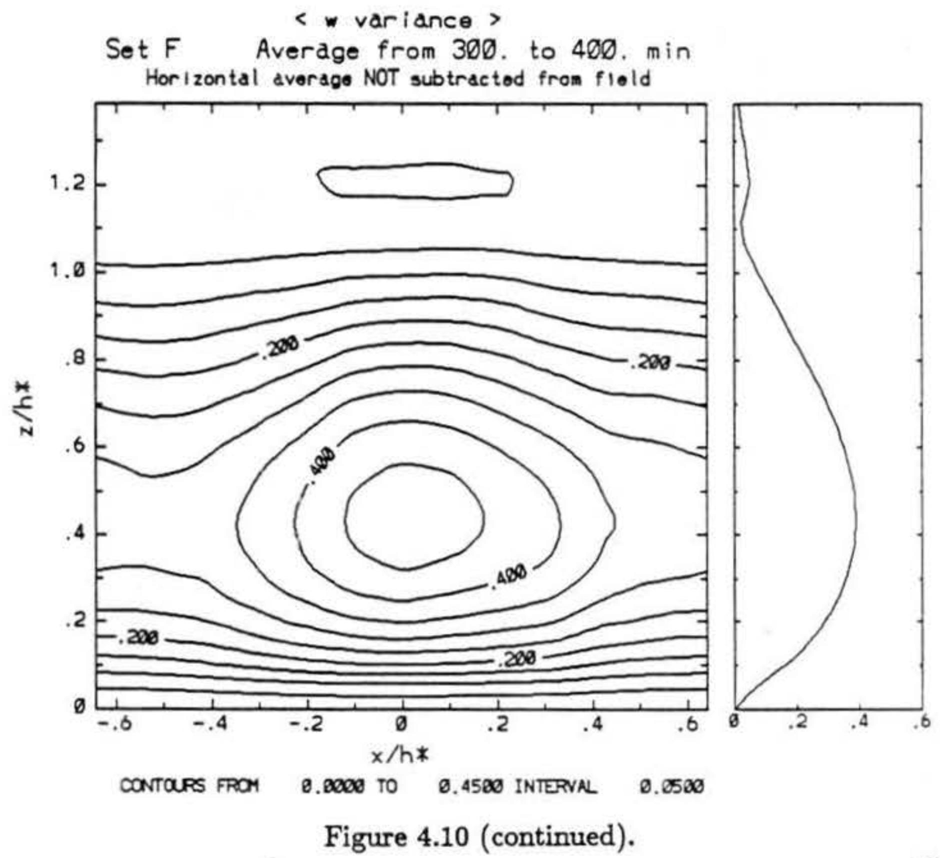

Figure 4.10 (continued).

Continued.

(d)

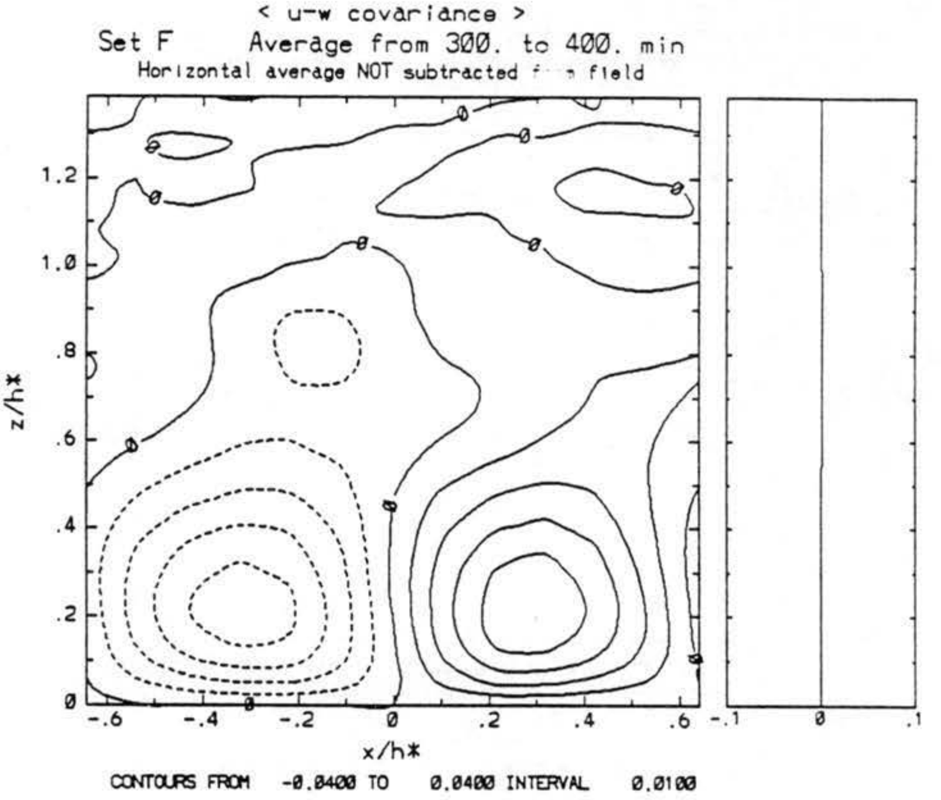

(e)

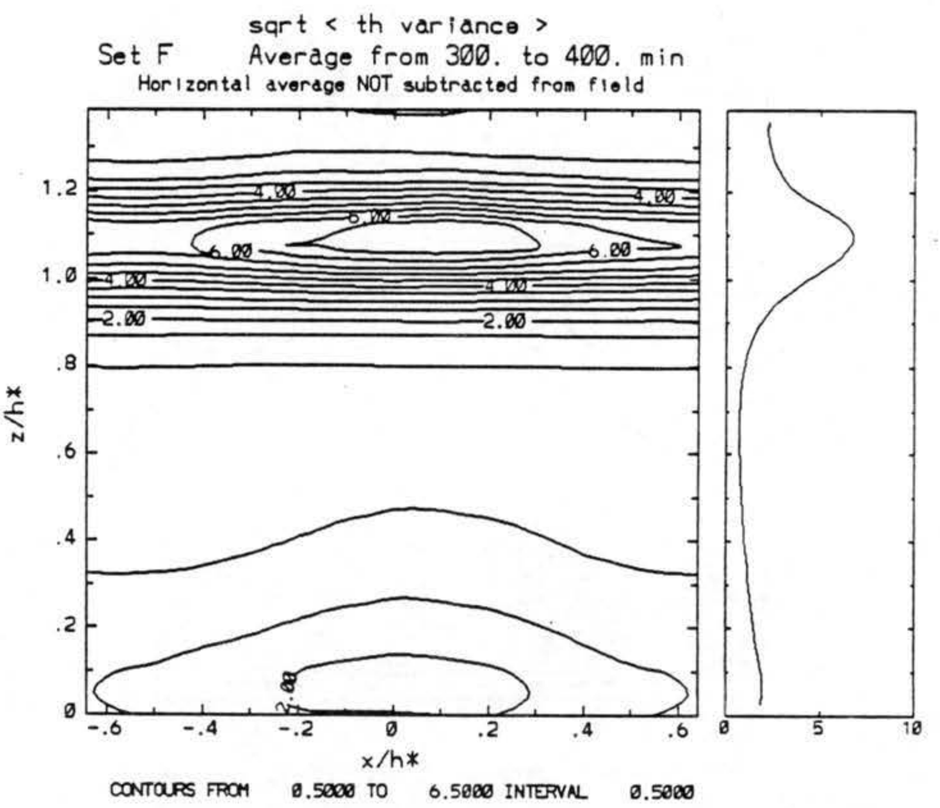

Figure 4.10 (continued).

Continued.

(f)

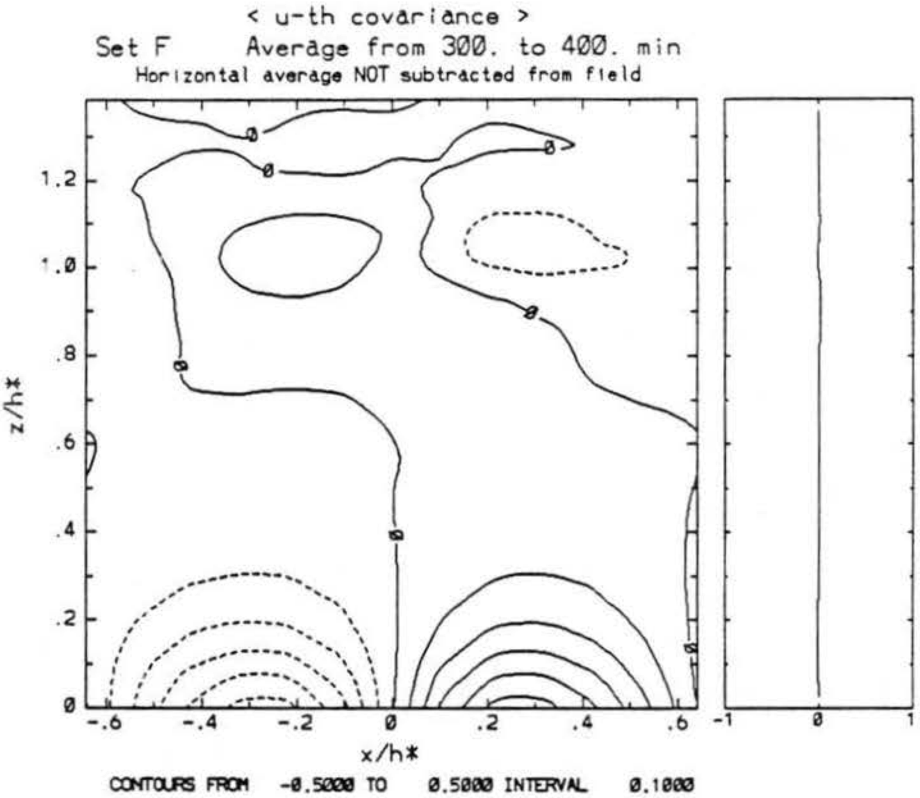

(g)

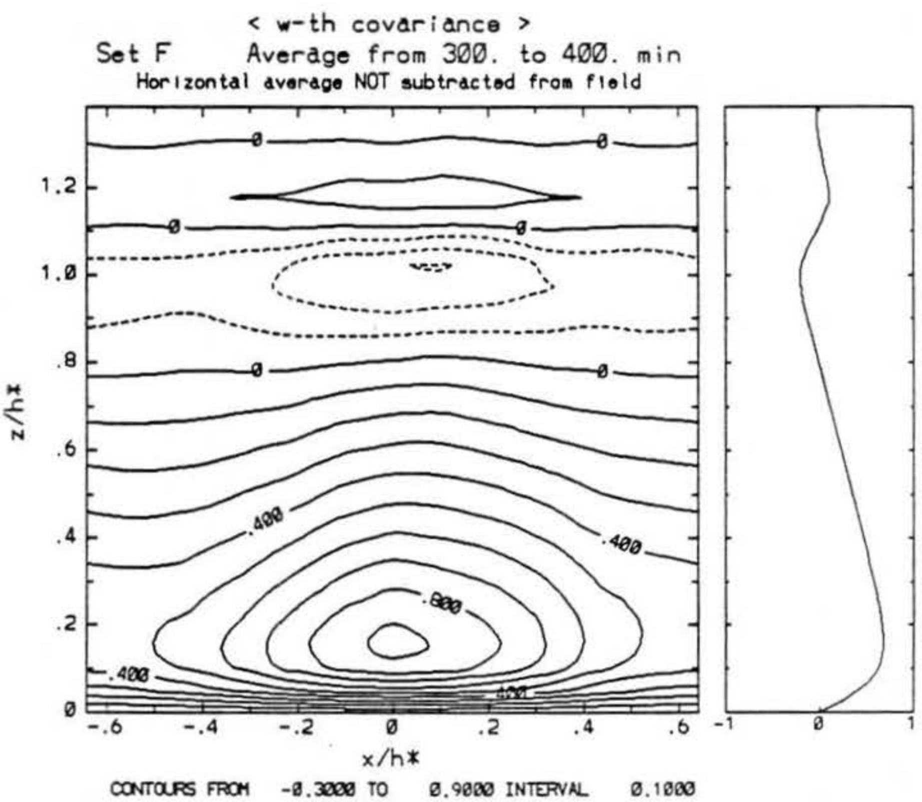

Figure 4.10 (continued).

The variance and covariance fields for Runs F1 to F4 have also been examined separately. In general the features described below are found in each of the individual simulations.

There is a wealth of information in the diagrams and they deserve careful study. Some of the conspicuous features are the pronounced low-level maxima in u variance and θ variance at $\hat{x}=0$, the very weak minimum in v variance in the same position, the low-level maximum in w/θ covariance and the mid-level maximum in w variance. The u/w and u/θ covariances are negative for $\hat{x} < 0$ and positive for $\hat{x} > 0$ in the lower boundary layer. They can be interpreted as horizontal fluxes in in w and θ away from $\hat{x}=0$; the u/w covariance can also be interpreted as a vertical flux in u directed downwards to the left of the mean updraught and upwards to its right. Near the inversion there is a negative-maximum in the w/θ covariance (i.e., more vigorous entrainment) at $\hat{x}=0$, and a corresponding maximum in θ variance. The horizontal velocity variances do not vary much with $\hat{x}$ in the upper boundary layer, although there is a slight maximum in u variance at $\hat{x} = -0.4h_* = -0.3\lambda_p$. The fact that this is displaced to the right of the heat-flux minimum suggests that it *may* be associated with the region of horizontal convergence at the top of the mean downdraught, which is also displaced to the right.

For some perspective on the amplitude of the horizontal variation in the w variance, one can calculate the variance that would be expected if the surface heat flux were constant at either the maximum or minimum value. Note that the minimum surface heat flux is $0.5\,w_*\theta_*$ and the maximum is $1.5\,w_*\theta_*$. The velocity scale based on the minimum flux and on depth h_* is

$$w_{*\min} \stackrel{\text{def}}{=} (0.5\, g\, \langle\Phi\rangle_h\, h_*/\theta_{0S})^{1/3} = (0.5)^{1/3} w_* = 0.79 w_*,$$

whereas the velocity scale based on the maximum flux is

$$w_{*\max} \stackrel{\text{def}}{=} (1.5\, g\, \langle\Phi\rangle_h\, h_*/\theta_{0S})^{1/3} = (1.5)^{1/3} w_* = 1.15 w_*,$$

Since the w variance in mid-boundary-layer over a surface with constant heat flux $w_*\theta_*$ is $0.4w_*^2$, a reasonable first guess for the w variance in mid-boundary-layer over the heat flux minimum is $0.4w_{*\min}^2 = 0.25w_*^2$ and over the heat-flux maximum it is $0.4w_{*\max}^2 = 0.53w_*^2$. The variation observed in Set F is somewhat smaller, from $0.30w_*^2$ to $0.45w_*^2$.

4.4.6 *Horizontal-average statistics*

The present section returns to the decomposition described in Equation 4.1, and used in analysing horizontally homogeneous simulations in chapter 3. The variance in a is now $\langle a'^2 \rangle_{h,t}$. It is related to the (circulation) variance described in Section 4.4.4 and the (turbulent) variance described in Section 4.4.5 by the relationship

$$\left\langle a'^2 \right\rangle_{h,t} = \left\langle \langle a' \rangle_{p,t}^2 \right\rangle_h + \left\langle \langle (a')_{p,t}^2 \rangle_{p,t} \right\rangle_h . \tag{4.11}$$

Figure 4.11 shows profiles of the velocity variances $\langle u_i'^2 \rangle_{h,t}$ for Runs F1 to F4, and Figure 4.12 shows the average over Set F. The most striking feature is that there are large differences between the u and v variance profiles. In two of the simulations (Runs F2 and F4) the u variance exceeds the v variance at all levels with the difference having a maximum ($\sim +0.20w_*^2$) near the surface, a minimum in the middle of the boundary layer, and a second maximum ($\sim +0.10w_*^2$) at around $z = 0.9h_*$. In the other two simulations (Runs F1 and F3) the difference is smaller near the surface ($\sim +0.10w_*^2$), it is essentially zero between $z = 0.3h_*$ and $z = 0.7h_*$, and above there it is positive (maximum $\sim +0.05w_*^2$)in one simulation and slightly negative in the other. Comparing this figure with Figure 4.6, there is a hint of a negative correlation between the time-averaged circulation on the one hand, and the difference between the u and v variances on the other. The two simulations with $\langle u'^2 \rangle_{h,t}$ significantly greater than $\langle v'^2 \rangle_{h,t}$ have a weaker circulation.

For some perspective on the statistical significance of the differences between the horizontal velocity variances, the quantity $\langle u'^2 \rangle_{h,t} - \langle v'^2 \rangle_{h,t}$ was calculated at three different levels for a sample of nine 100-minute averages from horizontally homogeneous simulations—the same sample that was used as a control in Section 3.4. The dimensionless means and standard deviations calculated over the sample are listed in ordered pairs as follows: (0.002, 0.025) at $z = 0.1h_*$, (0.002, 0.007) at $z = 0.5h_*$ and (0.005, 0.024)

(a) (b) (c) (d)

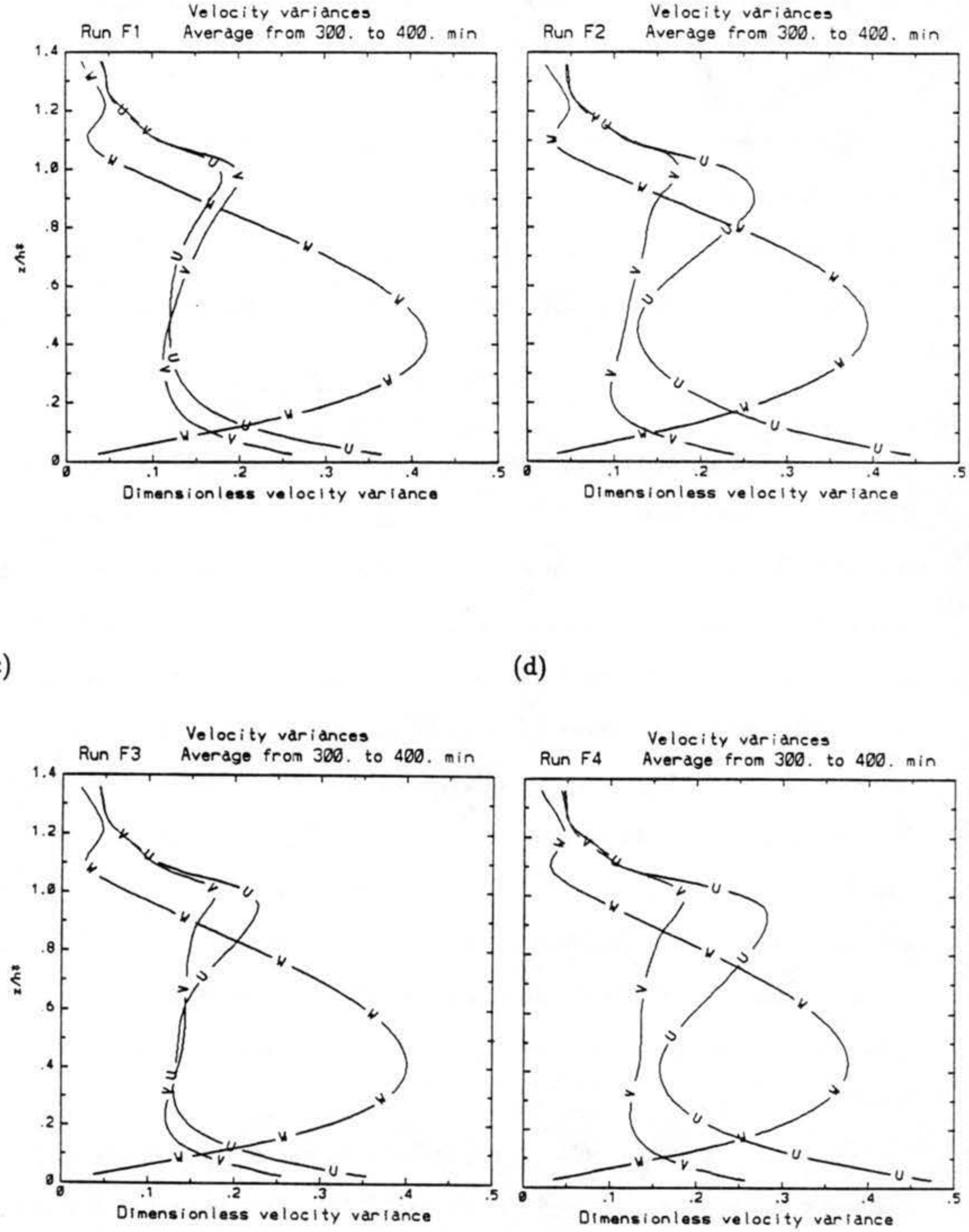

Figure 4.11. Profiles of dimensionless velocity variances $\langle u_i'^2 \rangle_{h,t}$ for (a) Run F1, (b) Run F2, (c) Run F3 and (d) Run F4.

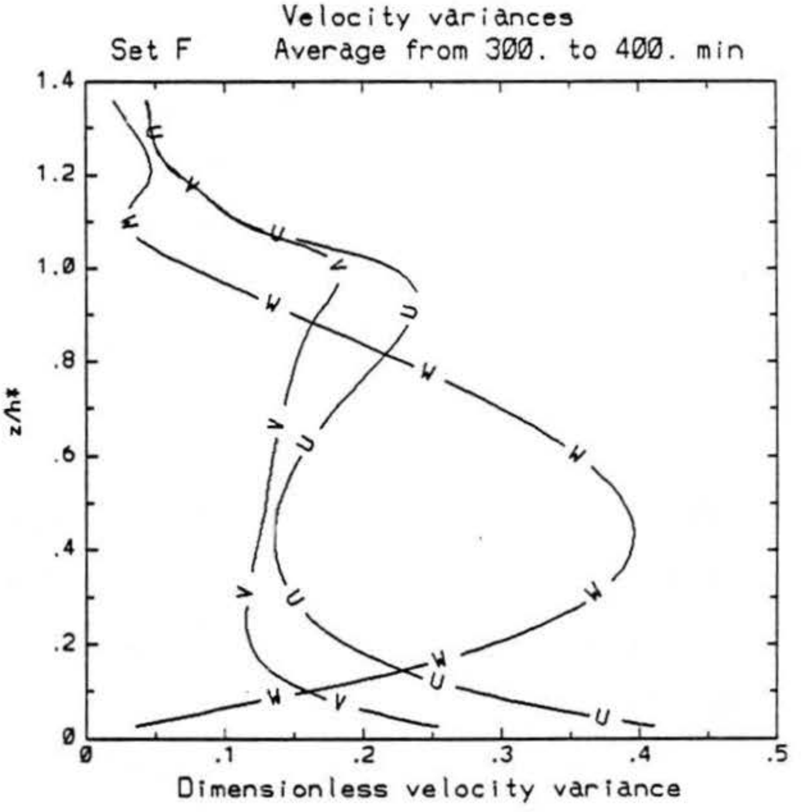

Figure 4.12. Profiles of dimensionless velocity variances $\langle u_i'^2 \rangle_{h,t}$ for Set F.

at $z = 0.9h_*$. Similar statistics based on the four averages of Figure 4.11 are: (0.122, 0.063) at $z = 0.1h_*$, (0.010, 0.016) at $z = 0.5h_*$ and (0.067, 0.065) at $z = 0.9h_*$. The sample standard deviations can be compared using an F test: at all levels the standard deviations are larger for the second sample (with the heat-flux perturbation) than for the first at a (one-tailed) confidence level of better than 95%, so the heat-flux perturbation increases the variability in $\langle u'^2\rangle_{h,t} - \langle v'^2\rangle_{h,t}$. To establish whether each sample mean is significantly different from zero one can use a single-sample t test (two-tailed this time because either a positive or a negative difference could be accepted). For the sample of horizontally homogeneous simulations the means are not significantly different from zero at any height—as one might expect—but for the perturbed sample the mean is significantly positive (95% confidence) at $z = 0.1h_*$, although not at $z = 0.5h_*$ and $z = 0.9h_*$.

One interpretation of the difference between the horizontal velocity variances is that it is a symptom of elongation of the large eddies in the y direction: inflow into the base of the updraughts then occurs mainly on the sides (as does outflow at the top) and appears as an excess of u variance over v variance. One of the cross-sections presented in the next section (Figure 4.15) supports this interpretation.

Another noticeable effect of the surface heat-flux perturbations is an increase in the temperature variance near the surface (Figure 4.13). The maximum difference is found at the lowest grid level ($z = \Delta z/2 = 0.03h_*$) and is $+1.9\,\theta_*^2$. For comparison, the variance associated with the time-averaged circulation $\langle\langle\theta'\rangle_{p,t}^2\rangle_h$ is $1.4\,\theta_*^2$, so most of the excess horizontal-average variance, but not all, can be interpreted as a direct result of the mean temperature perturbation.

Profiles of a number of other first, second and third order horizontal-average statistics have been examined and very little effect from the surface heat-flux perturbation has been found. Among the effects that *have* been identified are:

- A decrease in the height of the zero-crossing in the potential temperature gradient from $z = 0.37h_*$ to $z = 0.32h_*$.

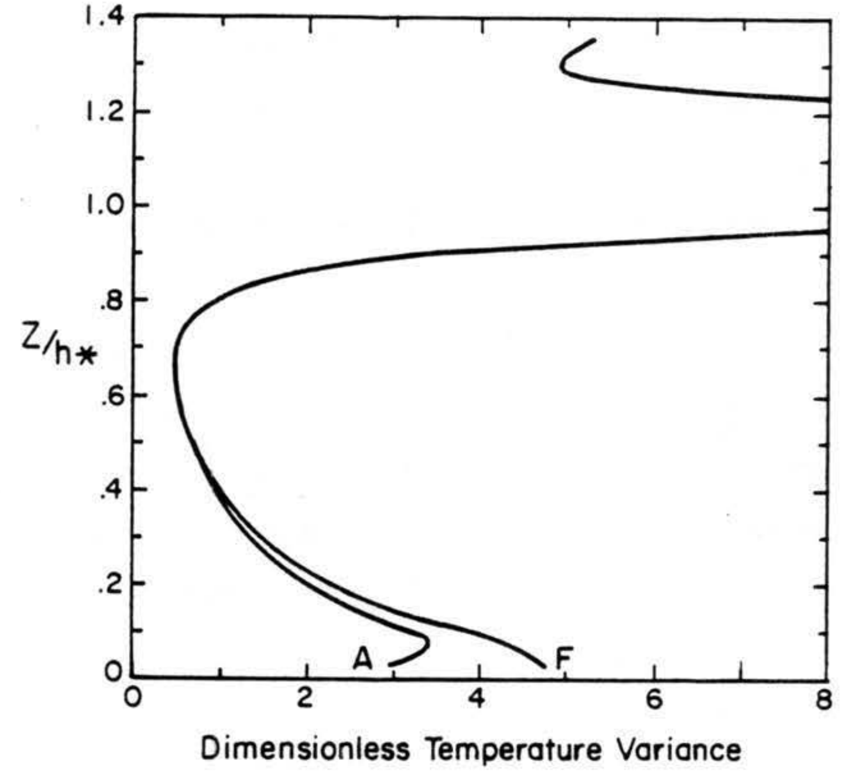

Figure 4.13. Profiles of dimensionless temperature variance $\langle \theta'^2 \rangle_{h,t}$ for Run A and Set F.

- An increase in the height (but not apparently the magnitude) of the maximum in w variance from $z=0.40h_*$ to $z=0.44h_*$.

- An increase in the magnitude (but not the height) of the maximum in $\langle w'^3\rangle_{h,t}/2$, from $0.11w_*^3$ to $0.12w_*^3$.

- An increase of about 10% in the standard deviation of pressure at all levels.

These effects are statistically significant, but none is very large: they would be *very* hard to detect in the atmosphere. The first three are consistent with an increase in the rate of vertical transfer of kinetic energy transfer and a compensating increase in stability in the middle and upper boundary layer. Regarding the fourth, it has already been mentioned (Section 3.4) that the standard deviation of pressure is sensitive to the horizontal scale of the large eddies. It can also be shown, by comparing the analytic solutions for the pressure fields associated with simple two- and three-dimensional fields of updraughts and downdraughts, that a two-dimensional field has substantially larger pressure fluctuations than a three-dimensional field for the same characteristic vertical velocity. The increase in the standard deviation of pressure can therefore be interpreted as a result of a change in the geometry of the large eddies.

Finally, spectra from Runs F1 to F4 have been examined. Figure 4.14 shows the one-dimensional power spectra of w in the x and y directions near the middle of the boundary layer (to be specific, an average over levels $z=0.25h_*$, $z=0.50h_*$ and $z=0.75h_*$). Note that the wavelength of the heat-flux perturbation is $\lambda = 1.28h_*$ so its wavenumber is $kh_*=4.9$. The spectra differ somewhat from simulation to simulation, but in all of them the x-spectral density is greater than the y-spectral density at $kh_*=4.9$ and less at the smallest wavenumber, $kh_*=1.6$.

4.4.7 *Cross-sections*

Many of the features described in previous sections are only evident after a great deal of averaging, so one should not expect to see them always reflected in the instantaneous fields. Several cross-sections have been examined, concentrating in particular on the

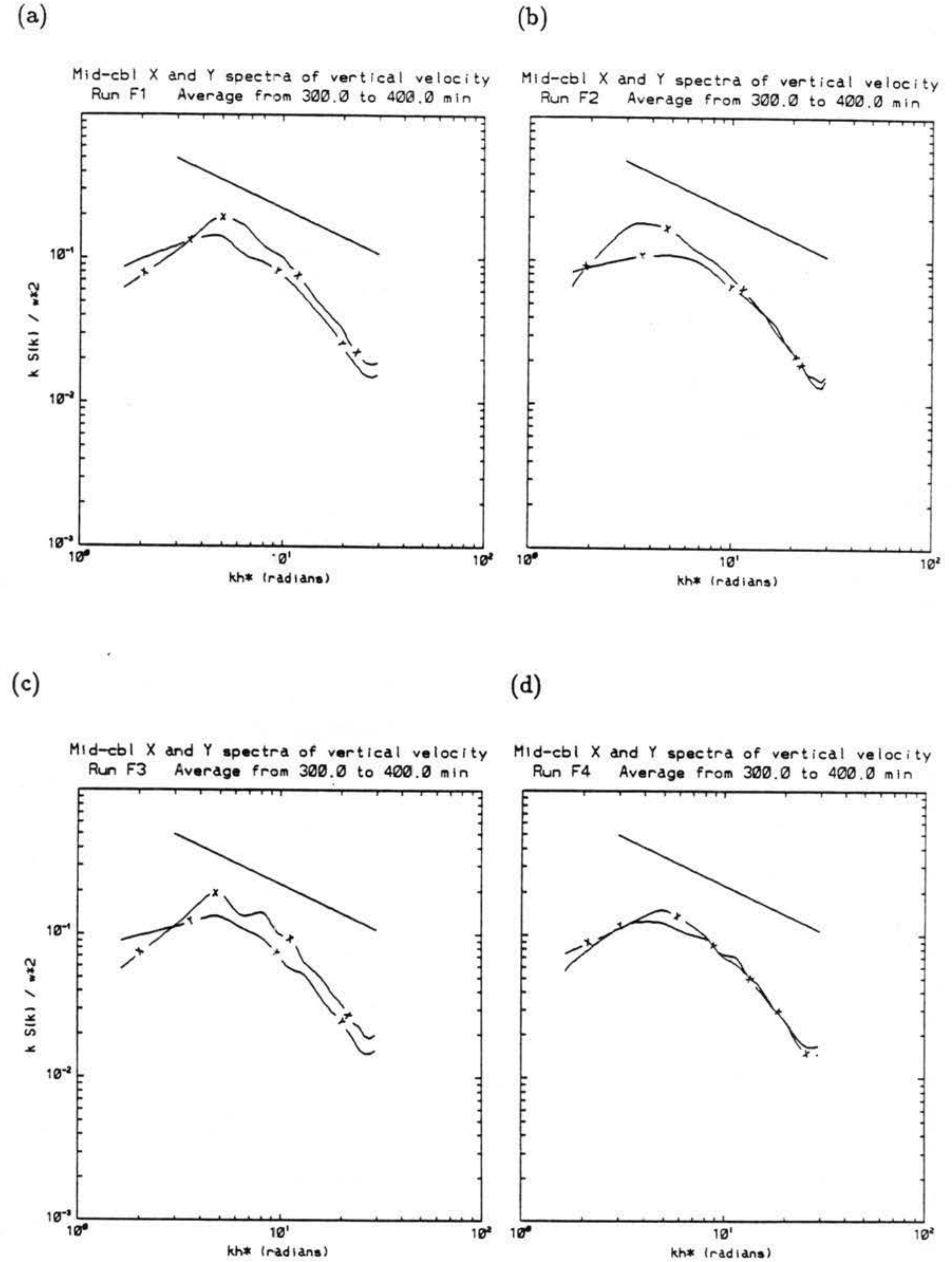

Figure 4.14. Dimensionless mid-boundary-layer spectra of vertical velocity in the x (—X—) and y (—Y—) directions for (a) Run F1, (b) Run F2, (c) Run F3 and (d) Run F4. Spectra are averaged over three levels: $z=0.25h_*$, $z=0.50h_*$ and $z=0.75h_*$.

configuration of the updraughts in the middle of the boundary layer. In some, the fields are not obviously different from what is observed in the horizontally homogeneous simulations; in some they are. Figure 4.15 shows horizontal cross-sections of w' from one of the simulations, Run F4, at $z = 0.25h_*$ at two selected times. The first time, $t = 330\,\mathrm{min}$, is chosen so that the difference $\langle u'^2 \rangle_{h,t} - \langle v'^2 \rangle_{h,t}$ is at a maximum. At the second time, $t = 360\,\mathrm{min}$, the difference is still positive, but a lot smaller. At both times the circulation kinetic energy E_c is fairly small, about $0.005\, w_*^2 h_{\rho *}$. Note that, in this simulation, the lines of maximum surface heat flux are at $x = \pm 0.75\,\mathrm{km}$ and $x = \pm 2.25\,\mathrm{km}$.

At $t = 330\,\mathrm{min}$ the configuration of the updraughts is reminiscent of the intersecting-ribbon structure seen in Run A (Figure 3.2a), but dominated by an updraught aligned along one of the heat-flux maxima ($x = -0.75\,\mathrm{km}$). There is no sign of organisation on a wavelength of λ_p in the x direction. The strongest downdraughts are found near the updraughts, but the region where descending motion is most frequent is along the heat-flux minimum at $x = 1.5\,\mathrm{km}$. At $t = 360\,\mathrm{min}$ the updraughts tend to form cells, more like Run A, and there is less evidence of alignment parallel to the heat-flux perturbations. Note, however, the upper half of the domain (i.e., $y > 0$) where there is organisation on a wavelength λ_p, with updraughts over each heat-flux maximum (more or less) and downdraughts between.

4.5 Simulations with $\lambda_p = 1500\,\mathrm{m}$ and $u_0 = 1\,\mathrm{m\,s^{-1}}$

4.5.1 *Evolution of surface-driven circulations*

There are two simulations with $\lambda_p = 1500\,\mathrm{m}$ and $u_0 = 1\,\mathrm{m\,s^{-1}}$: Runs G1 and G2. Collectively they are described as Set G. Again the circulation kinetic energy E_c has been calculated for the first member of the pair (Figure 4.16a) and for the average of the two (Figure 4.16b). Again it is not at all clear from the figures what the effect of the heat-flux perturbation is. Some insight is given by Figure 4.17, which shows the horizontal position of the maximum in $\langle w \rangle_p$ from Run G1 versus time. (Briefly, to calculate the position of the maximum, $\langle w \rangle_p$ is averaged through a layer in the middle boundary layer, then the phase of the Fourier component with $\lambda = 1500\,\mathrm{m}$ is calculated.) The

(a)

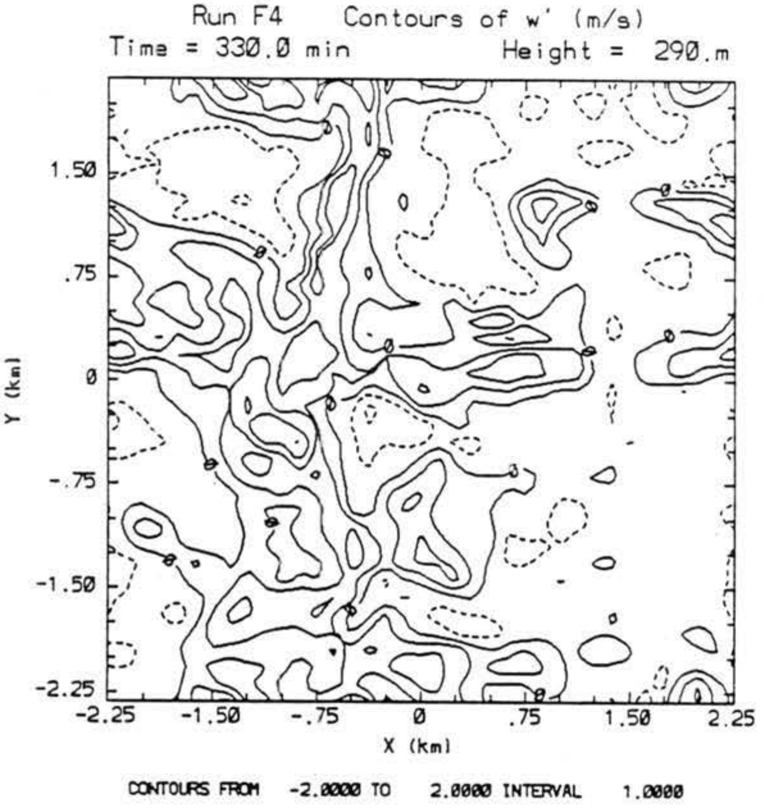

(b)

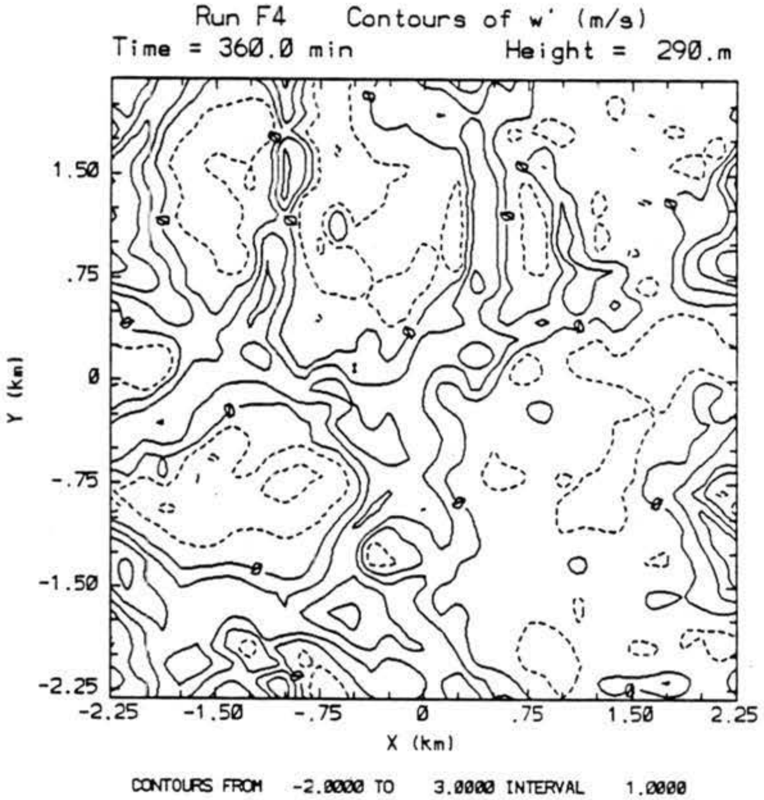

Figure 4.15. Cross-sections of w' at $z = 0.25h_*$ from Run F4. The times are (a) $t = 330$ min and (b) $t = 360$ min. The contour interval is $1.0\,\mathrm{m\,s^{-1}}$.

(a)

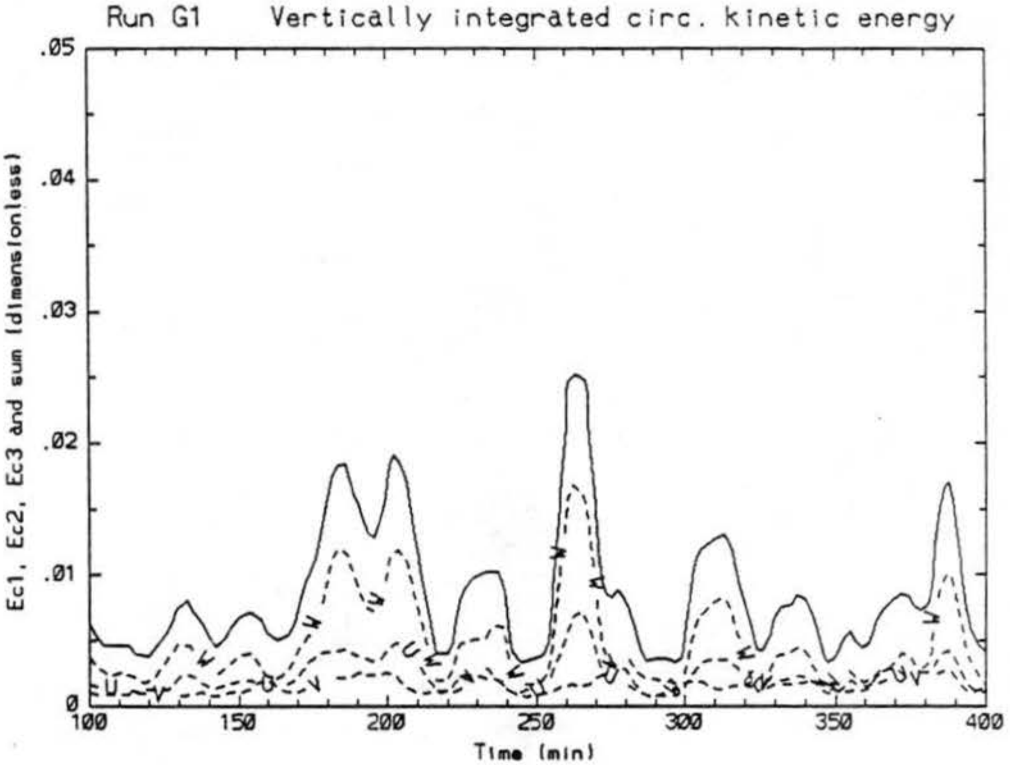

(b)

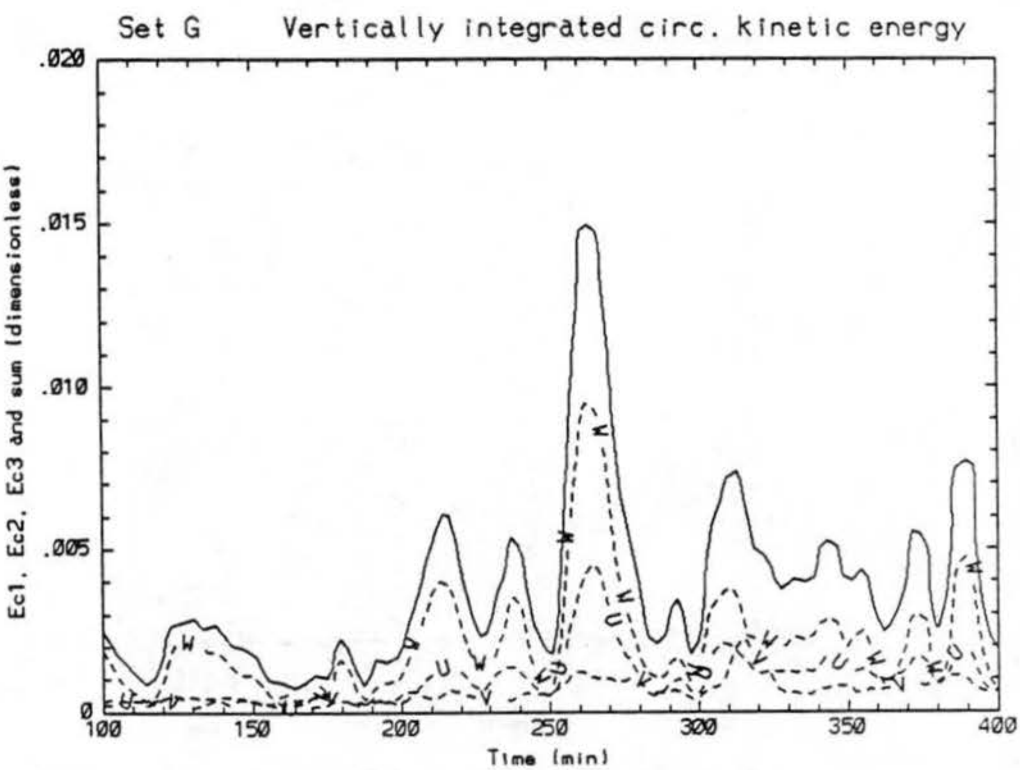

Figure 4.16. Evolution of circulation kinetic energy for (a) Run G1 and (b) Set G.

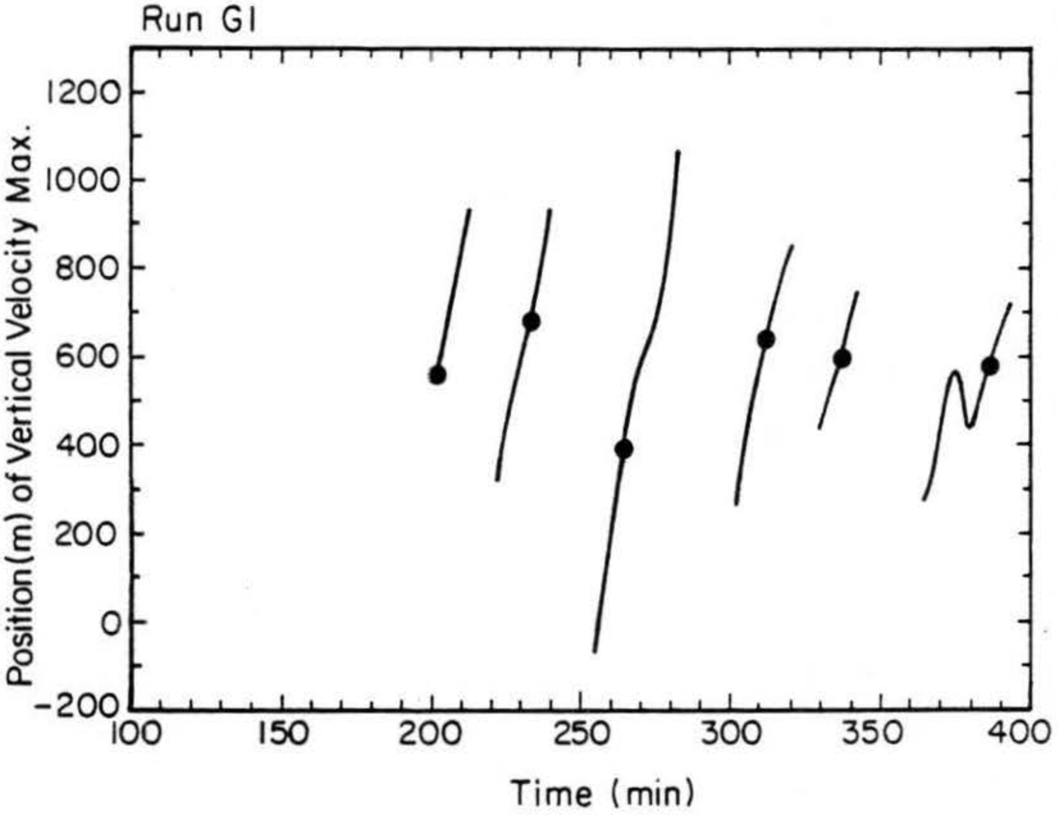

Figure 4.17. Position ($\hat{z}$) of the maximum in $\langle w' \rangle_p$ versus time for Run G1. Times when E_c (Figure 4.16a) reaches a local maximum are indicated by a "●".

curve has been suppressed when E_c is below a threshold value, and before $t = 200\,\mathrm{min}$. The times of the peaks in E_c are marked. The $\langle w \rangle_p$ maximum moves steadily in the x direction at $\sim 1\,\mathrm{m\,s^{-1}}$, with E_c typically reaching a peak when the $\langle w \rangle_p$ maximum is near $\hat{x} = 600\,\mathrm{m}$. It appears that the circulation periodically amplifies as its updraught moves into a favourable region downstream of the heat-flux maximum, then decays.

4.5.2 *Averages over individual simulations*

Figure 4.18 shows $\langle w' \rangle_{p,t}$ for Runs G1 and G2, averaged from $t = 300\,\mathrm{min}$ to $t = 400\,\mathrm{min}$. The similarity between the fields from the two simulations may look like a coincidence, given the high degree of variability amongst comparable figures for the $u_0 = 0\,\mathrm{m\,s^{-1}}$ simulations. Actually the mean wind greatly eases the problem of calculating stable time-averaged circulations, because it prevents stationary, long-lived large eddies from dominating. Again a parameter W is defined to capture the circulation—this time the definition is

$$W \stackrel{\mathrm{def}}{=} \left.\frac{\langle w' \rangle_{p,t}}{2}\right|_{\hat{x}=0.4\lambda_p, z=0.5h_*} - \left.\frac{\langle w' \rangle_{p,t}}{2}\right|_{\hat{x}=-0.1\lambda_p, z=0.5h_*}.$$

For the fields of Figures 4.18a and b, W equals $0.09w_*$ and $0.08w_*$ respectively. For the same simulations averaged from $t = 200\,\mathrm{min}$ to $t = 300\,\mathrm{min}$, W equals $0.05w_*$ and $0.08w_*$, and the fields are very similar in shape to the ones from the later period. For comparison, W calculated for two time-averages from a horizontally homogeneous simulation with $u_0 = 1\,\mathrm{m\,s^{-1}}$ (specifically Run C from $t = 200\,\mathrm{min}$ to $t = 300\,\mathrm{min}$, and from $t = 300\,\mathrm{min}$ to $t = 400\,\mathrm{min}$) has values $0.02w_*$ and $0.02w_*$. There is not really enough data to establish statistical significance, but the weight of evidence points to the conclusion there is an ensemble-average circulation driven by the heat-flux perturbation in Set G.

Further evidence is available from an earlier pair of simulations with $u_0 = 1\,\mathrm{m\,s^{-1}}$, averaged from $t = 80\,\mathrm{min}$ to $t = 100\,\mathrm{min}$ and reported by Cotton *et al.* (1988)—see their Figure 5.7. For this pair the general appearance of the fields is similar to those in Figure 4.18, and $W \approx 0.11$. It may not seem appropriate to draw on the simulations of Cotton *et al.* as evidence, because it was shown in Section 4.4.1 that, with $u_0 = 0\,\mathrm{m\,s^{-1}}$,

(a)

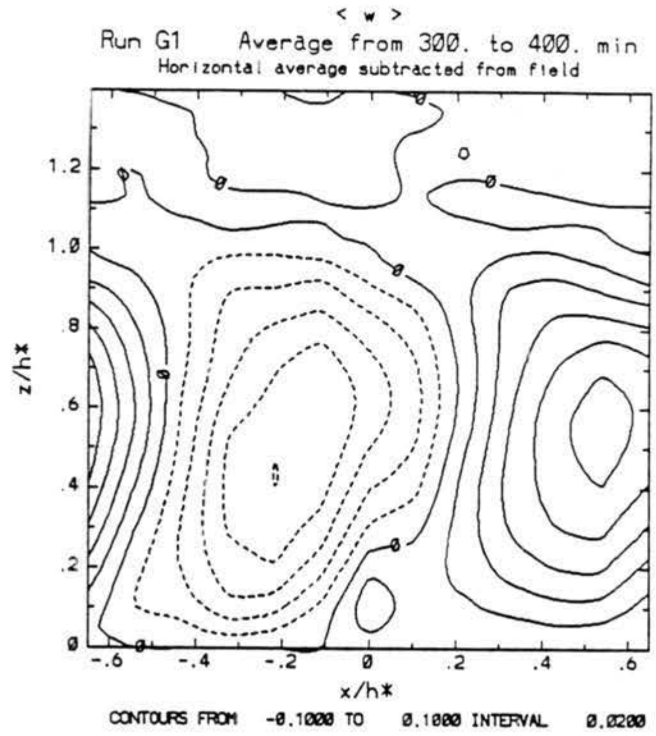

(b)

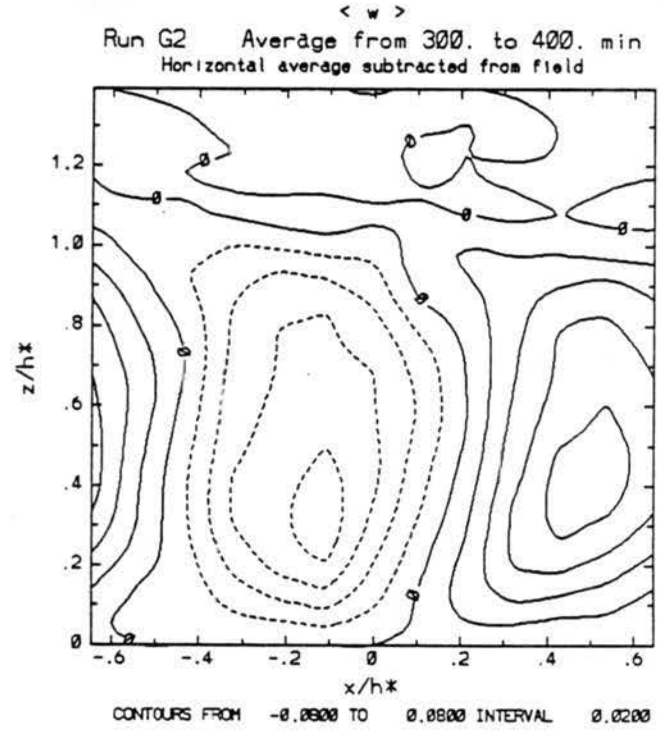

Figure 4.18. Circulation vertical velocity $\langle w' \rangle_{p,t}$ for (a) Run G1 and (b) Run G2. Contour interval $0.02 w_*$.

the Cotton *et al.* simulations differ from the present series in having stronger circulations initially, and this was attributed to their having weaker lateral mixing. However the temperature budgets to be presented in Section 5.1 suggest that lateral mixing is not as important with a mean wind as it is in the absence of one.

4.5.3 *Scaling parameters*

For Set G from $t = 300\,\text{min}$ to $t = 400\,\text{min}$, the boundary layer depth h_* is 1162 m, which implies

$$\frac{\lambda_p}{h_*} = 1.29 \quad \text{and} \quad \frac{u_0 h_*}{w_* \lambda_p} = 0.39.$$

(Recall from Section 2.3 that the latter is the ratio between the mixed layer time scale h_*/w_* and the time λ_p/u_0 required for advection at velocity u_0 through distance λ_p.) As with Set F, the horizontal variation in boundary layer depth h is found to be negligible.

4.5.4 *The time-averaged circulation*

Figure 4.19 shows $\langle u \rangle_{p,t}$, $\langle w \rangle_{p,t}$ and $\langle \theta \rangle_{p,t}$ fields averaged over Set G and over time from $t = 300\,\text{min}$ to $t = 400\,\text{min}$ (c.f. Figure 4.7 for Set F). The maximum in $\langle w' \rangle_{p,t}$ is somewhat reduced in magnitude by the mean wind ($0.08 w_*$ to the nearest contour interval for Set G versus $0.14 w_*$ for Set F) and is shifted downwind to $\hat{x} = 0.5 h_* = 0.4 \lambda_p$. The level of the $\langle w' \rangle_{p,t}$ maximum is also raised ($z = 0.5 h_*$ versus $z = 0.35 h_*$) and as a result the $\langle u' \rangle_{p,t}$ field is not as "bottom-heavy" as it was in Set F. Note also two features of the horizontal-average wind $\langle u \rangle_{h,t}$: first, in the interior of the boundary layer the velocity is about $0.45 w_*$, which is reduced by $\sim 10\%$ from the velocity of u_0 imposed at $t = 200\,\text{min}$; second, near $z = 0$ and $z = 1.1 h_*$ there are small maxima in the velocity, which are believed to be numerical wall/lid effects associated with mean advection in a gradient of vertical velocity variance. (It is believed that a Galilean transformation—i.e., subtraction of the mean wind—would eliminate the latter feature, but this would make calculation of the phase averages very difficult.)

The $\langle \theta' \rangle_{p,t}$ perturbation near the surface is hardly reduced in magnitude compared to Set F, but the maximum and minimum are shifted downwind and tilted. At $z = 0$ the

(a)

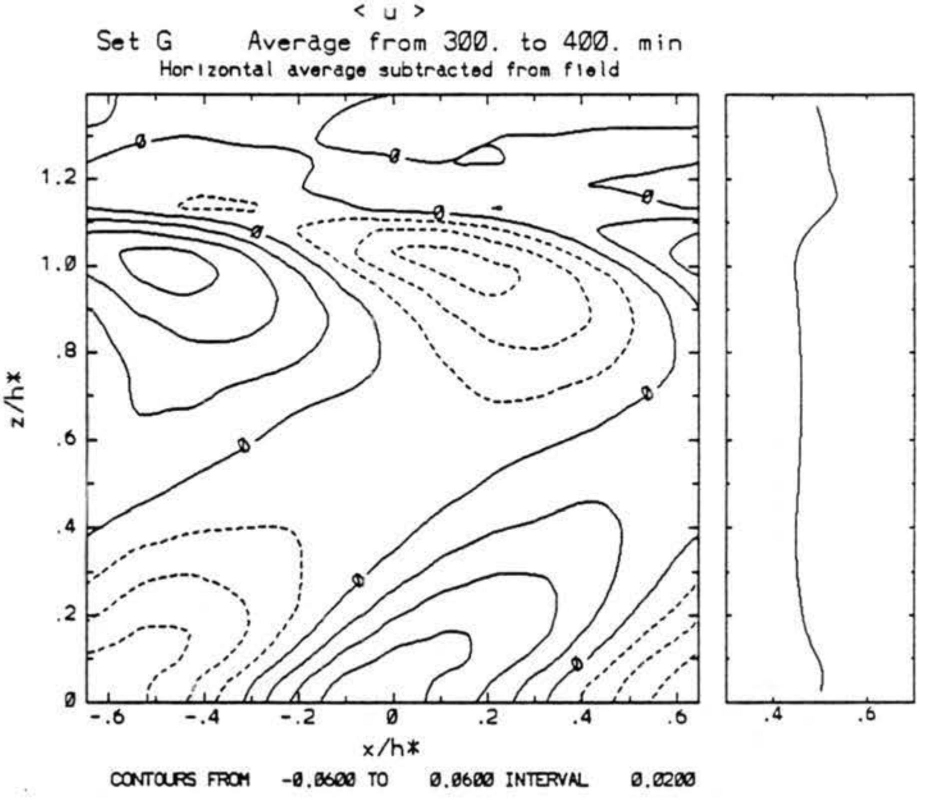

Figure 4.19. Phase-time averaged velocity and potential temperature fields for Set G.

(a) u (contour interval $0.02w_*$)

(b) w (contour interval $0.02w_*$)

(c) θ (contour interval $0.2\,\theta_*$)

Continued on following page.

(b)

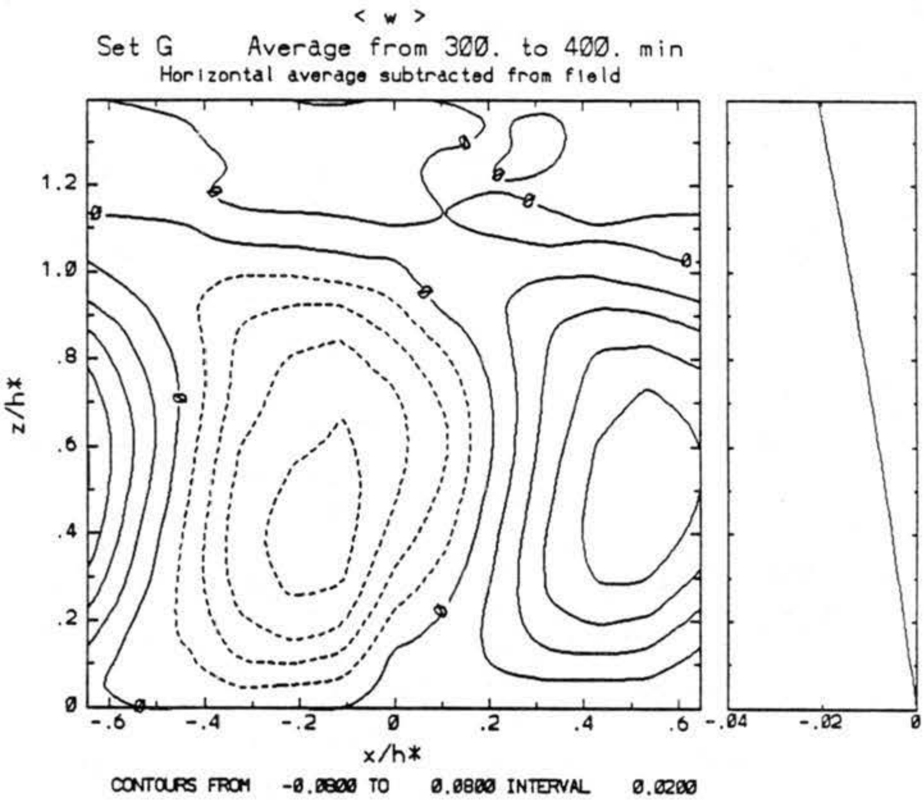

(c)

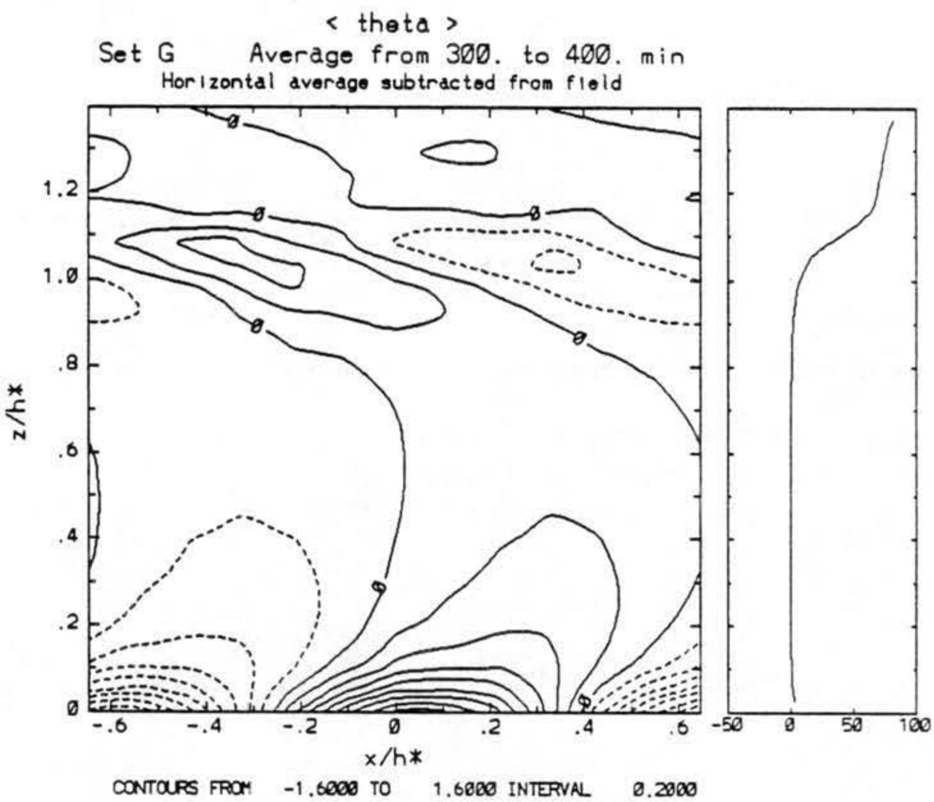

Figure 4.19 (continued).

maximum is at $\hat{x} = 0.06h_* = 0.05\lambda_p$ and at $z = 0.4h_*$ it is at $\hat{x} = 0.32h_* = 0.25\lambda_p$, which is $0.15\lambda_p$ upwind of the vertical velocity maximum. In and above the upper boundary layer the $\langle\theta'\rangle_{p,t}$ contour lines slope up and to the left at an angle of about 20° from horizontal. This feature was much better defined in the simulations of Cotton *et al.* (1988), where it was interpreted as a weak, stationary gravity wave with vertical wavelength $\sim 450\,\mathrm{m}$ and horizontal wavelength 1500 m. (The reason it was better defined in those simulations is that the spurious secondary circulations near $z = 1.2h_*$ had not developed by the time the averages were taken, so there was no significant minimum in the potential temperature gradient—see Sections 3.2.1 and 3.3.3.) An elevated maximum in the amplitude of the $\langle\theta'\rangle_{p,t}$ perturbation is found at $z = 1.05h_*$: its magnitude is $0.2\,\theta_*$, which is a little larger than in Set F.

The pressure field is shown in Figure 4.20 along with the buoyancy- and turbulence-induced components (c.f. Figure 4.8). The largest perturbations are associated with the buoyancy perturbations near the surface, as in Set F, but reduced in amplitude ($0.08\pi_*$ versus $0.14\pi_*$). Since the magnitude of the temperature perturbations is not much reduced, one suspects that the tilting of the $\langle\theta'\rangle_{p,t}$ fields is important here. The minimum in turbulence pressure in the middle of the boundary layer has been reduced in magnitude ($-0.02\pi_*$ versus $-0.05\pi_*$) and shifted downwind to about $\hat{x} = 0.4h_* = 0.3\lambda_p$, which is roughly the position of the maximum of turbulent w variance (Section 4.5.5 below).

Again several ratios characterising the circulation have been calculated—they are listed in Table 4.4 (c.f. Table 4.3). Ratios 1 to 7 are all smaller than in Set F, as expected with the weaker circulation. Ratios 8 and 9 have very similar values in both the $\lambda_p = 1500\,\mathrm{m}$ cases.

4.5.5 *Turbulence: deviations from the time-averaged circulation*

The turbulent second moments of velocity and temperature for Set G are shown in Figure 4.21 (c.f. Figure 4.10). As in Section 4.4.5 these are quantities of the form $\langle(a')^2_{p,t}\rangle_{p,t}$ and $\langle(a')_{p,t}(b')_{p,t}\rangle_{p,t}$. In most respects the fields resemble the fields of Set F,

(a)

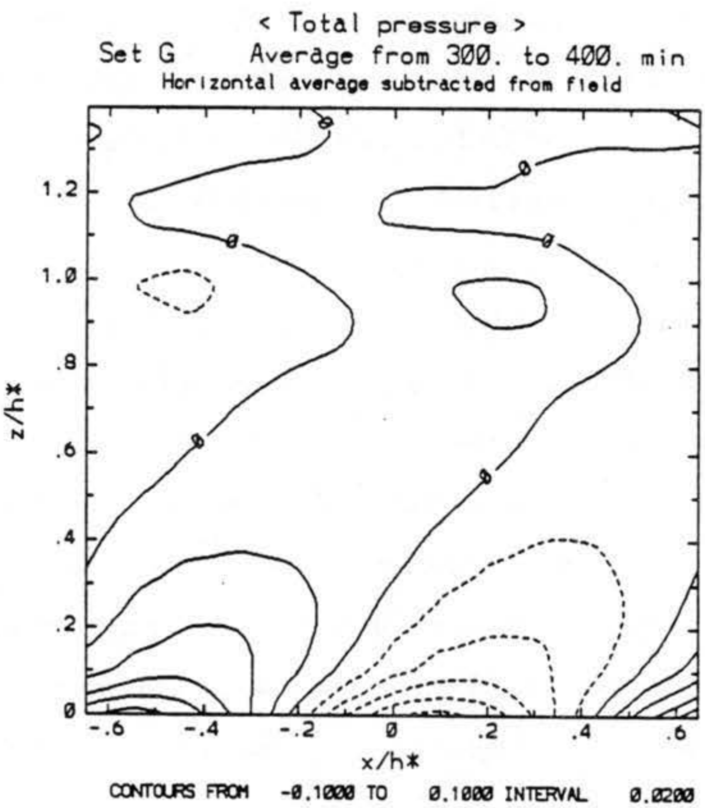

Figure 4.20. Phase-time averaged pressure fields for Set G.

(a) total pressure π (contour interval $0.02\pi_*$)

(b) buoyancy pressure π_b (contour interval $0.02\pi_*$)

(c) turbulence pressure π_t (contour interval $0.01\pi_*$)

Continued on following pages.

(b)

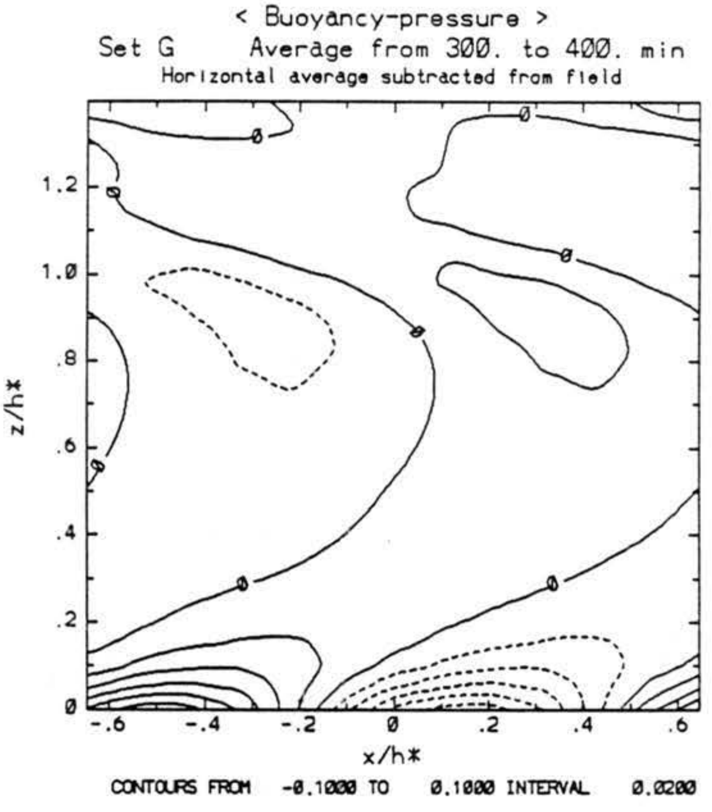

(c)

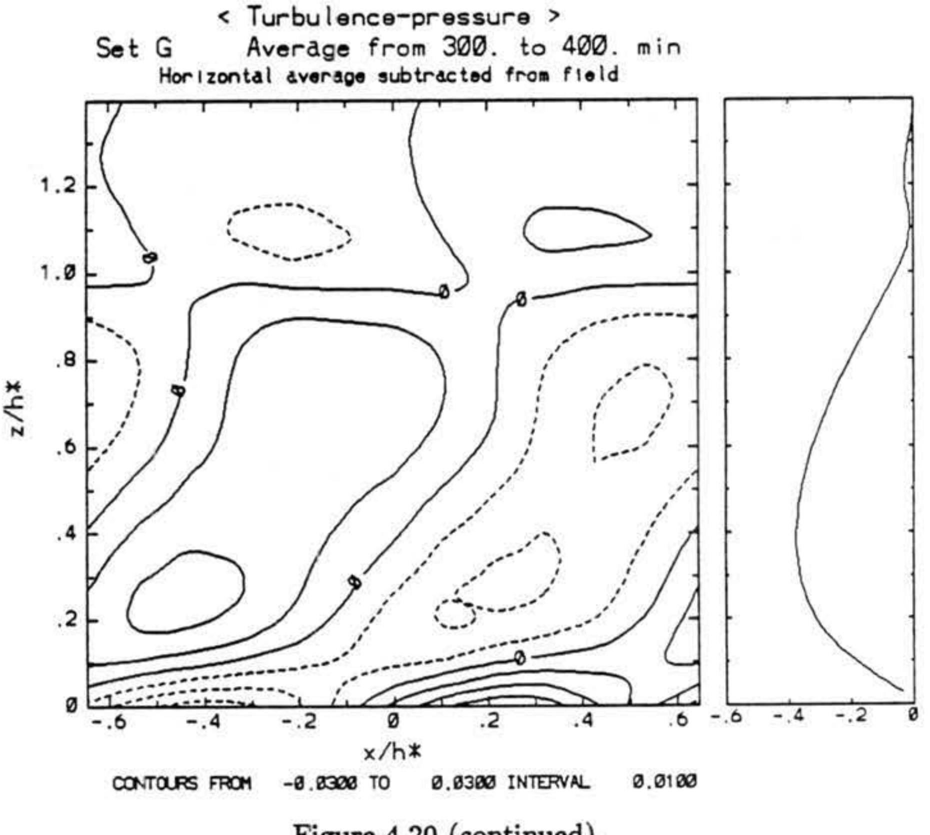

Figure 4.20 (continued).

Table 4.4. Ratios characterising the time-averaged circulation in Set G.

No.	Ratio	Height	Value
1	$\left\langle \langle u' \rangle_{p,t}^2 \right\rangle_h / \left\langle u'^2 \right\rangle_{h,t}$	$0.1h_*$	0.012
		$0.9h_*$	0.009
2	$\left\langle \langle w' \rangle_{p,t}^2 \right\rangle_h / \left\langle w'^2 \right\rangle_{h,t}$	$0.4h_*$	0.012
3	$\left\langle \langle \theta' \rangle_{p,t}^2 \right\rangle_h / \left\langle \theta'^2 \right\rangle_{h,t}$	$0.1h_*$	0.06
		$0.9h_*$	0.007
4	$\left\langle \langle \pi' \rangle_{p,t}^2 \right\rangle_h / \left\langle \pi'^2 \right\rangle_{h,t}$	$0.1h_*$	0.02
		$0.9h_*$	0.004
5	$\left\langle \langle w' \rangle_{p,t} \langle \theta' \rangle_{p,t} \right\rangle_h / \left\langle w'\theta' \right\rangle_{h,t}$	$0.2h_*$	0.012
		$1.0h_*$	0.017
6	$\sum_i \int_Z \left\langle \langle u_i' \rangle_{p,t}^2 \right\rangle_h / \sum_i \int_Z \left\langle u_i'^2 \right\rangle_{h,t}$	–	0.006
7	$\int_Z \left\langle \langle w' \rangle_{p,t} \langle \theta' \rangle_{p,t} \right\rangle_h / \int_Z \left\langle w'\theta' \right\rangle_{h,t}$	–	0.013
8	$\int_Z \left\langle \langle u' \rangle_{p,t}^2 \right\rangle_h / \sum_i \int_Z \left\langle \langle u_i' \rangle_{p,t}^2 \right\rangle_h$	–	0.32
9	$-(\theta_0^2/g) \int_Z \left\langle \langle w' \rangle_{p,t} \frac{\partial}{\partial z} \langle \pi_b' \rangle_{p,t} \right\rangle_h / \int_Z \left\langle \langle w' \rangle_{p,t} \langle \theta' \rangle_{p,t} \right\rangle_h$	–	0.49

(a)

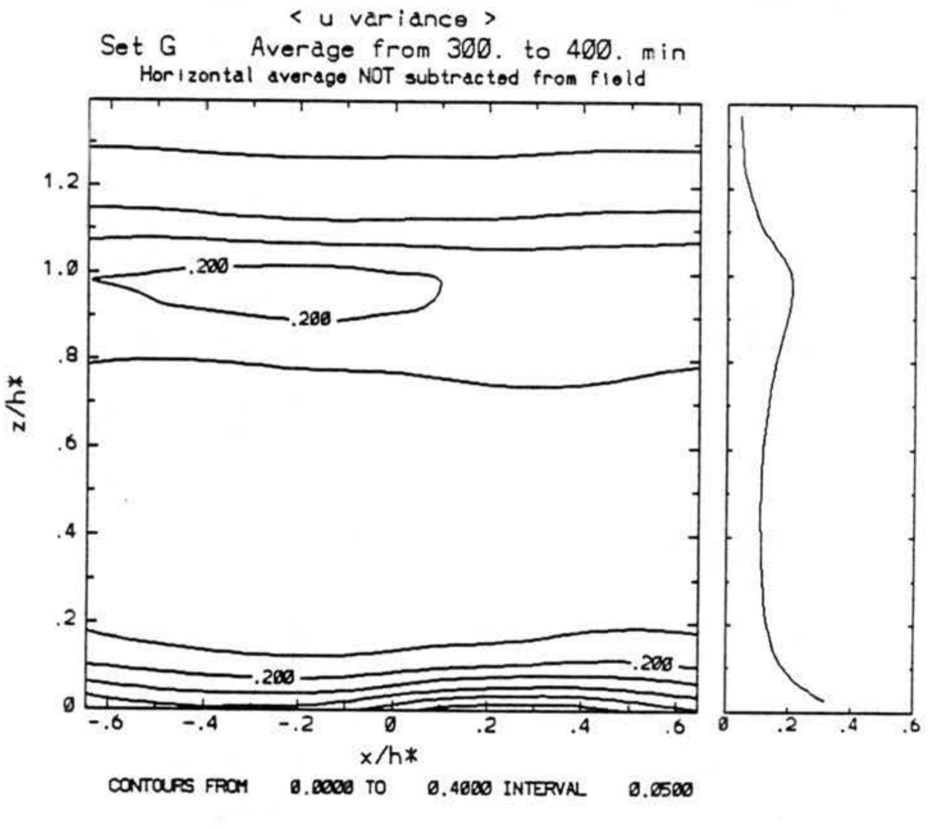

Figure 4.21. Fields of turbulent variances and covariances for Set G.

(a) u variance (contour interval $0.05w_*^2$)

(b) v variance (contour interval $0.05w_*^2$)

(c) w variance (contour interval $0.05w_*^2$)

(d) u/w covariance (contour interval $0.005w_*^2$)

(e) square root of θ variance (contour interval $0.5\,\theta_*$)

(f) u/θ covariance (contour interval $0.1w_*\theta_*$)

(g) w/θ covariance (contour interval $0.1w_*\theta_*$)

Continued on following pages.

(b)

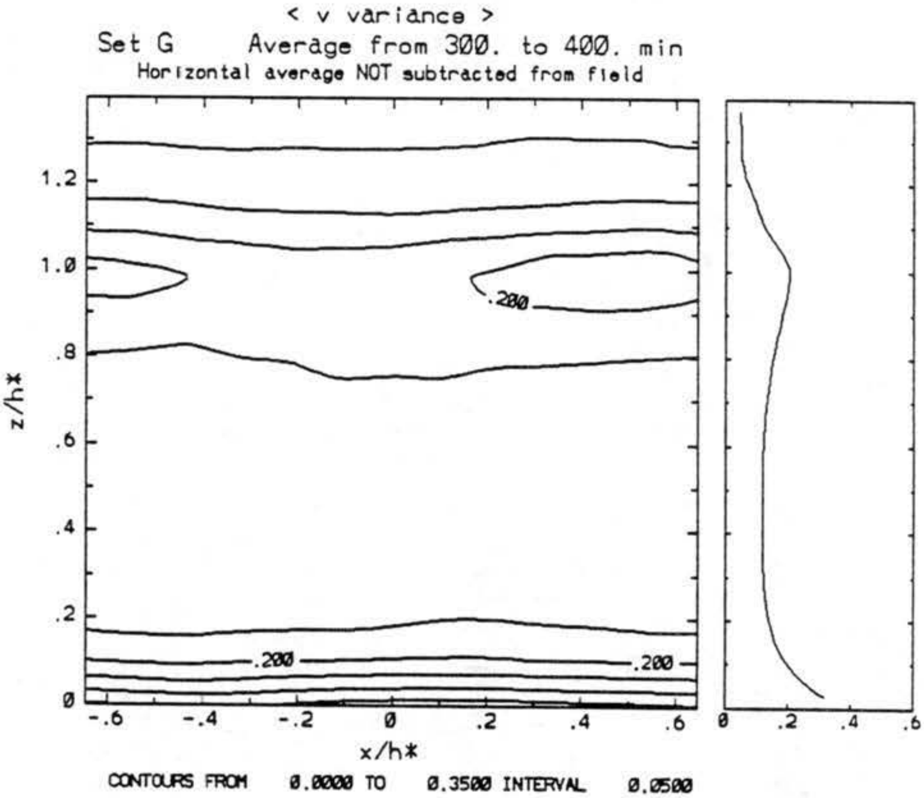

(c)

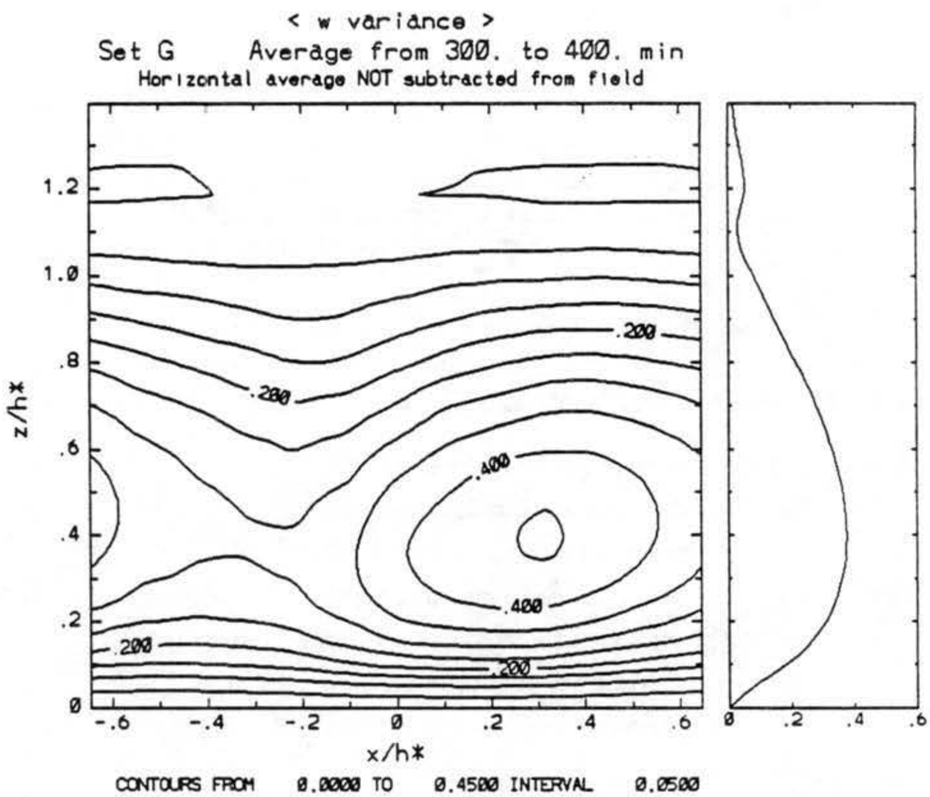

Figure 4.21 (continued).

Continued.

(d)

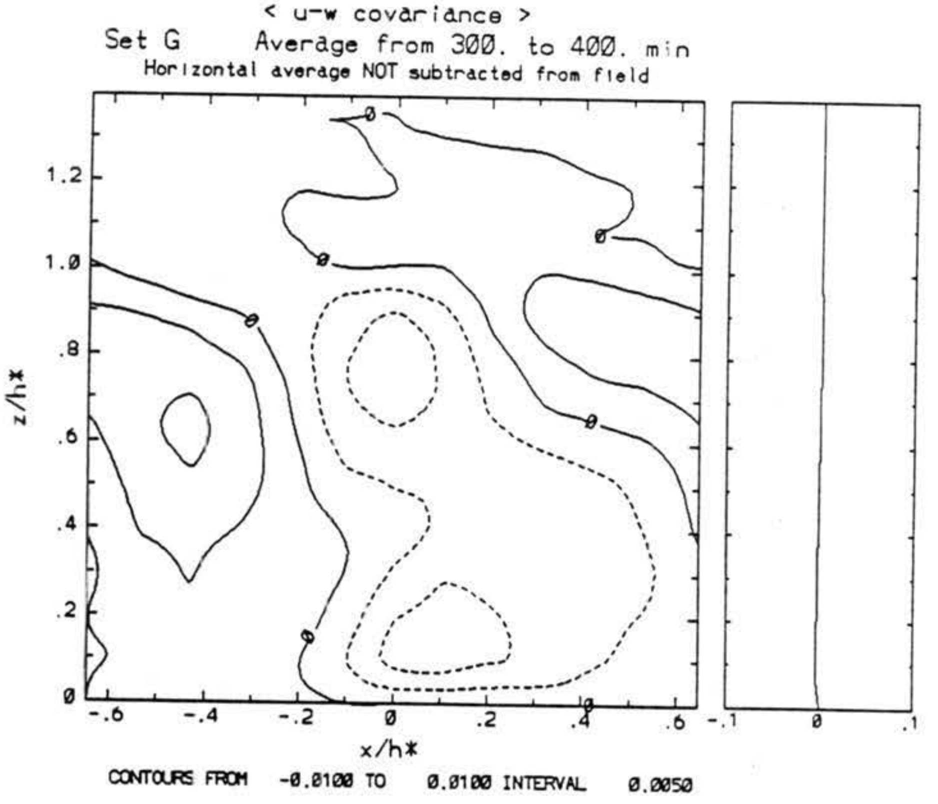

(e)

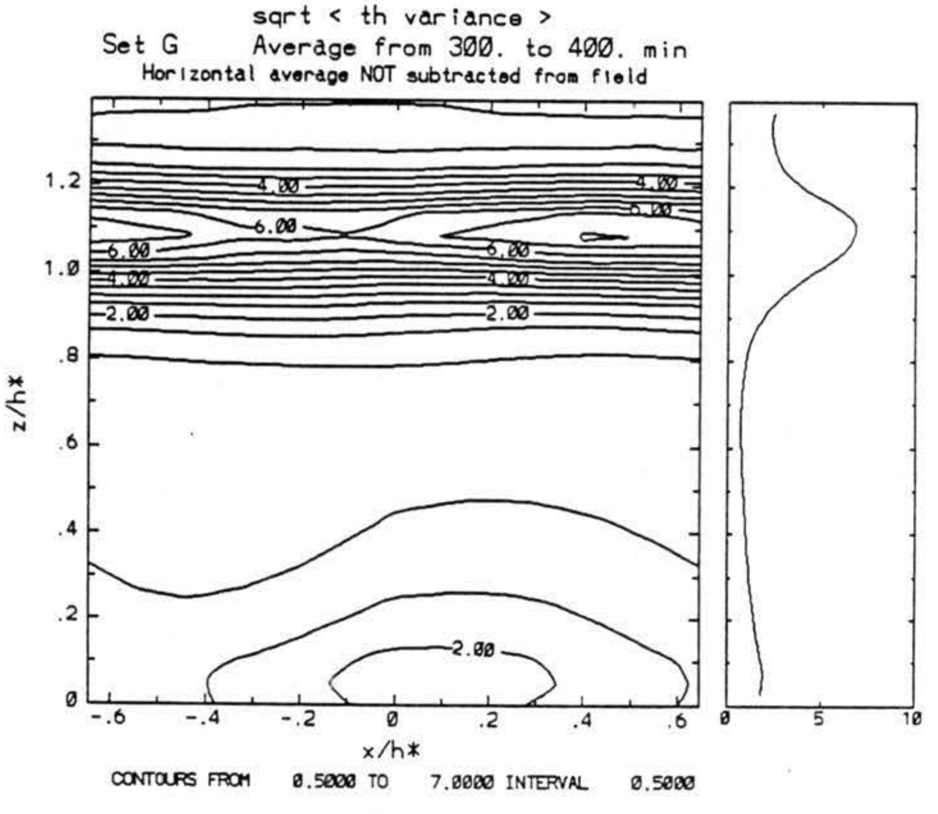

Figure 4.21 (continued).

Continued.

(f)

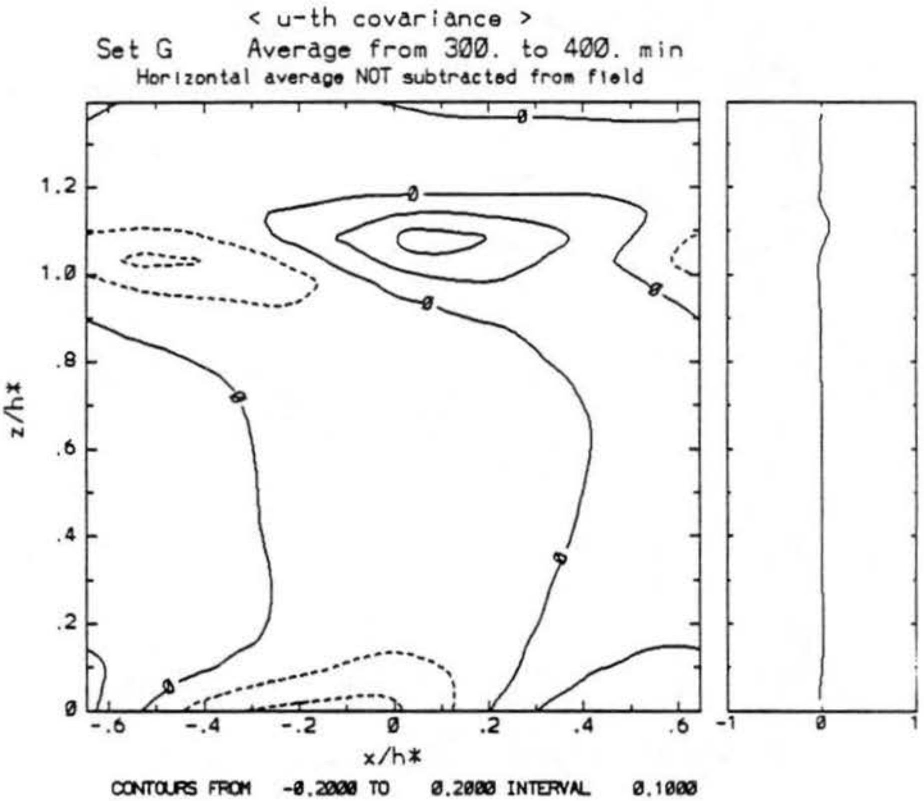

(g)

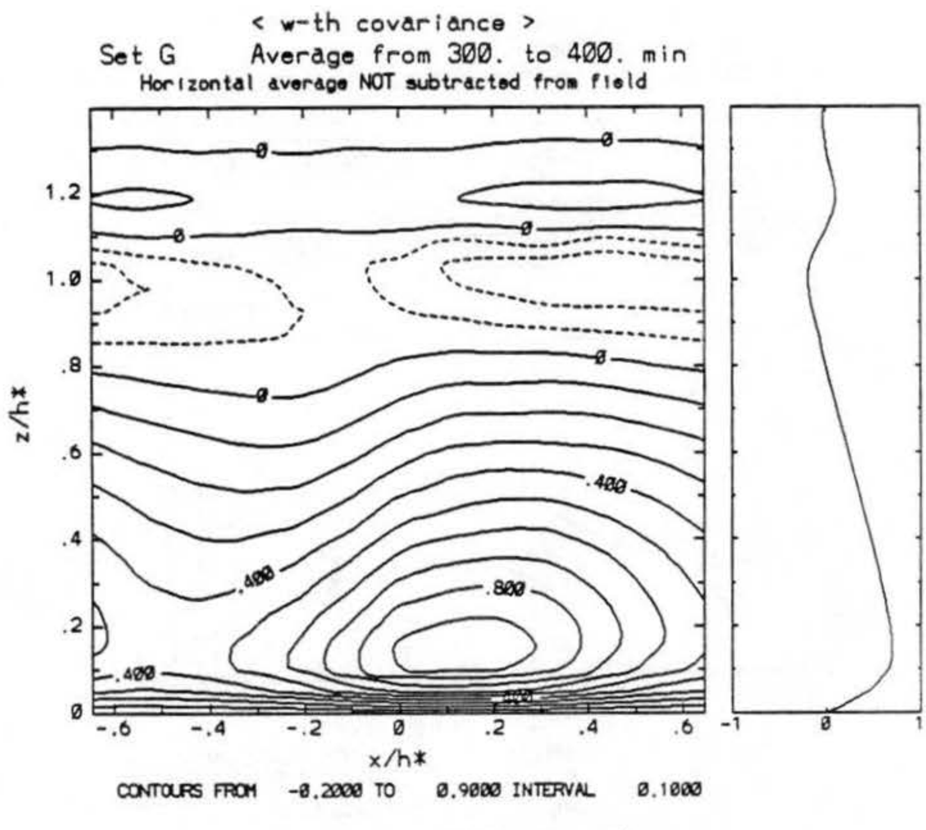

Figure 4.21 (continued).

but shifted downwind and sometimes tilted. The surface maximum in u variance is substantially reduced in magnitude and shifted downwind to $\hat{x} = 0.32h_* = 0.25\lambda_p$. There is now an elevated maximum in v variance at $\hat{x} = 0.5h_* = 0.4\lambda_p$, near the region of maximum entrainment discussed below, and a maximum in u variance downstream of that ($\hat{x} = -0.25h_* = -0.2\lambda_p$). The w variance maximum in the middle of the boundary layer is also shifted downwind to $\hat{x} = 0.32h_* = 0.25\lambda_p$, but its magnitude is not changed significantly. The near-surface maximum in w/θ covariance is at $\hat{x} = 0.13h_* = 0.10\lambda_p$, and coincides with a maximum in θ variance. The negative-maximum in w/θ covariance (i.e., maximum entrainment) at $z = h_*$ is at about $\hat{x} = 0.45h_* = 0.35\lambda_p$ and also coincides with a maximum in θ variance. Finally note that the u/w and u/θ covariances are substantially reduced in magnitude in the lower boundary layer, compared to Set F.

Imagine a line joining the near-surface maximum in w/θ covariance with the region of maximum entrainment. Since the w variance maximum in the middle of the boundary layer lies just to the right of the line, it can be loosely identified as the axis of maximum "turbulence intensity." An appealing interpretation is that convective updraughts accelerate as they ingest warm air from the surface in the regions of maximum heat flux, then propagate through the boundary layer at such a speed that they reach the inversion a horizontal distance $0.45\lambda_p$ downstream. The implied vertical velocity for propagation is approximately w_*, which seems a little large given that the maximum w variance is $0.45w_*^2$, corresponding to a standard deviation of $0.7w_*$. It is possible, of course, for energy to propagate faster than the typical fluid velocity via pressure effects. It is likely, however, that the above interpretation is wrong in ignoring the effects on the turbulence of the perturbations in temperature gradient above the surface. It will be shown in Appendix B that regions of maximum heat flux with approximately the right slope can be predicted by a model in which the heat flux is determined only by local gradients.

4.5.6 *Horizontal-average statistics*

Figure 4.22 shows profiles of the velocity variances $\langle u_i'^2 \rangle_{h,t}$ averaged over Set G. Whereas in Set F the surface heat-flux perturbation led to a substantial difference between

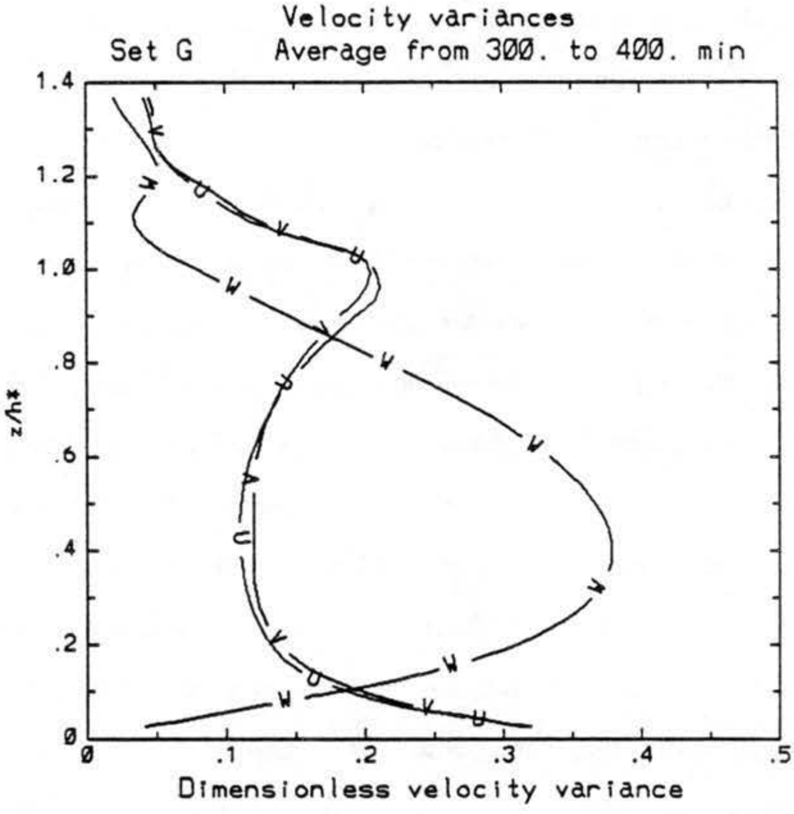

Figure 4.22. Profiles of dimensionless velocity variances $\langle u_i'^2 \rangle_{h,t}$ for Set G.

u and v variances (Figure 4.12), here no such difference is seen and the profiles are essentially identical to the ones for the horizontally homogeneous case. In examining various profiles of turbulence statistics the only effect of the heat-flux perturbation that has been detected is an increase in temperature variance near the surface similar to what was observed in Set F, but not so large and perceptible only below $z = 0.1h_*$. At the lowest level ($z = 0.03h_*$) the variance is $4.2\,\theta_*^2$ for Set G, versus $3.0\,\theta_*^2$ for Run A and $4.9\,\theta_*^2$ for Set F.

Figure 4.23 shows x- and y-spectra of vertical velocity from the middle of the boundary layer (c.f. Figure 4.14) There is no more than a hint of a peak in the x-spectra at wavelength λ_p ($kh_* = 4.9$) and the differences between x- and y-spectral density at low wavenumbers are smaller than in Set F. The slight excess of above $kh_* = 20$ of y-spectral density over x-spectral density is observed in a horizontally homogeneous simulation with the same u_0. It is presumed to be a consequence of phase-speed error in the advection scheme, given that there is no Galilean transformation.

4.6 Simulations with $\lambda_p = 4500\,\mathrm{m}$ and $u_0 = 0\,\mathrm{m\,s^{-1}}$

4.6.1 *Evolution of surface-driven circulations*

The simulations with $\lambda_p = 4500\,\mathrm{m}$ and $u_0 = 0\,\mathrm{m\,s^{-1}}$ are Runs H1 and H2. Figure 4.24 shows the evolution of the the circulation kinetic energy E_c and its components; since the curves from Runs H1 and H2 are similar, only the one calculated over the pair, Set H, is shown. After the heat-flux perturbation is imposed at $t = 200\,\mathrm{min}$, E_c develops to a maximum at $t = 245\,\mathrm{min}$, then settles down to an approximately steady value after $t = 280\,\mathrm{min}$. The magnitude is much higher than it was at the shorter wavelength, and it is also worth noting that $E_{c1} > E_{c3}$, i.e., there is more energy in the $\langle u' \rangle_p$ field than in the $\langle w' \rangle_p$ field.

With the strong, steady circulation, statistical significance is not an issue. The following sections look at statistics of Set H, averaged from $t = 300\,\mathrm{min}$ to $t = 400\,\mathrm{min}$.

(a)

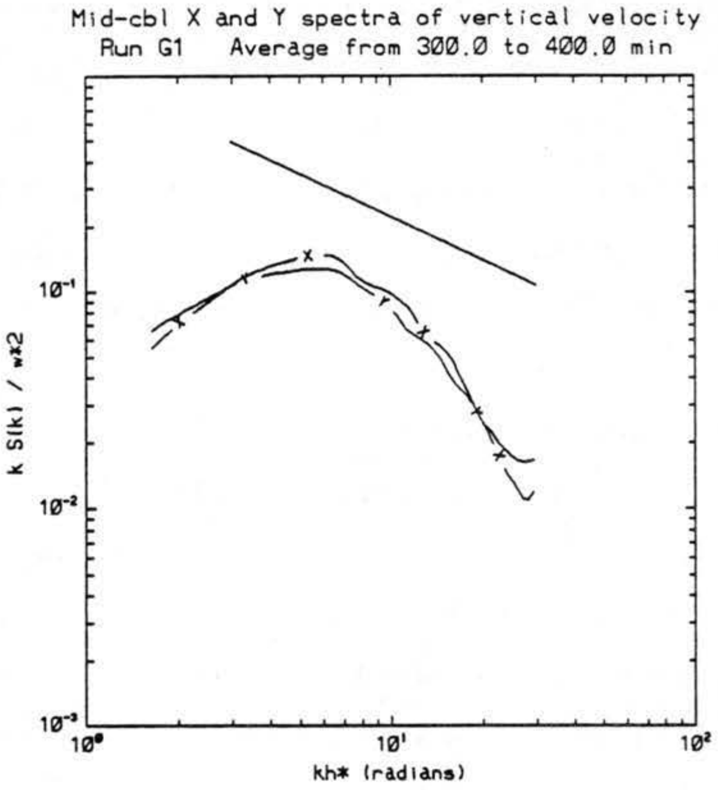

(b)

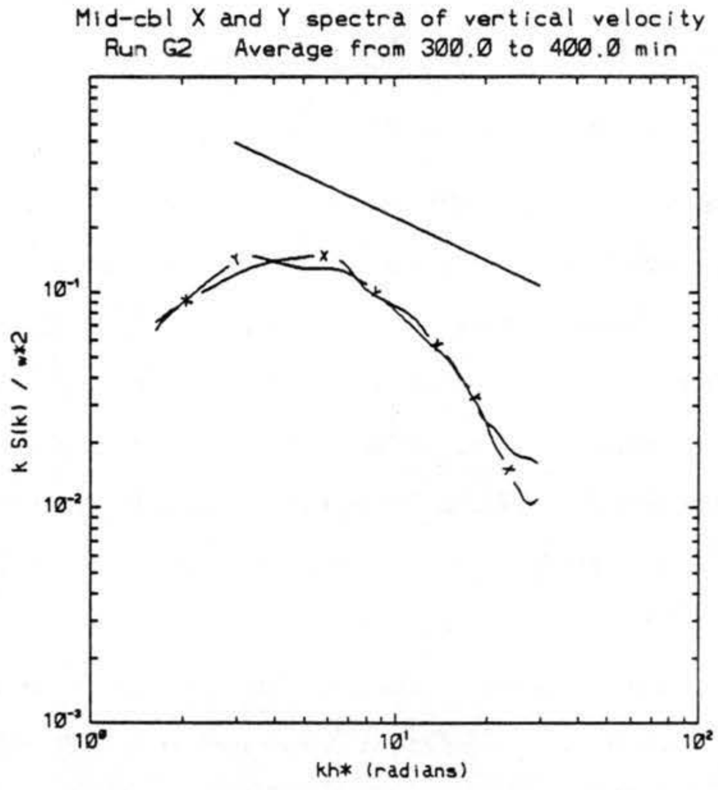

Figure 4.23. Dimensionless mid-boundary-layer spectra of vertical velocity in the x (—X—) and y (—Y—) directions for (a) Run G1 and (b) Run G2.

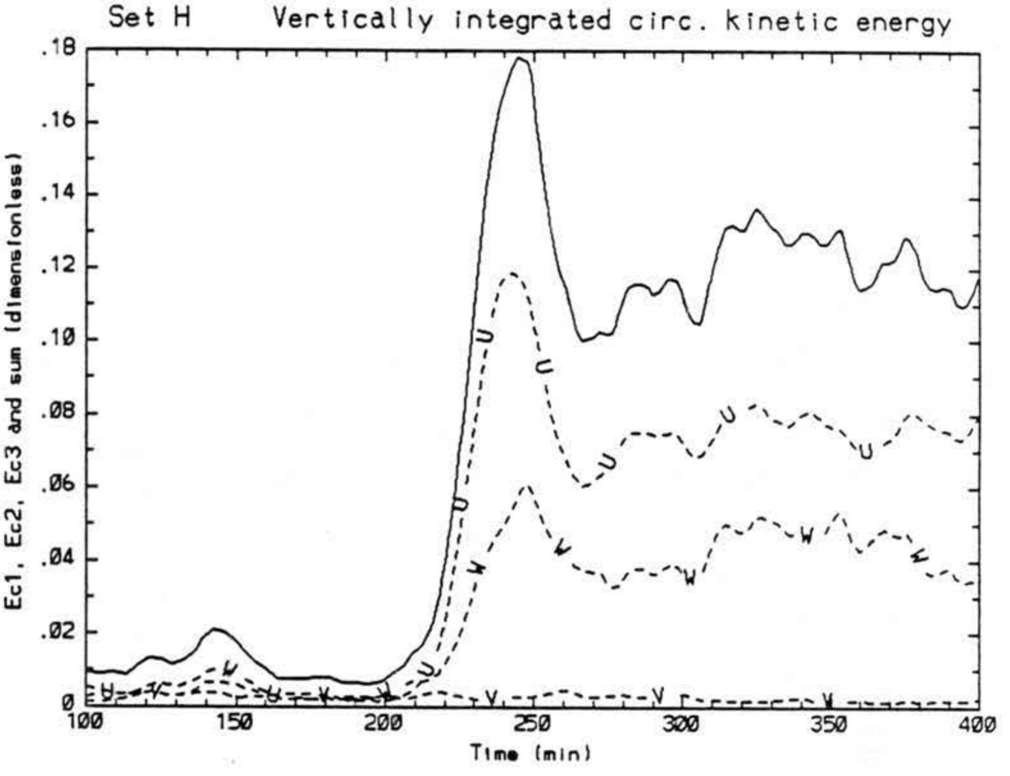

Figure 4.24. Evolution of circulation kinetic energy for Set H.

4.6.2 *Scaling parameters*

For the present case, $h_* = 1189\,\mathrm{m}$, which is 2.5% larger than the horizontally homogeneous value. The difference is presumably due to more vigorous horizontal-average entrainment (Section 4.6.5). The dimensionless wavelength of the surface perturbation is therefore

$$\frac{\lambda_p}{h_*} = 3.78.$$

Figure 4.25 shows fields (horizontal averages *not* subtracted) of two quantities relevant to the horizontal variation in the boundary layer depth, namely

$$\frac{\partial}{\partial t}\langle\theta\rangle_{p,t} + \langle w\rangle_{h,t}\frac{\partial}{\partial z}\langle\theta\rangle_{p,t} \quad \text{and} \quad \frac{\partial}{\partial z}\langle\theta\rangle_{p,t}.$$

Despite the pronounced horizontal variations that will be seen below in mean and turbulence fields, the boundary layer depth h, defined by the lowest zero contour in Figure 4.25a, varies by no more than a few percent. Similarly the height of maximum potential temperature gradient (Figure 4.25b) and the height of maximum temperature variance (Section 4.6.4 below) are constant with $\hat{x}$.

4.6.3 *The time-averaged circulation*

Figure 4.26 shows $\langle u\rangle_{p,t}$, $\langle w\rangle_{p,t}$ and $\langle\theta\rangle_{p,t}$ fields for Set H. They are very different from comparable fields with $\lambda_p = 1500\,\mathrm{m}$ (see Figure 4.7 for Set F and Figure 4.19 for Set G). The $\langle w'\rangle_{p,t}$ field has a central updraught of width $0.95h_* = 0.25\lambda_p$ and maximum vertical velocity $1.1w_*$, flanked by downdraughts with a most-negative velocity of $-0.3w_*$ at $z = 0.7h_*$, $\hat{x} = \pm 0.7h_* = \pm 0.18\lambda_p$. (Note that the vertical exaggeration of $\times 2.8$ in the figure distorts the appearance of the updraught somewhat; it is only a little taller than it is wide.) Away from the central region there is weaker descent with velocity $\sim 0.1w_*$. In the $\langle u'\rangle_{p,t}$ field the inflow and outflow velocities both have maxima at the edge of the updraught ($\hat{x} = \pm 0.5h_* = \pm 0.12\lambda_p$). The maximum inflow velocity is $0.9w_*$ and it is found at a height of $z = 0$; the maximum outflow velocity is $0.8w_*$ and it is found at at a height of $z = 0.9h_*$. In the $\langle\theta'\rangle_{p,t}$ field there is warm air at $\hat{x} = 0$ up to $z = 0.7h_*$ and a minimum above there, centred near $z = 1.1h_*$. At the surface the perturbations are in the range

(a)

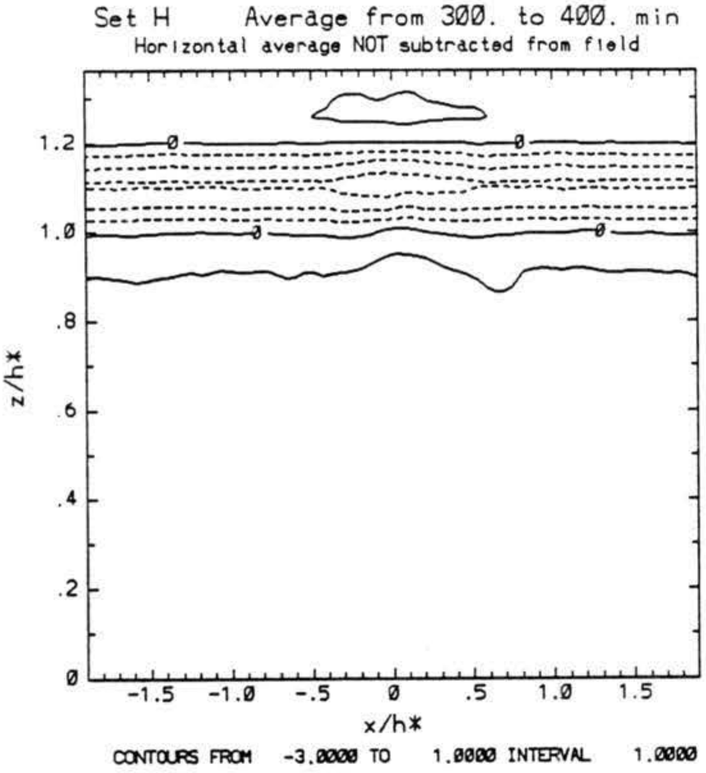

(b)

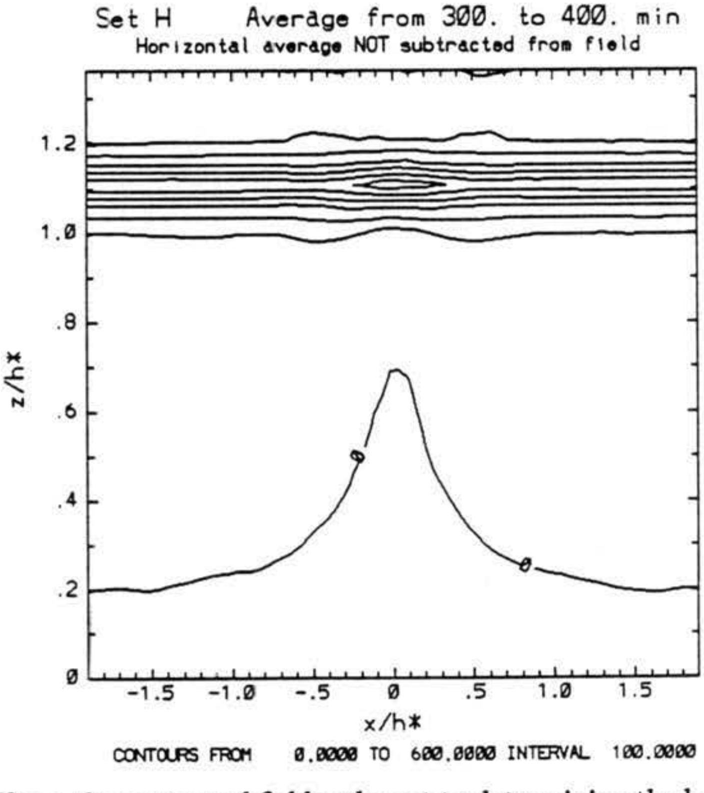

Figure 4.25. Phase-time averaged fields relevant to determining the boundary layer depth h for Set H. (a) Potential temperature tendency $\partial\langle\theta\rangle_{p,t}/\partial t + \langle w\rangle_{h,t}\,\partial\langle\theta\rangle_{p,t}/\partial z$ (contour interval $1.0 w_*\theta_*/h_{\rho*}$). (b) Potential temperature gradient $\partial\left\langle\theta\right\rangle_{p,t}/\partial z$ (contour interval $100 w_*/h_*$).

(a)

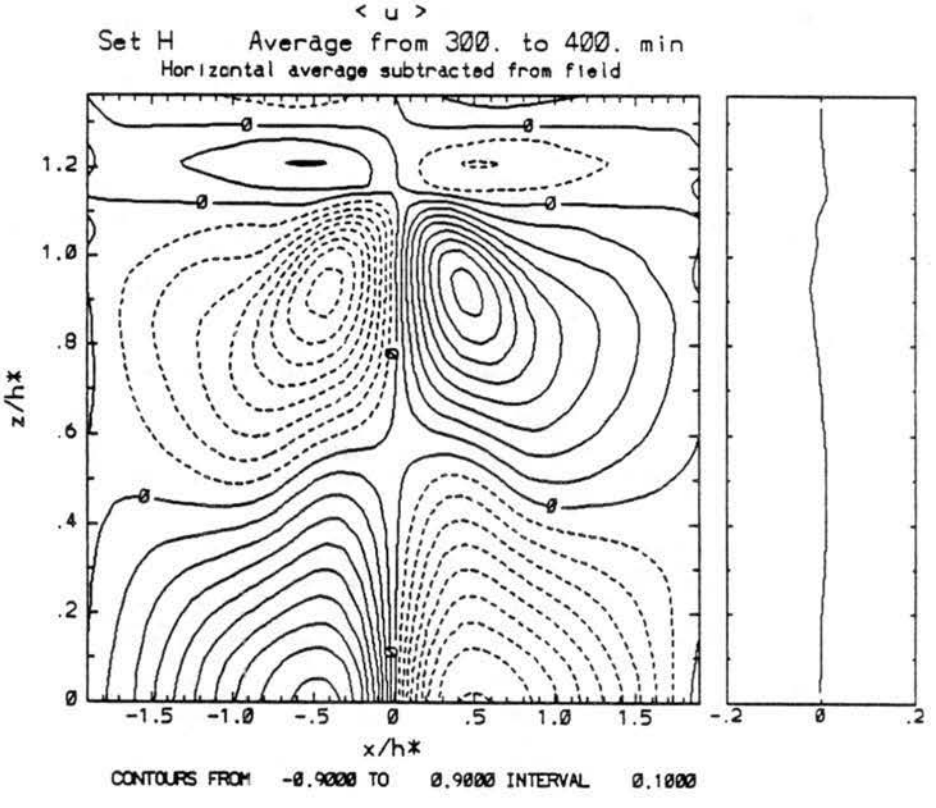

Figure 4.26. Phase-time averaged velocity and potential temperature fields for Set H.

(a) u (contour interval $0.1w_*$)

(b) w (contour interval $0.1w_*$)

(c) θ (contour interval $1.0\,\theta_*$)

Continued on following page.

(b)

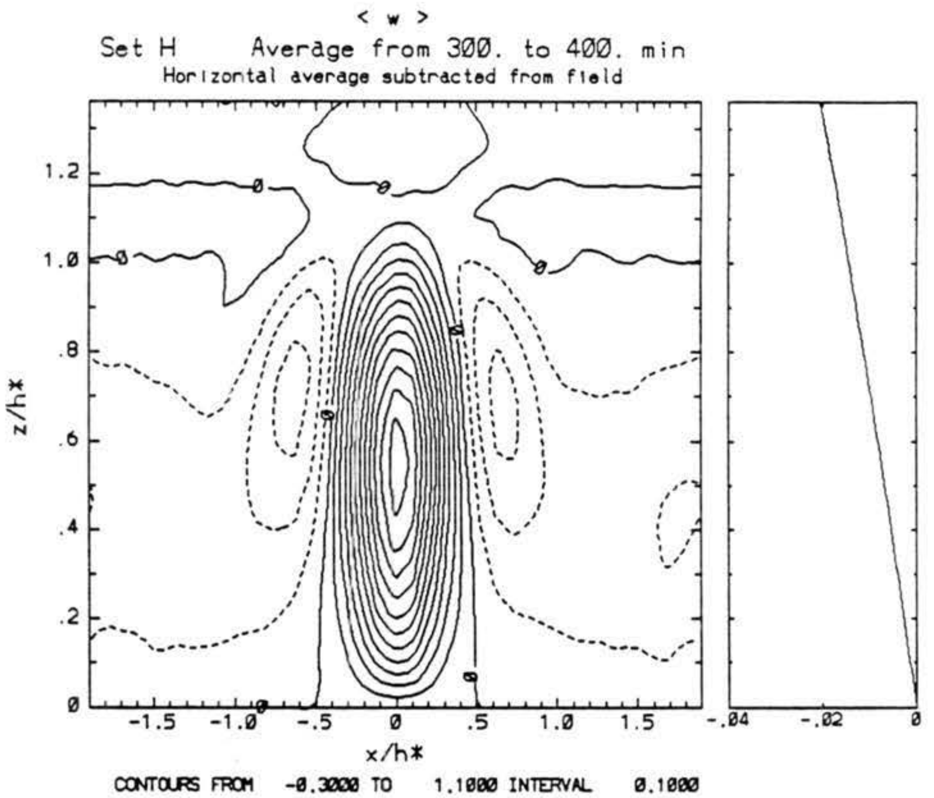

(c)

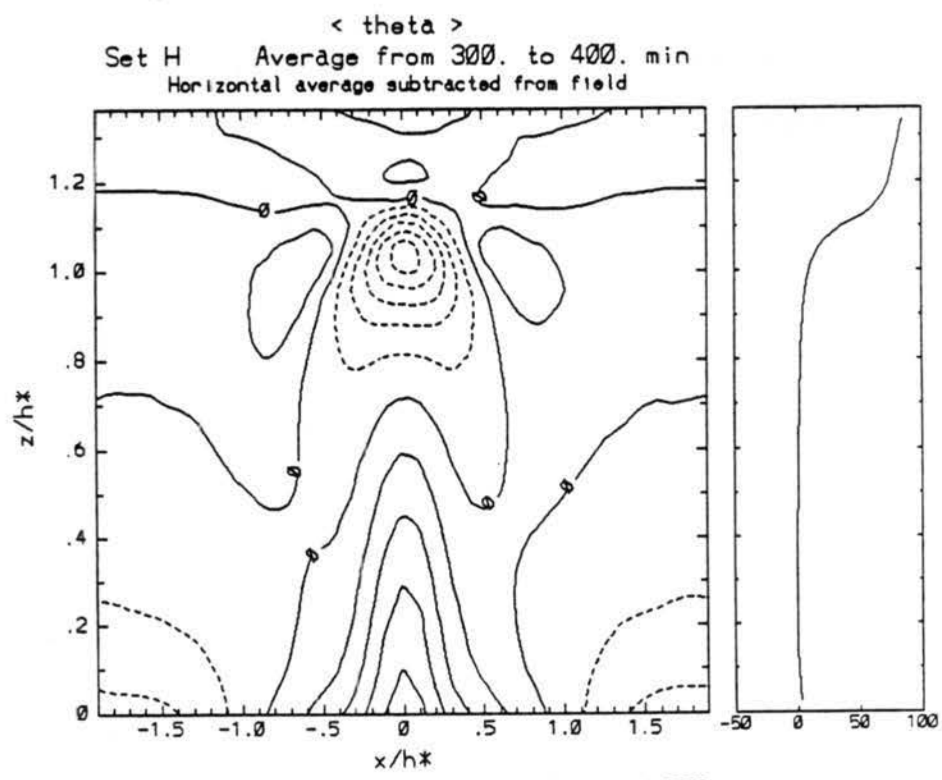

Figure 4.26 (continued).

$-2.4\,\theta_*$ to $+4.2\,\theta_*$, versus $\pm 2\,\theta_*$ for Set F. The elevated minimum in temperature is now *much* larger in magnitude ($-5.4\,\theta_*$ versus $-0.2\,\theta_*$).

Figure 4.27 shows the pressure fields (c.f. Figures 4.8 and 4.20). The intriguing structure of the total pressure field—a broad minimum over the heat-flux maximum with a narrow region of higher pressure along $\hat{x} = 0$—is more comprehensible when the pressure is broken down into its components. The basic structure of the buoyancy pressure and turbulence pressure fields is similar to what it was in Set F, but the magnitudes are greater. The circulation pressure π_c now makes a substantial contribution; it is interesting that it shows the features that were postulated for a positively-skewed updraught/ downdraught field in Section 3.3.1 and Figure 3.32,[12] namely pressure minima on either side of the updraught merging to give low pressure at the centre, and pressure maxima at the top and bottom of the updraught.

Table 4.5 summarises several characteristics of the circulation in Set H (c.f. Tables 4.3 and 4.4). Ratios 1 to 7 are of the order of 0.5, much larger than they were in either of the previous cases. Note also that ratios 8 and 9 (i.e., the ones comparing two different moments of the circulation fields) are larger than they were in the previous simulations, as expected with a decrease in aspect ratio.

Figure 4.28 shows the fraction of points with $w' > 0$ (c.f. Figure 4.9 for Set F). In the core of the updraught upward motion is found more than 90% of the time (the maximum is actually about 96%) whereas at $\hat{x} = \pm\lambda_p/2$, $z = 0.5h_*$ upward motion is found less than 10% of the time. Notice that the fraction has its lowest value within the region of broad, relatively weak descent at $\hat{x} = \pm\lambda_p/2$, not where $\langle w' \rangle_{p,t}$ is most negative.

4.6.4 *Turbulence: deviations from the time-averaged circulation*

Figure 4.29 shows the fields of the turbulence variances and covariances for Set H (c.f. Figures 4.10 and 4.21). There is a central column of large w variance and w/θ covariance, coinciding more or less with the updraught in the time-averaged circulation, and capped

[12]Note that the horizontal average has been subtracted from Figure 4.27d, but has not been subtracted from Figure 3.32d.

(a)

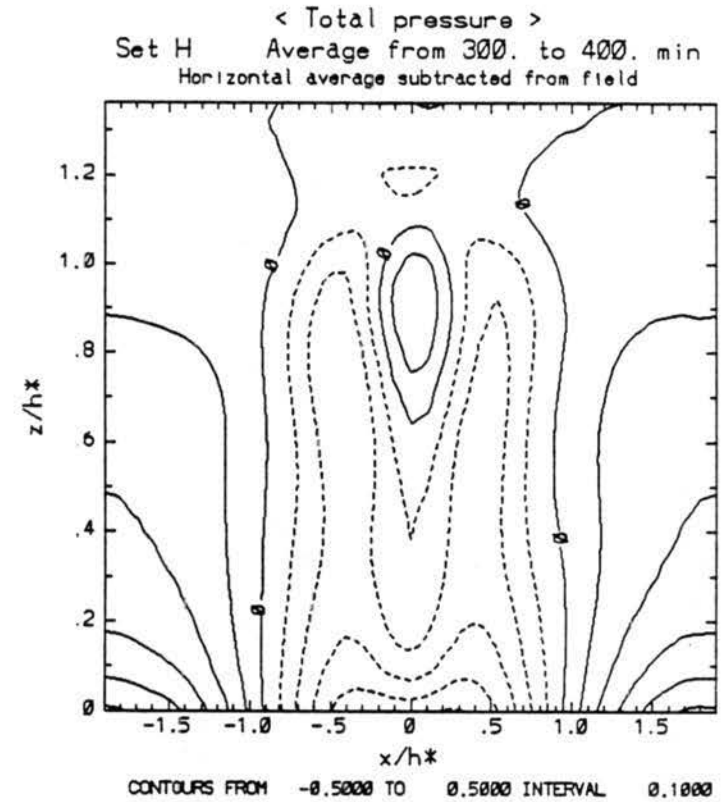

Figure 4.27. Phase-time averaged pressure fields for Set H.

(a) total pressure π (c) turbulence pressure π_t

(b) buoyancy pressure π_b (d) circulation pressure π_c

All contour intervals $0.1\pi_*$.

Continued on following pages.

(b)

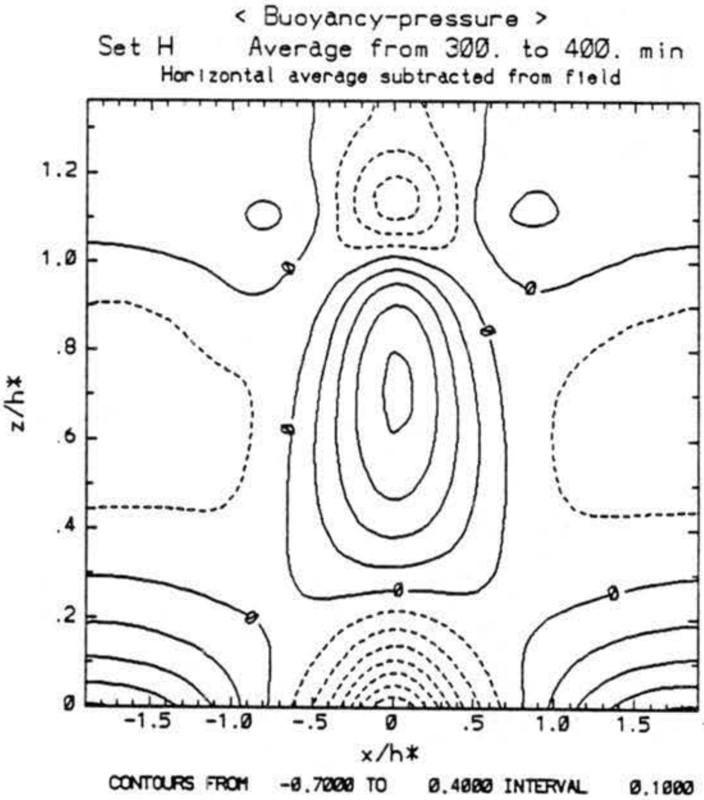

(c)

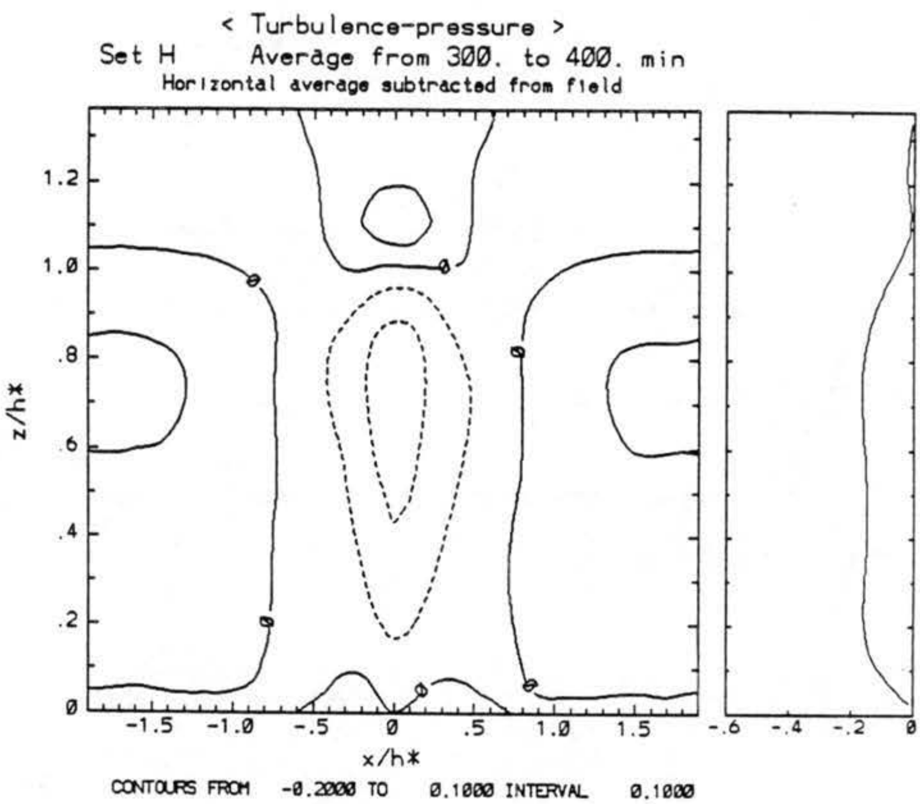

Figure 4.27 (continued).

Continued.

(d)

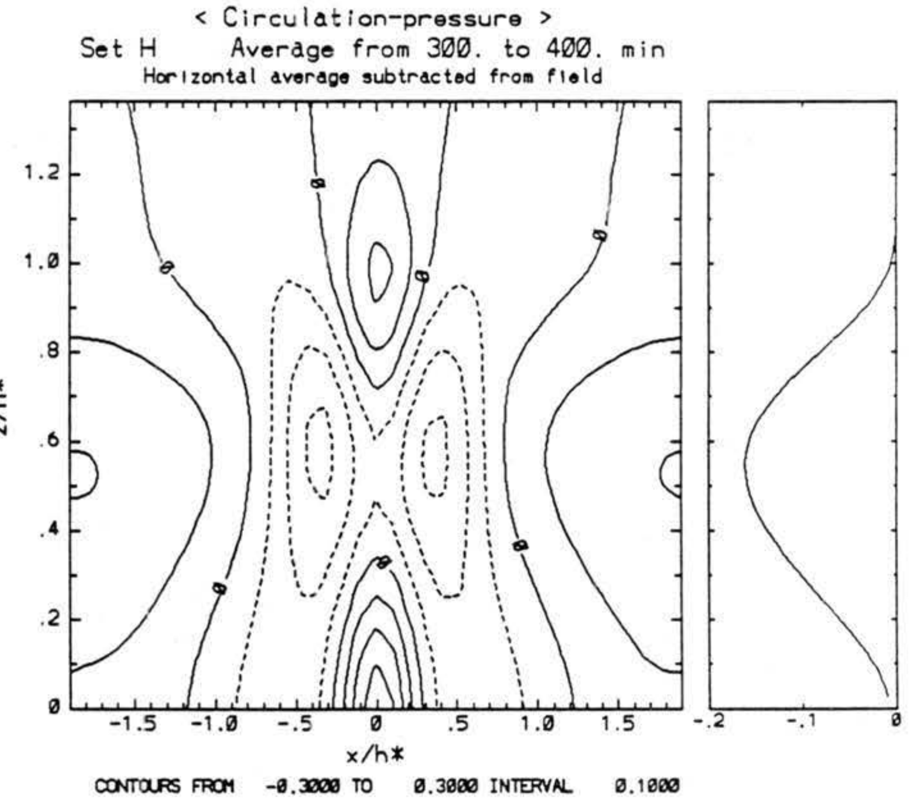

Figure 4.27 (continued).

Table 4.5. Ratios characterising the time-averaged circulation in Set H.

No.	Ratio	Height	Value
1	$\left\langle \langle u' \rangle_{p,t}^2 \right\rangle_h / \left\langle u'^2 \right\rangle_{h,t}$	$0.1h_*$	0.78
		$0.9h_*$	0.60
2	$\left\langle \langle w' \rangle_{p,t}^2 \right\rangle_h / \left\langle w'^2 \right\rangle_{h,t}$	$0.4h_*$	0.46
3	$\left\langle \langle \theta' \rangle_{p,t}^2 \right\rangle_h / \left\langle \theta'^2 \right\rangle_{h,t}$	$0.1h_*$	0.50
		$0.9h_*$	0.27
4	$\left\langle \langle \pi' \rangle_{p,t}^2 \right\rangle_h / \left\langle \pi'^2 \right\rangle_{h,t}$	$0.1h_*$	0.77
		$0.9h_*$	0.26
5	$\left\langle \langle w' \rangle_{p,t} \langle \theta' \rangle_{p,t} \right\rangle_h / \left\langle w'\theta' \right\rangle_{h,t}$	$0.2h_*$	0.43
		$1.0h_*$	0.50
6	$\sum_i \int_Z \left\langle \langle u_i' \rangle_{p,t}^2 \right\rangle_h / \sum_i \int_Z \left\langle u_i'^2 \right\rangle_{h,t}$	–	0.35
7	$\int_Z \left\langle \langle w' \rangle_{p,t} \langle \theta' \rangle_{p,t} \right\rangle_h / \int_Z \left\langle w'\theta' \right\rangle_{h,t}$	–	0.41
8	$\int_Z \left\langle \langle u' \rangle_{p,t}^2 \right\rangle_h / \sum_i \int_Z \left\langle \langle u_i' \rangle_{p,t}^2 \right\rangle_h$	–	0.63
9	$-(\theta_0^2/g) \int_Z \left\langle \langle w' \rangle_{p,t} \frac{\partial}{\partial z} \langle \pi_b' \rangle_{p,t} \right\rangle_h / \int_Z \left\langle \langle w' \rangle_{p,t} \langle \theta' \rangle_{p,t} \right\rangle_h$	–	0.86

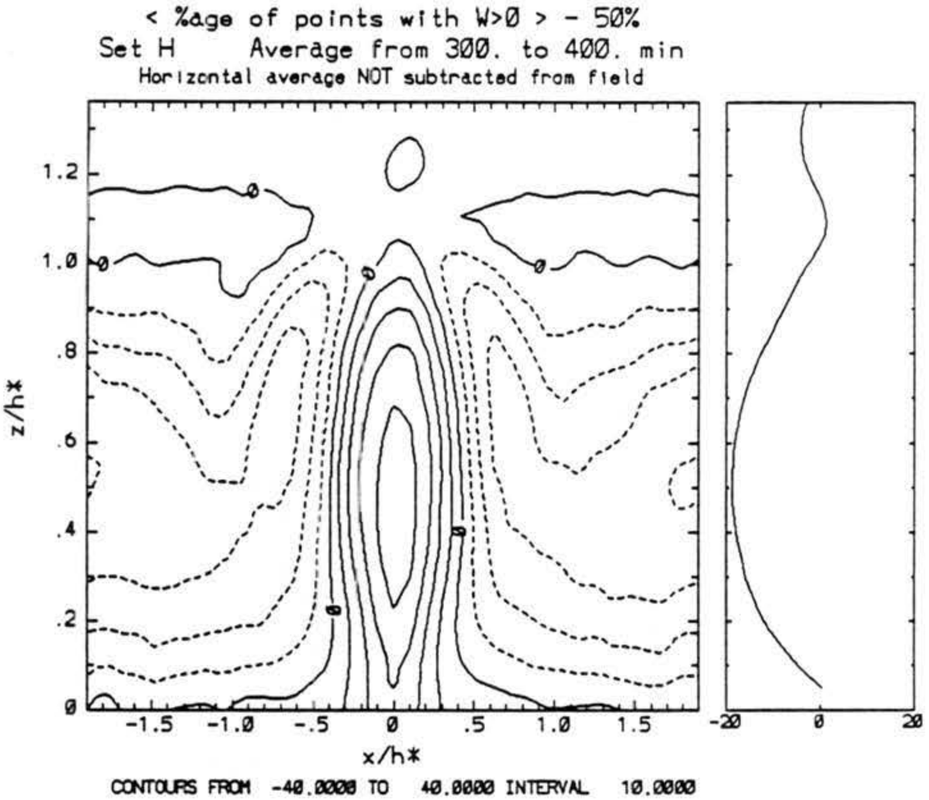

Figure 4.28. The percentage of points at each position $(\hat{x},z)$ with $w' > 0$, minus 50%, for Set H. Contour interval 10%.

(a)

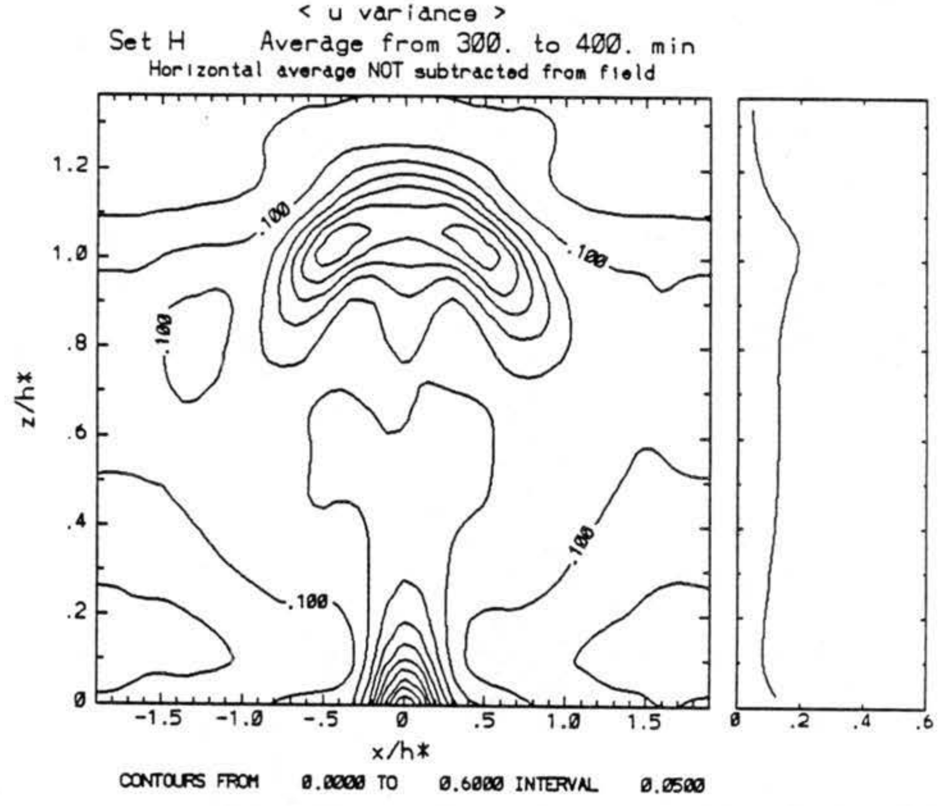

Figure 4.29. Fields of turbulent variances and covariances for Set H.

(a) u variance (contour interval $0.05w_*^2$)

(b) v variance (contour interval $0.05w_*^2$)

(c) w variance (contour interval $0.05w_*^2$)

(d) u/w covariance (contour interval $0.02w_*^2$)

(e) square root of θ variance (contour interval $1.0\,\theta_*$)

(f) u/θ covariance (contour interval $0.2w_*\theta_*$)

(g) w/θ covariance (contour interval $0.2w_*\theta_*$)

Continued on following pages.

(b)

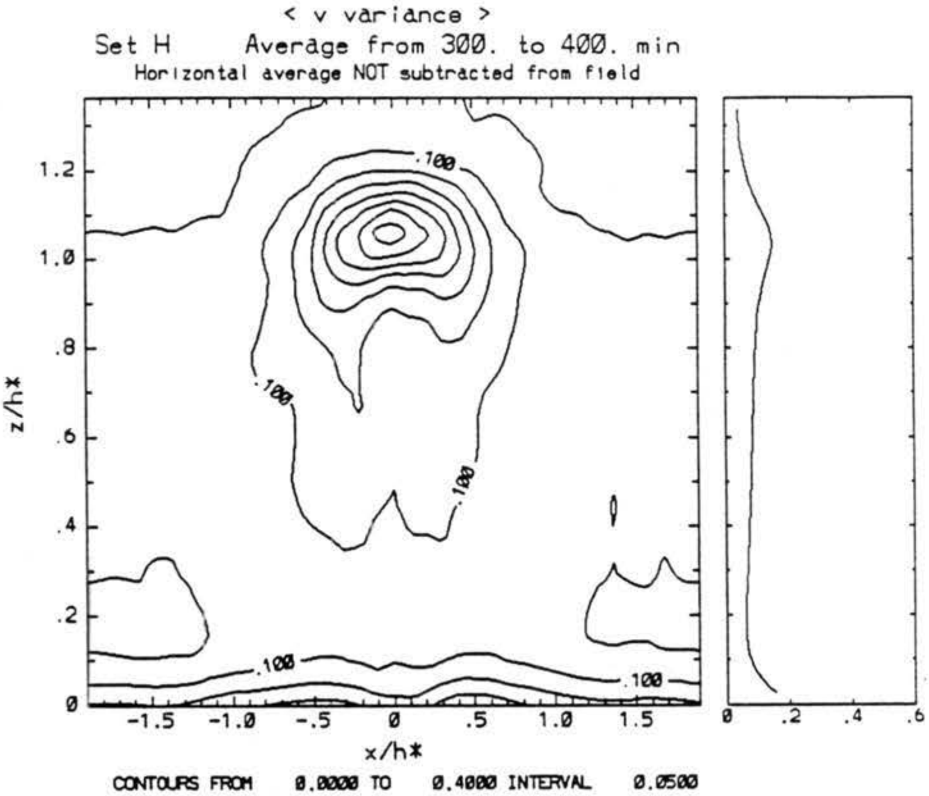

(c)

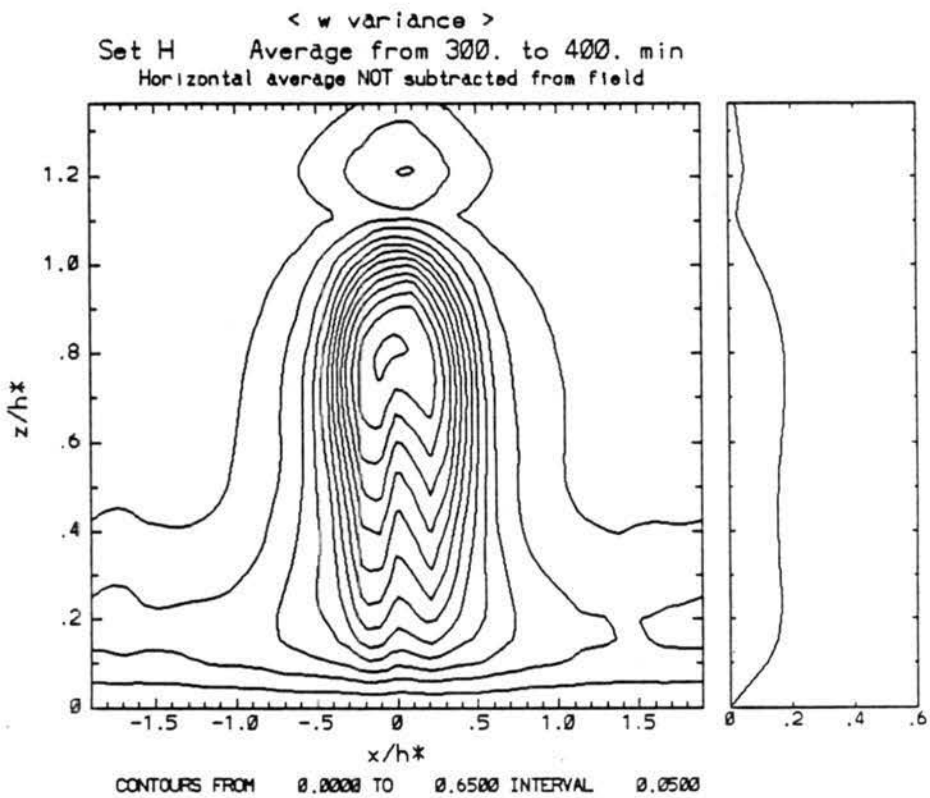

Figure 4.29 (continued).

Continued.

(d)

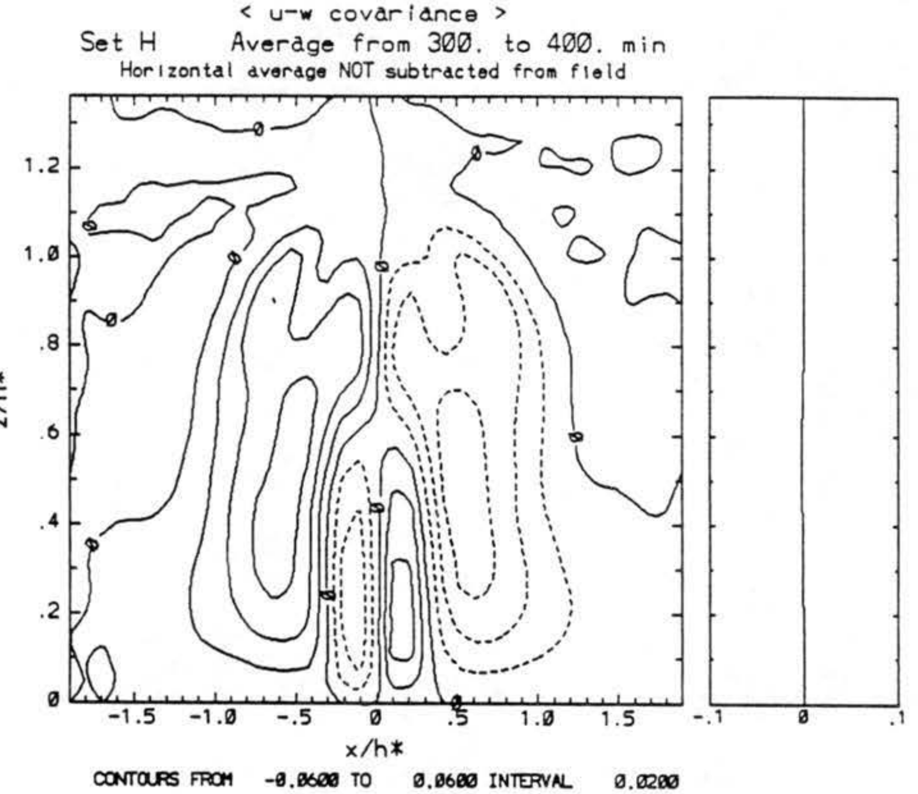

(e)

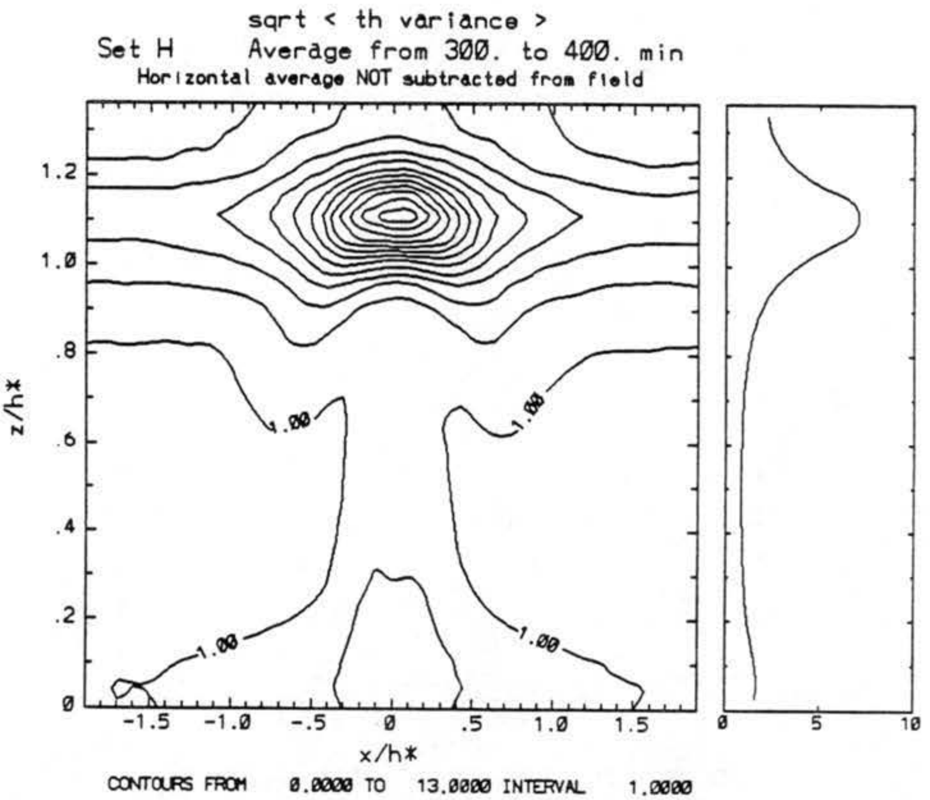

Figure 4.29 (continued).

Continued.

(f)

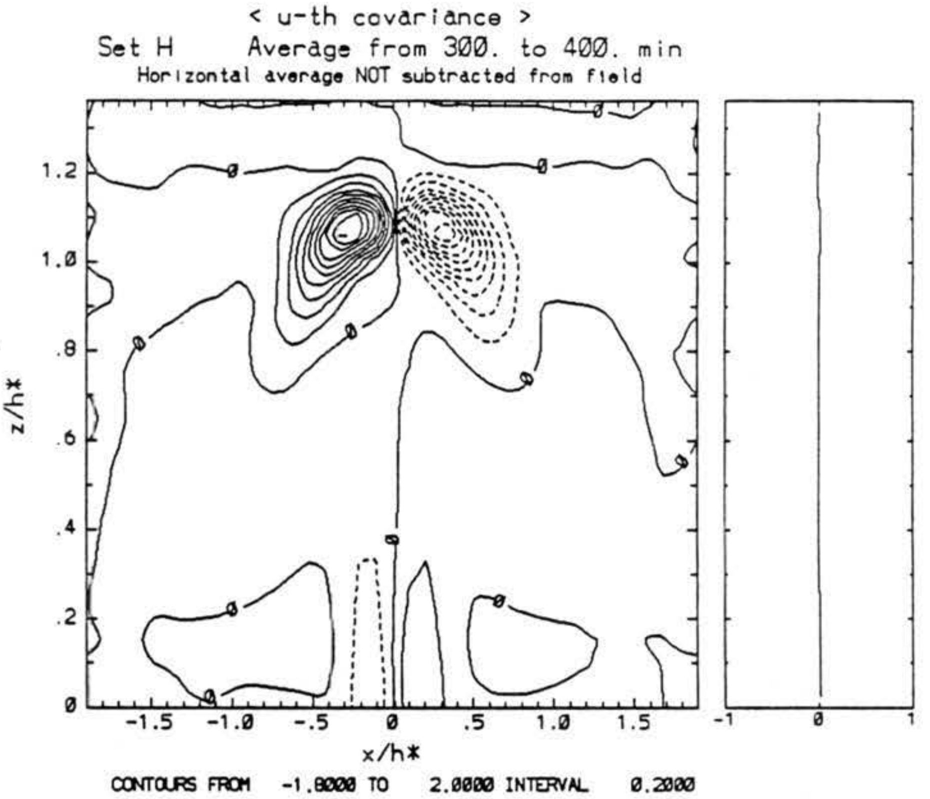

(g)

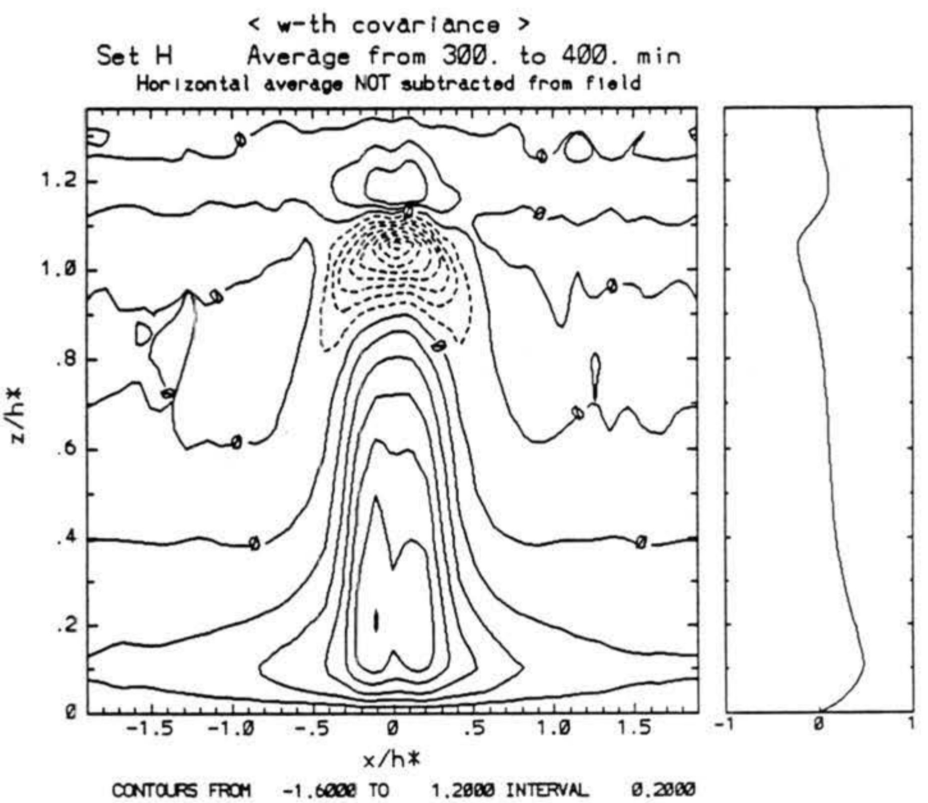

Figure 4.29 (continued).

by a region with intense entrainment and large horizontal velocity variances. On the sides of the $\hat{x}$-z domain all the variances are much lower than in the centre. There are several other interesting features—the following list is not exhaustive:

- At $\hat{x}=0$ the mid-boundary-layer maximum in w variance is at a higher level than it is in the horizontally homogeneous boundary layer ($z=0.8h_*$ versus $z=0.4h_*$) and is greater in magnitude ($0.65w_*^2$ versus $0.4w_*^2$), whereas at $\hat{x}=\pm\lambda_p/2$ it is lower ($z=0.2h_*$) and much weaker ($0.1w_*^2$).

- At $\hat{x}=\pm\lambda_p/2$ the minima in the u, v and θ variances are also at a lower level than they would be in a horizontally homogeneous boundary layer. The region above $z=0.4h_*$ is characterised by mean subsidence ($-0.1w_*$), very low w variance ($< 0.05w_*^2$) and weak w/θ covariance. There is still, nevertheless, a well-defined maximum in θ variance at $z=1.1h_*$, which has been identified as the height of the capping inversion.

- The u/w covariance is mostly positive for $\hat{x} < 0$ (it was negative in Set F), but below $z=0.6h_*$ there is a negative region of width $\sim 0.1\lambda_p$ just to the left of the $\hat{x}=0$ axis.

- Within the central maximum in w variance there is a very narrow minimum along $\hat{x}=0$. Similar features can be seen in the v variance, the θ variance and the w/θ covariance.

- The u/θ covariance is largest on either side of the elevated minimum in $\langle\theta'\rangle_{p,t}$, with the flux directed inwards.

4.6.5 *Horizontal-average statistics*

Whereas with previous simulations it has been difficult (with a few exceptions) to find horizontal-average statistics which are affected by the surface perturbation, in the present case the problem is to find ones that are not. Figure 4.30 shows the velocity variance profiles (c.f. Figures 4.12 and 4.22 for Sets F and G, also Figure 3.4 for Run A).

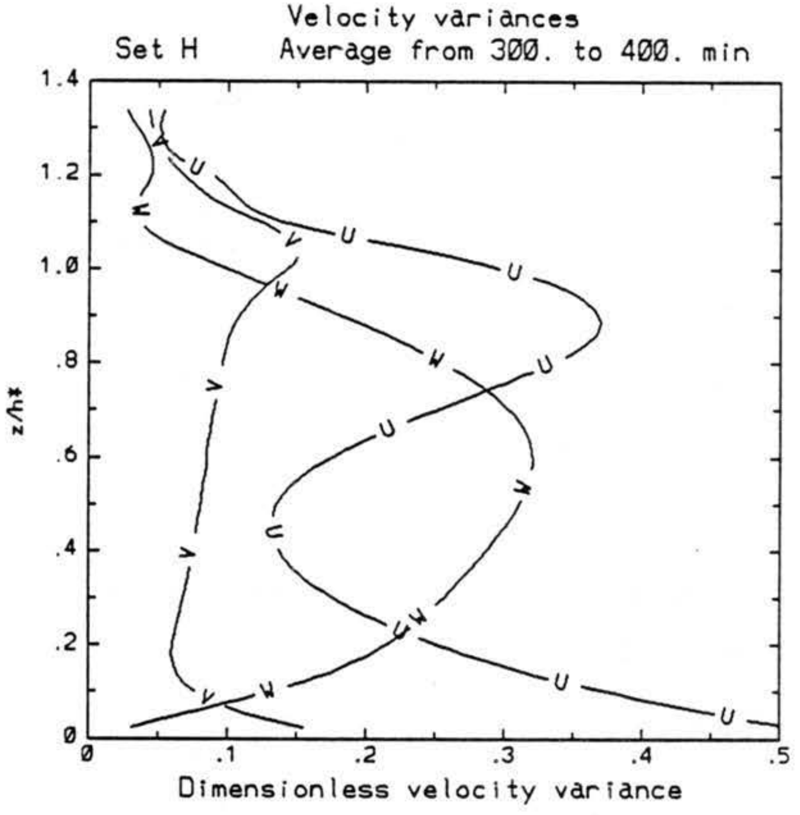

Figure 4.30. Profiles of dimensionless velocity variances $\langle u_i'^2 \rangle_{h,t}$ for Set H.

The u variance is considerably greater than the v variance and the maximum in the w variance, at $z=0.6h_*$, is about $0.2h_*$ higher than it was in the horizontally homogeneous simulation. Both these effects were seen in Set F, but were not so pronounced then.

A number of other differences from the horizontally homogeneous simulations have been detected and are listed below. Compared to the horizontally homogeneous simulations ...

- The height of the zero-crossing in the potential temperature gradient decreases from $z=0.37h_*$ to $z=0.27h_*$ and the middle boundary layer becomes more stable.
- The temperature variance increases at all levels (e.g. from $3.3\,\theta_*^2$ to $5.2\,\theta_*^2$ at $z=0.1h_*$, from $0.7\,\theta_*^2$ to $1.0\,\theta_*^2$ at $z=0.5h_*$, from $3.0\,\theta_*^2$ to $4.6\,\theta_*^2$ at $z=0.9h_*$).
- The standard deviation of pressure increases at all levels by about 25% (e.g. from $0.24\,\pi_*$ to $0.31\,\pi_*$ at $z=0.1h_*$, from $0.19\,\pi_*$ to $0.23\,\pi_*$ at $z=0.5h_*$, from $0.19\,\pi_*$ to $0.24\,\pi_*$ at $z=0.9h_*$).
- The magnitude of the peak in $\langle w'^3\rangle_{h,t}/2$ increases from $0.11w_*^3$ to $0.16w_*^3$,and its height increases slightly from $z=0.56h_*$ to $z=0.60h_*$.
- The magnitude of the minimum in resolved heat flux becomes more negative, from $-0.21w_*\theta_*$ to $-0.28w_*\theta_*$. The more vigorous entrainment results in an increase in the net warming rate $\partial\langle\theta\rangle_{h,t}/\partial t$ in the lower and middle boundary layer of 6%, or about $0.04\,\mathrm{K\,hr^{-1}}$.

One-dimensional x- and y-spectra for w in the middle of the boundary layer are shown in Figure 4.31 (c.f. Figures 4.14 for Set F and 4.23 for Set G). Remember that in this simulation the surface perturbation is at wavenumber 1 in the x direction, i.e., at $kh_*=1.65$. The x-spectral density exceeds the y-spectral density by a factor of about 2.0 at wavenumbers up to and including number 4 (i.e., $\lambda=\lambda_p/4$, $kh_*=6.6$). At wavenumber 5 and above the y-spectral density exceeds the x-spectral density slightly. The transition is quite sharp.

(a)

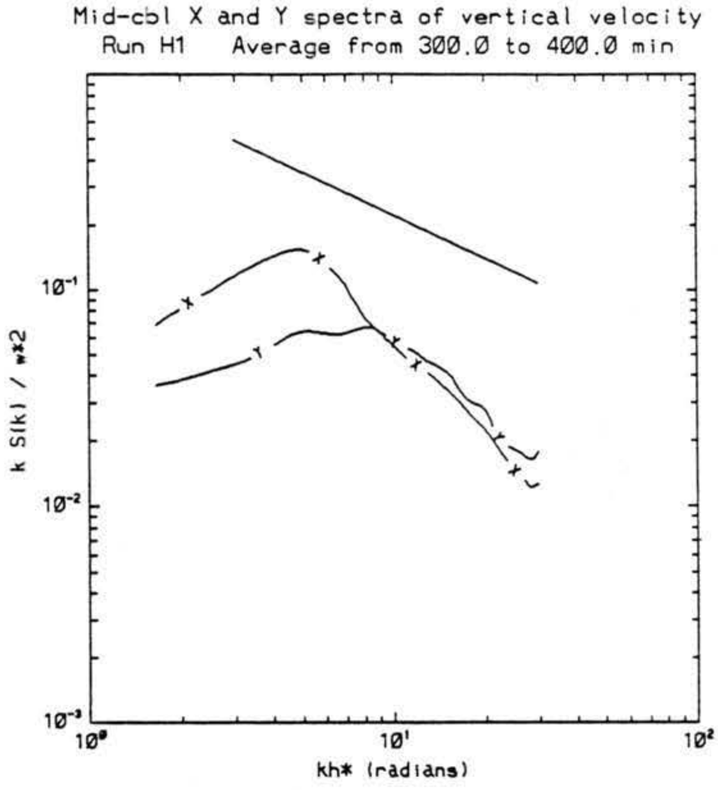

(b)

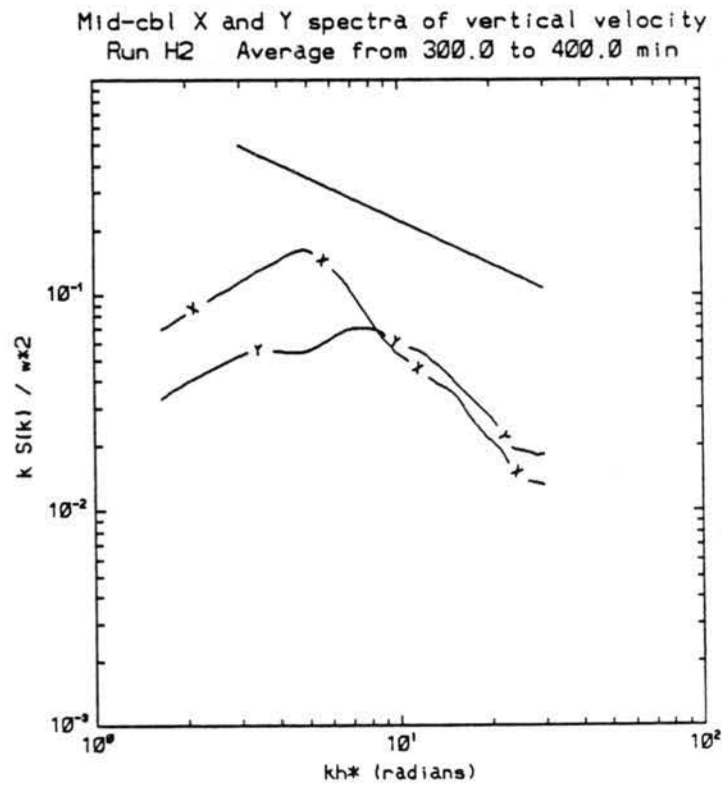

Figure 4.31. Dimensionless mid-boundary-layer spectra of vertical velocity in the x (—x—) and y (—Y—) directions for (a) Run H1 and (b) Run H2.

4.6.6 *Cross sections*

Figure 4.32 shows horizontal cross-sections of u', w' and θ' from Run H1 at $t = 350\,\mathrm{min}$; they are at two levels, $z = 290\,\mathrm{m} = 0.25\mathrm{h}_*$ and $z = 880\,\mathrm{m} = 0.74\mathrm{h}_*$. The surface heat-flux maximum is at $x = 0$ and the minimum is at $x = \pm\lambda_p/2 = \pm 2.25\,\mathrm{km}$.

At $z = 0.25h_*$ the dominant feature is a quasi-linear updraught of width $\sim 0.2\lambda_p$, aligned parallel to the y-axis and apparently meandering within a central region $\sim 0.3\lambda_p$ wide. The vertical velocity at the centre of the updraught is typically $\sim 2\,\mathrm{m\,s^{-1}}$ (i.e., $\sim w_*$), whereas the typical descending velocity outside it is less than $1\,\mathrm{m\,s^{-1}}$. Outside the central region there are secondary updraughts, for the most part parallel to the x-axis. The maximum temperature is found along the axis of the central updraught, with the region of $\theta' > 0$ somewhat wider than the region of $w' > 0$. Like vertical velocity, the temperature is highly skewed, having a maximum perturbation of $\sim 0.8\,\mathrm{K}$, but a most-negative perturbation between $-0.1\,\mathrm{K}$ and $-0.2\,\mathrm{K}$. The u' field is dominated by inflow into the central updraught, with a zero contour close to the w' maximum. It appears that the secondary updraughts are coincident with maxima in u' for $x < 0$ and minima in u' for $x > 0$, i.e., with maxima in the inflow velocity.

At $z = 0.74h_*$ the central updraught is still evident (and somewhat stronger) but the secondary updraughts are not. The minima in w' are mostly clustered on either side of the updraught, at $x = \pm 0.15\lambda_p$. Some of the most vigorous parts of the updraught have $\theta' > 0$, but at other places on the centre of the updraught, and on either side of it, θ' is negative. In the u' field, flow is generally away from $x = 0$ and strongest near $x = \pm 0.15\lambda_p$. It *seems* that maxima in outflow velocity are coincident with the minima in w' flanking the updraught in this region.

Some of the features in the circulations and turbulence can now be explained. ("Turbulence" is used here to mean deviations from the time-averaged circulation). The explanations rely too heavily on hindsight to have any predictive value, but it is worthwhile, nevertheless, to try to interpret the statistics in terms of structures in the flow.

It is hypothesised that variations in the position of the central updraught (i.e., meandering) are a major factor in causing variability in the vicinity of $\hat{x} = 0$. For

(a)

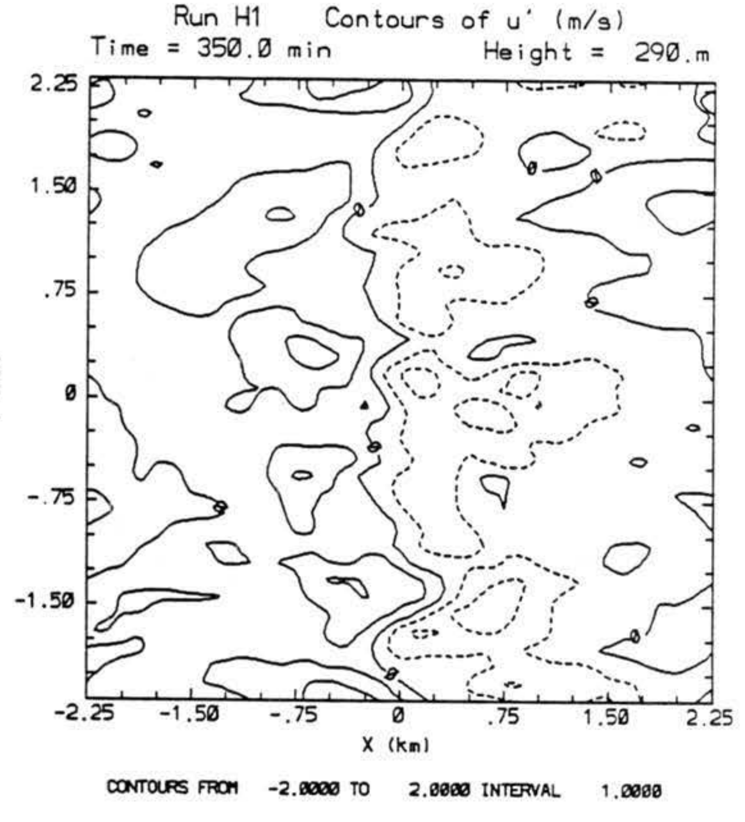

Figure 4.32. Cross-sections of u', w' and θ' from Run H1 at $t=350$ min.

(a) u' at $z=0.25h_*$ (d) u' at $z=0.74h_*$
(b) w' at $z=0.25h_*$ (e) w' at $z=0.74h_*$
(c) θ' at $z=0.25h_*$ (f) θ' at $z=0.74h_*$

Contour intervals are $1.0\,\mathrm{m\,s^{-1}}$ for u' and w' and 0.1 K for θ'.

Continued on following pages.

(b)

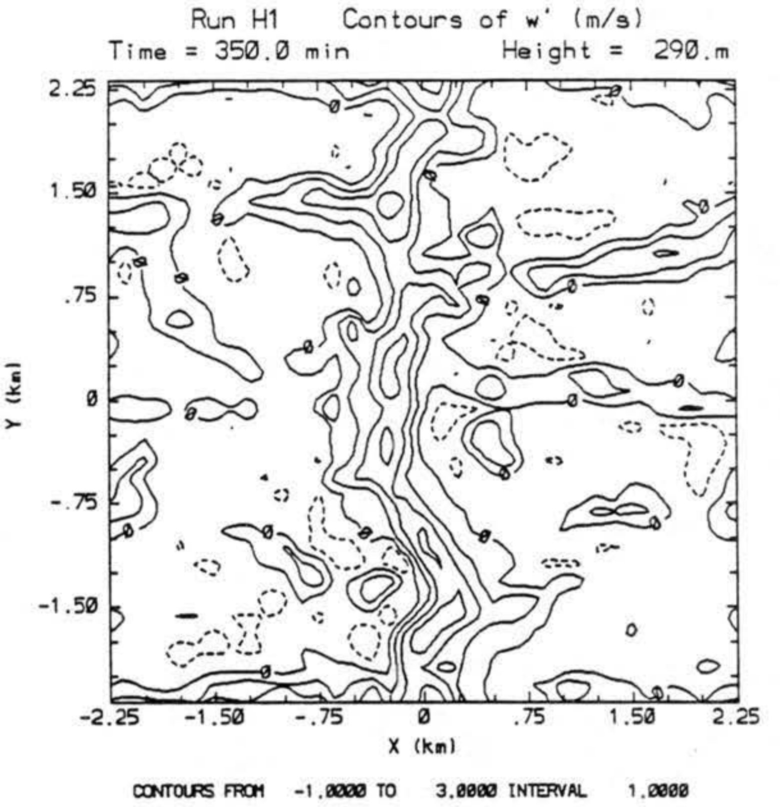

(c)

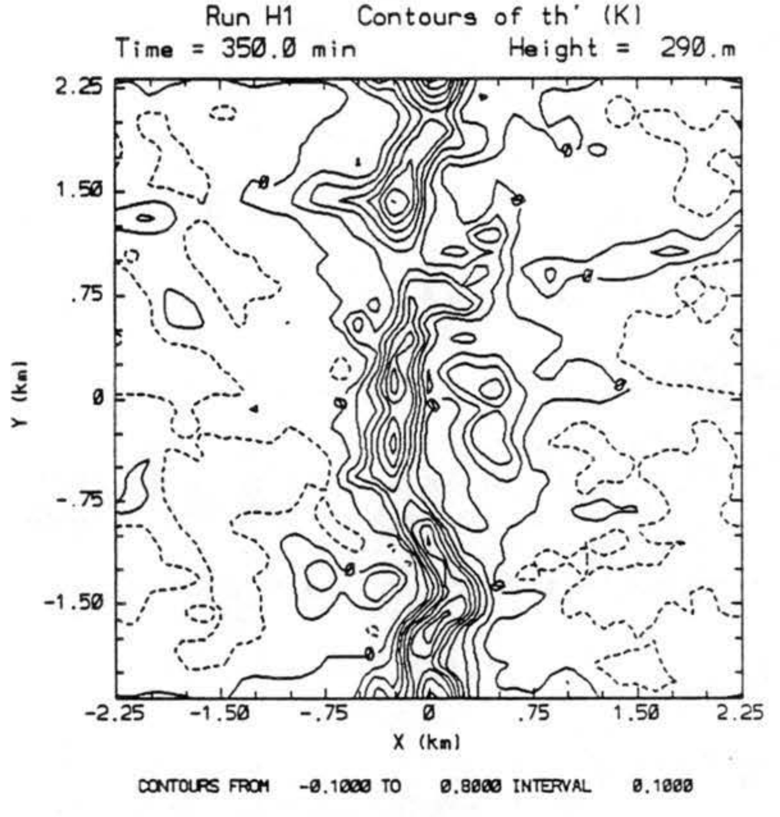

Figure 4.32 (continued).

Continued.

(d)

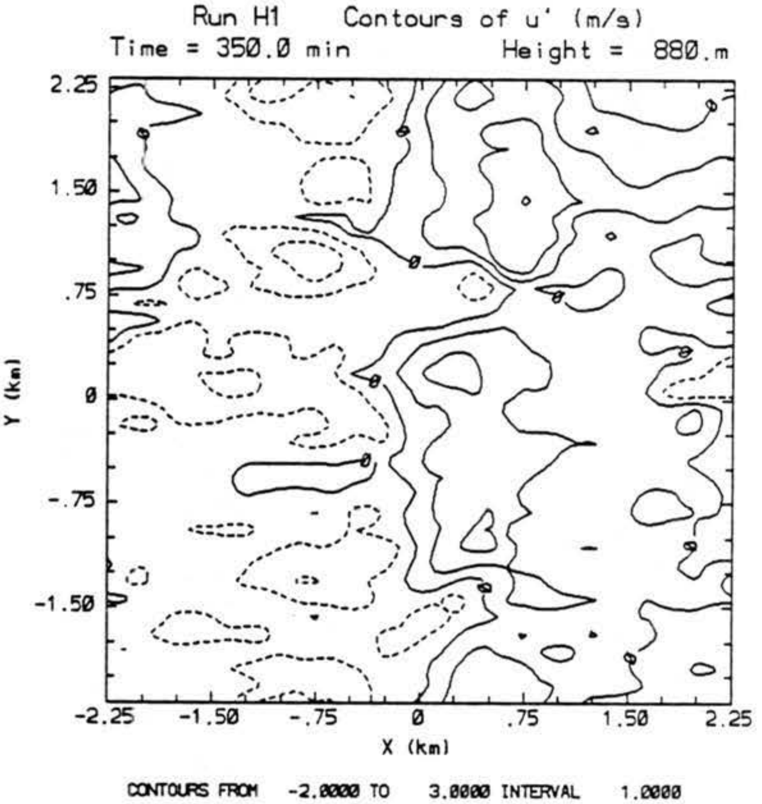

Figure 4.32 (continued).

Continued.

(e)

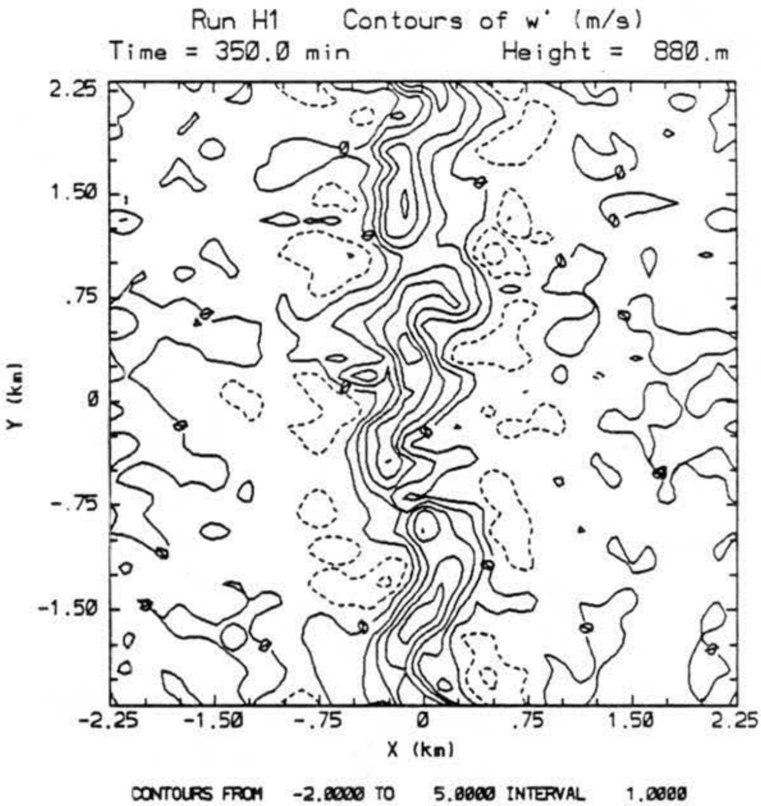

(f)

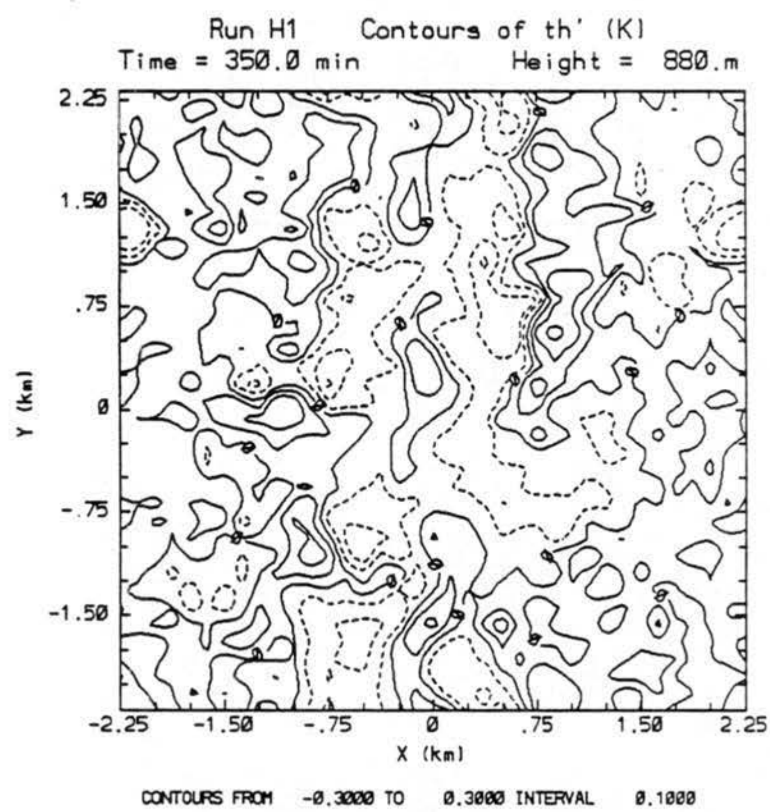

Figure 4.32 (continued).

example, the sharp, near-surface maximum in u variance arises because points at $\hat{x}=0$ variously find themselves in the region with $u' > 0$ to the left of the updraught or in the region with $u' > 0$ to the right. For similar reasons the broader maxima in w variance, θ variance and w/θ covariance occupy the region (roughly $1.0h_* \approx 0.3\lambda_p$ wide) within which the updraught meanders. It is also possible to explain the narrow central minima in w variance: points at $\hat{x}=0$ plane are (almost) always within the updraught and usually somewhere near the centre, but points on each side can be near the centre, on the margin, or in subsiding regions, and therefore have higher variance.

Now let us look at the u/w covariance, for simplicity only in the region where $\hat{x} < 0$. Consider a point in the lower boundary layer just to the left of $\hat{x}=0$. Usually it will be either in the inflow region on the left edge of the updraught (u' positive and w' small) or near the centre (u' small and w' positive), so the u/w covariance is negative; in the upper boundary layer outflow replaces inflow and the covariance is positive. Further from $\hat{x}=0$ matters are not so clear. It has been noted that the secondary updraughts in the lower boundary layer seem to be associated with strong inflow. This may be because they are penetrating from the surface where mean inflow is strongest, but, whatever the mechanism, the association contributes positively to the u/w covariance.

Finally, it has been noted that, away from the central updraught, the w variance is small above $z=0.4h_*$ and there are secondary updraughts at $z=0.25h_*$ that are not in evidence at $z=0.74h_*$ (nor at $z=0.5h_*$ although fields at that level have not been shown). One can visualise updraughts penetrating into a region dominated by the return flow of the central updraught. Subsidence limits the height reached by the secondary updraughts before they are advected into the central updraught, and the alignment of the secondary updraughts parallel to the x-axis is a result of deformation by the mean flow. Above $z=0.4h_*$ the turbulence is dominated by fluctuations in u and θ in the air flowing out of the central updraught.

4.7 Simulations with $\lambda_p = 4500\,\mathrm{m}$ and $u_0 = 1\,\mathrm{m\,s^{-1}}$

4.7.1 *Evolution of surface-driven circulations*

The simulations with $\lambda_p = 4500\,\mathrm{m}$ and $u_0 = 1\,\mathrm{m\,s^{-1}}$ are Runs I1 and I2, and averages over the two are labelled Set I. Figure 4.33 shows the evolution of the circulation kinetic energy and its components, calculated over the pair (c.f. Figure 4.2, Figure 4.16 and Figure 4.24). The curve is intermediate in character between those of Set H and Set G. After the perturbation is turned on at $t = 200\,\mathrm{min}$, E_c first rises to a peak at $t = 250\,\mathrm{min}$ then oscillates about a lower level.

The following sections describe time-averaged statistics—again the averaging period is from $t = 300\,\mathrm{min}$ to $t = 400\,\mathrm{min}$. Averages calculated for the individual simulations are very similar to each other, so only averages over the pair are described.

4.7.2 *Scaling parameters*

For the present case $h_* = 1170\,\mathrm{m}$, which is not significantly different from the horizontally homogeneous value for the same period. The following dimensionless numbers can be calculated:

$$\frac{\lambda_p}{h_*} = 3.85 \quad \text{and} \quad \frac{u_0 h_*}{w_* \lambda_p} = 0.13.$$

Regarding the horizontal variation in the boundary layer depth, it should come as no surprise after the results of Set H that it is less than 1%.

4.7.3 *The time-averaged circulation*

The value $(u_0 h_*)/(w_* \lambda_p) = 0.13$ implies that advection by a velocity u_0 through a distance λ_p will take $(0.13)^{-1} h_*/w_*$, i.e., about 75 minutes. In the previous ($u_0 = 0\,\mathrm{m\,s^{-1}}$) simulations at the same wavelength, the circulation started to develop strongly about 20 minutes after the surface perturbation was applied and reached a peak at 45 minutes. Given the strength of the circulation in that case, one might expect that a horizontal velocity of only $1\,\mathrm{m\,s^{-1}}$ would not modify it much: that the vertical velocity maximum in

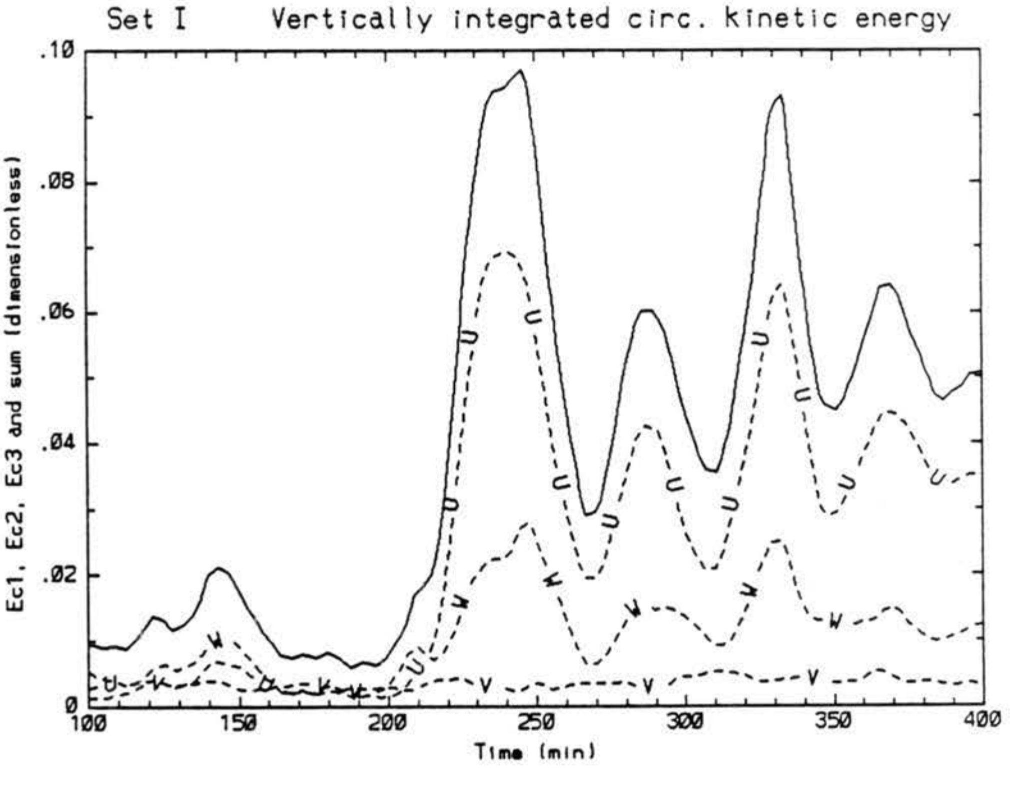

Figure 4.33. Evolution of circulation kinetic energy for Set I.

the mean circulation would be moved a short distance downstream of the surface heat-flux maximum and that its magnitude would be reduced slightly. This is not what is observed.

Figure 4.34 shows $\langle u \rangle_{p,t}$, $\langle w \rangle_{p,t}$ and $\langle \theta \rangle_{p,t}$ fields for Set I (c.f. Figures 4.7, 4.19 and 4.26 for Sets F, G and H, respectively). Whereas in Set H (same λ_p, $u_0 = 0\,\mathrm{m\,s^{-1}}$) there was a narrow updraught with maximum vertical velocity $1.1w_*$ and a much broader downdraught region with weaker vertical motion, in the present case the ascending and descending regions are approximately equal in width and the maximum vertical velocity is only $0.3w_*$. The present case can also be compared with Set G, with smaller λ_p but the same u_0. The maximum vertical velocity in that case was only about $0.075w_*$, but the position of the maximum, expressed as a fraction of λ_p, was about the same: in both cases it is at $\hat{x} = 0.4\lambda_p$. A few other points can be made. The maximum and minimum horizontal velocities are around $\pm 0.5w_*$, which is a little less than was found in Set H but a lot more than was found in either of the $\lambda_p = 1500m$ cases; in shape the $\langle u' \rangle_{p,t}$ field does not resemble that of any of the other cases. The temperature perturbations near the surface are around $\pm 2\,\theta_*$, which is comparable to what was found in Set F and Run G, but much smaller than was found in Set H. The shape of the $\langle \theta' \rangle_{p,t}$ field is similar to that found in Set G (both have a maximum in mid-boundary-layer at $\hat{x} = 0.25\lambda_p$, for example), but the perturbations at the level of the inversion are much larger in the present case. Again there is a suggestion in all the fields of contour lines in the stable layer sloping upwards and to the left, which is a signature of a stationary gravity wave.

One other feature should be mentioned, namely the short-wavelength fluctuations that are most apparent in the vertical velocity contours. These are a sign of stationary $2\Delta x$ structure in the fields. They were not apparent in phase-average fields from the earlier simulations. It is interesting, though, that in the spectra presented below (Figure 4.38) the spectral density at the $2\Delta x$ limit is no higher than it was in the other simulations; in fact the mean wind suppresses fine structure in the x direction slightly. The crucial point is that the structure is sufficiently steady to appear in the time-averaged fields. Possibly, the fine structure appears more in the present plots than in previous ones

(a)

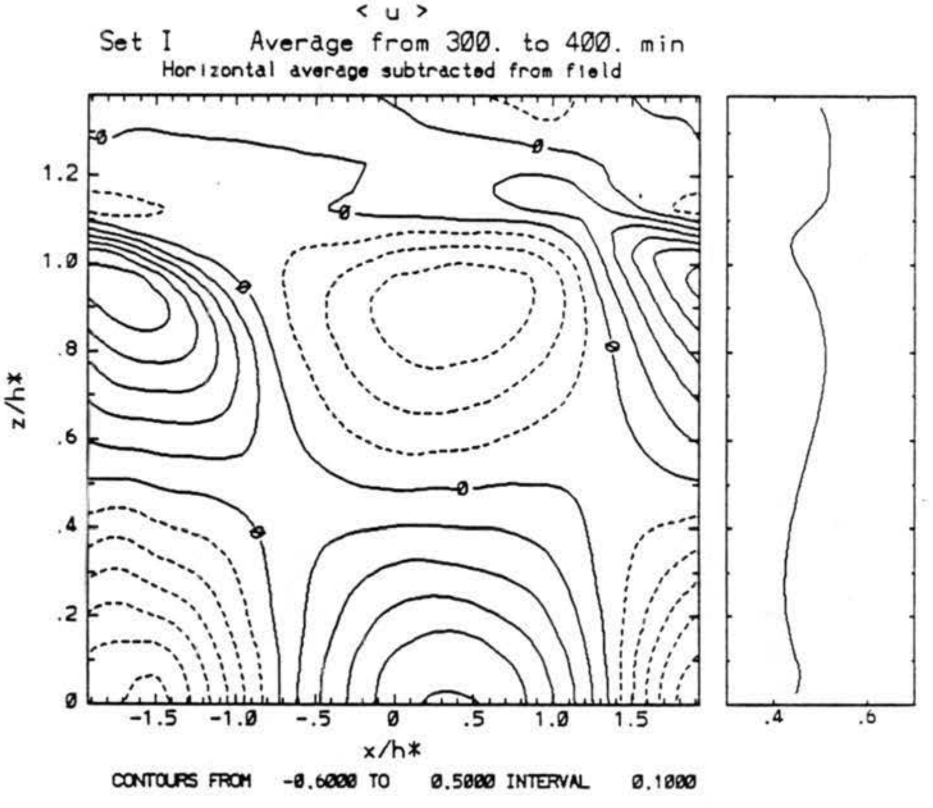

Figure 4.34. Phase-time averaged velocity and potential temperature fields for Set I.

- **(a)** **u (contour interval $0.1w_*$)**
- **(b)** **w (contour interval $0.05w_*$)**
- **(c)** **θ (contour interval $0.5\,\theta_*$)**

Continued on following page.

(b)

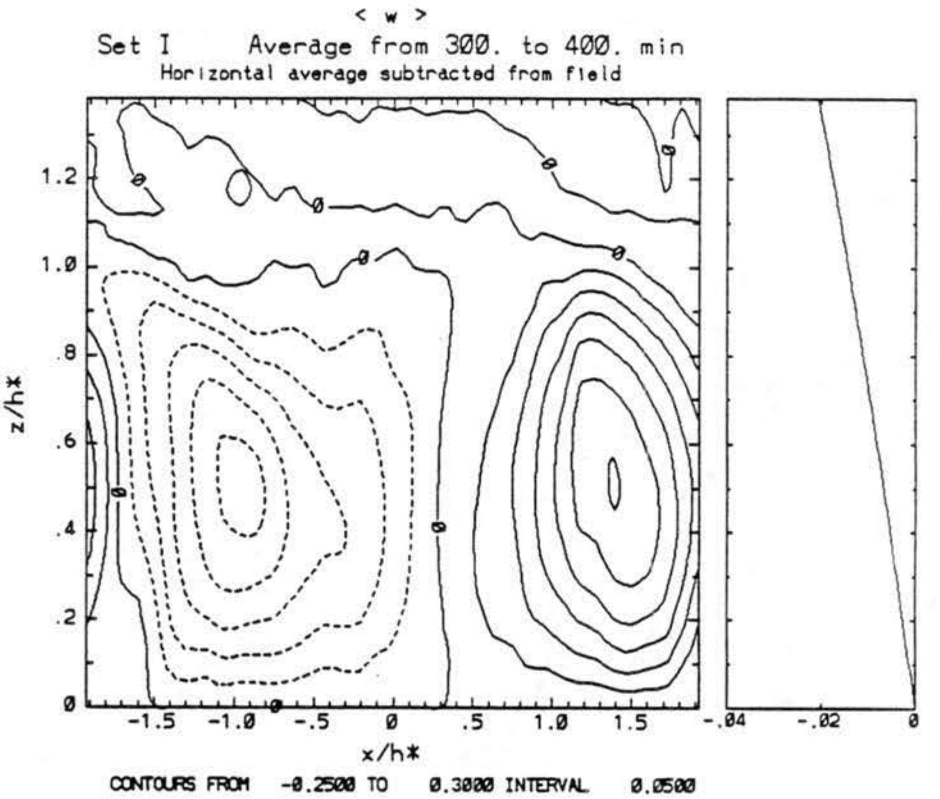

(c)

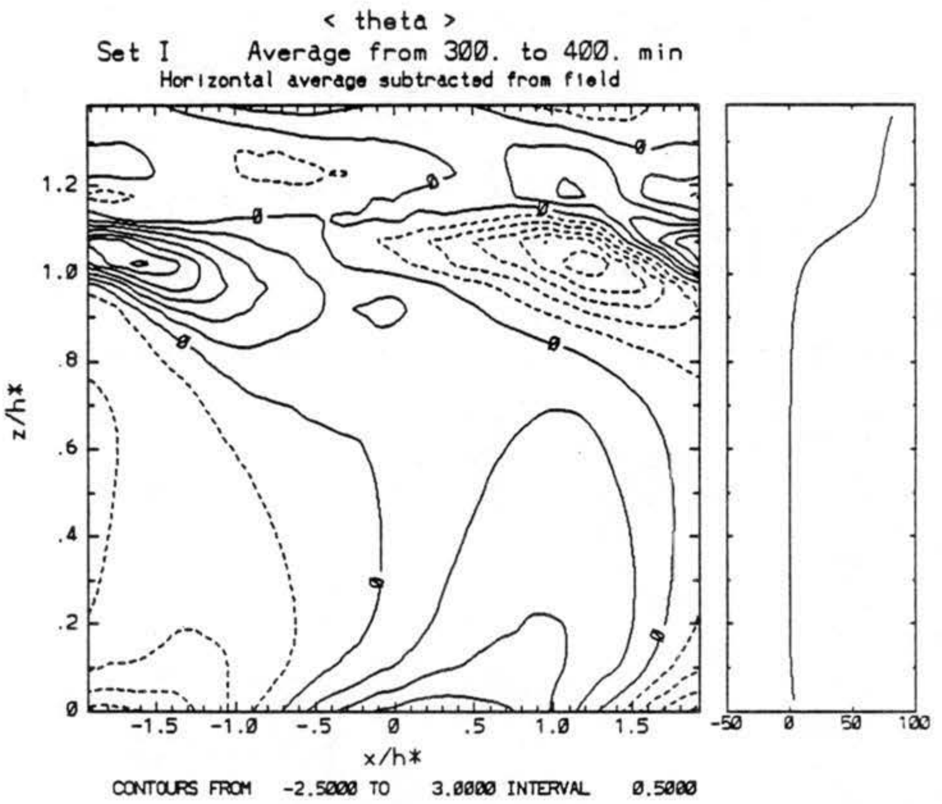

Figure 4.34 (continued).

because there is mean advection (not present in Set H) and because phase averages are calculated over only one cycle in the x-direction (versus three in Sets F and G).

Figure 4.35 shows the pressure field and its components (c.f. Figures 4.8, 4.20 and 4.27). The amplitude of the pressure perturbation at the surface ($0.30\pi_*$) is smaller than was found in Set H ($0.50\pi_*$), but larger than in Set F ($0.14\pi_*$) or Set G ($0.08\pi_*$). The total pressure field resembles the buoyancy pressure field more than in previous cases, because the turbulence pressure and circulation pressure perturbations are typically relatively small.

Table 4.6 presents comparable information to Tables 4.3, 4.4 and 4.5. In general ratios 1 to 7 are of the order of 0.1 (but somewhat larger for moments of u or π) and so are intermediate in magnitude between Set H and the other two cases. The fraction of the circulation kinetic energy in the $\langle u' \rangle_{p,t}$ field is now 0.86, versus 0.63 for Set H; presumably the difference reflects the lack of a strong, narrow ascending region in the present case.

4.7.4 *Turbulence: deviations from the time-averaged circulation*

Figure 4.36 shows the turbulent second moments of velocity and temperature for Set I (c.f. Figures 4.10, 4.21 and 4.29). As in Set G (same u_0, $\lambda_p = 1500\,\mathrm{m}$) one can imagine a line joining the θ-variance maximum near the surface ($\hat{x} = 0.3h_* = 0.08\lambda_p$, $z=0$) with the maximum at the inversion ($\hat{x} = 1.1h_* = 0.30\lambda_p$, $z = 1.1h_*$) and identify it loosely as the axis of maximum turbulence intensity. A number of other aspects of the fields are listed below.

- The w variance in the middle of the boundary layer varies from $\sim 0.25w_*^2$ to $\sim 0.50w_*^2$, which is a slightly larger range than was seen in the $\lambda_p = 1500\,\mathrm{m}$ simulations. The largest w variance is above and to the right of the maximum in w/θ covariance (buoyancy production), as in Set G. The height of maximum w variance, i.e., the value of z at which the largest w variance is encountered for a given value of $\hat{x}$, varies from a minimum of $\sim 0.3h_*$ to a maximum of $\sim 0.5h_*$.

(a)

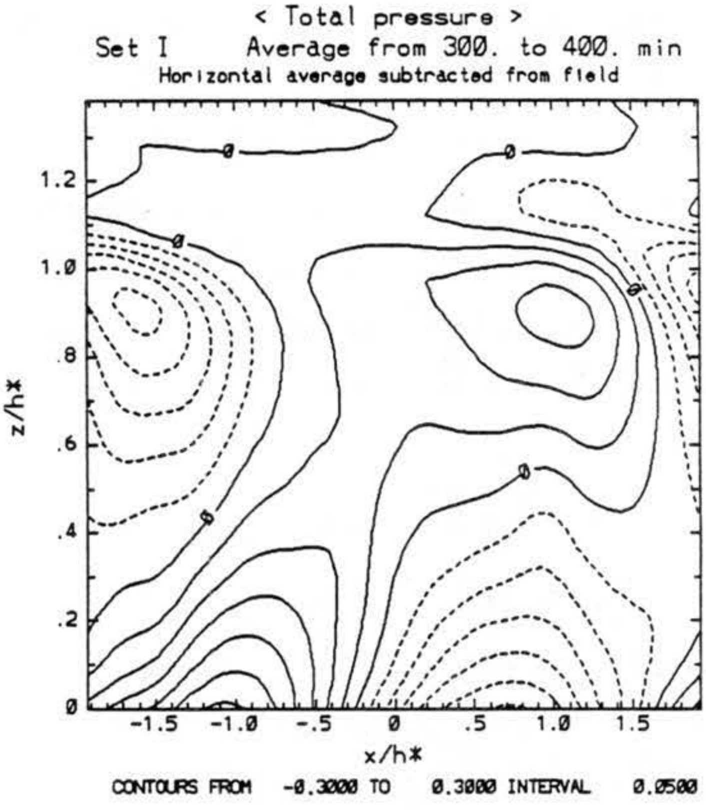

Figure 4.35. Phase-time averaged pressure fields for Set I.

(a) total pressure π (contour interval $0.05\pi_*$)

(b) buoyancy pressure π_b (contour interval $0.05\pi_*$)

(c) turbulence pressure π_t (contour interval $0.05\pi_*$)

(d) circulation pressure π_c (contour interval $0.02\pi_*$)

Continued on following pages.

(b)

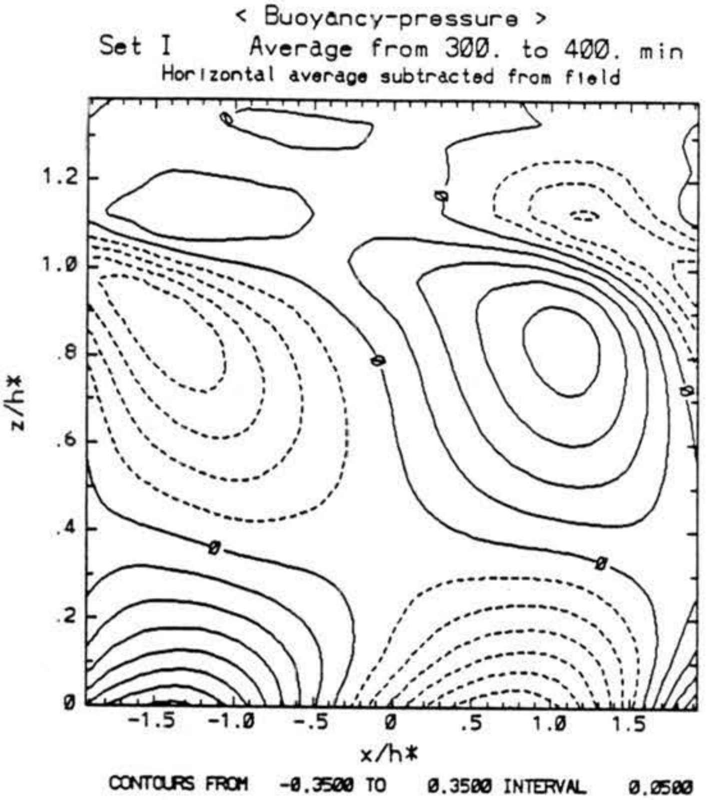

(c)

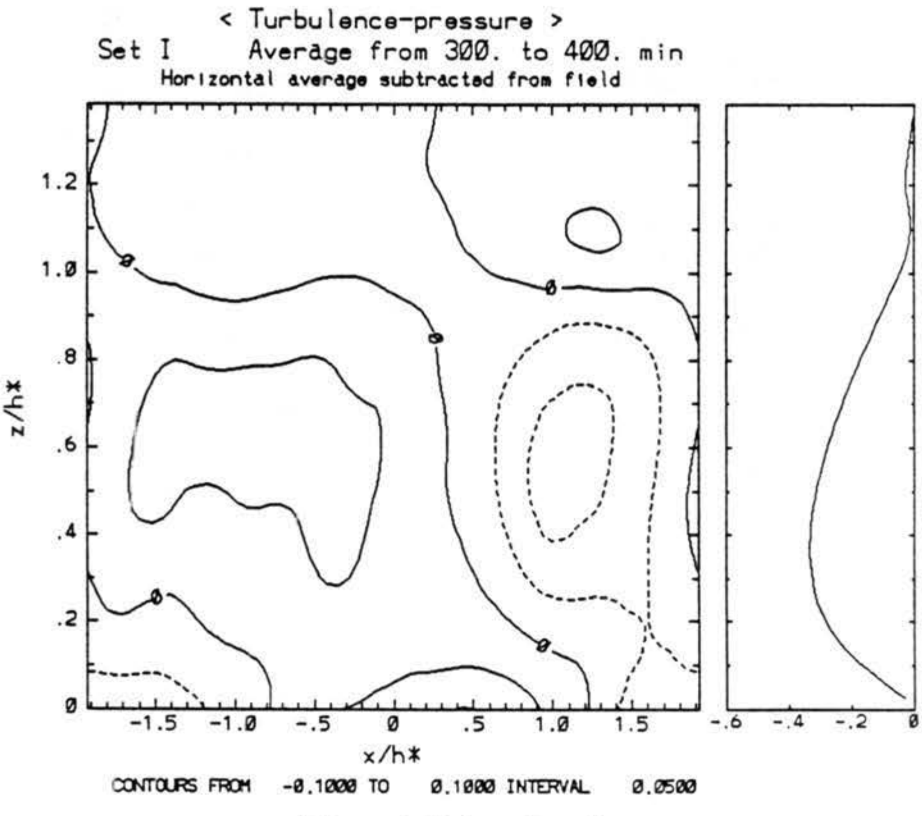

Figure 4.35 (continued).

Continued.

(d)

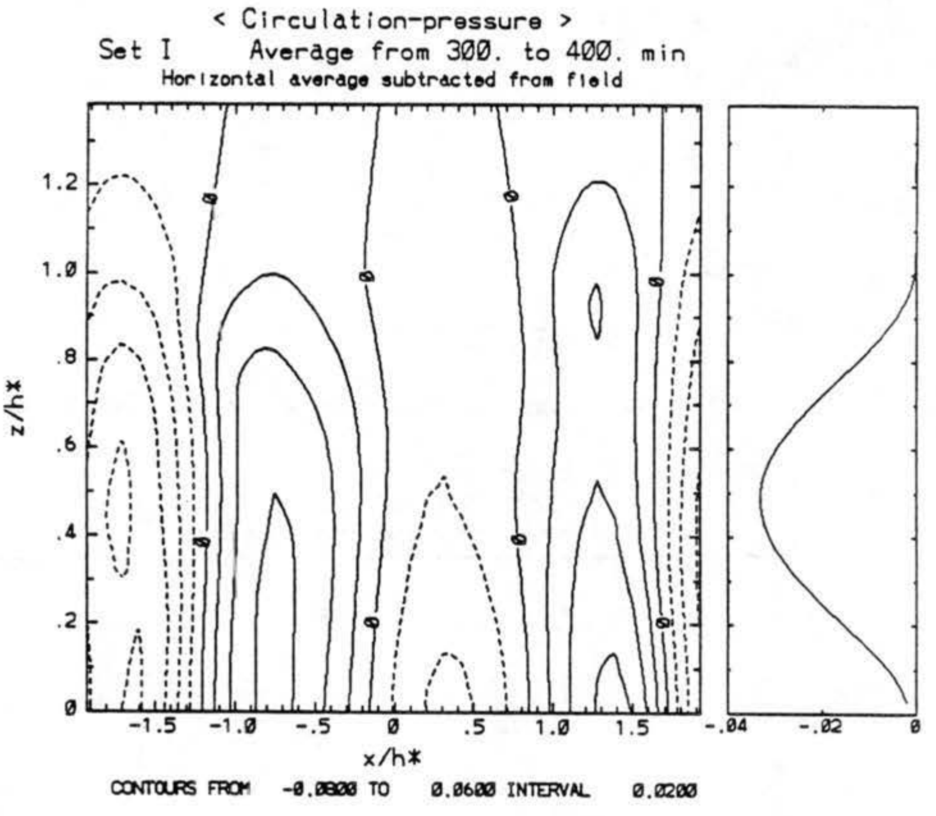

Figure 4.35 (continued).

Table 4.6. Ratios characterising the time-averaged circulation in Set I.

No.	Ratio	Height	Value
1	$\left\langle \langle u' \rangle_{p,t}^2 \right\rangle_h / \left\langle u'^2 \right\rangle_{h,t}$	$0.1h_*$	0.41
		$0.9h_*$	0.40
2	$\left\langle \langle w' \rangle_{p,t}^2 \right\rangle_h / \left\langle w'^2 \right\rangle_{h,t}$	$0.4h_*$	0.08
3	$\left\langle \langle \theta' \rangle_{p,t}^2 \right\rangle_h / \left\langle \theta'^2 \right\rangle_{h,t}$	$0.1h_*$	0.18
		$0.9h_*$	0.10
4	$\left\langle \langle \pi' \rangle_{p,t}^2 \right\rangle_h / \left\langle \pi'^2 \right\rangle_{h,t}$	$0.1h_*$	0.29
		$0.9h_*$	0.30
5	$\left\langle \langle w' \rangle_{p,t} \langle \theta' \rangle_{p,t} \right\rangle_h / \left\langle w'\theta' \right\rangle_{h,t}$	$0.2h_*$	0.08
		$1.0h_*$	0.11
6	$\sum_i \int_Z \left\langle \langle u_i' \rangle_{p,t}^2 \right\rangle_h / \sum_i \int_Z \left\langle u_i'^2 \right\rangle_{h,t}$	–	0.11
7	$\int_Z \left\langle \langle w' \rangle_{p,t} \langle \theta' \rangle_{p,t} \right\rangle_h / \int_Z \left\langle w'\theta' \right\rangle_{h,t}$	–	0.11
8	$\int_Z \left\langle \langle u' \rangle_{p,t}^2 \right\rangle_h / \sum_i \int_Z \left\langle \langle u_i' \rangle_{p,t}^2 \right\rangle_h$	–	0.78
9	$-(\theta_0^2/g) \int_Z \left\langle \langle w' \rangle_{p,t} \frac{\partial}{\partial z} \langle \pi_b' \rangle_{p,t} \right\rangle_h / \int_Z \left\langle \langle w' \rangle_{p,t} \langle \theta' \rangle_{p,t} \right\rangle_h$	–	0.89

(a)

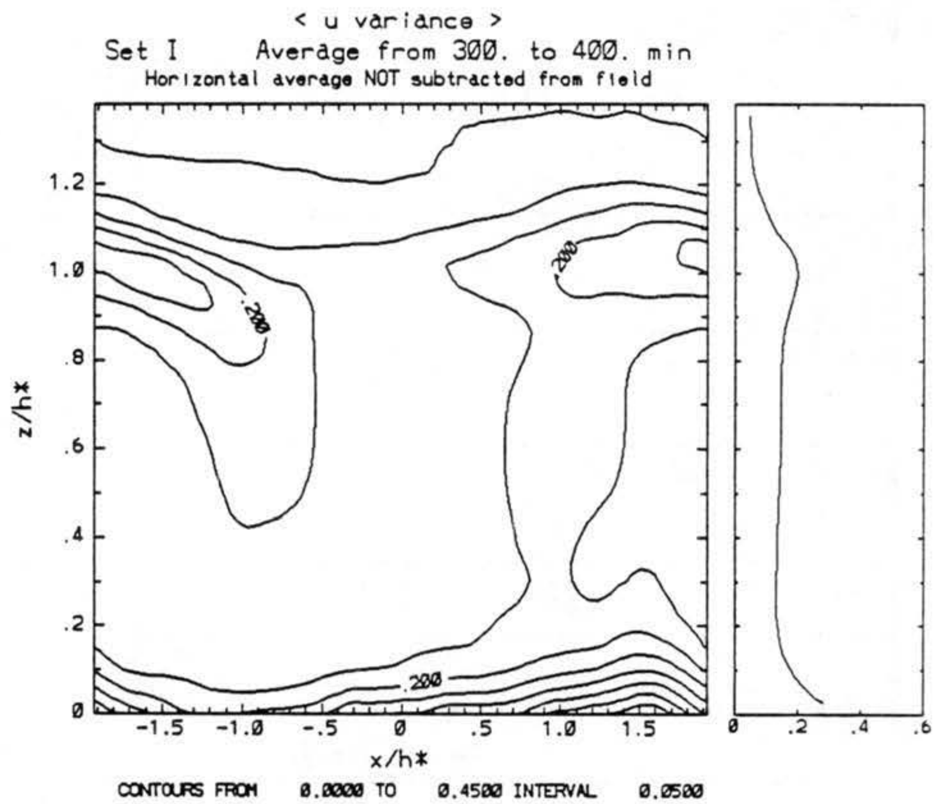

Figure 4.36. Fields of turbulent variances and covariances for Set I.

- (a) u variance (contour interval $0.05w_*^2$)
- (b) v variance (contour interval $0.05w_*^2$)
- (c) w variance (contour interval $0.05w_*^2$)
- (d) u/w covariance (contour interval $0.01w_*^2$)
- (e) square root of θ variance (contour interval $0.5\,\theta_*$)
- (f) u/θ covariance (contour interval $0.1w_*\theta_*$)
- (g) w/θ covariance (contour interval $0.1w_*\theta_*$)

Continued on following pages.

(b)

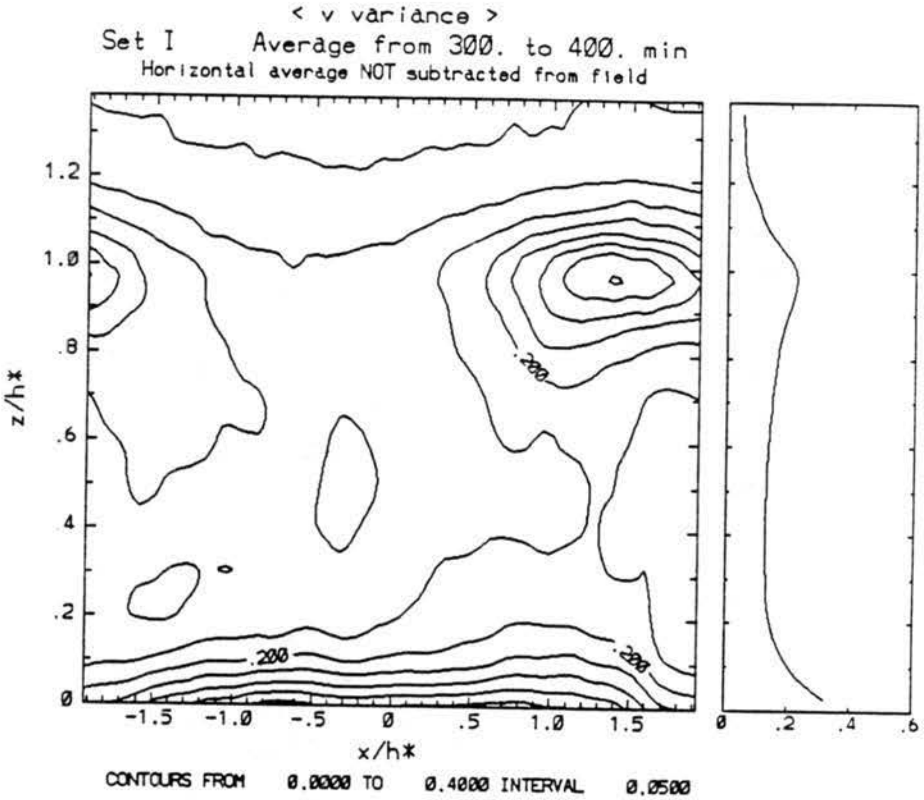

(c)

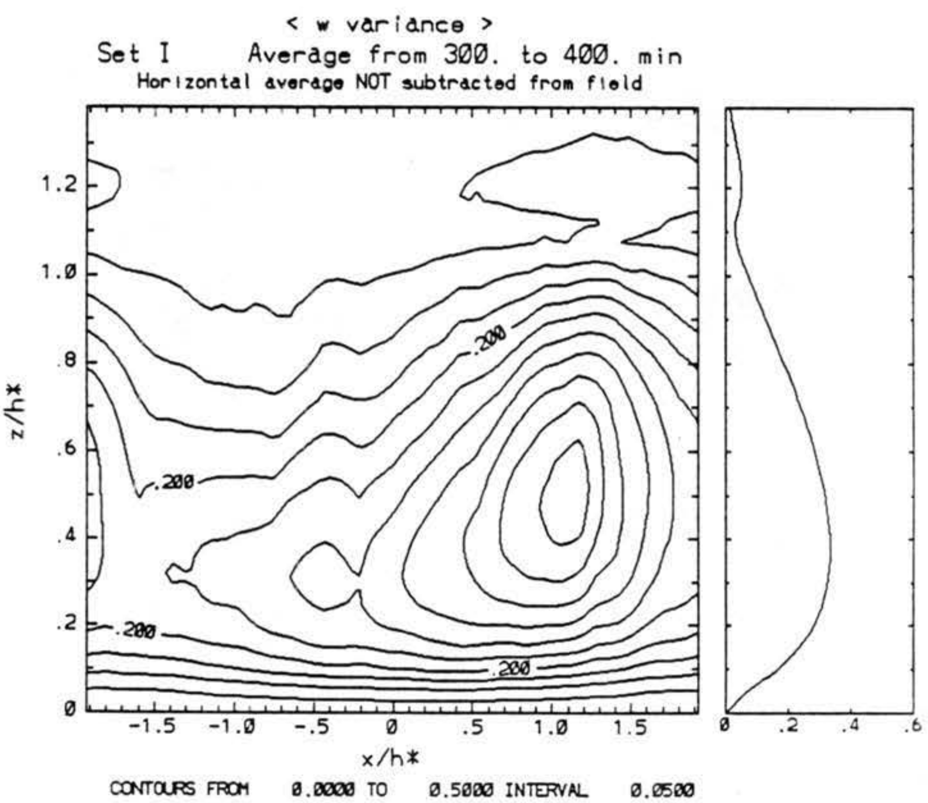

Figure 4.36 (continued).

Continued.

(d)

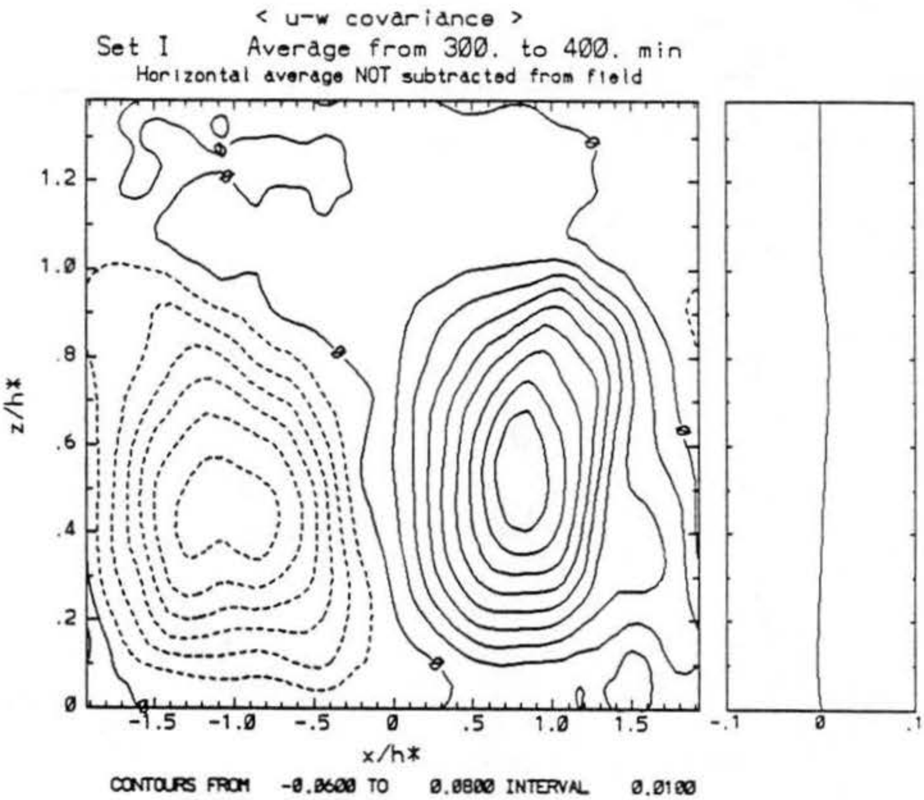

(e)

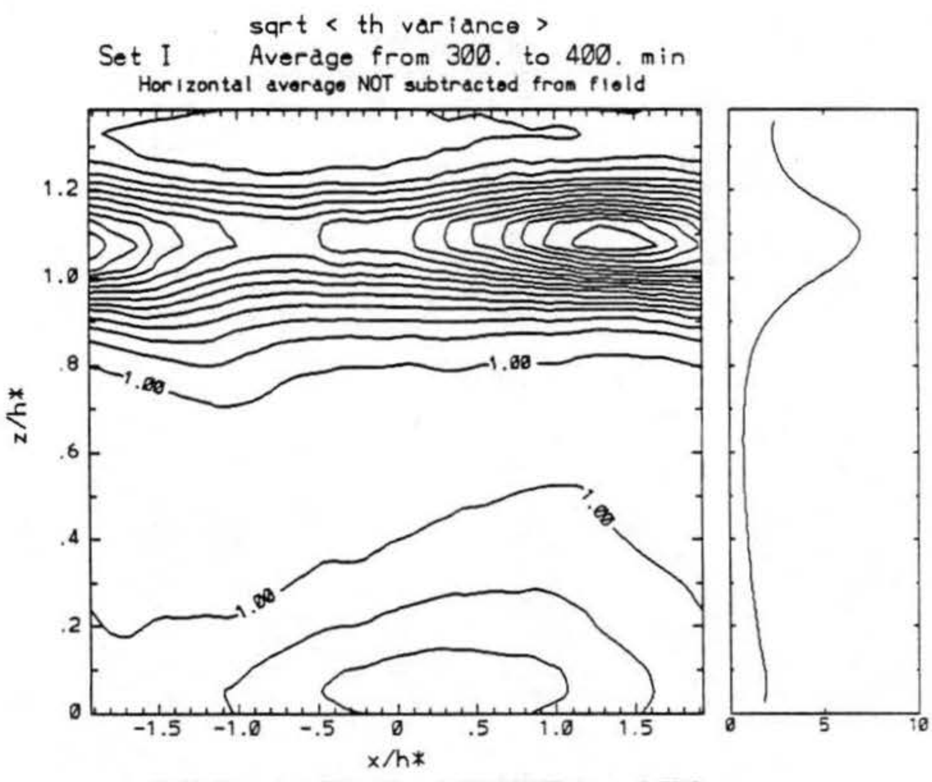

Figure 4.36 (continued).

Continued.

(f)

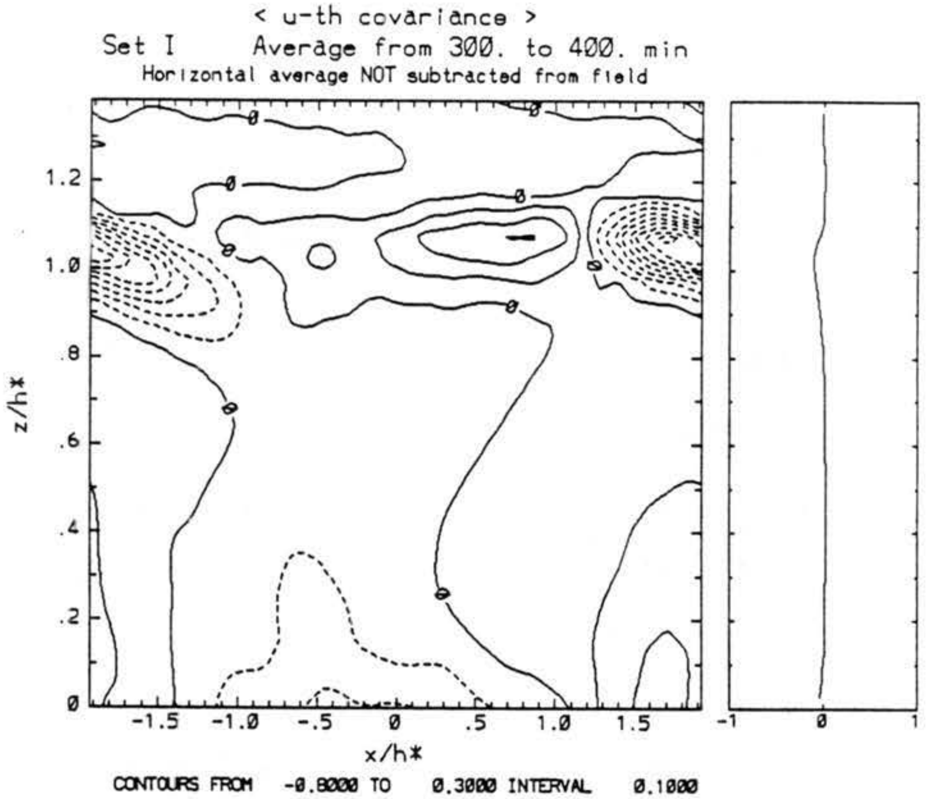

(g)

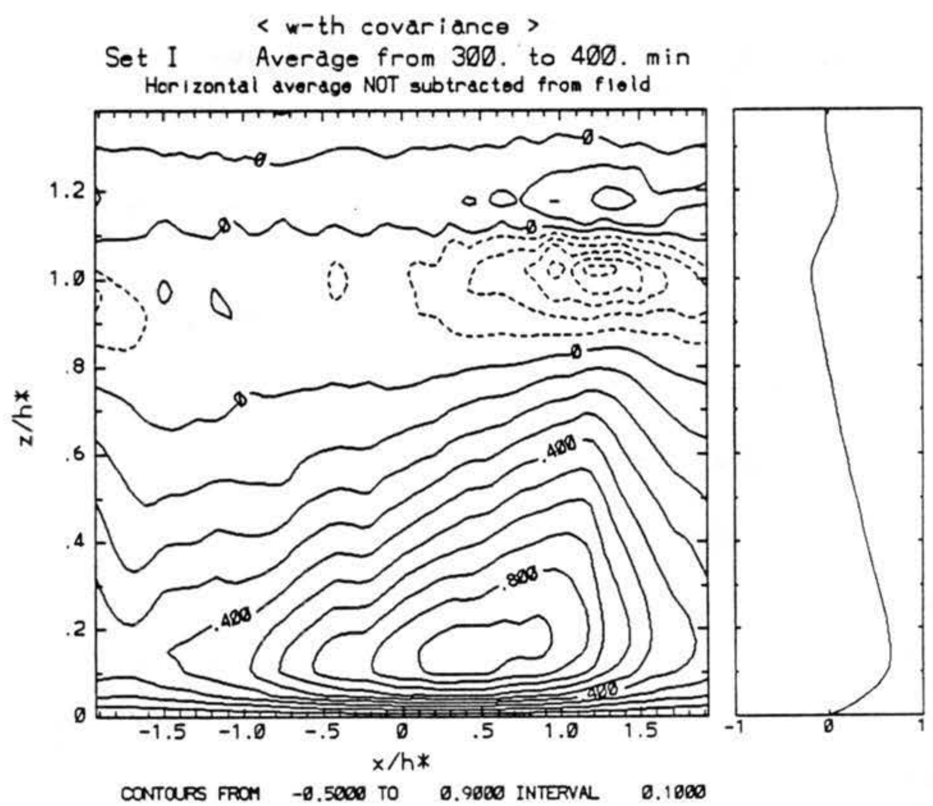

Figure 4.36 (continued).

- The w variance field shows evidence of vertically coherent modulation at a horizontal wavelength of $4\Delta x$. This feature is presumably related in some way to the $2\Delta x$ structure that has been observed in the $\langle w' \rangle_{p,t}$ field.

- In the u variance there is a broad surface maximum, more or less below the maximum in w/θ covariance, with a pronounced peak at its right-hand end at the base of the updraught.

- There are definite maxima in u variance and v variance near the inversion. The v-variance maximum is at the position of maximum entrainment. The u-variance maximum is tongue-shaped and extends downstream from the maximum-entrainment region.

- The u/w covariance has a pair of well-defined maxima and minima in the middle of the boundary layer, positioned about $0.1\lambda_p = 0.4h_*$ downstream of the mimima and maxima in the vertical gradient in $\langle u' \rangle_{p,t}$ (Figure 4.34a). (Note that the vertical exaggeration in the figures tends to mask the fact that the vertical shear is typically much larger than the horizontal shear in the circulation.)

- The u/θ covariance near the inversion has a maximum to the left of the $\langle \theta' \rangle_{p,t}$ minimum (Figure 4.34c) and a minimum to the right. The marked difference between the magnitudes of the maximum and minimum covariances reflects an asymmetry in the horizontal temperature gradients.

4.7.5 *Horizontal-average statistics*

Figure 4.37 shows the velocity variance profiles for Set I (c.f. Figures 4.12, 4.22 and 4.30, also Figure 3.4 for Run A). Again the u variance is greater than the v variance in the upper and lower boundary layer, with the difference being comparable to what was seen in Set F and smaller than was seen with Set H. Other differences from the horizontally homogenous simulations are as follows:

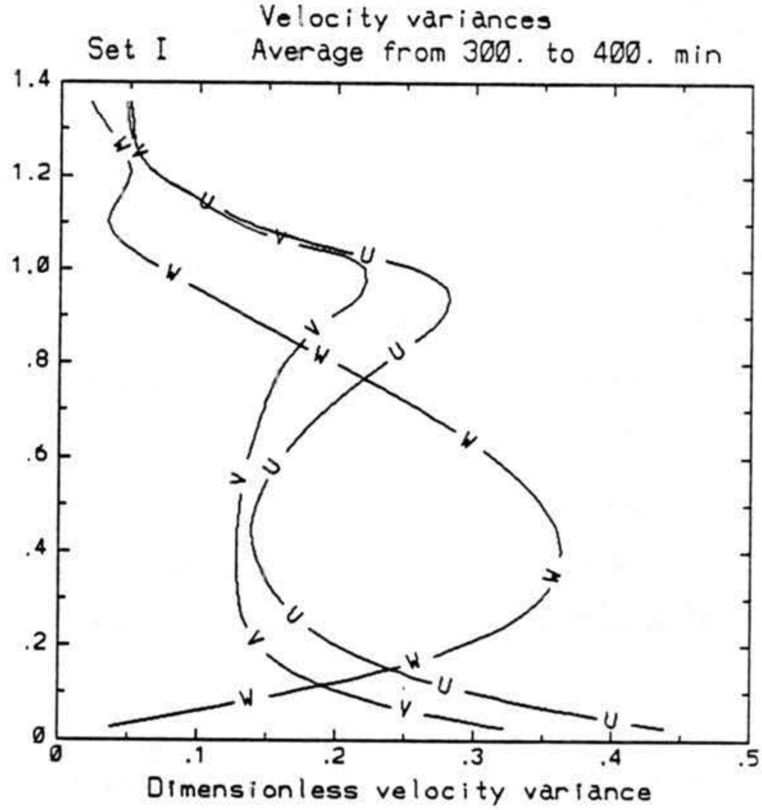

Figure 4.37. Profiles of dimensionless velocity variances $\langle u_i'^2 \rangle_{h,t}$ for Set I.

- The magnitude of the maximum in w variance is reduced from $0.40w_*^2$ to $0.36w_*^2$.
- The temperature variance increases at all levels (e.g. from $3.3\,\theta_*^2$ to $4.7\,\theta_*^2$ at $z = 0.1h_*$, from $0.7\,\theta_*^2$ to $0.9\,\theta_*^2$ at $z = 0.5h_*$, from $3.0\,\theta_*^2$ to $4.2\,\theta_*^2$ at $z = 0.9h_*$).
- The standard deviation of pressure increases at all levels (e.g. from $0.24\,\pi_*$ to $0.28\,\pi_*$ at $z = 0.1h_*$, from $0.19\,\pi_*$ to $0.22\,\pi_*$ at $z = 0.5h_*$, from $0.19\,\pi_*$ to $0.26\,\pi_*$ at $z = 0.9h_*$).

The latter two effects are similar in direction to what was observed in Set H, however a number of quanities that were significantly different from the horizontally homogeneous values in Set H are *not* different in the present case, including the height of the maximum in w variance, the height of the zero-crossing in temperature gradient, the magnitude of the minimum in heat flux, and the height and magnitude of the maximum in $\langle w'^3 \rangle_{h,t}/2$.

Figure 4.38 shows the mid-boundary-layer x- and y-spectra of w for Runs I1 and I2 (c.f. Figures 4.14, 4.23 and 4.31). The x-spectral density at $\lambda = 4500\,\mathrm{m}$ ($kh_* = 1.6$) is increased by a factor of 1.8 over the y-spectral density. At wavelengths of $\lambda = \lambda_p/2$ ($kh_* = 3.2$) and shorter the difference is reversed. As in Set G there is evidence of the y-spectra exceeding the x-spectra above $kh_* = 20$ owing to numerical dispersion.

4.7.6 *Cross sections*

Figure 4.39 shows horizontal cross-sections of w' at $z = 0.25h_*$ in Run I1 at two times: $t = 300\,\mathrm{min}$ and $t = 400\,\mathrm{min}$. In this simulation the surface heat-flux maximum is at $x = 0$ and the minimum is at $x = \pm\lambda_p/2 = \pm 2.25\,\mathrm{km}$. At $t = 300\,\mathrm{min}$ there is an updraught aligned parallel to the y-axis along $x = 2\,\mathrm{km}$, which is approximately the position of the updraught in the time-averaged circulation. There are also other updraughts, approximately three across the domain, aligned parallel to the x-axis. The structure resembles what was seen in Set H, but with the major updraught moved well downstream and not so dominant. At $t = 400\,\mathrm{min}$ upward motion still predominates near $x = 2\,\mathrm{km}$, but the organisation is less regular, not obviously different from a horizontally homogeneous simulation.

(a)

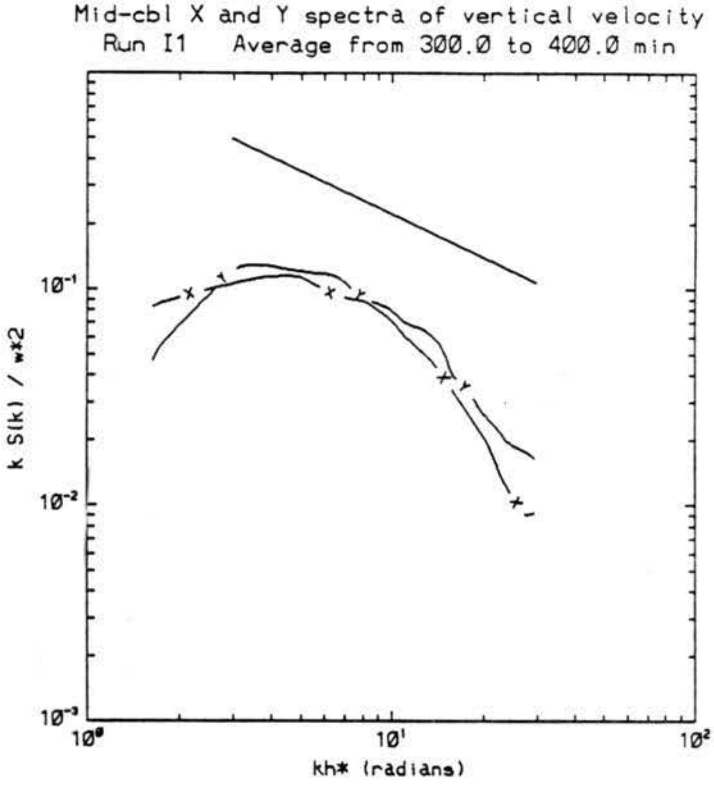

(b)

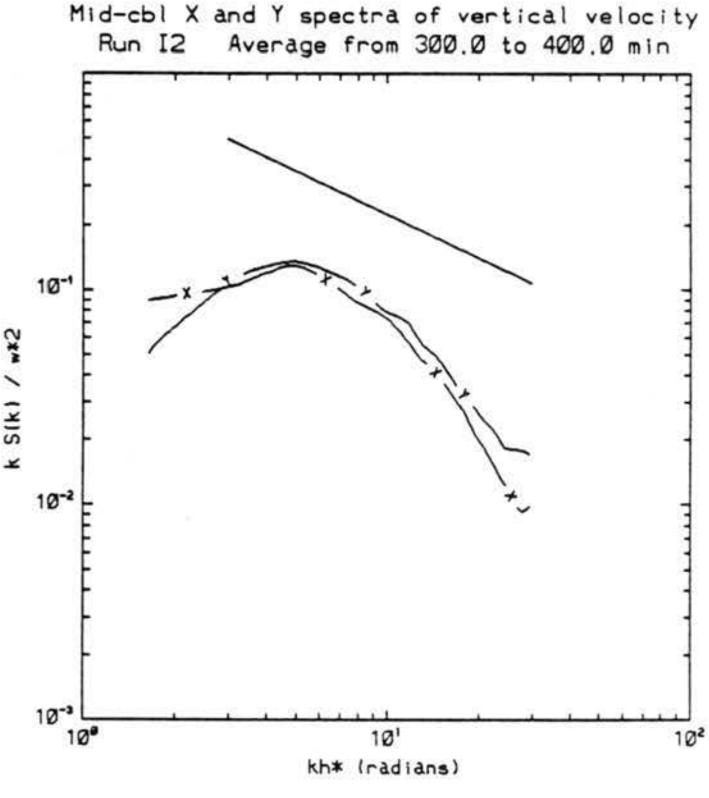

Figure 4.38. Dimensionless mid-boundary-layer spectra of vertical velocity in the x (—X—) and y (—Y—) directions for (a) Run I1 and (b) Run I2.

(a)

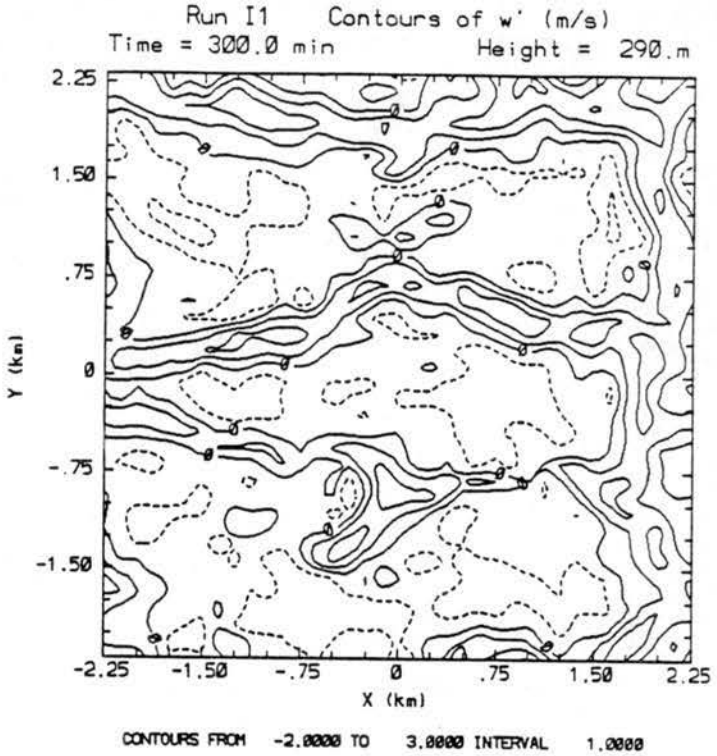

(b)

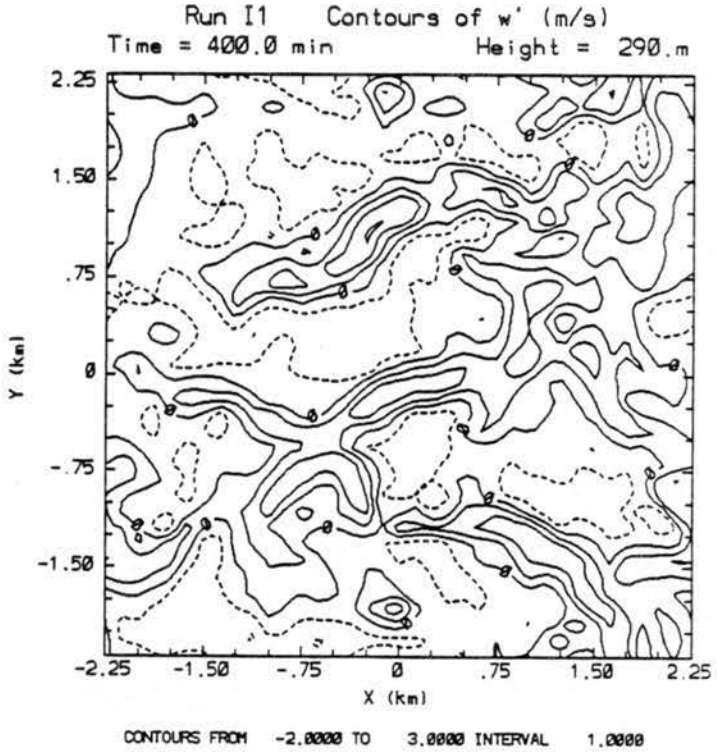

Figure 4.39. Cross-sections of w' at $z = 0.25h_*$ from Run I1. The times are (a) $t = 300$ min and (b) $t = 400$ min. Contour interval $1.0\,\mathrm{m\,s^{-1}}$.

4.8 Simulations with $\lambda_p = 4500\,\mathrm{m}$ and $u_0 = 2\,\mathrm{m\,s^{-1}}$

The simulations with $\lambda_p = 4500\,\mathrm{m}$ and $u_0 = 2\,\mathrm{m\,s^{-1}}$ are Runs J1 and J2, and the pair is labelled Set J. The E_c versus t curve is not shown—it is intermediate in character between those from Set G and Set I. Time-averages for the period from $t = 300\,\mathrm{min}$ to $t = 400\,\mathrm{min}$ are examined below.

4.8.1 *Scaling parameters*

As in Run I, $h_* = 1170\,\mathrm{m}$, and the following dimensionless numbers can be calculated:

$$\frac{\lambda_p}{h_*} = 3.85 \quad \text{and} \quad \frac{u_0 h_*}{w_* \lambda_p} = 0.26.$$

The boundary layer depth does not vary significantly in the horizontal.

4.8.2 *The time-averaged circulation*

Figure 4.40 shows $\langle u \rangle_{p,t}$, $\langle w \rangle_{p,t}$ and $\langle \theta \rangle_{p,t}$ for Set J (c.f. Figures 4.7, 4.19, 4.26 and 4.34), and Figure 4.41 shows $\langle \pi \rangle_{p,t}$, $\langle \pi_b \rangle_{p,t}$ and $\langle \pi_t \rangle_{p,t}$ (c.f. Figures 4.8, 4.20, 4.27 and 4.35). Compared with Set I, the maximum in $\langle w' \rangle_{p,t}$ is moved downstream (but not very far!), from $\hat{x} = 1.4h_* = 0.36\lambda_p$ to $\hat{x} = 1.7h_* = 0.43\lambda_p$, and reduced in magnitude by a factor of more than 3. The amplitude of the temperature perturbations in the middle of the boundary layer is also reduced, from something in excess of $0.5\,\theta_*$ in Set I to something less than $0.5\,\theta_*$ in Set J (the contour interval is too large to show the perturbations in this region, but if it were much smaller the lines would be too crowded in the stable region). The sloping contour lines above $z = h_*$—which have been interpreted before as a sign of a stationary gravity wave—are now more pronounced. The gravity wave is found to support a negative momentum flux and a positive energy flux, given by

$$\begin{aligned} \left\langle \langle w' \rangle_{p,t} \langle u' \rangle_{p,t} \right\rangle_h &\approx -0.001 w_*^2 \\ \theta_0 \left\langle \langle w' \rangle_{p,t} \langle \pi_b' \rangle_{p,t} \right\rangle_h &\approx 0.0007 w_*^3 . \end{aligned}$$

The absorbing layer is thus a source for horizontal-average momentum and a sink for circulation kinetic energy. The momentum flux is 0.17 times the surface drag. The

(a)

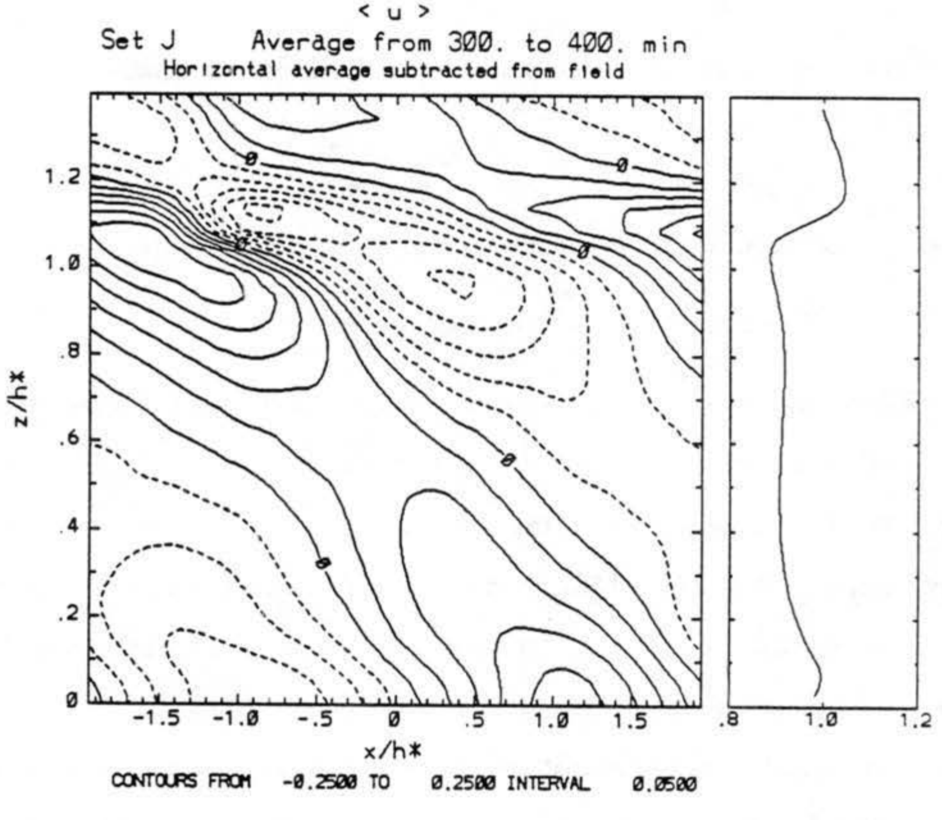

Figure 4.40. Phase-time averaged velocity and potential temperature fields for Set J.

(a) u (contour interval $0.05w_*$)

(b) w (contour interval $0.02w_*$)

(c) θ (contour interval $0.5\,\theta_*$)

Continued on following page.

(b)

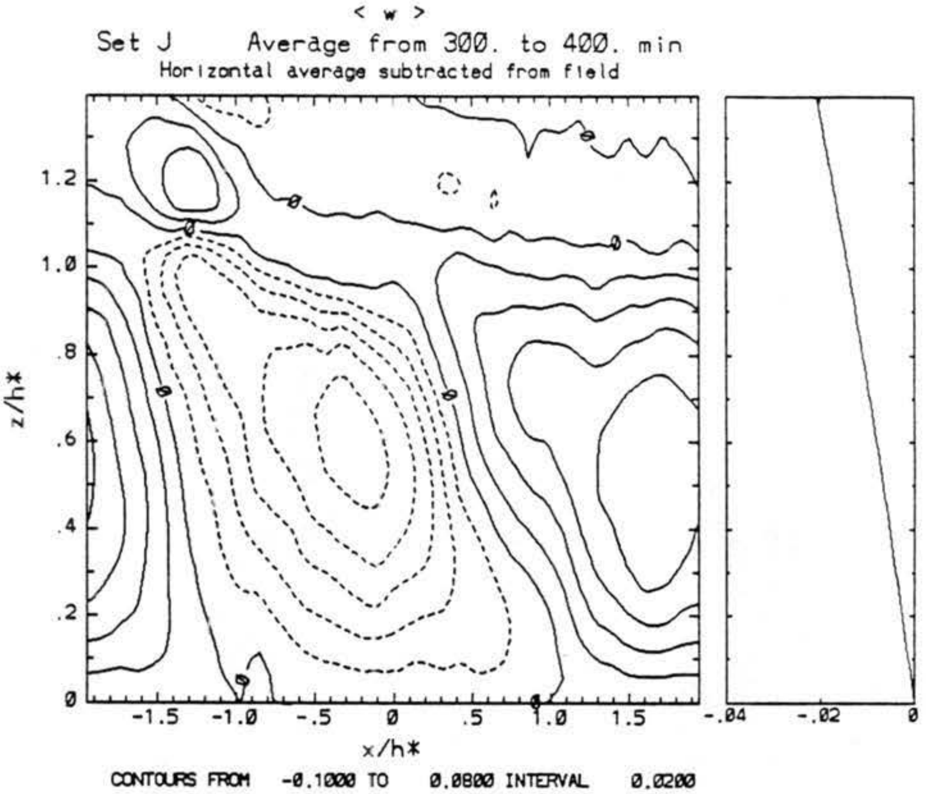

(c)

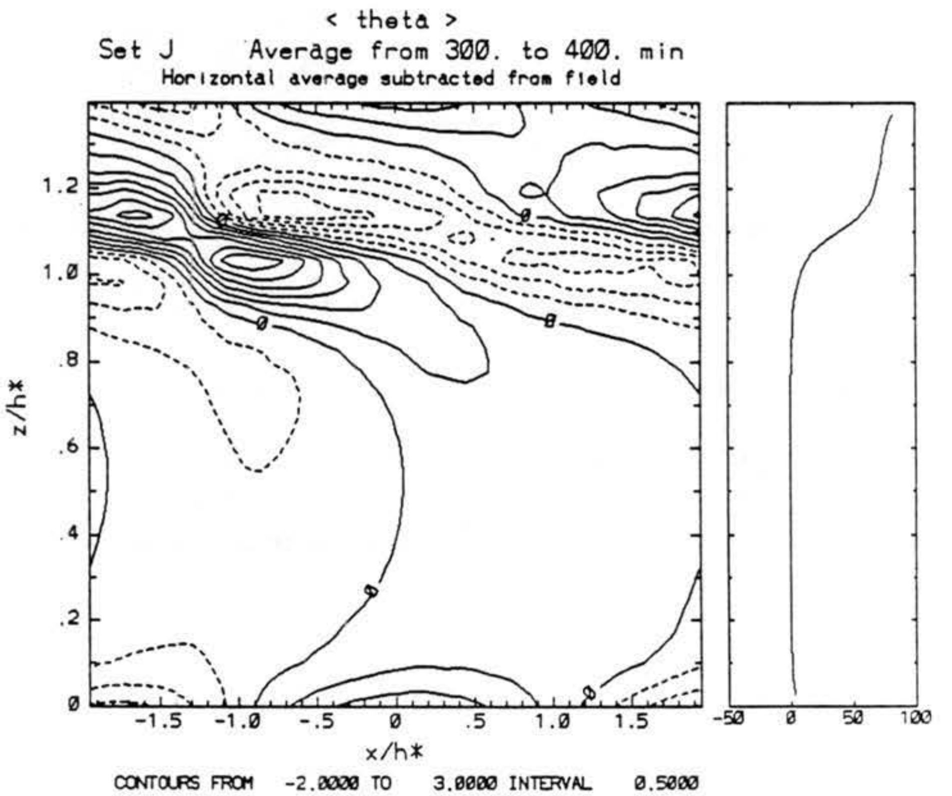

Figure 4.40 (continued).

(a)

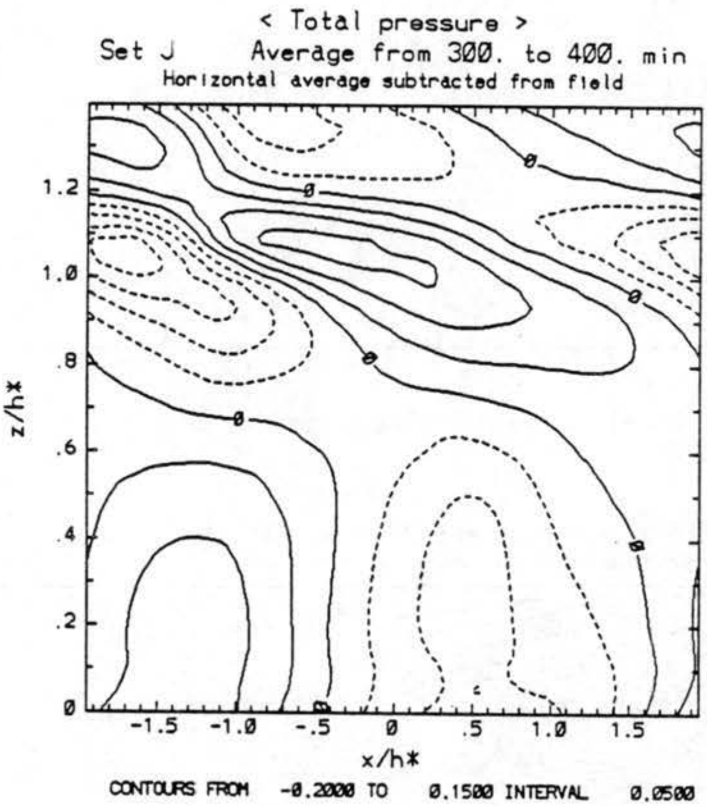

Figure 4.41. Phase-time averaged pressure fields for Set J.

(a) total pressure π (contour interval $0.05\pi_*$)

(b) buoyancy pressure π_b (contour interval $0.05\pi_*$)

(c) turbulence pressure π_t (contour interval $0.02\pi_*$)

Continued on following pages.

(b)

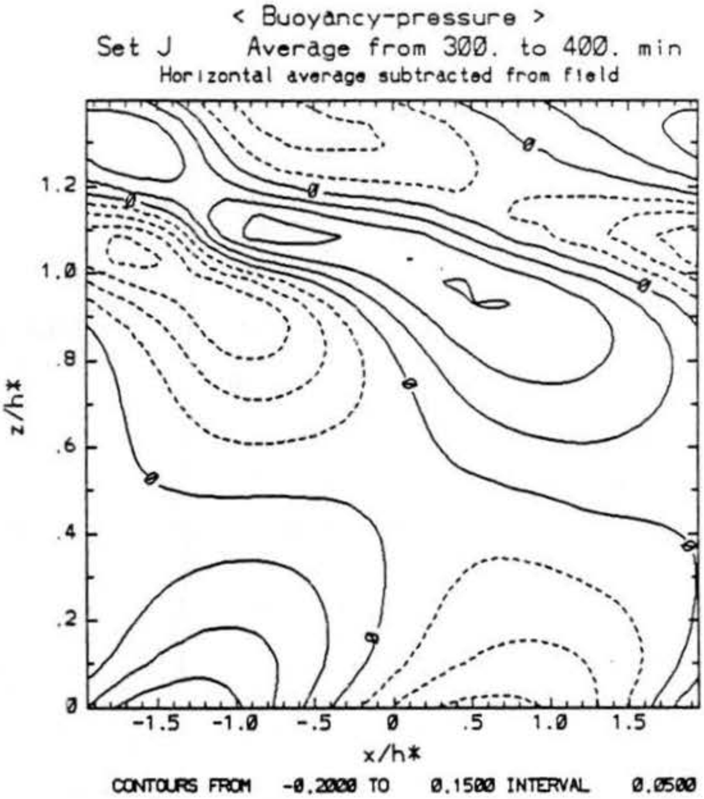

(c)

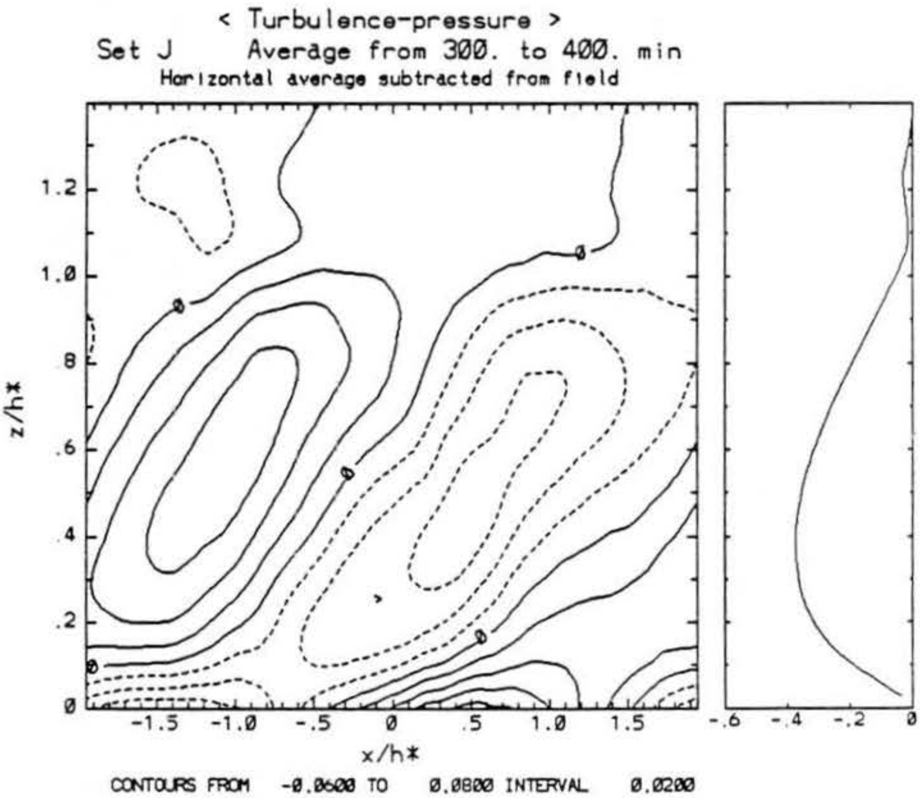

Figure 4.41 (continued).

energy flux is about one order of magnitude less than the total gravity-wave energy flux $\theta_0\langle w'\pi_b'\rangle_{h,t}$, of $0.005w_*^3$ (Section 3.3.1); its significance in the circulation kinetic energy budget will be discussed in Section 5.2.

Table 4.7 presents comparable information to Tables 4.3, 4.4, 4.5 and 4.6. Note that ratio number 5 is not very meaningful at $z=0.2h_*$ because that height is very near a zero crossing in $\langle\langle w'\rangle_{p,t}\langle\theta'\rangle_{p,t}\rangle_h$ (see Section 5.2). Otherwise ratios 1 to 7 are of the order of a few percent, but—as with Set I—generally larger for the moments of u and π. Ratios 8 and 9 have similar values to Set I.

4.8.3 *Turbulence: deviations from the time-averaged circulation*

Figure 4.42 shows the turbulence second moments for Set J (c.f. Figures 4.10, 4.21, 4.29 and 4.36). The fields resemble those from Set I (same λ_p, $u_0 = 1\,\mathrm{m\,s^{-1}}$) in many respects, but there are notable differences, the most surprising of which is that many of the features in the fields are now found further *upstream* despite the larger u_0. For example:

- In Set J the largest w variance is found at $\hat{x}=0.4h_*=0.09\lambda_p$ whereas with Set I it was at $\hat{x}=1.1h_*=0.28\lambda_p$.
- In Set J the surface maximum in θ variance is centred at $\hat{x}=0.1h_*=0.01\lambda_p$ and the elevated maximum is at $\hat{x}=1.2h_*=0.31\lambda_p$, whereas in Set I the surface maximum was at $\hat{x}=0.3h_*=0.08\lambda_p$ and the elevated maximum was at $\hat{x}=1.4h_*=0.36\lambda_p$.
- In Set J the low-level ($z=0.15h_*$) maximum in w/θ covariance is at $\hat{x}=0.2h_*=0.05\lambda_p$ whereas in Set I it was at $\hat{x}=0.5h_*=0.14\lambda_p$.

Another difference between the simulations is that in Set J the region of maximum entrainment is not so sharply defined, and the maxima in u variance and v variance that were near the entrainment maximum in Set I are not so pronounced. Finally, note that the height of maximum w variance in Set J is approximately constant with $\hat{x}$, at $z=0.4h_*$, whereas in Set I it varied between $z=0.3h_*$ and $z=0.5h_*$.

Table 4.7. Ratios characterising the time-averaged circulation in Set J.

No.	Ratio	Height	Value
1	$\left\langle \langle u' \rangle_{p,t}^2 \right\rangle_h / \left\langle u'^2 \right\rangle_{h,t}$	$0.1h_*$	0.06
		$0.9h_*$	0.13
2	$\left\langle \langle w' \rangle_{p,t}^2 \right\rangle_h / \left\langle w'^2 \right\rangle_{h,t}$	$0.4h_*$	0.010
3	$\left\langle \langle \theta' \rangle_{p,t}^2 \right\rangle_h / \left\langle \theta'^2 \right\rangle_{h,t}$	$0.1h_*$	0.04
		$0.9h_*$	0.07
4	$\left\langle \langle \pi' \rangle_{p,t}^2 \right\rangle_h / \left\langle \pi'^2 \right\rangle_{h,t}$	$0.1h_*$	0.09
		$0.9h_*$	0.15
5	$\left\langle \langle w' \rangle_{p,t} \langle \theta' \rangle_{p,t} \right\rangle_h / \left\langle w'\theta' \right\rangle_{h,t}$	$0.2h_*$	0.00
		$1.0h_*$	0.08
6	$\sum_i \int_Z \left\langle \langle u_i' \rangle_{p,t}^2 \right\rangle_h / \sum_i \int_Z \left\langle u_i'^2 \right\rangle_{h,t}$	–	0.029
7	$\int_Z \left\langle \langle w' \rangle_{p,t} \langle \theta' \rangle_{p,t} \right\rangle_h / \int_Z \left\langle w'\theta' \right\rangle_{h,t}$	–	0.017
8	$\int_Z \left\langle \langle u' \rangle_{p,t}^2 \right\rangle_h / \sum_i \int_Z \left\langle \langle u_i' \rangle_{p,t}^2 \right\rangle_h$	–	0.85
9	$-(\theta_0^2/g) \int_Z \left\langle \langle w' \rangle_{p,t} \frac{\partial}{\partial z} \langle \pi_b' \rangle_{p,t} \right\rangle_h / \int_Z \left\langle \langle w' \rangle_{p,t} \langle \theta' \rangle_{p,t} \right\rangle_h$	–	0.88

(a)

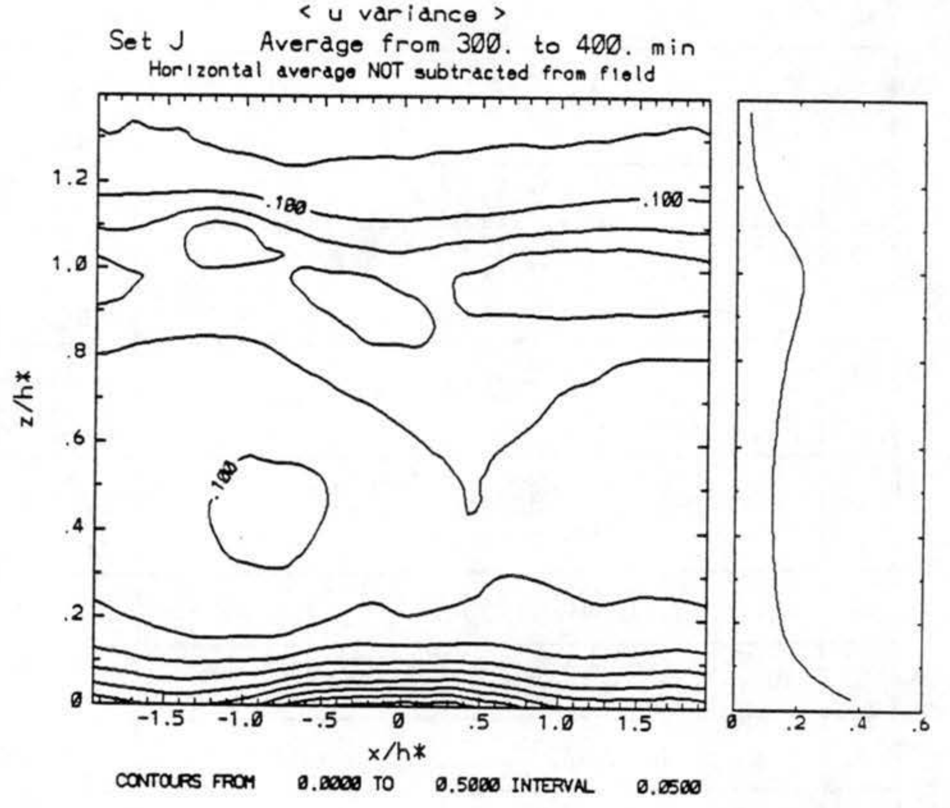

Figure 4.42. Fields of turbulent variances and covariances for Set J.

- (a) **u variance (contour interval $0.05w_*^2$)**
- (b) **v variance (contour interval $0.05w_*^2$)**
- (c) **w variance (contour interval $0.05w_*^2$)**
- (d) **u/w covariance (contour interval $0.01w_*^2$)**
- (e) **square root of θ variance (contour interval $0.5\,\theta_*$)**
- (f) **u/θ covariance (contour interval $0.1w_*\theta_*$)**
- (g) **w/θ covariance (contour interval $0.1w_*\theta_*$)**

Continued on following pages.

(b)

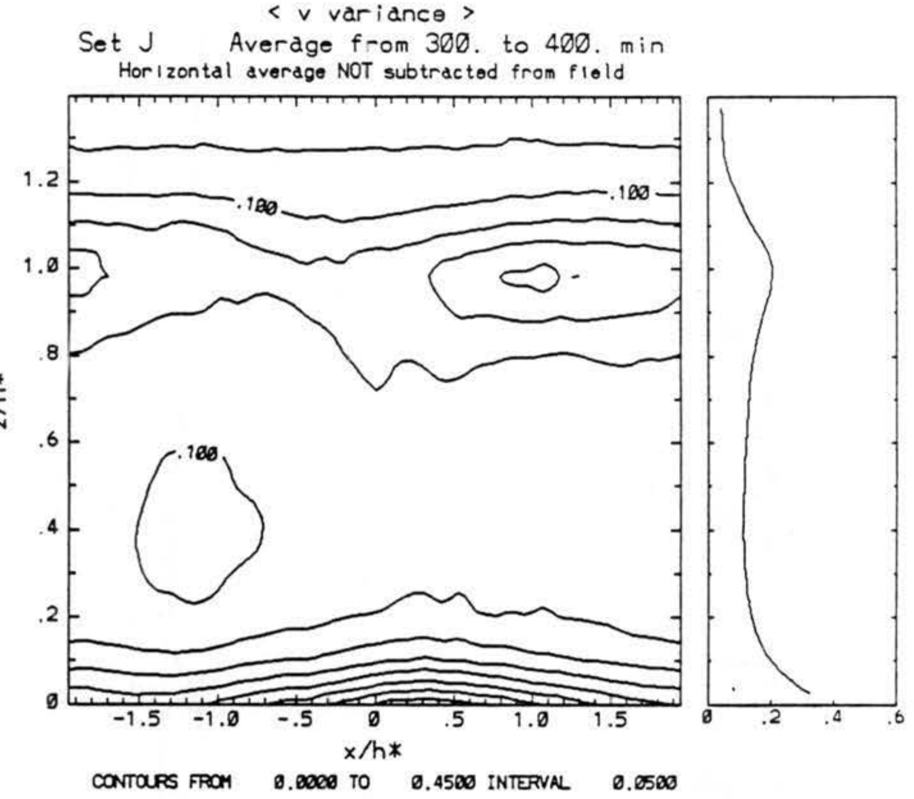

(c)

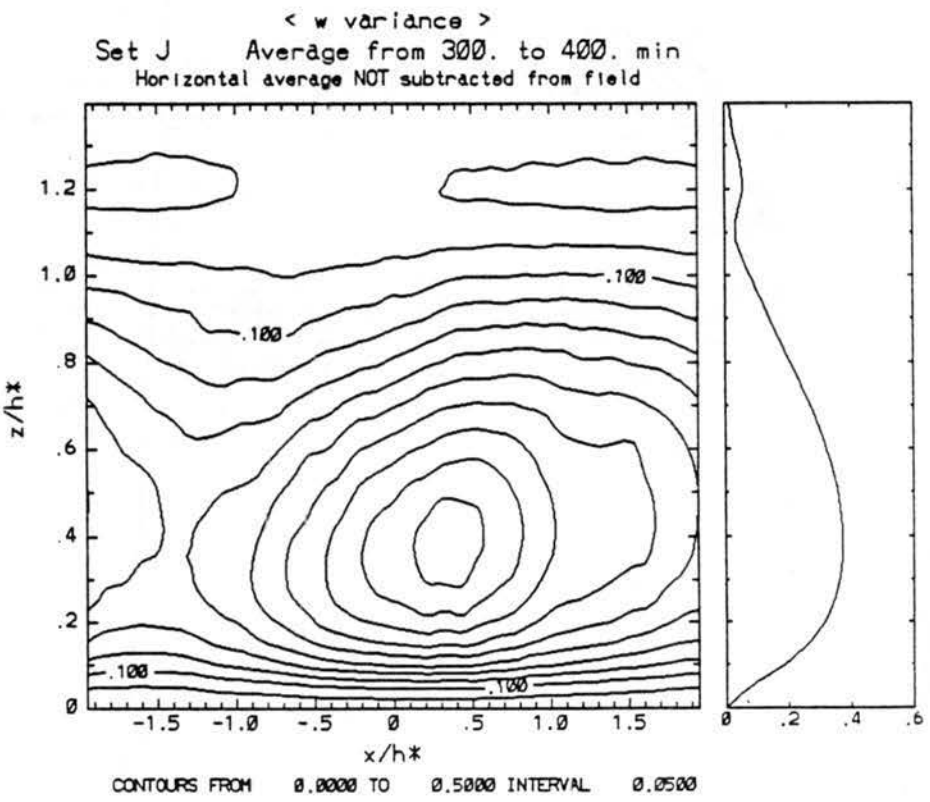

Figure 4.42 (continued).

Continued.

(d)

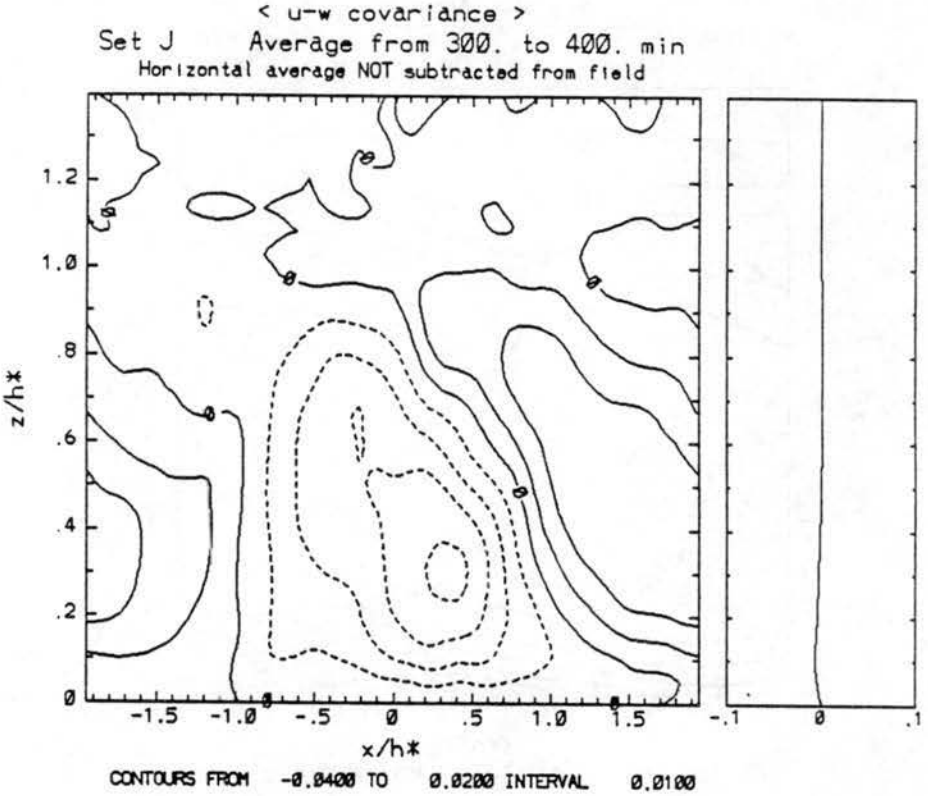

(e)

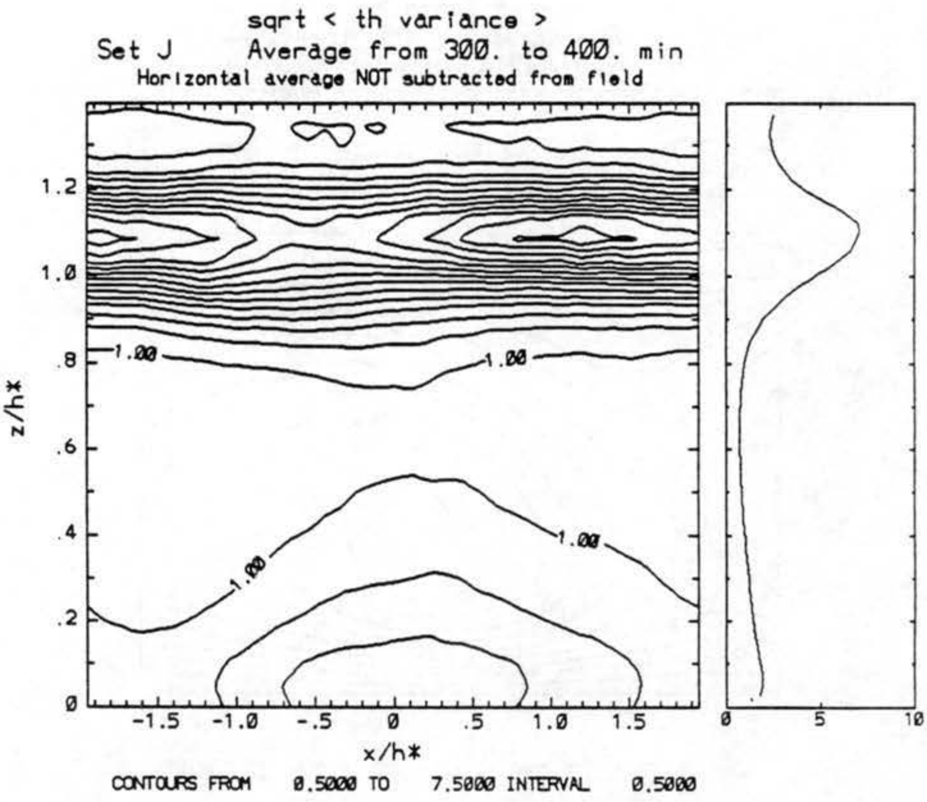

Figure 4.42 (continued).

Continued.

(f)

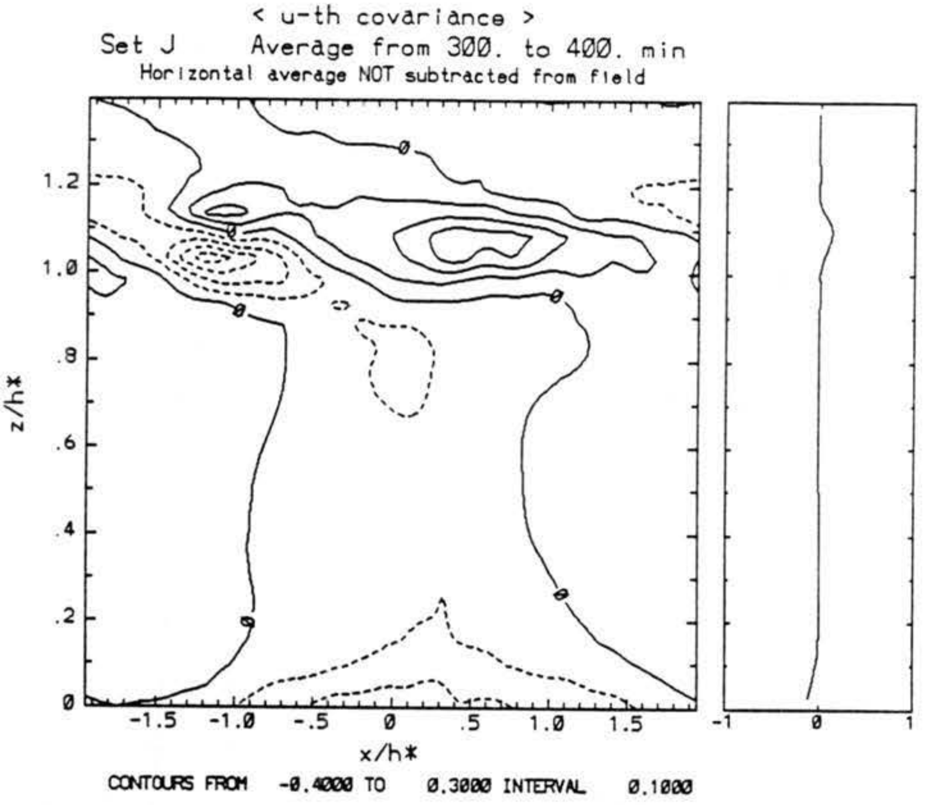

(g)

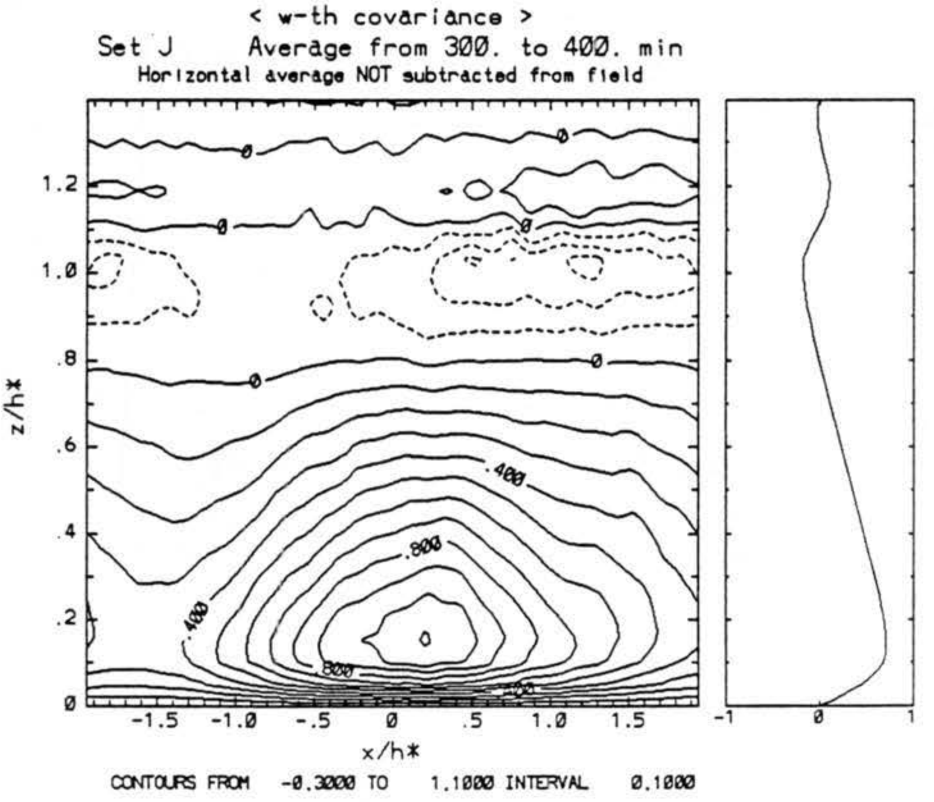

Figure 4.42 (continued).

The following explanation is proposed for the differences noted above. The crucial difference between the turbulence fields of Set I and Set J is that in the former there is a reasonably strong circulation, with maximum mean ascent (at $\hat{x}=1.4h_*=0.36\lambda_p$) well downstream of the surface heat-flux maximum. The circulation tends to increase the turbulence intensity—a deliberately vague term, but the mechanisms will be examined in Section 5.3—in the region of maximum ascent, thereby moving features like the w-variance maximum and the entrainment maximum downstream.

4.8.4 *Horizontal-average statistics*

Figure 4.43 shows the velocity variance profiles for Set J (c.f. Figures 4.12, 4.22, 4.30 and 4.37, also Figure 3.4 for Run A). As with the earlier simulations (with the exception of Set G) the u variance exceeds the v variance in the upper and lower boundary layer, with the difference being about $0.04\,w_*^2$ at $z=0.1h_*$ and $z=0.9h_*$. The differences are smaller than they were in Sets F, H and I. The differences are not statistically significant (based on a two-tailed, two-sample t test with 9 degrees of freedom, at 95% confidence), but they are likely to be real given the previous results. All the differences that were noted between Set I and the horizontally homogeneous control sample (see Section 4.7.5) are also seen in Set J, but reduced in magnitude:

- The magnitude of the maximum in w variance is reduced slightly from $0.40w_*^2$ (horizontally homogeneous) to $0.38w_*^2$.
- The temperature variance increases at all levels (from $3.3\,\theta_*^2$ to $3.6\,\theta_*^2$ at $z=0.1h_*$, from $0.7\,\theta_*^2$ to $0.8\,\theta_*^2$ at $z=0.5h_*$, from $3.0\,\theta_*^2$ to $3.9\,\theta_*^2$ at $z=0.9h_*$).
- The standard deviation of pressure increases at all levels (from $0.24\,\pi_*$ to $0.28\,\pi_*$ at $z=0.1h_*$, from $0.19\,\pi_*$ to $0.21\,\pi_*$ at $z=0.5h_*$, from $0.19\,\pi_*$ to $0.23\,\pi_*$ at $z=0.9h_*$).

Figure 4.44 shows spectra of vertical velocity for Runs J1 and J2 in the middle of the boundary layer. (c.f. Figures 4.14, 4.23, 4.31 and 4.37). There is a consistent small difference between x- and y-spectra at low wavenumbers (largest at $kh_*=3.2$, $\lambda=\lambda_p/2$).

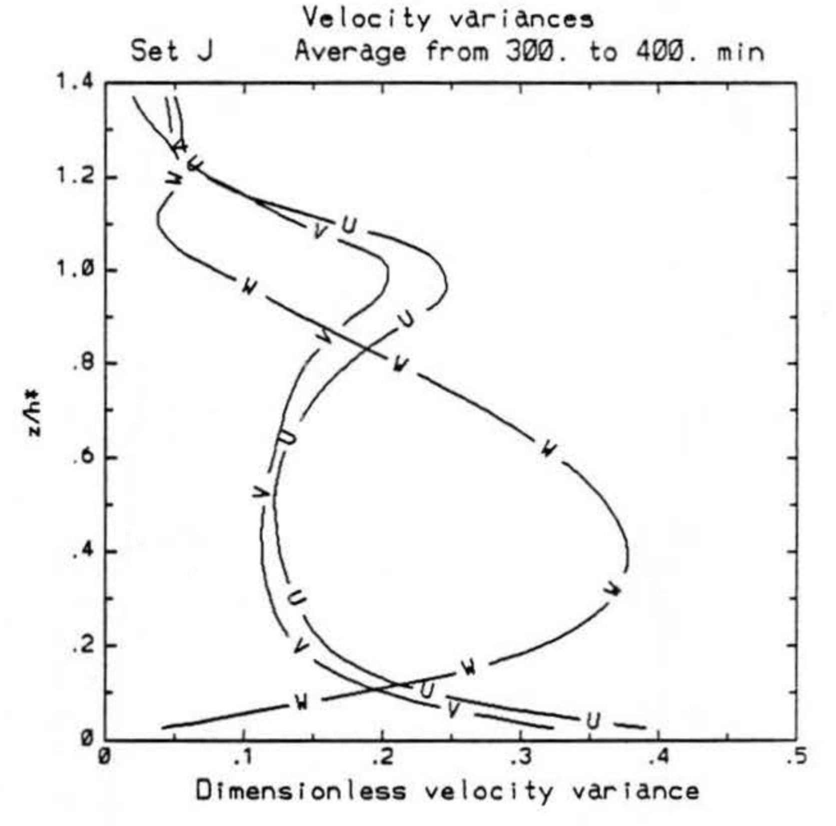

Figure 4.43. Profiles of dimensionless velocity variances $\langle u_i'^2 \rangle_{h,t}$ for Set J.

(a)

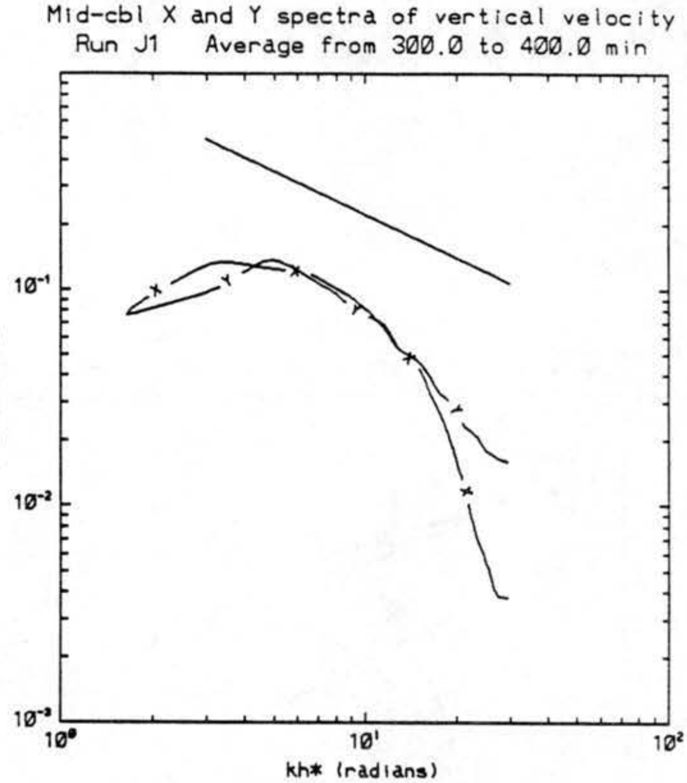

(b)

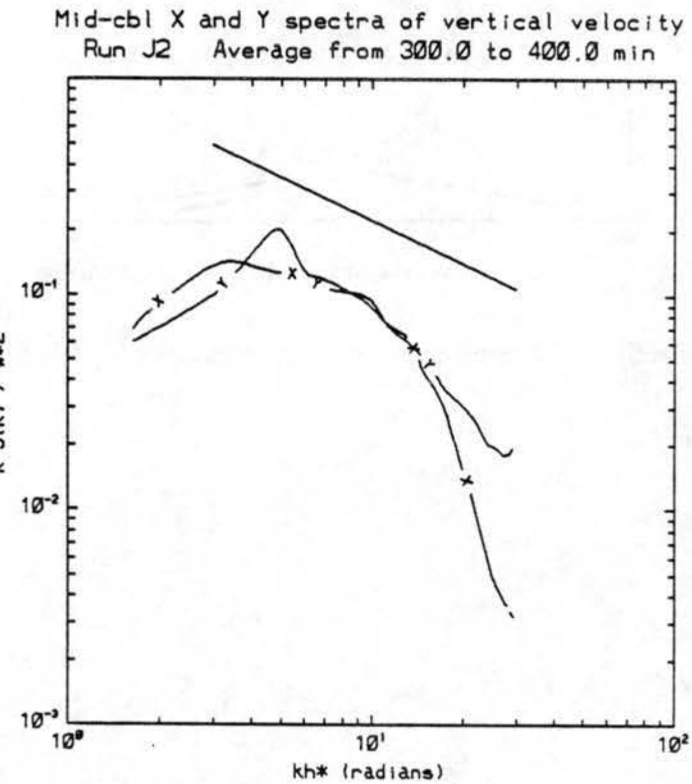

Figure 4.44. Dimensionless mid-boundary-layer spectra of vertical velocity in the x (—X—) and y (—Y—) directions for (a) Run J1 and (b) Run J2.

There is also an intriguing peak in the y-spectrum of Run J2 at $kh_* = 4.9$ ($\lambda = \lambda_p/3$). Such a peak has not been seen in any horizontally homogeneous simulations, but it is not necessarily real in an ensemble-average sense since it is much less prominent in Run J1 The pronounced difference between x- and y-spectra above $kh_* = 15$ is a result of the mean advection—it is also seen in a horizontally homogeneous simulation with the same u_0.

4.9 Discussion

The two questions posed in Chapter 1 and again at the start of the present chapter can be answered in the affirmative: spatial variations in the surface heat flux do cause changes in the structure of the simulated convective boundary layer and these changes are revealed when the boundary layer is analysed with respect to the phase average or the horizontal average.

The first case considered (Set F) is a very simple one, without the apparent complication of a mean wind and with a heat-flux perturbation having wavelength λ_p of 1500 m, a little larger than the boundary layer depth and comparable to the typical scale of the large eddies. A mean circulation is observed, with ascent over the heat-flux maxima and descent over the heat-flux minima, although its existence can be established with reasonable confidence only after considerable averaging. This amount of averaging is feasible in the large-eddy simulations because of the regularity in the imposed heat-flux perturbation and because of the ability to run the simulations several times with minor variations; it would be very difficult to achieve in the atmosphere. One reason the circulation is hard to detect is that it is "weak," in a sense that will be discussed further below. Another reason is that the lack of a mean wind allows stationary convective updraughts in random positions to appear in the phase-time averages. A further possible reason is that the large eddies may, depending on unknown details of their configuration, be sometimes much more sensitive to the surface perturbation than at other times.

Along with the circulation velocity there are variations in the buoyancy and pressure fields. These variations are all small in Set F in the sense that they account for only a few percent of the variability in the boundary layer. It will be shown in Chapter 5 that the circulation is weak in another sense: that terms in the circulation temperature and velocity budgets involving advection by the circulation are generally smaller than the turbulence terms. It will also be shown that the circulation tends to modify the circulation and turbulence fields in various ways, e.g. making the circulation updraught narrower and more vigorous than the downdraught, raising the level of maximum variance in the updraught and lowering it in the downdraught. It has been seen in the present chapter that these effects are not much in evidence in the actual fields, so this is another sense in which the circulation in Set F is weak.

Statistics of turbulent deviations from the time-averaged circulations generally vary significantly with horizontal position relative to the surface perturbation. The variations are "moderately large" in the sense that quantities like the variances in u, w and θ may be 50% larger or more over the heat-flux maxima than they are at the same height over the heat-flux minima. It is suspected that the variations are largely due to the larger w/θ covariance in the lower boundary layer over the surface heat-flux maxima. In Chapter 5 the significance of the turbulent heat fluxes in the circulation temperature budget will be examined, as will the dynamic effects of the turbulent buoyancy force on the turbulent stresses.

In the profiles of the horizontal-average statistics, the most noticeable effect of the surface heat-flux perturbation is a difference between the u and v variances, apparently related to a change in the geometry of the large eddies. The effect is much larger in two of the simulations than in the other two, which suggests that the large-eddy configuration is sometimes more sensitive to the surface perturbations than it is at other times. (A similar effect was postulated above in relation to variability in the circulations, but here there is strong evidence for it.) Of the other effects noted, the reduction in the height of the zero-crossing in potential temperature gradient and the increase in the height of maximum vertical velocity variance are consistent with the increase in the third moment of vertical velocity, which indicates more vigorous transfer of vertical velocity variance into the upper boundary layer. These effects are all small—statistically significant given the averaging available in the large-eddy model but probably undetectable in the atmosphere.

With a mean wind of only $1\,\mathrm{m\,s^{-1}}$ perpendicular to the heat-flux perturbations (Set G) all the phase-average fields are shifted downstream and the circulation velocity is reduced in amplitude and changed in shape. Although the circulation is weaker, it is no more difficult to detect because the mean wind prevents stationary large eddies from dominating the phase-time averages. It will be shown in Chapter 5 that advection by the mean wind is now comparable in magnitude to other processes in the circulation temperature and velocity budgets.

The mean wind also reduces the effects of the surface perturbations on profiles of the horizontal-average statistics. The only perceptible effect remaining is an increase in the temperature variance at low levels relative to a horizontally homogeneous simulation.

One feature that is not much reduced in magnitude by the mean wind in Set G is the horizontal variation in the turbulent w variance in the middle of the boundary layer ("turbulent" referring here to deviations from the time-averaged circulation). The maximum variance at $z = 0.4h_*$ remains about 1.5 times the minimum variance at the same level, although the maximum is shifted about $0.25\lambda_p$ downwind compared to Set F. This result suggests that horizontal variations in the turbulence statistics are more resistant to a mean wind than mean circulations.

In Set H, with a surface heat-flux perturbation with a longer wavelength ($\lambda_p = 4500\,\mathrm{m}$) and with zero mean wind, the circulation is much stronger than it is in Set F. The mean ascending motion is now concentrated in a relatively narrow (width $\sim h_*$) region surrounded by a broader region with weaker descending motion. It will be shown in Chapter 5 that advection by the circulation is significant in the circulation temperature and velocity budgets, in contrast to the shorter-wavelength simulations. The central updraught is much more turbulent than the downdraught, but it is interesting that the boundary layer depth, defined on the basis of several different criteria, does not vary by more than 1% or so in the horizontal. The instantaneous cross-sections show that the flow is dominated by a single, quasi-two-dimensional circulation, with a central updraught meandering near the axis of maximum surface heat flux. The change in large-eddy structure is also reflected in modifications to the horizontal-average statistics, including a large excess of u variance over v variance and an increase of about 50% in the third moment of w.

A mean wind of only $1\,\mathrm{m\,s^{-1}}$ (Set I) has a profound effect, despite the fact that the dimensionless horizontal velocity $(u_0 h_*)/(w_* \lambda_p)$ is apparently small at 0.13. The circulation updraught is moved downstream so that it is closer to the surface heat-flux minimum than to the heat-flux maximum, and it becomes broader and weaker. Significant horizontal modulation of the turbulence remains, and entrainment is much more vigorous near the top of the updraught than it is elsewhere. Horizontal-average statistics are again significantly different from those for a horizontally homogeneous boundary layer, but the differences are much smaller than in Set H.

When the mean wind is increased to $2\,\mathrm{m\,s^{-1}}$ (Set J) some of the expected trends are seen: the circulation becomes weaker and moves downstream (but not very far downstream), the horizontal modulation in turbulence is reduced and the profiles of horizontal-average statistics relax closer to the horizontally homogeneous profiles. One intriguing change is that the features in the turbulent variance and covariance fields are typically found further *upstream* with the stronger mean wind: this may be a consequence of the less vigorous circulation. There is now detectable transfer of energy and momentum through the stable layer by a stationary gravity wave. The energy transfer accounts for a significant fraction of the buoyancy production of circulation kinetic energy (Chapter 5) but is still an order of magnitude less than the total kinetic energy flux into the absorbing layer. Two comments are in order: The first is that the circulation may be sensitive to gravity-wave reflection above the boundary layer. (Clark *et al.*, 1986, have simulated gravity wave systems over a convective boundary layer and concluded that in some cases the organisation of the boundary-layer convection involves the full depth of the troposphere.) The second comment is that the generation of the gravity waves need not involve mechanisms any different from what occurs in a horizontally homogeneous boundary layer—presumably penetration of unsteady updraughts into the inversion—but simply requires that this process be organised spatially.

CHAPTER 5

BOUNDARY LAYER RESPONSE TO SURFACE HEAT-FLUX PERTURBATIONS: DYNAMICS

Having described the basic features of the time-averaged circulation and the deviations from it, let us now examine the processes that maintain these fields. Section 5.1 describes the budgets for the circulation potential temperature and suggests certain simplifying concepts that are investigated further in Appendix B. Section 5.2 examines the circulation velocity budgets and summarises them in terms of the profiles and vertical integrals of the circulation kinetic energy budget.[13] The effect of the turbulent stress fields arises during the course of Section 5.2, and a few of the terms that contribute to the turbulent stress budgets are then described in Section 5.3. The emphasis throughout is on using the description of *how* various tendency terms appear in the budgets to understand *why* the circulations and turbulence fields assume the forms they do, but it must be recognised that questions involving "why" are very hard to pose, let alone answer. An analysis of the state of a system does not directly explain why the system assumes a particular state or why it does not assume a substantially different state.

5.1 The circulation temperature budget

With the velocity and temperature fields decomposed as described in Equation 4.3 and with several small terms neglected (see Appendix A), the budget equation for the circulation temperature can be written

[13]The term "circulation kinetic energy" refers here to the kinetic energy of the *time-averaged* circulation, rather than kinetic energy of the *instantaneous* circulation introduced in Section 4.4.1.

$$
\begin{aligned}
\frac{\partial}{\partial t}\left\langle\theta'\right\rangle_{p,t} = & -\langle u_j\rangle_{h,t}\frac{\partial\langle\theta'\rangle_{p,t}}{\partial x_j} - \left\langle w'\right\rangle_{p,t}\frac{\partial\langle\theta\rangle_{h,t}}{\partial z} \\
& -\frac{1}{\rho_0}\frac{\partial}{\partial x_j}\Big(\rho_0\langle u_j'\rangle_{p,t}\langle\theta'\rangle_{p,t}\Big)' \\
& -\frac{1}{\rho_0}\frac{\partial}{\partial x_j}\Big\langle\rho_0(u_j')_{p,t}(\theta')_{p,t}\Big\rangle_{p,t}' - \frac{1}{\rho_0}\frac{\partial}{\partial x_j}\Big\langle\rho_0\phi_j\Big\rangle_{p,t}',
\end{aligned} \tag{5.1}
$$

where summation is implied over j. The first term on the right-hand side is horizontal-average/circulation interaction—i.e., advection *by* the horizontal average velocity *of* the circulation temperature—or "horizontal advection." The second term, circulation/horizontal-average interaction, involves vertical advection of the mean stratification. The third term is circulation/circulation interaction. The fourth is (resolved) turbulence/turbulence interaction, i.e., turbulent flux divergence, and the fifth is subgrid flux divergence. Below, the $\langle\theta'\rangle_{p,t}$ budgets for Sets F to J are described and discussed in turn.

Figure 5.1 shows several terms in the budget for Set F ($\lambda_p = 1500\,\mathrm{m}$, $u_0 = 0\,\mathrm{m\,s^{-1}}$). Horizontal advection is negligible with zero mean wind and has been omitted. Circulation/horizontal-average interaction tends to warm the base of the updraught and cool the top, with the reverse effect on the downdraught. The circulation/circulation term warms the base of the updraught *and* the base of the downdraught and cools in between; it thus tends to broaden the $\langle\theta'\rangle_{p,t}$ minimum near the surface and to narrow the $\langle\theta'\rangle_{p,t}$ maximum. These circulation terms are typically much smaller than the turbulence and subgrid tendencies. As was pointed out in Section 3.2.5, below about $z = 0.2h_*$ subgrid diffusion tends to warm and destabilise the atmosphere; the effect is much stronger over the heat-flux maximum, so the subgrid term acts to increase the temperature perturbations near the surface. The turbulence term opposes this process.

More insight into the turbulence and subgrid terms can be gained if they are combined as

$$
-\frac{1}{\rho_0}\frac{\partial}{\partial x_j}\left\langle\rho_0(u_j')_{p,t}(\theta')_{p,t} + \rho_0\phi_j\right\rangle_{p,t}'
$$

and the contributions from $j = 1$ and $j = 3$ are considered separately (Figures 5.1e and 5.1f). In the lower and middle boundary layer, vertical-flux divergence warms the air over the heat-flux maximum and horizontal-flux divergence cools it. The individual flux-divergence terms are at least as large as the other terms in the budget and it is proposed

(a)

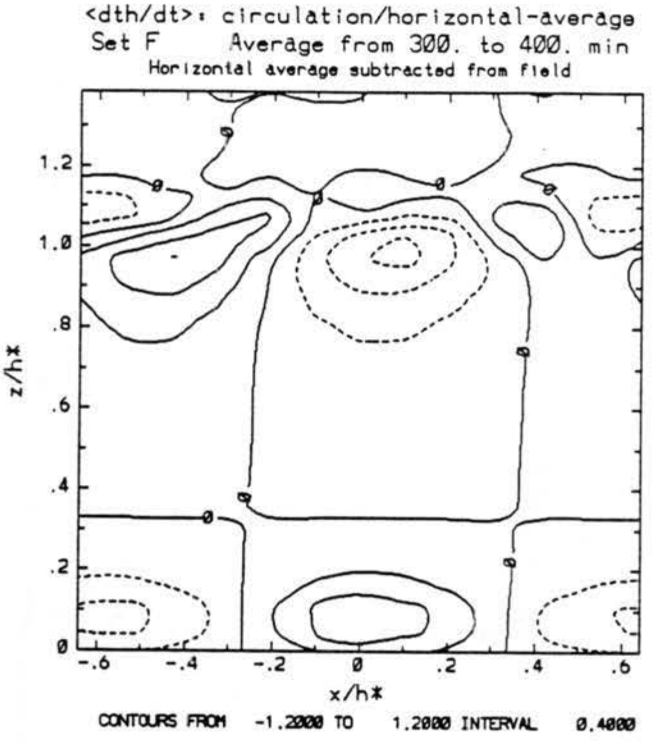

(b)

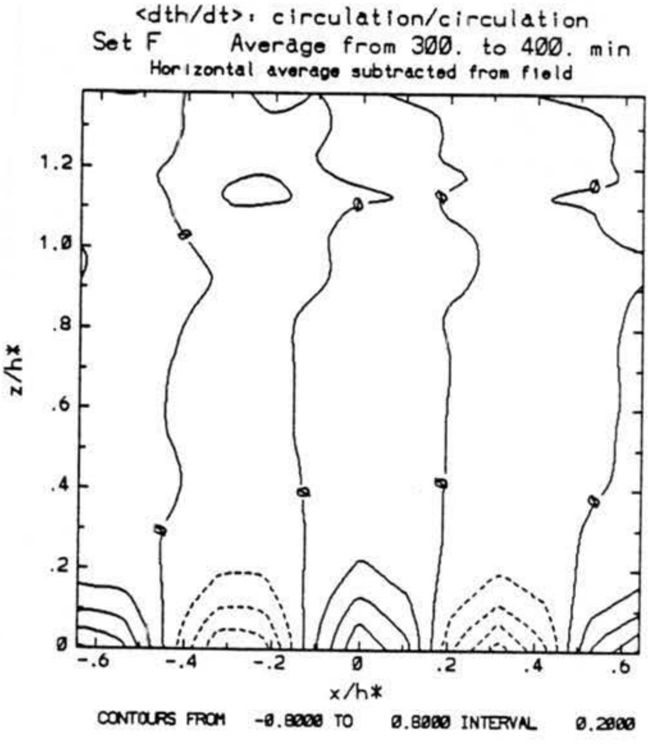

Figure 5.1. Tendencies in circulation potential temperature $\langle\theta'\rangle_{p,t}$ for Set F. (a) Circulation/horizontal-average interaction. (b) Circulation/circulation interaction. (c) Resolved turbulent flux divergence. (d) Subgrid flux divergence. (e) Horizontal-flux divergence. (f) Vertical-flux divergence. Contour interval $0.4w_*\theta_*/h_{\rho*}$ except (b) $0.2w_*\theta_*/h_{\rho*}$.

Continued on following pages.

(c)

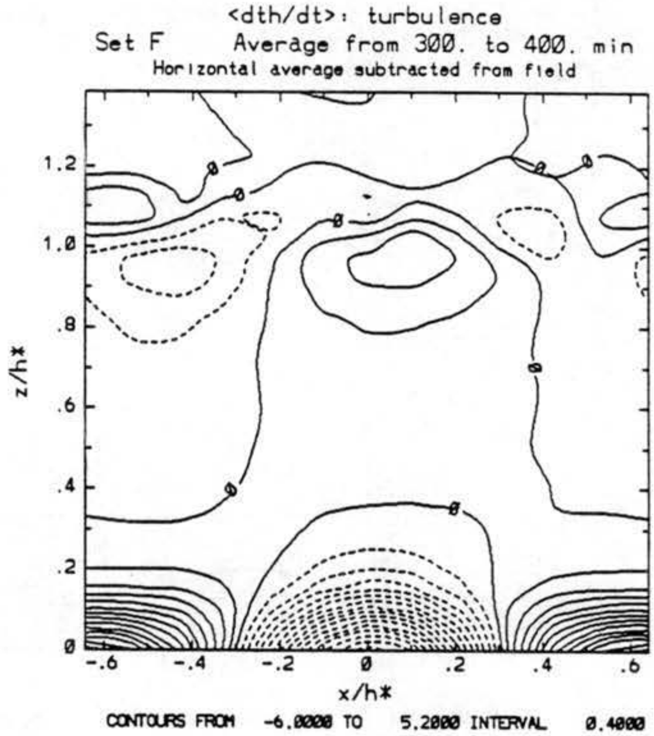

(d)

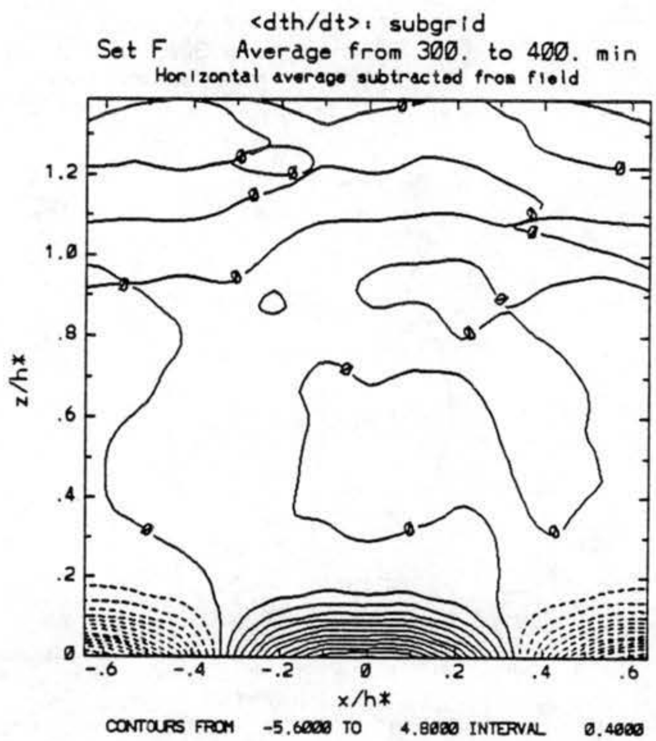

Figure 5.1 (continued).

Continued.

(e)

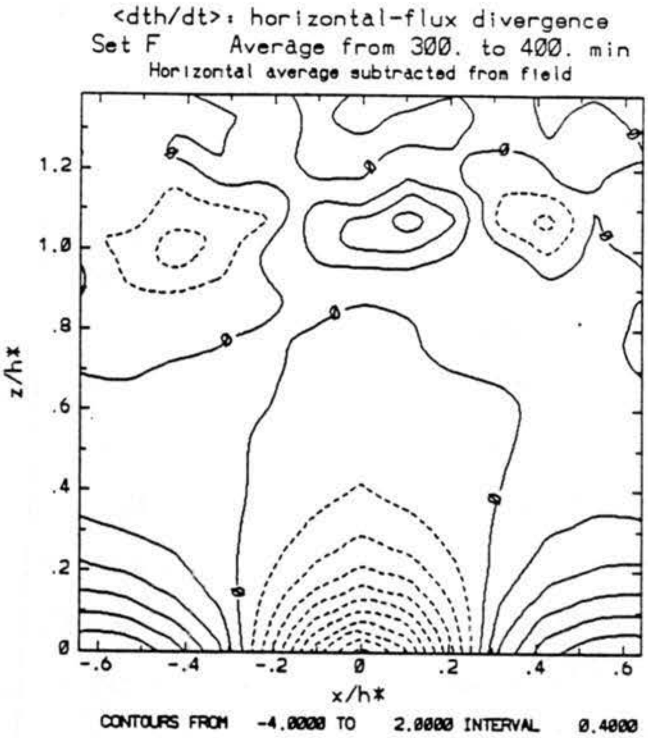

(f)

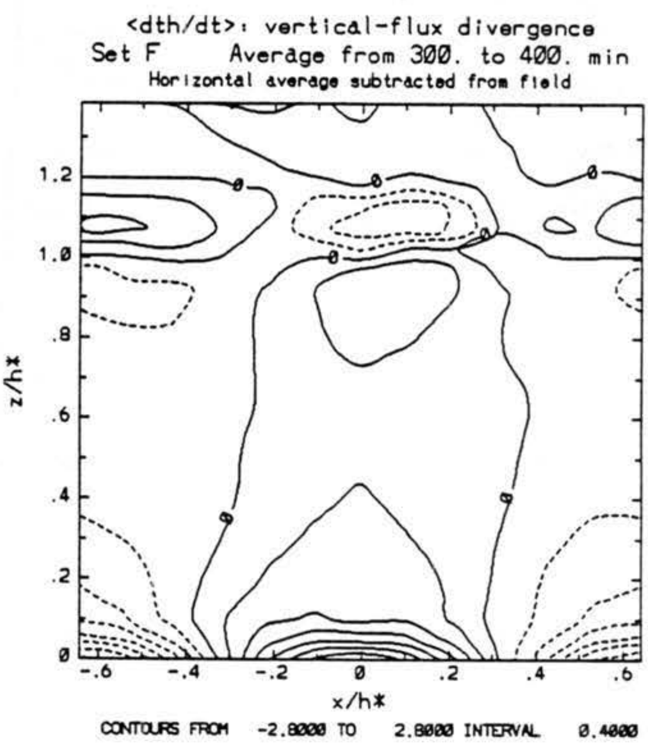

Figure 5.1 (continued).

that, to a first approximation, the temperature field can be understood in terms of the balance between them.

Consider the flux from which the flux-divergence budget term is calculated (let it be labelled f_j):

$$f_j \stackrel{\text{def}}{=} \left\langle (u_j')_{p,t}(\theta')_{p,t} + \phi_j \right\rangle'_{p,t}. \tag{5.2}$$

The components of f_j for Set F are shown in Figure 5.2. This figure resembles Figure 4.10 showing u/θ and w/θ covariances in the previous chapter, except that in Figure 5.2 the horizontal averages have been subtracted from the contoured fields and the subgrid term is included—it makes a significant contribution near the surface. The vertical component f_3 has a maximum dimensionless surface value of 0.5 and a minimum of -0.5, which is just the boundary condition imposed by the sinusoidal perturbation. In the lower boundary layer the horizontal component f_1 carries heat away from the region of maximum surface flux towards the region of minimum surface flux. Streamlines of f_j would originate at the surface near $\hat{x} = 0$ and terminate near $\hat{x} = \pm\lambda_p/2$; most of them would be concentrated near the surface where the horizontal flux is strongest.

Perhaps the relationship between the circulation temperature field and the flux can be understood in terms of a down-gradient diffusion equation? For the present this will be written as

$$f_j = -K \frac{\partial \langle \theta' \rangle_{p,t}}{\partial x_j}. \tag{5.3}$$

The temperature gradients are shown in Figure 5.3 and can be compared with the fluxes in Figure 5.2. In the horizontal component, the flux field and the gradient field are broadly similar in shape with dimensionless gradients about 10 to 15 times the dimensionless fluxes. In other words, Equation 5.3 fits the horizontal component fields with $K \approx 0.1 w_* h_*$, perhaps a little less near the surface. In the vertical the gradients are concentrated near the surface whereas the perturbations in the flux extend throughout the boundary layer, so Equation 5.3 as it stands is not satisfactory. In Appendix B a more general form of Equation 5.3 is investigated and it is shown that it is possible to describe the temperature field, and its gradients, fluxes and budget terms, reasonably well in terms of the down-gradient diffusion concept.

(a)

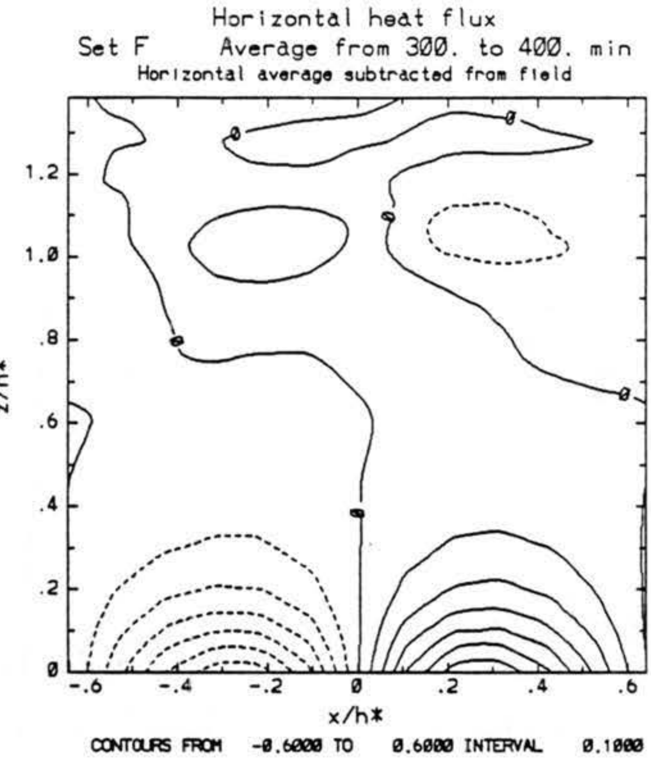

(b)

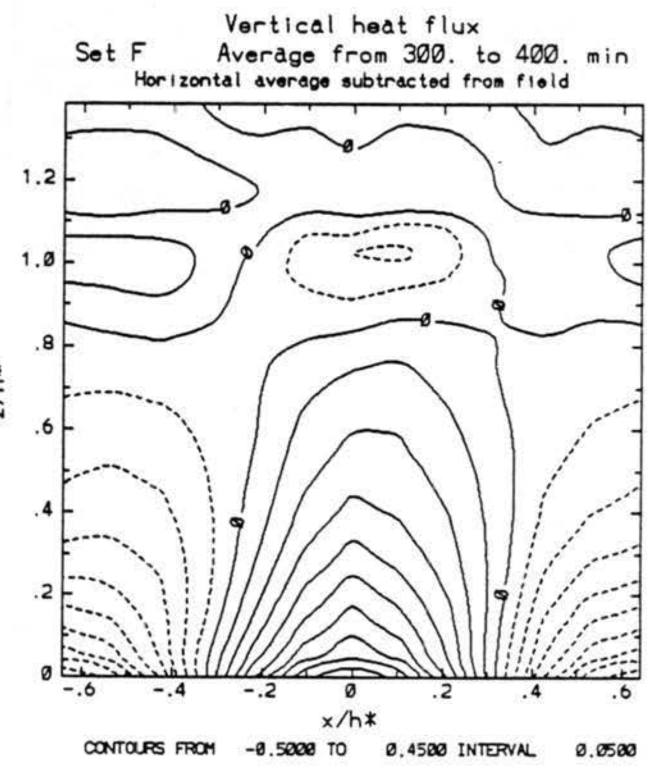

Figure 5.2. Components of the heat flux f_j for Set F. (a) Horizontal component ($j=1$), contour interval $0.1w_*\theta_*$. (b) Vertical component ($j=3$), contour interval $0.05w_*\theta_*$.

(a)

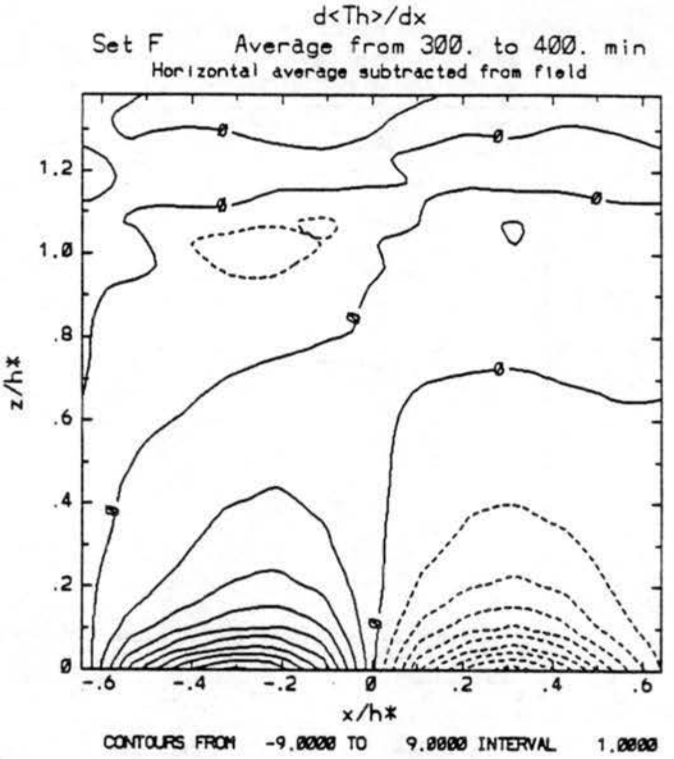

(b)

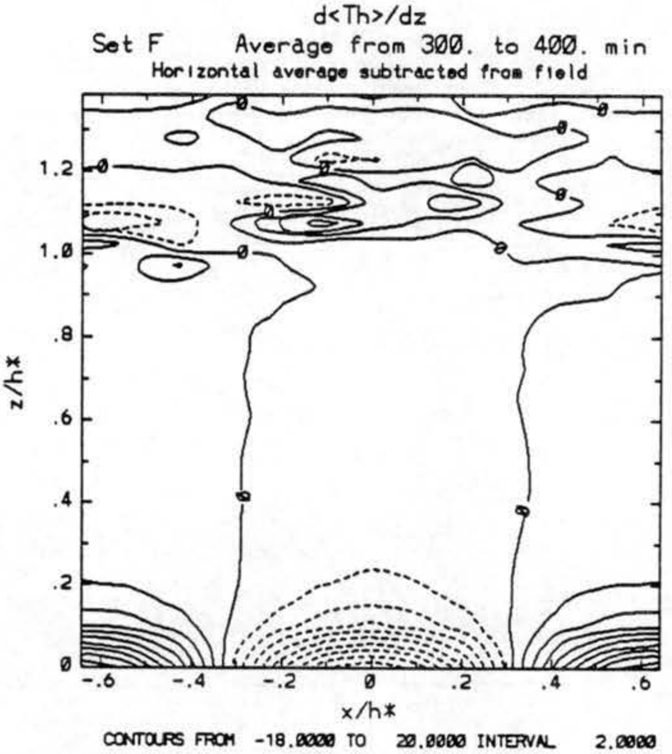

Figure 5.3. Components of the circulation potential temperature gradient $\partial\langle\theta'\rangle_{p,t}/\partial x_j$ for Set F. (a) Horizontal component ($j=1$), contour interval $1\theta_*/h_*$. (b) Vertical component ($j=3$), contour interval $2\theta_*/h_*$.

Let us now look briefly at the processes maintaining the region of negative temperature perturbation $\langle\theta'\rangle_{p,t}$ centred at $\hat{x}=0$, $z=h_*$ (Figure 4.7c). Here the salient features of the $\langle\theta'\rangle_{p,t}$ budget are a minimum in the circulation/horizontal-average term, a maximum in the horizontal-flux divergence, and a couplet in the vertical-flux divergence. Given that the minimum in the circulation/horizontal-average term coincides with the $\langle\theta'\rangle_{p,t}$ minimum, it is reasonable to assume that the latter is generated through cooling by upward motion in a region with a strongly stable temperature gradient. The horizontal heat flux is directed down-gradient into the $\langle\theta'\rangle_{p,t}$ minimum—with diffusivity implied by Figures 5.2a and 5.3a again of the order of $0.1w_*\theta_*$—and so tends to fill the minimum. The couplet in the vertical heat flux divergence is related to the minimum in vertical heat flux centred at $z=h_*$ and it tends to shift the $\langle\theta'\rangle_{p,t}$ minimum upwards.

The next case to be examined is Set G ($\lambda_p=1500\,\mathrm{m}$, $u_0=1\,\mathrm{m\,s^{-1}}$). Figure 5.4 shows various terms in the $\langle\theta'\rangle_{p,t}$ budget. They are similar in form to the terms shown for Set F in Figure 5.1, but with a few changes: First, horizontal advection was negligible with $u_0=0\,\mathrm{m\,s^{-1}}$, but is now shown. Second, the circulation/circulation term is small and has been omitted. Finally, since it has been established that the individual subgrid and turbulence terms are large and opposite near the surface, they are omitted and only their sum is shown. The component fluxes f_j are presented in Figure 5.5.

Let us look first at the lower and middle boundary layer. Here there is a balance in $\partial\langle\theta'\rangle_{p,t}/\partial t$ between horizontal advection and flux-divergence. The former is just proportional to the $\langle\theta'\rangle_{p,t}$ field displaced $\lambda_p/4$ downwind, so it follows that the latter is proportional to $\langle\theta'\rangle_{p,t}$ displaced $\lambda_p/4$ upwind. Near the surface the maximum in turbulence heating is at $\hat{x} = -0.2\lambda_p$, *upwind* of the position of maximum surface heat flux. This behaviour is a result of divergence in the vertical flux: owing to the downwind tilt of the maximum in f_3, contour lines are crowded together on the upwind side, hence the maximum heating there. It will be shown in Appendix B that such behaviour can be predicted by a simple model that includes only horizontal advection and gradient diffusion.

(a)

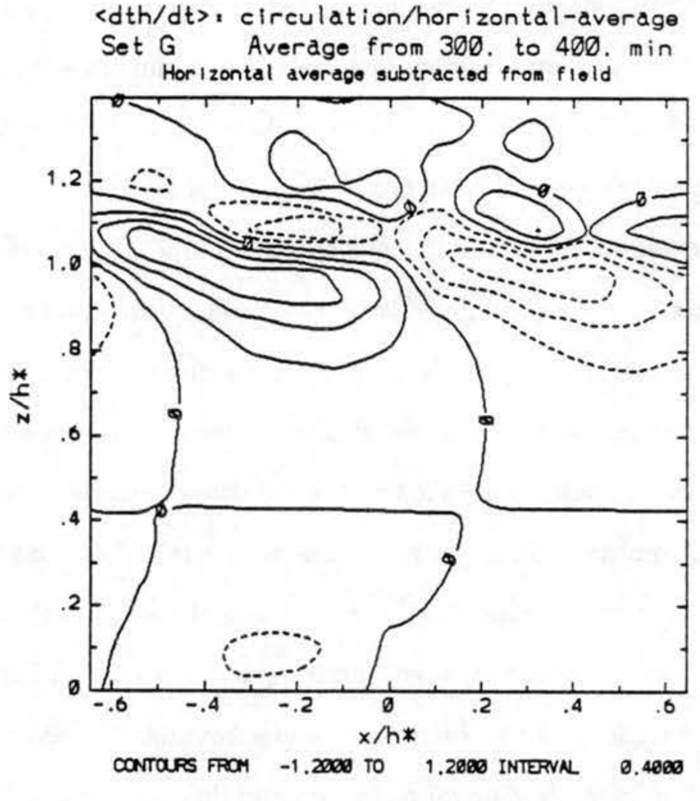

Figure 5.4. Tendencies in circulation potential temperature $\langle\theta'\rangle_{p,t}$ for Set G. (a) Circulation/horizontal-average interaction. (b) Horizontal advection. (c) Flux divergence. Contour interval $0.4w_*\theta_*/h_{\rho*}$.

Continued on following page.

(b)

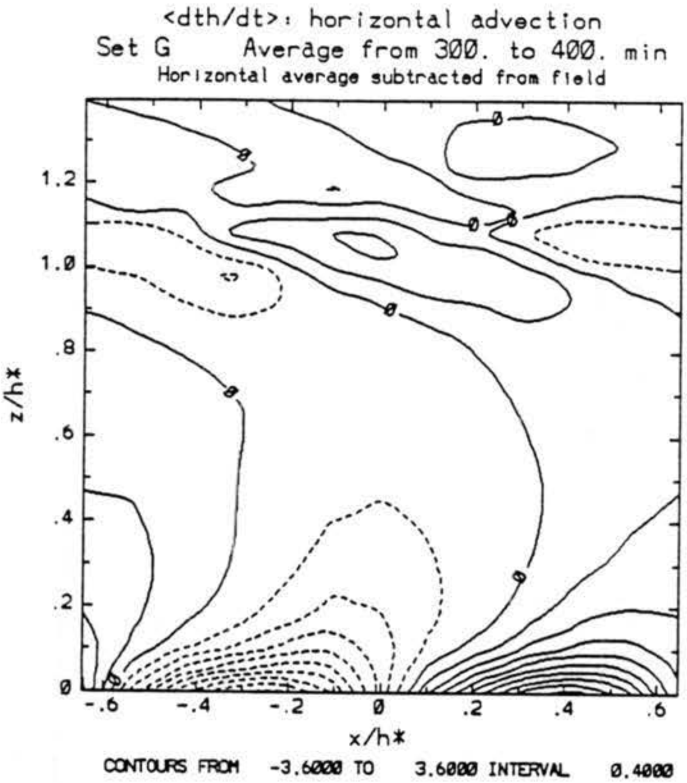

(c)

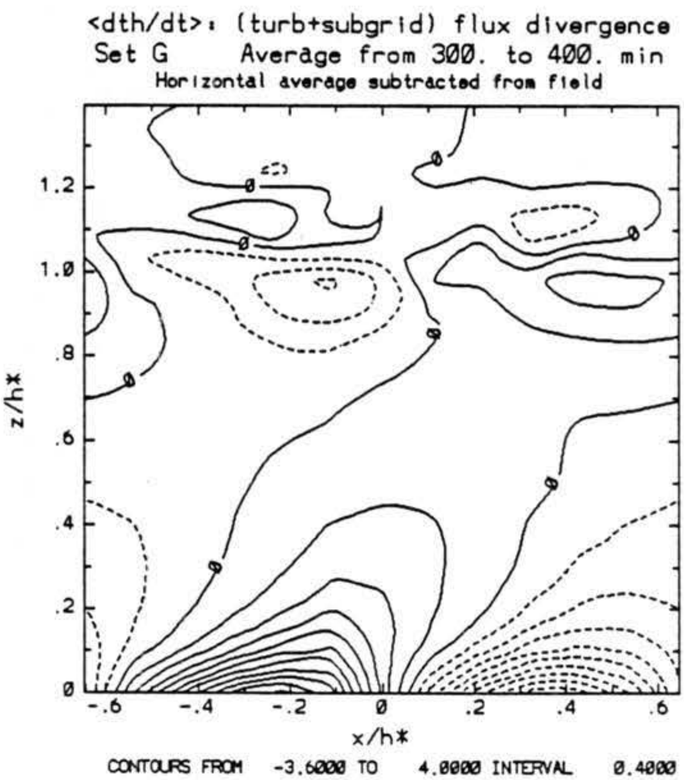

Figure 5.4 (continued).

(a)

(b)

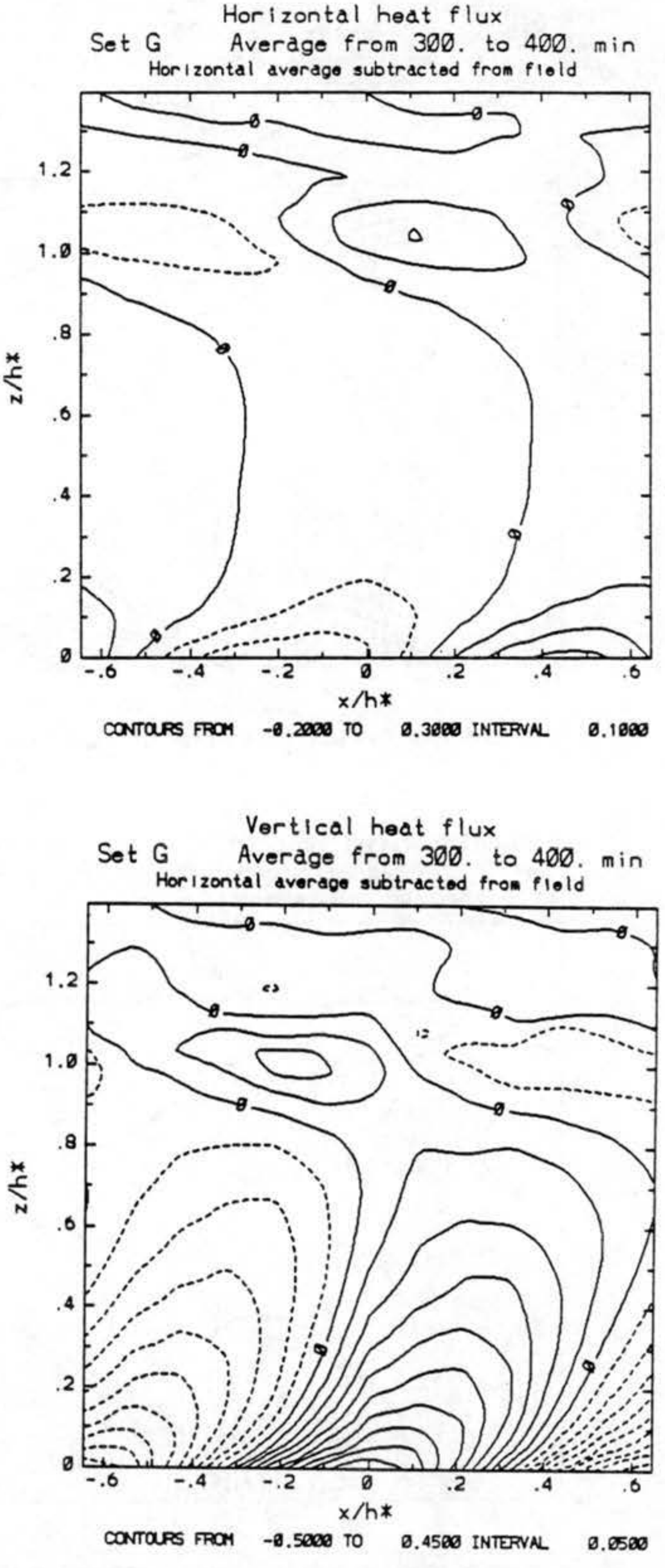

Figure 5.5. Components of the heat flux f_j for Set G. (a) Horizontal component ($j=1$), contour interval $0.1w_*\theta_*$. (b) Vertical component ($j=3$), contour interval $0.05w_*\theta_*$.

The $\langle\theta'\rangle_{p,t}$ budget in the vicinity of the inversion is quite complicated. It was argued in Section 4.5.4 that the sloping contour lines in the stable layer suggest a stationary gravity wave pattern of small amplitude. In that case the temperature perturbations would arise due to vertical deflection of streamlines, and the horizontal advection and circulation/horizontal-average terms of Equation 5.1 would balance, i.e.,

$$-\langle u_j\rangle_{h,t}\frac{\partial\langle\theta'\rangle_{p,t}}{\partial x_j}-\langle w'\rangle_{p,t}\frac{\partial\langle\theta\rangle_{h,t}}{\partial z}=0.$$

In Set G these terms are generally of opposite sign near $z=h_*$, but they do not sum to zero, since the flux-divergence term is also significant. As in Set F, the horizontal flux f_1 near the inversion is directed down-gradient and therefore tends to fill the maximum and minimum in $\langle\theta'\rangle_{p,t}$ (Figure 4.19c). The vertical flux f_3 is positive where the entrainment is at a minimum (Figure 4.21g) and negative where the entrainment is at a maximum, resulting in a pair of couplets in the vertical-flux divergence. The net flux divergence reflects the sum of these processes.

Let us now examine the $\langle\theta'\rangle_{p,t}$ budgets for the three cases with $\lambda_p=4500\,\mathrm{m}$. Figure 5.6 shows the budget for Set H ($\lambda_p=4500\,\mathrm{m}$, $u_0=0\,\mathrm{m\,s^{-1}}$) and Figure 5.7 shows the components of f_j. Whereas with $\lambda_p=1500\,\mathrm{m}$ (Sets F and G) advection by the time-averaged circulation was small or negligible, here it is significant. The circulation/horizontal-average and circulation/circulation tendencies are a reasonably straightforward consequence of the mean velocity and temperature fields, and they will not be discussed further except to note that the latter tends to focus the positive temperature perturbation at the base of the circulation updraught and to transport the perturbation into the upper boundary layer. On the axis of the mean updraught in the lower boundary layer, the flux-divergence term is negative, partly because the vertical heat flux increases with height (whereas it decreased with height at the same position in Set F) and partly because the horizontal flux is directed away from the axis. Overall the budget is very different from what has been seen in the previous cases. It is not easy to see how the velocity, temperature and flux fields adjust such that the budget balances.

(a)

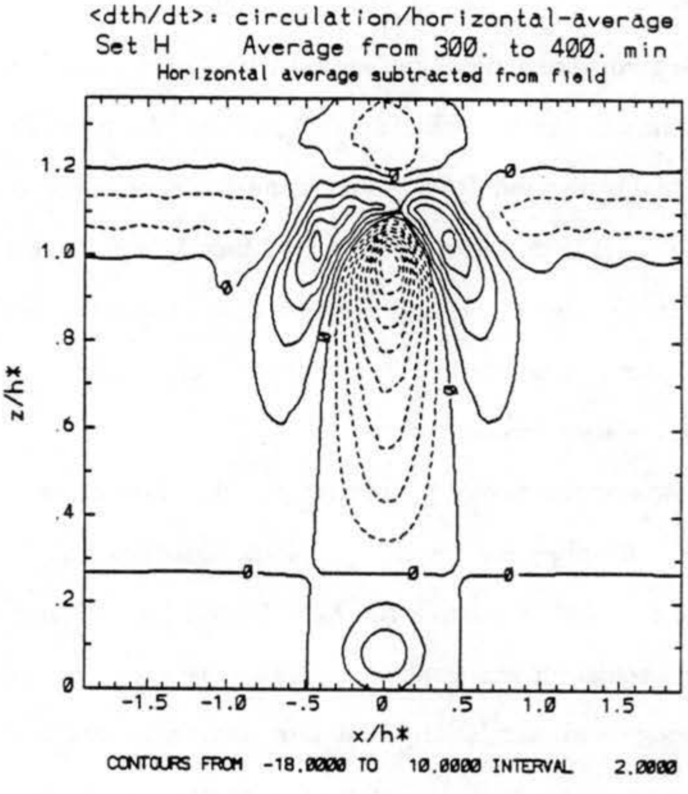

Figure 5.6. Tendencies in circulation potential temperature $\langle\theta'\rangle_{p,t}$ for Set H. (a) Circulation/horizontal-average interaction. (b) Circulation/circulation interaction. (c) Flux divergence. Contour interval $2w_*\theta_*/h_{\rho*}$.

Continued on following page.

(b)

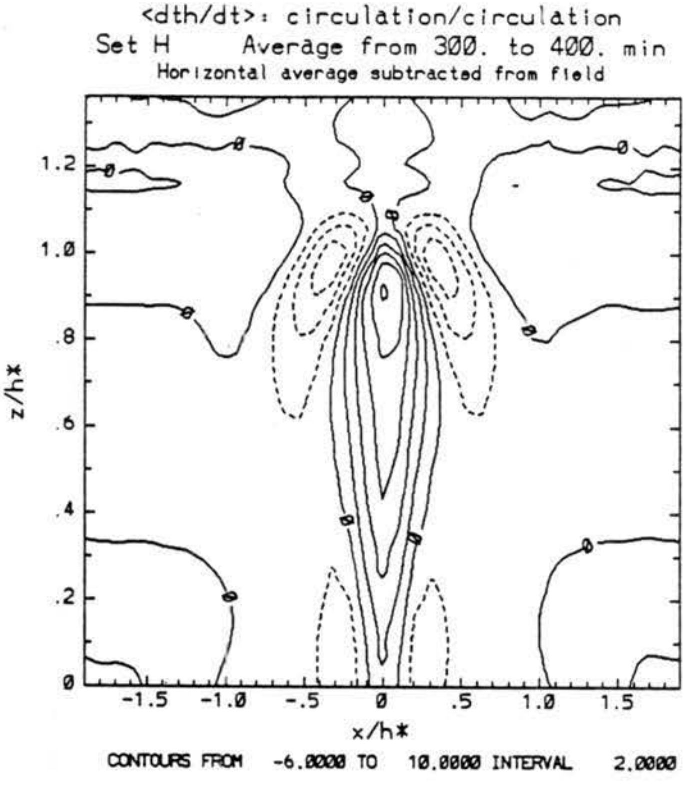

(c)

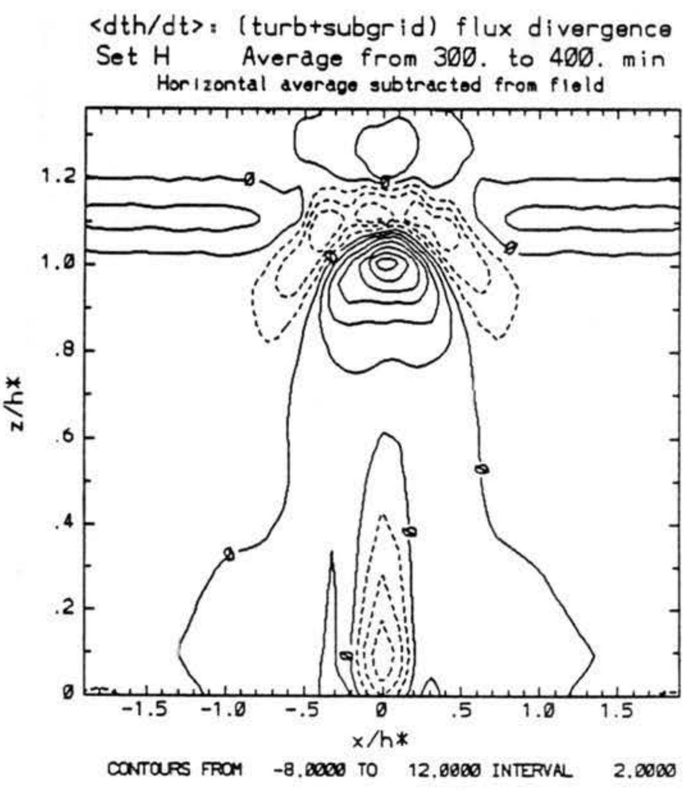

Figure 5.6 (continued).

(a)

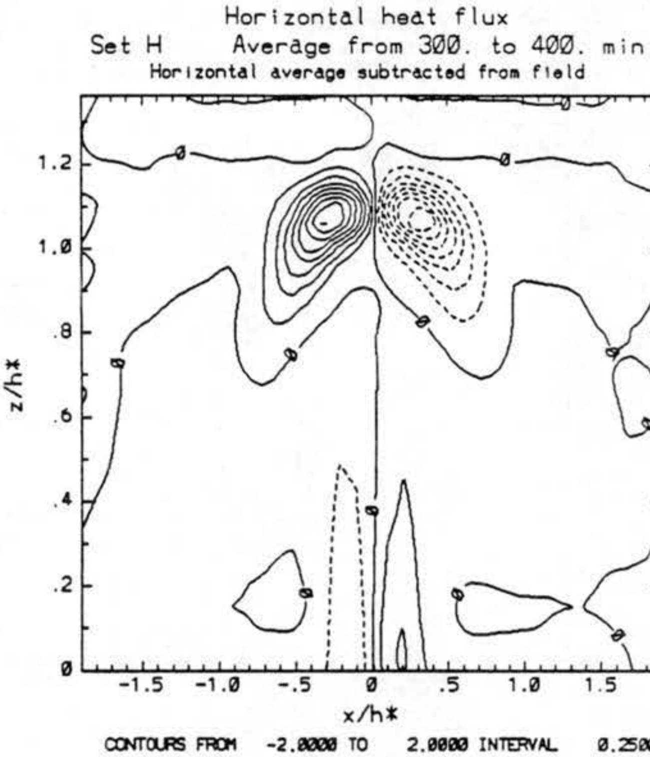

(b)

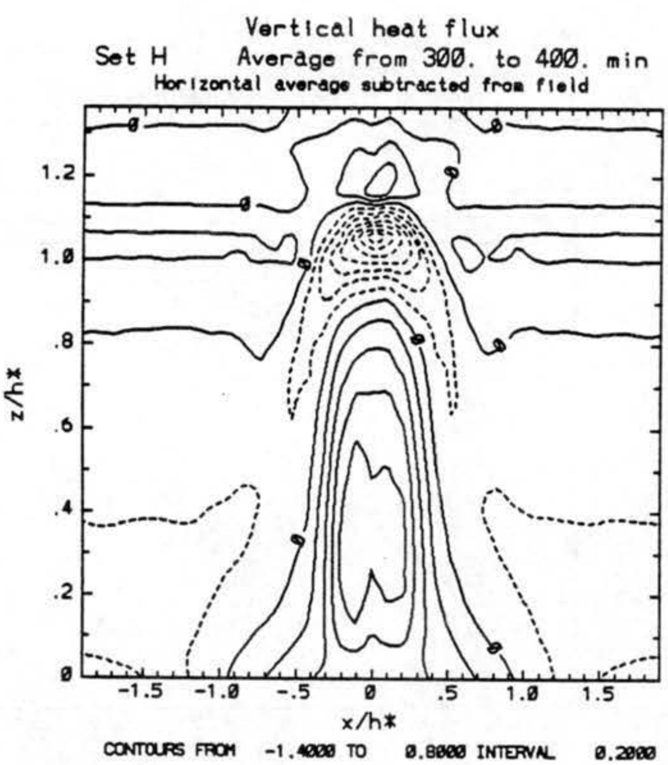

Figure 5.7. Components of the heat flux f_j for Set H. (a) Horizontal component ($j=1$), contour interval $0.25 w_* \theta_*$. (b) Vertical component ($j=3$), contour interval $0.2 w_* \theta_*$.

Figure 5.8 shows the $\langle\theta'\rangle_{p,t}$ budget for Set I ($\lambda_p = 4500\,\mathrm{m}$, $u_0 = 1\,\mathrm{m\,s^{-1}}$) and Figure 5.9 shows the vertical flux f_3. (The horizontal component of the flux has not been shown because its divergence is not a significant contributor to the budget.) Because of the fine structure in the mean and turbulence fields, the tendencies, which involve gradients, are not as smooth as they were in previous cases, but the main features of the budget are clear. In Set G there was a balance in the lower boundary layer between horizontal advection and flux divergence. In the present case these two terms do oppose each other, but the circulation/circulation and circulation/horizontal-average terms are also of comparable magnitude. In the vicinity of the inversion the budget resembles the one calculated for Set G, although the tendency terms are now much larger in magnitude. Again horizontal advection and circulation/horizontal-average interaction are both large and generally oppose each other. Again, however, the turbulence term is also significant: it has a couplet at the entrainment maximum and another at the entrainment minimum.

The potential temperature budget for Set J is not shown, since it resembles in most respects the budget for Set I. The differences are that the circulation/horizontal-average and circulation/circulation terms in Set J are smaller, essentially negligible, within the boundary layer and that the balance between horizontal advection and the circulation/horizontal-average term near the inversion is different owing to the better-defined stationary wave pattern in Set J. The vertical flux *is* shown, in Figure 5.10, mainly for later comparison with the calculations of Appendix B.

5.2 The circulation velocity and kinetic energy budgets

The budget equation for the circulation velocity is

$$\begin{aligned}\frac{\partial}{\partial t}\langle u_i'\rangle_{p,t} \;=\;& +\delta_{i3}\frac{g}{\theta_0}\langle\theta'\rangle_{p,t} - \theta_0\frac{\partial\langle\pi'\rangle_{p,t}}{\partial x_i} - \langle u_j\rangle_{h,t}\frac{\partial\langle u_i'\rangle_{p,t}}{\partial x_j}\\ &- \frac{1}{\rho_0}\frac{\partial}{\partial x_j}\Big(\rho_0\langle u_j'\rangle_{p,t}\langle u_i'\rangle_{p,t}\Big)' \qquad\qquad (5.4)\\ &- \frac{1}{\rho_0}\frac{\partial}{\partial x_j}\Big\langle\rho_0(u_j')_{p,t}(u_i')_{p,t}\Big\rangle'_{p,t} - \frac{1}{\rho_0}\frac{\partial}{\partial x_j}\Big\langle\rho_0\tau_{ij}\Big\rangle'_{p,t}.\end{aligned}$$

It differs from the $\langle\theta'\rangle_{p,t}$ budget (Equation 5.1) in that buoyancy and pressure-gradient terms have been added. (As has been pointed out previously, the $\langle\pi'\rangle_{p,t}$ field can be

(a)

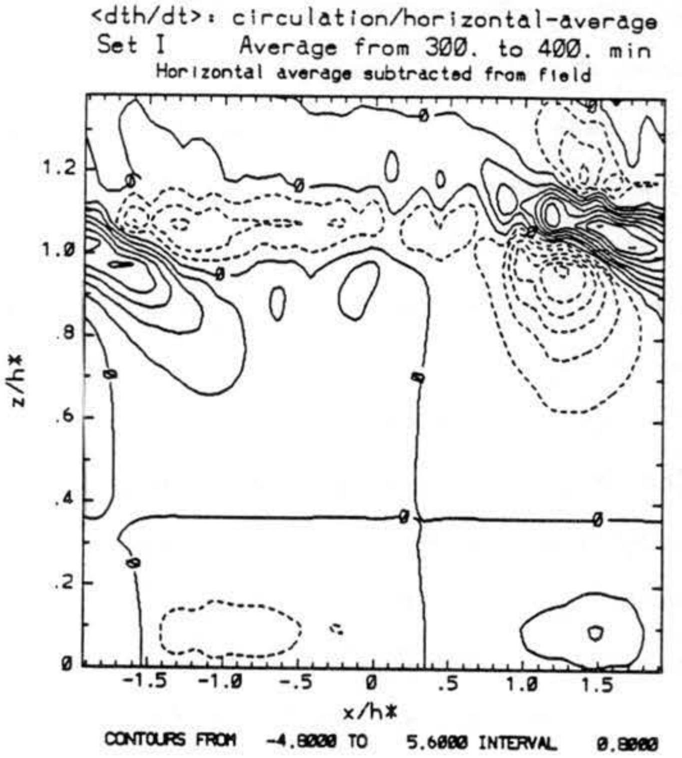

(b)

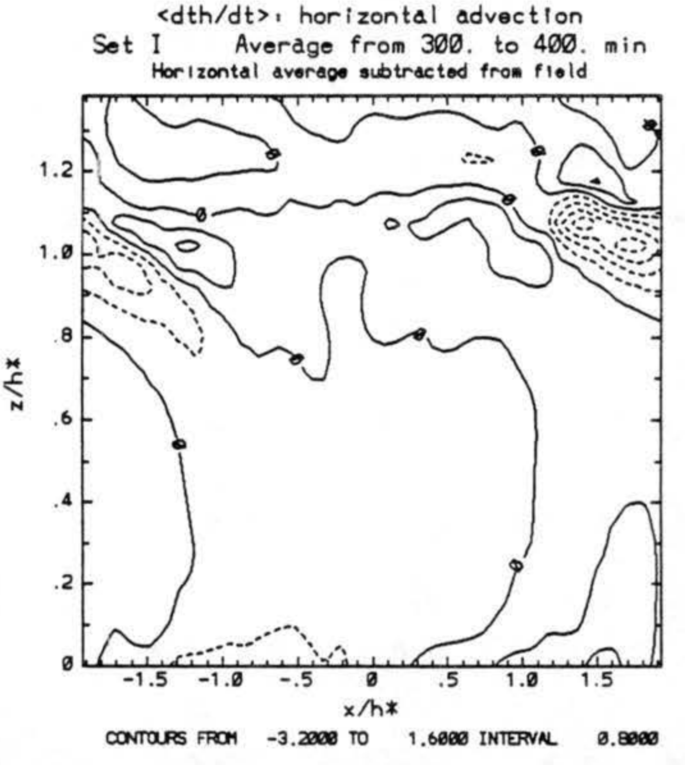

Figure 5.8. Tendencies in circulation potential temperature $\langle\theta'\rangle_{p,t}$ for Set I. (a) Circulation/horizontal-average interaction. (b) Horizontal advection. (c) Circulation/circulation interaction. (d) Flux divergence. Contour interval $0.8w_*\theta_*/h_{\rho *}$.

Continued on following page.

(c)

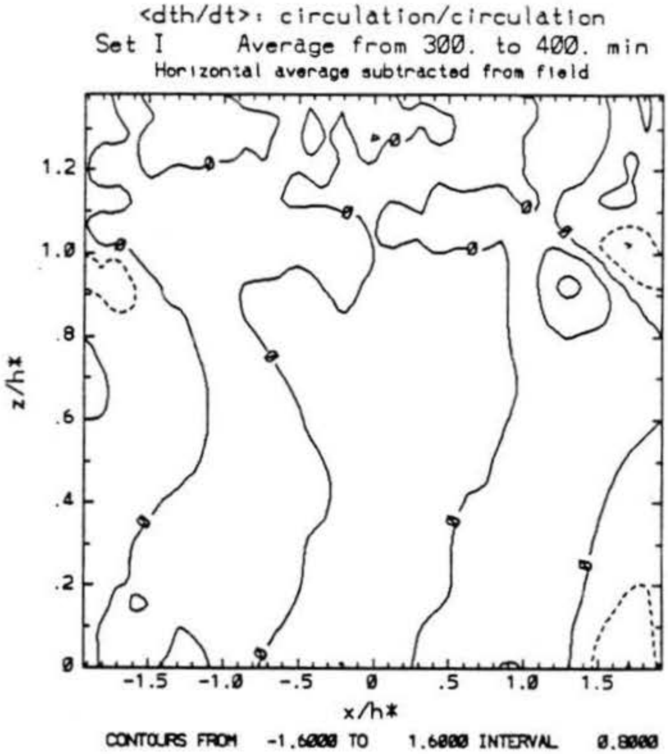

(d)

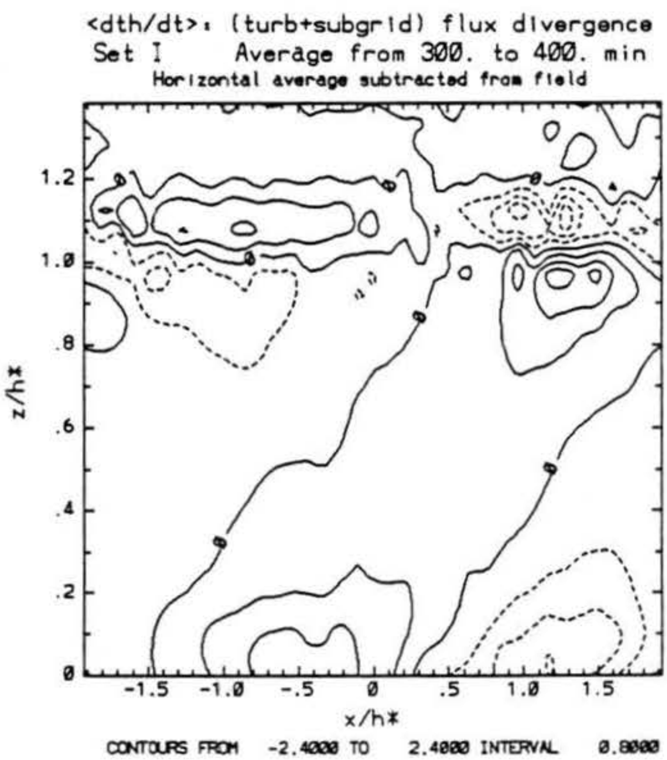

Figure 5.8 (continued).

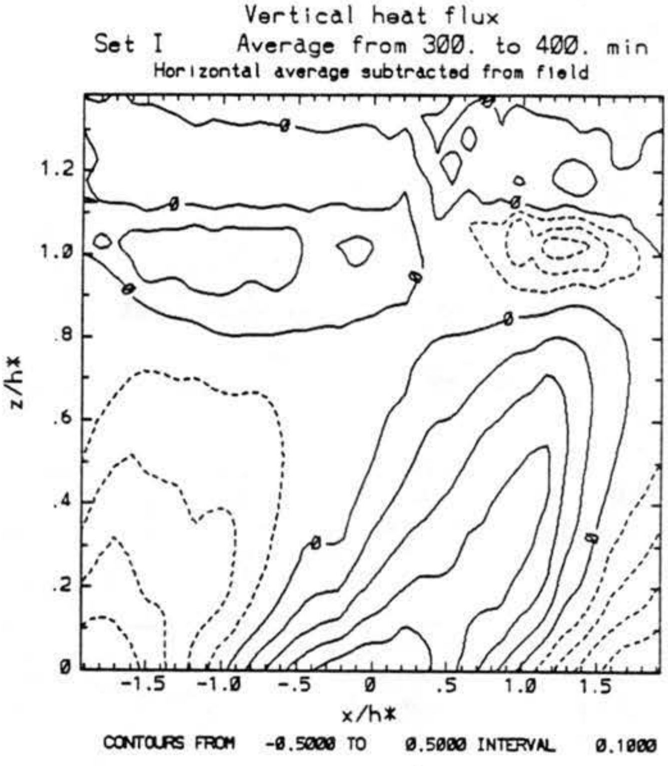

Figure 5.9. Vertical heat flux f_3 for Set I. Contour interval $0.1w_*\theta_*$.

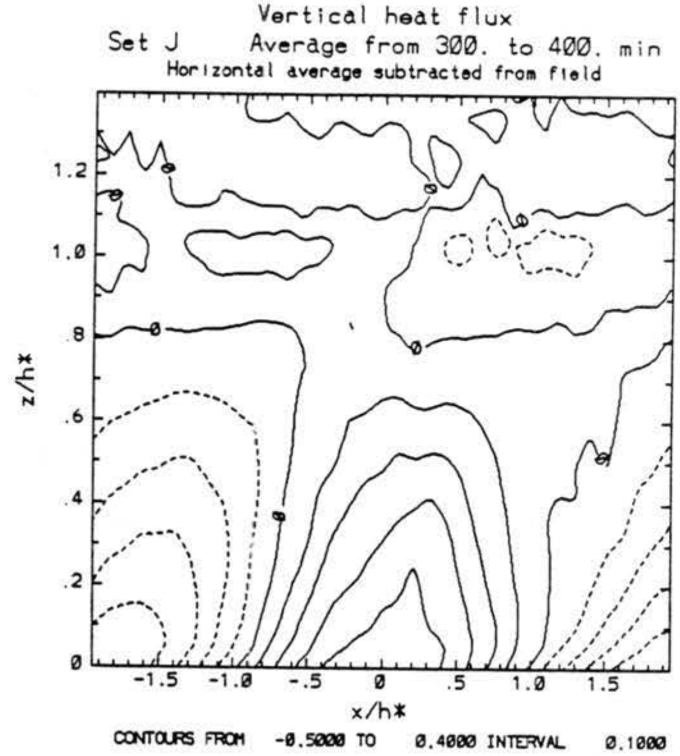

Figure 5.10. Vertical heat flux f_3 for Set J. Contour interval $0.1w_*\theta_*$.

decomposed into components induced by each of the other terms in the budget.) The other difference from the $\langle\theta'\rangle_{p,t}$ budget is that the circulation/horizontal-average term has been dropped, since the gradient in $\langle u_i\rangle_{h,t}$ is small. The only term associated with advection by the circulation is now circulation/circulation interaction, which will be called the "circulation" term without ambiguity.

Figure 5.11 shows tendencies in $\langle u'\rangle_{p,t}$ and $\langle w'\rangle_{p,t}$ for Set F ($\lambda_p = 1500\,\mathrm{m}$, $u_0 = 0\,\mathrm{m\,s^{-1}}$). The fields are the non-divergent parts of the tendencies, i.e., the sum of the tendency plus the associated pressure-gradient force. (The pressure fields have been described in Section 4.4.4 and plotted in Figure 4.8.) Because the divergence is zero, the vertical component determines the horizontal component uniquely (or vice versa), although the fields are easier to visualise when both components are presented.

Disposing of the minor terms of the budget first, the non-divergent[14] circulation term tends to focus the maximum in $\langle w'\rangle_{p,t}$ and to shift the low-level maximum and minimum in $\langle u'\rangle_{p,t}$ towards $\hat{x}=0$. It is very small, however. The subgrid term is largest in magnitude right next to the surface, where it resists inflow into the updraught. Even there it is substantially smaller than the other terms. The budget reduces, then, to a balance between buoyancy and turbulence. The (non-divergent) buoyancy force (Figure 5.11a) is similar in form to the $\langle u_i'\rangle_{p,t}$ field itself (Figures 4.7a and 4.b): Like the velocity, the buoyancy vector is directed upwards along $\hat{x}=0$ in the lower and middle boundary layer, with shallow horizontal convergence near the surface and deeper horizontal divergence above. On the other hand, the buoyancy vector differs from the velocity vector in that the maximum in its vertical component is at a lower level ($z=0.2h_*$ versus $z=0.35h_*$) and in that near $z=h_*$ it is directed downwards along $\hat{x}=0$.

The non-divergent buoyancy field would be directly proportional to the velocity field, *if* the sum of the turbulence and subgrid forces force were of the form of a Rayleigh friction, such as is used in the absorbing layer near the upper boundary—see Equation 2.14.

[14]In this and later paragraphs the qualifier "non-divergent" will generally be omitted where it is clearly implied by the context.

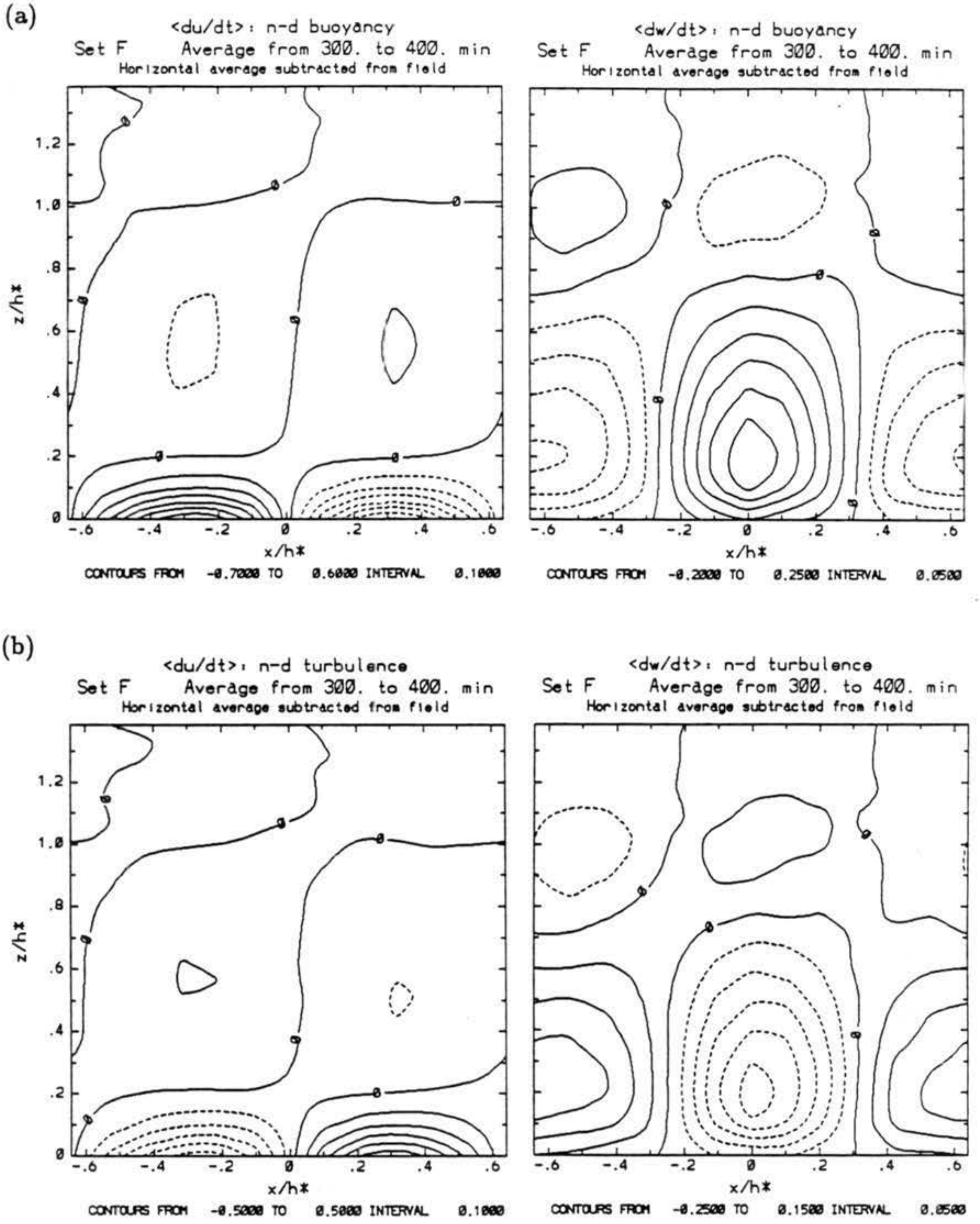

Figure 5.11. Non-divergent tendencies in circulation velocity $\langle u_i' \rangle_{p,t}$ for Set F. The figures are in pairs, with the left-hand one showing the tendency in $\langle u' \rangle_{p,t}$ and the right-hand one showing the tendency in $\langle w' \rangle_{p,t}$. (a) Buoyancy (contour intervals $0.1 w_*^2/h_*$ for u and $0.05 w_*^2/h_*$ for w). (b) Turbulence (contour intervals $0.1 w_*^2/h_*$ for u and $0.05 w_*^2/h_*$ for w). (c) Circulation (contour intervals $0.01 w_*^2/h_*$ for u and $0.005 w_*^2/h_*$ for w). (d) Subgrid (contour intervals $0.1 w_*^2/h_*$ for u and $0.02 w_*^2/h_*$ for w).

Continued on following page.

(c)

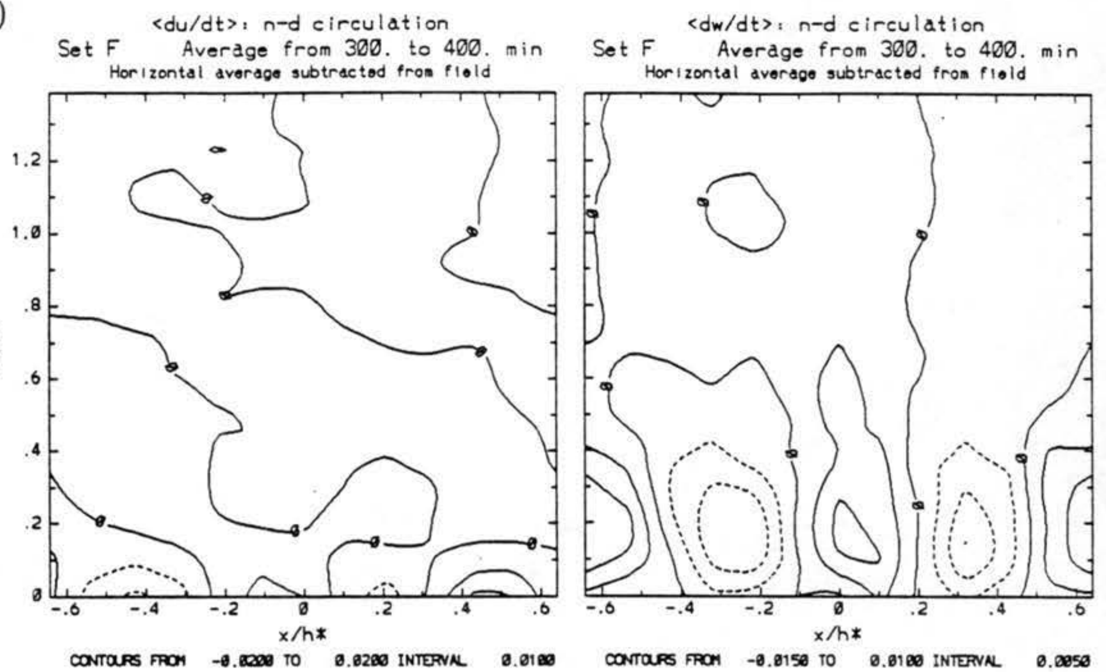

(d)

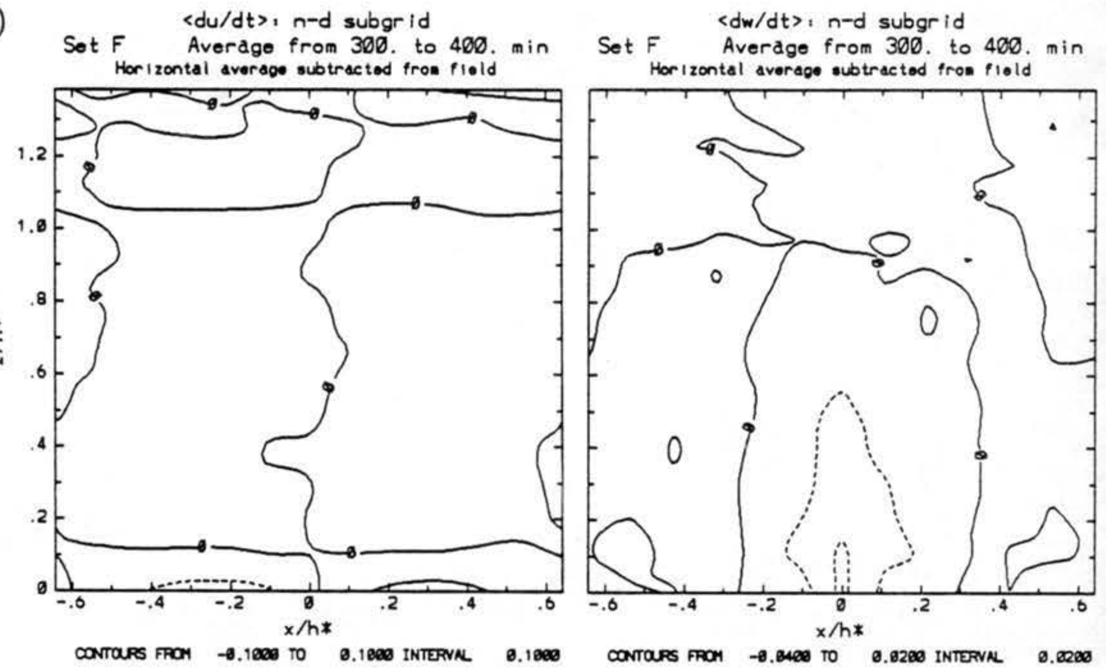

Figure 5.11 (continued).

Clearly this is not exactly so, and the turbulence term will be examined in more detail below. For the moment, however, let us calculate an effective value of the Rayleigh friction coefficient: For example, the maximum vertical velocity in the mean updraught is approximately $0.14w_*$ and the retarding force due to the turbulence plus subgrid tendencies in the same region is approximately $0.25w_*^2/h_*$, so the implied coefficient is of the order of $2w_*/h_*$. In the region of inflow at the base of the mean updraught the horizontal velocity is approximately $0.2w_*$ and the retarding force is approximately $0.6w_*^2/h_*$, so the coefficient is of the order of $3w_*/h_*$, whereas in the region of outflow in the upper boundary layer the horizontal velocity is approximately $0.04w_*$ and the retarding force is approximately $0.1w_*^2/h_*$, so the coefficient is of the order of $2.5w_*/h_*$. The inverse of the Rayleigh friction coefficient is a time scale, which is therefore in the range $0.3h_*/w_*$ to $0.5h_*/w_*$, or 3 min to 5 min. Later, a time scale will be calculated from the vertically integrated budget for the circulation kinetic energy, and it will be found to be within this range.

There are several advantages to describing the dynamics of the $\langle u_i' \rangle_{p,t}$ field in terms of the budget for the kinetic energy, $\langle \langle u_i' \rangle_{p,t}^2 \rangle_h / 2$: the amount of information to be comprehended is reduced, it is easier to describe the processes quantitatively, and certain integral constraints on the energy transformations appear. The budget equation, which is similar in form to the $\langle u_i'^2 \rangle_{h,t}/2$ budget that was examined in Section 3.3.1, is

$$\begin{aligned}
\frac{1}{2}\frac{\partial}{\partial t}\left\langle \langle u_i' \rangle_{p,t}^2 \right\rangle_h \quad = \quad & + \delta_{i3}\frac{g}{\theta_0}\left\langle \langle w' \rangle_{p,t} \langle \theta' \rangle_{p,t} \right\rangle_h - \theta_0 \left\langle \langle u_i' \rangle_{p,t} \frac{\partial}{\partial x_i} \langle \pi' \rangle_{p,t} \right\rangle_h \\
& - \frac{\partial}{\partial z}\left\langle \langle w' \rangle_{p,t} \langle u_i' \rangle_{p,t}^2 / 2 \right\rangle_h \\
& - \frac{1}{\rho_0}\left\langle \langle u_i' \rangle_{p,t} \frac{\partial}{\partial x_j} \left\langle \rho_0 (u_j')_{p,t} (u_i')_{p,t} \right\rangle_{p,t} \right\rangle_h \\
& - \frac{1}{\rho_0}\left\langle \langle u_i' \rangle_{p,t} \frac{\partial}{\partial x_j} \left\langle \rho_0 \tau_{ij} \right\rangle_{p,t} \right\rangle_h .
\end{aligned} \qquad (5.5)$$

The terms on the right-hand side correspond to the terms in the $\langle u_i' \rangle_{p,t}$ budget, except that the horizontal advection term in the velocity budget does not contribute to the energy budget, since horizontal advection does not change the kinetic energy at a given height. The first term is buoyancy production, and it is proportional to the heat flux carried by the time-averaged circulation. The second is the pressure term, which as usual can transport energy and transfer it between the component variances. The third term is vertical transport due to the circulation. (It was noted above that the circulation tends to focus the updraught—this effect is represented in the *third moment* budgets.) The fourth and fifth terms describe interaction with the turbulent and subgrid stresses, respectively.

It was shown in Section 3.3.1 that the buoyancy force (in that context the deviation from the horizontal average) tends to be opposed by the vertical gradient in the buoyancy pressure. By analogy one might expect the following relationship to hold:

$$-\theta_0 \left\langle \langle w' \rangle_{p,t} \frac{\partial}{\partial z} \langle \pi_b' \rangle_{p,t} \right\rangle_h = -A_c \frac{g}{\theta_0} \left\langle \langle w' \rangle_{p,t} \langle \theta' \rangle_{p,t} \right\rangle_h \tag{5.6}$$

where A_c is a ratio analogous to A in Equation 3.14. The π_b-gradient term in the $\langle \langle w' \rangle_{p,t}^2 \rangle_h / 2$ budget is plotted in Figure 5.12 and compared with the buoyancy term times -1. The profile of the ratio A_c is plotted in a graph on the right-hand edge of the figure (it is suppressed where the numerator or denominator approaches zero). At the lowest level ($z = 0.05h_*$) A_c is 0.9, and it drops off rapidly in the lower boundary layer, between $z = 0.55h_*$ and $z = 0.75h_*$ it is badly behaved, since the curves cross zero at different levels, and above $z = 0.75h_*$ it is approximately 0.6. One can also form the ratio between the *vertical integrals* of the π_b-gradient and buoyancy terms, although this ratio can be misleading when the curves have substantial negative area, since a large value of A_c in the negative region then tends to reduce the ratio. For Set F the ratio based on the vertical integrals has the value 0.45 (Table 4.3), i.e., in the absence of buoyancy-pressure transport out of the boundary layer, 45% of the total buoyancy production in $\langle \langle w' \rangle_{p,t}^2 \rangle_{h,t} / 2$ is transferred directly to $\langle \langle u' \rangle_{p,t}^2 \rangle_{h,t} / 2$ by the buoyancy pressure.

Figure 5.13 shows profiles of the non-divergent terms in the budgets for $\langle \langle u' \rangle_{p,t}^2 \rangle_h / 2$, $\langle \langle w' \rangle_{p,t}^2 \rangle_h / 2$ and their sum. It is thus a condensation of the information in Figures 4.7 (velocities) and 5.11 (tendencies). In the $\langle \langle u' \rangle_{p,t}^2 \rangle_h / 2$ budget there is a large buoyancy source term near the surface associated with inflow into the π_b minimum at the base of the mean updraught. The major sink term is turbulence (which will be examined further

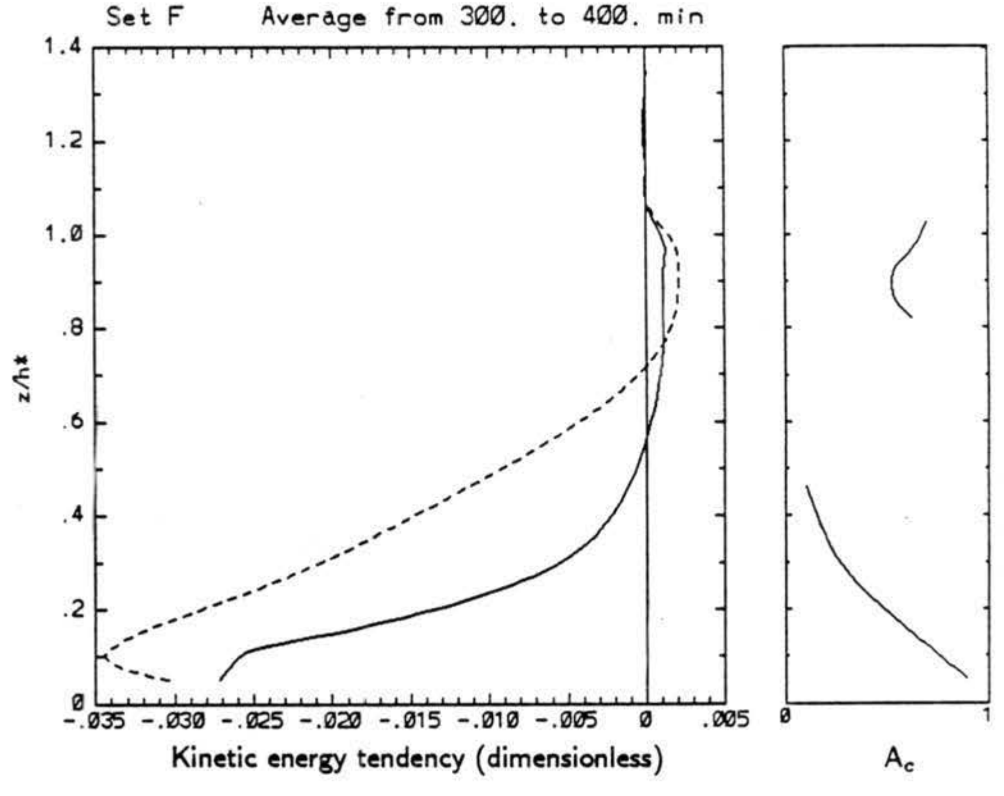

Figure 5.12. Profiles of the π_b-gradient term (solid) and -1 times the buoyancy term (dashed) in the budget for one-half the circulation vertical velocity variance $\langle\langle w'\rangle^2_{p,t}\rangle_h/2$ in Set F. The right-hand profile shows the ratio A_c between them.

(a) $\frac{1}{2}\frac{\partial}{\partial t}\left\langle\langle u'\rangle^2_{p,t}\right\rangle_h$:

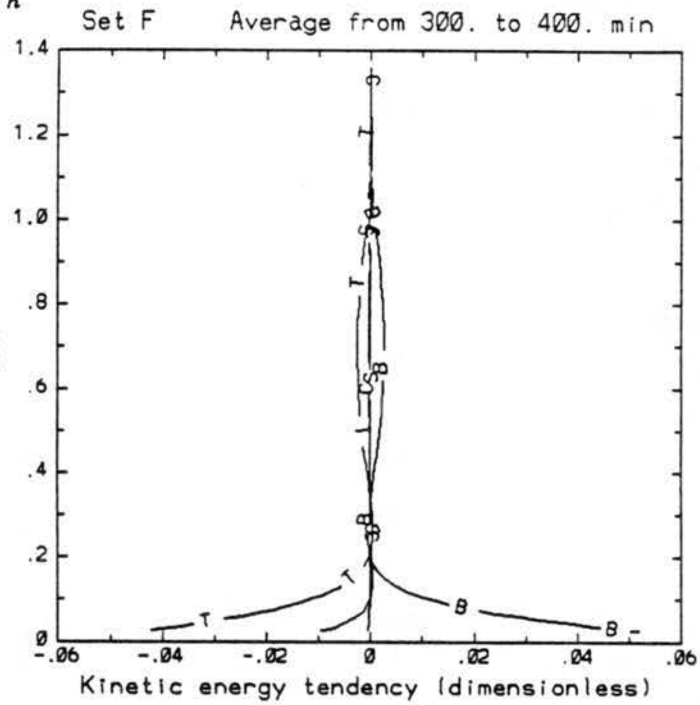

(b) $\frac{1}{2}\frac{\partial}{\partial t}\left\langle\langle w'\rangle^2_{p,t}\right\rangle_h$:

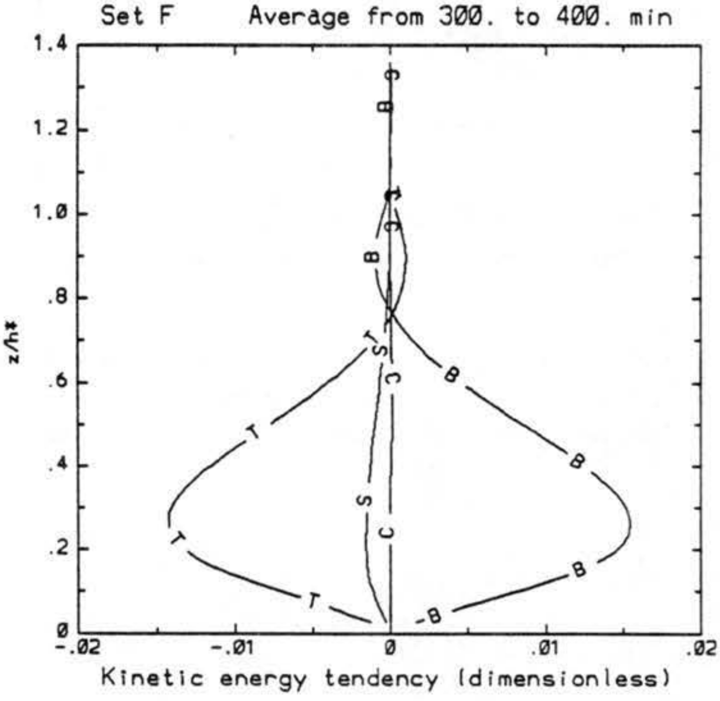

Figure 5.13. Profiles of non-divergent terms in the budgets for circulation kinetic energy $\langle\langle u_i'\rangle^2_{p,t}\rangle_h/2$ in Set F: (a) $i=1$, (b) $i=3$ and (c) sum. The terms are buoyancy (—B—), turbulence (—T—), circulation (—C—) and subgrid (—S—).

Continued on following page.

(c) $\frac{1}{2}\frac{\partial}{\partial t}\left\langle \langle u' \rangle_{p,t}^2 + \langle w' \rangle_{p,t}^2 \right\rangle_h$:

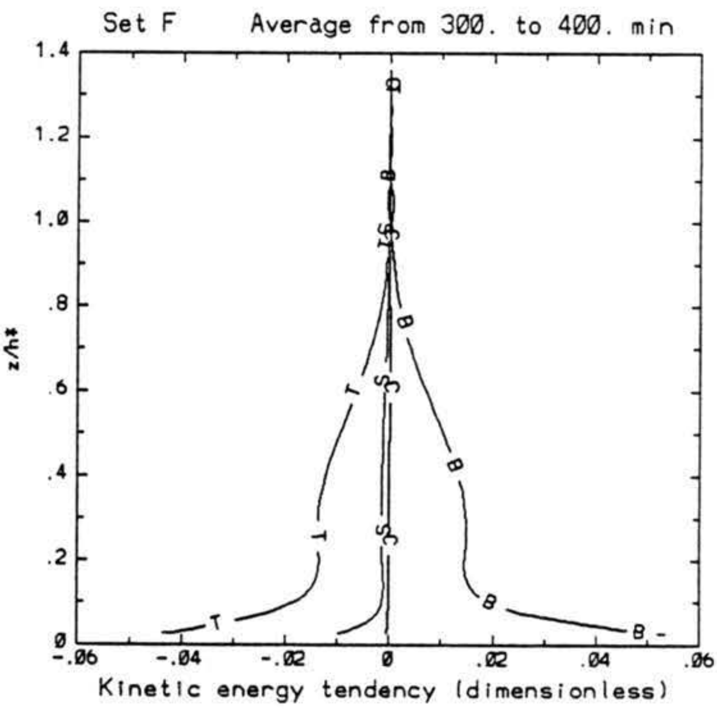

Figure 5.13 (continued).

below). Above $z = 0.3h_*$, in the outflow region, buoyancy is again a source—because there is outflow from the $\langle\pi_b'\rangle_{p,t}$ maximum in the middle and upper boundary layer—and turbulence a sink; the budget terms are small because the velocity and tendencies are both small. In the $\langle\langle w'\rangle_{p,t}^2\rangle_h/2$ budget the terms are largest near $z = 0.3h_*$: buoyancy is a source, turbulence a sink and the subgrid term a small sink. Above $z = 0.75h_*$ the buoyancy and turbulence terms reverse sign so that buoyancy becomes a sink and turbulence a source; the terms are small, not so much because the vertical velocity is small as because the tendencies are small. When the $\langle\langle u'\rangle_{p,t}^2\rangle_h/2$ and $\langle\langle w'\rangle_{p,t}^2\rangle_h/2$ budgets are combined to give the circulation kinetic energy budget, buoyancy is a source and turbulence a sink at all heights.

Let us examine the turbulence terms in more detail. In Figure 5.14a the non-divergent turbulence term in $\langle\langle u'\rangle_{p,t}^2\rangle_h/2$ is divided into its components,

$$-\frac{1}{\rho_0}\left\langle\langle u'\rangle_{p,t}\frac{\partial}{\partial x}\left\langle\rho_0(u')_{p,t}^2\right\rangle_{p,t}\right\rangle_h-\frac{1}{\rho_0}\left\langle\langle u'\rangle_{p,t}\frac{\partial}{\partial z}\left\langle\rho_0(w')_{p,t}(u')_{p,t}\right\rangle_{p,t}\right\rangle_h$$
$$-\theta_0\left\langle\langle u'\rangle_{p,t}\frac{\partial}{\partial x}\langle\pi_t'\rangle_{p,t}\right\rangle_h.$$

The net sink near the surface is associated with the first of these, i.e., with inflow into the maximum in u variance (Figure 4.10a). It is opposed by the second, which describes forcing of the inflow by the u/w covariance (Figure 4.10d) The third term is small near the surface, because the amplitude of the variation in $\langle\pi_t'\rangle_{p,t}$ (Figure 4.8c) is small there.

Figure 5.14b shows a similar decomposition of the non-divergent turbulence term in $\langle\langle w'\rangle_{p,t}^2\rangle_h/2$, namely

$$-\frac{1}{\rho_0}\left\langle\langle w'\rangle_{p,t}\frac{\partial}{\partial x}\left\langle\rho_0(u')_{p,t}(w')_{p,t}\right\rangle_{p,t}\right\rangle_h-\frac{1}{\rho_0}\left\langle\langle w'\rangle_{p,t}\frac{\partial}{\partial z}\left\langle\rho_0(w')_{p,t}^2\right\rangle_{p,t}\right\rangle_h$$
$$-\theta_0\left\langle\langle w'\rangle_{p,t}\frac{\partial}{\partial z}\langle\pi_t'\rangle_{p,t}\right\rangle_h.$$

(Note the change in the horizontal scale from Figure 5.14a.) The first term is negative everywhere, since the u/w covariance transports vertical momentum out of the updraught and into the downdraught. The second term is negative below $z = 0.4h_*$ and positive above, and its vertical integral is slightly negative. It arises because the updraught is opposed below the w-variance maximum and assisted above. The pressure term is,

(a) $\frac{1}{2}\frac{\partial}{\partial t}\left\langle\langle u'\rangle^2_{p,t}\right\rangle_h$:

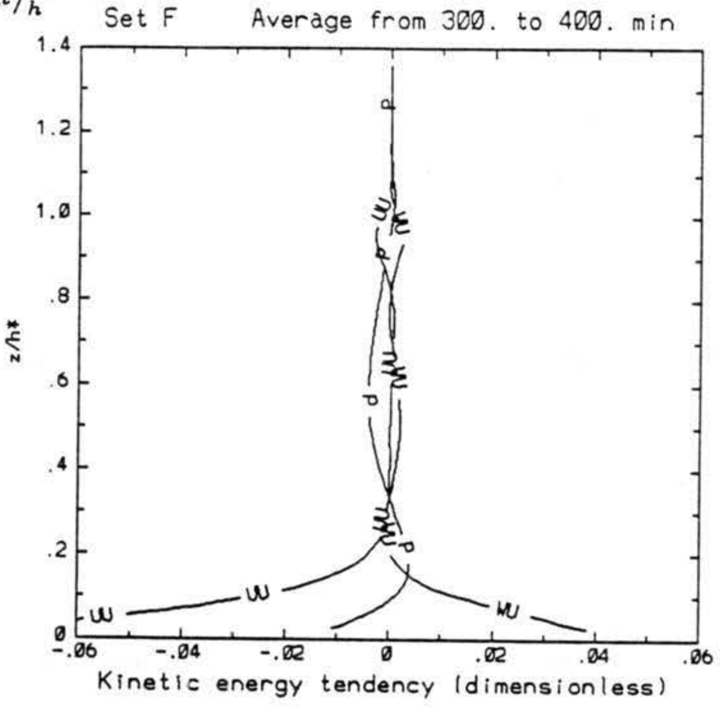

(b) $\frac{1}{2}\frac{\partial}{\partial t}\left\langle\langle w'\rangle^2_{p,t}\right\rangle_h$:

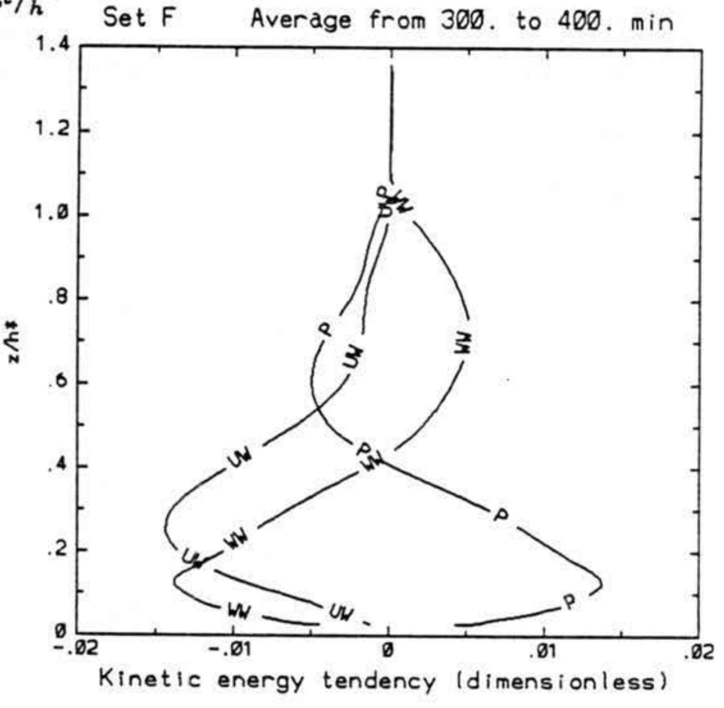

Figure 5.14. Decomposition of the non-divergent turbulence terms in the budgets for one-half the circulation velocity variances $\langle\langle u_i'\rangle^2_{p,t}\rangle_h/2$ in Set F. (a) Horizontal velocity ($i=1$) with terms due to u variance (—UU—), u/w covariance (—WU—) and turbulence pressure π_t (—P—). (b) Vertical velocity ($i=3$) with terms due to w variance (—WW—), u/w covariance (—UW—) and turbulence pressure π_t (—P—).

however, almost exactly equal and opposite, because the maximum in w variance is coincident with a minimum in turbulence pressure.

There is a similarity between the role of the w variance term in the $\langle\langle w'\rangle_{p,t}^2\rangle_h/2$ budget and the turbulent transport term in the budget for $\langle w'^2\rangle_{h,t}/2$ described in Section 3.3.1: Both the terms describe advection of w by w—in other words, the inertia in the vertical velocity field—and both terms absorb energy in the lower boundary layer, where buoyancy production in the vertical is positive, and release energy in the upper boundary layer, where buoyancy production is negative. Both terms also tend to be opposed by the pressure gradients induced by advection. The crucial difference is that the term in $\langle w'^2\rangle_{h,t}/2$ describes interaction of w' with itself, whereas the term in $\langle\langle w'\rangle_{p,t}^2\rangle_h/2$ describes interaction of the mean-circulation part of w', namely $\langle w'\rangle_{p,t}$, with the remainder. (In the present case, interaction of $\langle w'\rangle_{p,t}$ with itself—circulation transport—is negligible.) In other words, convective updraughts penetrate past the height where they become negatively buoyant largely because of *their own inertia,* but the weak mean updraught of Set F penetrates past the height where it becomes negatively buoyant because of *the inertia of the turbulence.* The coupling between the mean circulation and the turbulence is easier to understand when one thinks of the mean updraught not as single entity, but as a preferred location for the convective updraughts. One expects that if the surface heat-flux perturbation defines regions in the *lower* boundary layer where updraughts are more common than elsewhere, then those updraughts will penetrate into the *upper* boundary layer and be reflected in mean ascent there too. Thus the mean updraught will penetrate up to the maximum height reached by the convective updraughts. In Section 3.3.2 it was argued that this latter height is $z = 1.1h_*$ (although vertical motion in gravity-wave structures is found at higher levels). This is the maximum height reached by the weak mean updraught in Set F (Figure 4.7b) and it is also the maximum height reached by the much stronger mean updraught in Set H, described below.

To show the fate of the energy extracted from the circulation by the turbulent stresses, the turbulence term in Equation 5.5 can be rewritten as

$$
\begin{aligned}
-\frac{1}{\rho_0}\left\langle \langle u_i'\rangle_{p,t}\frac{\partial}{\partial x_j}\left\langle \rho_0 (u_j')_{p,t}(u_i')_{p,t}\right\rangle_{p,t}\right\rangle_h &= \\
-\frac{1}{\rho_0}\frac{\partial}{\partial z}\left\langle \langle u_i'\rangle_{p,t}\left\langle \rho_0 (w')_{p,t}(u_i')_{p,t}\right\rangle_{p,t}\right\rangle_h &+ \left\langle \left\langle (u_j')_{p,t}(u_i')_{p,t}\right\rangle_{p,t}\frac{\partial}{\partial x_j}\langle u_i'\rangle_{p,t}\right\rangle_h .
\end{aligned}
\tag{5.7}
$$

The first term on the right-hand side integrates to zero in the vertical and can be called "turbulent transport." The second is negative when the turbulent flux is directed down-gradient, and it can be called "turbulent dissipation," since there is an equal and opposite source term in the horizontally averaged budget for the turbulent velocity variance (Equation 5.8 with $i = j$). Turbulent dissipation, in other words, transfers energy from the time-averaged circulation to the turbulence.

There is a great deal of information, then, in the circulation kinetic energy and velocity variance budgets. It is convenient to summarise these budgets in terms of their vertical integrals. Figure 5.15 describes the vertically integrated kinetic energy transformations for the time-averaged circulation. The T_{ij} terms in Figure 5.15 represent the energy transfer resulting from interaction of the i'th component of the circulation velocity with the turbulent u_i/u_j covariance. The largest of them is T_{11} (u circulation, u variance) at 62% of the buoyancy production. Note also that the terms associated with the u/w covariance, T_{31} and T_{13}, are of opposite sign and their sum is small (14% of buoyancy production) so the u/w covariance achieves only a small fraction of the net energy transfer to turbulence. Incidentally there is no term in Figure 5.15 associated with a gravity-wave flux into the absorbing layer, because that flux is vanishingly small.

One can calculate a time scale based on the vertically integrated kinetic energy of the time-averaged circulation and the vertically integrated rate of dissipation by resolved and subgrid turbulence. For the present case the time scale is

$$
\frac{.0037\, w_*^2 h_{\rho *}}{.0117\, w_*^3 h_{\rho *}/h_*} = 0.32\, h_*/w_* = 3\,\mathrm{min}.
$$

This seems surprisingly small. For comparison, the time scale calculated in Section 3.3.1 for the subgrid dissipation of turbulence kinetic energy was $1.17 h_*/w_*$ (here "turbulence" is used in the sense assumed in Chapter 3).

$$B = 0.0117\, w_*^3 h_{\rho *}/h_*$$

$$\downarrow$$

$$\boxed{\frac{1}{2}\left\langle \langle w' \rangle^2_{p,t} \right\rangle_h} \quad \xrightarrow{\begin{array}{rcr} P_b & = & 0.45 \\ P_t & = & -0.15 \end{array}} \quad \boxed{\frac{1}{2}\left\langle \langle u' \rangle^2_{p,t} \right\rangle_h}$$

$$\downarrow \qquad\qquad\qquad\qquad \downarrow$$

$$\begin{array}{rcr} T_{31} & = & 0.50 \\ T_{33} & = & 0.13 \\ S & = & 0.07 \end{array} \qquad\qquad \begin{array}{rcr} T_{11} & = & 0.62 \\ T_{13} & = & -0.37 \\ S & = & 0.07 \end{array}$$

Figure 5.15. Vertically integrated kinetic energy budget for the time-averaged circulation in Set F. The terms are as follows: buoyancy (B), buoyancy pressure (P_b), turbulence pressure (P_t), turbulent u_i/u_j covariance (T_{ij}) and non-divergent subgrid (S). The buoyancy term is expressed in units of $w_*^3 h_{\rho *}/h_*$. The remaining terms are expressed as fractions of the buoyancy term.

Let us now examine the circulation velocity and kinetic energy budgets for Set G ($\lambda_p = 1500\,\mathrm{m}$, $u_0 = 1\,\mathrm{m\,s^{-1}}$). The non-divergent tendencies in the $\langle u_i' \rangle_{p,t}$ budget are shown in Figure 5.16. With $u_0 = 1\,\mathrm{m\,s^{-1}}$ the horizontal advection term,

$$-\langle u_j \rangle_{h,t}\, \partial \langle u_i' \rangle_{p,t} / \partial x_j,$$

has become important; it does not generate significant pressure fluctuations, since $\langle u_i' \rangle_{p,t}$ has zero divergence and $\langle u_j \rangle_{h,t}$ is approximately constant with height. As noted in the discussion of the temperature budget, the horizontal advection field is proportional to the velocity field displaced $\lambda_p/4$ downstream, so the sum of the other two significant terms—buoyancy and turbulence—is displaced $\lambda_p/4$ upstream of the velocity. As in Set F, the horizontal component of the turbulence tendency is generallly of opposite sign to the horizontal velocity, while the vertical component of the turbulence tendency is of opposite sign to the vertical velocity in the lower boundary layer and of the same sign above. Otherwise the relationship between the buoyancy and turbulence terms is not easily summarised (they are each of comparable magnitude) and again it is not clear how the velocity, buoyancy, pressure and stress fields adjust to achieve a balance. The following paragraphs will just look briefly at how the kinetic energy of the time-averaged circulation is maintained.

Figure 5.17 compares the buoyancy and π_b-gradient terms in the $\langle \langle w' \rangle_{p,t}^2 \rangle_h / 2$ budget. The ratio A_c between them is generally between 0.4 and 0.8, except between $z \approx 0.7h_*$ and $z \approx 0.9h_*$ where it is badly behaved. The profile of A_c is rather different from what was found for $u_0 = 0\,\mathrm{m\,s^{-1}}$, but again the ratio based on the vertical integrals is a little under 0.5 (Table 4.4).

Figure 5.18 shows profiles of the non-divergent terms in the $\langle \langle u_i' \rangle_{p,t}^2 \rangle_h / 2$ budgets of Set G. The budget again reduces to a balance between buoyancy and turbulence, with the subgrid term smaller and the circulation term negligible. In $\langle \langle u' \rangle_{p,t}^2 \rangle_h / 2$ the buoyancy forcing is positive everywhere within the boundary layer, with a maximum near the surface and a weaker maximum near $z = 0.9h_*$. In $\langle \langle w' \rangle_{p,t}^2 \rangle_h / 2$ the buoyancy forcing is positive below $z = 0.7h_*$ and negative above. For the kinetic energy the buoyancy term is

(a)

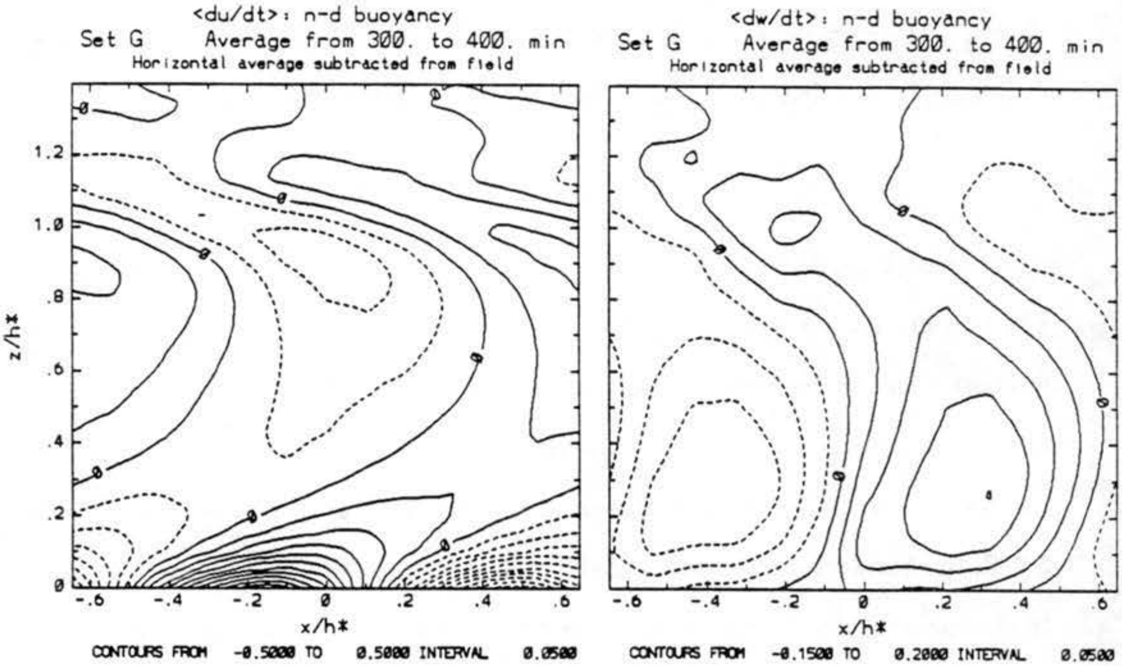

(b)

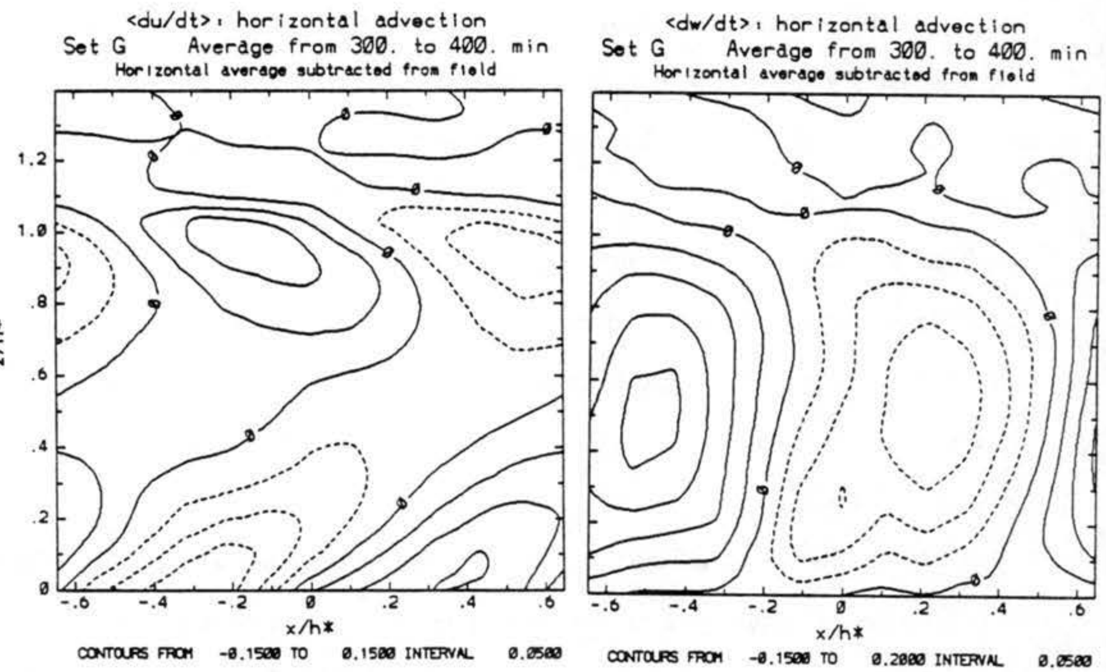

Figure 5.16. Non-divergent tendencies in circulation velocity $\langle u_i' \rangle_{p,t}$ for Set G. The format is similar to that used in figure 5.11. (a) Buoyancy. (b) Horizontal advection. (c) Turbulence. All contour intervals $0.05 w_*^2/h_*$.

Continued on following pages.

(c)

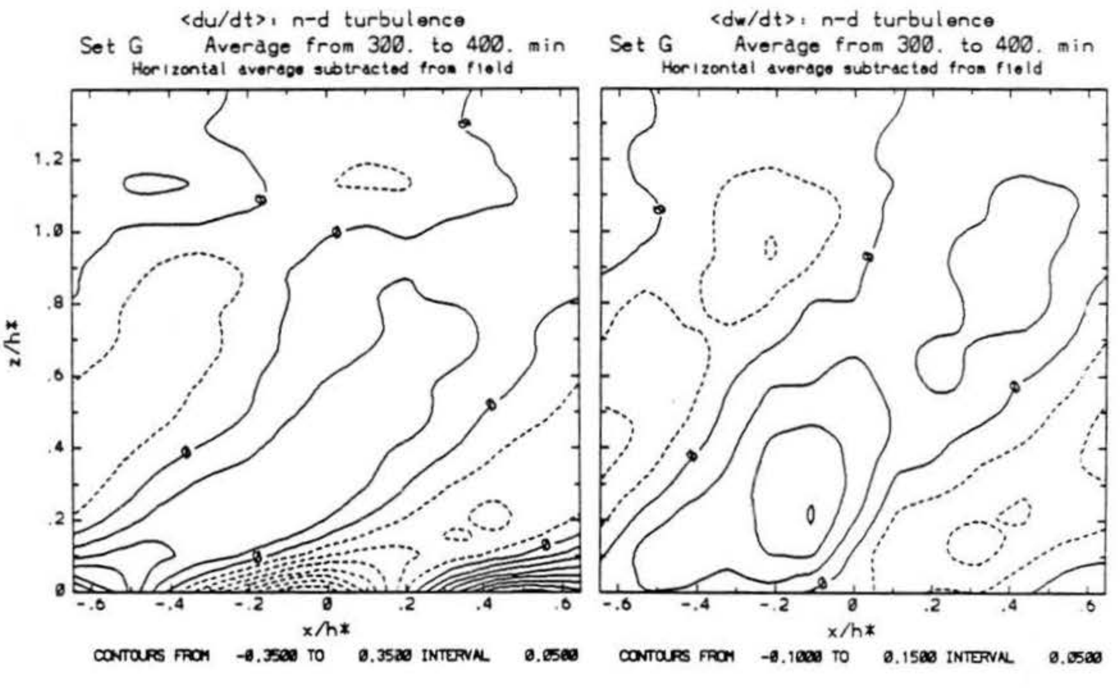

Figure 5.16 (continued).

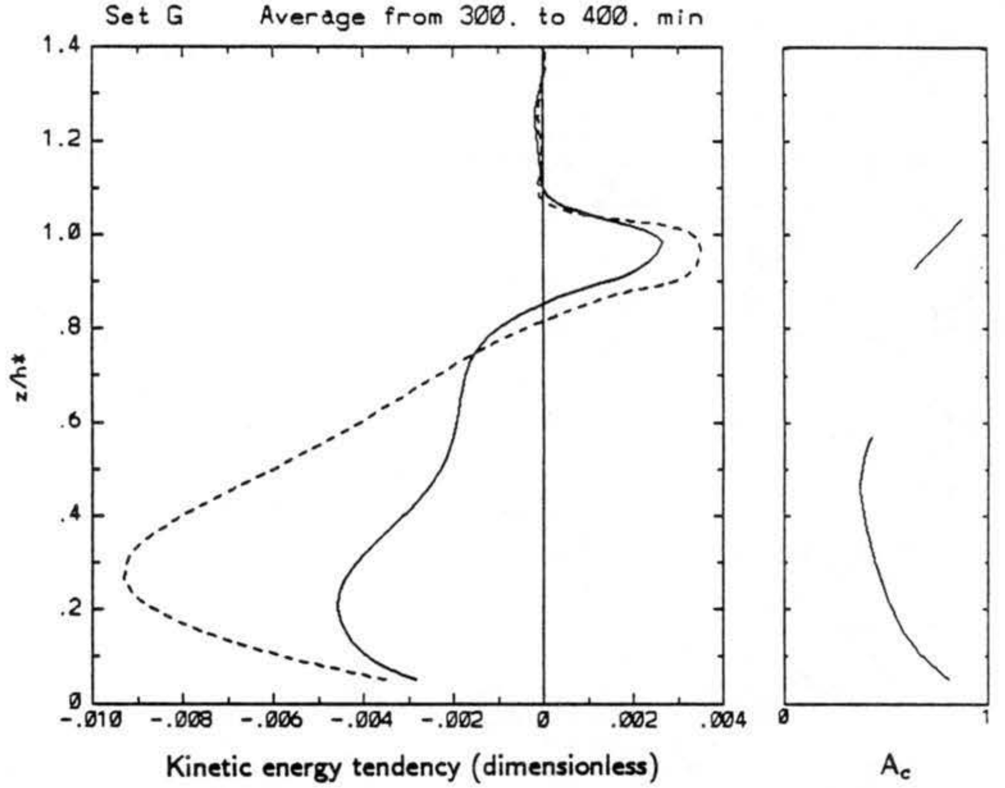

Figure 5.17. Profiles of the π_b-gradient term (solid) and -1 times the buoyancy term (dashed) in the budget for one-half the circulation vertical velocity variance $\langle\langle w'\rangle^2_{p,t}\rangle_h/2$ in Set G. The right-hand profile shows the ratio A_c.

(a) $\frac{1}{2}\frac{\partial}{\partial t}\left\langle \langle u' \rangle_{p,t}^2 \right\rangle_h$:

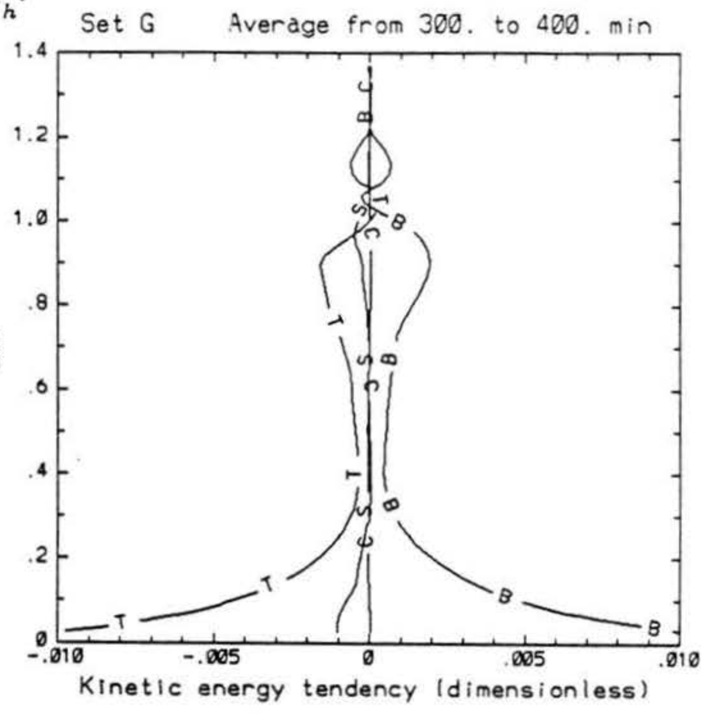

(b) $\frac{1}{2}\frac{\partial}{\partial t}\left\langle \langle w' \rangle_{p,t}^2 \right\rangle_h$:

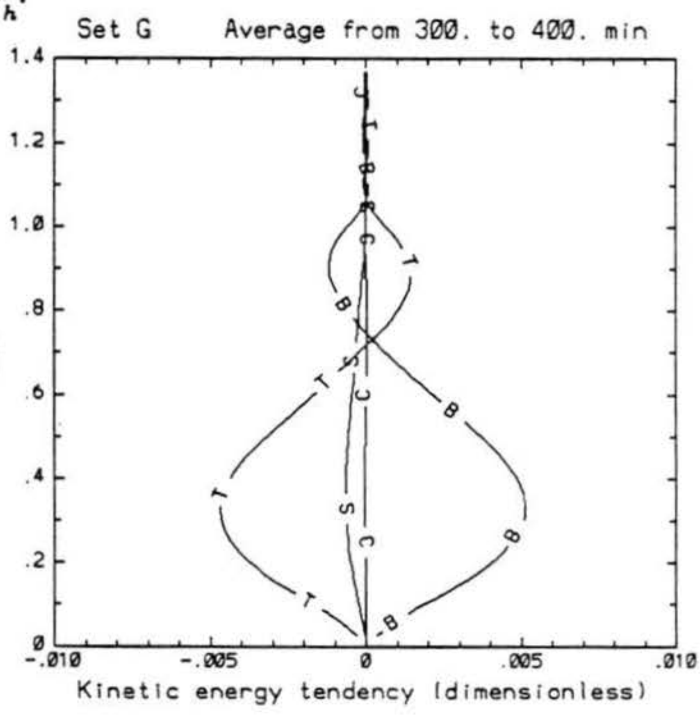

Figure 5.18. Profiles of non-divergent terms in the budgets for circulation kinetic energy $\langle\langle u_i' \rangle_{p,t}^2\rangle_h/2$ in Set G: (a) $i=1$, (b) $i=3$ and (c) sum. The terms are buoyancy (—B—), turbulence (—T—), circulation (—C—) and subgrid (—S—).

Continued on following page.

(c) $\frac{1}{2}\frac{\partial}{\partial t}\left\langle \langle u' \rangle_{p,t}^2 + \langle w' \rangle_{p,t}^2 \right\rangle_h$:

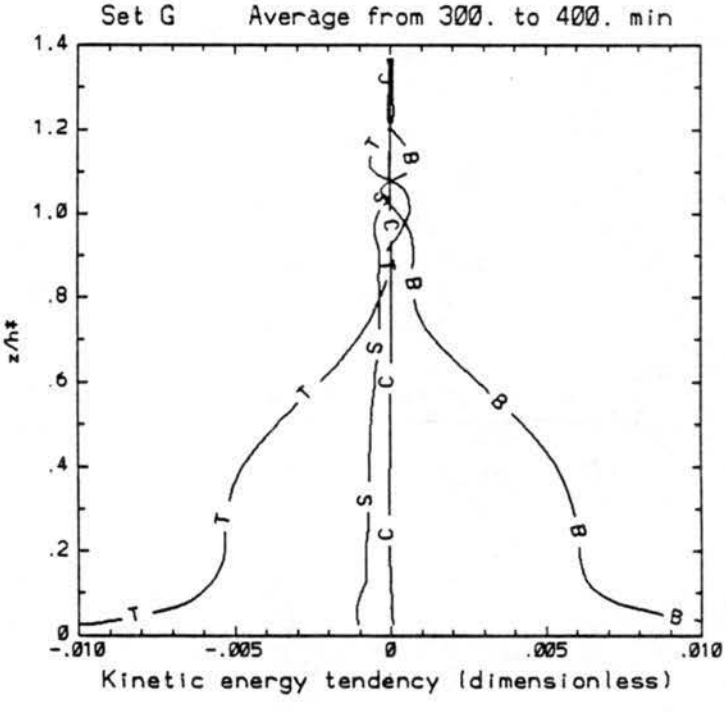

Figure 5.18 (continued).

positive everywhere and the budget resembles the corresponding budget for Set F despite the substantial differences between the tendency fields.

In Figure 5.19 the non-divergent turbulence terms in the $\langle\langle u'\rangle^2_{p,t}\rangle_h/2$ and $\langle\langle w'\rangle^2_{p,t}\rangle_h/2$ budgets are divided into components associated with the turbulent stresses and the turbulence pressure, as described above. In the $\langle\langle u'\rangle^2_{p,t}\rangle_h/2$ budget the u variance term is a sink near the surface and the u/w covariance term is a weaker source, as they were in Set F, but now the pressure term is also a significant sink, associated with the maximum in turbulence pressure (Figure 4.20c) in the region of surface horizontal convergence (Figure 4.19a) near the base of the mean updraught. In the upper boundary layer the u variance term is again a sink, the u/w covariance is again a source, and the pressure term is (mostly) a sink. In the $\langle\langle w'\rangle^2_{p,t}\rangle_h/2$ budget the u/w covariance term is again a sink at all levels, with a maximum in the middle of the boundary layer, and the w variance term is again a sink at low levels and a source at high levels, with its negative area larger than its positive area. (Incidentally, the zero-crossing in the w variance term is now higher than it was in Set F, $z=0.6h_*$ versus $z=0.4h_*$, but it is not easy to see at a glance from the mean w and w variance fields why this is so.) The pressure term again opposes the w variance term.

The $\langle\langle u'_i\rangle^2_{p,t}\rangle_h/2$ budget for Set G is therefore qualitatively similar to the budget for Set F, but there are significant quantitative differences. Figure 5.20 summarises the vertical integrals. All the terms have the same sign as they did in Set F, but the proportions are somewhat different. The term T_{11} accounts for 32% of the buoyancy production (versus 62% in Set F), term T_{33} for 39% (versus 13%), and $T_{13}+T_{31}$ for 15% (versus 14%). The time scale for dissipation of the circulation is

$$\frac{.0019\, w_*^2 h_{\rho*}}{.0041\, w_*^3 h_{\rho*}/h_*} = 0.46\, h_*/w_*,$$

which is 40% larger than the corresponding time scale in Set F. At risk of over-simplifying, it is hypothesised that the longer time scale occurs because of the weaker transfer of energy to the turbulence by the T_{11} term, and that the transfer is weaker in Set G

(a) $\frac{1}{2}\frac{\partial}{\partial t}\left\langle \langle u' \rangle^2_{p,t} \right\rangle_h$:

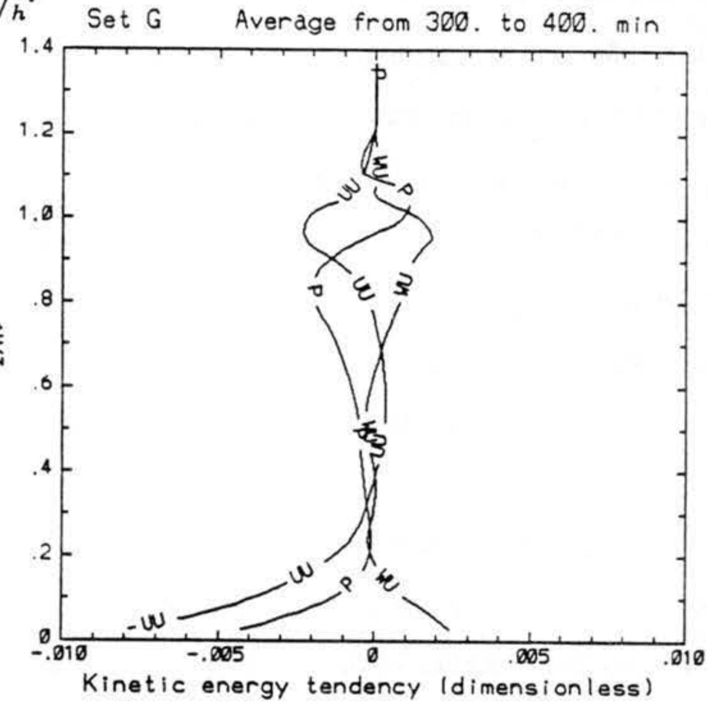

(b) $\frac{1}{2}\frac{\partial}{\partial t}\left\langle \langle w' \rangle^2_{p,t} \right\rangle_h$:

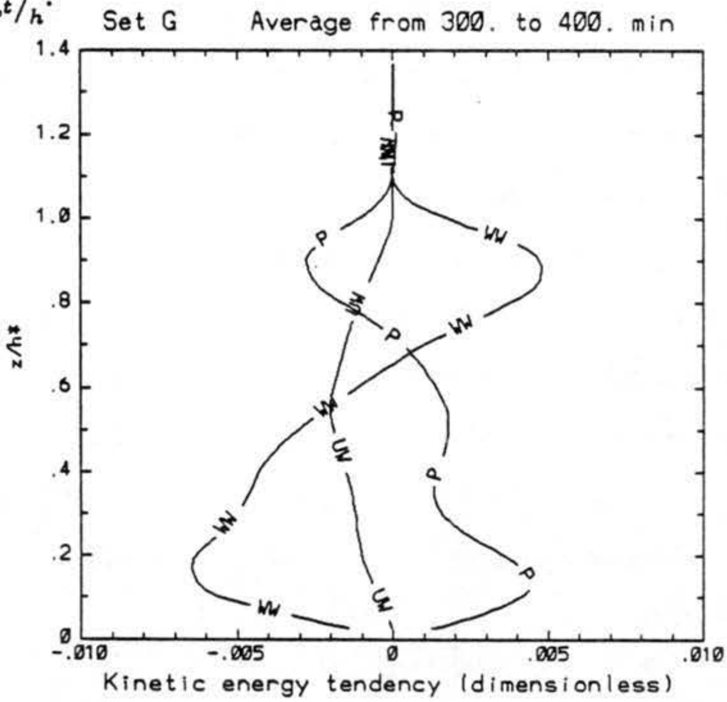

Figure 5.19. Decomposition of the non-divergent turbulence terms in the budgets for one-half the circulation velocity variances $\langle\langle u_i' \rangle^2_{p,t}\rangle_h/2$ in Set G. (a) Horizontal velocity ($i=1$) with terms due to u variance (—UU—), u/w covariance (—WU—) and turbulence pressure π_t (—P—). (b) Vertical velocity ($i=3$) with terms due to w variance (—WW—), u/w covariance (—UW—) and turbulence pressure π_t (—P—).

$$B = 0.0041\, w_*^3 h_{\rho *}/h_*$$

$$\downarrow$$

$$\boxed{\frac{1}{2}\left\langle \langle w' \rangle_{p,t}^2 \right\rangle_h} \quad \xrightarrow{\begin{array}{rl} P_b = & 0.49 \\ P_t = & -0.24 \end{array}} \quad \boxed{\frac{1}{2}\left\langle \langle u' \rangle_{p,t}^2 \right\rangle_h}$$

$$\downarrow \qquad\qquad\qquad\qquad \downarrow$$

$$\begin{array}{rl} T_{31} = & 0.27 \\ T_{33} = & 0.39 \\ S = & 0.07 \end{array} \qquad\qquad \begin{array}{rl} T_{11} = & 0.32 \\ T_{13} = & -0.12 \\ S = & 0.07 \end{array}$$

Figure 5.20. Vertically integrated kinetic energy budget for the time-averaged circulation in Set G. Terms are as defined in Figure 5.15.

because there is not such a pronounced near-surface maximum in the u variance, nor is the inflow into the base of the updraught so shallow or so vigorous.

Figure 5.21 shows the $\langle u_i' \rangle_{p,t}$ tendencies for Set H ($\lambda_p = 4500\,\mathrm{m}$, $u_0 = 0\,\mathrm{m\,s^{-1}}$). As one might expect from the form of the temperature, pressure and stress fields shown in Section 4.4, the tendency fields are more complicated than they were in Sets F and G. Note that there is a broad similarity in shape between the (non-divergent) turbulence and circulation forces. This is not surprising given that the same entity—a quasi-two-dimensional updraught meandering about the axis of maximum heat flux (Section 4.6.6)—is involved in both turbulence/turbulence advection and circulation/circulation advection. To digress for a moment: The surface heat-flux perturbation in Set H has "trapped" a convective eddy in a preferred location such that it makes a strong contribution to the phase-average statistics. One can study the dynamics of the eddy in terms of the phase averages. Unfortunately such an exercise has limited relevance to the dynamics of eddies in the *horizontally homogeneous* boundary layer because (as is clear from the horizontal-average statistics described in Section 4.6.5) the surface perturbation changes the eddy structure significantly.

Returning to the non-divergent $\langle u_i' \rangle_{p,t}$ tendencies, the horizontal component of the buoyancy force is directed towards the $\hat{x} = 0$ axis near the surface and away from it in the middle and upper boundary layer, with maxima and minima near the axis. As in Set F the horizontal velocity (Figure 4.26a) is generally in the same sense as the horizontal component of the buoyancy (which suggests the unremarkable conclusion that the non-divergent buoyancy force is in some sense *driving* the horizontal velocity) but the height at which the buoyancy changes from being horizontally convergent to horizontally divergent at the axis ($z = 0.3h_*$) is lower than the height of the corresponding transition in the velocity ($z = 0.5h_*$).

The vertical component of the (non-divergent) buoyancy has three maxima and one minimum, in roughly the same positions as the extrema in the temperature field (Figure 4.26c) but different in magnitude and shape. There is a maximum at $\hat{x} = 0$ in the lower and middle boundary layer, a minimum centred near $\hat{x} = 0$, $z = h_*$ with

(a)

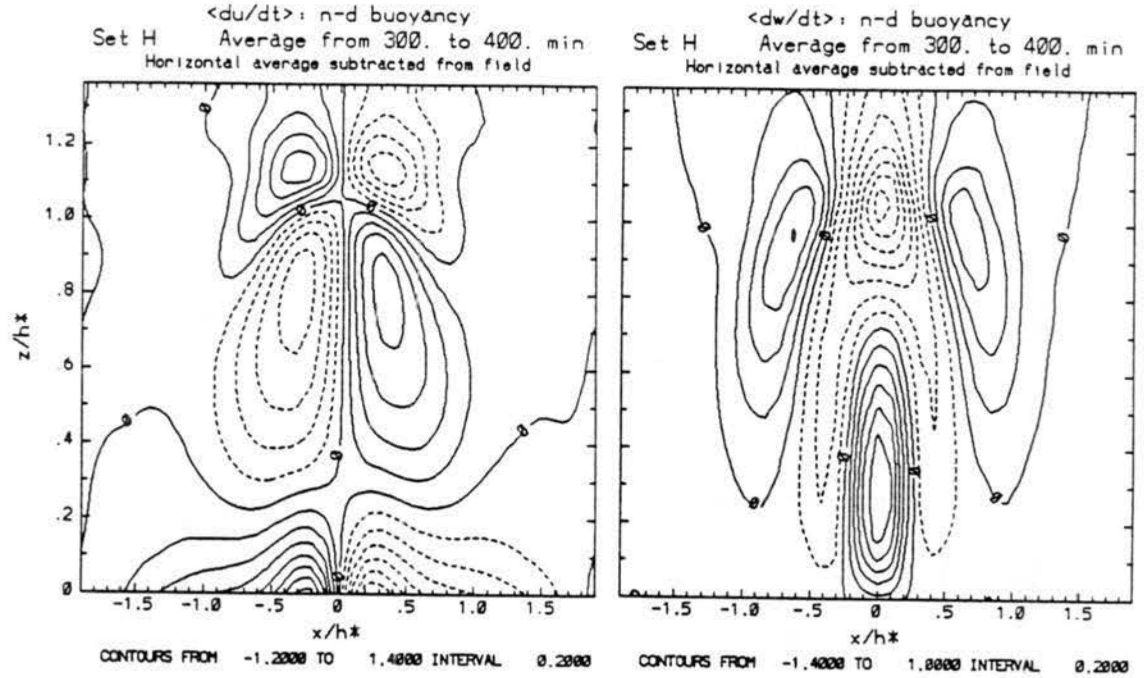

(b)

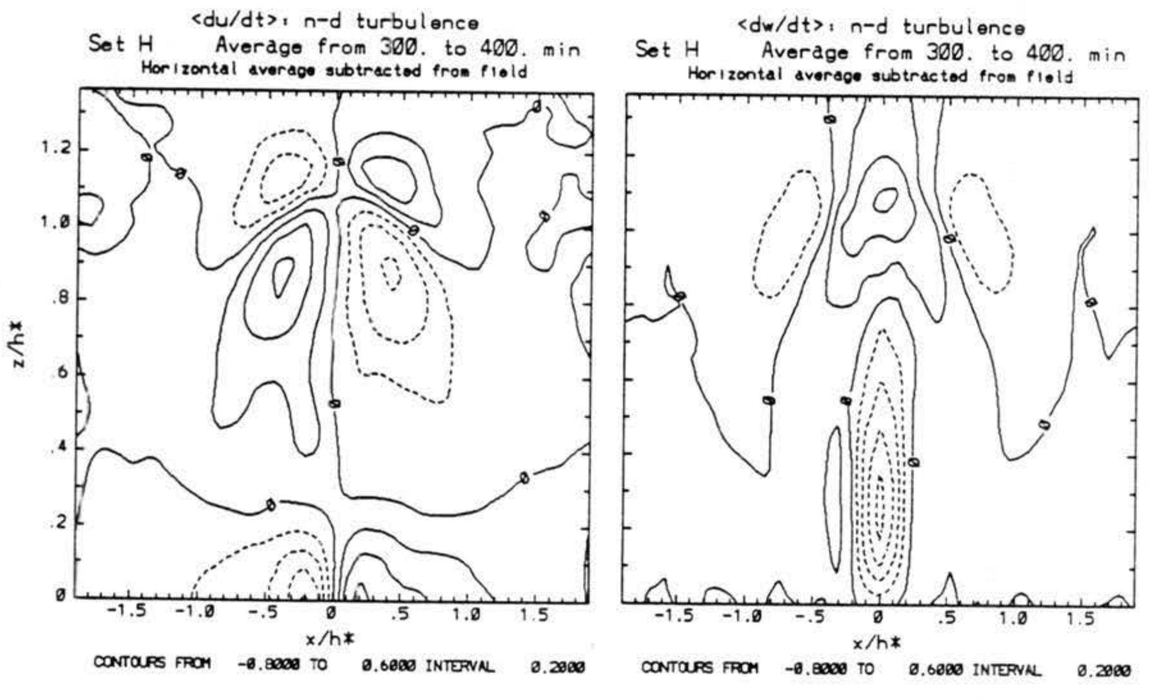

Figure 5.21. Non-divergent tendencies in circulation velocity $\langle u_i' \rangle_{p,t}$ for Set H. The format is similar to that used in figure 5.11. (a) Buoyancy. (b) Turbulence. (c) Circulation. All contour intervals $0.2w_*^2/h_*$.

Continued on following pages.

(c)

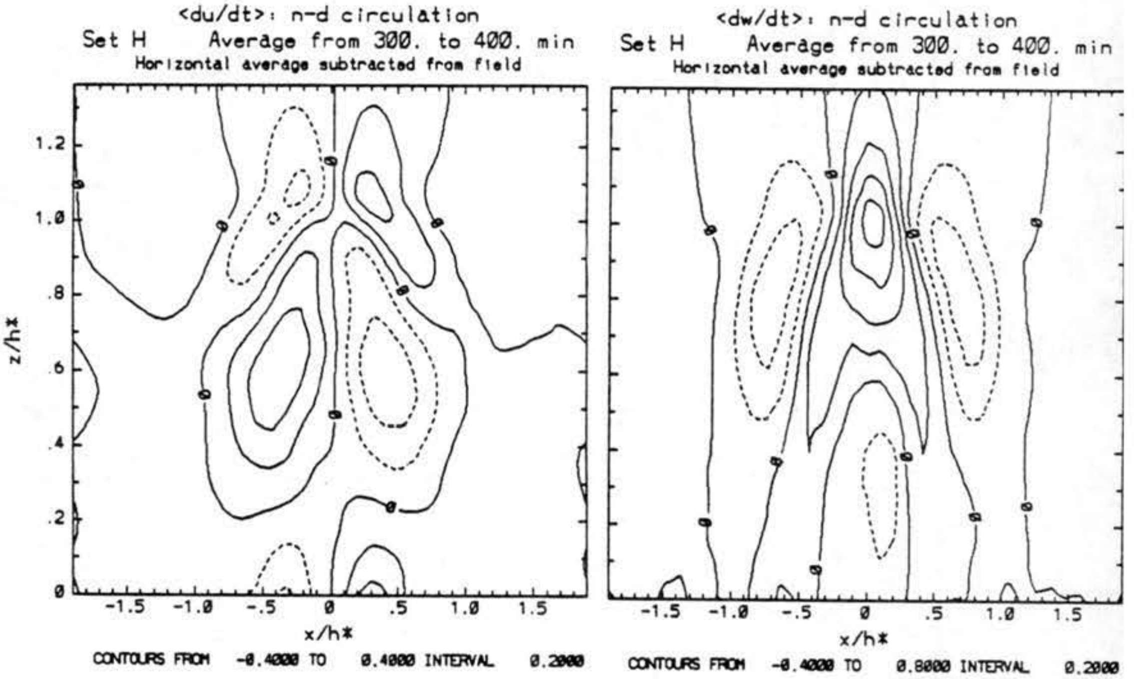

Figure 5.21 (continued).

negative lobes extending down on either side of the maximum below, and a pair of maxima centred at $\hat{x}=\pm0.17\lambda_p$, $z=h_*$. The first of the maxima is quite narrow (width$=$ $0.5h_*=0.13\lambda_p$) and is associated with the narrow region of large $\langle\theta'\rangle_{p,t}$ along the centre of the mean updraught. On either side of this region, $\langle\theta'\rangle_{p,t}$ is still positive but the (non-divergent) buoyancy force is directed downwards because of the vertical gradient in buoyancy pressure (Figure 4.27b). The mean updraught has a width of approximately $1.0h_*$ ($0.25\lambda_p$ and along its margins ascent is driven (mainly) by turbulence. At the top of the mean updraught, upward motion along the axis penetrates up to $z=1.1h_*$ and is maintained against the negative buoyancy by the turbulence and circulation tendencies.

It is interesting to consider the balance of forces maintaining the negative vertical velocity in the downdraughts flanking the mean updraught in the upper boundary layer. These regions are manifestations of the downdraughts found in the instantaneous cross-sections (Figure 4.32e) on each side of the central updraught. Such downdraughts are also evident in the vicinity of the updraughts in the cross-sections from the horizontally homogeneous Run A (Figure 3.2c), so—notwithstanding the caution a few paragraphs above—there is an opportunity to investigate a ubiquitous feature of boundary-layer convection while it is "trapped" in the phase-time average fields. Consider the minimum in $\langle w'\rangle_{p,t}$ to the right of the updraught, at $\hat{x}=0.65h_*=0.17\lambda_p$, $z=0.7h_*$. This point is near zero contours in the non-divergent buoyancy, tubulence and circulation tendencies. To the left of the maximum the buoyancy tendency is negative and to the right it is positive, and the other two tendencies are opposite in sign to the buoyancy, with the circulation tendency being the larger of the two. In the temperature budget (Figure 5.6) there is warming by circulation/horizontal-average interaction and cooling by circulation/circulation interaction. Let us ignore the turbulence to a first approximation and follow a hypothetical parcel moving with the mean circulation, beginning to the left of the $\langle w'\rangle_{p,t}$ minimum. The parcel is initially in a region where the vertical component of the non-divergent buoyancy force is negative. Since there is strong horizontal outflow ($\langle u'\rangle_{p,t}\approx0.5w_*$) it accelerates downwards through the stable horizontal-average temperature gradient until the buoyancy perturbation changes sign. At that point (a proximately) the vertical velocity reaches a minimum. The argument is complicated b the need to consider the components of the vertical pressure-gradient force (which ha been examined but are not shown) but basically the downdraught is a response to th negative temperature perturbation in air leaving the mean updraught.

In Figure 5.22 the buoyancy and π_b-gradient terms in the $\langle\langle w'\rangle_{p,t}^2\rangle_h/2$ budget a compared. The ratio A_c varies smoothly from approximately 1.0 near the surface to 0. at $z=h_*$, and is badly behaved only in a shallow layer near the zero-crossings at $z=0.7h$. The ratio based on the vertical integrals is 0.86, which is substantially larger than th corresponding values (0.45 to 0.50) for the simulations with $\lambda_p=1500\,\mathrm{m}$. The increase i to be expected with a decrease in the aspect ratio.

Figure 5.23 shows profiles of the non-divergent terms in the $\langle\langle u_i'\rangle_{p,t}^2\rangle_h/2$ budgets. Th buoyancy term in $\langle\langle u'\rangle_{p,t}^2\rangle_h/2$ has maxima near the surface and in the upper boundar layer, as in Set F and Set G, and it is opposed by turbulence, but the circulation ter is now clearly non-zero, though still smaller than buoyancy or turbulence. The vertic integral of the circulation term is negative, which implies intercomponent transfer fro the horizontal to the vertical by the π_c-gradient force. In the $\langle\langle w'\rangle_{p,t}^2\rangle_h/2$ budget th buoyancy term is positive in the lower boundary layer and negative in the upper boundar layer, as in the previous case, but the negative area is now almost as large as the positiv area owing to the large, negative buoyancy perturbations in the upper part of the mea updraught. Turbulence remains the largest sink term in the lower boundary layer, bu in the upper boundary layer the largest source is the circulation term. The budget fo kinetic energy $\langle\langle u_i'\rangle_{p,t}^2\rangle_h/2$ has the buoyancy term positive up to $z=h_*$, the turbulenc term negative and the circulation transporting energy from the lower boundary layer t the upper boundary layer.

The turbulence terms are decomposed in Figure 5.24. The u variance term i $\langle\langle u'\rangle_{p,t}^2\rangle_h/2$ is negative near the surface as usual—because of the maximum in u var ance at the base of the circulation updraught (Figure 4.29a)—and small, but mostl negative elsewhere. The u/w covariance term is now a sink near the surface and in th

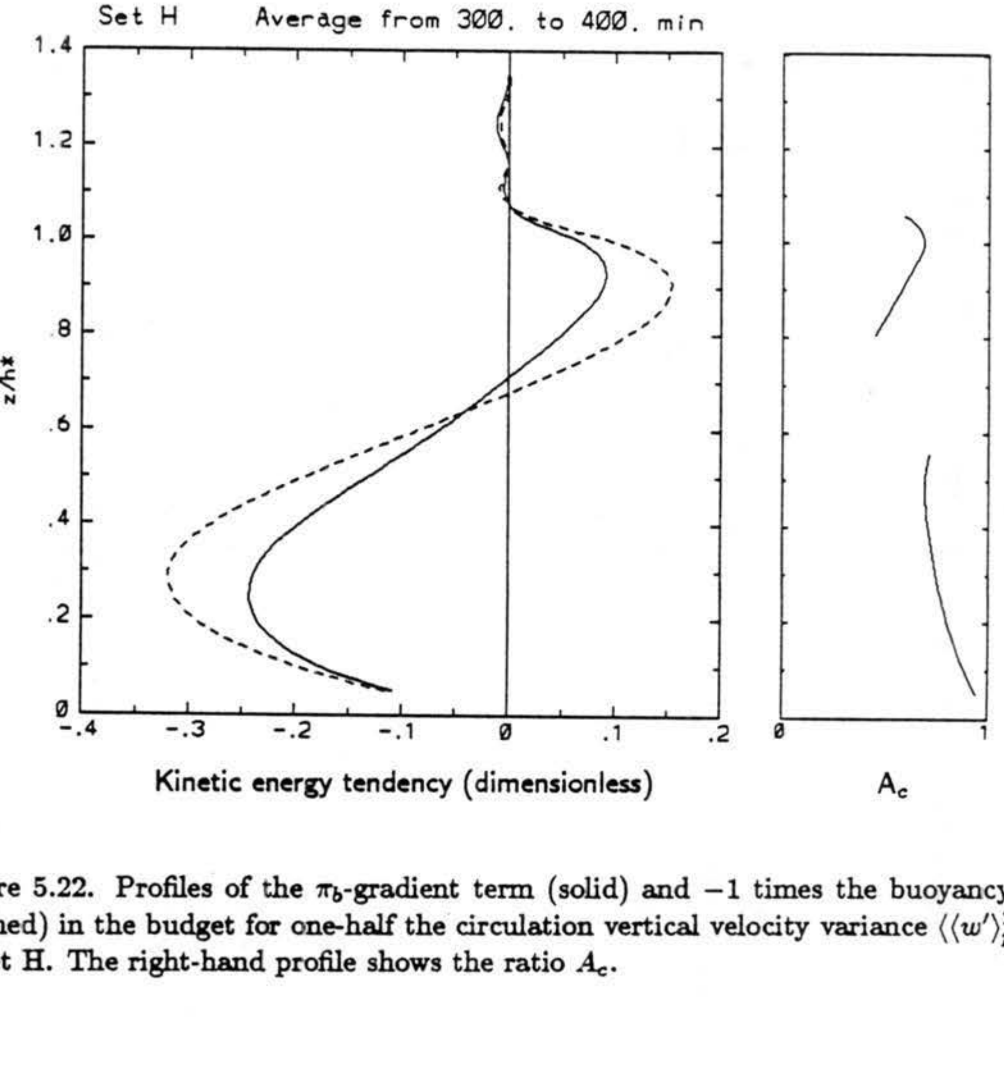

Figure 5.22. Profiles of the π_b-gradient term (solid) and -1 times the buoyancy term (dashed) in the budget for one-half the circulation vertical velocity variance $\langle\langle w'\rangle^2_{p,t}\rangle_h/2$ in Set H. The right-hand profile shows the ratio A_c.

(a) $\frac{1}{2}\frac{\partial}{\partial t}\left\langle \langle u' \rangle_{p,t}^2 \right\rangle_h$:

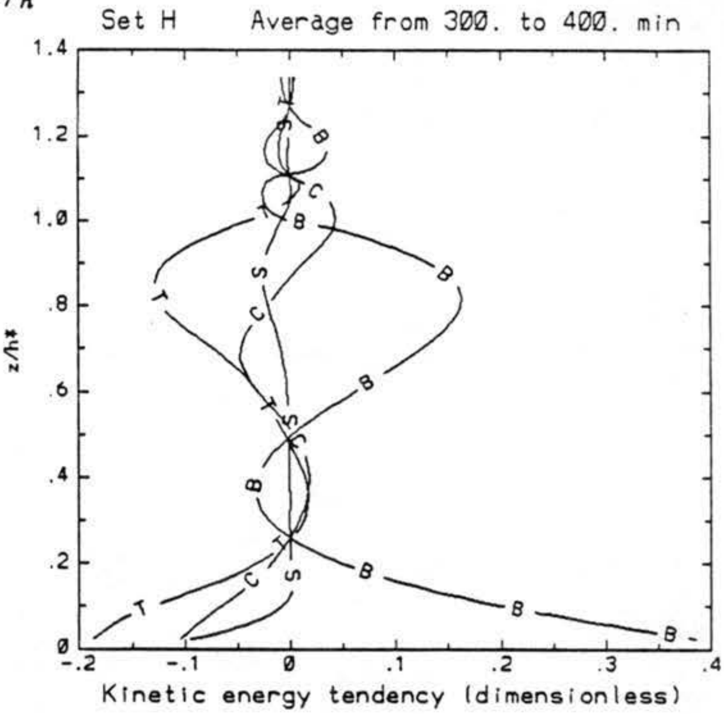

(b) $\frac{1}{2}\frac{\partial}{\partial t}\left\langle \langle w' \rangle_{p,t}^2 \right\rangle_h$:

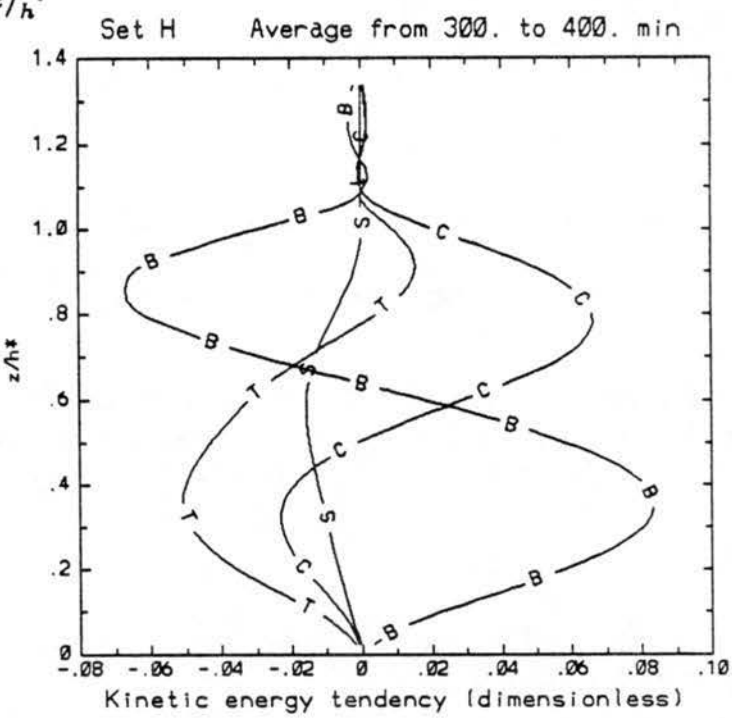

Figure 5.23. Profiles of non-divergent terms in the budgets for circulation kinetic energ $\langle\langle u_i' \rangle_{p,t}^2\rangle_h/2$ in Set H: (a) $i=1$, (b) $i=3$ and (c) sum. The terms are buoyancy (—B— turbulence (—T—), circulation (—C—) and subgrid (—S—).

Continued on following pag

(c) $\frac{1}{2}\frac{\partial}{\partial t}\left\langle \langle u' \rangle_{p,t}^2 + \langle w' \rangle_{p,t}^2 \right\rangle_h$:

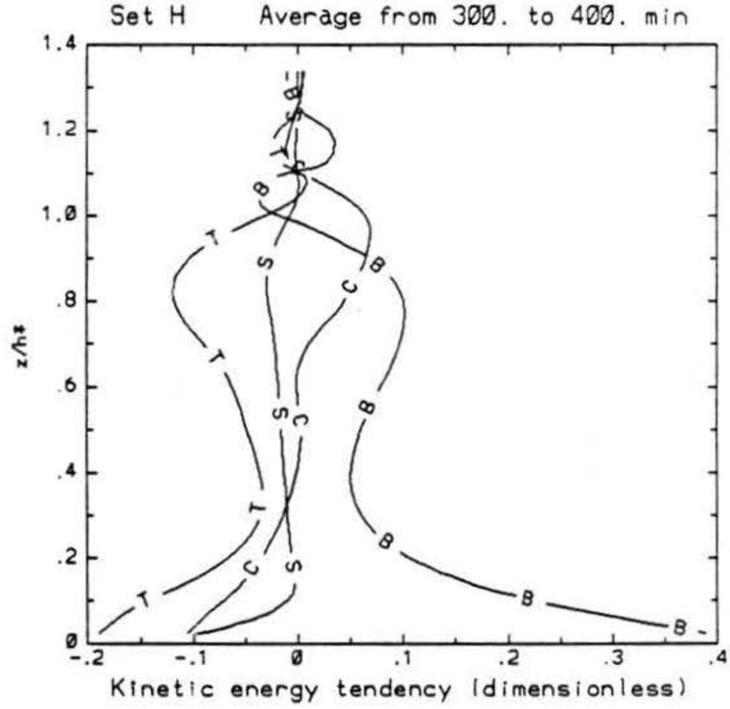

Figure 5.23 (continued).

(a) $\frac{1}{2}\frac{\partial}{\partial t}\left\langle \langle u' \rangle_{p,t}^2 \right\rangle_h$:

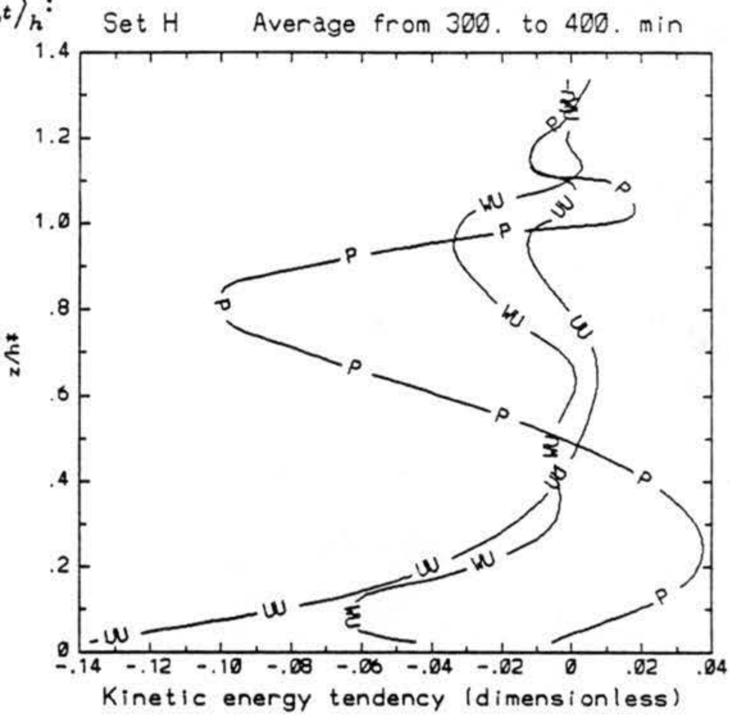

(b) $\frac{1}{2}\frac{\partial}{\partial t}\left\langle \langle w' \rangle_{p,t}^2 \right\rangle_h$:

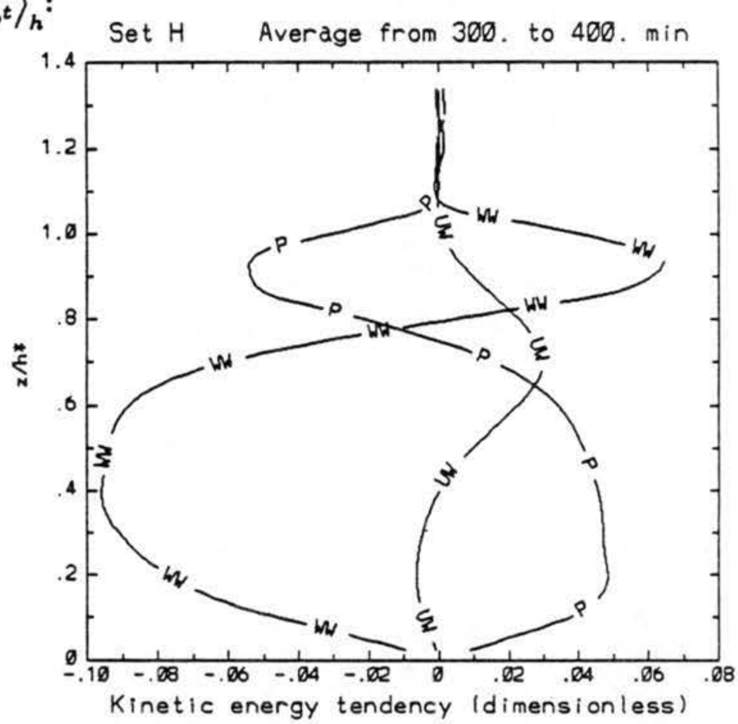

Figure 5.24. Decomposition of the non-divergent turbulence terms in the budgets f one-half the circulation velocity variances $\langle\langle u_i' \rangle_{p,t}^2\rangle_h/2$ in Set H. (a) Horizontal veloci ($i=1$) with terms due to u variance (—UU—), u/w covariance (—WU—) and turbulen pressure π_t (—P—). (b) Vertical velocity ($i=3$) with terms due to w variance (—WW– u/w covariance (—UW—) and turbulence pressure π_t (—P—).

upper boundary layer, however, whereas in previous cases it was generally a source. The reason is that the u/w covariance (Figure 4.29d) is positive in (most) of the region to the left of the circulation updraught, whereas in the simulations with smaller λ_p it was negative. (It will be argued below in connection with Set I that a change of this sort is to be expected as the aspect ratio of the circulation decreases.) The pressure term is positive in the lower boundary layer and negative in the upper boundary layer because of the turbulence pressure minimum throughout most of the depth of the boundary layer at $\hat{x} = 0$ (Figure 4.27c). In the $\langle\langle w'\rangle^2_{p,t}\rangle_h/2$ budget the w variance term is negative below $z = 0.8h_*$, which is the height of the maximum in w variance (Figure 4.29c), and positive above there. The negative area greatly exceeds the positive area (presumably because the $\langle w'\rangle_{p,t}$ maximum is well below the variance maximum). The pressure term is generally opposed to the w variance term, as has been observed before. The u/w covariance term is generally a source, for the reason outlined above.

The vertically integrated circulation kinetic energy budget is described in Figure 5.25. As mentioned previously, a large fraction (86%) of the net buoyancy production is transferred directly to $\langle\langle u'\rangle^2_{p,t}\rangle_h/2$ by π_b-gradient forces, but the π_t- and π_c-gradient forces transfer much of that (30% of buoyancy production) back to $\langle\langle w'\rangle^2_{p,t}\rangle_h/2$, which therefore still accounts for a substantial fraction of the kinetic energy transfer to the turbulence. The largest of the turbulent dissipation terms is T_{33} (43% of buoyancy production) which, as indicated above, extracts energy from the $\langle w'\rangle_{p,t}$ field in the strong circulation updraught below the w-variance maximum. The u variance term T_{11} which has been significant in the previous cases, is also a significant sink here (23% of buoyancy production). The u/w covariance terms are a source for $\langle\langle w'\rangle^2_{p,t}\rangle_h/2$, but a sink for $\langle\langle u'\rangle^2_{p,t}\rangle_h/2$ respectively (the opposite of earlier cases). Their sum, $T_{31} + T_{13}$, accounts for 13% of buoyancy production.

The dissipation time scale is

$$\frac{0.117\, w_*^2 h_{\rho *}}{0.106\, w_*^3 h_{\rho *}/h_*} = 1.10\, h_*/w_*,$$

$$B = 0.106\, w_*^3 h_{\rho *}/h_*$$

$$\frac{1}{2}\left\langle \langle w' \rangle_{p,t}^2 \right\rangle_h \xrightarrow{\begin{array}{l} P_b = 0.86 \\ P_t = -0.15 \\ P_c = -0.14 \end{array}} \frac{1}{2}\left\langle \langle u' \rangle_{p,t}^2 \right\rangle_h$$

$$\begin{aligned} T_{31} &= -0.08 \\ T_{33} &= 0.43 \\ S &= 0.08 \end{aligned} \qquad\qquad \begin{aligned} T_{11} &= 0.23 \\ T_{13} &= 0.21 \\ S &= 0.12 \end{aligned}$$

Figure 5.25. Vertically integrated kinetic energy budget for the time-averaged circulation in Set H. Terms are as defined in Figure 5.15, with the addition of circulation-pressure (P_c).

which is substantially larger than the corresponding time scales for the earlier simulations: $0.32\,h_*/w_*$ for Set F and $0.46\,h_*/w_*$ for Set G.

In Set I ($\lambda_p = 4500\,\mathrm{m}$, $u_0 = 1\,\mathrm{m\,s^{-1}}$) the fields of the non-divergent terms in the $\langle u_i' \rangle_{p,t}$ budget are qualitatively similar to those of Set G. For the sake of brevity they will not be shown, but their contributions to the kinetic energy budget for the time-averaged circulation will be described. Figure 5.26 shows the buoyancy and π_b-gradient terms in the $\langle\langle w' \rangle_{p,t}^2\rangle_h/2$ budget. The ratio between them is everywhere very close to 0.9, consistently larger than it was in any of the previous cases. The ratio based on the vertical integrals (Table 4.6) is 0.89, only slightly larger than the value of 0.86 calculated for Set H—as mentioned before the ratio of the vertical integrals can sometimes be misleading.

Figure 5.27 shows profiles of the non-divergent terms in the circulation kinetic energy budgets. In $\langle\langle u' \rangle_{p,t}^2\rangle_h/2$ the buoyancy term is positive (except for a shallow layer in the middle of the boundary layer) with maxima near the surface and in the upper boundary layer, the turbulence term is negative and the subgrid term is significant only right next to the surface. In $\langle\langle w' \rangle_{p,t}^2\rangle_h/2$ the buoyancy term is positive in the lower and middle boundary layer and negative in the upper boundary layer, and it is generally opposed by turbulence. The circulation terms are larger than than they are in Set F and Set G, but much smaller than in Set H. Note also that the $\langle\langle w' \rangle_{p,t}^2\rangle_h/2$ budget terms are typically smaller than the $\langle\langle u' \rangle_{p,t}^2\rangle_h/2$ terms by almost an order of magnitude. The disparity is larger than in Set H or the previous cases; it arises because the vertical component of each force is nearly cancelled by the vertical gradient in the pressure it induces.

Figure 5.28 shows the contributions to the non-divergent turbulence terms. In the $\langle\langle u' \rangle_{p,t}^2\rangle_h/2$ budget the terms are all similar to what was seen with Set H, although the negative peak in the π_t-gradient term in the upper boundary layer is now much less pronounced. Note again that the u/w covariance term is negative near the surface and in the upper boundary layer, like Set H, but unlike the cases with $\lambda_p = 1500\,\mathrm{m}$. From the circulation u field (Figure 4.34a) and the u/w covariance field (Figure 4.36d) one can see (a little more clearly than in Set H) that this occurs because the u/w covariance is transporting horizontal momentum upwards from the region of horizontal inflow on the

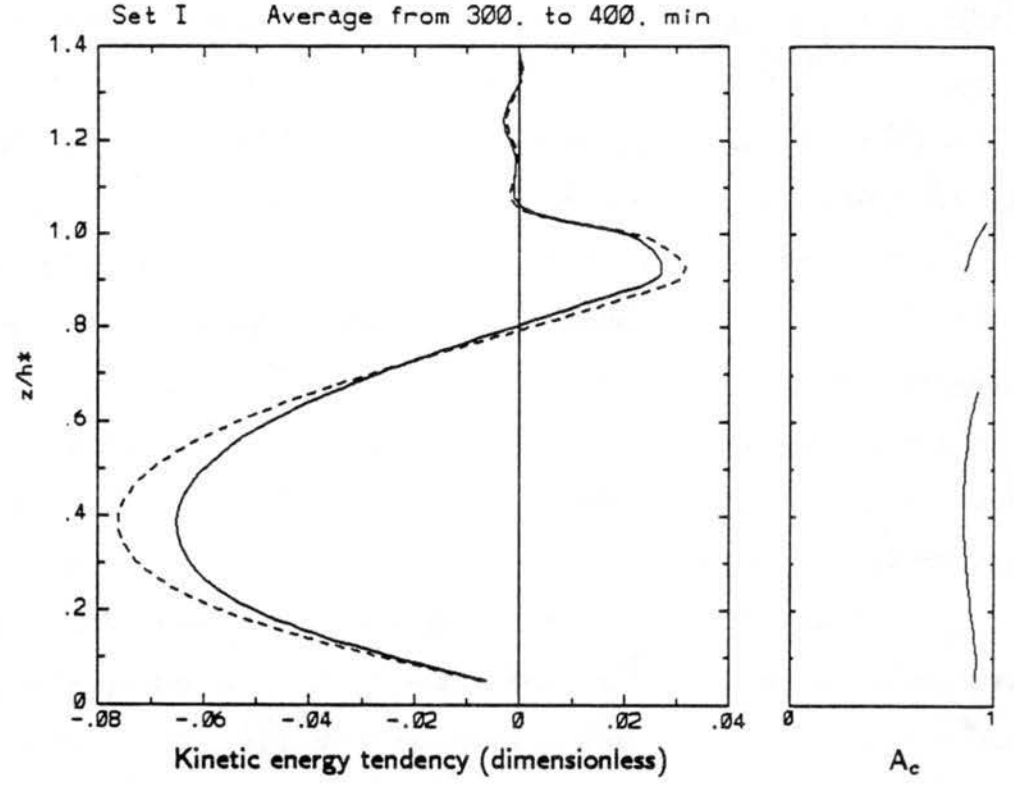

Figure 5.26. Profiles of the π_b-gradient term (solid) and -1 times the buoyancy term (dashed) in the budget for one-half the circulation vertical velocity variance $\langle\langle w'\rangle^2_{p,t}\rangle_h/2$ in Set I. The right-hand profile shows the ratio A_c.

(a) $\frac{1}{2}\frac{\partial}{\partial t}\left\langle \langle u' \rangle_{p,t}^2 \right\rangle_h$:

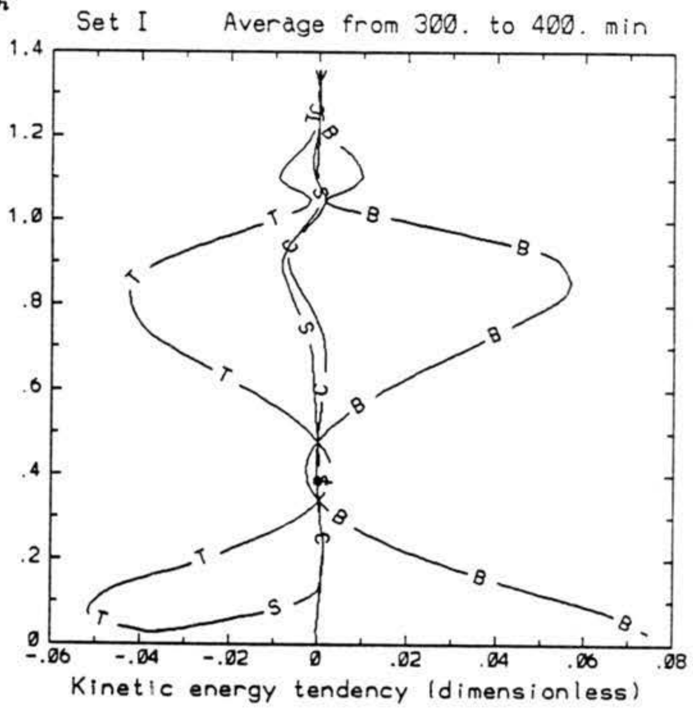

(b) $\frac{1}{2}\frac{\partial}{\partial t}\left\langle \langle w' \rangle_{p,t}^2 \right\rangle_h$:

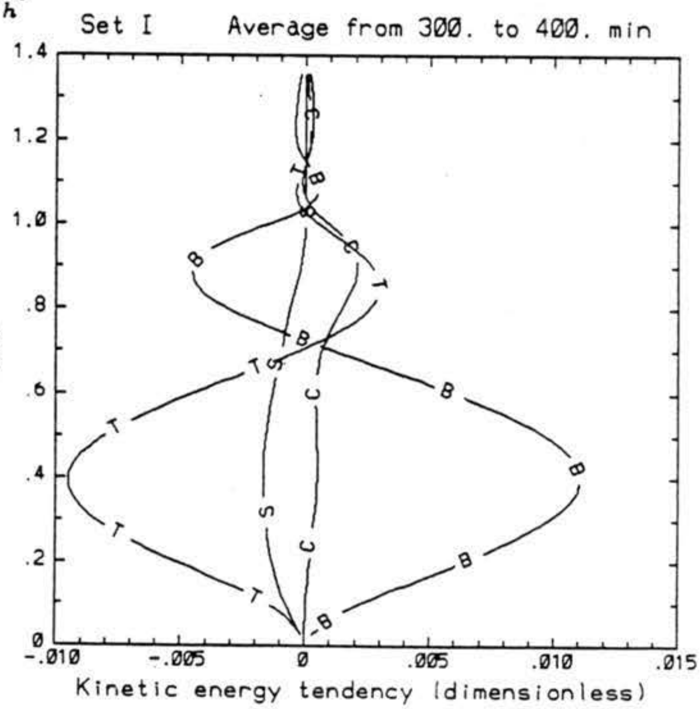

Figure 5.27. Profiles of non-divergent terms in the budgets for circulation kinetic energy $\langle \langle u_i' \rangle_{p,t}^2 \rangle_h / 2$ in Set I: (a) $i = 1$, (b) $i = 3$ and (c) sum. The terms are buoyancy (—B—), turbulence (—T—), circulation (—C—) and subgrid (—S—).

Continued on following page.

(c) $\frac{1}{2}\frac{\partial}{\partial t}\left\langle \langle u' \rangle^2_{p,t} + \langle w' \rangle^2_{p,t} \right\rangle_h$:

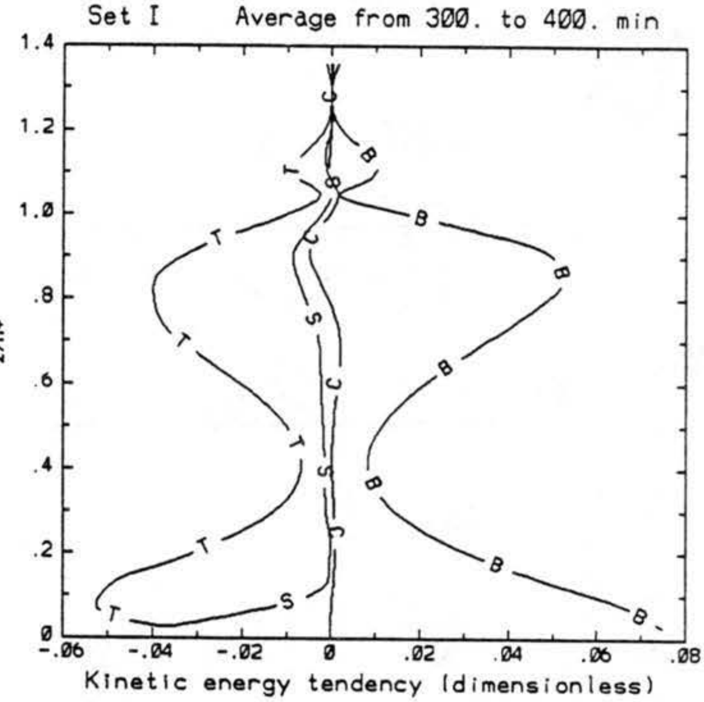

Figure 5.27 (continued).

(a) $\frac{1}{2}\frac{\partial}{\partial t}\left\langle \langle u' \rangle_{p,t}^2 \right\rangle_h$:

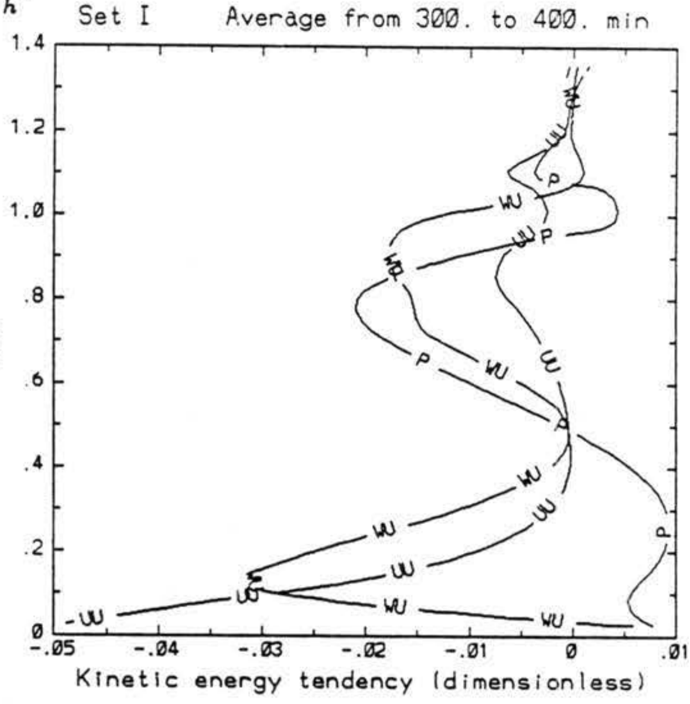

(b) $\frac{1}{2}\frac{\partial}{\partial t}\left\langle \langle w' \rangle_{p,t}^2 \right\rangle_h$:

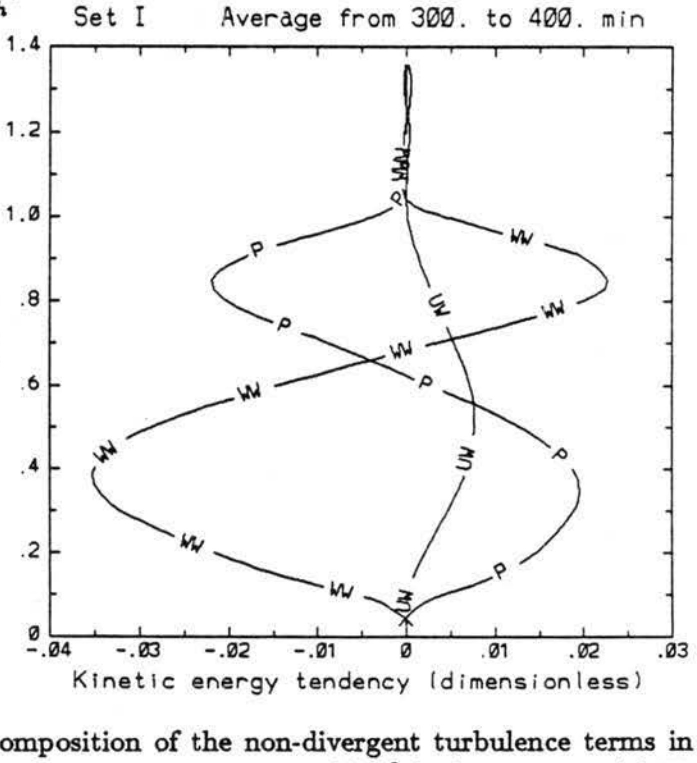

Figure 5.28. Decomposition of the non-divergent turbulence terms in the budgets for one-half the circulation velocity variances $\langle \langle u_i' \rangle_{p,t}^2 \rangle_h / 2$ in Set I. (a) Horizontal velocity ($i=1$) with terms due to u variance (—UU—), u/w covariance (—WU—) and turbulence pressure π_t (—P—). (b) Vertical velocity ($i=3$) with terms due to w variance (—WW—), u/w covariance (—UW—) and turbulence pressure π_t (—P—).

left of the circulation updraught to the region of outflow above (and vice versa to the right of the updraught). In the $\langle\langle w'\rangle_{p,t}^2\rangle_h/2$ budget there is also a strong similarity to Set H, but now the w variance term crosses zero at a lower level and its positive and negative areas are more nearly equal.

The vertically integrated circulation kinetic energy budget is described in Figure 5.29. As with Set H a large fraction of the buoyancy production is transferred to the horizontal by π_b-gradient forces—89% versus 86% in Set H—but the transfer back by the advection pressure (i.e., $P_t + P_c$) is now smaller—9% of buoyancy production versus 30% in Set H. Note that there is now a sink term, labelled E, standing for export of energy to the absorbing layer by buoyancy-pressure transport. It is large enough to be measurable, but still very small compared to the other terms in the budget—about 0.3% of buoyancy production. The dissipation time scale is

$$\frac{0.040\, w_*^2 h_{\rho*}}{0.034\, w_*^3 h_{\rho*}/h_*} = 1.17\, h_*/w_*,$$

which is similar to the value for Set H despite the substantially different configuration of the circulation and turbulence.

For Set J ($\lambda_p = 4500\,\mathrm{m}$, $u_0 = 2\,\mathrm{m\,s^{-1}}$) the non-divergent terms in the $\langle u_i'\rangle_{p,t}$ budget are again not shown. Figure 5.30 shows the buoyancy and π_b-gradient terms in the $\langle\langle w'\rangle_{p,t}^2\rangle_h/2$ budget. The profile of the buoyancy term differs in an important respect from all the previous cases in that it is negative below $z = 0.22h_*$, since the circulation updraught is so far downstream of the surface heat-flux maximum that it is drawing on cool air from the vicinity of the heat-flux minimum. The way in which the circulation is maintained in this region will be discussed below. The ratio A_c between the π_b-gradient and buoyancy terms is everywhere between 0.9 and 1.0. The ratio based on the vertical integrals is 0.88 (Table 4.7). Even though A_c is generally highest in Set J, the ratio of the vertical integrals, is not much different from the values found in the other two $\lambda_p = 4500\,\mathrm{m}$ cases because A_c takes its highest values where the buoyancy term is negative.

Figure 5.31 shows the non-divergent terms in the $\langle\langle u_i'\rangle_{p,t}^2\rangle_h/2$ budgets for Set J. In the $\langle\langle u'\rangle_{p,t}^2\rangle_h/2$ budget the buoyancy term near the surface ($z < 0.1h_*$) is negative

$$B = 0.034\, w_*^3 h_{\rho *}/h_*$$

$$\downarrow$$

$$\boxed{\frac{1}{2}\left\langle \langle w' \rangle_{p,t}^2 \right\rangle_h} \quad \xrightarrow{\begin{aligned} P_b &= 0.89 \\ P_t &= -0.06 \\ P_c &= -0.03 \end{aligned}} \quad \boxed{\frac{1}{2}\left\langle \langle u' \rangle_{p,t}^2 \right\rangle_h}$$

$$\downarrow \qquad\qquad\qquad\qquad\qquad\qquad \downarrow$$

$$\begin{aligned} T_{31} &= -0.12 \\ T_{33} &= 0.26 \\ S &= 0.03 \\ E &= 0.003 \end{aligned} \qquad\qquad\qquad \begin{aligned} T_{11} &= 0.29 \\ T_{13} &= 0.35 \\ S &= 0.12 \end{aligned}$$

Figure 5.29. Vertically integrated kinetic energy budget for the time-averaged circulation in Set I. Terms are as defined in Figure 5.15, with the addition of circulation pressure (P_c) and export to the absorbing layer (E).

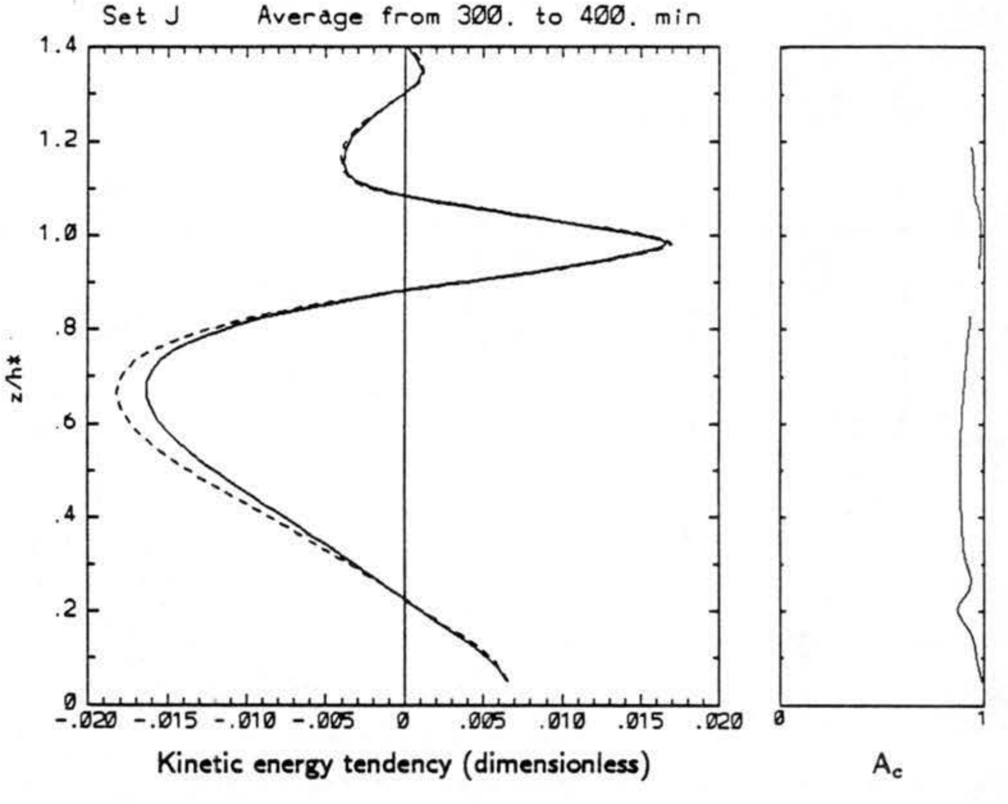

Figure 5.30. Profiles of the π_b-gradient term (solid) and -1 times the buoyancy term (dashed) in the budget for one-half the circulation vertical velocity variance $\langle \langle w' \rangle_{p,t}^2 \rangle_h / 2$ in Set J. The right-hand profile shows the ratio A_c.

(a) $\frac{1}{2}\frac{\partial}{\partial t}\left\langle\langle u'\rangle^2_{p,t}\right\rangle_h$:

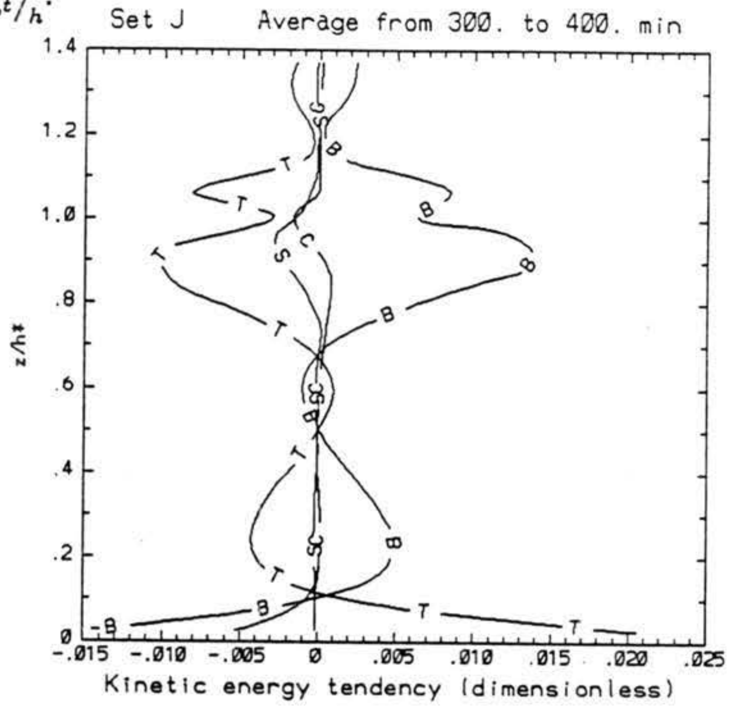

(b) $\frac{1}{2}\frac{\partial}{\partial t}\left\langle\langle w'\rangle^2_{p,t}\right\rangle_h$:

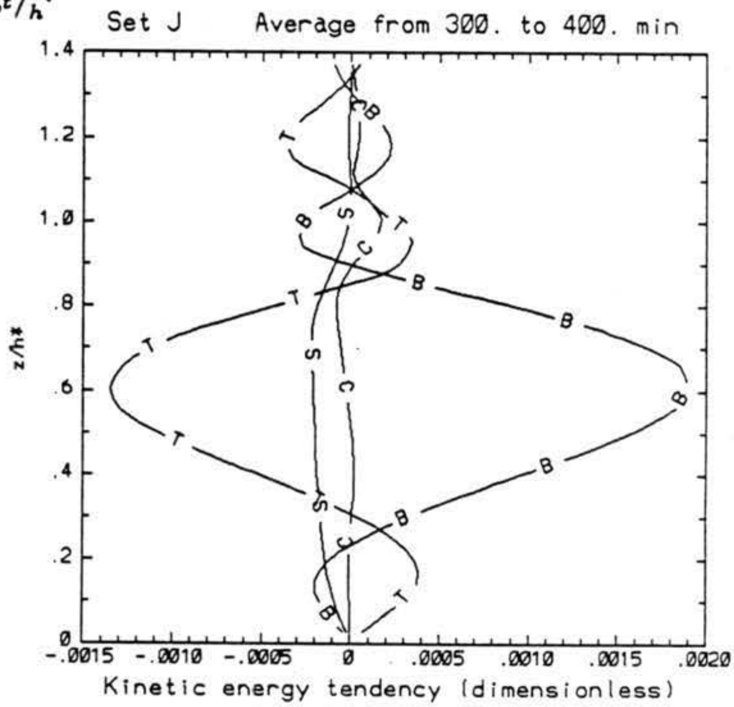

Figure 5.31. Profiles of non-divergent terms in the budgets for circulation kinetic energy $\langle\langle u_i'\rangle^2_{p,t}\rangle_h/2$ in Set J: (a) $i=1$, (b) $i=3$ and (c) sum. The terms are buoyancy (—B—), turbulence (—T—), circulation (—C—) and subgrid (—S—).

Continued on following page.

(c) $\dfrac{1}{2}\dfrac{\partial}{\partial t}\left\langle \langle u' \rangle^2_{p,t} + \langle w' \rangle^2_{p,t} \right\rangle_h$:

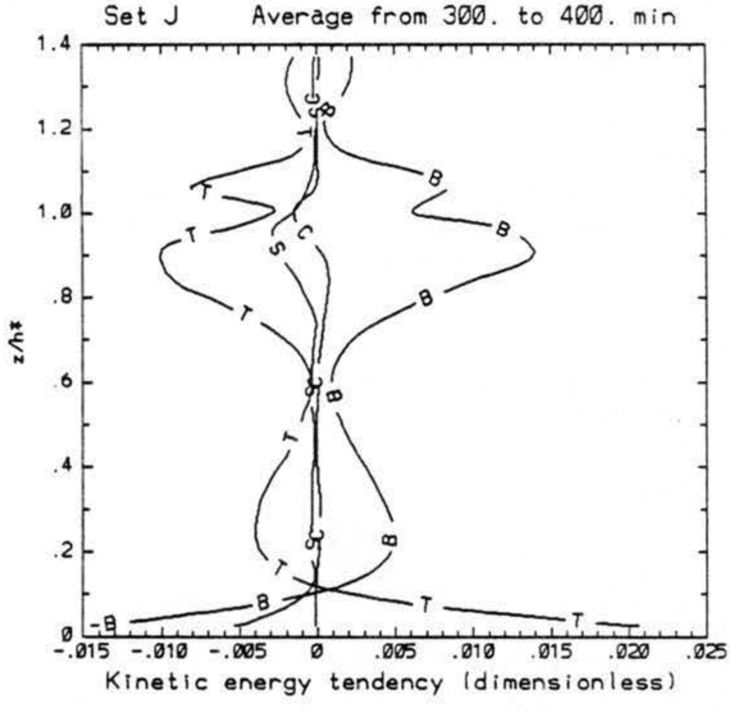

Figure 5.31 (continued).

because the maximum in $\langle u' \rangle_{p,t}$ (Figure 4.40a) is somewhat downstream of the minimum in $\langle \pi_b' \rangle_{p,t}$ (Figure 4.41b). The subgrid term is also negative near the surface, as usual, and the turbulence term is positive. The axis of the horizontal velocity maximum slopes to the left with height and the axis of the buoyancy-pressure minimum slopes to the right, so above $z = 0.12h_*$, the buoyancy term becomes positive and the budget resembles the budgets for previous cases (especially Set I). Similarly in the $\langle \langle w' \rangle_{p,t}^2 \rangle_h / 2$ budget the buoyancy term is negative near the surface and is balanced by turbulence, but above $z \approx 0.25h_*$ it changes sign.

The non-divergent turbulence terms are decomposed in Figure 5.32. The profiles are more complicated than they were in previous cases (especially the $\langle \langle u' \rangle_{p,t}^2 \rangle_h / 2$ tendency profiles), which appears to be a consequence of the way the phase-averaged velocity, pressure and stress fields (Figures 4.40, 4.41 and 4.42) slope variously to the left or to the right. Let us look at the region near the surface, where the non-divergent turbulence terms are forcing the circulation against buoyancy. In the $\langle \langle u' \rangle_{p,t}^2 \rangle_h / 2$ decomposition all the contributions are positive. As regards the u variance term and π_t-gradient term, the positive contributions arise because the surface maxima in u variance and $\langle \pi_t' \rangle_{p,t}$ are both near $\hat{x} = 0$ and therefore more or less coincident with the $\langle \pi_b' \rangle_{p,t}$ minimum; the fact that the π_b-gradient term is a net sink for $\langle \langle u' \rangle_{p,t}^2 \rangle_h / 2$ then implies that the u-variance gradient and π_t-gradient terms will be sources. In considering the u/w covariance term, compare the $\langle u' \rangle_{p,t}$ and u/w covariance fields from Set I (Figures 4.34a and 5.36d) and the present case (Figures 4.40a and 4.42d). In both cases the covariance maximum is found in the middle of the boundary layer about $0.4h_*$ $(0.1\lambda_p)$ downstream of the surface velocity maximum. In Set I the configuration resulted in a net sink for $\langle \langle u' \rangle_{p,t}^2 \rangle_h / 2$ at low levels, whereas in the present case it results in a net source. The differences between the fields that account for the different net contributions to the budget are subtle, but possibly associated with the fact that in Set J the u/w covariance maxima and minima are displaced to the right near the surface. In the $\langle \langle w' \rangle_{p,t}^2 \rangle_h / 2$ budget the fact that the non-divergent turbulence term is positive arises from a small imbalance between a positive w-variance term and a negative π_t-gradient term (just as the fact that

(a) $\frac{1}{2}\frac{\partial}{\partial t}\left\langle \langle u' \rangle_{p,t}^2 \right\rangle_h$:

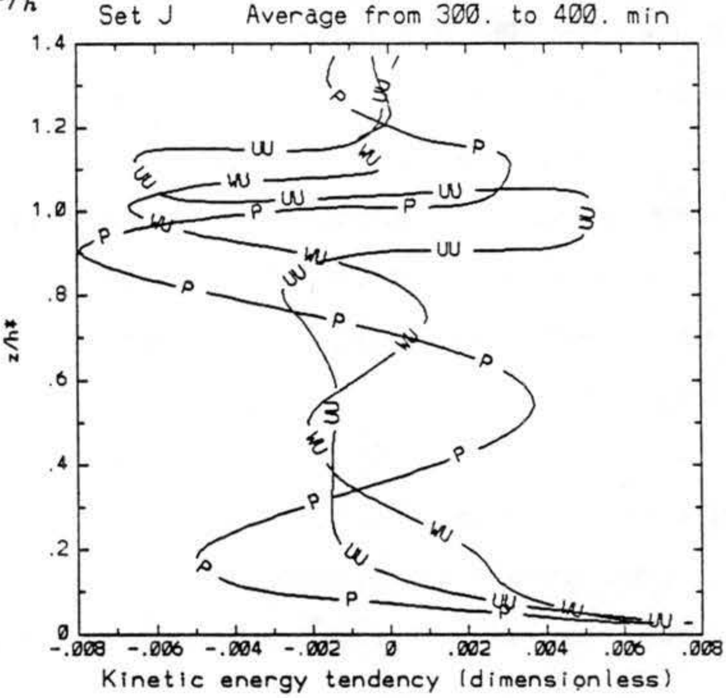

(b) $\frac{1}{2}\frac{\partial}{\partial t}\left\langle \langle w' \rangle_{p,t}^2 \right\rangle_h$:

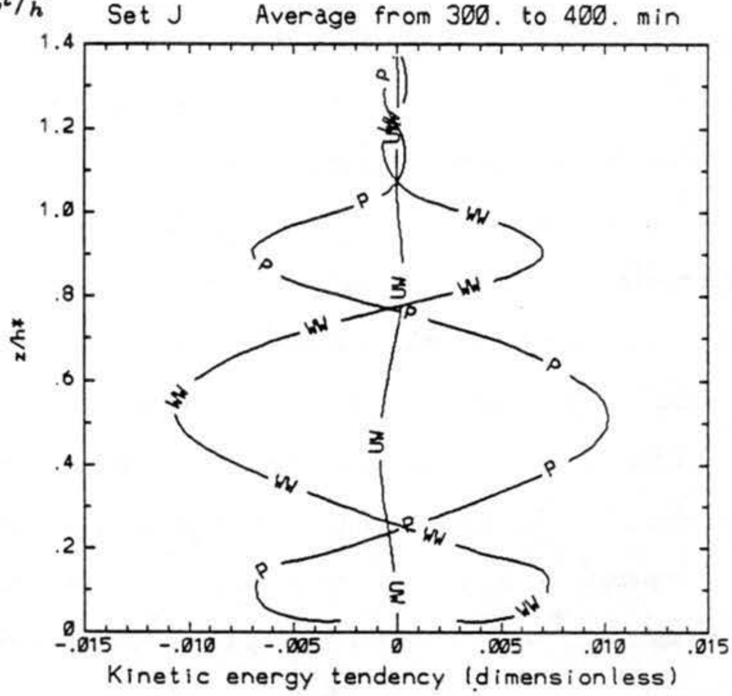

Figure 5.32. Decomposition of the non-divergent turbulence terms in the budgets for one-half the circulation velocity variances $\langle \langle u_i' \rangle_{p,t}^2 \rangle_h / 2$ in Set J. (a) Horizontal velocity ($i = 1$) with terms due to u variance (—UU—), u/w covariance (—WU—) and turbulence pressure π_t (—P—). (b) Vertical velocity ($i = 3$) with terms due to w variance (—WW—), u/w covariance (—UW—) and turbulence pressure π_t (—P—).

the non-divergent buoyancy term is negative arises from a small imbalance between a negative buoyancy term and a positive π_b-gradient term). Based on previous experience one suspects that the π_t-gradient force tends to oppose the force due to the gradient in w variance, but not completely. The w-variance term is positive—whereas it has been negative in the previous cases—because the maximum in w variance is near the surface heat-flux maximum, whereas the circulation updraught is a long way downstream.

Figure 5.33 shows the vertically integrated circulation kinetic energy budget for Set J. (Given that the profiles of the kinetic energy terms are generally more complicated than they were in previous cases, a summary in terms of vertical integrals may be less relevant.) In this case, 88% of the total buoyancy production in the vertical is opposed by the π_b-gradient force, but not all of this energy is transferred to the horizontal velocity field, since there is also export to the absorbing layer. The largest vertically integrated sink is T_{33} (w circulation, w variance). The dissipation time scale (excluding the E term) is

$$\frac{.0100\, w_*^2 h_{\rho*}}{.0039\, w_*^3 h_{\rho*}/h_*} = 2.56\, h_*/w_*,$$

which is more than twice as large as has been found in any of the previous cases. A possible explanation is that quite a large fraction of the vertically integrated kinetic energy of the circulation is accounted for by horizontal motion above $z = h_*$, in structures that have a noticeable gravity-wave character and may therefore be dissipated less efficiently.

5.3 Turbulence budgets

The present section looks at the turbulence stress budgets, and compares the effects of the non-divergent buoyancy force on the one hand, and of interaction with the time-averaged circulation on the other. (In the discussion of Set H the effect of the advection pressure is also described.) The budget for the u_i/u_j covariance is discussed in Appendix A. The relevant terms here are

$$B = 0.0051\, w_*^3 h_{\rho *}/h_*$$

$$\downarrow$$

$$\boxed{\frac{1}{2}\left\langle \langle w' \rangle_{p,t}^2 \right\rangle_h} \quad \xrightarrow{\begin{aligned} P_b &= 0.75 \\ P_t &= -0.22 \end{aligned}} \quad \boxed{\frac{1}{2}\left\langle \langle u' \rangle_{p,t}^2 \right\rangle_h}$$

$$\downarrow \qquad\qquad\qquad\qquad\qquad\qquad \downarrow$$

$$\begin{aligned} T_{31} &= 0.06 \\ T_{33} &= 0.24 \\ S &= 0.02 \\ E &= 0.14 \end{aligned} \qquad\qquad \begin{aligned} T_{11} &= 0.16 \\ T_{13} &= 0.10 \\ S &= 0.20 \end{aligned}$$

Figure 5.33. Vertically integrated kinetic energy budget for the time-averaged circulation in Set J. Terms are as defined in Figure 5.15, with the addition of export to the absorbing layer (E).

$$
\begin{aligned}
\frac{\partial}{\partial t}\left\langle (u_i')_{p,t}(u_j')_{p,t}\right\rangle_{p,t} = \; & + \delta_{j3}\frac{g}{\theta_0}\left\langle (u_i')_{p,t}(\theta')_{p,t}\right\rangle_{p,t} + \delta_{i3}\frac{g}{\theta_0}\left\langle (u_j')_{p,t}(\theta')_{p,t}\right\rangle_{p,t} \\
& - \theta_0\left\langle (u_i')_{p,t}\frac{\partial}{\partial x_j}(\pi_b')_{p,t}\right\rangle_{p,t} - \theta_0\left\langle (u_j')_{p,t}\frac{\partial}{\partial x_i}(\pi_b')_{p,t}\right\rangle_{p,t} \\
& + \cdots \\
& - \left\langle u_k'\right\rangle_{p,t}\frac{\partial}{\partial x_k}\left\langle (u_i')_{p,t}(u_j')_{p,t}\right\rangle_{p,t} \\
& - \left\langle (u_i')_{p,t}(u_k')_{p,t}\right\rangle_{p,t}\frac{\partial\langle u_j'\rangle_{p,t}}{\partial x_k} - \left\langle (u_j')_{p,t}(u_k')_{p,t}\right\rangle_{p,t}\frac{\partial\langle u_i'\rangle_{p,t}}{\partial x_k} \\
& + \cdots
\end{aligned} \tag{5.8}
$$

where i and j each takes values 1 or 3 and summation over k is implied. The first two terms are buoyancy production. They appear in the budgets for w variance and u/w covariance, where they are proportional to the vertical heat flux and horizontal heat flux, respectively. The next pair of terms (velocity/π_b-gradient covariance) appears in all the turbulent stress budgets and is the only way the buoyancy fluctuations explicitly affect the u variance field. The first of the advective terms results from advection *by* the time-averaged circulation *of* turbulent fluctuations in velocity; it takes the form of mean advection of the turbulent stress. The last two terms result from advection *by* the turbulent fluctuations *of* the circulation velocity field; they take the form of gradient production terms. It would be desirable to take account also of the pressure fluctuations generated by the interaction between the circulation and the turbulent fluctuations. It is not practicable to do so, however, for reasons that are explained in Appendix A.

Figure 5.34 shows fields of the non-divergent buoyancy term (the sum of the first four terms in Equation 5.8) and the circulation term (the sum of the last three terms in Equation 5.8) in the budgets of the u variance, w variance and the u/w covariance for Set F ($\lambda_p = 1500\,\mathrm{m}$, $u_0 = 0\,\mathrm{m\,s^{-1}}$). In the u variance budget both the (non-divergent) buoyancy force and the circulation tend to produce a low-level maximum in the region of the maximum surface heat flux. A maximum in this position is a prominent feature in the u variance field itself (Figure 4.10a) and therefore appears to be a result of both effects. In the w variance budget the maximum in the buoyancy term at $\hat{x}=0$, $z=0.2h_*$ is found just below the maximum seen in the variance at $\hat{x}=0$, $z=0.4h_*$ (Figure 4.10c). One presumes

(a)

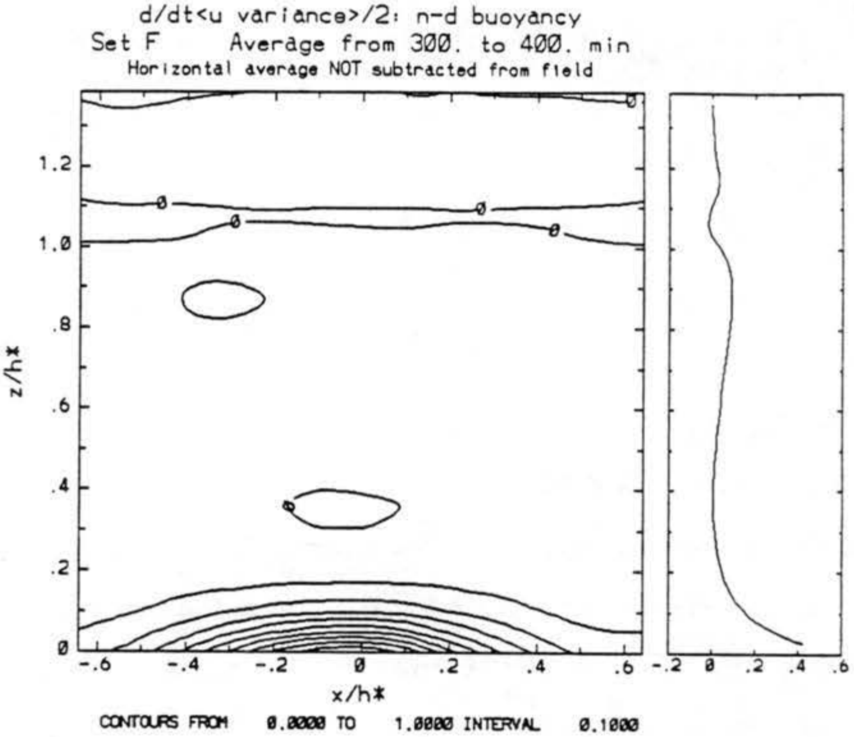

(b)

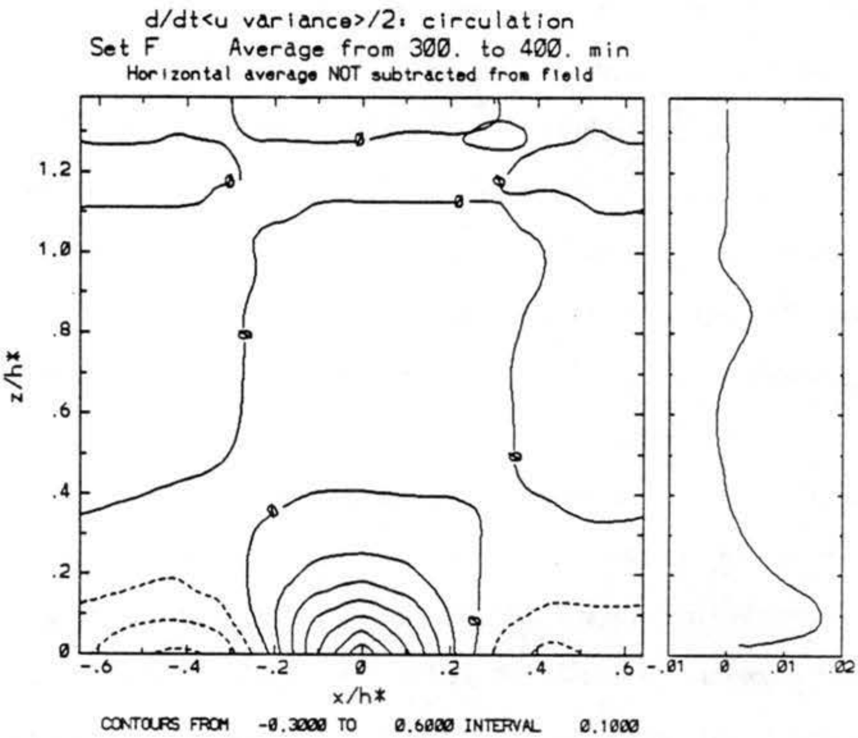

Figure 5.34. Terms in the turbulence stress budgets for Set F. (a) Buoyancy and (b) circulation terms in one-half the u variance, contour interval $0.1w_*^3/h_*$. (c) Buoyancy and (d) circulation terms in one-half the w variance, contour interval $0.1w_*^3/h_*$. (e) Buoyancy and (f) circulation terms in u/w covariance, contour interval $0.025w_*^3/h_*$.

Continued on following pages.

(c)

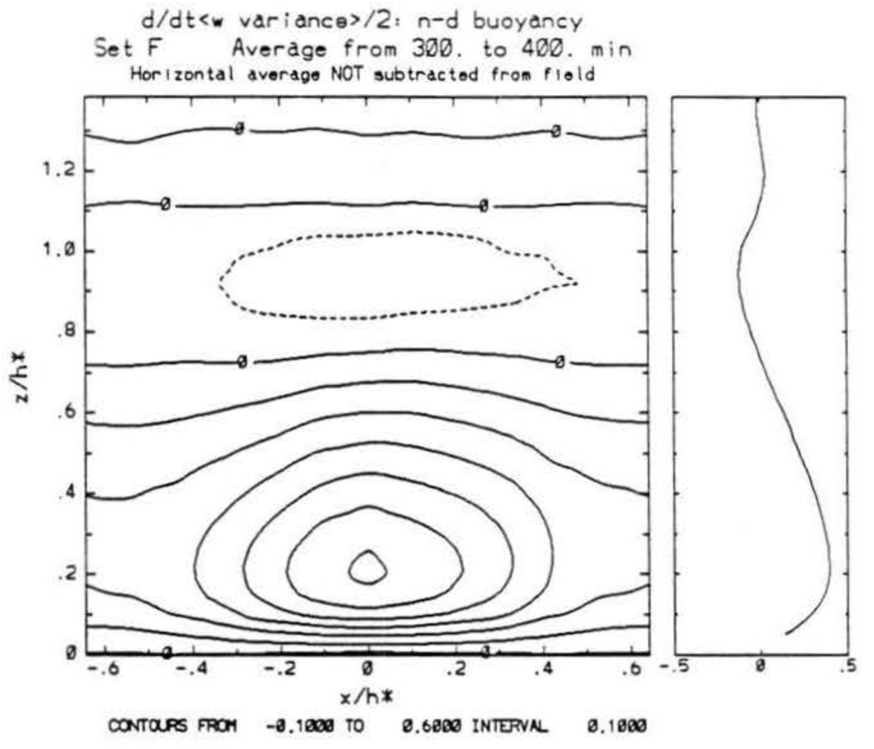

(d)

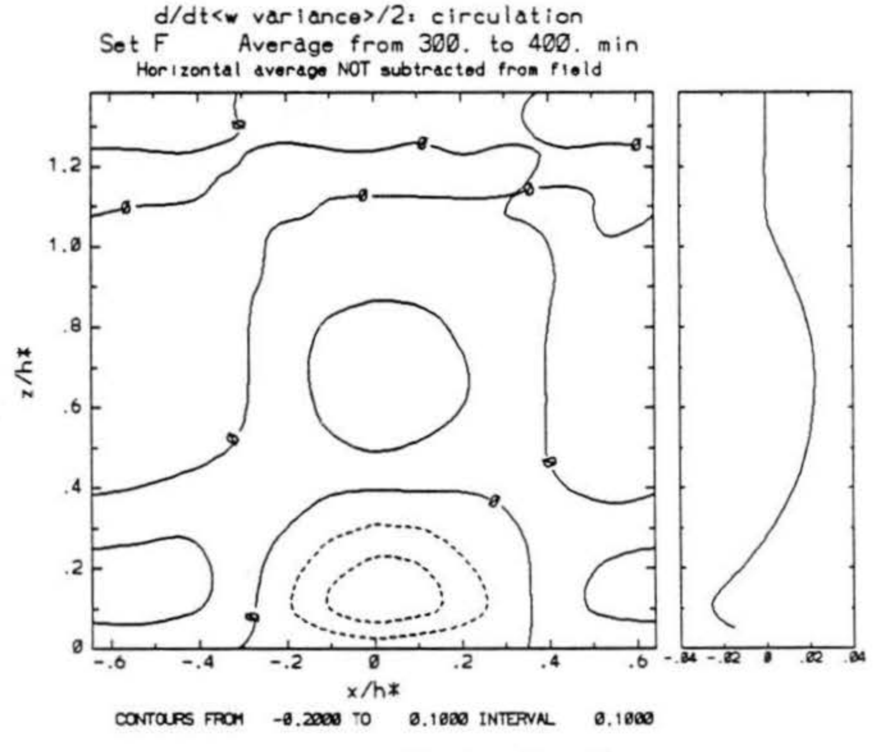

Figure 5.34 (continued).

Continued.

(e)

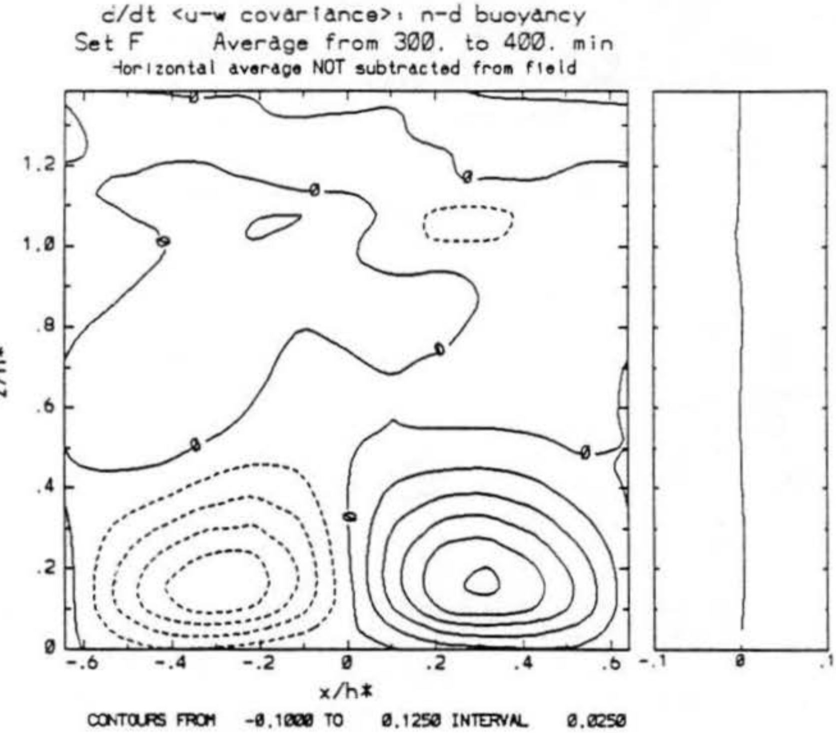

(f)

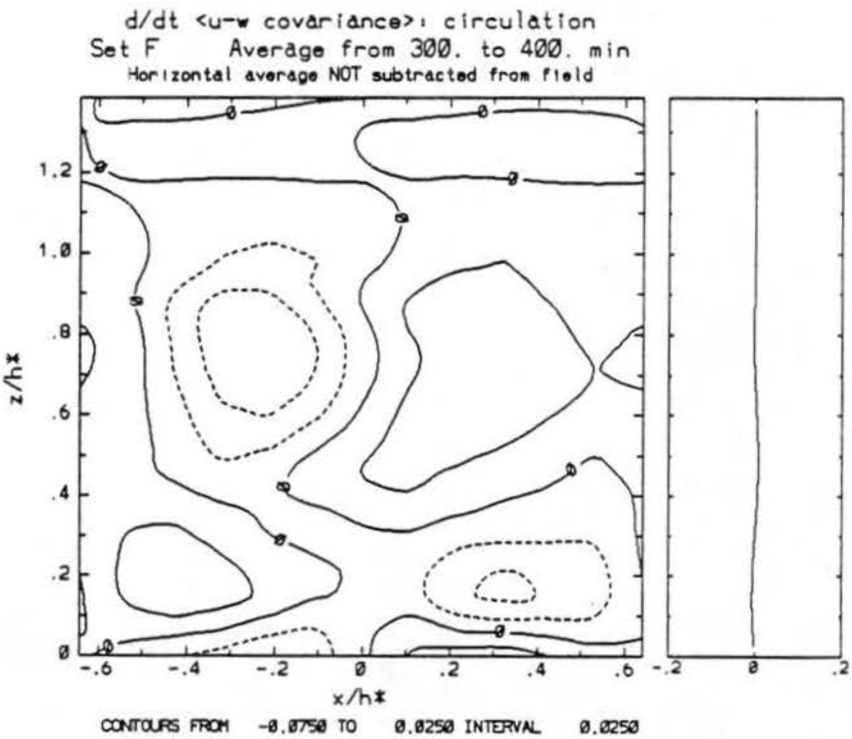

Figure 5.34 (continued).

from what was seen in the horizontally homogeneous budgets (Section 3.3.1) that the variance maximum is primarily a *result* of the buoyancy-term maximum and that the difference between the levels of the two is a result of turbulent transport. The circulation tends to force the variance maximum upwards in the updraught and downwards in the downdraught. It is apparent from Figure 5.10c that the height of maximum w variance does *not* vary significantly with $\hat{x}$, which therefore suggests that that the circulation is too weak in this case to have a significant effect. Finally in the u/w covariance budget, buoyancy drives negative flux for $\hat{x} < 0$ in the lower boundary layer and positive flux for $\hat{x} > 0$. This is the pattern observed in the covariance field itself (Figure 4.10d), which again suggests that the u/w covariance is driven predominantly by buoyancy forcing. Near the surface that flux is against the gradient in $\langle u_i' \rangle_{p,t}$. The circulation term is generally smaller (except right next to the surface) although it may be responsible for the somewhat asymmetric maxima and minima in flux on either side of $\hat{x} = 0$ at $z = 0.8h_*$.

The above analysis suggests that the form of the turbulent stress fields in Set F is determined both by turbulent buoyancy effects and by interaction with the circulation velocity field, with the buoyancy being (broadly speaking!) more important. One can consider the buoyancy terms to arise as a direct consequence of the constraint that (given the relatively small heat transfer by the circulation) the turbulence must distribute heat uniformly throughout the boundary layer, and the circulation terms to arise in a more indirect way as a consequence of the circulation driven by the mean buoyancy, although there is really too much coupling between the circulation and the turbulence for this separation to be well-defined. Note in particular that the surface maximum in u variance at the base of the circulation updraught was found to be important in opposing the circulation (Section 5.2). The fact that the turbulent buoyancy force tends to force this maximum may help explain the small dissipation time scale for the circulation. In principle it even appears feasible for the buoyancy fluctuations to drive a reverse circulation, in the opposite sense to the circulation buoyancy force, via their effects on the u variance.

Figure 5.35 shows the circulation and non-divergent buoyancy terms in the turbulent stresses for Set G ($\lambda_p = 1500\,\mathrm{m}$, $u_0 = 1\,\mathrm{m\,s^{-1}}$). As in Set F there is a broad surface maximum in buoyancy production of u variance; it is shifted downwind, but remains directly below the maximum in w/θ covariance (Figure 4.21g). The maximum in the circulation term is found in the region of horizontal convergence at the base of the circulation updraught, therefore to the right of the maximum in the buoyancy term. Both the u variance terms—especially the circulation term—show less-pronounced surface maxima than in Set F, which may explain the smaller amplitude of the variation in the u variance at the surface. The maximum in the buoyancy term in w variance is found below and just to the left of the maximum in the variance itself (Figure 4.21c) and so buoyancy is presumably the main factor in forcing that maximum. The circulation term in the w variance again tends mainly to raise the level of maximum variance in the updraught and to lower it in the downdraught. In the u/w covariance budget the buoyancy and circulation terms are of comparable magnitude to each other and neither leaves a clear signature in the actual covariance field (Figure 4.21d).

Figure 5.36 shows terms in the turbulent stress budgets for Set H ($\lambda_p = 4500\,\mathrm{m}$, $u_0 = 0\,\mathrm{m\,s^{-1}}$). In addition to the buoyancy and circulation terms described above, Figure 5.36 also includes the u and w variance budget terms associated with the advection pressure,

$$-\,\theta_0 \left\langle (u_i')_{p,t} \frac{\partial}{\partial x_i} (\pi_a')_{p,t} \right\rangle_{p,t}$$

where π_a is defined in Section 2.2.1. The form of the π_a field in convective updraughts and downdraughts was discussed in Section 3.3.1 and sketched in Figure 3.31.

Recall that in the u variance field for Set H (Figure 4.29a) there is a narrow peak near the surface at $\hat{x} = 0$, which has been attributed to meandering of the central updraught. Based on the discussion of large-eddy structure in Section 3.3.1, one expects the base of the central updraught to be flanked by regions of inflow where the π_b-gradient force is directed inwards, so meandering should be reflected in a positive buoyancy term in the u variance budget. In addition the horizontal convergence, $\partial\langle u'\rangle_{p,t}/\partial x$, is large and negative at the base of the circulation updraught (which is a manifestation in the mean of

(a)

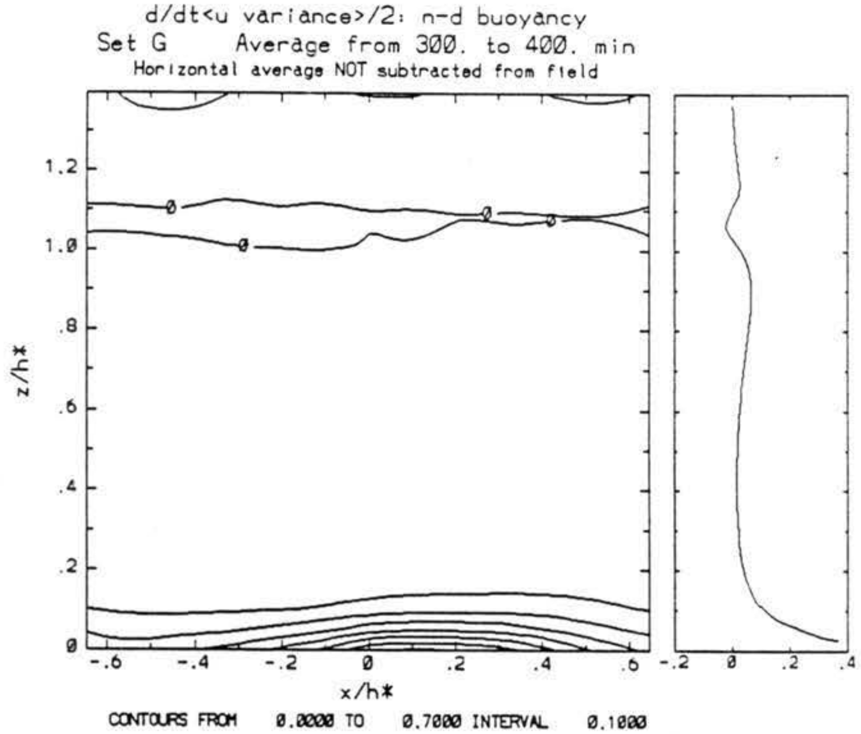

(b)

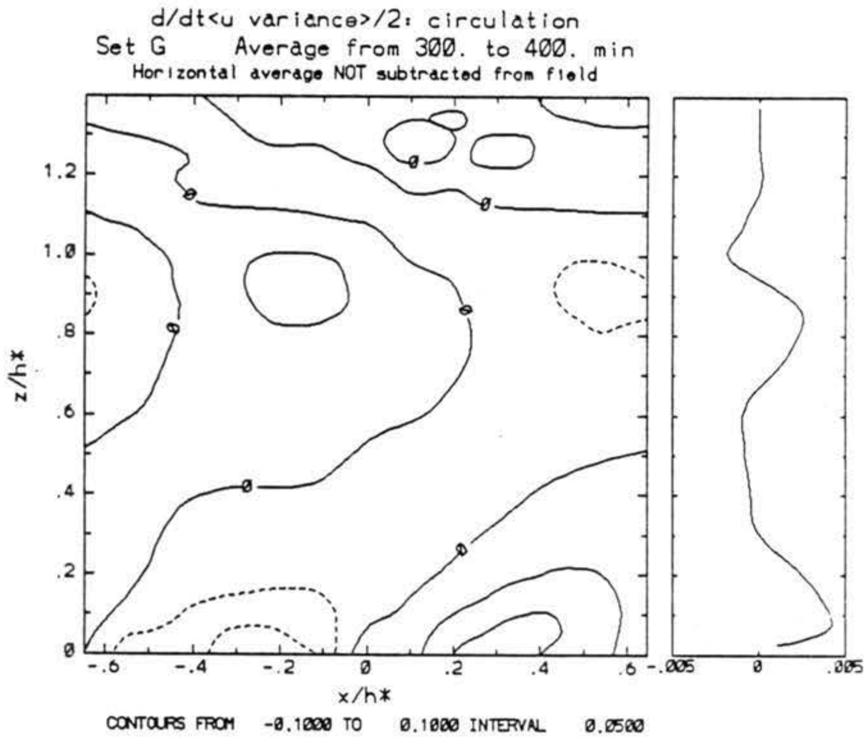

Figure 5.35. Terms in the turbulence stress budgets for Set G. (a) Buoyancy and (b) circulation terms in one-half the u variance, contour intervals $0.1w_*^3/h_*$ and $0.05w_*^3/h_*$ respectively. (c) Buoyancy and (d) circulation terms in one-half the w variance, contour intervals $0.1w_*^3/h_*$ and $0.05w_*^3/h_*$ respectively. (e) Buoyancy and (f) circulation terms in u/w covariance, contour interval $0.02w_*^3/h_*$.

Continued on following pages.

(c)

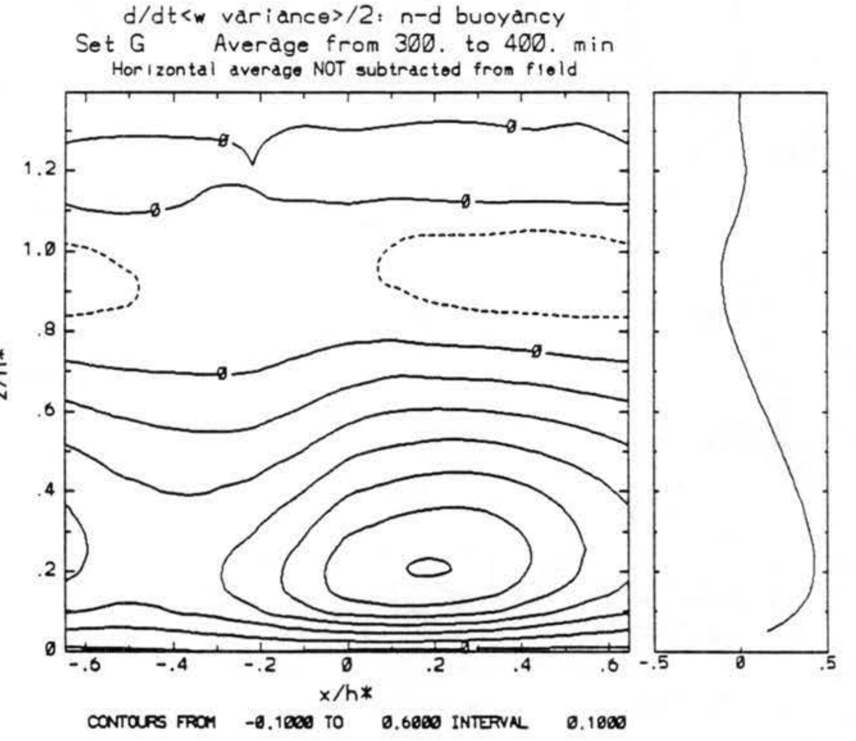

(d)

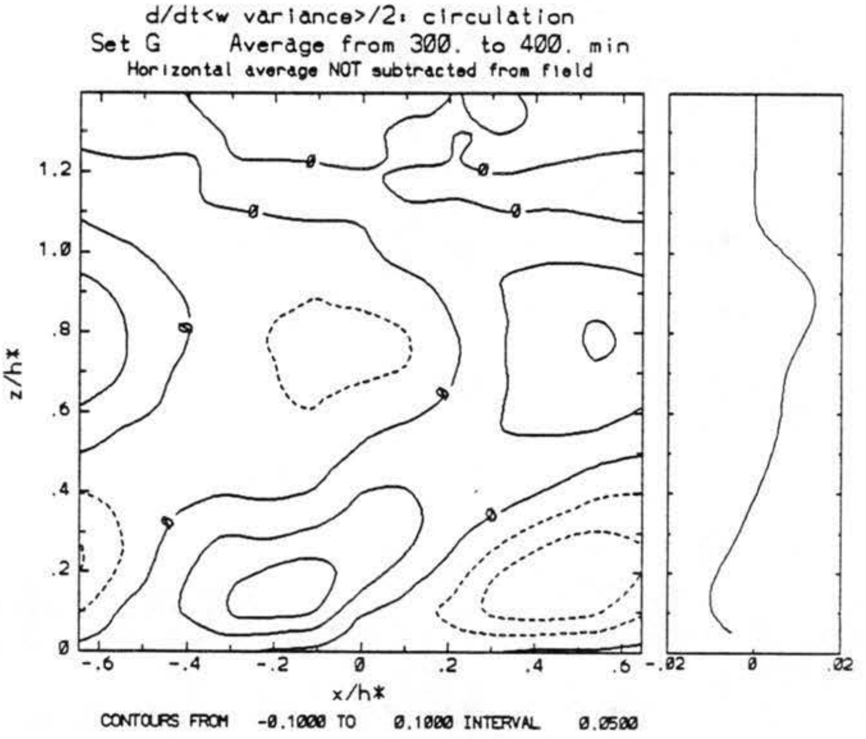

Figure 5.35 (continued).

Continued.

(e)

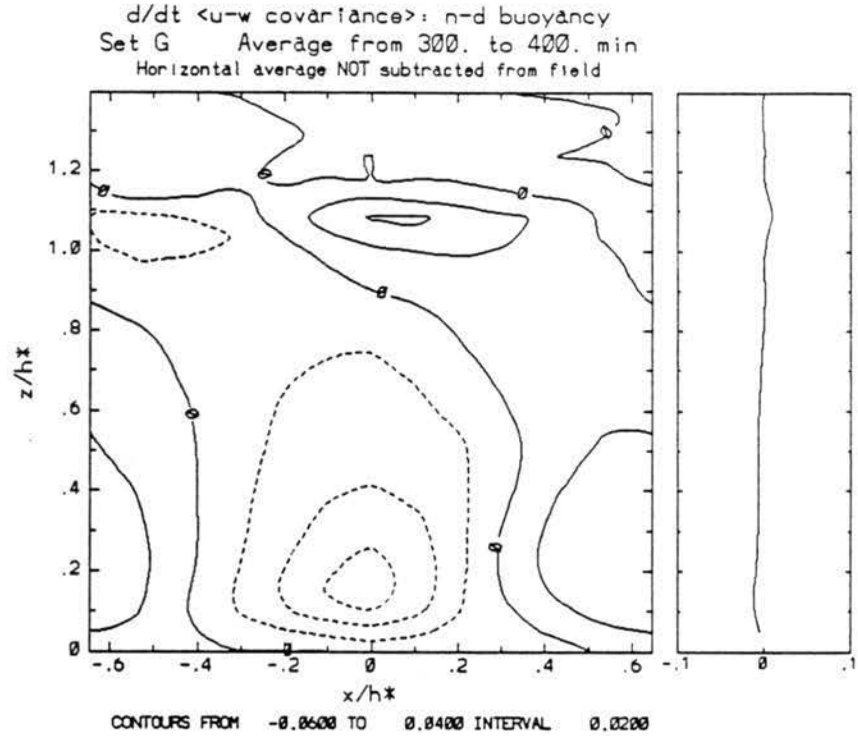

(f)

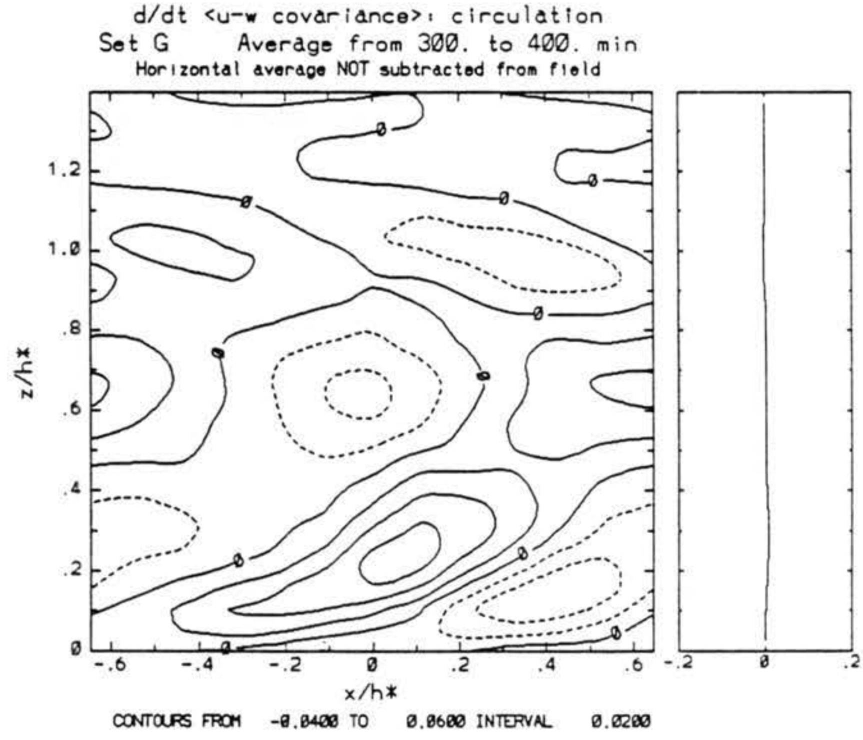

Figure 5.35 (continued).

(a)

(b)

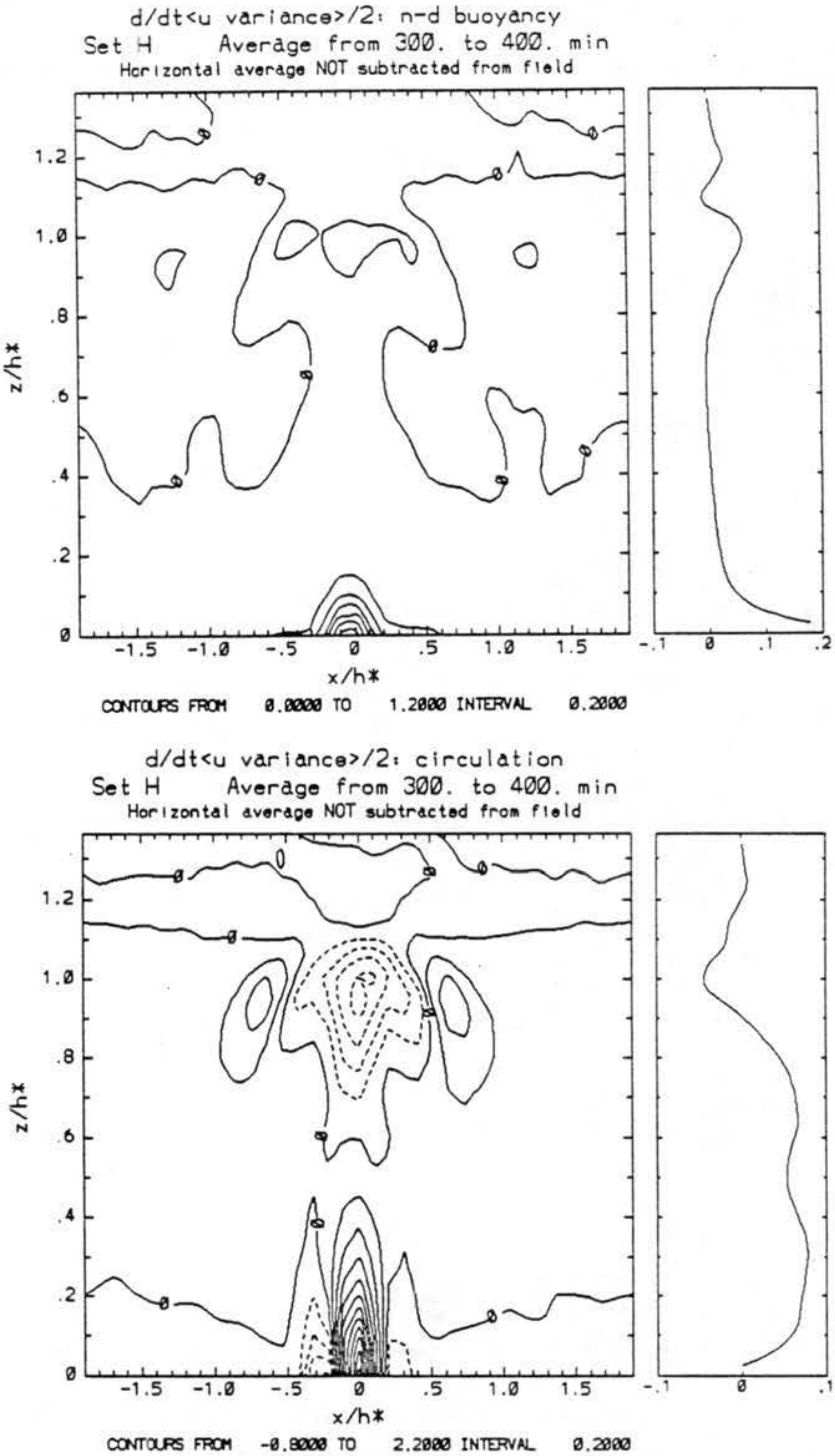

Figure 5.36. Terms in the turbulence stress budgets for Set H. (a) Buoyancy, (b) circulation and (c) advection-pressure terms in one-half the u variance, contour interval $0.2w_*^3/h_*$. (d) Buoyancy, (e) circulation and (f) advection-pressure terms in one-half the w variance, contour interval $0.2w_*^3/h_*$. (g) Buoyancy and (h) circulation terms in u/w covariance, contour interval $0.1w_*^3/h_*$.

Continued on following pages.

(c)

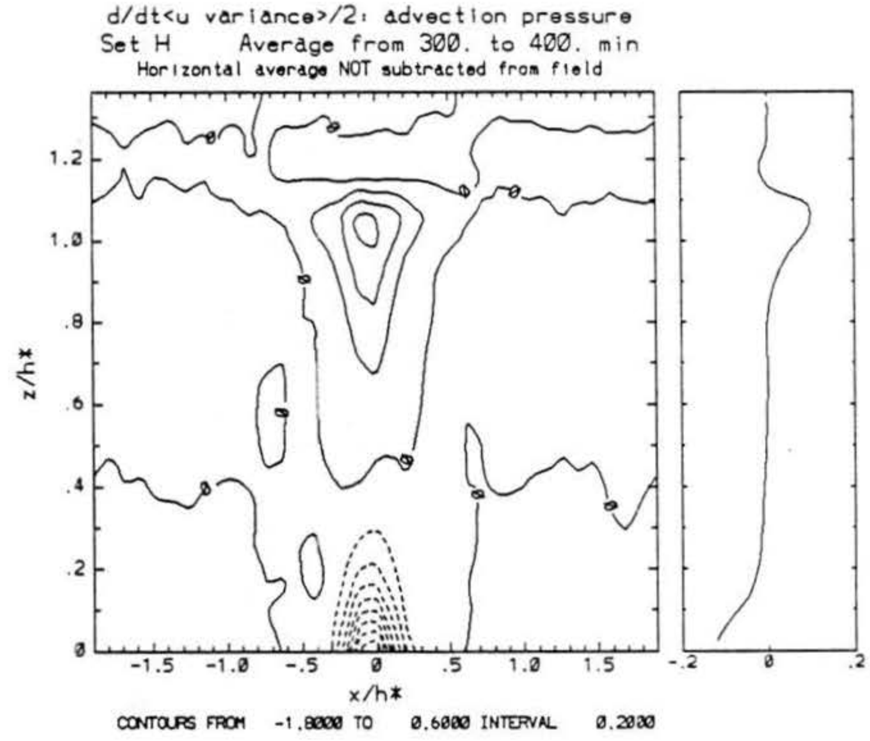

Figure 5.36 (continued).

Continued.

(d)

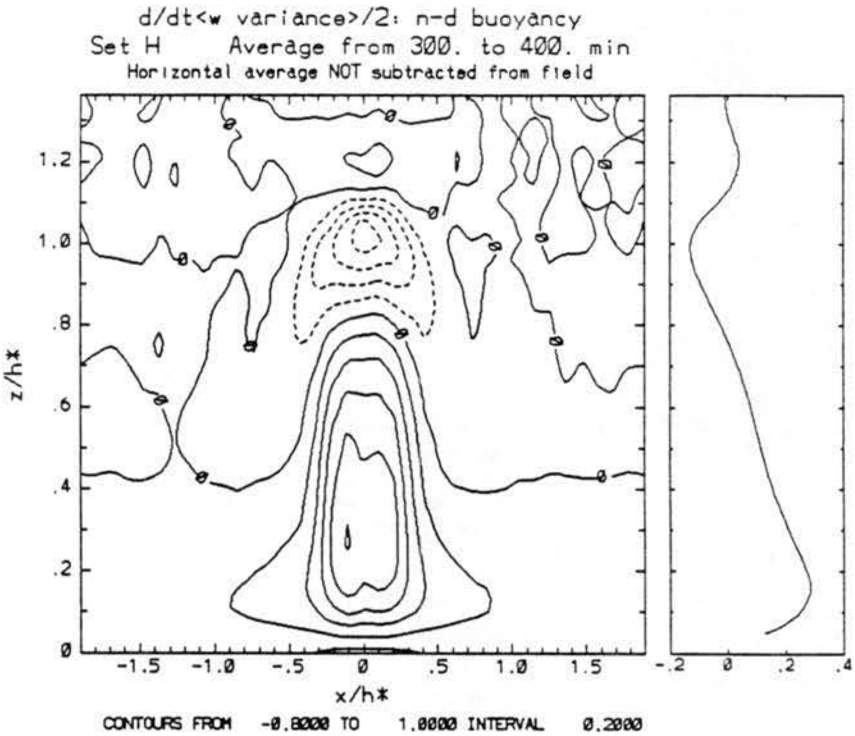

(e)

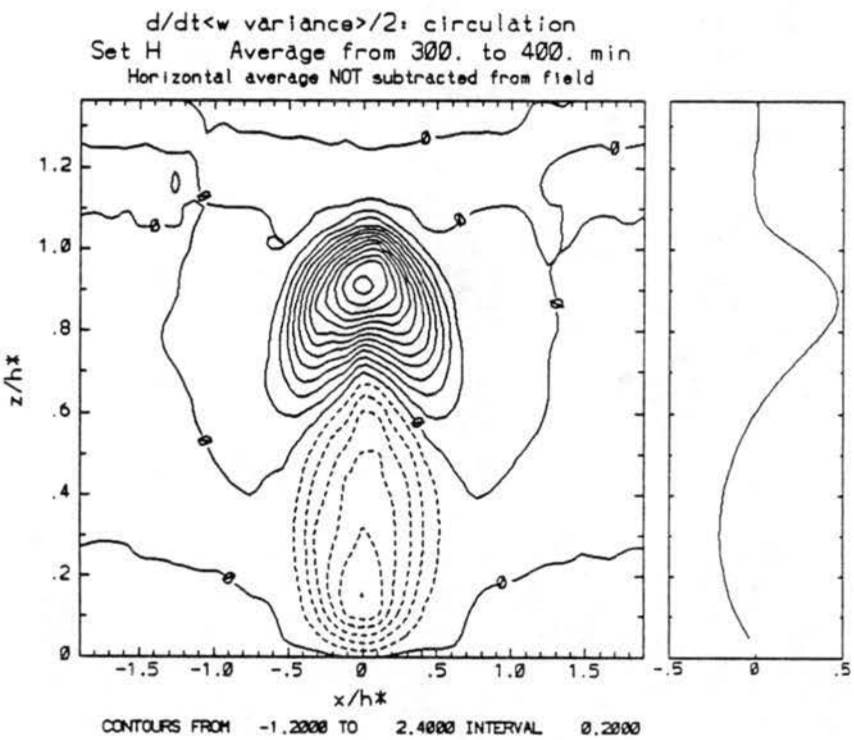

Figure 5.36 (continued).

Continued.

(f)

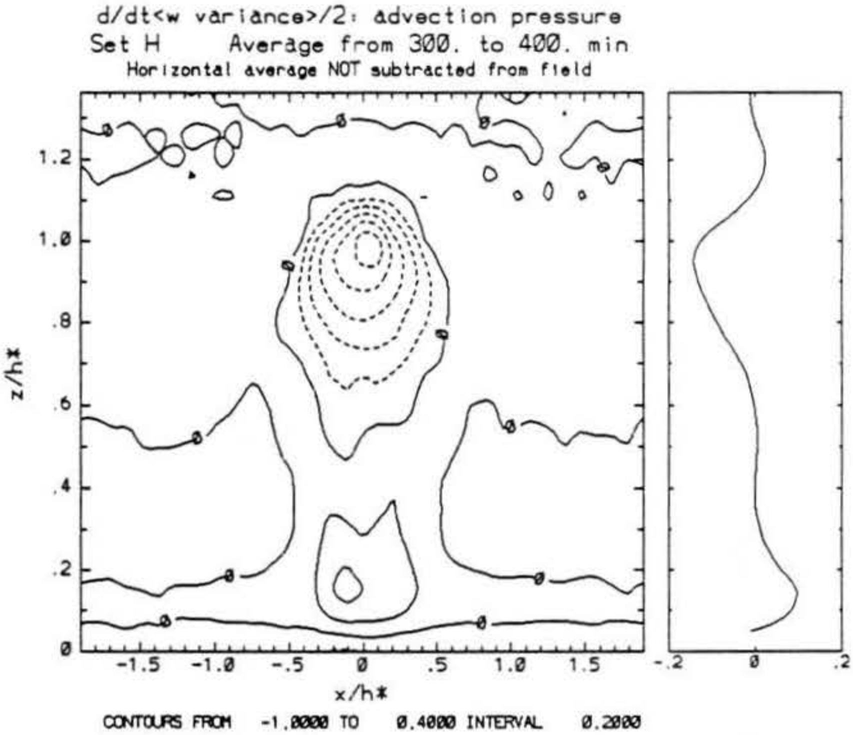

Figure 5.36 (continued).

Continued.

(g)

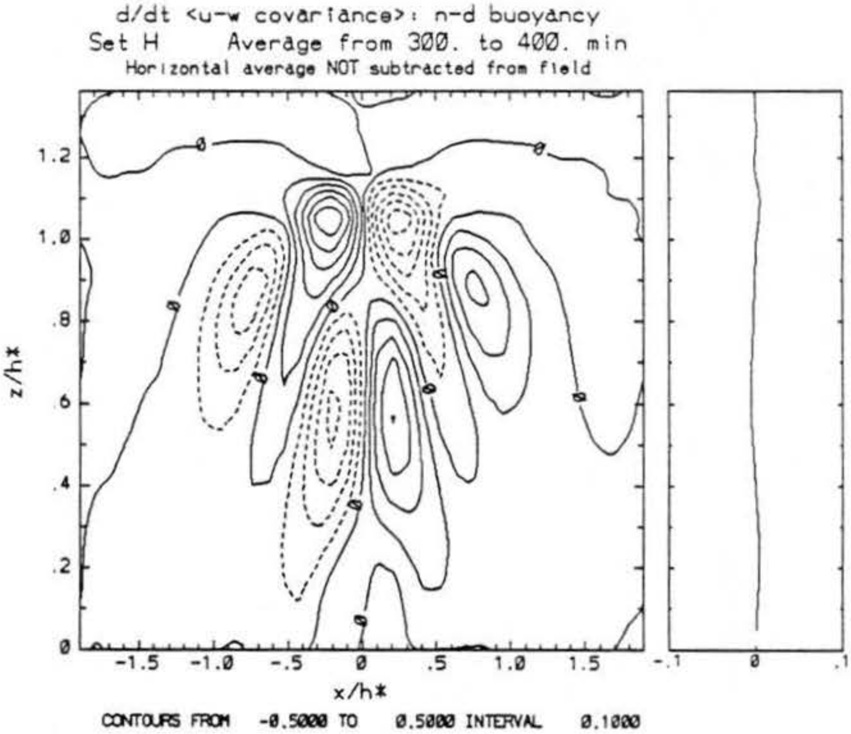

(h)

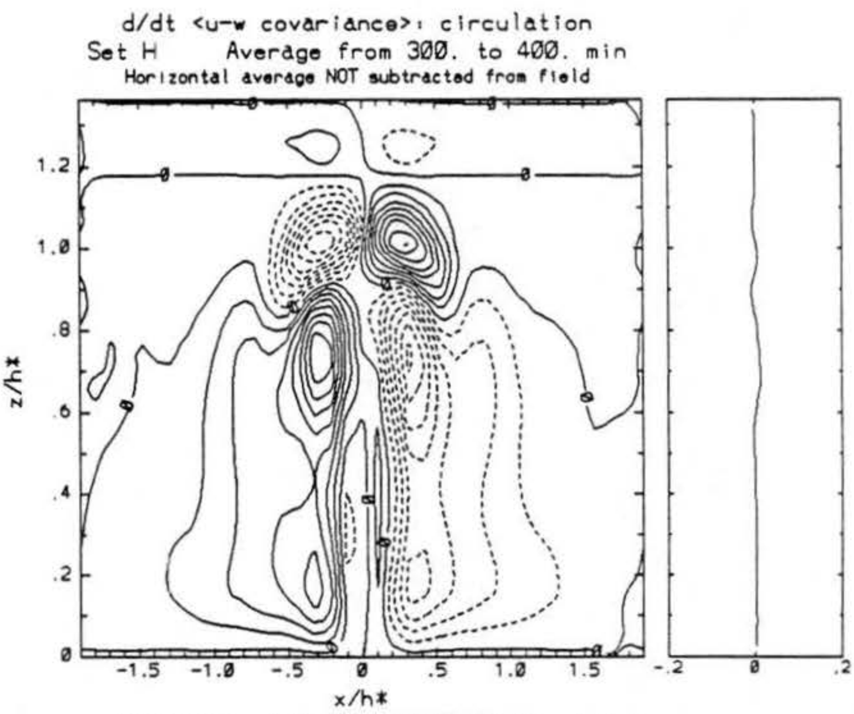

Figure 5.36 (continued).

the strong *instantaneous* gradients in u), so one expects the circulation term, specifically its gradient production part, to be positive. From Figure 5.36 one can see that both the buoyancy and circulation terms both have sharp positive maxima near the surface at $\hat{x}=0$, and that the circulation term is the larger, so both processes can be considered responsible for the existence of the maximum. The advection pressure term is a sink, but not large enough to balance the sum of the other two terms; presumably there is also enhanced subgrid dissipation in the region, and maybe turbulent transport out of it.

At $\hat{x}=0$, $z=h_*$—at the centre of the elevated maximum in u variance—the buoyancy term in the u variance budget is weakly positive, but the circulation term is larger and negative, and it is hard to view either of them as responsible for the elevated maximum. From the form of the u variance budget in the horizontally homogeneous boundary layer (Section 3.3.1 and Figure 3.20) one would suspect that the elevated maximum is forced primarily by fluctuations in π_a, generated by velocity gradients as the air in the updraughts is decelerated at the inversion. The figure showing the π_a-gradient term confirms the suspicion. In terms of the meandering-updraught model this process can be visualised as meandering of a pressure maximum at the top of the updraught; the maximum also appears in the phase-time averages as a maximum in the sum of π_t and π_c (Figure 4.27).

In the w variance, the buoyancy term is positive everywhere below $z=0.4h_*$ (which was identified earlier as the maximum height reached by the secondary updraughts in the subsiding region) and in a central column reaching up to $z=0.8h_*$; it has a pronounced negative maximum in the region of maximum entrainment. In general the (non-divergent) buoyancy term resembles the w/θ covariance (Figure 4.29g), but multiplied by a factor $(1-A)$ where A is between ~ 0.2 (in the ascending region) and ~ 0.5 (almost everywhere else). The circulation term is negative in the lower half of the ascending region and positive in the upper half; upon looking at various contributions to the circulation term separately (not shown) it has been found that the gradient production term is generally the largest of them and that the maximum centred at ($\hat{x}=0$, $z=0.9h_*$) is associated with a maximum in

$$-\left\langle (w')^2_{p,t} \right\rangle_{p,t} \frac{\partial}{\partial z} \langle w' \rangle_{p,t} ,$$

i.e., with vertical convergence in the upper half of the ascending branch of the circulation. Recall that this energy is extracted from the $\langle w' \rangle_{p,t}$ field via the turbulence term, plotted in Figure 5.23b and represented as T_{33} in Figure 5.25. On comparing the circulation and buoyancy terms in the w variance budget, one finds that there is substantial excess production near the inversion at $\hat{x}=0$. One of the sinks is the π_a-gradient term; since this term destroys w variance at a higher rate than it generates u variance it is presumably also forcing the elevated maximum in v variance and/or transporting turbulence kinetic energy away from the region.

The buoyancy and circulation terms in the u/w covariance budget are included in Figure 5.36 for completeness, and to show how complicated their structure is relative to the previous cases. The structure of the circulation term away from the inversion—a narrow negative region flanking the central updraught on its left-hand side and a broader positive region further away—may account for the somewhat similar structure in the covariance itself (Figure 4.31d). A kinematic explanation of the u/w covariance field has been attempted in Section 4.6.4, but there appears to be no simple correspondence between this and the budget analysis.

Figure 5.37 shows the buoyancy and circulation terms in the turbulent stress budgets for Set I ($\lambda_p = 4500\,\mathrm{m}$, $u_0 = 1\,\mathrm{m\,s^{-1}}$). In the variance budgets the buoyancy term acts similarly to previous cases, i.e., it is a source for w variance in the region of maximum w/θ covariance (Figure 4.36g), a source for u variance near the surface in a broad region below that, and a sink for w variance where the entrainment is greatest. In the u variance budget the circulation term has a maximum near the surface located at the position ($\hat{x} = 1.5h_* = 0.40\lambda_p$) where the horizontal convergence is greatest (Figure 4.34). As in Set G, this maximum is sharper, and well to the right of, the maximum in the buoyancy term, but in the present case it is much stronger than than in Set G and its signature can be seen more clearly in the u variance field (Figure 4.36a). Together, buoyancy and

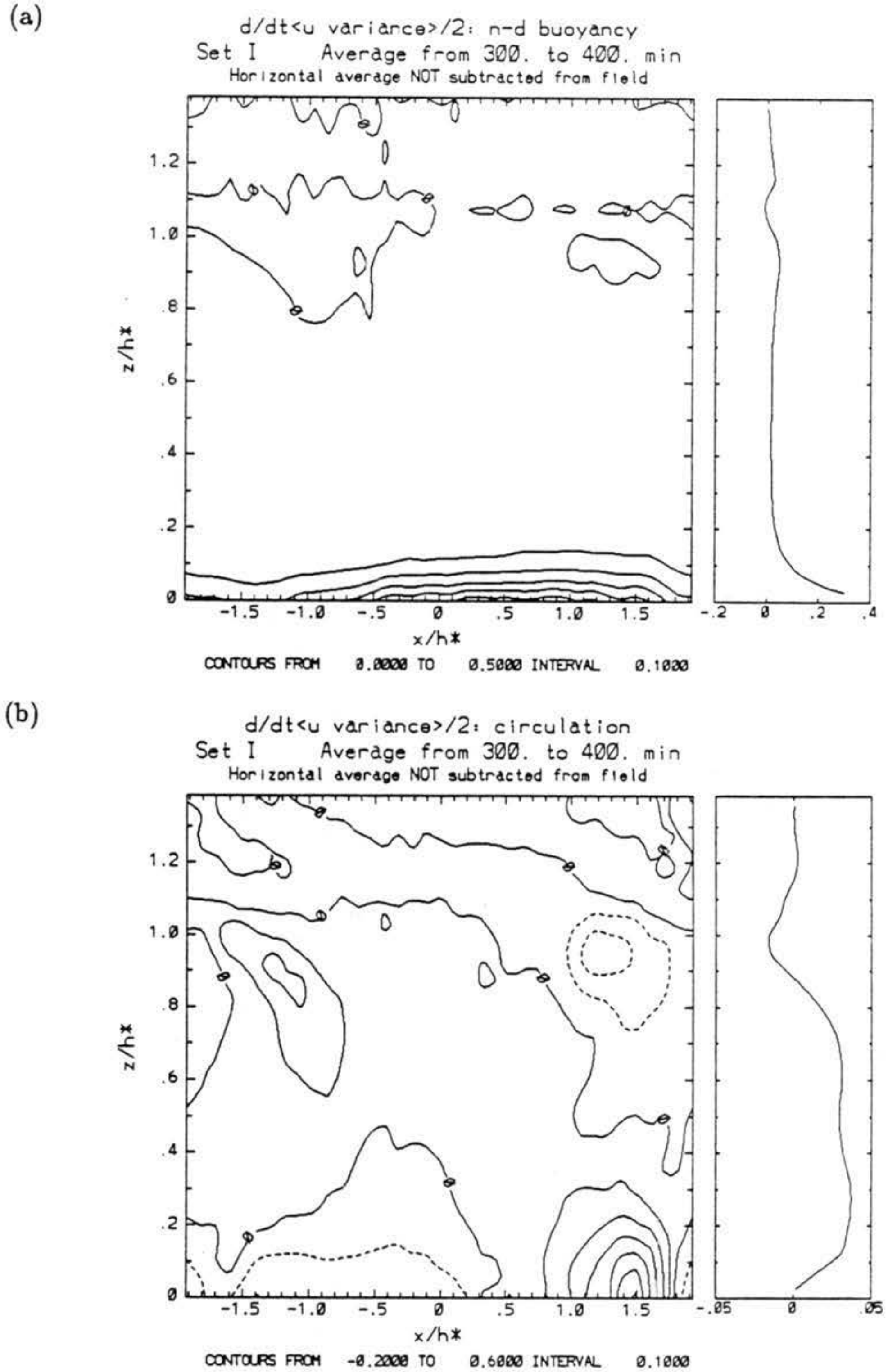

Figure 5.37. Terms in the turbulence stress budgets for Set I. (a) Buoyancy and (b) circulation terms in one-half the u variance, contour interval $0.1w_*^3/h_*$. (c) Buoyancy and (d) circulation terms in one-half the w variance, contour interval $0.1w_*^3/h_*$. (e) Buoyancy and (f) circulation terms in u/w covariance, contour interval $0.05w_*^3/h_*$.

Continued on following pages.

(c)

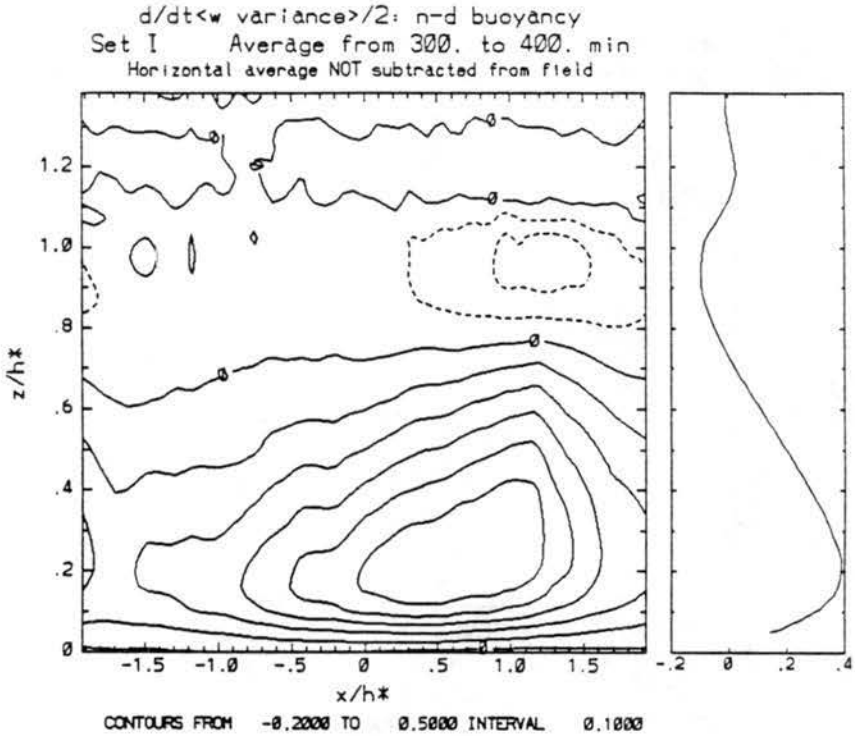

(d)

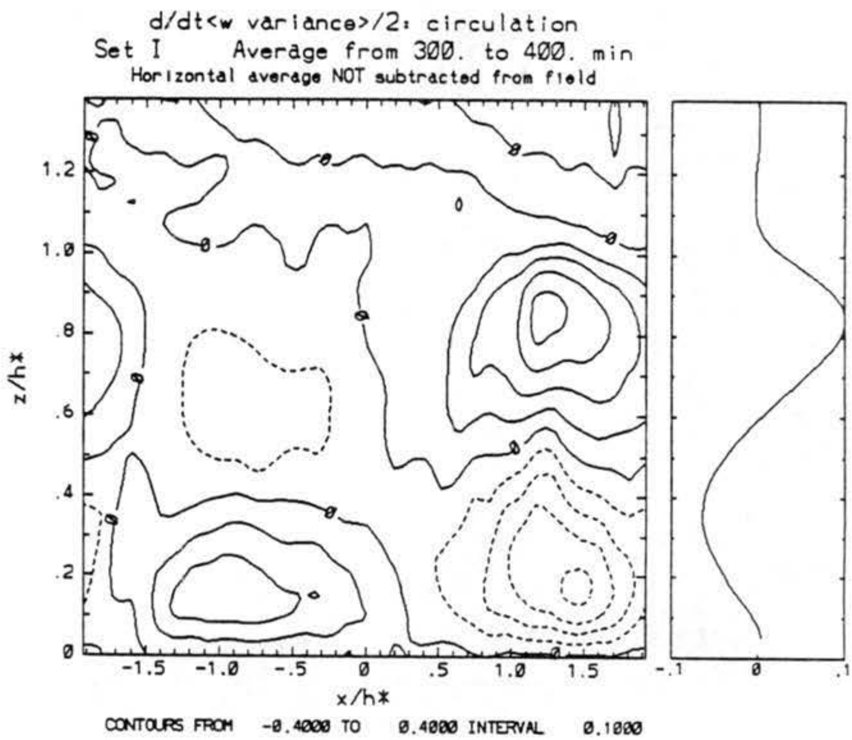

Figure 5.37 (continued).

Continued.

(e)

(f)

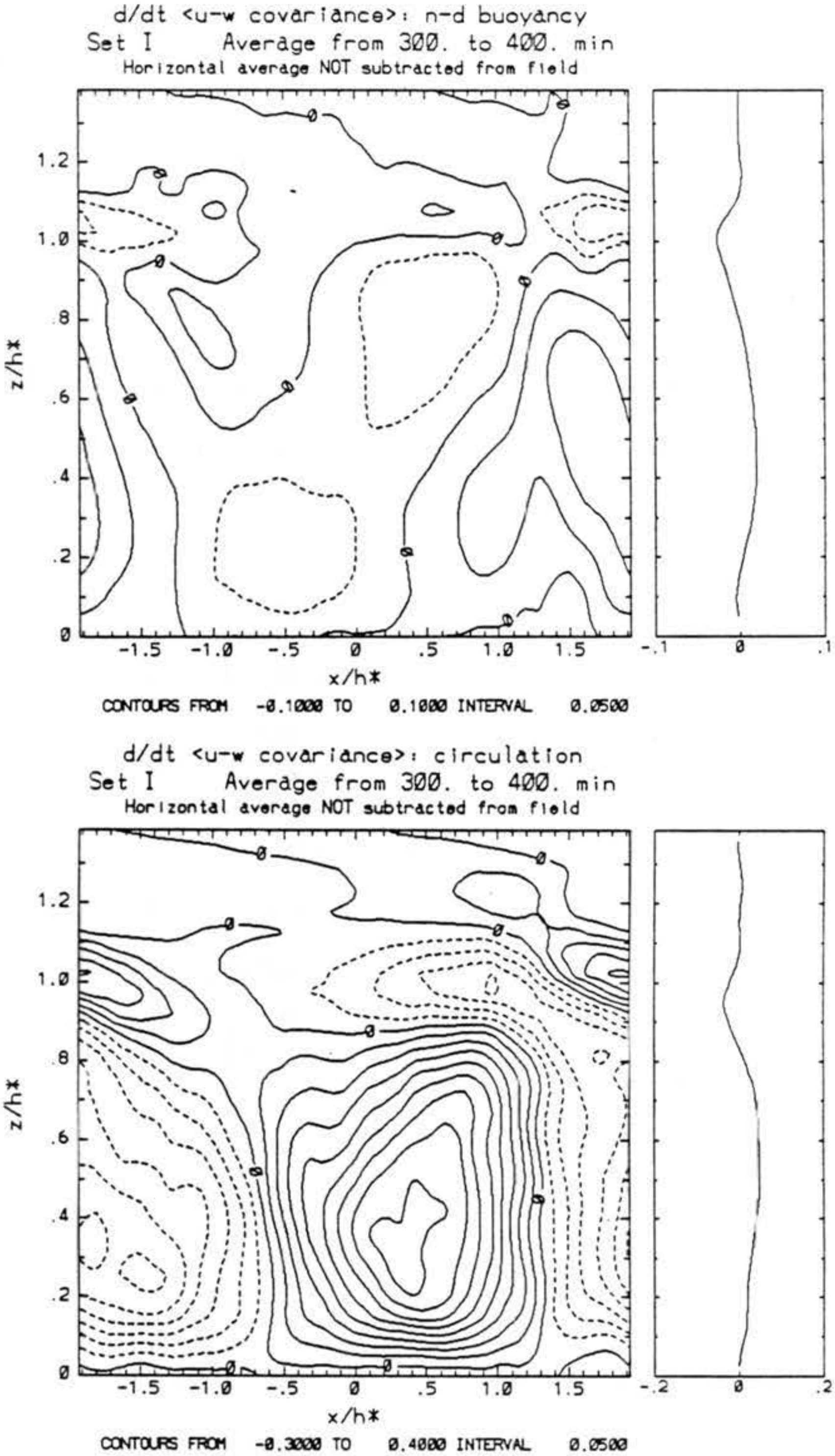

Figure 5.37 (continued).

circulation effects seem to account for the strongly asymmetrical maximum at the surface in the u variance field. In the w variance budget the circulation term is a source in the upper boundary layer and a sink in the lower boundary layer in the mean updraught, and vice versa in the mean downdraught, so one expects it to produce a horizontal variation in the height of maximum w variance; such a variation is observed (Figure 4.36c) and is more pronounced than in Set G.

In the u/w covariance budget for Set I the buoyancy term is much smaller than the circulation term. The latter is dominated by production associated with *vertical* shear in the *horizontal* circulation velocity, namely

$$-\left\langle (w')^2_{p,t} \right\rangle_{p,t} \frac{\partial \langle u' \rangle_{p,t}}{\partial z},$$

which is positive to the left of the mean updraught. The other production term,

$$-\left\langle (u')^2_{p,t} \right\rangle_{p,t} \frac{\partial \langle w' \rangle_{p,t}}{\partial x},$$

is smaller and negative to the left of the mean updraught. (Note that the vertical stretching in the figures showing the circulation (Figure 4.34) tends to exaggerate the horizontal gradient in $\langle w' \rangle_{p,t}$ and diminish the vertical gradient in $\langle u' \rangle_{p,t}$. In fact the latter is much the larger of the two.) The u/w covariance itself (Figure 4.36d) has a pattern similar to its circulation production term, but shifted $\sim 0.1\lambda_p$ downstream (maybe by advection in the mean wind). In the discussion of the circulation velocity budgets it was pointed out that the u/w covariance in Sets H and I tends to decelerate the horizontal circulation velocity and accelerate the vertical circulation velocity but had the opposite effect in Sets F and G. This difference is to be expected with a change in aspect ratio.

Finally, Figure 5.38 shows the turbulent stress budgets for Set J ($\lambda_p = 2500\,\mathrm{m}$, $u_0 = 2\,\mathrm{m\,s^{-1}}$). In general the u- and w-variance budget terms are qualitatively similar to the corresponding terms for Set I, but the circulation terms are much smaller in magnitude, as one expects with the weaker circulation. In the u/w covariance budget the circulation term is generally of larger magnitude than the non-divergent buoyancy term, but not so dominant as in Set I. The maximum and minimum in the covariance

(a)

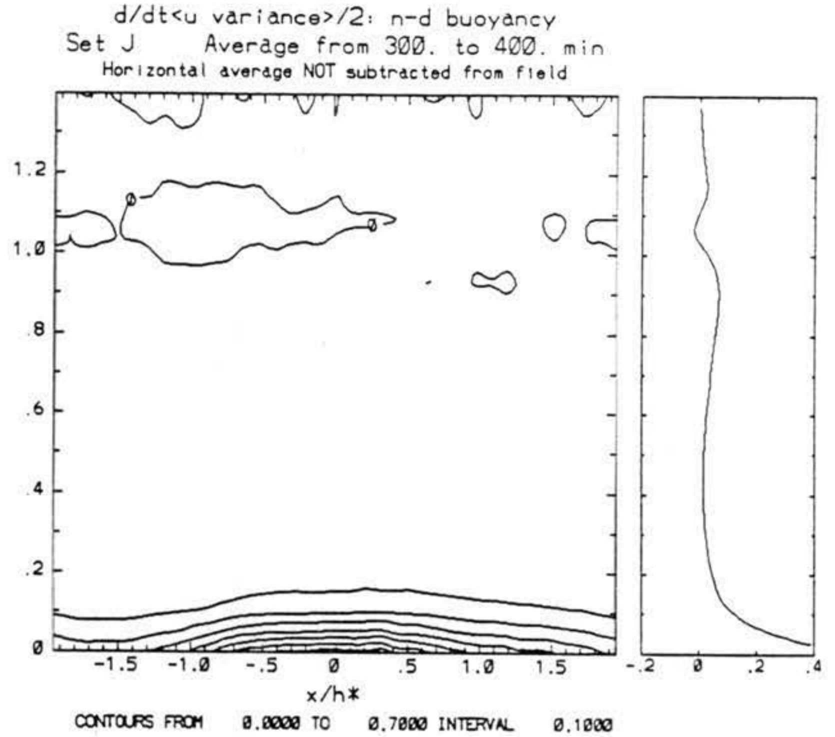

(b)

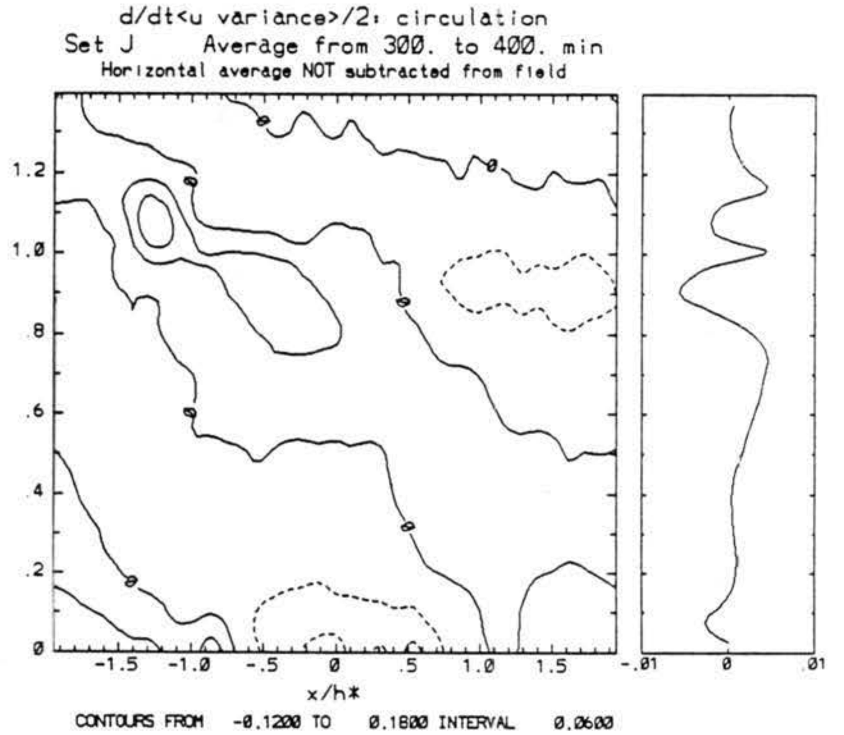

Figure 5.38. Terms in the turbulence stress budgets for Set J. (a) Buoyancy and (b) circulation terms in one-half the u variance, contour intervals $0.1w_*^3/h_*$ and $0.06w_*^3/h_*$ respectively. (c) Buoyancy and (d) circulation terms in one-half the w variance, contour intervals $0.1w_*^3/h_*$ and $0.05w_*^3/h_*$ respectively. (e) Buoyancy and (f) circulation terms in u/w covariance, contour intervals $0.03w_*^3/h_*$ and $0.08w_*^3/h_*$ respectively.

Continued on following pages.

(c)

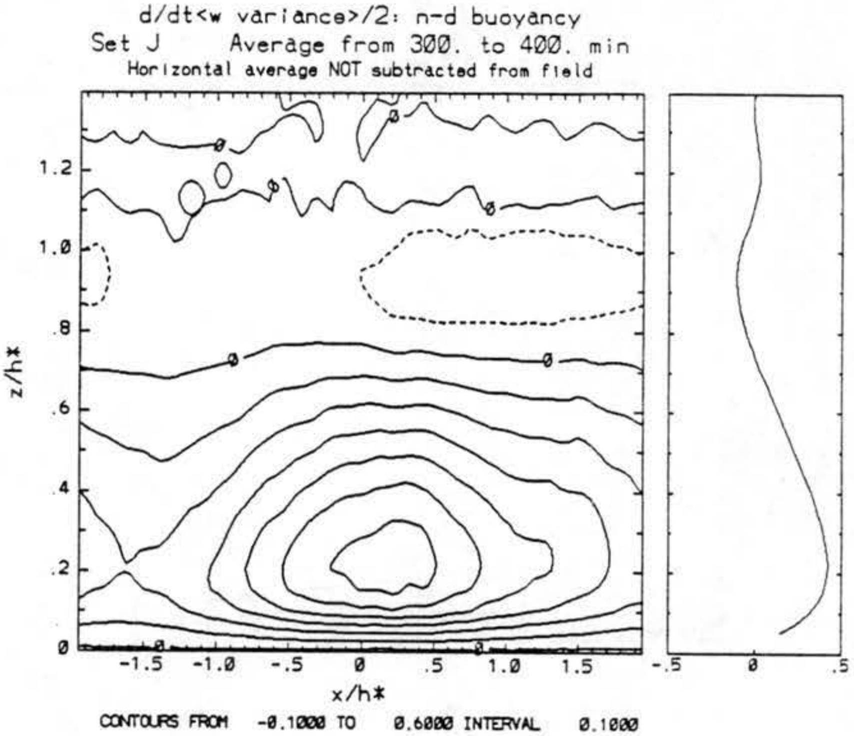

(d)

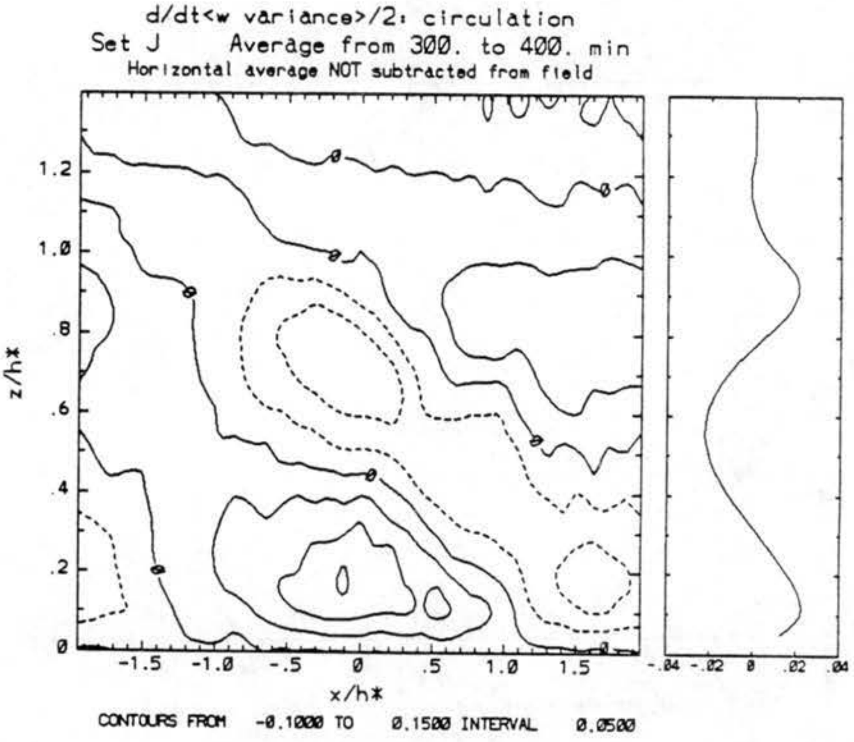

Figure 5.38 (continued).

Continued.

(e)

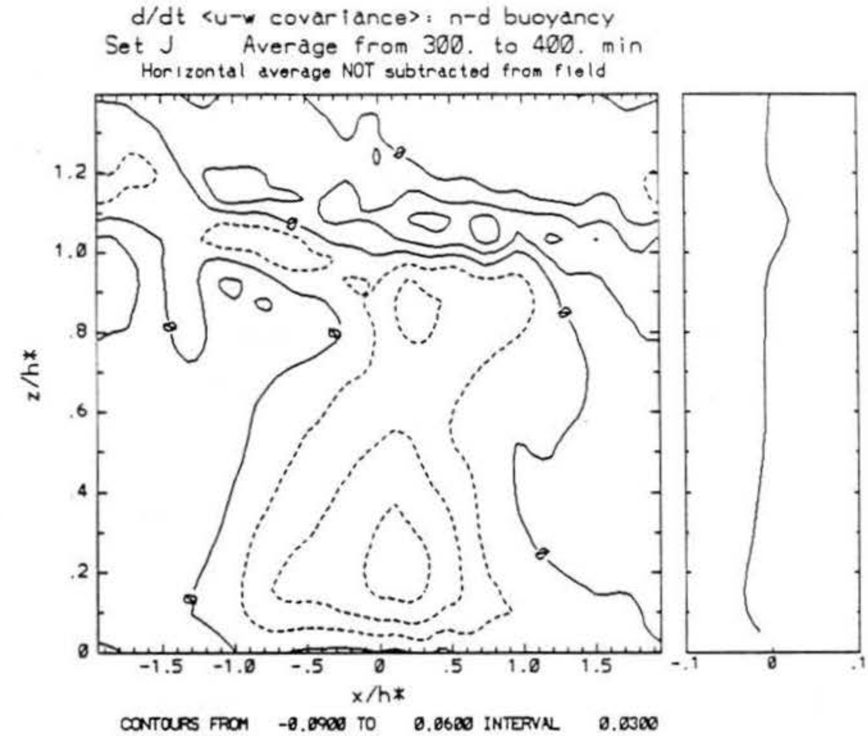

(f)

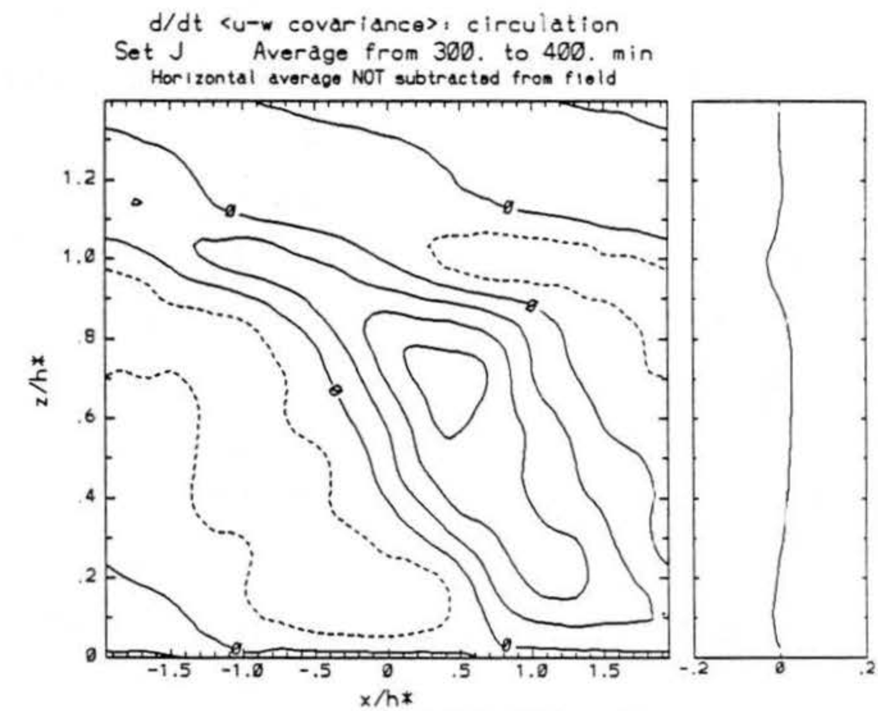

Figure 5.38 (continued).

(Figure 4.45d) are found about $0.2\lambda_p$ downstream of the maximum and minimum in the circulation term (versus about $0.1\lambda_p$ in Set I). In Section 5.2 it was pointed out that the u/w covariance tends to accelerate the $\langle u' \rangle_{p,t}$ field at low levels, in contrast to Set I, and that this might be related to the sloping maxima and minima in the covariance field. This slope seems to be in part a consequence the slope in the circulation term (associated with the slope in the regions where vertical shear is greatest), maybe also with the presence of a negative centre in the buoyancy term in the lower boundary layer near $\hat{x} = 0$. On the whole, however, the reorganisation of the stresses that leads to the different form of the $\langle \langle u' \rangle^2_{p,t} \rangle_h / 2$ budget in Set J, as compared to Set I, is not easy to understand.

5.4 Discussion

Let us consider first the set of simulations with zero mean wind and $\lambda_p = 1500\,\mathrm{m}$ (Set F). It was shown in Chapter 4 that the velocity, temperature and pressure perturbations associated with the time-averaged circulations are all "small," in the various senses discussed in that chapter. Do the budget analyses in the present chapter explain why this is so? In the budget for the buoyancy perturbation $\langle \theta' \rangle_{p,t}$ it has been argued that the dominant process is a redistribution of heat uniformly throughout the boundary layer by the horizontal and vertical turbulent fluxes. The flux f_j is generally directed from the warmer region immediately above the maximum in surface heat flux to the cooler region above the surface heat-flux minimum, although the relationship between the flux and the gradient in the temperature $\langle \theta' \rangle_{p,t}$ is not a simple down-gradient one—at least not with a single, constant diffusivity. In Appendix B a down-gradient diffusion model will be investigated further and it will be shown that a plausible, non-isotropic diffusivity can be constructed that reproduces the LES fluxes and gradients reasonably well. It is noteworthy that the required horizontal diffusivity is not especially large in dimensionless terms—it is of the order of $0.1 w_* h_*$—so perhaps the small magnitude of the circulation perturbations should not come as a surprise. Still, *owing to its large velocity and length scales, the convective boundary layer is a highly diffusive medium.*

Given a higher mean temperature over the heat-flux maxima, what mean circulation is to be expected? The circulation velocity budget is predominantly a balance between the non-divergent buoyancy force and the non-divergent turbulence force. The former is entirely determined by the circulation temperature perturbation discussed above. The buoyancy perturbation induces a pressure π_b, the vertical gradient of which tends to oppose the buoyancy force in the vertical. A ratio A_c has been defined to relate the vertical component of the π_b-gradient force to the buoyancy. In Set F, A_c has a limiting value of one at $z=0$ and drops off rapidly towards zero in the lower half of the boundary layer. As a result, whereas the buoyancy force vector acts entirely in the vertical and has maximum magnitude at the surface, the non-divergent buoyancy vector has an elevated maximum ($z=0.2h_*$) in its vertical component and assumes a pattern not too different from the circulation velocity vector. In particular, it appears that the shallow region of relatively strong inflow into the base of the mean updraught arises because of the even shallower region of strong horizontal forcing by the non-divergent buoyancy vector.

The non-divergent turbulence force transfers kinetic energy from the circulation to the turbulence; a time scale has been defined for that transfer and found to be quite short, only $0.32h_*/w_*$ or 3 min. *The convective boundary layer therefore appears to be a highly dissipative medium for two-dimensional circulations on a scale comparable to the boundary layer depth.* The roles of the various stresses and pressure-gradient forces in the circulation kinetic energy budgets have been examined; furthermore the buoyancy and circulation terms in the stress budgets have been calculated and compared. It seems that the stress fields are strongly affected by the turbulent buoyancy fluxes, which are constrained by the requirement that they redistribute heat more or less uniformly throughout the boundary layer. The pronounced surface maximum in u variance, centred at $\hat{x}=0$, is important in extracting energy from the circulation. It is generated partly by turbulent buoyancy-pressure forces (associated with the near-surface maximum in w/θ covariance) and partly by the circulation itself. The combination of relatively strong horizontal convergence at the base of the mean updraught, turbulent forcing of a maximum in u variance in the same position and interaction between the two may therefore be responsible for the short dissipation time scale.

With the same λ_p and a mean wind of $1\,\mathrm{m\,s^{-1}}$ (Set G), *horizontal advection becomes significant in the circulation temperature and velocity budgets.* The horizontal advection tendency in $\langle\theta'\rangle_{p,t}$ is proportional to the temperature field displaced $\lambda_p/4$ downwind, therefore, in the absence of other significant terms in the budget, the turbulence tendency is proportional to the temperature field displaced $\lambda_p/4$ upwind. It will be shown in Appendix B that the balance can be achieved by a model with horizontal advection plus down-gradient diffusion through downwind tilting of the fields; the behaviour of that model is qualitatively similar to what is seen in the LES simulations. In the circulation velocity budget there is a similar balance between horizontal advection, on one hand, and the sum of the non-divergent buoyancy and turbulence terms, on the other, but it is not clear what the feedbacks are that allow this balance to be achieved. The circulation kinetic energy budgets, from which horizontal advection vanishes, are qualitatively similar to the budgets for Set F but there are quantitative differences (beside an overall reduction in magnitude) including a reduction in the fraction of the vertically integrated buoyancy production accounted for by term T_{11} (u circulation, u variance). The dissipation time scale is $0.46h_*/w_*$, somewhat larger than in Set F. In the turbulent stress budgets most of the processes that were seen in Set F are still detectable, but generally weaker; one feature of these budgets is still very evident, namely a low-level maximum in the non-divergent buoyancy production of w variance coinciding more or less with the maximum in w/θ covariance. As in Set F the maximum in the buoyancy term appears to produce a maximum in w variance; with the mean wind these maxima are shifted downwind, but not much reduced in magnitude.

The case with zero wind and $\lambda_p = 4500\,\mathrm{m}$, namely Set H, is very different from Set F. *Here the time-averaged circulation is strong enough for advection by the circulation to be significant in the circulation budgets.* The circulation is also strong enough to reorganise the turbulent stresses significantly and it presumably modifies the turbulent heat fluxes and feeds back onto the circulation temperature field, although this process has not been explored. Much of the energy transfer from the circulation to the turbulence occurs in the mean updraught, through interaction between the circulation vertical velocity and the w variance, and in the process w variance is generated in the upper part of the updraught. This process is presumably important in driving strong entrainment at the top of the updraught and, through pressure-gradient coupling, in supporting the elevated maxima in the horizontal velocity variances.

In Set I ($\lambda_p = 4500\,\mathrm{m}$, $u_0 = 1\,\mathrm{m\,s^{-1}}$) the mean wind has similar effects to those it had in Set G ($\lambda_p = 1500\,\mathrm{m}$, same u_0): it introduces horizontal advection into the circulation temperature and velocity budgets, tilts the fields and moves them downwind. There are several differences from Set G however. Advection by the circulation is more significant in Set I, because the circulation is stronger. A larger fraction of the circulation buoyancy production is transferred to the horizontal velocity component by the π_b-gradient force, as expected with the smaller aspect ratio. The u/w covariance budget is dominated by gradient production due to vertical shear in the horizontal wind, leading to a u/w covariance field that opposes the horizontal component of the circulation velocity. The time scale for dissipation of the circulation kinetic energy is now $1.17h_*/w_*$, similar to the time scale for subgrid dissipation of the total turbulence kinetic energy (Section 3.3.1) and substantially larger than it was in either of the $\lambda_p = 1500\,\mathrm{m}$ cases. It was hypothesised in Chapter 4 that the circulation in Set I moves the maxima in w variance and w/θ covariance further downstream than they would otherwise be. A *possible* mechanism suggested by the budget analyses described in this chapter is that convergence at the base of the mean updraught forces the maximum in u variance, which drives turbulent fluctuations in w above through pressure-gradient coupling.

The budgets for Set J ($\lambda_p = 4500\,\mathrm{m}$, $u_0 = 2\,\mathrm{m\,s^{-1}}$) might be expected to be qualitatively similar to those of Set I, but with stronger horizontal advection. Actually there are several differences, mainly in the circulation kinetic energy budgets. *The mean updraught has moved far enough downstream that it draws on the relatively cold air in the vicinity of the heat-flux minimum.* The circulation heat flux (buoyancy production) is therefore negative near the surface. The adjustments in the stress and pressure fields that maintain the circulation at low levels have been described briefly. The profiles of the circulation kinetic energy budgets are more complicated than in previous cases, apparently because of the way the various velocity, pressure and stress fields slope variously to the left or right. At the end of it all one is not left with a clear idea of why the velocity and stress fields do not assume substantially different forms. It seems intuitively reasonable that the circulation updraught could not be supported if it moved very far downwind of its position in Set J, so one expects that a further increase in wind speed should result in very little change in position in the updraught, but in a substantial further reduction in strength (basically a continuation in the trend seen between Set I and Set J). Another distinguishing feature of Set J is that a significant fraction (14%) of the vertically integrated buoyancy production propagates up to the absorbing layer. (A similar flux was detectable in Set I, but much smaller.) *This raises the issue of the sensitivity of the circulations to the structure of the atmosphere above the boundary layer, an issue which has been avoided in the design of the present numerical experiments.*

CHAPTER 6

PASSIVE PLUME DISPERSION

6.1 The Lagrangian particle dispersion scheme

Concentration fields are calculated from the LES model using a Lagrangian particle dispersion scheme, very similar to the one used by Lamb (1978, 1982). The pollutant plume is modelled as a large number of particles, each with velocity[15] q_i calculated as the sum of a deterministic part and a random part:

$$q_i = \bar{q}_i + q_i''. \tag{6.1}$$

The deterministic velocity $\bar{q}_i$ is simply estimated for each particle at its current position by linear interpolation from the resolved velocity fields and the random part q_i'' is constructed using a first-order Markov process,

$$q_i''(t + \Delta t_p) = \beta\, q_i''(t) + \gamma \left(\frac{2\bar{e}}{3}\right)^{\frac{1}{2}} r_i(t) + \Delta t_p \, \frac{2}{3}\frac{\partial \bar{e}}{\partial x_i}, \tag{6.2}$$

where Δt_p is the time step for the Markov process, $\bar{e}$ is the subgrid kinetic energy interpolated to the particle position and $r_i(t)$ is drawn from a sequence of independent, Gaussian, random numbers with zero mean and unit variance. To calculate the coefficients β and γ, a Lagrangian decorrelation time scale is estimated from the subgrid energy and length scale,

$$t_L = \bar{e}^{1/2} / \bar{l}, \tag{6.3}$$

---

[15]The symbol q_i denotes the components of particle velocity, as distinct from the fluid velocity u_i.

and the coefficients are given by

$$\beta = \exp -(\Delta t_p / t_L) \qquad \gamma = (1 - \beta^2)^{1/2}. \tag{6.4}$$

The q_i'' sequence is initialized at its release time t_s with

$$q_i''(t_s) = \left(\frac{2\bar{e}}{3}\right)^{\frac{1}{2}} r_i(t_s). \tag{6.5}$$

Given the particle velocities q_i, positions p_i are calculated by stepping forward in time,

$$p_i(t + \Delta t_p) = p_i(t) + q_i(t)\Delta t_p, \tag{6.6}$$

with reflection at the upper and lower boundaries.

The third term in Equation 6.2 was not used by Lamb. It is a "drift correction" of the type used by Legg and Raupach (1982) in a one-dimensional particle model to compensate for a tendency for particles to accumulate in regions of low velocity variance. The extension of such a correction to an unsteady, three-dimensional field of subgrid turbulence is *ad hoc*, and is justified by the observation that without such a correction the particles show a slight tendency to gather in the less-turbulent downdraughts and be carried to the lower boundary layer. *With* the drift correction an initially uniform concentration profile remains uniform to within better than 2%.

It should be noted that the second-order Markov model proposed by Lamb (1981, 1982) has *not* been used, because it is believed that not enough is known about the subgrid turbulence in a large-eddy model to support anything other than a very simple subgrid dispersion scheme. Furthermore, dispersion from an elevated source is achieved largely by the resolved eddies. Several of the dispersion simulations described below have been repeated with q_i'' set identically to zero, with very little change in the results, so it appears that the subgrid dispersion model is not critical in estimating mean concentration fields.

The concentration field is defined as the probability density for finding a particle near a given point and must be estimated from the particle positions. This is done with a kernel function technique (Gingold and Monaghan, 1982). With the large number of particles used here (typically $\sim 10^4$) the choice of kernel shape and width is not critical.

6.2 Dispersion in the horizontally homogeneous boundary layer

The obvious way to simulate a continuous source in a homogeneous boundary layer is to release particles at regular intervals from a single point. Mean concentration fields can then be found by averaging over time. The problem with this method is that it may take a long time before a single release point is exposed to all the different types of turbulent eddy in the flow. A more efficient approach is to release a large number of particles simultaneously at a given height over the entire model domain and record the horizontal position of each particle *relative to its release point.* Let $p_i{}^l(t)$ be the position in the i'th direction of the l'th particle, where $l = 1, \ldots, N$, and let the relative position $r_i{}^l(t)$ be defined by

$$r_i{}^l(t) = \begin{cases} p_i{}^l(t) - p_i{}^l(t_s) & i = 1, 2 \\ p_i{}^l(t) & i = 3 \end{cases}$$

where t_s is the release time. One can look at the statistics of the "cloud" of N values of $r_i{}^l$. An average over the cloud is indicated by the symbol $\langle\,\rangle_c$. Thus the mean and standard deviation of the particle positions at time t are written

$$\langle r_i \rangle_c \quad \text{and} \quad \left\langle r_i^2 - \langle r_i \rangle_c^2 \right\rangle_c^{1/2},$$

with the superscripts deleted for clarity. (Following the usual convention the standard deviations will also be labelled σ_x, σ_y and σ_z.) The method is essentially similar to that used by Willis and Deardorff (1976) in their laboratory experiments, except that they released particles along a horizontal line and measured dispersion only in directions perpendicular to that line; they were not, of course, able to track individual particles.

The dimensionless, horizontally-integrated concentration of the cloud is defined as

$$C^* = Ch_*/N,$$

where C is the density of particles per unit interval in height r_3. Willis and Deardorff show that, if the wind speed U in the boundary layer is constant with height and large enough for streamwise diffusion to be ignored, then C^* at dimensionless time

$$t^* = (t - t_s)\frac{w_*}{h_*}$$

after release is equivalent to the dimensionless *cross-wind integrated* concentration in a plume at a dimensionless distance

$$x^* = (x - x_s)\frac{w_*}{h_* U}$$

downwind of a point source.

To compare the present LES/dispersion model with previous work, particles were released in a layer at $z = 290m = 0.25h_*$ in the fields from Run A and tracked for 40 minutes.[16] There were three releases conducted at different times during the period between $t = 300\,\mathrm{min}$ and $t = 400\,\mathrm{min}$ and the particle trajectories from the different releases were then combined for an ensemble average. The technique of averaging over several releases was developed for use in simulations with surface heat-flux perturbations, below; it is not really necessary for the horizontally homogeneous calculations. Figure 6.1 shows the evolution of the dimensionless horizontally integrated concentration: Figure 6.1a shows contours of C^* on a dimensionless height-time plane and Figure 6.1b shows the ground-level value of C^*. The height of maximum concentration descends from the source height, reaching the surface at $t^* \sim 0.5$, then lifts off again at $t^* \sim 1$. The maximum dimensionless concentration at ground level—let it be called $C^*_{\mathbf{max}}$—is 2.7 and it is reached at $t^* = 0.6$. By $t^* = 4$ the concentration is almost uniform throughout the boundary layer at a dimensionless value of about 1.0. (Paradoxically this results in apparent noisiness in the figure as small fluctuations then lead to large deflections in the $C^* = 1.0$ contour.) The final concentration profile will be discussed further below. The results agree very well with those from Lamb's (1978) numerical model and Willis and Deardorff's (1978) laboratory tank model (Figure 6.2). Lamb's model does show, however, a secondary maximum at ground level, which persists after the cloud lifts off and which is not observed in the laboratory tank. This was encountered in the present model too, until the subgrid scheme was set up to *reverse* the vertical component of subgrid

[16]See Chapter 3 for a description of the simulation. All scaling parameters quoted in this chapter are based on statistics time-averaged from 300 to 400 minutes.

(a)

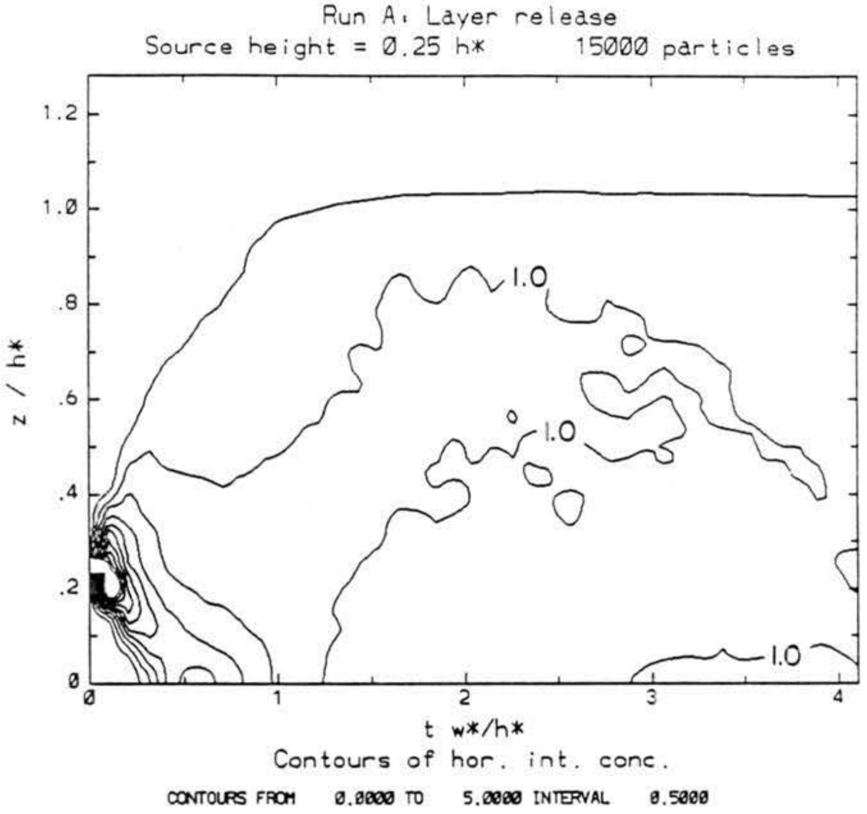

(b)

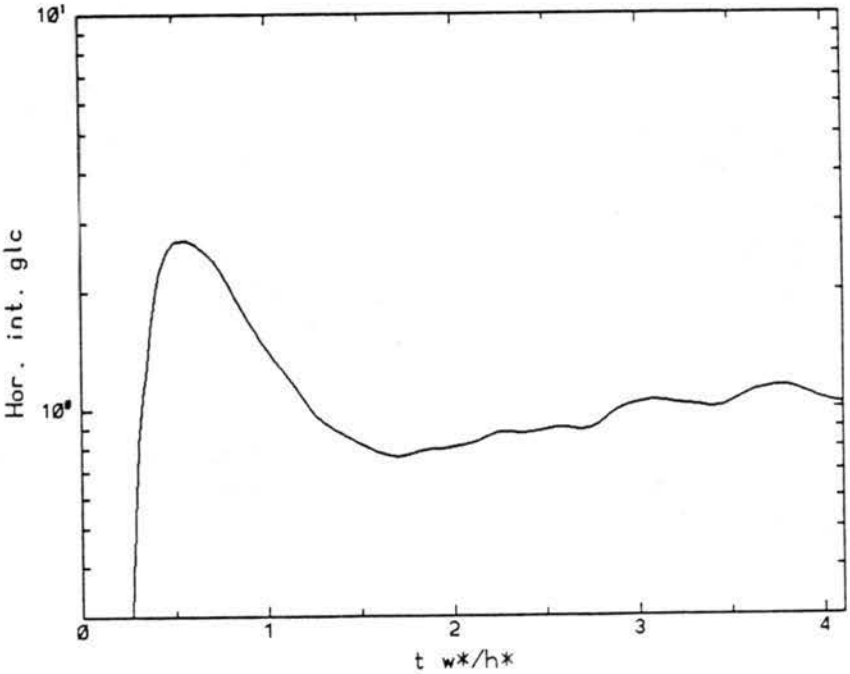

Figure 6.1. Dimensionless, horizontally integrated concentration C^* for the release in Run A. (a) Contours of C^* versus dimensionless height and dimensionless time after release (contour interval 0.5). (b) Ground-level value of C^* versus dimensionless time.

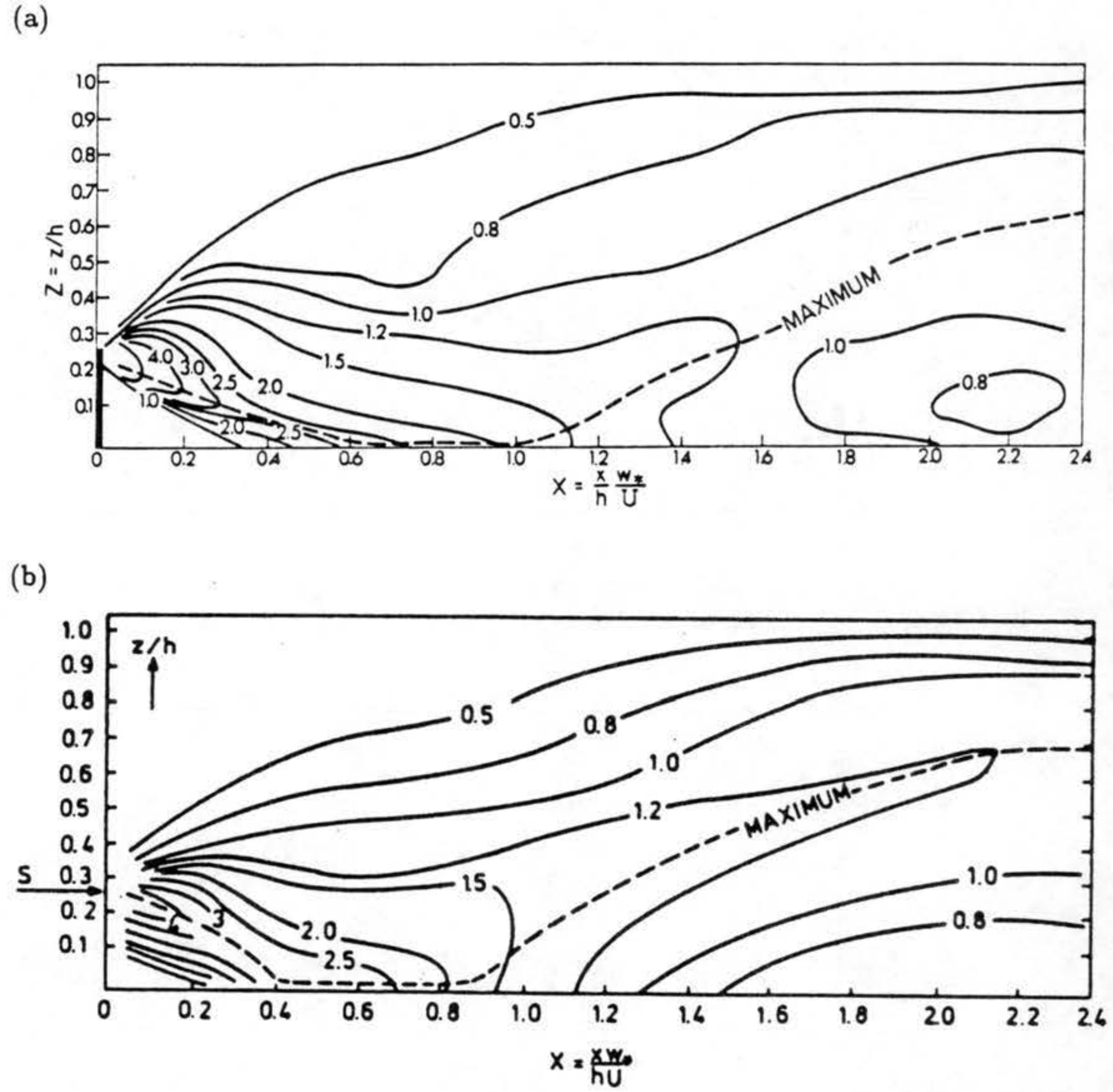

Figure 6.2. Dimensionless, cross-wind integrated concentration for releases at $z = 0.25h$, from (a) the numerical model of Lamb (1978) and (b) the laboratory model of Willis and Deardorff (1978). Figures copied from Lamb (1982).

particle velocities on reflection from the surface, rather than *re-initialising* the Markov chain as suggested by Lamb.

Figure 6.3 shows various distances characterising the particle cloud: Figure 6.3a shows the height of the maximum in C^* and the mean height $\langle r_3 \rangle_c$. The mean height initially remains constant, as required by mass continuity,[17] then approaches its final value of $0.5h_*$, overshoots and finally relaxes back towards it. There is very good agreement with Willis and Deardorff (1978, Figure 1).

The height of maximum concentration initially descends at such a rate that it would intersect the surface at $t^* = 0.63$—this implies a mode of $-0.40w_*$ in the distribution of particle velocities—however between $t^* = 0.45$ and $t^* = 0.50$ it jumps down to the surface, presumably as a result of downdraughts containing faster-descending particles reaching the surface and spreading out. There is nothing remarkable about an abrupt jump in the height of maximum concentration—such behaviour is shown by a Gaussian plume model with reflection at the surface, for example—but it is mentioned here to draw attention to the fact that the concentration maximum need not be always associated with the same particles. At $t^* = 1.2$ the height of maximum concentration lifts off again, as noted above; again the movement is abrupt. After $t^* \approx 2$ it is not well-defined.

Figure 6.3b shows the standard deviations, defined above. They are within 10% of the numerical and laboratory results shown by Lamb (1982, Figure 5.11).[18]

One presumes that the concentration profile tends towards a final state in which the particles are mixed throughout the boundary layer. If the top of the boundary layer were a rigid, impervious wall at $z = h_*$ (which it clearly is not) then in the final state C^* would be 1.0 below $z = h_*$ and zero above. With such a profile the mean height would be $0.50h_*$ and the standard deviation would be $0.29h_*$. For comparison, the mean height and standard deviation at $t^* = 4.1$ are $0.51h_*$ and $0.30h_*$, respectively. Figure 6.4 shows

---

[17]The mean subsidence velocity at $z = 0.25h_*$ is $-0.003w_*$, which is negligible.

[18]Lamb plots the *root-mean-square displacement from the source position,* which in the vertical is not the same as the standard deviation. The present data has also been expressed in this form and agreement is good.

(a)

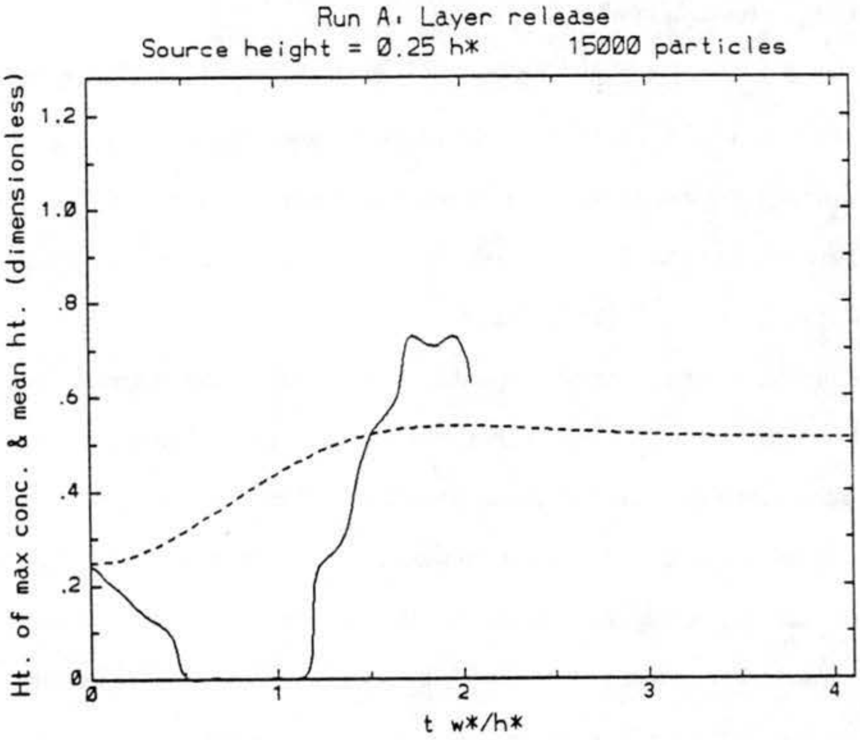

(b)

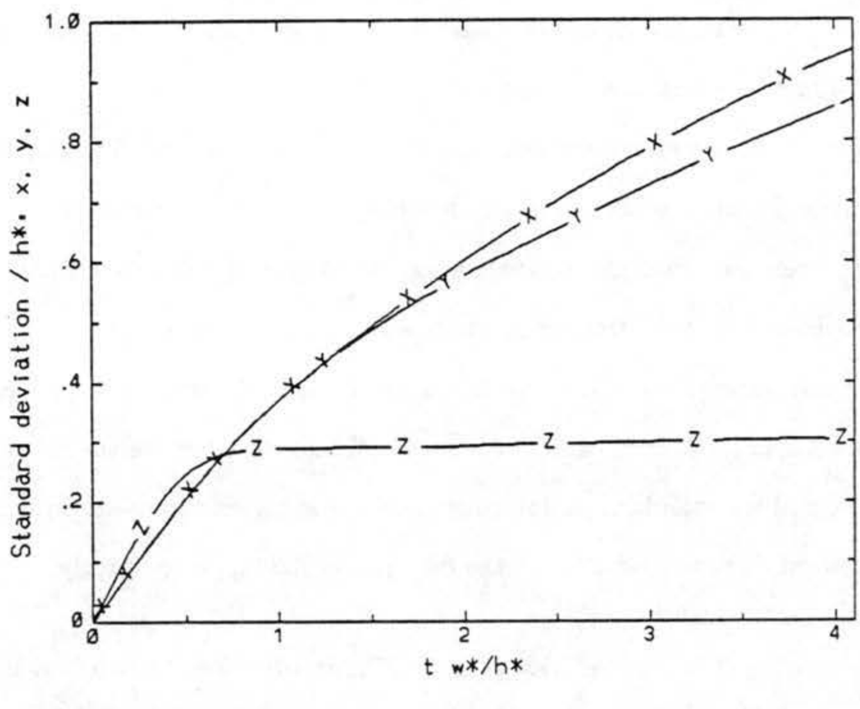

Figure 6.3. Position and size of the particle cloud for the release in Run A. (a) Height of maximum concentration (——) and mean height (- - -). (b) Width (standard deviation) in the x (—X—), y (—Y—) and z (—Z—) directions.

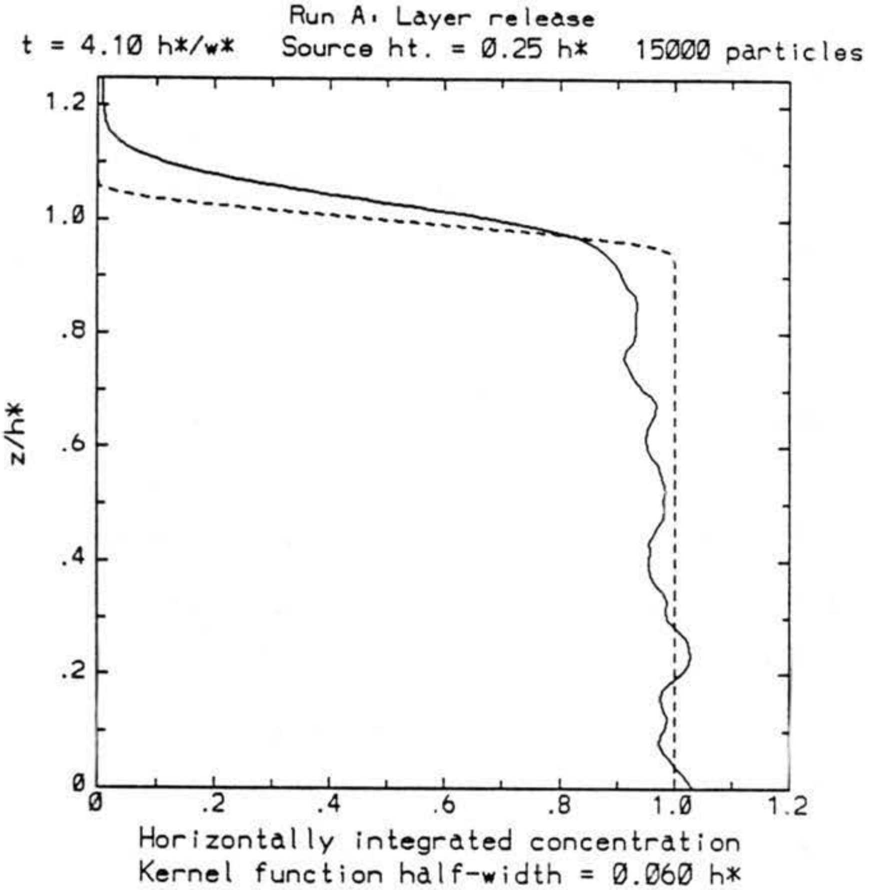

Figure 6.4. Profile of C^* (solid line) at time $t^* = 4.1$ for the release in Run A. The dashed line shows a uniform distribution up to $z = h_*$ evaluated with the same kernel width.

the concentration profile at $t^* = 4.1$. It also shows the profile that would be computed if an infinite number of particles were uniformly distributed below $z = h_*$; owing to the non-zero width of the kernel function the discontinuity is smoothed over a layer of thickness $0.10h_*$. The small-scale variability in the simulated concentration profile is due to the finite number of particles; the concentration estimate at each height is based on ~ 2000 particles, so the standard deviation should be approximately 2% of the mean. Ignoring the random fluctuations the concentration is around 1.0 near the surface and drops off more or less linearly in the lower and middle boundary layer according to

$$C^* \approx 1 - 0.07z/h_*. \tag{6.7}$$

This decrease cannot be accounted for by random fluctuations, nor does it result from any tendency of the model to generate spurious concentration gradients. Instead it appears from Figures 6.1 and 6.4 that the concentration maximum is oscillating between the lower and upper boundary layer with a period of $\sim 3h_*/w_*$, and that at $t^* = 4.1$ the oscillation has not died down completely.

Given that C^* is a weak function of height within the boundary layer, the rapid decrease of C^* near $z = h_*$ can be interpreted as a decrease in the fractional coverage of mixed-layer air. Let the entrainment layer be defined as the region between heights $\tilde{h}_0$, where the fractional coverage is 0.95, and $\tilde{h}_2$, where the fractional coverage is 0.01. (The motivation behind the definitions and notation will become clear below.) By comparing the actual C^* profile with the linear profile of Equation 6.7 one can estimate that $\tilde{h}_0 = 0.92h_*$ and $\tilde{h}_2 = 1.20h_*$. The entrainment layer thickness is therefore $0.28h_*$. There is some uncertainty in $\tilde{h}_0$ owing to uncertainty in Equation 6.7, and there is a tendency to ovestimate the thickness slightly owing to the non-zero kernel width.

Deardorff *et al.* (1980) defined the bottom of the entrainment layer (h_0) as the height of the lowest zero-crossing in the heat flux and the top of the entrainment layer (h_2) as the height where the heat flux vanishes. In a series of laboratory simulations they found the entrainment layer thickness to be between 0.2 and 0.3 times the mixed-layer depth (i.e., comparable with the present result) when the fluid above the mixed layer was strongly stratified. For the laboratory data, h_0 and h_2 coincide with $\bar{h}_0$ and $\bar{h}_2$ as defined above. For the LES model h_0 is $0.8h_*$ and h_2 is not well-defined (owing to the non-zero heat fluxes well above the boundary layer) but the most closely comparable height is the second zero-crossing in the heat flux at $z = 1.1h_*$. These heights are about $0.1h_*$ below $\bar{h}_0$ and $\bar{h}_2$, respectively, which suggests some differences between the entrainment processes in the LES model and the laboratory. On the other hand it is reassuring that very few particles penetrate to $z = 1.2h_*$: whatever the nature of the flow structures that contribute to the spurious heat-flux maximum at that level in the model, they do not exchange significant mass with the boundary layer.

6.3 Dispersion with a surface heat-flux perturbation

The layer-source experiment described above was repeated for each set of simulations described in Chapter 4, namely Set F ($\lambda_p = 1500\,\mathrm{m}$, $u_0 = 0\,\mathrm{m\,s^{-1}}$), Set G ($\lambda_p = 1500\,\mathrm{m}$, $u_0 = 1\,\mathrm{m\,s^{-1}}$), Set H ($\lambda_p = 4500\,\mathrm{m}$, $u_0 = 0\,\mathrm{m\,s^{-1}}$), Set I ($\lambda_p = 4500\,\mathrm{m}$, $u_0 = 1\,\mathrm{m\,s^{-1}}$) and Set J ($\lambda_p = 4500\,\mathrm{m}$, $u_0 = 2\,\mathrm{m\,s^{-1}}$). In each case there were two separate releases, at $t = 300\,\mathrm{min}$ and $t = 350\,\mathrm{min}$, in each of the simulations comprising the set.

The only case in which the heat-flux perturbation has a conspicuous effect on the dispersion from the layer source is Set H. Figure 6.5 shows the evolution of the C^* profile and the standard deviations. The maximum horizontally-integrated concentration at ground-level is only slightly different from the horizontally homogeneous simulation ($C^*_{\mathrm{max}} = 3.0$ in Set H versus $C^*_{\mathrm{max}} = 2.7$ in Run A) and it is reached slightly later ($t^* = 0.71$ in Set H versus $t^* = 0.56$ in Run A) but the subsequent lift-off of the concentration maximum is substantially delayed (it occurs at $t^* = 2.3$ in Set H and at $t^* = 1.2$ in Run A). A likely explanation is that the typical time required for a fluid element in the lower boundary layer to be carried into the upper boundary layer is large in Set H owing to the relatively large horizontal distances that must be travelled to enter the base of the dominant, quasi-two-dimensional updraught. The other major effect is that σ_x grows about twice as fast as σ_y, which is consistent with the difference between the horizontal velocity variances, $\langle u'^2 \rangle_{h,t}$ and $\langle v'^2 \rangle_{h,t}$.

(a)

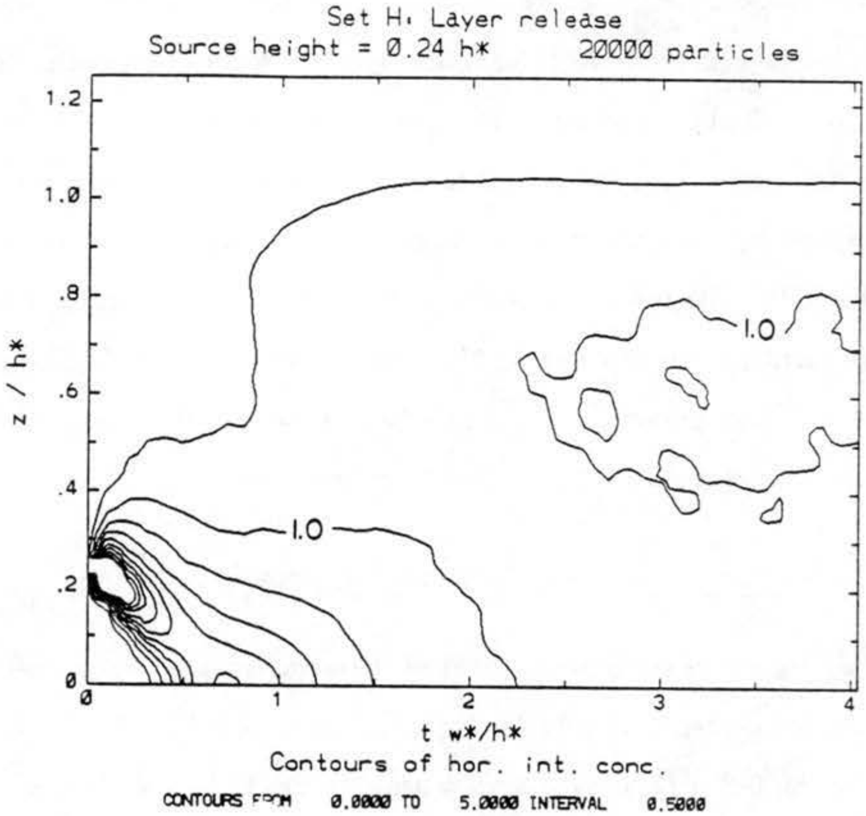

(b)

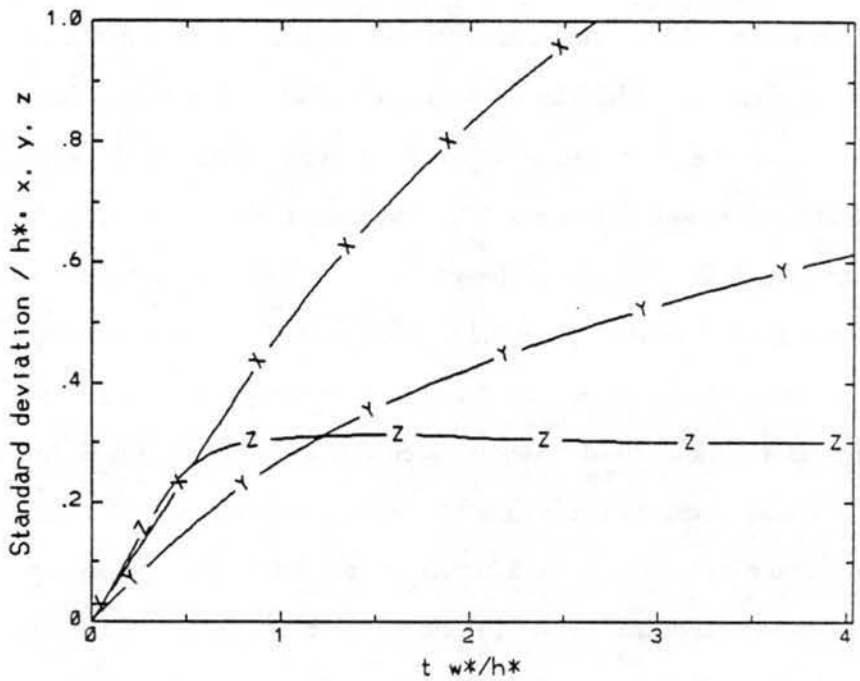

Figure 6.5. Layer release in Set H. (a) Contours of C^* versus dimensionless height and dimensionless time (contour interval 0.5). (b) Width (standard deviation) in the x (—X—), y (—Y—) and z (—Z—) directions.

In the remaining cases (not shown), namely Sets F, G, I and J, the C^* profile evolves in very much the same way as it did in the horizontally homogeneous case. In general, growth in σ_x is a little faster than growth in σ_y, the difference becoming larger with t^* as the scale of the eddies dispersing the cloud becomes larger. At $t^*=1$ ($t^*=3$) the ratio σ_x/σ_y is 1.15 (1.18) in Set F, 1.00 (1.00) in Set G, 1.08 (1.20) in Set I and 1.06 (1.14) in Set J.

The surface heat-flux perturbation has a more pronounced effect when the particles are released only at a given value of $\hat{x}$. The source is then a series of lines parallel to the y-axis, one in each cycle of the surface heat-flux perturbation. One expects that where the mean vertical velocity is negative a larger fraction of particles will be carried towards the surface and the ground-level concentration will be increased, and that where it is positive the ground-level concentration will be reduced. In each set of simulations particles have been released at two different values of $\hat{x}$, but still at $z=290\,\mathrm{m}$. One of the particle sources was chosen to be near the position where $\langle w' \rangle_{p,t}$ at $z=290\,\mathrm{m}$ is most negative (the downdraught source) and the other was near the position where $\langle w' \rangle_{p,t}$ is most positive (the updraught source). The source positions are described in Table 6.1, along with other information discussed below.

It has already been seen that the strength of the instantaneous circulation (Chapter 4) fluctuates so that an estimate of the ensemble-average circulation typically requires averaging over several simulations and over time. The particle clouds have therefore also been averaged over several releases. In Set F, which includes four separate simulations, there were two releases from each source in each simulation, at $t = 300\,\mathrm{min}$ and at $t = 350\,\mathrm{min}$. In Sets G to J, each of which includes two simulations, there were four releases from each source in each simulation, at $t = 300\,\mathrm{min}$, $t = 325\,\mathrm{min}$, $t = 350\,\mathrm{min}$ and $t = 375\,\mathrm{min}$. The particles were followed for 40 minutes after release, except for the releases at $t = 375\,\mathrm{min}$ which could be followed for only 25 minutes. Each particle cloud described below is therefore an average over a total of eight releases, more or less covering the averaging period ($t=300\,\mathrm{min}$ to $t=400\,\mathrm{min}$) over which statistics have been calculated in Chapters 3, 4 and 5.

Table 6.1. Statistics of line-source releases. The columns are labelled "D" for the downdraught source and "U" for the updraught source. The first pair of columns shows the source position, as a fraction of λ_p, for each source. The second pair of columns shows the dimensionless, phase-time averaged vertical velocity at the source. The third pair of columns shows the initial, dimensionless, cloud-mean vertical velocity.

Set	Position $(\hat{x}/\lambda_p)$		$\langle w\rangle_{p,t}/w_*$		$\langle q_3(t_s)\rangle_c/w_*$	
	D	U	D	U	D	U
F	−0.50	0.00	−0.11	0.14	−0.08	0.10
G	−0.17	0.33	−0.08	0.07	−0.09	0.02
H	−0.50	0.00	−0.12	0.80	−0.11	0.78
I	−0.25	0.33	−0.20	0.20	−0.23	0.17
J	−0.10	0.40	−0.05	0.08	0.04	0.12

The line-source geometry coincides with the geometry over which the phase averages are calculated, so one expects that if the releases are sufficiently dense in time then the mean vertical velocity of the cloud $\langle q_i(t_s)\rangle_c$ at the time of release should equal the phase-time averaged velocity $\langle u_i\rangle_{p,t}$ at the source. The vertical components of these two velocities are compared in Table 6.1; the difference is typically of the order of $\pm 0.04 w_*$ (standard deviation) with no apparent bias. This variability is comparable to the circulation velocity in some of the sets of simulations—note in particular that for the downdraught source in Set J the mean cloud velocity is *positive*—but in general there is clearly a correlation between the cloud-averaged velocity and the circulation velocity.

Figures 6.6ff show the results of the line-source releases in two of the sets of simulations. (The format of the figures follows Figure 6.5. Note that the slight discontinuities in some of the figures at $t^* \approx 2.5$ are a result of a change of the number of particles in the cloud as the $t = 375$ min releases are terminated.) In Set H (Figures 6.6 and 6.7) the difference between the downdraught and updraught sources is pronounced. The majority of particles released from the downdraught source (Figure 6.6) descend to the surface so $C^*_{\max} = 5.6$, almost twice as large as in the horizontally homogeneous boundary layer. The top boundary of the cloud, indicated roughly by the $C^* = 0.5$ contour, reaches $z = 0.45h_*$ quite rapidly, but does not rise much further until after $t^* = 3$. Recall that the convective updraughts in the descending branch of the circulation in Set H reach a maximum height of $z \approx 0.5h_*$; particles cannot penetrate to higher levels until they reach the deeper updraught centred over the surface heat-flux maximum. Initially σ_x, σ_y and σ_z all grow at the same rate, substantially more slowly than in the horizontally homogeneous boundary layer, but after $t^* = 0.5$ growth of σ_x accelerates and growth of σ_z decelerates as the cloud impinges on the surface and spreads laterally. The cloud from the updraught source (Figure 6.7) is carried rapidly up to the top of the boundary layer and then mixes slowly back down. Some particles *are* carried directly down to the surface, arriving at $t^* \approx 0.5$, but there are too few to appear on the contour plot. Again there is a period of accelerated growth in σ_x and develerated (even negative) growth in σ_z, this time occurring as the cloud reaches the capping inversion.

(a)

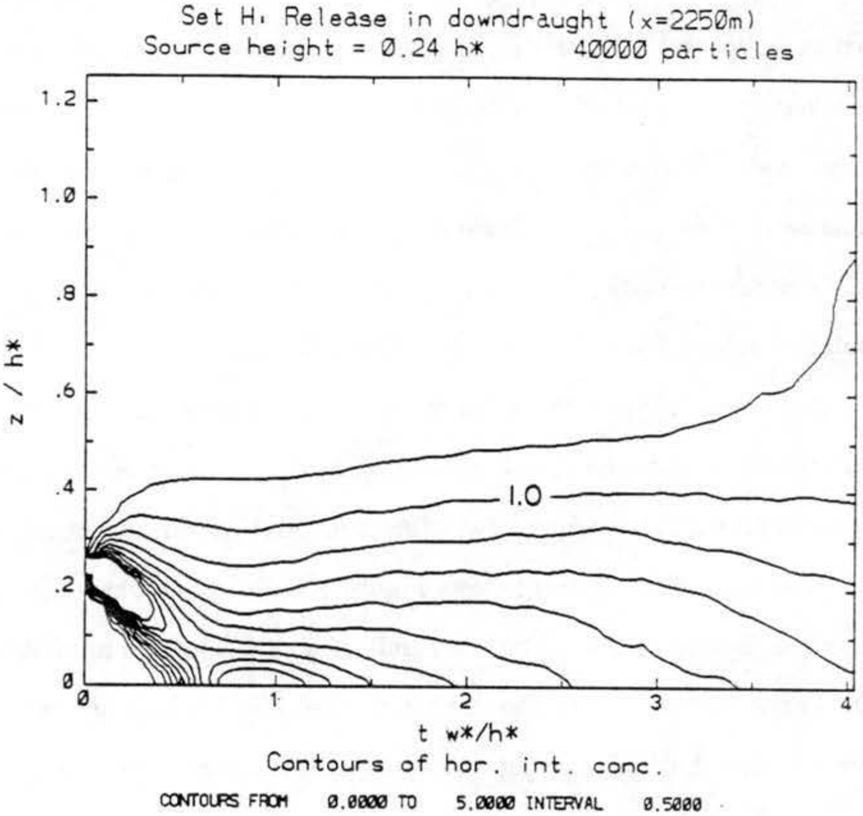

(b)

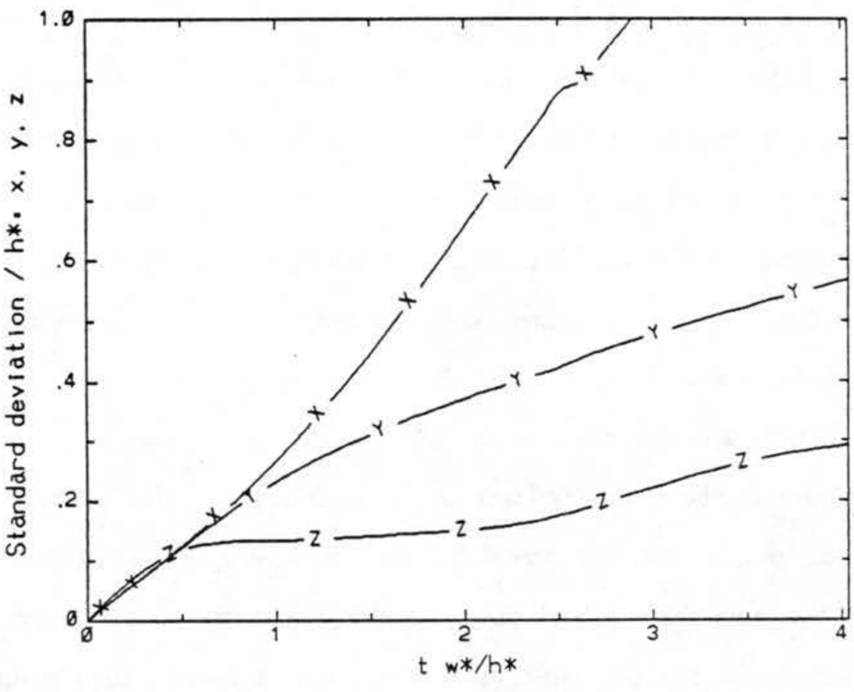

Figure 6.6. As Figure 6.5 but downdraught release ($\hat{x} = -0.5\lambda_p$) in Set H.

(a)

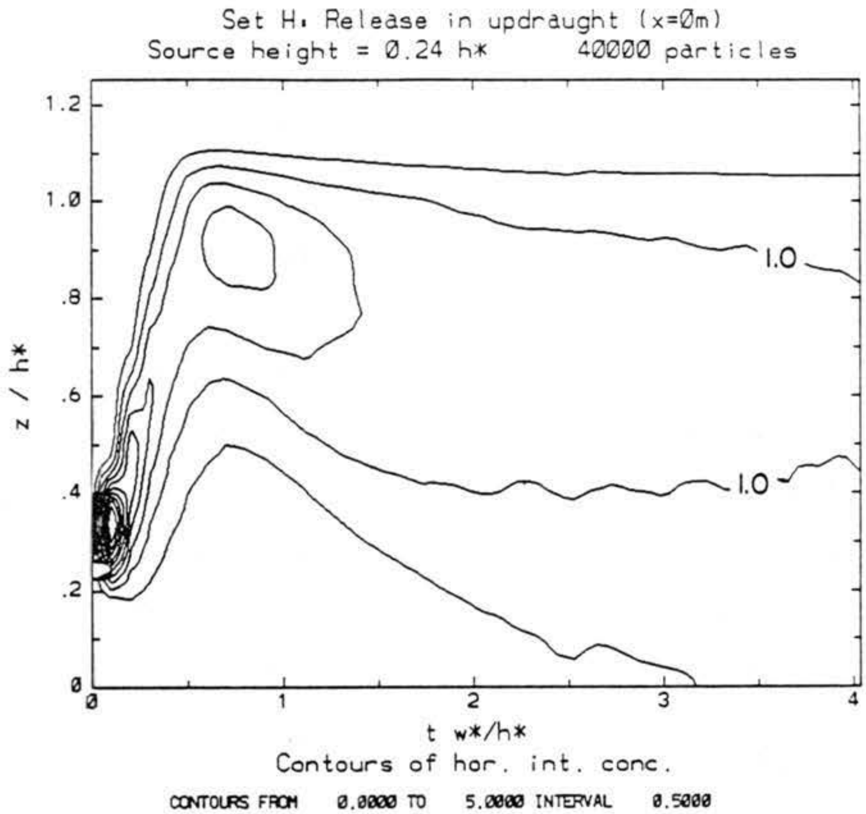

(b)

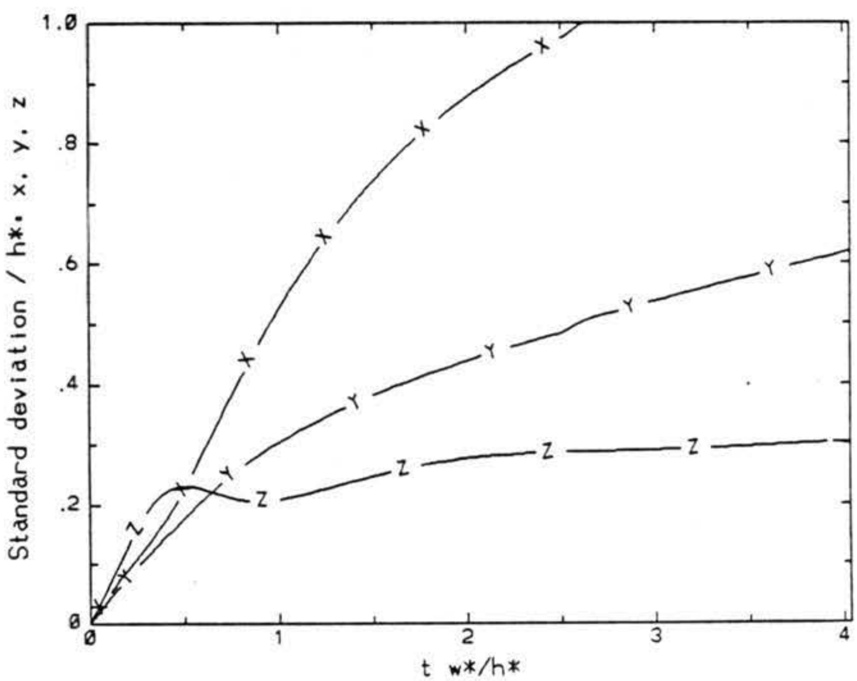

Figure 6.7. As Figure 6.5 but updraught release ($\hat{x}=0$) in Set H.

In Set I (Figures 6.8 and 6.9) the position of the source clearly has a significant effect on the dispersion of the particle clouds, but less so than in Set H. With the downdraught source (Figure 6.8) the height of maximum concentration descends at about the same velocity ($-0.40w_*$) as it does for a layer source in the horizontally homogeneous boundary layer, but the fraction of particles descending is larger and so is the maximum ground-level concentration ($C^*_{\mathrm{max}} = 4.6$ for the downdraught source in Set I versus $C^*_{\mathrm{max}} = 2.7$ for Run A). The σ curves are not very different from the corresponding curves for Run A except that σ_z takes much longer to reach its final value and σ_x/σ_y is greater than 1 (and also slightly greater than it was for the layer source in Set I). With the updraught source (Figure 6.9) the concentration profile is either bimodal or has a broad maximum for some time after release and the maximum ground-level concentration is lower ($C^*_{\mathrm{max}} = 1.2$). By $t^* = 1.5$ there is a pronounced upper-level maximum, which then descends to the surface by $t^* = 3.5$ and presumably oscillates vertically for some time thereafter. In this case σ_x/σ_y is slightly smaller than it was for the layer source.

Table 6.2 summarises the values of the maximum dimensionless ground-level concentration C^*_{max} for the layer- and line-source releases in Sets F to J. There is, however, a minor subtlety in the definition of C^*_{max}. Typically the C^* versus t^* curve at ground level (e.g., Figure 6.1b) has at least two maxima, the first one at $0.5 < t^* < 1$ associated with the initial impingement of the cloud on the surface and the second one much later associated with oscillation of the concentration profile about its final state. For the updraught releases the second maximum can be larger than the first; this is the case, for example, in Set I (Figure 6.9a). The first maximum is more important for short-range dispersion of a plume from a point source, because the plume width is smaller at the earlier time and the plume centreline concentration proportionally higher, and it is this maximum that is listed in Table 6.2. In general C^*_{max} shows the expected dependence on the vertical velocity at the source. The maximum concentration from the downdraught source is always larger than the maximum concentration from the updraught source. The maximum concentrations of Table 6.2 are plotted against the initial cloud-mean vertical velocities of Table 6.1 in Figure 6.10. (The initial vertical velocity of the layer-source

(a)

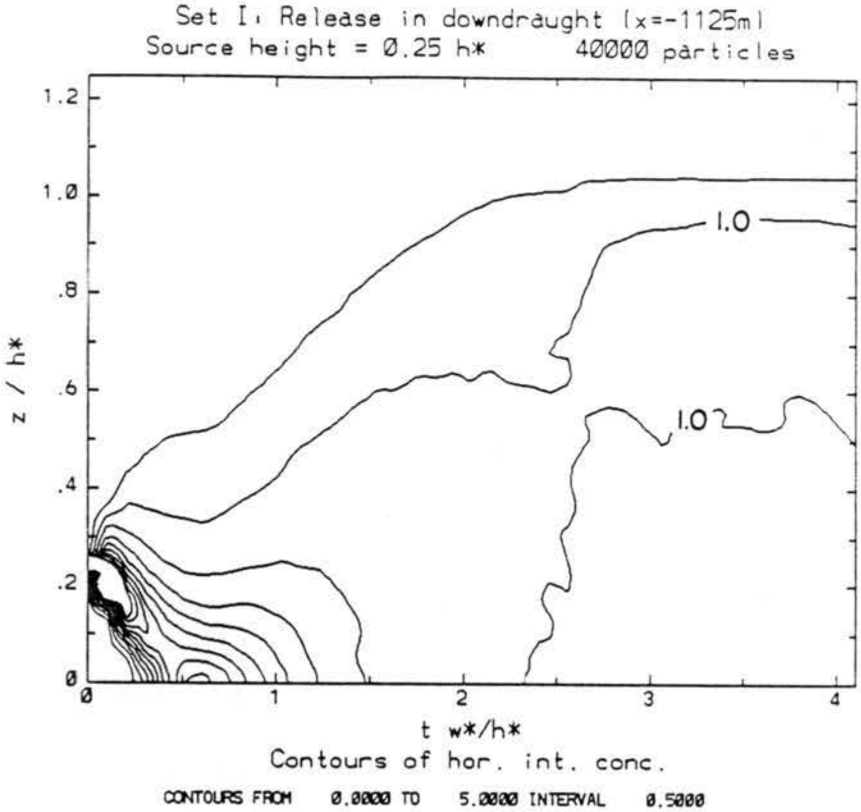

(b)

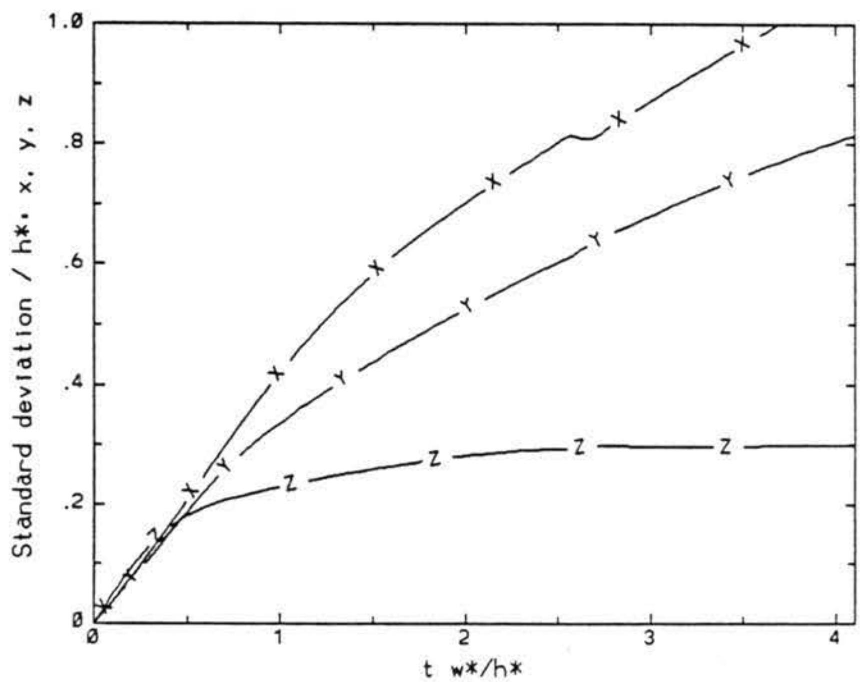

Figure 6.8. As Figure 6.5 but downdraught release ($\hat{x} = -0.25\lambda_p$) in Set I.

(a)

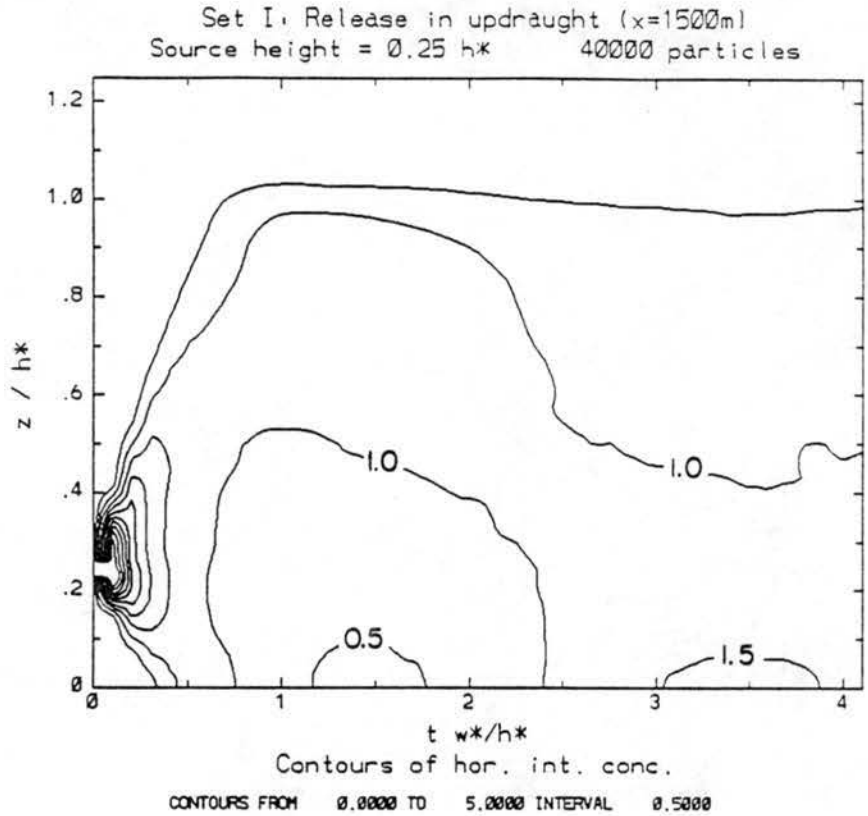

(b)

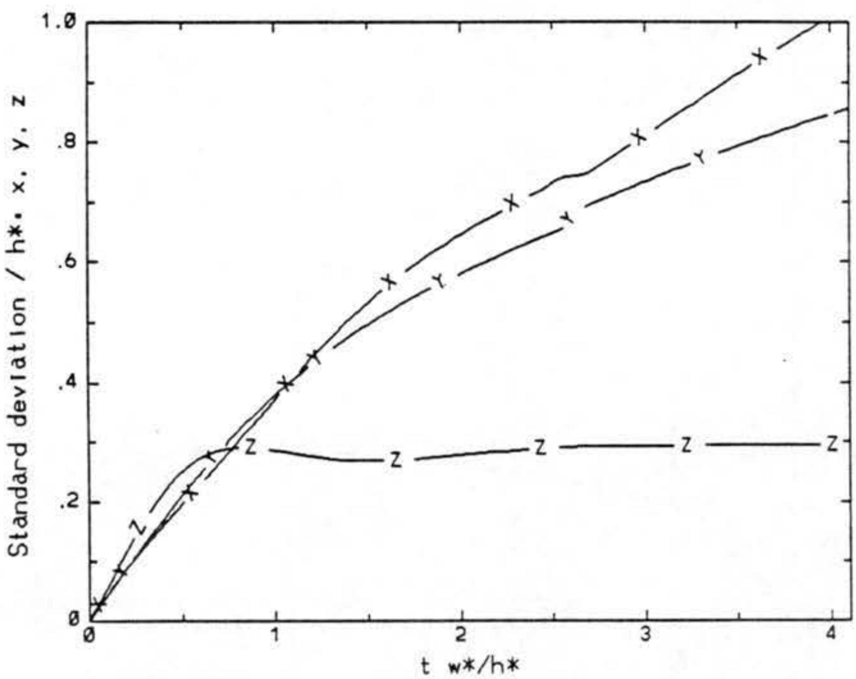

Figure 6.9. As Figure 6.5 but updraught release ($\hat{x} = 0.33\lambda_p$) in Set I.

Table 6.2. The maximum ground-level concentration $C^*_{\max}$ for layer- and line-source releases. The columns are labelled "D" for the downdraught source, "L" for the layer source and "U" for the updraught source.

Set	$C^*_{\max}$		
	D	L	U
F	3.9	2.5	1.4
G	3.1	2.6	2.4
H	5.6	3.0	0.1
I	4.6	2.5	1.2
J	3.0	2.4	1.8

clouds is zero, of course.) If Set H is excluded, the data can be described with a linear relationship

$$C^*_{\max} = 2.65 - 8.6 \left\langle q_3(t_s)\right\rangle_c / w_* \qquad -0.2 \leq \left\langle q_3(t_s)\right\rangle_c / w_* \leq 0.2 \tag{6.8}$$

with coefficient of determination $r^2 = 0.88$. *It is hereby proposed that Equation 6.8 is a useful first approximation for the effect of moderate mean vertical velocities on the ground-level concentration, with a source height of* $0.25h_*$.

The data from Set H clearly do not follow Equation 6.8. For the updraught source the predicted $C^*_{\max}$ is negative, so the initial cloud-averaged vertical velocity is well outside the range over which Equation 6.8 applies. For the downdraught source the initial vertical velocity is of modest magnitude, but $C^*_{\max}$ is substantially higher than predicted. In this case the turbulent vertical velocity variance at the source is very low, therefore the effect of the mean descending motion is enhanced.

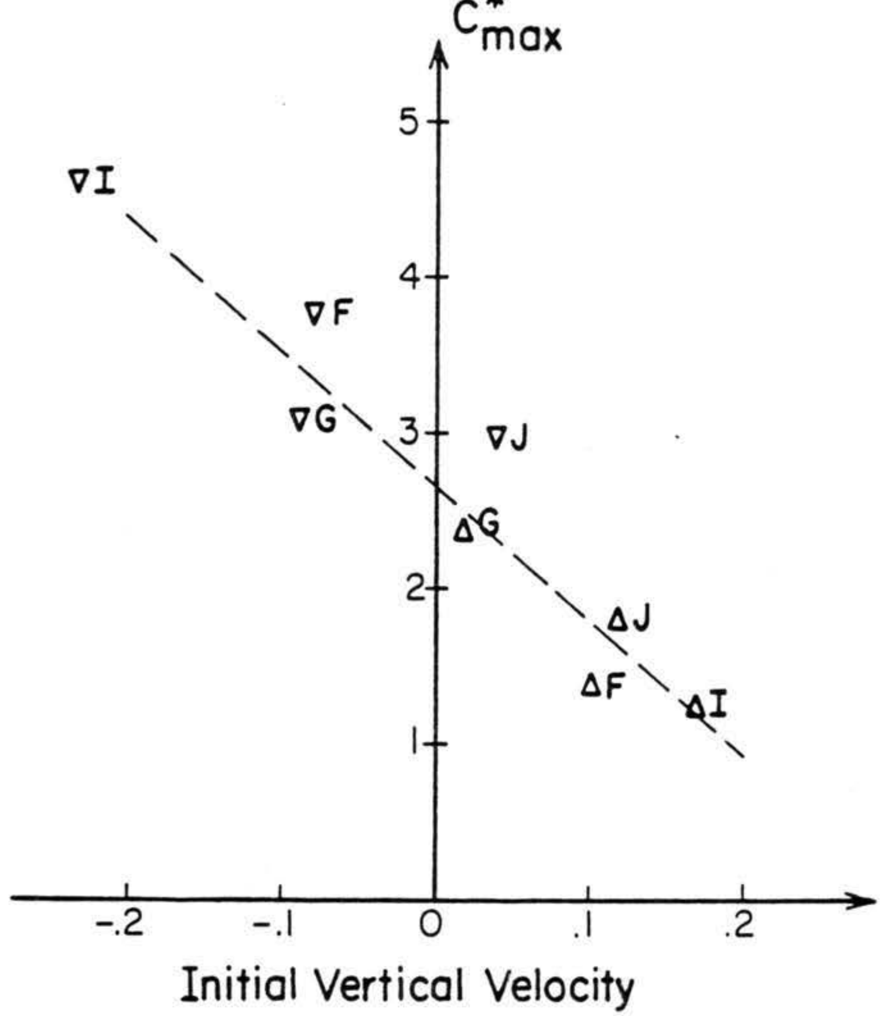

Figure 6.10. Maximum dimensionless, ground-level concentration C^*_{max} versus dimensionless, initial, cloud-mean vertical velocity for updraught ($\triangle$) and downdraught ($\triangledown$) releases. The dashed line shows the relationship defined by Equation 6.8.

Chapter 7

Summary and Conclusions

7.1 Synthesis

A large-eddy simulation of a horizontally homogeneous boundary layer has been compared with simulations conducted by other workers, and with atmospheric and laboratory studies. In most respects the large-eddy models are similar to each other. They simulate a field of convective eddies having approximately the correct velocity and spatial scale, and they correctly predict that the updraughts are narrower and stronger than the downdraughts, which implies vigorous vertical transport of kinetic energy. Compared to the convective boundary layers observed in the atmosphere and the laboratory, the numerically simulated boundary layers have the potential temperature variance too small in the lower and middle and boundary layer, which implies too high a correlation between vertical velocity and temperature fluctuations. It is interesting, however, that the updraught-mean and downdraught-mean temperature perturbations are similar to those measured in the atmosphere. Other common failings of the models are a pressure variance that is too small, a vertical velocity skewness that is too large in the upper half of the boundary layer and a horizontal velocity variance profile with too-pronounced a maximum near the surface.

The dynamics of the eddies in the simulated boundary layer have been described in terms of the budgets for turbulence kinetic energy, heat flux and temperature variance. Following Moeng and Wyngaard (1986b) the pressure field has been divided into contributions induced by each of the other "forces" (buoyancy, advection, subgrid) in the Eulerian momentum equation. As expected, kinetic energy is generated in the vertical component of velocity via buoyancy production in the lower boundary layer, transported into the upper boundary layer, and transferred to the horizontal velocity field by the pressure-gradient forces. About one percent of the total buoyancy production is transported by gravity waves to the artificial absorbing layer near the upper boundary. In the vertical, the buoyancy-pressure (π_b) gradient force tends to oppose the buoyancy: whereas Moeng and Wyngaard proposed a constant ratio (A) of around 0.5 between them, here it is found that A varies with height, with much the same vertical profile in all the second and third moment budgets. Gradients in the advection pressure (which is dominated by the contribution (π_t) induced by turbulence/turbulence interaction) oppose kinetic energy transport in mid-boundary-layer. Intercomponent transfer due to π_t has commonly been parameterised in the past by a return-to-isotropy expression. Such an expression does not work well in the present model, but it is also found that the net transfer of kinetic energy from the vertical to the horizontal is not as vigorous in the model as it should be—or, to be more exact, not as vigorous as it would have to be if the model were to resolve eddies well into the inertial subrange. Similarly, in discussion of the heat flux budget it is concluded that the temperature/π_t-gradient covariance is not as large a sink for heat flux in the lower boundary layer as it should be. A qualitative model for the temperature, velocity and pressure structure of updraughts and downdraughts has been developed which is consistent with several aspects of the turbulence statistics, but it appears that the large-eddy model—at the resolution used here—is not a convincing tool for investigating the details of the turbulence dynamics, especially those details involving unsteady or small-scale structures.

The sensitivity of the large-eddy model to a doubling of the subgrid length scale has been investigated. The subgrid diffusivity increases with the length scale, so that at the larger value of the length scale there is less fine-scale structure in the fields. There are also substantial changes in the heat flux, temperature variance and potential temperature gradient in the lowest one-tenth of the boundary layer, but otherwise the changes are more subtle. In many respects the profiles of turbulence statistics become more realistic with an increase in the length scale (a less-pronounced surface maximum in horizontal velocity variance, larger pressure variance, smaller skewness in the upper boundary layer), but there is also a substantial decrease in the intercomponent transfer of energy by the π_t-gradient force, which is already too small.

The large-eddy model therefore captures several of the important features of the eddies in the horizontally homogeneous, convective boundary layer, although it is by no means perfect. Several improvements are possible, including a general improvement in resolution or a selective improvement near the surface and the capping inversion using stretched or nested grids.

The model has next been applied to simulations of the convective boundary layer over a surface with a spatially varying heat flux, for which long averaging times and/or multiple simulations are necessary. For this problem a substantial improvement in resolution is not practicable. It remains to be seen just how accurate a simulation is necessary for this problem. Verification, although beyond the scope of the present study, is an essential next step and will be discussed below.

The perturbation in the surface heat flux was chosen to be sinusoidal in the x direction and constant in the y direction, with an amplitude equal to one-half the horizontally averaged flux and with wavelengths λ_p of 1500 m or 4500 m. A mean wind u_0 of $0\,\mathrm{m\,s^{-1}}$, $1\,\mathrm{m\,s^{-1}}$ or $2\,\mathrm{m\,s^{-1}}$ was imposed in the x direction (but the combination of $\lambda_p = 1500\,\mathrm{m}$, $u_0 = 2\,\mathrm{m\,s^{-1}}$ was not considered). In all the simulations but one,[19] the boundary layer was first allowed to develop over a surface with constant heat flux for 200 minutes, then the perturbation was applied suddenly and the simulation continued to 400 minutes. Subsidence was imposed such that the boundary layer depth remained approximately constant throughout, at a little less than 1200 m. The analysis has concentrated on time averages from $t = 300$ min to $t = 400$ min.

With the smaller wavelength ($\lambda_p = 1500\,\mathrm{m}$) and zero mean wind, a mean circulation is set up with ascent over the heat-flux maxima (maximum positive velocity $0.14w_*$)

[19]The exception is Run F5, see Section 4.4.1.

and slightly weaker descent (maximum negative velocity $0.12w_*$) over the heat-flux minima. The amplitude of the vertical velocity is at a maximum at $z = 0.35h_*$; below this level there is inflow into the updraught (maximum velocity $0.18w_*$) and above there is much weaker outflow. There is considerable variability in the strength of the circulation, however, and time averages from four separate simulations have been combined to give reasonable confidence that the mean circulation is real. Associated with the circulation, there are also mean variations in the temperature and pressure fields. In general the mean variations are small in the sense that they account for only a few percent of the variances and covariances of fluctuations from the horizontal average.

The surface heat-flux perturbation causes horizontal variations in the turbulence throughout the depth of the boundary layer. If one compares the regions over the heat-flux maxima with the regions over the heat-flux minima, one finds the following features over the former: the vertical velocity variance is larger, by about 50% in the middle of the boundary layer; near the surface the u variance is much larger; the temperature variance is larger in the lower boundary layer and near the capping inversion; the w/θ covariance is larger in the lower boundary layer and more negative in the entrainment layer.

Analyses of the budgets for temperature, velocity and turbulence stresses yield some further insight. In the temperature budget the effects of advection by the mean circulation are small—although not entirely negligible—so the turbulent heat flux is constrained to distribute heat more or less uniformly throughout the boundary layer. The relationship between the flux and the mean temperature perturbation in the lower boundary layer can be described reasonably well in terms of a down-gradient diffusion process, with a horizontal diffusivity of approximately $0.1w_*h_*$ and a vertical diffusivity equal to that calculated for horizontally homogeneous, bottom-up diffusion by Wyngaard and Brost (1984). The circulation velocity budget is dominated by a balance between the mean buoyancy force and the turbulent stress, once account has been taken of the induced pressure gradients. Energy extracted from the mean circulation by the turbulent stress is transferred to the turbulence kinetic energy, and the integral time scale for the process is quite short at $0.32h_*/w_*$, or 3 min. The largest of the turbulence sink terms in a vertically integrated sense is associated with horizontal convergence into the u variance maximum at the base of the updraught. Although the turbulent stresses are crucial in the dynamics of the circulation, the converse is not the case. The major features of the stress fields appear to arise as a result of forcing by the turbulent buoyancy and buoyancy-pressure fluctuations although transport and production by the circulation are not negligible. The buoyancy terms in the stress budgets are related to the horizontal and vertical heat fluxes, which, as mentioned above, are constrained by the need to distribute heat uniformly throughout the boundary layer.

One can look at the effect of the surface heat-flux perturbation in a fundamentally different way by examining the profiles of the horizontal averages and the deviations from them. (Collectively they are labelled "horizontal-average statistics.") For the case with $\lambda_p = 1500\,\mathrm{m}$ and $u_0 = 0\,\mathrm{m\,s^{-1}}$ the most noticeable effect of the heat-flux perturbation appears in the horizontal velocity variance profiles as an excess of u variance over v variance, the difference being largest near the surface and very small in the middle of the boundary layer. It is noteworthy that this difference is much larger in two of the simulations over which the averages have been calculated than in the other two. There is also a substantial increase in temperature variance near the surface. Other effects are more subtle—they can be detected in the model because there is a large control group of time averages from horizontally homogeneous simulations with which to make the comparison, but they would be difficult, if not impossible, to detect in the atmosphere. They include a small increase in the flux of vertical velocity variance through the middle of the boundary layer and an increase in the standard deviation of the pressure.

A light mean wind ($\lambda_p = 1500\,\mathrm{m}$, $u_0 = 1\,\mathrm{m\,s^{-1}}$) has a profound effect. The velocity, temperature and pressure fields are all moved and/or tilted downwind. The maximum mean updraught velocity is reduced to $0.08w_*$ and is found in mid-boundary-layer ($z = 0.5h_*$) about $0.5h_*$ ($0.4\lambda_p$) downwind of the heat-flux maxima. The layers of mean inflow and outflow are equal in depth and have similar maximum horizontal velocities ($\pm 0.06w_*$). The main features in the turbulence fields are moved downwind, too, and in some respects (e.g., the u variance at the surface) the amplitude of the horizontal variation is much reduced, but the maximum w variance in mid-boundary-layer remains about 50% larger than the minimum variance at the same level. The region of maximum entrainment is about $0.45h_*$ $(0.35\lambda_p)$ downwind of the surface heat-flux maximum, and a line joining the two can be loosely identified as the axis of maximum "turbulence intensity."

In the temperature budget there is a balance between horizontal advection and flux divergence, the latter being dominated by the gradient in the vertical flux. The budget can be described tolerably well by a model in which horizontal advection is added to the gradient-diffusion relationship developed for the previous case. In the circulation velocity budget there is a balance between horizontal advection, buoyancy and turbulence, but how these three adjust to give the observed velocity fields is not clear. The interaction between the horizontal velocity and the u variance is now a less significant sink for the kinetic energy of the circulation than it was with $u_0 = 0\,\mathrm{m\,s^{-1}}$, and the time scale for transfer of energy to the turbulence is a little larger at $0.46h_*/w_*$.

Most of the profiles of horizontal-average statistics are indistinguishable from the corresponding profiles in the horizontally homogeneous boundary layer. There is, however, still an increase in temperature variance near the surface.

In the simulations with the longer wavelength $(\lambda_p = 4500\,\mathrm{m})$ and zero mean wind, the circulation is much stronger than with the shorter wavelength. There is a relatively narrow (width $\approx 1.0h_* \approx 0.25\lambda_p$), turbulent region of strong ascending motion (maximum mean velocity $1.1w_*$) over the surface heat-flux maximum and a broader region with weaker and less turbulent descending motion on either side. The instantaneous fields are dominated by a narrow updraught meandering within a region $1.1h_*$ $(0.3\lambda_p)$ wide centred on the heat-flux maximum, with secondary updraughts elsewhere penetrating to a height of about $0.5h_*$ in the surrounding subsidence. There are pronounced variations in the intensity of turbulence at the capping inversion, but the boundary layer depth does not vary by more than one or two percent in the horizontal.

Several of the effects of the circulation that were evident as small tendencies in the *budgets* in the previous cases are now apparent in the *fields* themselves, i.e., focusing of the vertical velocity and temperature perturbations in the updraught, raising of the level of maximum w variance in the updraught and lowering it in the downdraught. The time scale for transfer of kinetic energy from the mean circulation to the turbulence is $1.10h_*/w_*$, larger than in either of the $\lambda_p = 1500\,\mathrm{m}$ cases and similar to the dissipation time scale of convective eddies in the horizontally homogeneous boundary layer. The horizontal-average statistics are strongly affected by the surface heat-flux perturbation: there is a large difference between the u and v variance profiles; the third moment of w is about 50% larger than in a horizontally homogeneous boundary layer; and the height of maximum w variance is raised to about $z = 0.6h_*$.

Given the strength of the circulation in the case just mentioned, one might expect a light mean wind to have little effect. However in the next set of simulations ($\lambda_p = 4500\,\mathrm{m}$, $u_0 = 1\,\mathrm{m\,s^{-1}}$), the mean updraught is moved about $1.4h_*$ ($0.36\lambda_p$) downwind and its maximum velocity is reduced to $0.3w_*$, the pronounced disparity between the width of the updraught and the downdraught is eliminated, and the horizontal variation in the turbulent variances is much reduced. In the horizontal-average statistics the difference between the u variance and v variance is much reduced (comparable to what it was with $\lambda_p = 1500\,\mathrm{m}$ and $u_0 = 0\,\mathrm{m\,s^{-1}}$) and the third moment of w is not significantly different from its value in a horizontally homogeneous boundary layer.

The circulation with $\lambda_p = 4500\,\mathrm{m}$ and $u_0 = 1\,\mathrm{m\,s^{-1}}$ remains substantially stronger than in either of the $\lambda_p = 1500\,\mathrm{m}$ cases, and the circulation terms in the temperature and velocity budgets are significant. Because of the small aspect ratio (vertical scale divided by horizontal scale) of the circulation, forces acting in the vertical tend to generate opposing pressure gradients that are almost as large: for example, the ratio between buoyancy-pressure gradient force and the buoyancy force is about -0.9. Both buoyancy and circulation effects in the turbulent stress budgets can be distinguished: for example, there is an asymmetric maximum in the u variance at the surface that can be explained as a consequence of a broad region of buoyancy forcing beneath the maximum in w/θ covariance, plus a sharp maximum in the circulation term further downwind where there is horizontal convergence at the base of the updraught.

With a further increase in wind ($\lambda_p = 4500\,\mathrm{m}$, $u_0 = 2\,\mathrm{m\,s^{-1}}$) the mean updraught becomes weaker (maximum vertical velocity $0.08w_*$) and moves downwind (but not very far) compared to the $u_0 = 1\,\mathrm{m\,s^{-1}}$ case. At the base of the updraught the temperature perturbation is negative, which implies that the vertical heat flux carried by the circulation near the surface is negative, therefore a sink for kinetic energy. There are two other interesting aspects of this case: First, there is significant export of kinetic energy to the absorbing layer near the top boundary of the model via a correlation between the mean vertical velocity and buoyancy pressure fields. This flux is about one order of magnitude less than the kinetic energy transport by fluctuating gravity waves and is equal to 14% of the vertically integrated buoyancy production of circulation kinetic energy. Second, despite the stronger wind compared to the $u_0 = 1\,\mathrm{m\,s^{-1}}$ case, several features of the turbulence fields (e.g., the maximum in w variance and the minimum in entrainment) are found further upwind. It is hypothesised that this is a result of the stronger circulation that existed with the smaller u_0 and a mechanism has been tentatively proposed in Section 5.4.

A Lagrangian particle model driven by the LES fields has been used to investigate the effect of the heat-flux perturbations on dispersion of passive contaminants released from an elevated source ($z = 0.25h_*$). Since in some cases the mean circulations are evident only after much averaging, it has been necessary to average particle concentrations over several releases at different times and in different simulations. As expected the maximum ground level concentration $C^*_{\max}$ is higher when the releases are made into the mean downdraught than when they are made into the mean updraught. A linear relationship between $C^*_{\max}$ and the mean vertical velocity at the release point has been developed. It fits all the data well, with the exception of the case with $\lambda_p = 4500\,\mathrm{m}$ and $u_0 = 0\,\mathrm{m\,s^{-1}}$.

7.2 Discussion

A large number of effects of the surface heat-flux perturbations have been identified for the five combinations of λ_p and u_0 considered. Some of these effects have been mentioned in the previous section, but many have not. Certain trends can be discerned. Most of the effects become stronger with an increase in λ_p. Most of them are substantially reduced by mean winds of only one or two metre per second perpendicular to the axes of constant heat flux. (On the other hand, a wind parallel to the axes of constant heat flux should have little effect, unless it is strong enough for mean shear to organise the flow.) Each case is substantially different—at least in some important respects—from all the others.

One can imagine, very tentatively, how the boundary layer would behave with intermediate values of the parameters of λ_p and u_0, or with a larger or smaller amplitude in the perturbation. With zero mean wind there is a pronounced difference in the strength and character of the circulation between $\lambda_p = 1500\,\mathrm{m}$ and $\lambda_p = 4500\,\mathrm{m}$. There may be a transitional value of λ_p, between 1500 m and 4500 m, above which the circulation is strong enough to organise itself and below which it is not. It is not at all clear whether the transition will be abrupt. (It may be that the transition is abrupt for a given simulation, but not in an ensemble-average sense.) If there is a well-defined transition, one expects it to occur at smaller λ_p as the amplitude of the perturbation increases.

Regarding the mean wind u_0, it appears that this would have to be very small to be negligible. It is interesting that, in the three simulations with u_0 non-zero, the distance of the vertical velocity maximum from the surface heat-flux maximum (expressed as a fraction of λ_p) varies very little, at most between $0.35\lambda_p$ and $0.45\lambda_p$. With large u_0 there is evidence of a rapid increase in the importance of coupling with the rest of the troposphere via gravity waves, which raises the issue of the sensitivity of the boundary-layer circulations to the structure of the atmosphere above.

How can one reconcile the weak circulations found when $\lambda_p = 1500\,\mathrm{m}$ with the experience of glider pilots that small areas can be consistently good sources of vigorous updraughts? The answer is probably that a higher frequency of vigorous updraughts in a given location does not necessarily imply a significant *mean* vertical velocity: if downdraughts are more vigorous there as well, then it is the *variance* of the vertical velocity that is increased. A significant enhancement of the vertical velocity variance above or downwind of the heat-flux maxima *is* found in the present study, and it is not reduced as drastically by a mean wind as the mean circulation is.

The strong circulation, with a maximum vertical velocity of $1.1w_*$ ($2.2\,\mathrm{m\,s^{-1}}$), found when $\lambda_p = 4500\,\mathrm{m}$ and $u_0 = 0\,\mathrm{m\,s^{-1}}$ appears to be in disagreement with Abe and Yoshida's (1982) simulations, which find a much smaller maximum vertical velocity in the sea-breeze circulation over an 8 km wide peninsula. However, Abe and Yoshida's model has too coarse a grid interval ($\Delta x = 4\,\mathrm{km}$) to resolve the narrow convergence zone seen in the present model (and also frequently observed in sea breezes, e.g., Lyons and Olsson, 1972). Their observation that a narrow (10 km) peninsula does not enhance deep convection during the daytime, whereas wider (30 km and 50 km) peninsulas do, can be explained in terms of the present work as a result of the effect of a mean wind—even a very light one—in reducing the vertical velocity in the circulation over the narrow peninsula.

As mentioned in Chapter 1, previous observations and large-eddy simulations of the convective boundary layer over moderately inhomogeneous surfaces have failed to identify any effects of the inhomogeneity. The present study has used an idealised one-dimensional perturbation in the heat flux, which can be expected (although it is not certain) to be more efficient in organising convection and altering the profiles of turbulence statistics than the inhomogeneities in the other studies. Various effects have been detected, but they are generally small except in the case where $\lambda_p = 4500\,\mathrm{m}$ and $u_0 = 0\,\mathrm{m\,s^{-1}}$. (The most conspicuous effect is the difference between the u variance and the v variance, which should not occur if the surface inhomogeneity were more two-dimensional.) The positive, but small, result in the present study is consistent with the null results from the other studies.

7.3 Major conclusions

1. At the modest resolution used here, the large-eddy model captures several of the important aspects of observed convective boundary layer structure: the large eddies have approximately the correct spatial scale and velocity scale, and the updraughts

are narrower and more vigorous than the downdraughts. Nevertheless it has several failings: the temperature variance and the pressure variance are underpredicted, the vertical velocity skewness is overpredicted in the upper boundary layer, and the smallest scales are definitely not isotropic. As far as is known, the present model shares the above features to a greater or lesser extent with other LES models.

2. Small-scale perturbations in the surface sensible heat flux ($\lambda_p = 1500\,\mathrm{m}$, $u_0 = 0\,\mathrm{m\,s^{-1}}$ and $u_0 = 1\,\mathrm{m\,s^{-1}}$) drive *weak* mean circulations. They are weak in the following senses: they account for only a small fraction ($\sim 1\%$) of the kinetic energy of the boundary layer convection, they can be detected only after a lot of averaging, and advection by the circulation is relatively unimportant in the circulation temperature and velocity budgets.

3. A larger-scale perturbation in the surface heat flux ($\lambda_p = 4500\,\mathrm{m}$, $u_0 = 0\,\mathrm{m\,s^{-1}}$) drives a strong mean circulation with a vigorous, relatively narrow updraught. However, a mean wind of only $1\,\mathrm{m\,s^{-1}}$ weakens the circulation drastically.

4. With zero mean wind the mean updraught is centred over the heat-flux maximum, but a light mean wind moves it downwind. The amount of this shift is about 0.4 times the wavelength λ_p and it does not vary much (as a fraction of λ_p) with u_0 or λ_p.

5. At the largest—but still meteorologically small—u_0 (namely, $2\,\mathrm{m\,s^{-1}}$) there is significant coupling between the mean boundary-layer circulation and the atmosphere above. With an absorbing layer at the top of the model, the mean circulation exports energy (14% of its total buoyancy production) to the absorbing layer.

6. The maximum dimensionless ground-level concentration from an elevated source of pollutant is larger when the source is in a mean downdraught than in a mean updraught. Unless the circulation is very strong (e.g., in the case when when $lambda_p = 4500\,\mathrm{m}$ and $u_0 = 0\,\mathrm{m\,s^{-1}}$) a great deal of averaging is needed to detect this difference, so it is probably not of practical significance.

7. In all cases there are substantial horizontal variations in the turbulence throughout the depth of the boundary layer. The vertical velocity variance in the middle of the boundary layer is generally at a maximum above and downwind of the surface heat-flux maximum. Above and downwind of this, there is a region of maximum entrainment.

8. Although the entrainment rate can vary considerably with horizontal position relative to the heat-flux maxima, the boundary layer depth does not vary with position by more than $\pm 1\%$.

9. In all cases but one, the horizontal variation of the vertical velocity variance in the middle of the boundary layer is not very sensitive to λ_p and u_0: the maximum is between 1.5 and 2.0 times the minimum (0.45–0.50w_*^2 versus 0.20–0.30w_*^2). The exception is the case with $\lambda_p = 4500\,\mathrm{m}$ and $u_0 = 0\,\mathrm{m\,s^{-1}}$, where the vertical velocity variance is *much* higher in the central updraught than elsewhere.

10. An analysis of the circulation temperature budget shows that, owing to the large length and velocity scales of the turbulence, the convective boundary layer is a highly diffusive medium for small-scale temperature perturbations.

11. The time scale for transfer of kinetic energy from the mean circulation to the turbulence is small ($0.3h_*/w_*$–$0.5h_*/w_*$) when $\lambda_p = 1500\,\mathrm{m}$, so the convective boundary layer is a highly dissipative medium for small-scale circulations.

12. When the circulation is not too strong, the mean temperature can be approximated as a passive scalar. A model that includes horizontal advection and down-gradient diffusion (with an anisotropic diffusivity) describes the temperature and temperature-flux fields tolerably well.

13. An analysis of the "buoyancy" and "circulation" terms[20] in the turbulent stress budgets suggests certain causal mechanisms—in *some* cases—for the form of the

[20]For definitions see Section 5.3 and Equation 5.8.

turbulent stress fields. In particular, at the shorter wavelength ($\lambda_p = 1500\,\mathrm{m}$), forcing by the turbulent buoyancy fluctuations and the associated pressure fluctuations appears to explain the major features of the stresses.

14. A small-scale perturbation in the heat flux ($\lambda_p = 1500\,\mathrm{m}$) has little or no effect on the profiles of the horizontal-average statistics. What effects there are decrease with a mean wind.

15. With $\lambda_p = 1500\,\mathrm{m}$ and $u_0 = 0\,\mathrm{m\,s^{-1}}$, the most conspicuous effect of the heat-flux perturbation on the horizontal-average profiles is an increase in u variance at the expense of v variance, which suggests a change in the geometry of the convective updraughts. This increase is much larger in some simulations than in others.

16. A larger-scale perturbation in the heat flux ($\lambda_p = 4500\,\mathrm{m}$) modifies many profiles of horizontal-average statistics substantially when the mean wind is zero, but again these effects are reduced drastically by a light mean wind.

7.4 Suggestions for future research

The immediate need is to establish that the model is basically correct in the idealised situations that have been considered. The comparison that has been done between simulations and observations for the horizontally homogeneous boundary layer is reassuring, on the whole, but it is not conclusive. It would be straightforward to set up a laboratory simulation of a convective boundary layer over heat-flux perturbations in the absence of a mean wind using a facility like Deardorff and Willis's (1985) water tank. It should be possible to carry out laboratory simulations *with* a mean wind in a wind tunnel (Cermak, 1987). Another way of producing the effect of a mean wind is to generate moving perturbations in the surface heat flux beneath a stationary fluid.

Several existing sets of convective boundary layer data could be examined for phenomena of the type seen in the LES model, e.g., the BLX83 experiments in Oklahoma and the Phoenix experiments in Colorado. It is probably too much to hope for *verification* of the model in this context but it may be possible to look at the relevance of its predictions to the atmosphere. Verification of the model against atmospheric data will probably require further simulations specific to the case under study and maybe new field measurements.

The present study has concentrated on establishing ensemble averages as accurately as possible. In doing so, it has taken full advantage of the comprehensive and detailed information available from the large-eddy model. It has not considered in any depth the question of what could be discovered using various subsets of that information. Nevertheless, it appears that in the atmosphere—even if one could find sinusoidal perturbations in the surface sensible heat flux and steady, light winds—the mean circulations found in the model would be difficult or impossible to detect with point sensors (towers, aircraft). They *might* be detected with instruments that can observe three-dimensional velocity fields (Doppler radar, lidar). It does not appear to be fruitful to expend energy searching for mean circulations unless they are reasonably strong (vertical velocity $\sim 0.5w_*$ or greater?) The circulations become stronger and easier to detect as the wavelength of the surface perturbation increases.

Horizontal variations in the intensity of boundary-layer turbulence are a robust feature of the simulations. They might be detectable by repeated aircraft flights of a few kilometres length over a well-defined surface feature (roughly the pattern that a glider pilot might use in searching for thermals). Again, Doppler radar or lidar could increase drastically the temporal and spatial coverage, and allow visualisation of the flow. Horizontal variations in the entrainment rate would be hard to measure (reliable estimates of the *horizontally averaged* entrainment rate are difficult to achieve in the atmosphere), but should in many circumstances be visible as variations in the density of fair-weather cumulus (Gibson, 1988, personal communication).

The problem of passive scalar diffusion in the presence of a spatially varying surface flux is an interesting one, for its own sake and because it appears that potential temperature can behave like a passive scalar when the mean circulation is weak. The mean concentration distribution resulting from a continuous area source can be calculated by superposing instantaneous point sources. Lagrangian particle simulations of horizontal and vertical dispersion from surface (strictly *near*-surface) sources have been carried out by Lamb (1982) and they agree well with laboratory simulations. It would be easy to repeat such a simulation with the current model. A single simulation could then be used to construct concentration fields for surface flux perturbations of arbitrarily complicated geometry.

One interesting approach is to develop a two- or three-dimensional ensemble average model with second or higher order closure, using the large-eddy simulations to guide the choice of closure assumptions and to check the results. A consideration of the requirements for such a model is beyond the scope of the present work, but it is clear that it would require a reasonably complete parameterisation of the effect of buoyancy fluctuations on the turbulent stress fields, including forcing of the horizontal velocity variance at the base of the convective updraughts via buoyancy-pressure gradients. The ensemble average model could be cheaper to run than an LES model because in simple geometries the domain can be contracted (to two dimensions rather than three if the surface perturbation is one-dimensional, for example), while in complicated geometries there is no need to run the model several times and/or for long periods to accumulate statistically significant averages. It could then be used for more complicated situations than is feasible with an LES model or for examining a larger number of cases. At the moment the large-eddy model requires verification before such work can be justified.

REFERENCES

Ackerman, B., 1974a: METROMEX: Wind fields over St. Louis in undisturbed weather. *Bull. Amer. Meteor. Soc.*, **55**, 93–94.

Ackerman, B., 1974b: Wind fields over the St. Louis metropolitan area. *J. Air Pollut. Control Soc.*, **24**, 232–23.

Businger, J.A., and A.S. Frisch, 1972: Cold plumes. *J. Geoph. Res.*, **77**, 3270–3271.

Businger, J.A., J.C. Wyngaard, Y. Izumi, and E.F. Bradley, 1971: Flux-profile relationships in the atmospheric surface layer. *J. Atmos. Sci.*, **28**, 181–189.

Calder, K.L., 1986: On the equation of atmospheric diffusion. *Quart. J. R. Met. Soc.*, **91**, 514–517.

Caughey, S.J., 1982: Observed characteristics of the atmospheric boundary layer. *Atmospheric Turbulence and Air Pollution Modelling*, F.T.M. Nieuwstadt and H. van Dop, Ed., Reidel, Dordrecht, 107–158.

Caughey, S.J., M. Kitchen and J.R. Leighton, 1983: Turbulence structure in convective boundary layers and implications for diffusion. *Boundary-Layer Meteorol.*, **25**, 345–352.

Carruthers, D.J., and J.C.R. Hunt, 1987: Waves, turbulence and entrainment near an inversion layer. Submitted to *J. Fluid Mech.*

Carruthers, D.J., and C.-H. Moeng, 1987: Waves in the overlying inversion of the convective boundary layer. *J. Atmos. Sci.*, **44**, 1801–1808.

Cermak, J.E., 1987: Advances in physical modelling for wind engineering. *J. Eng. Mech.*, **113**, 737–756.

Clark, T.L., T. Hauf and J.P. Kuettner, 1986: Convectively forced gravity waves: results from two-dimensional numerical experiments. *Quart. J. R. Met. Soc.*, **112**, 899–925.

Cotton, W.R., M.G. Hadfield, R.A. Pielke, C.J. Tremback and R.L. Walko, 1988: Large-eddy simulations of plume transport and dispersion over flat and hilly terrain. Final Report for EPRI Contract #1630-53, Department of Atmospheric Science, Colorado State University.

Deardorff, J.W., 1966: The counter-gradient heat flux in the lower atmosphere and in the laboratory. *J. Atmos. Sci.*, **23**, 503–506.

Deardorff, J.W., 1970: Convective velocity and temperature scales for the unstable planetary boundary layer and for Rayleigh convection. *J. Atmos. Sci.*, **27**, 1211–1213.

Deardorff, J.W., 1972: Numerical investigation of neutral and unstable planetary boundary layers. *J. Atmos. Sci.*, **29**, 91–115.

Deardorff, J.W., 1973a: The use of subgrid transport equations in a three-dimensional model of atmospheric turbulence. *J. Fluids Eng.*, **95**, 429–438.

Deardorff, J.W., 1973b: Three-dimensional numerical modeling of the planetary boundary layer. *Workshop on Micrometeorology*, D.A. Haugen, Ed., Amer. Meteor. Soc., Boston, 429–438.

Deardorff, J.W., 1974a: Three-dimensional numerical study of the height and mean structure of a heated planetary boundary layer. *Boundary-Layer Meteorol.*, **7**, 81–106.

Deardorff, J.W., 1974b: Three-dimensional numerical study of turbulence in an entraining mixed layer. *Boundary-Layer Meteorol.*, **7**, 199–226.

Deardorff, J.W., 1978: Closure of second- and third-moment rate equations for diffusion in homogeneous turbulence. *Phys. Fluids*, **21**, 525–530.

Deardorff, J.W., 1980: Stratocumulus-capped mixed layers derived from a three-dimensional model. *Boundary-Layer Meteorol.*, **18**, 495–527.

Deardorff, J.W., and G.E. Willis, 1985. Further results from a laboratory model of the convective planetary boundary layer. *Boundary-Layer Meteorol.*, **32**, 205–236.

Defant, F., 1951: Local winds. *Compendium of Meteorology*, Amer. Meteor. Soc., Boston, 655–672.

Devore, J.L., 1982: *Probability and Statistics for Engineering and the Sciences.* Brooks/ Cole, Monterey, 640pp.

Druilhet, A., J.P. Frangi, D. Guedalia and J. Fontan, 1983: Experimental studies of the turbulence structure parameters of the convective boundary layer. *J. Cl. Appl. Met.*, **22**, 594–608.

Drogemeier, K.K., 1985: *The numerical simulation of thunderstorm outflow dynamics*, Ph.D. thesis, Dept. of Atmos. Sci., University of Illinois, 695pp.

Fiedler, B.H., 1984: An integral closure model for the vertical turbulent flux of a scalar in a mixed layer. *J. Atmos. Sci.*, **41**, 674–680.

Gal-Chen, T., and R.A. Kropfli, 1984: Buoyancy and pressure perturbations derived from dual-Doppler radar observations of the planetary boundary layer: applications for matching models with observations. *J. Atmos. Sci.*, **41**, 3007–3020.

Gingold, R.A., and J.J. Monaghan, 1982: Kernel estimates as a basis for general particle methods in hydrodynamics. *J. Comput. Phys.*, **46**, 429–453.

Hadfield, M.G., W.R. Cotton and R.A. Pielke, 1988: Comments on an analysis of closures for pressure-scalar covariances in the convective boundary layer. *J. Atmos. Sci.*, (in press).

Hechtel, L.M., and R.B. Stull, 1985: Statistical measures of surface inhomogeneity and its potential impact on boundary layer turbulence. *Seventh Symposium on Turbulence and Diffusion*, Amer. Meteor. Soc., Boston, 144–146.

Hechtel, L.M., 1988a: Large-eddy simulations of the effects of nonhomogeneous surface fluxes on the planetary boundary layer. M.Sc. Thesis, University of Wisconsin, Madison.

Hechtel, L.M., 1988b: The effects of nonhomogeneous surface heat and moisture fluxes on the convective boundary layer. *Eighth Symposium on Turbulence and Diffusion*, Amer. Meteor. Soc., Boston, 37–40.

Hildebrand, P.H., and B. Ackerman, 1984: Urban effects on the convective boundary layer. *J. Atmos. Sci.*, **41**, 76–91.

Holmes, R.M., 1969. Note on low-level airborne observations of temperature near prairie oases. *Mon. Wea. Rev.*, **97**, 333–339

Hooke, W.H. (ed), 1979: Project Phoenix—The September 1978 Field Operation, BAO Report No. 1.

Hussain, A.K.M.F., and W.C. Reynolds, 1970: The mechanics of an organized wave in turbulent shear flow. *J. Fluid Mech.*, **41**, 241–258.

Jochum, A.M., 1988: Turbulent transport in the convective boundary layer over complex terrain. *Eighth Symposium on Turbulence and Diffusion*, Amer. Meteor. Soc., Boston, 417–420.

Kaimal, J.C., R.A. Eversole, D.H. Lenschow, B.B. Stankov, P.H. Kahn and J.A. Businger, 1982: Spectral characteristics of the convective boundary layer over uneven terrain. *J. Atmos. Sci.*, **39**, 1098–1114.

Lamb, R.G., 1978: A numerical simulation of dispersion from an elevated point source in the convective planetary boundary layer. *Atmos. Environ.*, **12**, 1297–1304.

Lamb, R.G., 1981: A scheme for simulating particle pair motions in turbulent fluid. *J. Comput. Phys.*, **39**, 329–346.

Lamb, R.G., 1982: Diffusion in the convective boundary layer. *Atmospheric Turbulence and Air Pollution Modelling*, F.T.M. Nieuwstadt and H. van Dop, Ed., Reidel, Dordrecht, 159–230.

Launder, B.E., 1974: On the effects of a gravitational field on the turbulent transport of heat and momentum. *J. Fluid Mech.*, **67**, 569–581.

Legg, B.J., and M.R. Raupach, M.R., 1982: Markov-chain simulation of particle dispersion in inhomogeneous flows: the mean drift velocity induced by a gradient in Eulerian velocity variance. *Boundary-Layer Meteorol.*, **24**, 3–13.

Lenschow, D.H., and J.A. Dutton, 1964: Surface temperature variations measured from an airplane over several surface types. *J. Appl. Meteor.*, **3**, 65–69.

Lenschow, D.H., J.C. Wyngaard and W.T. Pennell, 1980: Mean-field and second-moment budgets in a baroclinic, convective boundary layer. *J. Atmos. Sci.*, **37**, 1313–1326.

Lenschow, D.H., M.-Y. Zhou and B.B. Stankov, 1985: The scalar gradient near the top of the convective boundary layer. *Seventh Symposium on Turbulence and Diffusion*, Amer. Meteor. Soc., Boston, 67–70.

Leonard, A., 1974: Energy cascade in large-eddy simulations of turbulent fluid flows. *Adv. Geoph.*, **18A**, 237–248.

Lilly, D.K., 1967: The representation of small-scale turbulence in numerical simulation experiments. *Proc. IBM Sci. Comput. Symp. Environmental Sci.*, Thomas J. Watson Research Center, Yorktown Heights, NY, 195–210.

Long, R.R., 1978: A theory of mixing in stably stratified fluids. *J. Fluid Mech.*, **84**, 113–124.

Lumley, J.L., 1978: Computational modeling of turbulent flows. *Advances in Applied Mechanics*, C.-S. Yih, Ed., Academic Press, **18**, 123–176.

Mason, P.J. and N.S. Callen, 1986: On the magnitude of the subgrid-scale eddy coefficient in large-eddy simulations of turbulent channel flow. *J. Fluid Mech.*, **162**, 439–462.

Moeng, C.-H., 1984: A large-eddy-simulation model for the study of planetary boundary-layer turbulence. *J. Atmos. Sci.*, **41**, 2052–2062.

Moeng, C.-H., and J.C. Wyngaard, 1984: Statistics of conservative scalars in the convective boundary layer. *J. Atmos. Sci.*, **41**, 2052–2062.

Moeng, C.-H., and J.C. Wyngaard, 1986a: Recalculation of the pressure-gradient/scalar covariance in top-down and bottom-up diffusion. *J. Atmos. Sci.*, **43**, 1182–1183.

Moeng, C.-H., and J.C. Wyngaard, 1986b: An analysis of closures for pressure-scalar covariances in the convective boundary layer. *J. Atmos. Sci.*, **43**, 2499–2513.

Moeng, C.-H., and J.C. Wyngaard, 1988: Spectral analysis of large-eddy simulations of the convective boundary layer. Submitted to *J. Atmos. Sci.*

Moninger, W.R., W.L. Eberhard, G.A. Briggs, R.A. Kropfli and J.C. Kaimal, 1983: Simultaneous radar and lidar observations of plumes from continuous point sources. *21st Conference on Radar Meteorology*, Amer. Meteor. Soc., Boston, 246–250.

Nieuwstadt, F.T.M., and J.P.J.M. de Valk, 1987: A large eddy simulation of buoyant and non-buoyant plume dispersion in the atmospheric boundary layer. *Atmospheric Environment*, **21**, 2573–2587.

Panofsky, H.A., and J.A. Dutton: *Atmospheric Turbulence*. John Wiley and Sons, New York.

Poreh, M., and J.E. Cermak: A study of neutrally buoyant plumes in a convective boundary layer with mean velocity and shear. *Symposium on Turbulence and Diffusion*, Amer. Meteor. Soc., Boston, 119–122.

Reiter, E.R., 1969: Mean and eddy motions in the atmosphere. *Mon. Wea. Rev.*, **97**, 200–204.

Raynor, G.S., S. Sethuraman and R.M. Brown, 1979: Formation and characteristics of coastal internal boundary layers during onshore flows. *Boundary-Layer Meteorol.*, **16**, 487–514.

Segal, M., R. Avissar, M.C. McCumber, and R.A. Pielke, 1988a: Evaluation of vegetation effects on the generation and modification of mesoscale circulations. *J. Atmos. Sci.*, (in press).

Segal, M., W.E. Schreiber, G. Kallos, J.R. Garratt, A. Rodi and R.A. Pielke, 1988b: The impact of crop areas in Northeast Colorado on mid-summer mesoscale thermal circulations. Submitted to *Mon. Wea. Rev.*

Stull, R.B., 1984: Transilient turbulence theory. Part I: the concept of eddy mixing across finite distances. *J. Atmos. Sci.*, **41**, 3351–3367.

Tripoli, G.J., and W.R. Cotton, 1982: The Colorado State University Three-Dimensional Cloud/Mesoscale Model—1982. Part I: general theoretical framework and sensitivity experiments. *Journal de Recherches Atmospheriques*, **16**, 185–219.

Turner, J.S., 1973: *Buoyancy Effects in Fluids*. The Cambridge University Press, Cambridge.

Wallington, C.E., 1961: *Meteorology for Glider Pilots*. John Murray.

Willis, G.E., and J.W. Deardorff, 1974: A laboratory model of the unstable planetary boundary layer. *J. Atmos. Sci.*, **31**, 1297–1307.

Willis, G.E., and J.W. Deardorff, 1976: A laboratory model of diffusion into the convective planetary boundary layer. *Quart. J. R. Met. Soc.*, **102**, 427–445.

Willis, G.E., and J.W. Deardorff, 1978. A laboratory study of dispersion from an elevated source within a modelled convective planetary boundary layer. *Atmos. Environ.*, **12**, 1305–1311.

Wyngaard, J.C., 1980: The atmospheric boundary layer—modeling and measurements. *Turbulent Shear Flows 2*, Springer-Verlag, Berlin, 352–365.

Wyngaard, J.C., 1983: Lectures on the planetary boundary layer. *Mesoscale Meteorology—Theories, Observations and Models*, Gal-Chen and Lilly, eds.

Wyngaard, J.C., and R.A. Brost, 1984: Top-down and bottom-up diffusion of a scalar in the convective boundary layer. *J. Atmos. Sci.*, **41**, 102–112.

Wyngaard, J.C., O.R. Cote, and Y. Izumi, 1971. Local free convection, similarity, and the budgets of shear stress and heat flux. *J. Atmos. Sci.*, **28**, 1171–1182.

Wyngaard, J.C., and A. Sundarajan, 1979: The temperature skewness budget in the lower atmosphere and its implications for turbulence modeling. *Turbulent Shear Flows I*, F. Durst *et al.*, Ed., Springer-Verlag, Berlin, 319–326.

Young, G.S., 1986: The dynamics of thermals and their contribution to mixed layer processes. Colorado State University Atmospheric Science Paper No. 402, 292pp.

Young, G.S., 1988a: Turbulence structure of the convective boundary layer. Part I: Variability of normalized turbulence statistics. *J. Atmos. Sci.*, **45**, 719–726.

Young, G.S., 1988b: Turbulence structure of the convective boundary layer. Part II: Phoenix 78 aircraft observations of thermals and their environment. *J. Atmos. Sci.*, **45**, 727–735.

Appendix A

Miscellaneous Aspects of Averaging and Analysis

A.1 A satisfactory definition of the time average

One wishes to define a time average $\langle a \rangle_t$ of a variable $a(t)$—which itself will normally be some sort of spatial average—and write budget equations for statistics such as $\langle a \rangle_t$, $\langle a^2 \rangle_t$ and $\langle a \rangle_t^2$. It is desirable that the averaging operator satisfy the Reynolds postulates (Equations 2.3) and the commutativity properties (Equations 2.5), in particular

$$\begin{aligned} \langle a \rangle_{t,t} &= \langle a \rangle_t \quad (A.1) \\ \frac{\partial}{\partial t} \langle a \rangle_t &= \left\langle \frac{\partial a}{\partial t} \right\rangle_t . \quad (A.2) \end{aligned}$$

Consider first a running average of $a(t)$ over an interval Δ centered around the current time t, i.e.,

$$\langle a \rangle_t (t) = \frac{1}{\Delta} \int_{t-\Delta/2}^{t+\Delta/2} a(\tau)\, d\tau. \quad (A.3)$$

This satisfies Equation A.2 but not Equation A.1. Alternatively the average can be defined to be constant over an interval $[t_1, t_2]$ of duration Δ, i.e.,

$$\langle a \rangle_t (t) = \frac{1}{\Delta} \int_{t_1}^{t_2} a(\tau)\, d\tau \qquad \forall\, t_1 \leq t \leq t_2. \quad (A.4)$$

Now Equation A.1 holds, but

$$\frac{\partial}{\partial t} \langle a \rangle_t = 0 \quad \text{whereas} \quad \left\langle \frac{\partial a}{\partial t} \right\rangle_t = \frac{a(t_2) - a(t_1)}{\Delta},$$

so in general Equation A.2 is not satisfied. It is not entirely clear, in fact, what a budget equation means with such an average.

To define a more useful time average, consider an instant t at which there is an ensemble of simulations, each initialised at a different time within an interval. Say the youngest realisation was initialised at time $t - t_1$ and the oldest at $t - t_2$ where $t_2 - t_1 = \Delta$ as before. The value of the variable a in the realisation of age τ at time t will be written as $a(\tau; t)$. The realisations could correspond in a broad sense to different regions in an atmospheric flow, each with different histories. The time average is defined as an average over this ensemble, i.e.,

$$\langle a \rangle_t (t) = \frac{1}{\Delta} \int_{t_1}^{t_2} a(\tau; t)\, d\tau. \tag{A.5}$$

Equations A.2 and A.1 are both satisfied, the first by definition and the second because integration over τ and differentiation with respect to t are commutative, giving

$$\frac{\partial}{\partial t} \langle a \rangle_t = \frac{1}{\Delta} \frac{\partial}{\partial t} \int_{t_1}^{t_2} a(\tau; t)\, d\tau = \frac{1}{\Delta} \int_{t_1}^{t_2} \frac{\partial}{\partial t} a(\tau; t)\, d\tau = \left\langle \frac{\partial a}{\partial t} \right\rangle_t .$$

Of course one does not normally have a large number of independent realisations available, however let us assume that all the realisations were initialised in an identical way and integrated with identical prognostic equations and boundary conditions, i.e., they are all drawn from the same simulation. The average now has the same value as the one defined in Equation A.4 but still satisfies the Reynolds postulates. (The proof of these postulates did not depend on the realisations being independent or otherwise.) The average has been defined to be the same for all the realisations, but still evolves with time, so meaningful budget equations can be written for it.

The reference above to regions with different histories in an atmospheric flow leads to the second of the reasons described in Section 2.1.4 for dealing with the time average.

A.2 Advection in the budget equations for $\langle a \rangle_h$ and $\langle a'b' \rangle_h$

Given the decomposition used in Chapter 3,

$$u_j = \langle u_j \rangle_h + u_j' \qquad a = \langle a \rangle_h + a',$$

the advective tendency in a can be written as the sum of four components,

$$-u_j\frac{\partial a}{\partial x_j} = -\underbrace{\langle w\rangle_h\frac{\partial\langle a\rangle_h}{\partial z}}_{(1)} - \underbrace{\langle u_j\rangle_h\frac{\partial a'}{\partial x_j}}_{(2)} - \underbrace{w'\frac{\partial\langle a\rangle_h}{\partial z}}_{(3)} - \underbrace{u'_j\frac{\partial a'}{\partial x_j}}_{(4)}, \tag{A.6}$$

with summation over j.

When a horizontal average is taken of Equation A.6 all terms but (1) and (4) vanish. The advective tendency in $\langle a\rangle_h$ is therefore

$$-\left\langle u_j\frac{\partial a}{\partial x_j}\right\rangle_h = -\underbrace{\langle w\rangle_h\frac{\partial\langle a\rangle_h}{\partial z}}_{(1)} - \underbrace{\frac{1}{\rho_0}\frac{\partial}{\partial z}\langle\rho_0 w'a'\rangle_h}_{(4)} \tag{A.7}$$

where term (4) can be written in flux-divergence form since u'_j satisfies the anelastic continuity equation (Equation 2.19) and only the vertical derivative of the flux is retained since the horizontal derivatives are identically zero. This is the form used in the $\langle\theta\rangle_h$ budget described in Section 3.2.5 (Equation 3.8).

The advective tendency in a covariance $\langle a'b'\rangle_h$ is

$$\begin{aligned} -\left\langle a'u_j\frac{\partial b}{\partial x_j}\right\rangle_h - \left\langle b'u_j\frac{\partial a}{\partial x_j}\right\rangle_h &= \\ -\underbrace{\langle w\rangle_h\frac{\partial\langle a'b'\rangle_h}{\partial z}}_{(2)} - \underbrace{\langle w'b'\rangle_h\frac{\partial\langle a\rangle_h}{\partial z}}_{(3a)} &- \underbrace{\langle w'a'\rangle_h\frac{\partial\langle b\rangle_h}{\partial z}}_{(3b)} - \underbrace{\frac{1}{\rho_0}\frac{\partial}{\partial z}\langle w'a'b'\rangle_h}_{(4)}. \end{aligned} \tag{A.8}$$

Term (2) is usually described as mean advection. It arises in the present case only because there is subsidence in the model and it tends to be largest near the top of the boundary layer. Even there it is generally small in comparison with the other terms and can be ignored. Terms (3a) and (3b) are both derived from term (3) in Equation A.6 and are labelled gradient production. They are typically small unless either a or b is a scalar, like temperature, with strong vertical gradients. Note that when either a or b is vertical velocity, terms involving the gradient in $\langle w\rangle_h$ are introduced. For example, in the vertical velocity variance budget the gradient production term is

$$\frac{\partial}{\partial t}\left\langle w'^2/2\right\rangle_h = \ldots - \left\langle w'^2\right\rangle_h\frac{\partial\langle w\rangle_h}{\partial z}\ldots$$

The mean vertical velocity is a (more or less) linear function of height and its value at $z = h_*$ in the present simulations is $-0.014w_*$, so $\partial \langle w \rangle_h / \partial z = -0.014w_*/h_*$. Gradient production therefore feeds back positively on the variance with a time scale of $\sim 35h_*/w_*$. Since time scales in the second moment budgets are generally of the order of h_*/w_* (e.g. see Section 3.3.1), this process is not expected to be significant. There is no sign of the vertical velocity variance being higher in a simulation with subsidence than in one without. Term (4) is turbulent transport; it is typically one of the principal terms in the second-moment budgets.

A.3 Advection in the budget equations for $\langle a \rangle_{p,t}$ and $\langle (a')_{p,t}(b')_{p,t} \rangle_{p,t}$

If the horizontal-deviation parts of u_j and a are divided into a phase-time average and the remainder,

$$u_j = \langle u_j \rangle_h + \left\langle u_j' \right\rangle_{p,t} + \left(u_j'\right)_{p,t} \qquad u_j = \langle u_j \rangle_h + \left\langle u_j' \right\rangle_{p,t} + \left(u_j'\right)_{p,t},$$

as described in Section 4.2, the advective tendency in a can be written as the sum of nine components:

$$\begin{aligned} u_j \frac{\partial a}{\partial x_j} \quad = \quad & -\underbrace{\langle w \rangle_h \frac{\partial \langle a \rangle_h}{\partial z}}_{(1)} - \underbrace{\langle u_j \rangle_h \frac{\partial \langle a' \rangle_{p,t}}{\partial x_j}}_{(2)} - \underbrace{\langle u_j \rangle_h \frac{\partial (a')_{p,t}}{\partial x_j}}_{(3)} \\ & -\underbrace{\langle w' \rangle_{p,t} \frac{\partial \langle a \rangle_h}{\partial z}}_{(4)} - \underbrace{\left\langle u_j' \right\rangle_{p,t} \frac{\partial \langle a' \rangle_{p,t}}{\partial x_j}}_{(5)} - \underbrace{\left\langle u_j' \right\rangle_{p,t} \frac{\partial (a')_{p,t}}{\partial x_j}}_{(6)} \\ & -\underbrace{(w')_{p,t} \frac{\partial \langle a \rangle_h}{\partial z}}_{(7)} - \underbrace{\left(u_j'\right)_{p,t} \frac{\partial \langle a' \rangle_{p,t}}{\partial x_j}}_{(8)} - \underbrace{\left(u_j'\right)_{p,t} \frac{\partial (a')_{p,t}}{\partial x_j}}_{(9)} \end{aligned} \tag{A.9}$$

The advective tendency in $\langle a \rangle_{p,t}$ is derived by taking the phase-time average of Equation A.9. A number of simplifications are possible using the Reynolds postulates (Equations 2.3), the commutativity properties (Equations 2.5) and the properties of the phase average and horizontal average listed in Equations 2.13. Term (1) can be simplified by assuming that the subsidence is constant with time (which is true during the periods over which analyses have been done) so that $\langle w\rangle_h = \langle w\rangle_{h,t}$ and

$$\Big\langle(1)\Big\rangle_{p,t} = -\langle w\rangle_{h,t}\,\frac{\partial}{\partial z}\,\langle a\rangle_{h,t}\,.$$

The most difficult terms are (3) and (7), which are similar to each other in form. To simplify $\langle(3)\rangle_{p,t}$ note that a can be decomposed in two ways,

$$\langle a'\rangle_{p,t} + (a')_{p,t} = a = \langle a'\rangle_p + (a')_p\,,$$

and that equating them implies that

$$(a')_{p,t} = (a')_p + \langle a'\rangle_p - \langle a'\rangle_{p,t} = (a')_p + \Big(\langle a'\rangle_p\Big)_t.$$

Substituting into term (3) gives

$$\Big\langle(3)\Big\rangle_{p,t} = -\left\langle \langle u_j\rangle_h \frac{\partial\,(a')_p}{\partial x_j}\right\rangle_{p,t} - \left\langle \langle u_j\rangle_h \frac{\partial((\langle a'\rangle_p)_t}{\partial x_j}\right\rangle_{p,t}.$$

The first term on the right-hand side vanishes when the outer phase average is taken, since

$$\langle\langle c\rangle_h (d)_p\rangle_p \equiv 0.$$

The second term is unaffected by the outer phase average, since

$$\langle\langle c\rangle_h \langle d\rangle_p\rangle_p \equiv \langle c\rangle_h \langle d\rangle_p,$$

but when the time average is taken one can use the property

$$\langle c\,(d)_t\rangle_t \equiv \langle (c)_t (d)_t\rangle_t$$

to get finally

$$\Big\langle(3)\Big\rangle_{p,t} = \left\langle (\langle u_j\rangle_h)_t \frac{\partial((\langle a'\rangle_p)_t}{\partial x_j}\right\rangle_t.$$

With a similar simplification of term (7), and with a number of other, simpler manipulations, one finds

$$\left\langle u_j \frac{\partial a}{\partial x_j}\right\rangle_{p,t} = -\underbrace{\langle w\rangle_{h,t}\frac{\partial\,\langle a\rangle_{h,t}}{\partial z}}_{(1)} - \underbrace{\langle u_j\rangle_{h,t}\frac{\partial\,\langle a'\rangle_{p,t}}{\partial x_j}}_{(2)} - \underbrace{\left\langle (\langle u_j\rangle_h)_t \frac{\partial((\langle a'\rangle_p)_t}{\partial x_j}\right\rangle_t}_{(3)}$$

$$- \underbrace{\langle w' \rangle_{p,t} \frac{\partial \langle a \rangle_{h,t}}{\partial z}}_{(4)} - \underbrace{\frac{1}{\rho_0} \frac{\partial}{\partial x_j} \left(\rho_0 \left\langle u'_j \right\rangle_{p,t} \langle a' \rangle_{p,t} \right)}_{(5)} \tag{A.10}$$

$$- \underbrace{\left\langle (\langle w' \rangle_p)_t \frac{\partial (\langle a \rangle_h)_t}{\partial z} \right\rangle_t}_{(7)} - \underbrace{\frac{1}{\rho_0} \frac{\partial}{\partial x_j} \left\langle \left(u'_j \right)_{p,t} (a')_{p,t} \right\rangle_{p,t}}_{(9)}$$

Terms (1), (2), (4), (5) and (9) are straightforward. Terms (1) to (4) describe the various interactions between the time-averaged horizontal flow ($\langle u_j \rangle_{h,t}$ and $\langle a \rangle_{h,t}$) and the time-averaged circulation ($\langle u'_j \rangle_{p,t}$ and $\langle a' \rangle_{p,t}$). Term (9) describes the interaction of turbulence ($(u'_j)_{p,t}$ and $(a')_{p,t}$) with itself. Term (1) is entirely a result of subsidence. It is significant if $a \equiv \theta$, when it warms the stable layer and so limits the boundary layer growth, but is otherwise negligible. Term (2) also includes a subsidence contribution (advection of the circulation downwards) which is generally negligible.

Terms (3) and (7) arose in Equation A.9 from interaction between the horizontal flow and turbulence. Their contributions to Equation A.10 are non-zero if there is a correlation between the fluctuations in the horizontal average (i.e., $(\langle u_j \rangle_h)_t$ and $(\langle a \rangle_h)_t$) and the fluctuations in the circulation (i.e., $(\langle u'_j \rangle_p)_t$ and $(\langle a' \rangle_p)_t$). It is not obvious *a priori* that either of these terms is small. In particular note that when $a \equiv \theta$ term (7) could be significant near the top of the boundary layer if there were a trend in $\langle w' \rangle_p$ over the averaging period coupled with a trend in $\partial \langle \theta \rangle_h / \partial z$, associated with either a change in the temperature jump across the inversion or a change in the boundary layer depth. (In the latter case $\partial \langle \theta \rangle_h / \partial z$ at a given height changes as the region of strongest gradients moves up or down.) All the terms in Equation A.10 have been evaluated individually. (Owing to the limitations imposed by the structure of the analysis programs the task is non-trivial.) It has been found that terms (3) and (7) are generally small. With these terms omitted, with the horizontal average subtracted and with the subgrid term included, Equation A.10 becomes the circulation temperature budget (Equation 5.1) discussed in Section 5.1. The circulation velocity budget (Equation 5.4) discussed in Section 5.2 is similar except that buoyancy and pressure-gradient terms are added and the circulation/horizontal-average term (4) is neglected.

In principle the advective terms in the budget for the turbulent covariance, $\langle (a')_{p,t}(b')_{p,t}\rangle_{p,t}$, can be found by substituting Equation A.9 into

$$\frac{\partial}{\partial t}\left\langle (a')_{p,t}(b')_{p,t}\right\rangle_{p,t} = \left\langle (a')_{p,t}\frac{\partial (b')_{p,t}}{\partial t}\right\rangle_{p,t} + \left\langle (b')_{p,t}\frac{\partial (a')_{p,t}}{\partial t}\right\rangle_{p,t}$$

and simplifying. The process is straightforward, but tedious. It leads to a number of "non-standard" terms associated with interactions between the temporal fluctuations in the horizontal average and/or the circulation. It is not practicable to evaluate all these terms directly and it is not obvious that they are negligible. However the decision has been made in the present study to look at only those turbulence budgets involving moments of velocity. (The decision to ignore temperature flux and variance budgets was made partly because of the difficulties just mentioned, but mainly because of a suspicion that analysing terms in these budgets is not an effective way of gaining insight into the constraints that govern heat transport.) It has been found that for velocity components the fluctuating (or evolving) part of the horizontal average $(\langle u_i\rangle_h)_t$ is small, in the sense that it accounts for a negligible fraction of the boundary layer kinetic energy. Therefore one can make the approximations

$$\langle u_i\rangle_h \approx \langle u_i\rangle_{h,t} \qquad \text{and} \qquad (u_i')_{p,t} \approx (u_i)_{p,t}\,,$$

and the two decompositions discussed in Section 4.2 (Equations 4.3 and 4.5) become equivalent. With these approximations the advective tendency in the covariance $\langle (a')_{p,t}(b')_{p,t}\rangle_{p,t}$, where a and b are velocity components, is given by

$$\begin{aligned}
-\left\langle (a')_{p,t}\left(u_j\frac{\partial b}{\partial x_j}\right)'_{p,t}\right\rangle_{p,t} - \left\langle (b')_{p,t}\left(u_j\frac{\partial a}{\partial x_j}\right)'_{p,t}\right\rangle_{p,t} \approx& \\
-\underbrace{\left\langle u_j\right\rangle_{h,t}\frac{\partial}{\partial x_j}\left\langle (a')_{p,t}(b')_{p,t}\right\rangle_{p,t}}_{(3)} - \underbrace{\left\langle u_j'\right\rangle_{p,t}\frac{\partial}{\partial x_j}\left\langle (a')_{p,t}(b')_{p,t}\right\rangle_{p,t}}_{(6)}& \\
-\underbrace{\left\langle (w')_{p,t}(b')_{p,t}\right\rangle_{p,t}\frac{\partial \langle a\rangle_{h,t}}{\partial z}}_{(7a)} - \underbrace{\left\langle (w')_{p,t}(a')_{p,t}\right\rangle_{p,t}\frac{\partial \langle b\rangle_{h,t}}{\partial z}}_{(7b)}& \qquad \text{(A.11)} \\
-\underbrace{\left\langle (u_j')_{p,t}(b')_{p,t}\right\rangle_{p,t}\frac{\partial \langle a'\rangle_{p,t}}{\partial x_j}}_{(8a)} - \underbrace{\left\langle (u_j')_{p,t}(a')_{p,t}\right\rangle_{p,t}\frac{\partial \langle b'\rangle_{p,t}}{\partial x_j}}_{(8b)}&
\end{aligned}$$

$$-\underbrace{\left\langle (u_j')_{p,t}(a')_{p,t}(b')_{p,t}\right\rangle_{p,t}}_{(9)} .$$

Terms (3) and (6) are mean advection by the horizontal average flow and the circulation respectively. Terms (7a) and (7b) are production terms associated with gradients in the horizontal average; since a and b are velocity components they are generally small. Terms (8a) and (8b) are production terms associated with gradients in the circulation. Term (9) is turbulent transport.

A.4 The model analysis

The dynamic analyses start, as all such analyses should, with the forces and tendency terms *as they are calculated by the model.* Typically these tendencies—which are written to model output files every few minutes—are used to estimate the average rate of change in some model statistic over a period of a few tens of minutes, then the actual change in that statistic between the beginning and end of the period is calculated.[21] If agreement is good, as it normally is, one has confidence in extending the analysis. For example, the advective tendencies are stored on the output files, but the model's advection algorithms are also duplicated in the analysis program and used to reconstruct the tendencies. Having checked the reconstructed tendencies against the model-output ones, one can use the same algorithms to subdivide the advection process into different contributions as in Equation A.6 or Equation A.9. The terms in the budget equations (Equations A.7, A.8 and A.10) are then calculated by taking appropriate averages of these contributions. For example, the turbulent transport term in $\langle a'b'\rangle_h$ is estimated by calculating the tendencies in a and b due to advection of turbulent fluctuations by the turbulent velocity field (i.e., $u_j'\partial a'/\partial x_j$ and $u_j'\partial b'/\partial x_j$), then taking the covariances of these tendencies with b and a respectively, and not by differentiating a triple covariance.

[21]No account is taken, incidentally, of the details of the model's finite-differencing in time. This can be done, one suspects, because the leapfrog scheme is non-dissipative and because the model typically operates at low Courant numbers at the majority of grid points.

With the pressure-gradient force, which is calculated by the acoustic routines, there is a problem that arises because of a tendency for the pressure and divergence fields to relax towards equilibrium over several short time steps. It is difficult to gain access to the pressure fields on the short time steps, so the pressure-gradient force is estimated by differentiating the pressure fields that are written by the model on the long time steps. This procedure leads to an overestimate of about 10% in the rate of transfer of kinetic energy from the vertical velocity field to the horizontal velocity fields. The discrepancy can be reduced by by increasing the speed of sound in the model, but it should be stressed that all the model fields but pressure are insensitive to such a change and the problem is one of *analysis* not of an error in the model *integration*. When the pressure is calculated from the tendency terms using the anelastic assumption, as described in Section 2.2.1, the resultant field is very similar to the model-output pressure field, albeit a little smoother. More to the point, the reconstructed pressure field gives an estimate of the rate of transfer of kinetic energy from the vertical to the horizontal that is consistent with the remaining terms in the kinetic energy budget. In other words the anelastically reconstructed pressure field is a *better* indicator of the action of pressure forces on the short time step than the model-output pressure field.

There are two separate programs to calculate the various averages, variances, co-variances and tendencies. The first program was used for Chapter 3. It deals with only one simulation at a time and calculates horizontal-average statistics. At each time the program makes one pass through the three-dimensional fields to compute horizontal averages, then on subsequent passes the deviations are computed so that moments like $\langle a'b' \ldots \rangle_h$ of any order can be calculated. The second program was used for Chapters 4 and 5. It deals with several simulations at a time and calculates phase-average statistics as well as horizontal-average statistics. At each time this program can make only one pass through the data from each simulation; this restriction limits the statistics that can practically be calculated. Horizontal averages are available only when all simulations at a given time have been processed and phase-time averages are available only when all the times within the averaging period have been processed. Fields of quantities like a'

and $(a')_{p,t}$ are therefore never available to the program. It is straightforward to calculate second-order moments like $\langle a'b'\rangle_h$ and $\langle (a')_{p,t}(b')_{p,t}\rangle_{p,t}$ by keeping track of averages of a, b and ab, then using the identities

$$\begin{aligned} \langle a'b'\rangle_h &\equiv \langle a\,b\rangle_h - \langle a\rangle_h \, \langle b\rangle_h \\ \left\langle (a')_{p,t}(b')_{p,t}\right\rangle_{p,t} &\equiv \left\langle a'\,b'\right\rangle_{p,t} - \left\langle a'\right\rangle_{p,t} \left\langle b'\right\rangle_{p,t} . \end{aligned}$$

Doing the same for third-order moments would require storing many more averages and has not been done.

The above restriction affects the budget analyses described in Section 5.3. Consider Equation A.11 for the advective tendency in $\langle (a')_{p,t}(b')_{p,t}\rangle_{p,t}$. The left-hand side of Equation A.11 is a second moment and is calculated, as are the buoyancy, pressure and subgrid terms in the budget. The turbulent transport term (9) on the right-hand side is a third moment and is not calculated, but one can calculate reasonable approximations to the other terms on the right-hand side and therefore obtain the turbulent transport term as a residual. ("Reasonable approximations" because the calculations use simple finite-difference analogues to the continuum equations rather than a decomposition of the advective tendencies.) A problem arises, however, in subdividing the pressure term in the budget. It *is* possible to divide the pressure field into contributions from buoyancy, advection and subgrid forces and calculate $\langle (a')_{p,t}(b')_{p,t}\rangle_{p,t}$ budget terms for each one, but it *is not* possible to divide the advection pressure further into parts associated with each of the advection processes in Equation A.9. For this reason the pressure term associated with the circulation term in the $\langle (u_i')_{p,t}(u_j')_{p,t}\rangle_{p,t}$ budget (Section 5.3, Equation 5.8) is not known.

APPENDIX B

A DOWN-GRADIENT DIFFUSION MODEL FOR SCALAR FIELDS

In the discussion of the temperature budget for Set F (Section 5.1), it was suggested that the $\langle\theta'\rangle_{p,t}$ field in the lower boundary layer in the presence of a spatially-varying surface heat flux can be understood in terms of a balance between vertical-flux divergence and horizontal-flux divergence, where the flux is the sum of the (resolved) turbulent flux in θ and the subgrid flux. This appendix considers an analogous problem involving a *passive* scalar, and investigates a gradient-diffusion expression for the scalar flux.

Consider a boundary layer with a horizontally homogeneous surface heat flux and assume that there is a sinusoidally-varying surface flux of a passive scalar c. For convenience let this scalar have the dimensions of potential temperature and let the surface flux f_s have the same amplitude and wavelength as the surface heat-flux perturbation specified in Equation 4.6, i.e.,

$$f_s = F\cos k\hat{x}, \qquad \text{where} \quad F = 0.5w_*\theta_* \quad \text{and} \quad k = 2\pi/\lambda_p. \tag{B.1}$$

Let us assume that the flux f_i in c is related to the gradient by

$$f_i = -K_{ij}\frac{\partial c}{\partial x_j}, \tag{B.2}$$

where K_{ij} is the diffusivity, in general a tensor (Calder, 1965), and summation over j is implied. For the present problem variations in the y-direction are ignored, so the diffusivity can be expanded into components in the x- and z-directions as follows,

$$K_{ij} = \begin{pmatrix} K_{11} & K_{13} \\ K_{31} & K_{33} \end{pmatrix}. \tag{B.3}$$

In principle the diffusivity can be allowed to vary in any way required to satisfy Equation B.2, but to be of any value it should depend only on the properties of the flow, and maybe on the general configuration of the scalar field. Wyngaard and Brost (1984) have shown that, for horizontally homogeneous, vertical diffusion in the convective boundary layer, the diffusivity depends on the relative contributions of fluxes at the surface ("bottom-up" diffusion) and at the top of the boundary layer ("top-down" diffusion). In the present case the flux is imposed at the surface and it will be assumed that the flux perturbations do not penetrate to the level of the inversion, so there is *spatially-varying, bottom-up diffusion.*

Since the flow is dynamically horizontally homogeneous, the diffusivity components are assumed to be functions of height only. Furthermore, it is assumed that the surface shear is zero or negligible, so there is no preferred direction in the horizontal and by symmetry

$$K_{13} \equiv 0 \equiv K_{31}.$$

Consider a case with uniform wind u_0 in the x-direction and assume that a steady state exists, satisfying

$$\frac{\partial c}{\partial t} = -u_0 \frac{\partial c}{\partial x} - \frac{\partial f_i}{\partial x_i} = 0. \tag{B.4}$$

Substituting Equation B.2 for f_i and applying the restrictions on K_{ij} gives the following elliptic equation for c,

$$K_{11} \frac{\partial^2 c}{\partial x^2} + K_{33} \frac{\partial^2 c}{\partial z^2} - u_0 \frac{\partial c}{\partial x} + \frac{\partial K_{33}}{\partial z} \frac{\partial c}{\partial z} = 0. \tag{B.5}$$

Solutions to this equation are described below on the domain

$$-\lambda_p/2 \le \hat{x} \le \lambda_p/2 \quad \text{and} \quad 0 \le z < \infty,$$

with the vertical flux at $z = 0$ defined by Equation B.1, with periodic lateral boundary conditions on c and f_i, and with all solutions assumed to tend to zero as $z \to \infty$. The equation and solutions will be described as the "advection/diffusion model." It is hereby proposed that the model can give a useful first approximation to the $\langle \theta' \rangle_{p,t}$ field and the fluxes in the lower boundary layer, for the simulations that have been described in

Chapters 4 and 5. There are, however, several possible problems:

- The concept of local, down-gradient diffusion is fundamentally flawed. Even in homogeneous turbulence, the diffusivity has to be made a function of time after release (a dependence that is not allowed here) to predict dispersion from a point-source correctly (Deardorff, 1978). Since area sources can be constructed by superposing point sources, a relationship like Equation B.2 is at best a *satisfactory approximation* to area-source dispersion. Furthermore it is known that the diffusivity based on the horizontal-average temperature gradient and the horizontal-average heat flux in the middle of the convective boundary layer is negative or very small (Deardorff, 1966). The bottom-up/top-down decomposition proposed by Wyngaard and Brost restores positive, apparently well-behaved diffusivities, although a similar study by Moeng and Wyngaard (1984) still finds that the bottom-up diffusivity is negative above $z=0.6h_*$. Non-local descriptions of diffusion (e.g. Fiedler, 1984, Stull, 1984) can also restore positive diffusivities, but at the cost of having the flux respond to gradients at remote locations. In the present case Equation B.2 is applied to a *bottom-up* scalar in the *lower* boundary layer and may be satisfactory.

- Since temperature is not a passive scalar, the mean temperature perturbations drive circulations which modify the temperature field. It has been found, however, that in most of the cases (with the conspicuous exception of Set H) the circulations are weak in the sense that the circulation/circulation and circulation/horizontal-average terms in the temperature budget are smaller than the horizontal advection and/or flux-divergence terms.

- The surface heat-flux perturbation has been found to modulate the turbulence significantly, even when the circulation is weak. In principle this might be incorporated into the gradient-diffusion model by allowing K_{ij} to vary with $\hat{x}$ and between simulations, and to have non-zero off-diagonal components. These complexities will be avoided.

Below, plausible profiles of K_{11} and K_{33} will be established using the results of Set F ($\lambda_p = 1500\,\mathrm{m}$, $u_0 = 0\,\mathrm{m\,s^{-1}}$), then the behaviour of the advection/diffusion model will be investigated with different values of λ_p and u_0.

The temperature, horizontal flux and vertical flux fields from Set F to be compared with the results of the advection/diffusion model are shown in Figures 4.7c, 5.2a and 5.2b. In all three fields the amplitude of the horizontal variation has a maximum at the surface and decreases with height. One can define the scale height for each field as the height at which the amplitude drops to $1/e$ times its surface value. For temperature the scale height is approximately $0.13h_*$ (but recall that the surface temperature in the contour plot is estimated by linear extrapolation and is not very meaningful), for horizontal flux it is $0.18h_*$ and for vertical flux it is $0.36h_*$.

Let us consider first a very simple—but not very realistic—form for the diffusivity tensor, namely

$$K_{11} = K_{33} = K,$$

where K is a constant. Equation B.5 then reduces to the Laplace equation and the solution is

$$\begin{aligned} c &= \frac{F}{kK} \cos k\hat{x} \, \exp^{-kz} \\ f_1 &= F \sin k\hat{x} \, \exp^{-kz} \\ f_3 &= F \cos k\hat{x} \, \exp^{-kz} . \end{aligned}$$

Note two properties of the solution: all the fields have the same scale height (as defined above) of $1/k = \lambda_p/2\pi$, and the amplitude of the horizontal flux is equal to the amplitude of the vertical flux. The solution has been evaluated with $\lambda_p = 1500\,\mathrm{m}$, $h_* = 1170\,\mathrm{m}$ and $F = 0.5w_*\theta_*$ and plotted on the same domain as the results of Set F. The diffusivity K is chosen to be $0.07w_*h_*$, which is roughly the *horizontal* diffusivity implied by the fluxes and gradients in Figures 5.2 and 5.3. The scalar is labelled "temperature" and made dimensionless with θ_*, and the fluxes are made dimensionless with $w_*\theta_*$; Figures B.1a, B.1b and B.1c are thus comparable with Figures 4.7c, 5.2a and 5.2b respectively. The

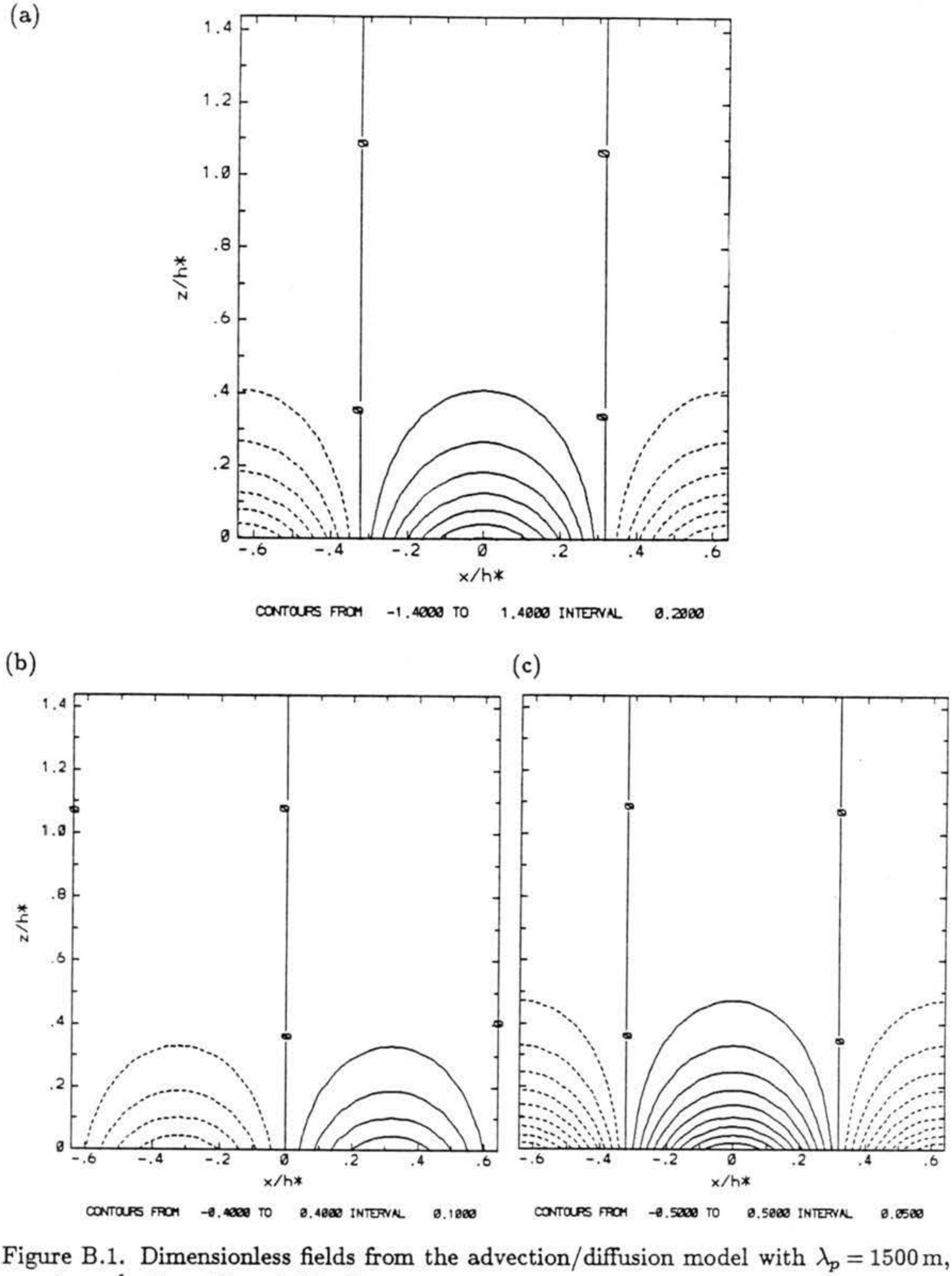

Figure B.1. Dimensionless fields from the advection/diffusion model with $\lambda_p = 1500\,\mathrm{m}$, $u_0 = 0\,\mathrm{m\,s^{-1}}$, $K_{11} = K_{33} = 0.07 w_* h_*$.

(a) Temperature c (contour interval 0.2)

(b) Horizontal flux f_1 (contour interval 0.1)

(c) Vertical flux f_3 (contour interval 0.05)

amplitude of the temperature perturbation in Figure B.1a is equal to the amplitude in Figure 4.7c at $z = 0.1h_*$ and $z = 0.4h_*$, but the advection/diffusion model lacks the region of tight vertical gradients in temperature below $z = 0.1h_*$. The height scale $\lambda_p/2\pi$ is $0.20h_*$, which is approximately correct for the horizontal flux, but too large for the temperature and too small for the vertical flux.

In principle, Equation B.2 should also describe the vertical gradient in a horizontally homogeneous, bottom-up scalar, although for that problem there is no steady solution for c. The vertical diffusivity K_{33} should therefore equal the bottom-up diffusivity calculated by Wyngaard and Brost (1984),

$$K_b = 2.5\, w_* h_* \,(1 - z/h_*)\,(z/h_*)^{3/2}. \tag{B.6}$$

(It was shown in Section 3.2.1 that the present LES model gives a temperature-gradient profile near the surface consistent with this diffusivity.) Figure B.2 shows the results of the advection/diffusion model with *both* K_{11} and K_{33} equal to K_b. (Actually, the diffusivity was clipped above $z = 0.5h_*$ at a value of approximately $0.4w_*h_*$.) The elliptic equation was evaluated numerically, with the same vertical grid spacing as the LES model ($\Delta z = 60\,\mathrm{m}$) and the same staggered-grid configuration, and the surface temperature plotted in Figure B.2a was calculated by linear extrapolation from above in the same way as it is in the LES model analysis. Several features of the advection/diffusion model are now more realistic than they were with constant K: the scale height of the temperature perturbation is now reduced, the scale height of the vertical flux is increased, and the amplitude of the temperature perturbation at the surface is now correct ($2.0\,\theta_*$). However, the temperature perturbations away from the surface are too small (the $+0.2\theta_*$ and $-0.2\theta_*$ contours reach a maximum height of $z = 0.24h_*$ instead of $z \approx 0.4h_*$), and the maximum horizontal flux is not at the surface but at $z = 0.18h_*$ and its magnitude is too small.

It does not seem to be possible to describe simultaneously the large vertical temperature gradients near the surface and the surface maximum in horizontal heat flux with $K_{11} = K_{33}$. The advection/diffusion model was next evaluated with $K_{11} = 0.07w_*h_*$

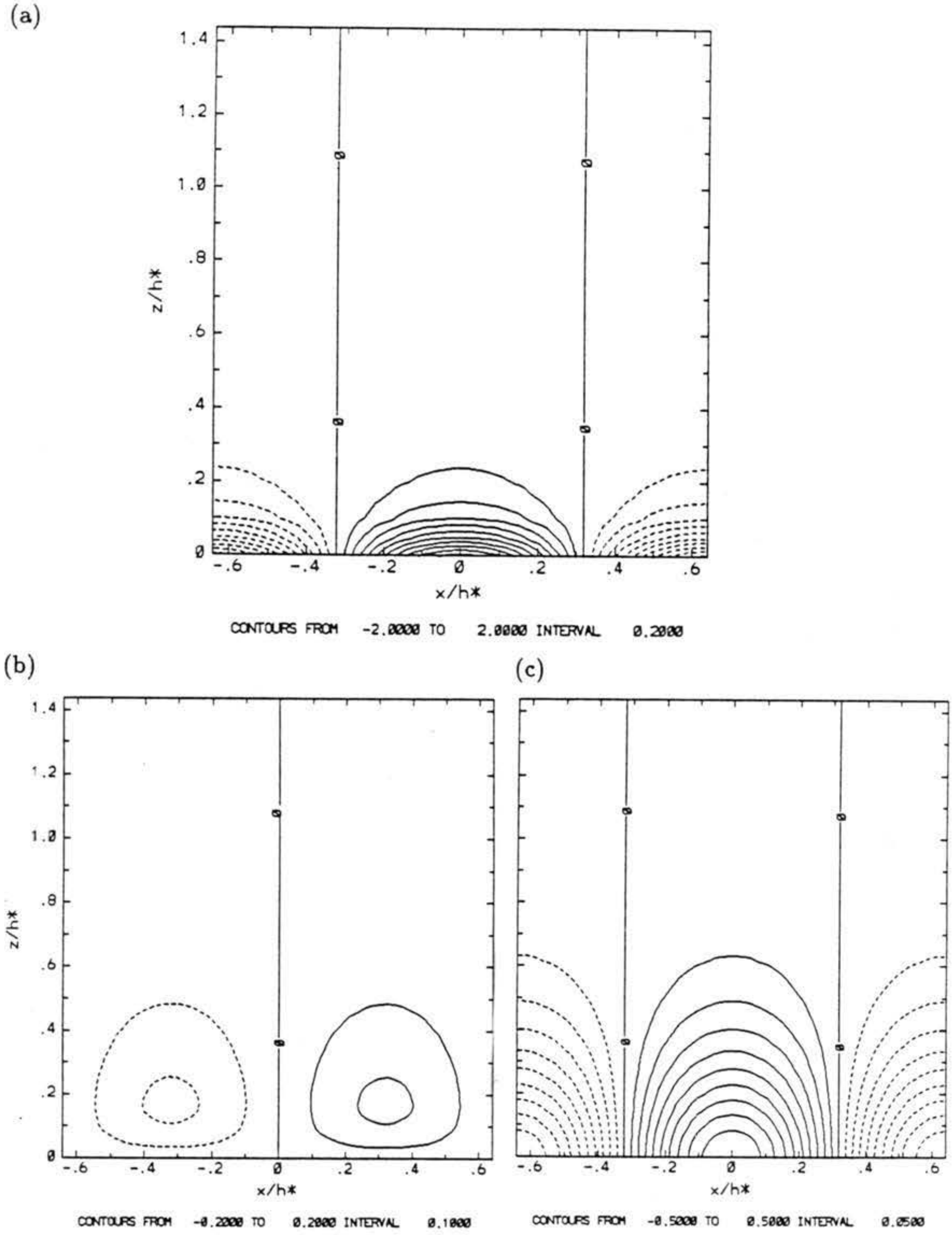

Figure B.2. Dimensionless fields from the advection/diffusion model with $\lambda_p = 1500\,\mathrm{m}$, $u_0 = 0\,\mathrm{m\,s^{-1}}$, $K_{11} = K_{33} = K_b$.

(a) Temperature c (contour interval 0.2)

(b) Horizontal flux f_1 (contour interval 0.1)

(c) Vertical flux f_3 (contour interval 0.05)

and $K_{33} = K_b$ (Figure B.3). With these diffusivities $K_{11} > K_{33}$ below $z = 0.10h_*$ and $K_{11} < K_{33}$ above, which seems reasonable given that the profiles of horizontal velocity variance and vertical velocity variance cross at about the same level ($z = 0.12h_*$). The form of the temperature field in Set F is now reproduced well, although the amplitude is generally under-estimated a little. The vertical flux is reproduced very well up to $z = 0.6h_*$; above there an expression like Equation B.2 clearly cannot describe the LES model's vertical flux field. The assumption of constant horizontal diffusivity constrains the amplitude of the horizontal flux to be proportional to the amplitude of the temperature perturbation, so the variation of the horizontal flux in the vertical is not reproduced well, although the magnitude at the surface is approximately correct. One could probably improve agreement by allowing K_{11} to vary with height (but not as rapidly as K_{33}), but the extra sophistication is not justified. Overall agreement is very good, given the reservations about the applicability of the advection/diffusion model.

With plausible profiles of K_{11} and K_{33} having been established for a single case, subject to the dual constraints of minimum complexity and consistency with results for horizontally homogeneous bottom-up diffusion, Figures B.4 to B.7 present the results of the advection/diffusion model for values of u_0 and λ_p corresponding to Sets G, H, I and J, respectively.

Figure B.4 has $\lambda_p = 1500\,\mathrm{m}$ and $u_0 = 1\,\mathrm{m\,s^{-1}}$; the temperature field in Figure B.4a can be compared with the temperature field from Set G in Figure 4.19c and the horizontal and vertical fluxes in Figures B.4b and B.4c can be compared with fluxes in Figure 5.5a and 5.5b. The advection/diffusion model correctly predicts that the fields are shifted downstream and tilted to the right by the mean wind. It underpredicts the amount of the shift somewhat: for example, at $z = 0.4h_*$ the maximum temperature perturbation in Set G is at $\hat{x} = 0.32h_* = 0.25\lambda_p$, whereas the prediction is $\hat{x} = 0.27h_* = 0.21\lambda_p$, and the maximum vertical flux is at $\hat{x} = 0.24h_* = 0.19\lambda_p$, whereas the prediction is $\hat{x} = 0.17h_* = 0.14\lambda_p$. The advection/diffusion model generally underpredicts the magnitude of the temperature and vertical-flux perturbations, but overpredicts the horizontal flux at the surface. (These errors are all consistent with the horizontal diffusivity being overestimated, which

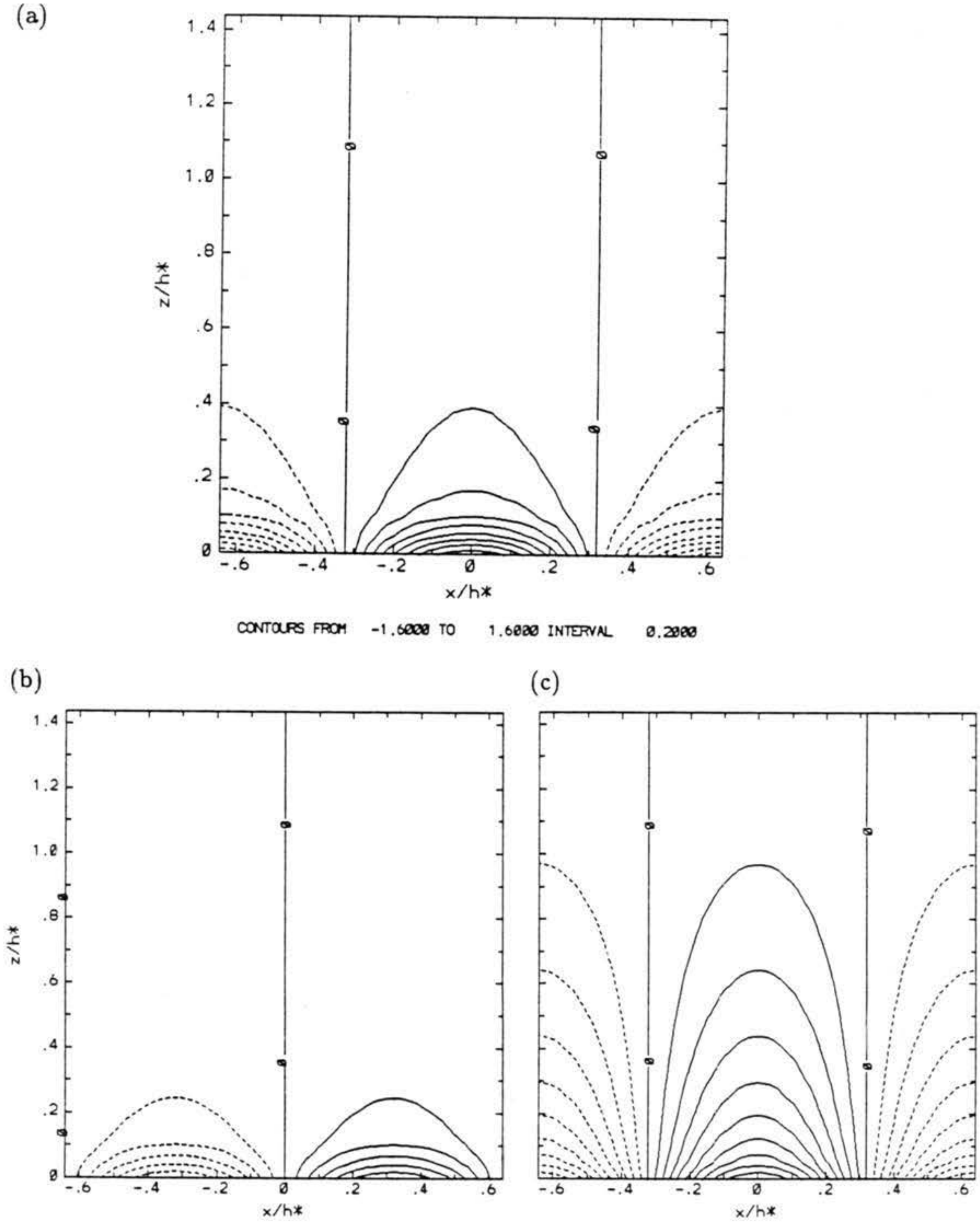

Figure B.3. Dimensionless fields from the advection/diffusion model with $\lambda_p = 1500\,\mathrm{m}$, $u_0 = 0\,\mathrm{m\,s^{-1}}$, $K_{11} = 0.07 w_* h_*$, $K_{33} = K_b$.

(a) Temperature c (contour interval 0.2)

(b) Horizontal flux f_1 (contour interval 0.1)

(c) Vertical flux f_3 (contour interval 0.05)

(a)

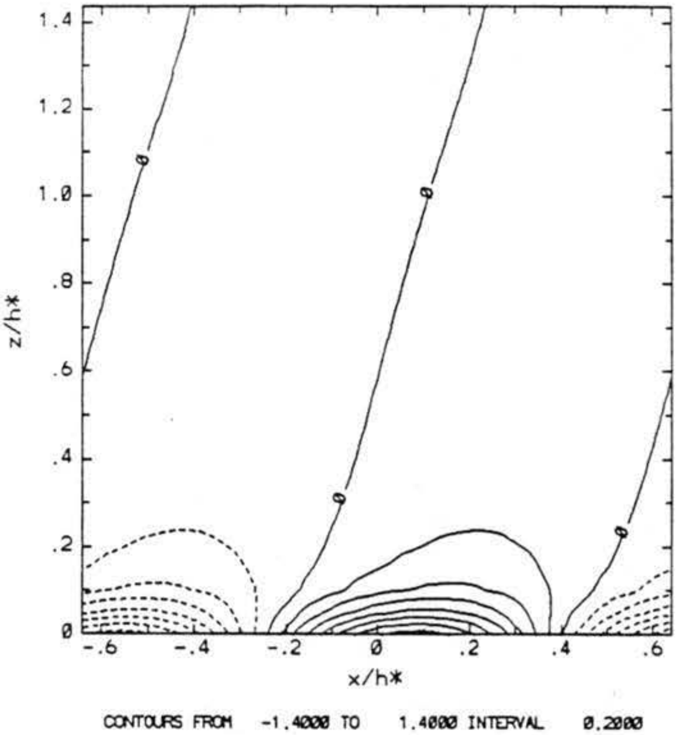

(b)

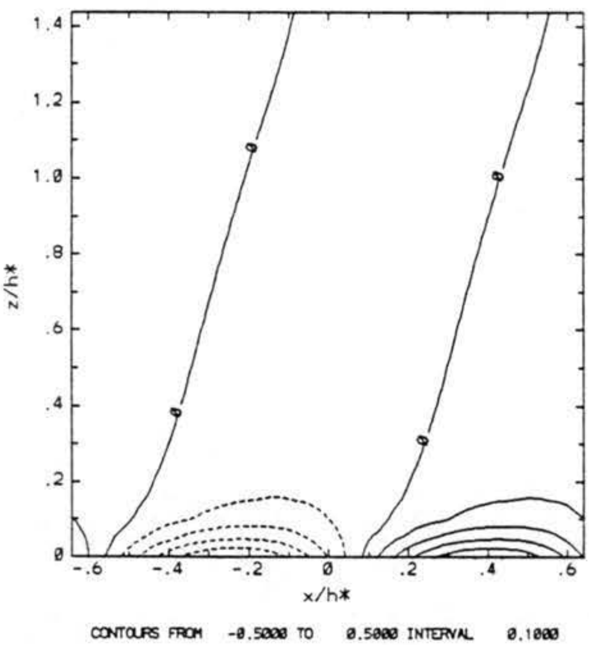

(c)

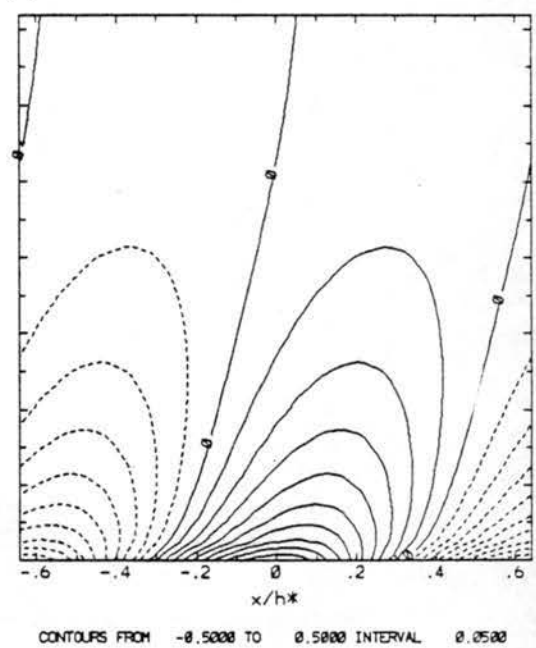

Figure B.4. Dimensionless fields from the advection/diffusion model with $\lambda_p = 1500\,\mathrm{m}$, $u_0 = 1\,\mathrm{m\,s^{-1}}$, $K_{11} = 0.07 w_* h_*$, $K_{33} = K_b$.

(a) Temperature c (contour interval 0.2)

(b) Horizontal flux f_1 (contour interval 0.1)

(c) Vertical flux f_3 (contour interval 0.05)

could be a consequence of the calibrating the model against simulation Set F, which has the u variance near the surface larger than a horizontally homogeneous simulation.)

Figure B.5 has $\lambda_p = 4500\,\mathrm{m}$ and $u_0 = 0\,\mathrm{m\,s^{-1}}$; the temperature field in Figure B.5a can be compared with the temperature field from Set H in Figure 4.26c and the horizontal and vertical fluxes in Figures B.5b and B.5c can be compared with the fluxes in Figure 5.7a and 5.7b. The advection/diffusion model predicts large temperature perturbations ($\sim \pm 1.5\theta_*$) throughout the depth of the boundary layer, but clearly it does not agree at all well with the large-eddy simulation. This is not at all surprising because the assumptions of the advection/diffusion model (weak circulation, small perturbations in the upper boundary layer) are seriously violated in Set H.

Figure B.6 has $\lambda_p = 4500\,\mathrm{m}$ and $u_0 = 1\,\mathrm{m\,s^{-1}}$; the temperature field in Figure B.6a can be compared with the temperature field from Set I in Figure 5.34c and the vertical flux in Figure B.6c can be compared with the vertical flux in Figure 5.10. The horizontal flux f_1 from Set I has not been shown, but it is approximately equal to the resolved u/θ covariance of Figure 4.36f. Note the large effect that the (apparently small) advecting velocity has on the passive scalar fields of Figure B.6 compared to Figure B.5—this observation may help explain the large difference in the magnitude of the circulations between Sets H and I. As with Set G the advection/diffusion model underpredicts the temperature perturbations somewhat and also underpredicts the downwind shift in the maximum and minimum. It fails more dramatically with the vertical heat flux, however, predicting that the maximum flux at $z = 0.4h_*$ should be at $\hat{x} = 0.3h_* = 0.08\lambda_p$, whereas in the simulation it is at $\hat{x} = 0.9h_* = 0.24\lambda_p$.

Figure B.7 has $\lambda_p = 4500\,\mathrm{m}$ and $u_0 = 2\,\mathrm{m\,s^{-1}}$, and is therefore comparable with Set J (Figures 4.40c, 4.42f and 5.10). The advection/diffusion model *overpredicts* the magnitude of the temperature perturbations slightly, but has the position of the maximum at $z = 0.4h_*$ correct ($\hat{x} = 1.0h_* = 0.25\lambda_p$). It now predicts that the vertical heat flux maximum at $z = 0.4h_*$ is at $\hat{x} = 0.5h_* = 0.13\lambda_p$, whereas the simulation has it further upwind at $\hat{x} = 0.3h_* = 0.07\lambda_p$. The horizontal heat flux perturbations are of roughly the right amplitude, although the simulation has a non-zero horizontal average flux, which

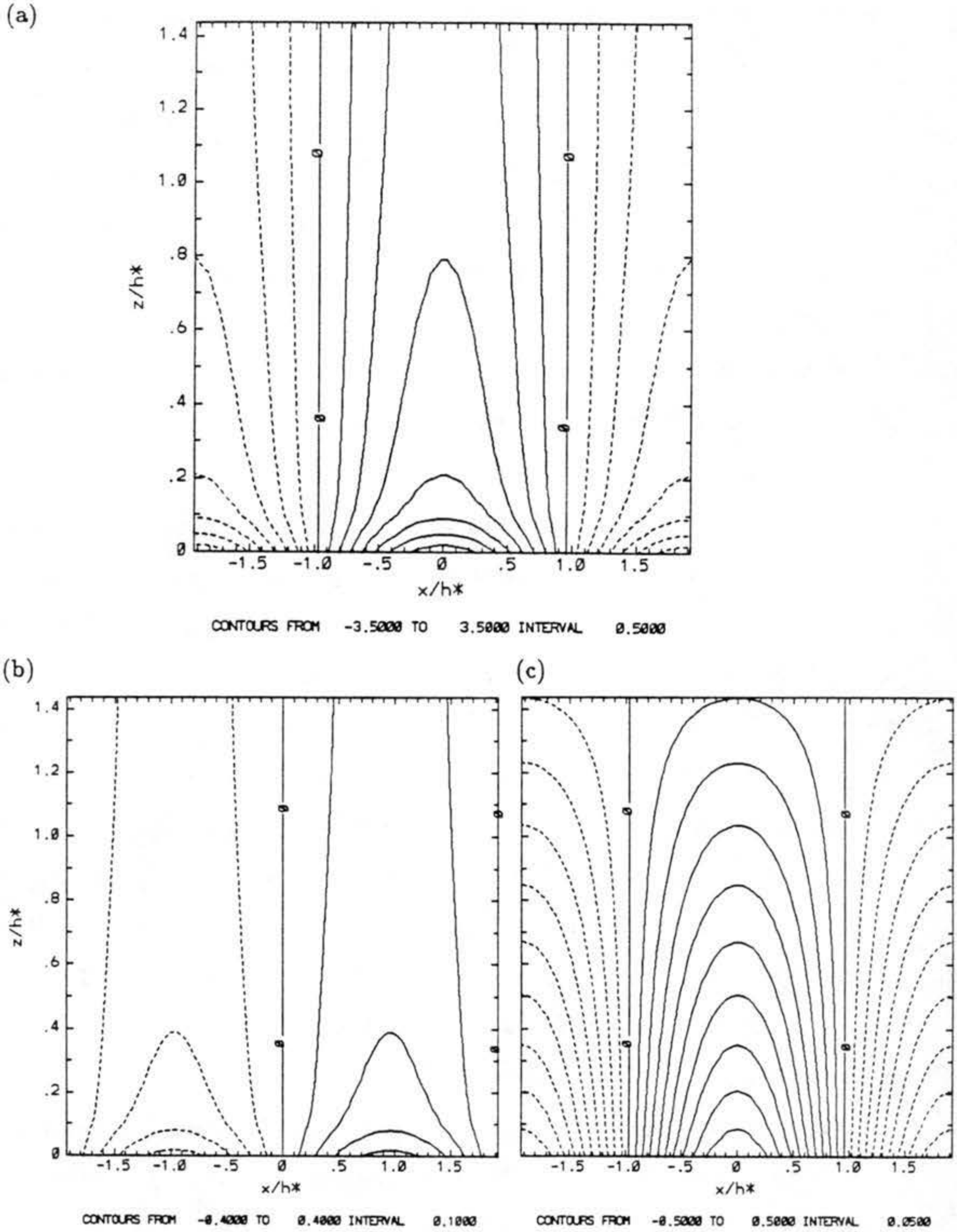

Figure B.5. Dimensionless fields from the advection/diffusion model with $\lambda_p = 4500\,\mathrm{m}$, $u_0 = 0\,\mathrm{m\,s^{-1}}$, $K_{11} = 0.07 w_* h_*$, $K_{33} = K_b$.

(a) Temperature c (contour interval 0.5)

(b) Horizontal flux f_1 (contour interval 0.1)

(c) Vertical flux f_3 (contour interval 0.05)

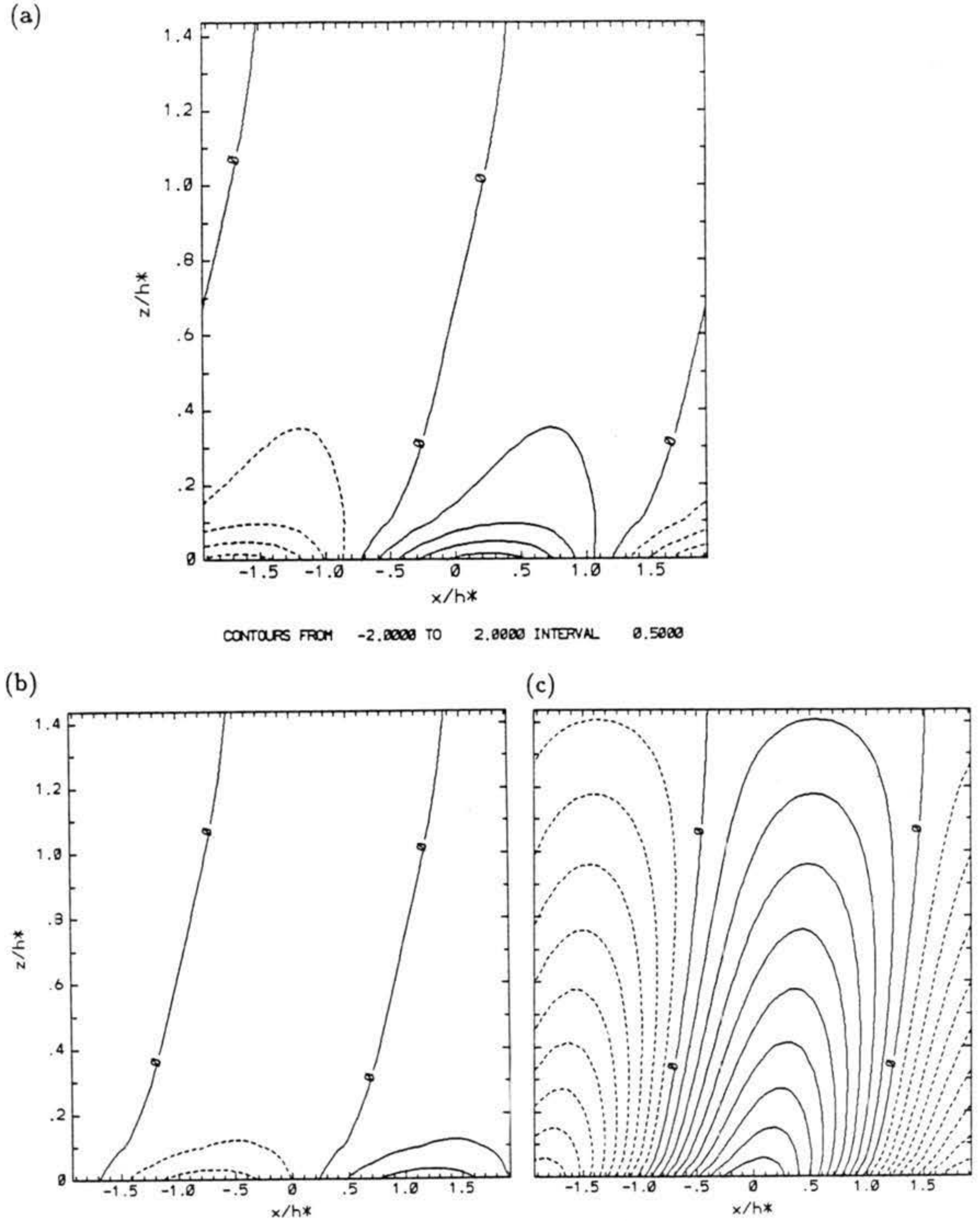

Figure B.6. Dimensionless fields from the advection/diffusion model with $\lambda_p = 4500\,\mathrm{m}$, $u_0 = 1\,\mathrm{m\,s^{-1}}$, $K_{11} = 0.07 w_* h_*$, $K_{33} = K_b$.

(a) Temperature c (contour interval 0.5)

(b) Horizontal flux f_1 (contour interval 0.1)

(c) Vertical flux f_3 (contour interval 0.05)

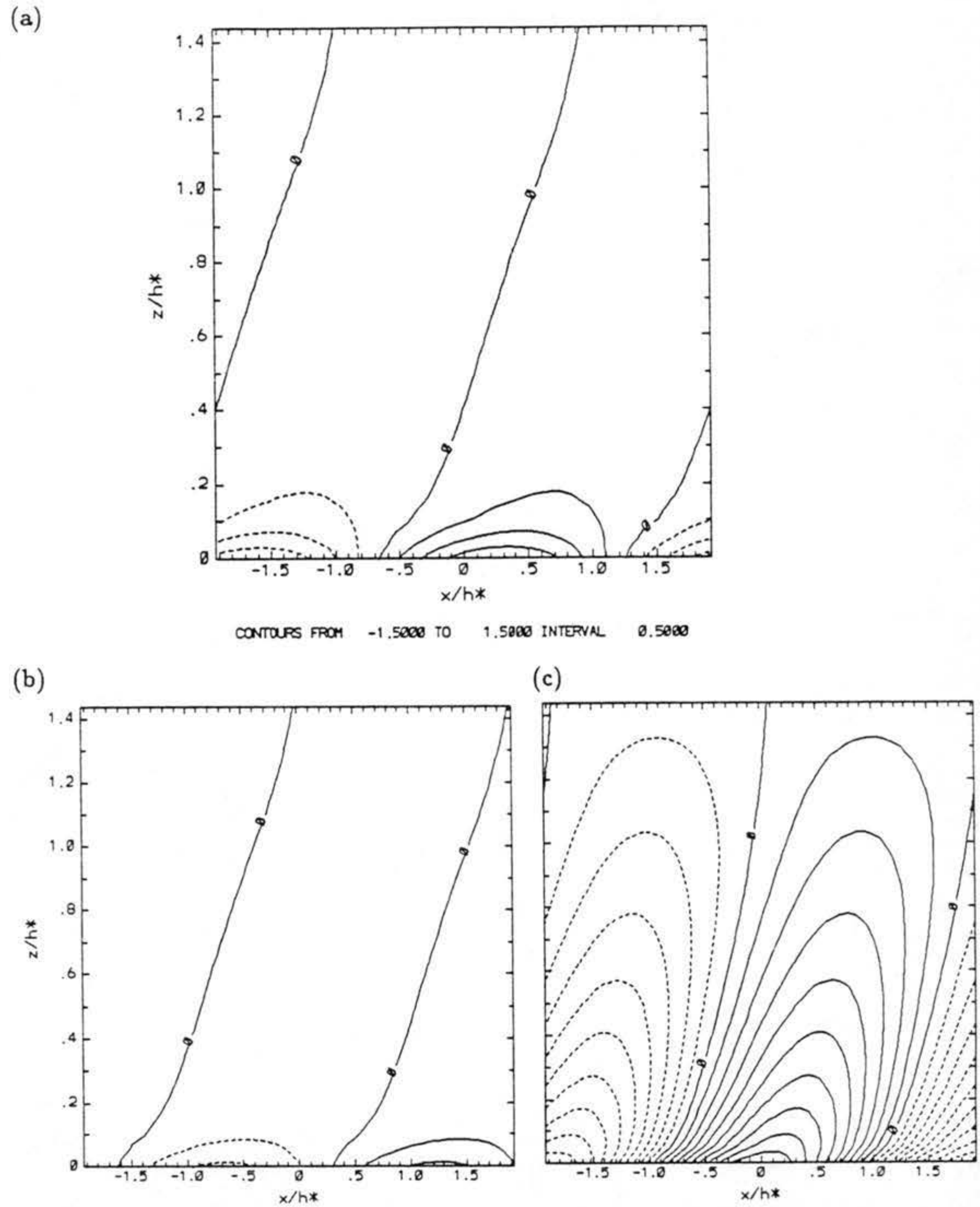

Figure B.7. Dimensionless fields from the advection/diffusion model with $\lambda_p = 4500\,\mathrm{m}$, $u_0 = 2\,\mathrm{m\,s^{-1}}$, $K_{11} = 0.07 w_* h_*$, $K_{33} = K_b$.

(a) Temperature c (contour interval 0.5)

(b) Horizontal flux f_1 (contour interval 0.1)

(c) Vertical flux f_3 (contour interval 0.05)

the advection/diffusion model cannot predict. Overall, agreement is better than with Set I, which is consistent with the hypothesis that the circulation in Set I moves the maxima in the turbulence fields (specifically the vertical heat flux) downwind.

The advection/diffusion model does not achieve good quantitative agreement with the simulations although it really only fails dramatically when the surface heat-flux perturbation drives a strong circulation (simulations Set H and, to a lesser extent, Set I). It does predict the temperature perturbations in the lower boundary layer to within a factor of two or so, and it does predict the major features of the fields (in particular the downwind tilting and shifting) reasonably well. This degree of success suggests that, in the absence of a strong circulation, the temperature and flux fields can be understood to a first approximation in terms of turbulence that is more or less homogeneous horizontally interacting with a *passive* scalar. Further investigation of the process of scalar diffusion would be worthwhile. As pointed out in Chapter 7, a large-eddy simulation of the horizontally homogeneous boundary layer could be used to calculate the mean concentration field from a surface, point-source release, whereupon an area source of arbitrary geometry could be constructed by superposition.

GLOSSARY

$\tilde{a}$	a general variable
a	$\langle\tilde{a}\rangle_g$, the resolved part of $\tilde{a}$
a'	deviation of a from horizontal average, $a' \equiv (a)_h$
C_e	constant in the expression for the dissipation rate of subgrid kinetic energy
C_g	constant in the expression for the grid scale l_g
C_K	constant in the expression for subgrid diffusivity
c_s	speed of sound in the model's acoustic scheme
C^*	dimensionless, horizontally integrated concentration
$C^*_{\max}$	maximum, dimensionless, horizontally integrated concentration at ground level
E_{ci}	i'th component of the circulation kinetic energy, $E_c = \langle\langle u_i\rangle_c^2\rangle_h/2$
e	subgrid kinetic energy
g	acceleration due to gravity
h	convective boundary layer depth based on phase-average statistics
H_ρ	scale height for base state density variation
H_θ	scale height for base state potential temperature variation
h_*	convective boundary layer depth based on horizontal-average statistics
$h_{\rho *}$	density-weighted h_*
K_h	subgrid diffusivity for potential temperature
K_m	subgrid diffusivity for momentum
l	subgrid length scale
l_g	length scale based on grid spacing
l_s	length scale based on stability
L	surface-layer Monin-Obukhov length
p_i	particle position
p_*	convective boundary layer pressure scale
q_i	particle velocity
$\bar{q}_i$	resolved particle velocity
q''_i	subgrid particle velocity

t	time after model initialization
t_s	particle release time
x_i	spatial coordinates, $x_1 \equiv x$, $x_2 \equiv y$, $x_3 \equiv z$
x_p	phase of the surface heat-flux perturbation
$\hat{x}$	position in x direction relative to the nearest surface heat-flux maximum, modulo λ_p
u_i	velocity components, $u_1 \equiv u$, $u_2 \equiv v$, $u_3 \equiv w$
u_{i0}	base state velocity
w_e	entrainment velocity, $(\partial h_* / \partial t) - w_s$
w_s	subsidence velocity, $\langle w \rangle_h$ at $z = h_*$
w_*	convective boundary layer velocity scale
X_1, X_2	lateral boundaries of the model
Y_1, Y_2	lateral boundaries of the model
z_0	surface roughness length
Z	upper boundary of the model
α_R	Rayleigh friction relaxation constant
Δt_l	"long" model time step
Δt_p	time step for particle dispersion
Δt_s	"short" model time step
Δx_i	model grid interval
λ_p	wavelength of the surface heat-flux perturbation
ϕ_i	subgrid heat (potential temperature) flux
Φ	surface heat flux $\phi_3(z=0)$
Φ_p	amplitude of surface heat flux variation
π	Exner pressure, $C_p T / \theta$
π_a	pressure induced by advection
π_b	pressure induced by buoyancy
π_m	pressure induced by turbulence/mean-flow interaction
π_s	pressure induced by the subgrid force
π_t	pressure induced by turbulence/turbulence interaction
π_0	base state Exner pressure
π_*	convective boundary layer Exner pressure scale
ρ	density
ρ_0	base state density
ρ_{0s}	surface value of ρ_0
θ	potential temperature

θ_0	base state potential temperature
θ_{0s}	surface value of θ_0
θ_*	convective boundary layer potential temperature scale
τ_{ij}	subgrid stress
$\langle\rangle_r$	a general averaging operator
$()_r$	deviation from $\langle\rangle_r$
$\langle\rangle_g$	grid average
$\langle\rangle_h$	horizontal average
$\langle\rangle_p$	phase average
$\langle\rangle_t$	time average